NOVEL SEARCHES FOR PHYSICS BEYOND THE STANDARD MODEL

A DISSERTATION
SUBMITTED TO THE DEPARTMENT OF PHYSICS
AND THE COMMITTEE ON GRADUATE STUDIES
OF STANFORD UNIVERSITY
IN PARTIAL FULFILLMENT OF THE REQUIREMENTS
FOR THE DEGREE OF
DOCTOR OF PHILOSOPHY

Kevin Zhou
August 2024

I certify that I have read this dissertation and that, in my opinion, it is fully adequate in scope and quality as a dissertation for the degree of Doctor of Philosophy.

Natalia Toro, Primary Adviser

I certify that I have read this dissertation and that, in my opinion, it is fully adequate in scope and quality as a dissertation for the degree of Doctor of Philosophy.

Peter Graham

I certify that I have read this dissertation and that, in my opinion, it is fully adequate in scope and quality as a dissertation for the degree of Doctor of Philosophy.

Jason Hogan

I certify that I have read this dissertation and that, in my opinion, it is fully adequate in scope and quality as a dissertation for the degree of Doctor of Philosophy.

Philip Schuster

Approved for the Stanford University Committee on Graduate Studies.

Stacey F. Bent, Vice Provost for Graduate Education

This signature page was generated electronically upon submission of this dissertation in electronic format.

Abstract

Progress in fundamental physics requires new experimental data. The point of view of this thesis is that there are a finite, manageable number of signals that new physics could produce in the laboratory, and that each of them can be precisely searched for by dedicated experiments using modern technology. For example, axions only have three qualitatively different leading couplings, to photons, gluons, and fermions. I will discuss a new way to probe axion dark matter through each of these couplings, using excited superconducting cavities for the axion-photon coupling, nuclear spin-polarized haloscopes for the axion-gluon coupling, and magnetized multilayers for the axion-fermion coupling. Dark matter could also exist in the form of macroscopic clumps, or light particles. In the former case, I show that collisions of these clumps with stars produce distinctive transients, which can be effectively searched for with ultraviolet telescopes. In the latter case, I show that production of dark matter particles through the decays of light vector mesons can be detected in "missing energy" experiments. In all of the cases discussed, it is possible to improve sensitivity to these effects by orders of magnitude, using only existing technology. Finally, I will discuss the intriguing possibility that the known massless particles in nature actually have "continuous" spin. Though most effects of new physics emerge in the ultraviolet, I will show that this particular question can only be settled by looking in the far infrared, motivating an entirely new class of experiments.

Acknowledgments

First and foremost, I must thank my advisor, Natalia Toro. Throughout my PhD, Natalia has been an amazing mentor, teacher, and collaborator. She guided me through the entire process, from learning the fundamentals and giving my first conference talks and seminars, to applying for postdocs and becoming an independent researcher. As a physicist, Natalia has an incredible intuition for the mathematical structure underlying physical theories. She also has an apparent photographic memory, and on one occasion figured out an exact solution just by seeing that one of its series coefficients was 11/46080. Of course, I'll never be able to do that. But I will always strive to emulate her breadth of knowledge and clarity of thought.

I must also thank Philip Schuster. Throughout my PhD, Philip has been an endless source of new ideas and new directions. He taught me to cut to the conceptual heart of any technical problem. As a team, Philip and Natalia are a model of scientific collaboration. They showed me how to boldly pursue research programs, from theoretical idea to experimental realization, regardless of disciplinary boundaries or temporary obstacles. They also taught me a lot about the bigger picture of doing science, including the mechanics of building collaborations and consensus, and the history of its greatest discoveries. These skills are rare, and essential in our field's uncertain times.

I would also like to thank my other collaborators: Asher Berlin, Raffaele Tito D'Agnolo, Anirban Das, Sebastian Ellis, Alex Millar, and Tanner Trickle. Together, we figured out a lot of interesting things, in subfields ranging from astrophysics to solid state physics. In particular, Asher's boundless energy for learning new fields of physics has inspired me to always keep learning myself. And though I didn't end up collaborating with any other PhD students during my time here, Payel, Aidan, Gowri, Shayarneel, and Anthony kept the office lively at SLAC, while Zach, Samuel, Yawen, and Cynthia generated fun conversations on campus.

It's not possible to spend every waking moment of a PhD thinking about research. In between projects, I recharged by teaching physics, in particular through the USA Physics Olympiad. I thank the American Association of Physics Teachers for running it, as well as our director Tengiz Bibilashvili, the entire coaching staff, and the wonderful students who participated. In retrospect, I believe the process of distilling ideas in modern physics into tricky questions, and using those questions as a springboard to learn more physics, was a positive feedback loop that enhanced my research.

Besides physicists, I thank SCOAP^3, AnnaArchivist, and Alexandra Elbakyan for making work possible, and Hagoromo, Idåsen, Rotring, and Leuchtturm for making it more enjoyable. I thank Jellycat, Fluffy, Helix, and Prof. Planty for making life softer. I thank the people at Varian for not noticing as I used dozens of pounds of their free printer paper. I especially thank Glenna Paige for keeping our building running, and fueling us with a steady stream of ice cream sandwiches.

I thank my family for their constant support, especially during the pandemic. They set me on this path, long ago, by giving me a copy of the Feynman lectures. My parents have always encouraged me to explore the directions that interest me the most, and I'm grateful for their patience as my time as a student entered its third decade.

Finally, I thank the algorithm for allowing me to meet my partner, Yiwen. Yiwen is the perfect blend of smart, silly, and sweet. Together we've scaled mountains, explored caves, solved puzzles, and made a home full of light and memories. I could have finished this degree alone, but now I can't imagine living without her. Submitting this dissertation marks the end of our wonderful time here, and the start of a new life together.

Contents

List of Tables

List of Figures

Chapter 1

Introduction

1.1 Progress and Stagnation

What is the root cause of progress in fundamental physics? We imagine a balding professor sunk deep in an armchair. Hours pass with no discernable motion until – suddenly – the moment of inspiration arrives. At an instant, a totally new conception of reality is born, fully formed, owing nothing to anything but the physicist's own creativity. He knows, from its mathematical perfection, that his idea must be right. All that's left to do is to collect the Nobel prizes.

Such a corny picture would be offered by the vast majority of laypeople, and even the majority of physics students. The wiser students might offer a more refined story: creativity comes from collaboration. In this more modern picture, we imagine several physicists from around the world, with hair, huddling together while sipping espresso in a beautiful sunlit room. Chalk dust flies until the true description of Nature appears on the board. The new friends triumphantly elbow bump and submit a paper to arXiv with an alphabetically ordered author list.

In my opinion, both of these pictures miss the true root cause of progress, which has more to do with the electricians installing power lines and solar panels outside the physics building. The problem is that it is very, very difficult to guess laws of nature, because of the combinatorial explosion of the number of possibilities, and the mental effort required to investigate each one. When we look at the history of physics we find (with perhaps the sole exception of general relativity) that every correct guess came only when it was forced by experiment. Experimental null results rule out entire classes of theories, anomalies sharply focus attention on a place existing theories broke down, and when the way forward is unclear, a large collection of new data presents patterns to explain. After a huge number of incorrect guesses, now forgotten, the correct theoretical guess is finally made once it becomes one of the two or three simplest remaining options. (And of course, it isn't even identified as the correct one until later experimental data arrives.) This is the story of the Standard Model, which was assembled by dozens of theorists, one particle at a time.

So we have experimentalists to thank, but experimentalists in turn rely on the level of technology and industrial production in their society [89], and external financial support. This is illustrated by countless examples from the history of physics. The Carnot cycle came from the mind of Carnot in 1824, but it was a consequence of exposure to a variety of steam engines, funded by the French government to compete with the British. Maxwell's derivation of the speed of electromagnetic waves was brilliant, but it was inspired by Faraday's physical picture of retardation in telegraph cables, which had been laid at great expense to connect the British empire. Special relativity was motivated by experiments by Fizeau, Michelson and Morley, Lodge, and Trouton and Noble; Michelson and Morley's experiment, which cost a significant fraction of their department's entire budget, required tons of stone and mercury, fitted with the finest optical equipment. More generally, many advances in physics are rooted in improvements in optics. Quantum mechanics owes a debt to atomic spectroscopy, and for centuries, our changing view of our place in the universe has come from telescopes with ever larger mirrors. Certainly, experiments can stimulate advances in technology, but more commonly technology is developed for economic or military ends, and applied to experiment.

One might object that this viewpoint is too broad to be useful, but I believe it gives the best explanation of the incredible pace of progress in particle physics in the mid-20^{th} century, and its present situation. Discoveries in that era were made with better particle colliders, and colliders are big infrastructure, requiring enormous amounts of concrete, steel, magnets, coolant, and electrical power. In the United States, the maximum attainable particle energy rose exponentially in the postwar period, from the Bevatron in the 1950s to the Tevatron in the 1980s, ending with the cancellation of the Superconducting Super Collider (SSC) in 1993 [90]. At the same time, the United States became the preeminent industrial power in the world, its government invested heavily in R&D, and particle physics received a larger share of that funding partly due to its proximity to the prestigious Manhatten Project. But after the cancellation of the SSC, particle colliders ceased to grow larger, and improvements in particle energy dramatically slowed. The European particle physics community, scrambling to make up for the loss of the SSC, designed the Large Hadron Collider to fit in a tunnel originally dug for another collider in the 1980s. That tunnel is now 40 years old, and remains the longest used for particle physics in the world.

Why hasn't another tunnel been dug? On paper, there seems to be no obstacle. The costs for larger colliders are higher, but the American GDP (adjusted for inflation) has tripled since 1980. By now, we should be able to afford the Superconducting Super Collider! But the more important limiting factor is that measures of industrial production, such as American energy consumption and steel production, have stayed flat or declined since 1980. It is unrealistic to expect particle physics to claim an ever increasing share of a society's material budget. As a result, our field predominantly reuses old infrastructure, and when their use is exhausted, further scientific advances seem unlikely. No amount of new thinking can replace getting new data, and new data can only be gathered when we gain the ability to make measurements we couldn't before.

This "materialist" explanation of progress and stagnation in particle physics works far better than the common narratives one finds in popular science. For example, one often hears a "vitalist" argument that progress in particle physics ceased because of a depletion of bold ideas sprung from creative genius. But in the golden age of particle physics, correct new ideas were incremental. They relied on the same principles of relativistic quantum field theory, introduced only one or two new particles or interactions at a time, and often were discovered by many workers simultaneously, as was the case for the Englert–Brout–Higgs–Guralnik–Hagen–Kibble (now just "Higgs") mechanism. If anything, theoretical ideas have been steadily growing bolder since the golden age, introducing more parameters at once, discarding more cherished principles, or requiring higher energies to test.

There is also the "metaphysical" argument that the entire endeavor of fundamental physics is intrinsically doomed, for some reason beyond human comprehension. For example, some claim that anthropic arguments can explain the mass of the Higgs boson, removing any pressing need for new particles. That might be true at the TeV scale, but anthropic arguments can't explain most of the Standard Model's open questions, such as the nature of dark matter, the origin of baryons, the strong CP problem, or the detailed structure of fermion masses. Furthermore, even in the absence of such problems, it would still be surprising for new particles to be roughly evenly distributed in mass on a logarithmic scale, only to abruptly and permanently stop at the TeV scale; that in itself would require a compelling explanation.

One such explanation is the "great desert" hypothesis. In order to speculate about grand unification, a phenomenon which might occur at energies a trillion times above experimental reach, one must know the properties of all particles coupled to Standard Model gauge fields up to that scale. A priori, this is as difficult as trying to guess the entirety of the Standard Model (up to $m_H \sim 10^2\,\mathrm{GeV}$) in the 1800s, when the highest energy particles we were aware of were visible light. The traditional assumption is that many supersymmetric particles sit at the TeV scale, followed by a desert containing no particles all the way up to the unification scale. This is a reasonable first guess, for which there is no strong evidence. But it is thought that since we've passed the TeV scale and found nothing, we are presumably now in the desert and can't find anything else. This feeling isn't just unjustified, it's logically self-contradictory: the failure of models of weak-scale supersymmetry decreases our confidence in traditional grand unification and the great desert, *increasing* the chance that new particles exist above the TeV scale.

Still, the materialist narrative seems even more pessimistic than the others. Under the metaphysical narrative, we have done excellently, and found all there is to find. According to the vitalists, we simply need to adjust how we think, or tweak the academic funding system. But if progress requires ever larger quantities of steel and electricity, there seems to be nothing a particle physicist can do.

A common comforting response is simply to declare that this isn't a theorist's problem, and retreat to the study of toy models, or thought experiments centuries beyond experimental test. (Indeed, I have been told that if a theorist does *not* work on untestable physics, then that theorist is "merely"

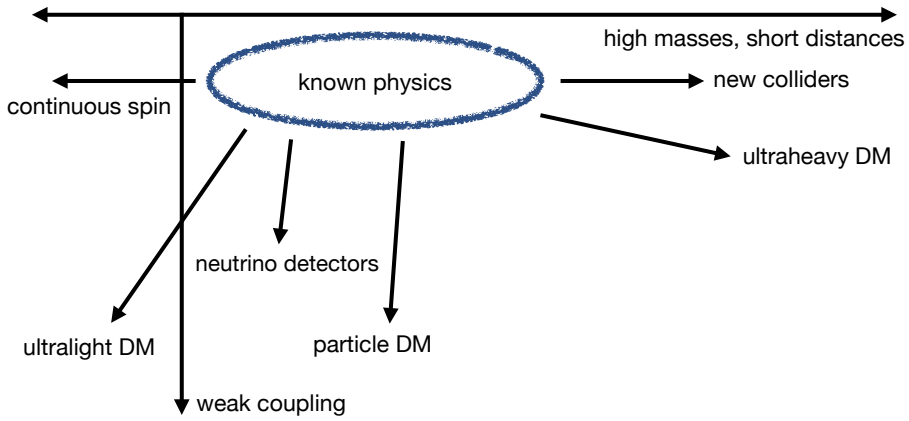

Figure 1.1: A schematic of known physics, and several directions to search for new physics.

an experimentalist – as if this were an insult!) But in my view, physics is interesting precisely because it can relate abstract mathematics to the real world. Quantum fields certainly exhibit some tricky mathematical subtleties, but they're fascinating because nature apparently "breathes life" into some of them. Without its connection to reality, physics would just become an undistinguished branch of pure mathematics.

Fortunately, there is a way forward. Though our capacity to build larger colliders has stagnated, other aspects of technology have advanced rapidly since the 1980s. We can now prepare and control particles to much greater precision than before. Detectors are more sensitive, with some using quantum mechanical effects to go beyond the standard quantum limit. Telescopes are larger, and can measure a broader range of radiation than ever before – including, for the first time, gravitational radiation. The key question is to find a way to put this technology to work, in the search for new fundamental physics.

1.2 The Landscape of New Physics

But where might this new fundamental physics be hiding? A rough schematic of the situation is shown in Fig. 1.1. Known particles, encapsulated in the Standard Model, feature a reasonably strong coupling to other known particles, as well as a mass within reach of the Large Hadron Collider. Smaller masses correspond to longer distances, and long-distance physics is tested through precision terrestrial and astrophysical experiments.

If funded, new large-scale colliders would extend the energy frontier upward in mass. However, the largest American particle physics experiment currently being built is the Deep Underground Neutrino Detector (DUNE), which seeks to measure the properties of neutrinos more precisely. If one doesn't count telescopes, the next-largest effort is the search for Weakly Interacting Massive

Particles (WIMPs), which are particles with masses comparable to nuclei, that could comprise the dark matter that seems to account for most of the universe's matter content.

These are well-motivated efforts which explore important places where new physics could be hiding, but far from exhaustive. For example, one of the main motivations to search for WIMPs was the fact that they emerged naturally in theories of weak-scale supersymmetry, which have since failed experimental test. Without this anchor, the possibilities are much broader. For example, dark matter could exist in the form of macroscopic clumps. If they are comparable in mass to asteroids, then they would be too rare to detect via impacts on Earth, and too light to detect at a distance through gravitational lensing. Alternatively, dark matter could consist of discrete particles lighter than a WIMP, which would deposit too little energy in each impact to be detectable in existing experiments. Furthermore, in the "ultralight" limit, each field mode is occupied by many dark matter particles, so that they collectively act on detectors like a classical field. The resulting experimental signatures look nothing like discrete impacts. Instead, they are extremely weak, but persistent signals, which penetrate conventional shielding.

Particle physics also has an underappreciated frontier, associated with low energies and long distances. It is usually assumed that if one understands a perturbative theory at some energy scale, then one automatically understands it at all lower energy scales; it is only at higher energies that unknown interactions and particles can enter. This is true for many familiar examples, but it breaks down dramatically for theories containing massless particles with "continuous spin". Counterintuitively, such particles can behave like the known photon or graviton at high energies, but also carry additional degrees of freedom, which are only revealed by interactions at very low energies. This immediately raises the question of whether the photon and graviton actually have continuous spin. Answering this question requires probing them in the exact opposite regime that particle physics experiments traditionally focus on.

A common theme of the above discussion is the diversity of possible signals of new physics, and their often unexpected nature. Discovering these kinds of signals requires a plan. Sometimes new effects are discovered through serendipitous accident – the cosmic microwave background, superfluidity, and superconductivity come to mind – but this generally only happens when a new technology makes it possible to rapidly explore a previously unknown frontier. By contrast, the Standard Model is *very* well-tested, and experiments that probe well beyond it generally need to be designed intentionally.

As a historical example, the sensitivity of the Michelson–Morley experiment was not surpassed for 40 years, when a series of new experiments were performed to test special relativity. It is therefore completely plausible that, if not for Michelson and Morley, the first ether wind null result would only have come decades later. By performing a careful search for a well-motivated signal, using the maximum available sensitivity from the technology of their time, these experimentalists accelerated the development of modern physics. We may hope that the same strategy employed today can accelerate the discovery of physics beyond the Standard Model.

1.3 Searching for Signals

One key challenge of such an approach is to know where and how to look. How can we know what we don't know? For instance, should we entertain the possibility that a distant star isn't there when nobody is looking at it? If not, what separates that hypothesis from more reasonable ones?

I once received a kindly worded, nicely illustrated letter from a gentleman who wanted to explain why the universe seems to have more matter than antimatter. He reasoned that by symmetry, the amounts of matter and antimatter were actually equal. However, stars made of antimatter would emit anti-photons which, compared to ordinary photons, would "anti-refract" upon entering a lens. Since telescopes are designed to focus the light from ordinary stars, they would *defocus* light from antimatter stars, rendering them invisible. To test this theory, one simply has to build a single telescope with an inverted lens.

To the layperson, this proposal probably seems reasonable, and possibly more reasonable than most searches for dark matter. But the particle physicist can see many reasons that it's completely impossible given what we already know about the universe, which sharply limits the kinds of experimental signatures that can appear.

First, we know that special relativity works. Generations of successors to the Michelson–Morley experiment have found no deviations, time dilation is routinely measured, and observations of gamma rays show that light of different frequencies travels at the same limiting speed, to extreme precision. It is possible that there are very small deviations to special relativity, which can be parametrized with Lorentz-violating terms in the Lagrangian, but the physical effects of these terms are often equivalent to those of additional external fields, such as ultralight dark matter fields.

Second, we know that quantum mechanics works: time evolution is linear and measurements obey the Born rule, which together logically imply that time evolution is unitary. The linearity of quantum mechanics is tested through interference experiments with increasingly large objects, and "loophole-free" Bell tests show that measurements on entangled states yield the expected results, regardless of how the entangled state is produced. Quantum mechanics admits a huge variety of interpretations, but interpretations by definition imply the same experimental results. *Modifications* of quantum mechanics, which do change experimental results, usually do so by introducing an additional source of wavefunction collapse. Such effects would appear in relevant experiments as an irreducible source of decoherence. Again, the same signature can be produced by other effects, such as collisions with dark matter particles.

As a result, for determining potential experimental signatures, we might as well assume that special relativity and quantum mechanics hold exactly. However, these two assumptions together imply a great deal about nature [91]. First, they sharply restrict the kinds of fundamental particles that can exist in nature, and the way these particles can interact. They imply that massive particles are classified by a mass m and a integer or half-integer spin s, while massless particles with zero spin scale are classified by an integer or half-integer helicity h. They further imply that interactions

between these particles can be written in the Lagrangian in terms of local products of relativistic fields, which create and annihilate the particles.

Massless bosonic particles are particularly interesting, as in the regime of high mode occupancy, they collectively behave like classical fields. These fields mediate the familiar macroscopic forces, with the electromagnetic field corresponding to $h = 1$, and the gravitational field corresponding to $h = 2$. For $h \geq 1$, the mismatch between the number of degrees of freedom of a particle and the simplest tensor field that can create it implies that the Lagrangian must have gauge symmetry. This in turn requires the fields to couple to appropriate tensorial conserved quantities, so that the electromagnetic field couples to ordinary charge and the gravitational field couples to stress-energy. (These considerations also doom our polite gentleman's idea: since only two polarizations of light are observed, the photon must be its own antiparticle, and particles and antiparticles must couple to it in the same way, up to an unimportant sign.) The absence of other observed macroscopic fields is neatly explained by the fact that for $h = 0$ there is no gauge symmetry, and thereby no reason the particle's mass is protected from quantum corrections, while for $h > 2$ a "minimal" coupling is impossible, as there are no appropriate conserved tensors to couple to.

Another important piece of information comes from thinking about how physics at a high energy scale Λ impacts physics at lower energy scales E. Terms in the Lagrangian have mass dimension 4. Given a set of fields, one can typically write a small number of interaction terms with dimension less than 4, some more with precisely dimension 4, and an arbitrarily larger number at progressively higher dimensions. However, by dimensional analysis, the coefficient of a term with mass dimension $n > 4$ must have dimensions $1/M^{n-4}$, where M is a mass scale. It can be shown quite generally that if the unknown high energy physics is perturbative with order-one couplings, can induce such a term, and has no other special structure, then we have $M \sim \Lambda$. By dimensional analysis, the physical effect of this term at the lower energy E is weighted by powers of E, so that the relative effect depends on $(E/\Lambda)^{n-4}$, and therefore smaller the higher n becomes. This heuristic works very well throughout physics as a whole, so much so that practitioners outside of particle physics often use it without explicitly realizing it, and it has led to successful predictions in particle physics as well [92].

This paradigm of parametrizing the unknown effects of high energy physics in terms of a series of increasingly suppressed terms involving low energy fields is known as effective field theory. For our purposes, effective field theory is useful because it strongly constrains how new physics can appear. For example, suppose that a new spin 1/2 field ψ couples to the electromagnetic field. The simplest, "minimal" coupling is the dimension 4 term $A_\mu \bar{\psi}\gamma^\mu\psi$, which gives the particle an electric charge. The next-simplest possibilities are the dimension 5 terms $i\bar{\psi}[\gamma^\mu, \gamma^\nu]\psi F_{\mu\nu}$ and $\bar{\psi}[\gamma^\mu, \gamma^\nu]\gamma^5\psi F_{\mu\nu}$, which give the particle a magnetic or electric dipole moment, respectively. At dimension 6, we can write down terms like $\bar{\psi}\gamma^\mu\psi\partial^\nu F_{\mu\nu}$ and $\bar{\psi}\gamma^\mu\gamma^5\psi\partial^\nu F_{\mu\nu}$, which correspond to charge radii and anapole moments. Each term yields different experimental signatures, but they can be enumerated and sorted by importance. Furthermore, because the high energy physics induces all terms allowed by symmetries,

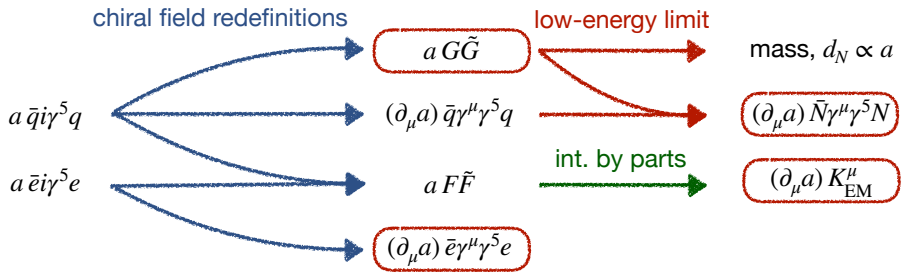

Figure 1.2: A schematic of how the low-energy axion couplings arise from the ultraviolet. The final boxed expressions are the axion-gluon coupling, the axion-photon coupling, and the axion-fermion couplings, to electrons and nucleons.

the search space is finite. It only makes sense to search for a higher dimensional term if there exists a plausible reason that effects from all lower dimensional terms would be suppressed.

Even though the choices of terms in the Lagrangian are quite restricted, the number of potential models of new physics suffers from a combinatorial explosion, whenever one introduces multiple families of particles with independent properties. Worse, within each model the number of possible terms in the Lagrangian can range from dozens to hundreds, due to the same combinatorial explosion, which can make it difficult to determine when a model is thoroughly tested. The solution to the problem is to insist on absolute minimality. For example, if one wants to explain dark matter, one could suppose it is due to a single new field with a single coupling of interest. If one must introduce a second field (such as a force mediator between Standard Model and dark matter particles), then the interactions of the mediator should be as simple as possible.

Certainly, it's true that the physics of dark matter can be extremely complex, just as the Standard Model is. But if it's complex, the chances of guessing it correctly are exponentially small. Fortunately, complex models often yield the same basic types of observable signals as minimal ones, so that searches targeting minimal models still automatically cover the complex ones.

Motivated by these considerations, let's consider one of the simplest possible models of dark matter: that it is a single light scalar field. As discussed earlier, scalar fields are not naturally light, and require a mechanism to protect their mass. This can happen when they are the Goldstone bosons of a spontaneously broken global symmetry. The simplest cases are when the symmetry is dilation symmetry, yield a parity-even scalar called the dilaton, and when it is a fermion's chiral symmetry, yielding a parity-odd scalar called an axion. Here we'll focus on the latter case.

The breaking of chiral symmetry at a high energy scale f_a gives the axion a coupling to fermions of the form $a\bar{\psi}i\gamma^5\psi$. As illustrated in Fig. 1.2, performing chiral field redefinitions converts these couplings to the form $(\partial_\mu a)\bar{\psi}\gamma^\mu\gamma^5\psi$ which explicitly contains a derivative on the axion field, reflecting its status as a Goldstone boson. In the presence of chiral anomalies, this redefinition can also produce couplings to gauge fields, $aF\tilde{F}$ and $aG\tilde{G}$ where F and G are the photon and gluon field strengths.

The first coupling can be rewritten in the form $(\partial_\mu a)K^\mu_{\rm EM}$ by integration by parts, where $K^\mu_{\rm EM}$ is the electromagnetic Chern–Simons current. The second coupling can't be simply rewritten in this way, because of QCD instanton field configurations, and accordingly it can give the axion a small mass, suppressed by powers of f_a.

One could have arrived at the same couplings (minus the axion-gluon coupling) by naively applying effective field theory. Here, one would simply enumerate terms consistent with the axion's odd parity and shift symmetry. One finds that no terms are possible at dimension 4 or lower. The leading terms at dimension 5 are precisely the axion-fermion and axion-photon couplings, and are accordingly suppressed by $1/f_a$. Dimension 6 couplings would be suppressed by $1/f_a^2$, and thus usually have negligible effects. Another consequence of the smallness of axion couplings is that laboratory searches for axion dark matter are typically never sensitive to processes which depend on pairs of couplings, as these would be suppressed by at least $1/f_a^2$, which implies that we can search for each single coupling independently.

Through either route, we conclude that axion dark matter has only a few leading experimental signatures. This theoretical background, largely already known in the 1980s, allows us to focus on developing experiments sensitive to each one.

1.4 Outline

The first half of this thesis is devoted to new experimental searches for axion dark matter.

In chapter 2, we propose a new search for the axion-photon coupling. In the presence of axion dark matter and a background electric or magnetic field, this coupling induces "effective" currents which yield other electric or magnetic fields, shifted in angular frequency from the background field by the axion mass m_a. Previously, most proposals to search for such effects considered a static background field, and used the axion to drive an electromagnetic resonator with resonant angular frequency m_a. We instead propose to excite a "loaded" mode of a microwave cavity, and detect axion-induced transitions to a "signal" mode whose angular frequency differs by m_a. This approach tends to generate a higher signal power, particularly at low m_a, and allows orders of magnitude in m_a to be scanned by slightly tuning the frequency difference for a single cavity. To effectively store energy in the loaded mode, one must use superconducting cavities, which have fortuitously been developed for decades for particle accelerators; the sensitivity is determined by how well one can cool the cavity and isolated the signal mode from the loaded mode. Experimental efforts in this direction are underway at both the SLAC National Accelerator Laboratory and the Fermi National Accelerator Laboratory.

In chapter 3, we adapt the analysis of chapter 2 to the case where the signal and loaded mode frequencies are set equal to each other, and one searches for energy off-resonance in the signal mode. This method has the advantage of broadband sensitivity, covering a large range of axion masses

without any need for scanning, at the cost of lower sensitivity at each individual axion mass. The work also contains a detailed exploration of the subtler noise sources relevant in such an experiment, such as drifts in the cavity mode frequencies and the frequency of the driving oscillator.

In chapter 4, we turn to the axion-gluon coupling. Famously, this coupling allows the axion field value to influence the electric dipole moment of the neutron. One of the strongest theoretical motivations for the axion is that when it minimizes its potential, the neutron's electric dipole moment is set to zero, explaining why this quantity is much smaller than the Standard Model expectation. However, if the axion carries the energy density of dark matter, then it oscillates about its potential minimum, producing a small neutron electric dipole moment which oscillates with angular frequency m_a. For appropriate atoms, we show that these such effects can propagate to a comparable oscillating atomic electric dipole moment, parallel to the nuclear spin. In a solid sample of such atoms, with nuclear spins aligned, these dipole moments correspond to an oscillating polarization and therefore a polarization current, which can excite a microwave cavity surrounding the sample. We find that if the axion mass is identified by other experiments, and lies in the well-motivated microwave regime $m_a \sim \mu$eV, then existing cavity and detector technology outfitted with a hyperpolarized sample of an appropriate rare earth element can detect the axion's coupling to gluons.

In chapter 5, we turn to the axion-fermion couplings, and in particular the coupling of the axion to electrons. The main physical effects of this coupling are a torque on electron spins, proportional to ∇a, and a force on electrons proportional to $\ddot{a}\,\mathbf{S}_e$. We review a variety of mechanical, electromagnetic, and solid state experiments sensitive to such effects throughout the entire axion mass range. We also explain why the axion does *not* induce an electron electric dipole moment proportional to a, contrary to several recent proposals. Finally, we outline a new proposal which centers around the use of layers of ferromagnetic material. The axion's torque on the electron spins causes the magnetization of such materials to precess, yielding a oscillating magnetization current on the surface of each layer. This current produces radiation, whose amplitude can be increased through constructive interference using multiple layers, and focused on a detector. Furthermore, the resonant frequency of each layer can be easily adjusted by tuning an external magnetic field. This proposal requires only mass produced magnetic materials and existing detector technology. It yields the strongest projected sensitivity for a axion search in the μeV to meV range.

In chapter 6, we consider a completely different possibility: that dark matter might come in the form of macroscopic clumps. Such clumps could arise in various ways in the early universe, and are worth considering because almost all experiments would be blind to them. There is no simple way to enumerate all possible interactions of clumps with Standard Model matter, so in the spirit of minimality, we suppose they are characterized by a mass M and a radius R, and scatter Standard Model matter elastically with geometric cross section. We identify a new experimental signature, relevant if the clumps have asteroid-like mass, within a few orders of magnitude of $M \sim 10^{15}\,\text{kg}$. In this case, "dark asteroids" colliding with stars dissipate their energy to shock waves in the star's

interior, which subsequently travel to the star's surface and produce a burst of ultraviolet light. Unlike other known transients, these events would occur to all types of main sequence stars, and produce unusually powerful transients which track the local dark matter distribution. We show that ultraviolet space telescopes such as Hubble can effectively search for such events, potentially improving sensitivity to macroscopic dark matter by orders of magnitude.

In chapter 7, we turn to the most well-studied possibility that dark matter is a particle of mass m_χ. "Direct" detection experiments search for the energy deposited in scattering events. However, for $m_\chi \lesssim$ GeV, WIMP searches lose sensitivity since the energy deposited becomes too low to detect. Moreover, some of the simplest theories of particle dark matter predict an extremely suppressed scattering rate, due to the fact that dark matter moves nonrelativistically with speed $v_{\rm DM}/c \sim 10^{-3}$. However, in these cases, dark matter can still be effectively *produced* in relativistic scattering events. The resulting dark matter travels out of the experiment undetected, and its signal is apparently "missing" energy and momentum. Detecting such anomalous events is the focus of the proposed Light Dark Matter eXperiment (LDMX). In this work, we refine sensitivity projections for LDMX by considering the case where dark matter is produced through the decay of a light meson, such as the ρ, ω, or ϕ. Considering these processes improves the sensitivity of LDMX by several orders of magnitude for $m_\chi \gtrsim 0.1\,\text{GeV}$, where previously considered production channels become ineffective.

Finally, in chapter 8, we consider a radical new possibility which, on its face, has nothing to do with dark matter. As mentioned above, massless particles are generally classified by a spin scale, which is traditionally assumed to be zero. A particle with nonzero spin scale can carry *arbitrary* integer helicity, with the spin scale quantifying how much the helicity states mix under boosts. We show, however, that one can formulate a theory with fields that create and annihilate massless particles of nonzero spin scale, and couple the fields to matter. The result is that at high energies, the behavior of the field automatically mimics that of a minimally coupled scalar, photon, or graviton; at low energies, the response remains well-behaved, but arbitrarily many helicity states play an important role. These results spectacularly break conventional effective field theory intuition, and are possible because the effective Lagrangian necessarily contains an infinite series of dimension 3 operators, which conspire to guarantee good behavior in the infrared. Deriving our results requires the use of a new mathematical tool called vector superspace, within which the entire Lagrangian can be neatly encapsulated in a few terms. They motivate an entirely new set of experimental searches focused on the deep infrared.

Chapter 2

Superconducting Resonant Frequency Conversion

This chapter is based on *Axion Dark Matter Detection by Superconducting Resonant Frequency Conversion*, by A. Berlin, R. T. D'Agnolo, S. A. R. Ellis, C. Nantista, J. Neilson, P. Schuster, S. Tantawi, N. Toro, K. Zhou, JHEP 07, 088 (2020).

Abstract

We propose an approach to search for axion dark matter with a specially designed superconducting radio frequency cavity, targeting axions with masses $m_a \lesssim 10^{-6}$ eV. Our approach exploits axion-induced transitions between nearly degenerate resonant modes of frequency $\sim$ GHz. A scan over axion mass is achieved by varying the frequency splitting between the two modes. Compared to traditional approaches, this allows for parametrically enhanced signal power for axions lighter than a GHz. The projected sensitivity covers unexplored parameter space for QCD axion dark matter for 10^{-8} eV $\lesssim m_a \lesssim 10^{-6}$ eV and axion-like particle dark matter as light as $m_a \sim 10^{-14}$ eV.

2.1 Introduction

The axion is a hypothetical parity-odd real scalar, protected by a shift symmetry and derivatively coupled to Standard Model fields. It is predicted by the Peccei–Quinn solution to the strong CP problem [93, 94, 95, 96] and expected to arise generically from string theory compactifications [97, 98, 99]. It was shown to be a viable dark matter (DM) candidate four decades ago [100, 101]. A generic prediction of axion models is the coupling to photons [102, 103, 104, 105, 106],

$$\mathcal{L} \supset -\frac{g_{a\gamma\gamma}}{4}\, a\, F\tilde{F} = -g_{a\gamma\gamma}\, a\, \mathbf{E}\cdot\mathbf{B}\,. \tag{2.1}$$

This interaction can induce axion-photon conversion in the presence of a background electromagnetic field via the Primakoff process [107], which has been exploited in various axion searches [6, 7, 9, 10, 12, 13, 18, 108, 109, 110, 4]. These searches have started to cover parameter space motivated by the Peccei–Quinn solution to the strong CP problem [102, 103, 104, 105, 106], $g_{a\gamma\gamma} \simeq 3\times10^{-16}\,\mathrm{GeV}^{-1}\,(m_a/\mu\mathrm{eV})$, but for now without a positive detection.[1]

More generally, an attractive motivation for axion-like particles (axions that do not solve the strong CP problem) is that they are a simple DM candidate. A very light axion can acquire a cosmological abundance from the misalignment mechanism that is in agreement with the observed DM energy density if $g_{a\gamma\gamma} \sim 10^{-16}\ \mathrm{GeV}^{-1}(m_a/\mu\mathrm{eV})^{1/4}$, where we have taken $g_{a\gamma\gamma} \sim \alpha_{\mathrm{em}}/2\pi f_a$ and assumed an $\mathcal{O}(1)$ initial misalignment angle (see Ref. [19] for a recent discussion). This relation thus provides a cosmologically motivated target for axion-like particle searches.

Cold axion DM produced by any mechanism generically virializes in the galactic halo. The typical virial velocity dispersion $v_a \sim 10^{-3}$ leads to an *effective* quality factor of $Q_a \sim 1/\langle v_a^2\rangle \sim 10^6$. For timescales shorter than the axion coherence time $\tau_a \sim Q_a/m_a$, we can thus treat the axion as a monochromatic field of the form

$$a(t) = \frac{\sqrt{2\rho_{\mathrm{DM}}}}{m_a}\cos m_a t\,, \tag{2.2}$$

where $\rho_{\mathrm{DM}} \simeq 0.4\ \mathrm{GeV/cm}^3$ is the local DM energy density. Properly speaking, we model the axion DM field in the galaxy as a Gaussian random field[2] with $\langle a(t)\rangle = 0$ and $\langle a(t)^2\rangle = \rho_{\mathrm{DM}}/m_a^2$, since it is a superposition of a large number of waves with random phases. This implies $\mathcal{O}(1)$ amplitude fluctuations on timescales $t \lesssim \tau_a$, which we suppress in Eq. (2.2) for simplicity.[3]

Resonant detectors are well-suited to exploit the coherence of the axion field. To date, most axion search experiments have matched the resonant frequency of the experiment to the mass of the axion DM being searched for. For $m_a \sim \mu$eV, the axion oscillates at $\sim$ GHz frequencies. This enables resonant searches using high-Q normal-conducting cavities in static magnetic fields [6, 7, 9, 10, 12, 13, 18],

[1] The value quoted is the average of the DFSZ [102, 103] and KSVZ [104, 105, 106] predictions.

[2] Detailed coherence properties of the axion DM field have been discussed in Refs. [111, 112], but do not change the features noted above.

[3] These fluctuations lead to statistical subtleties for $t \lesssim \tau_a$, as discussed in Appendix 2.10, but these will not be relevant.

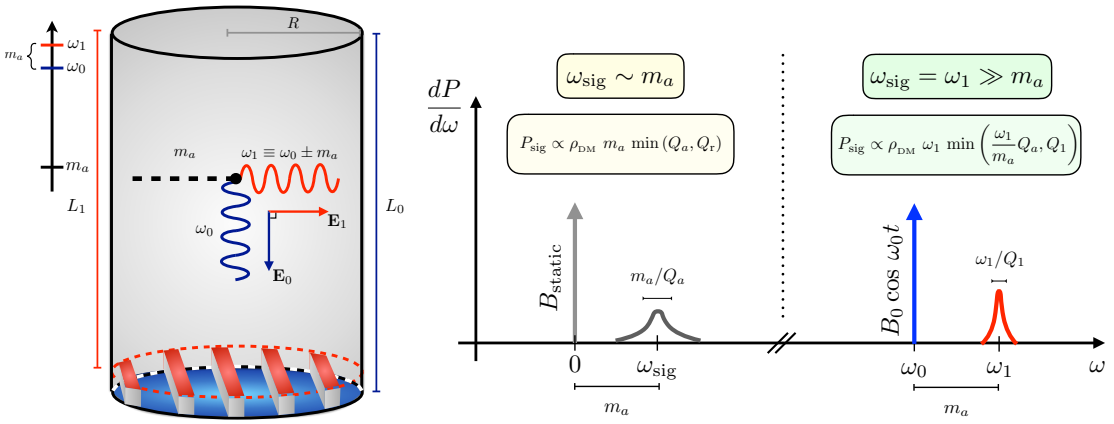

(a) Cartoon of cavity setup. (b) Signal parametrics.

Figure 2.1: **(a)** A schematic depiction of a potential cavity setup. A photon of frequency ω_0 is converted by the axion dark matter background into a photon of frequency $\omega_0 \pm m_a$, where m_a is the axion mass. The cavity is designed to have two nearly degenerate resonant modes at ω_0 and $\omega_1 = \omega_0 + m_a$. One possibility, as discussed in Section 2.4, is to split the frequencies of the two polarizations of a hybrid HE_{11p} mode in a corrugated cylindrical cavity. These two polarizations effectively see distinct cavity lengths, L_0 and L_1, allowing ω_0 and ω_1 to be tuned independently. In this case, larger frequency steps could be achieved by adjusting the fins (shown in red), while smaller frequency steps could be achieved with piezo-actuator tuners.
(b) A schematic comparison between the proposed frequency conversion scheme (right of the dotted line) and typical searches using static magnetic fields (left of the dotted line). The vertical and horizontal axes correspond to differential power and frequency, respectively, of either the driven field (vertical arrows) or the axion-induced signal (resonant curves). The parametric signal power derived in Section 2.2 is shown for both setups, where we assume $\omega_{\rm sig} \sim V^{-1/3}$ for our proposed scheme and factored out a common volume dependence of $V^{5/3}$.

where a cavity mode is rung up through the interaction of Eq. (2.1), sourced by the axion field and the external B field. These experiments take advantage of strong magnetic fields, the large quality factors ($Q \lesssim 10^6$) achievable in GHz normal-conducting cavities, and low-noise readout electronics operating at the GHz scale. However, extending this approach to smaller axion masses would require the use of prohibitively large cavities. To probe lighter axions, experiments have been proposed using systems whose resonant frequencies are not directly tied to their size, such as lumped-element LC circuits [113, 114, 115] or nuclear magnetic resonance [116].[4]

In this chapter, we explore an alternative approach to resonant axion detection, where the frequency *difference* between two modes is tuned to be on-resonance with the axion field, while the mode frequencies themselves remain parametrically larger. Because of their very large quality factors ($Q \gtrsim 10^{10}$), superconducting radio frequency (SRF) cavities are ideal resonators for such a setup. More concretely, as illustrated in Figure 2.1, we consider an SRF cavity with a small, tunable

[4] Ideas for resonant detection of axions heavier than a GHz can also involve decoupling the resonant frequency from the size of the apparatus, for instance via modifications to the photon dispersion relation in tunable plasmas [117] and dielectrics [118, 119].

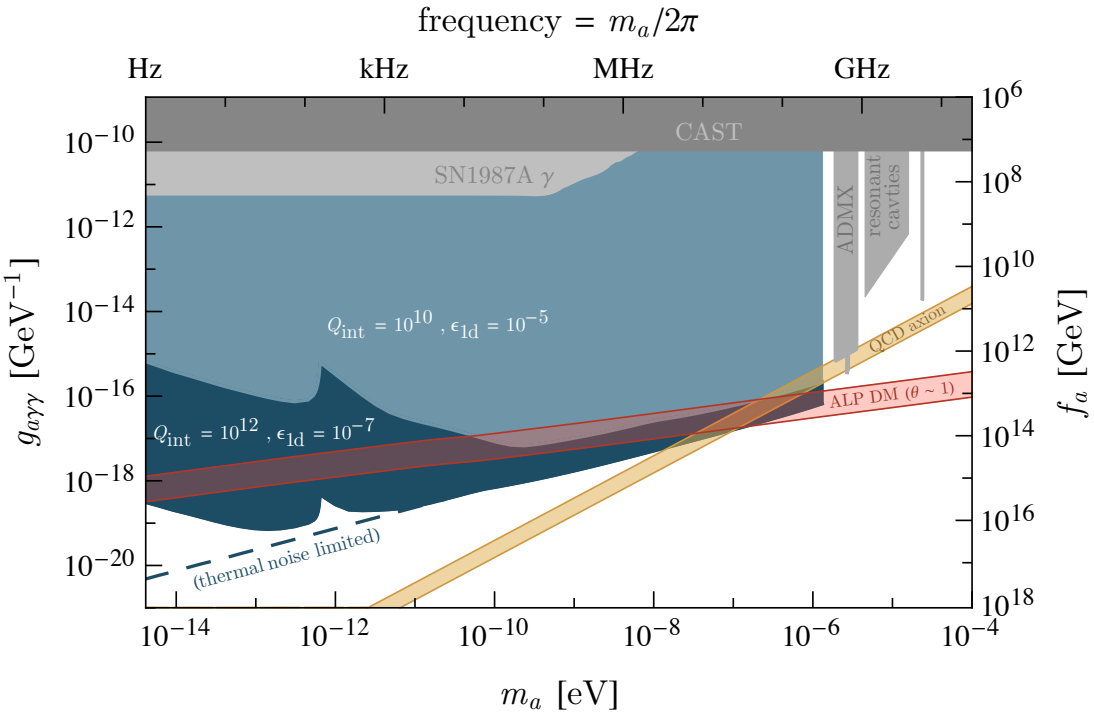

Figure 2.2: The anticipated reach to axion dark matter in the $g_{a\gamma\gamma} - m_a$ plane, for various experimental configurations, compared to existing constraints, shown in gray. Along the right axis, we relate the axion-photon coupling to the symmetry breaking scale f_a by $g_{a\gamma\gamma} \sim \alpha_{\rm em}/2\pi f_a$. As two representative examples, we show the projected sensitivity assuming an intrinsic quality factor and readout-pump mode coupling (see Section 2.5.2) of $Q_{\rm int} = 10^{10}$, 10^{12} and $\varepsilon_{\rm 1d} = 10^{-5}$, 10^{-7}, respectively. The dashed line shows the thermal noise limited sensitivity for $Q_{\rm int} = 10^{12}$ and $\varepsilon_{\rm 1d} = 10^{-7}$. In all cases, we assume a pump mode frequency of $\omega_0/2\pi =$ GHz, a cavity volume of $V = 1\,{\rm m}^3$, a peak magnetic field of $B_0 = 0.2$ T, a mode overlap of $\eta_{10} = 1$ (see Eq. (2.21)), a cavity temperature of $T = 1.8\,{\rm K}$, an average wall displacement of $q_{\rm rms} = 10^{-1}\,{\rm nm}$ (as defined in Section 2.5.3), and an e-fold time of $t_e = 10^7\,{\rm s}$. The orange band denotes the range of couplings and masses as motivated by the strong CP problem. Along the red band, axion production through the misalignment mechanism is consistent with the observed dark matter energy density, assuming an $\mathcal{O}(1)$ initial misalignment angle. As discussed in Section 2.5.3, the feature near $m_a \sim$ kHz is due to our assumption that there are no mechanical resonances below a kHz.

frequency difference between two low-lying modes, which we call the "pump mode" and the "signal mode." The cavity is prepared by driving the pump mode, which has frequency $\omega_0 \sim \text{GHz} \gg m_a$. If the signal mode is tuned to a frequency $\omega_1 \simeq \omega_0 \pm m_a$, then the axion DM field resonantly drives power from the pump mode to the signal mode.

The idea of detecting axions through photon frequency conversion has been studied in other contexts.[5] These include axion detection with optical cavities [124, 125, 126] and frequency conversion in SRF cavities with GHz-scale mode splittings [127]. More generally, frequency conversion is a commonly used technique in signal processing, under the name of "heterodyne detection."

However, frequency conversion in SRF cavities is particularly powerful because of the combination of high Q-factors and the large amount of stored energy in the pump mode. In this chapter, we highlight the parametric advantages of this approach at low axion masses, discuss scenarios for realizing the mode overlap and tunability requirements for such an experiment, and analyze key sources of noise. In the latter two aspects, we benefit from the decades-long effort to detect kHz-to-MHz gravitational waves with SRF cavity resonators [128]. The results from the prototypes of Refs. [129, 130, 131, 132] are particularly useful in anticipating the experimental challenges of our proposed approach.

Our study shows that axion-induced frequency conversion in SRF cavities could be sensitive to QCD axions for $10^{-8}\,\text{eV} \lesssim m_a \lesssim 10^{-6}\,\text{eV}$ and axion DM as light as $m_a \sim 10^{-14}$ eV. The projected sensitivity for two representative sets of experimental parameters is shown in Figure 2.2, with a larger set of parameters shown in Figure 2.5. Compared to traditional resonant searches, fixing the signal to GHz frequencies leads to several advantages for lower axion masses:

1. High frequency readout leverages the large quality factors of SRF cavities, which are typically of order $Q \gtrsim 10^{10}$. In this case, the signal power saturates once $Q \gtrsim (\text{GHz}/m_a)\, Q_a$, unlike static-field detectors whose signal power saturates once $Q \gtrsim Q_a$.

2. Only a small fraction of the signal power ($m_a/\text{GHz} \ll 1$) is sourced directly by the axion DM field. Therefore, the signal is not suppressed by the small axion mass when its Compton wavelength is much larger than the detecting apparatus. This is unlike static-field electromagnetic resonators, where the signal power scales as m_a in this limit.

3. Operating readout electronics near the standard quantum limit has been demonstrated at GHz frequencies [9].

In the next section, we present a parametric estimate of the axion-induced signal power and compare it to that of other resonant setups. In Section 2.3, we provide a more detailed calculation, using a simple model without explicit reference to cavity parameters. We discuss a more complete

[5] Different SRF setups have also been considered for production and detection of light, non-DM axions [120, 121]. Another, distinct idea is the proposal of Refs. [122, 123] to drive two modes and detect the resulting axion-induced frequency shifts.

experimental setup in Section 2.4, deferring a detailed discussion of SRF cavity geometries to Appendix 2.8. In Section 2.5, we study the expected sources of noise, with additional details in Appendix 2.9. In Section 2.6, we estimate the physics reach, with further detail regarding optimization of the readout coupling presented in Appendix 2.10. Finally, we conclude in Section 2.7.

2.2 Conceptual Overview

At the level of Maxwell's equations, an oscillating axion DM field sources a time-dependent effective current density, $J_{\rm eff}$, in the presence of an applied magnetic field $B_0(t)$, of magnitude

$$J_{\rm eff}(t) \sim g_{a\gamma\gamma}\, B_0(t)\, \sqrt{\rho_{\rm DM}}\, \cos m_a t\,. \tag{2.3}$$

This effective current density leads to a real magnetic field, $B_a \propto J_{\rm eff}$. The oscillations of this field generate a small electromotive force

$$\mathcal{E}_a \sim V^{2/3}\, \partial_t B_a\,, \tag{2.4}$$

which can drive power into a resonant detector of volume V. In typical setups, the applied magnetic field is static, such that $\mathcal{E}_a^{(\rm static)} \propto m_a$. In the approach we advocate for here, the applied magnetic field oscillates in time, $B_0(t) = B_0 \cos\omega_0 t$. Compared to static-field detectors of comparable size, the electromotive force is significantly larger,

$$\frac{\mathcal{E}_a^{(\rm osc.)}}{\mathcal{E}_a^{(\rm static)}} \sim \frac{\omega_0 + m_a}{m_a} \sim \frac{\omega_1}{m_a}\,. \tag{2.5}$$

This is the essential reason for the parametric enhancement of our approach at low axion masses ($m_a \ll \omega_0$).[6]

To make this intuition more precise, it is useful to compute the signal power explicitly and compare it to that of static-field resonators. In general, the power delivered to a resonator of volume V and resistance R is

$$P_{\rm sig}^{(\rm r)} \sim \frac{\mathcal{E}_a^2}{R}\, \min\!\left(1, \frac{\tau_a}{\tau_{\rm r}}\right) \sim \omega_{\rm sig}^2\, B_a^2 V \min(Q_{\rm r}/\omega_{\rm sig}, Q_a/m_a)\,, \tag{2.6}$$

where $\tau_{\rm r} \sim Q_{\rm r}/\omega_{\rm sig}$ is the ring-up time for a resonator with quality factor $Q_{\rm r}$ and readout frequency $\omega_{\rm sig}$, and in the second equality, we expressed R in terms of $Q_{\rm r}$. Note that as a function of $Q_{\rm r}$, the signal power saturates once the axion coherence time is smaller than the resonator ring-up time, since only a fraction of the axion power resides within the resonator bandwidth, as encapsulated in

[6] There is a well-known argument that axion signals must degrade at small m_a, since the massless limit at fixed axion field amplitude would be equivalent to a static QED θ-angle. The scaling of Eq. (2.4) does not violate this argument because $J_{\rm eff} \propto \sqrt{\rho_{\rm DM}} \sim m_a\, a$. Thus, for a fixed axion field amplitude, the electromotive force in our setup scales as m_a, compared to m_a^2 for static-field experiments.

the second factor in both equalities.

To date, most resonant experiments searching for electromagnetically coupled axion DM employ static magnetic fields, since these are more easily sourced at large field strengths. In this case, $J_{\rm eff}(t) \propto \cos m_a t$ implies that this current density sources photons of energy and frequency comparable to m_a, which can be detected with an apparatus whose resonant frequency is matched to the axion rest mass. For $m_a \sim$ GHz, this is the strategy employed by resonant cavity experiments such as ADMX [6, 7]. However, for any static-field cavity detector, this approach becomes increasingly difficult for $m_a \ll$ GHz, since the resonant frequency is typically controlled by the inverse length-scale of the apparatus.

By contrast, LC resonators can search for sub-GHz axions because their resonant frequency is not directly tied to the geometric size of their circuit components. In such a setup, when the Compton wavelength of the axion is much larger than the shielded detection region of volume $V_{\rm LC}$, the size of the axion-induced magnetic field follows simply from the quasistatic expectation, $B_a \sim J_{\rm eff} V_{\rm LC}^{1/3}$. Since the readout frequency of static-field setups is dictated by the axion mass, the signal power of an LC circuit with quality factor $Q_{\rm LC}$ is parametrically

$$P_{\rm sig}^{\rm (LC)} \sim m_a \, J_{\rm eff}^2 \, V_{\rm LC}^{5/3} \min(Q_{\rm LC}, Q_a) \,. \tag{2.7}$$

The saturation of signal power at $Q_{\rm r} \gtrsim Q_a$ as well as the overall suppression at small axion masses is characteristic of static-field setups. This latter point can also be understood from the fact that for a static-field configuration, the axion-induced electromotive force vanishes for zero axion mass and fixed DM energy density, since $\mathcal{E}_a \propto m_a$.

Our setup instead involves driving a resonant cavity at a frequency $\omega_0 \gg m_a$. An axion DM background converts the frequency, sourcing an effective current oscillating at $\omega_{\rm sig} = \omega_1 = \omega_0 \pm m_a$,

$$J_{\rm eff}(t) \sim g_{a\gamma\gamma} \, B_0 \sqrt{\rho_{\rm DM}} \, \cos\left(\omega_0 \pm m_a\right) t \,, \tag{2.8}$$

which drives power into the signal mode. In this case, $B_a \sim J_{\rm eff}/\omega_1$, and for a fixed DM energy density, the electromotive force is not suppressed for $m_a \ll$ GHz since $\mathcal{E}_a \propto \omega_1$. By the same logic as the previous calculation, the axion-induced signal power is

$$P_{\rm sig} \sim J_{\rm eff}^2 \, V \min(Q_{\rm r}/\omega_1, Q_a/m_a) \,, \tag{2.9}$$

which yields a parametric advantage[7] over LC resonators when $m_a \ll V_{\rm LC}^{-1/3}$. Intuitively, this is because each axion-photon interaction in the cavity involves a photon of energy ω_0, and so only a small fraction ($m_a/\omega_0 \ll 1$) of this signal power is contributed by the axion background, with the remainder originating from the pump mode. Since $\omega_1 \gg m_a$, maximizing the signal power in our setup requires

[7] Axion detection by frequency conversion in a radio frequency cavity was also briefly considered in Ref. [122], but the authors did not find the same parametric enhancement we demonstrate here.

resonator quality factors much larger than Q_a, saturating only when $Q_r \gtrsim (\omega_1/m_a)\, Q_a \gg 10^6$. This motivates the choice of using an SRF cavity, as superconducting resonators have been built with quality factors as large as $Q_r \sim \text{few} \times 10^{11}$.

To complete our overview, we give a parametric comparison of the reach. This can be done straightforwardly when our approach is thermal noise limited, which occurs in the right half of Figure 2.2. As we will see in Section 2.6, accounting for the scan rate and coupling optimization leads to simple expressions for the signal-to-noise ratio (SNR), which do not require the casework of Eqs. (2.7) and (2.9). Instead, for general quality factors,

$$\frac{\text{SNR}}{\text{SNR}^{(\text{LC})}} \sim \frac{(\omega_1 V^{1/3})^{-1}}{m_a V_{\text{LC}}^{1/3}} \left(\frac{V}{V_{\text{LC}}}\right)^{4/3} \left(\frac{Q_{\text{int}}}{Q_{\text{LC}}}\right)^{1/2} \left(\frac{T_{\text{LC}}}{T}\right)^{1/2} \left(\frac{B_0}{B_{\text{LC}}}\right)^2 \tag{2.10}$$

$$\sim \frac{\omega_1}{m_a} \left(\frac{Q_{\text{int}}}{Q_{\text{LC}}}\right)^{1/2} \left(\frac{T_{\text{LC}}}{T}\right)^{1/2} \left(\frac{B_0}{B_{\text{LC}}}\right)^2 , \tag{2.11}$$

where Q_{int} is the intrinsic quality factor of the SRF cavity, and for comparison we took $\omega_1 V^{1/3} \sim 1$, appropriate for low-lying cavity modes, and $V = V_{\text{LC}}$ in the second line. For the reference parameters $Q_{\text{int}} \sim 10^{12}$, $T \sim 1.8\,\text{K}$, and $B_0 \sim 0.2\,\text{T}$, and comparison parameters $Q_{\text{LC}} = Q_a \sim 10^6$, $T_{\text{LC}} = 0.1\,\text{K}$, and $B_{\text{LC}} = 4\,\text{T}$, the last three factors roughly cancel, leaving only the factor ω_1/m_a which enhances our frequency conversion approach compared to an LC resonator operating in the quasistatic regime.[8] In the next section, we begin the work of establishing these results, by directly solving the relevant equations of motion to compute the signal power.

2.3 Signal Power

In this section, we explicitly compute the signal induced by axion DM interacting with a loaded cavity. For this calculation, it suffices to use a simplified model that treats the cavity as a collection of fixed cavity modes. In the following two sections, we refine this model by including the additional layers of complexity needed to describe the system in the presence of noise.

Our starting point is Maxwell's equations modified by the axion interaction of Eq. (2.1),

$$\begin{aligned} \nabla \cdot \mathbf{E} &= \rho - g_{a\gamma\gamma} \mathbf{B} \cdot \nabla a \ , \\ \nabla \times \mathbf{B} &= \partial_t \mathbf{E} + \mathbf{J} - g_{a\gamma\gamma} \left(\mathbf{E} \times \nabla a - \mathbf{B}\, \partial_t a\right) . \end{aligned} \tag{2.12}$$

Since the spatial gradients of the axion field are small, the dominant effect is that the axion sources an effective current, $\mathbf{J}_{\text{eff}} = g_{a\gamma\gamma} \mathbf{B} \partial_t a$. The effective current $\mathbf{J}_{\text{eff}}$ inherits its time-dependence from the oscillating axion and pump mode magnetic field and can resonantly drive power into other cavity

[8] Fixing the geometry and other factors, scaling up both approaches in volume would decrease the relative advantage of the SRF approach. However, increasing the volume of either approach much beyond $\mathcal{O}(1)$ m^3 would constitute an engineering challenge.

modes with matching characteristic frequency.

To compute the steady state signal power, it is convenient to work in frequency space. In doing so, we adopt the following convention for the Fourier transform of a function f,

$$f(t) = \frac{1}{2\pi} \int d\omega \; e^{i\omega t} f(\omega) \,, \quad f(\omega) = \int dt \; e^{-i\omega t} f(t) \,.$$

When unspecified, the region of integration for ω or t is implicitly $-\infty$ to ∞. We define the power spectral density (PSD) of f, denoted as $S_f(\omega)$, by

$$\langle f(\omega) f^*(\omega') \rangle = S_f(\omega) \, \delta(\omega - \omega') \;, \tag{2.13}$$

so that the steady state average power can be expressed as[9]

$$\langle \, f(t)^2 \, \rangle = \frac{1}{(2\pi)^2} \int d\omega \; S_f(\omega) \;. \tag{2.14}$$

Note that all PSDs in this chapter are two-sided.

Given the tiny backreaction of the axion field on the cavity, it is useful to decompose the electric and magnetic fields into a set of vacuum cavity modes:

$$\begin{aligned} \mathbf{E}(t, \mathbf{r}) &= \sum_n \mathbf{E}_n(t, \mathbf{r}) = \sum_n e_n(t) \, \tilde{\mathbf{E}}_n(\mathbf{r}) \;, \\ \mathbf{B}(t, \mathbf{r}) &= \sum_n \mathbf{B}_n(t, \mathbf{r}) = \sum_n b_n(t) \, \tilde{\mathbf{B}}_n(\mathbf{r}) \;, \end{aligned} \tag{2.15}$$

where the resonant modes satisfy the conditions

$$\begin{gathered} \nabla^2 \tilde{\mathbf{E}}_n = -\omega_n^2 \, \tilde{\mathbf{E}}_n \;, \quad \nabla^2 \tilde{\mathbf{B}}_n = -\omega_n^2 \, \tilde{\mathbf{B}}_n \,, \\ \int_V \tilde{\mathbf{E}}_n^* \cdot \tilde{\mathbf{E}}_l = \delta_{nl} \int_V |\tilde{\mathbf{E}}_n|^2, \quad \int_V \tilde{\mathbf{B}}_n^* \cdot \tilde{\mathbf{B}}_l = \delta_{nl} \int_V |\tilde{\mathbf{B}}_n|^2 \,. \end{gathered} \tag{2.16}$$

Here, V is the volume of the cavity and ω_n are the resonant frequencies. Using the above definitions, Maxwell's equations in Eq. (2.12) can be rewritten as an equation of motion for the cavity's electric field in the presence of background axion and magnetic fields,

$$\sum_n \left(\omega^2 - \omega_n^2 - i \, \frac{\omega \, \omega_n}{Q_n} \right) \mathbf{E}_n(\omega) = g_{a\gamma\gamma} \int dt \; e^{-i\omega t} \; \partial_t (\mathbf{B} \, \partial_t a) \,, \tag{2.17}$$

where we have neglected terms proportional to the small axion velocity. Each mode has a distinct quality factor, Q_n, that is dictated by the electric field profile near the walls and power losses through

[9] In Eq. (2.13), the brackets denote an ensemble average, where a signal $f(t)$ is Fourier transformed in many different time intervals, which are then averaged in a given frequency bin. Eq. (2.14) then defines $\langle f(t)^2 \rangle$, which can equivalently be described as a time average of $f(t)^2$.

the loading and readout ports, and determines the dissipative terms on the left-hand side. Above, we have neglected the motion of the cavity walls, which can couple distinct modes and shift their resonant frequencies; we account for this source of noise in Section 2.5.3.

To complete the calculation, we note that the magnetic field in Eq. (2.17) is dominated by the pump mode such that $\mathbf{B} \simeq \mathbf{B}_0$. We then define the characteristic amplitude of the pump mode magnetic field as

$$B_0 \equiv \sqrt{\frac{1}{V}\int_V |\tilde{\mathbf{B}}_0|^2} \,. \tag{2.18}$$

The steady state average power delivered to the signal mode ($n = 1$) can be written in terms of a signal PSD defined analogously to Eq. (2.14),

$$P_{\rm sig} = \frac{\omega_1}{Q_1} U_1 = \frac{1}{(2\pi)^2}\int d\omega \; S_{\rm sig}(\omega) \,, \tag{2.19}$$

where U_1 is the electromagnetic energy stored in the signal mode. From Eq. (2.17), we find that

$$S_{\rm sig}(\omega) = \frac{\omega_1}{Q_1}\,(g_{a\gamma\gamma}\,\eta_{10}\,B_0)^2\,V\,\frac{\omega^2}{(\omega^2-\omega_1^2)^2+(\omega\,\omega_1/Q_1)^2}\int\frac{d\omega'}{(2\pi)^2}\,(\omega'-\omega)^2\,S_{b_0}(\omega')\,S_a(\omega-\omega')\,, \tag{2.20}$$

where $S_a(\omega)$ is the axion PSD, $S_{b_0}(\omega)$ is the PSD for $b_0(t)$ (defined in Eq. (2.15)), and η_{10} is an $\mathcal{O}(1)$ mode overlap factor,

$$\eta_{10} \equiv \frac{\left|\int_V \tilde{\mathbf{E}}_1^* \cdot \tilde{\mathbf{B}}_0\right|}{\sqrt{\int_V |\tilde{\mathbf{E}}_1|^2}\,\sqrt{\int_V |\tilde{\mathbf{B}}_0|^2}} \leq 1\,. \tag{2.21}$$

We have ignored backreaction on the axion field, as this is negligible even for very large quality factors. We note that Eq. (2.20) is only valid when the experimental integration time $t_{\rm int}$ exceeds both the ring-up time of the signal mode, $\tau_r \sim Q_1/\omega_1$, and the axion coherence time, $\tau_a \sim Q_a/m_a$. The steady state power is achieved when $t_{\rm int} \gtrsim \tau_r$, but if $t_{\rm int} \lesssim \tau_a$, the axion PSD is not resolved, and $S_a(\omega)$ must be convolved with a window function.[10]

If the spectral width of the pump mode magnetic field is sufficiently narrow, then it may be approximated as a monochromatic source, $b_0(t) = \cos\omega_0 t$, which corresponds to

$$S_{b_0}(\omega) = \pi^2\left[\delta(\omega-\omega_0)+\delta(\omega+\omega_0)\right] \,. \tag{2.22}$$

[10] Our result also breaks down in the extreme case $m_a \lesssim \omega_1/Q_1 \sim 10^{-17}\,\text{eV} \times (10^{12}/Q_1)$, where the axion oscillates on a longer timescale than the ring-up time. In this case, the signal power does not reach a steady value, but rather depends on the instantaneous phase of the axion field. Eq. (2.24) remains valid only if $P_{\rm sig}$ is taken to denote the average power over an entire axion field oscillation. This is not relevant for any of the parameter space shown in Figure 2.2. For the smaller intrinsic quality factors or e-fold times shown in Figure 2.5 (which affect Q_1, as described in Section 2.6), we restrict our calculations to $m_a \gtrsim \omega_1/Q_1$.

Eq. (2.20) then reduces to

$$S_{\rm sig}(\omega) = \frac{\omega_1}{4Q_1} \left(g_{a\gamma\gamma}\, \eta_{10}\, B_0\right)^2 V \;\; \frac{\omega^2 \left[(\omega-\omega_0)^2\, S_a(\omega-\omega_0) + (\omega+\omega_0)^2\, S_a(\omega+\omega_0)\right]}{(\omega^2-\omega_1^2)^2 + (\omega\,\omega_1/Q_1)^2}\,. \tag{2.23}$$

As we will see in Section 2.6, this is a valid approximation in most of the parameter space considered in this chapter. This is possible because the magnetic field can have a much narrower width than the pump mode itself, as its width is determined by the frequency stability of the oscillator that loads the cavity.

To understand Eq. (2.23) parametrically, we assume the signal mode frequency is on resonance and consider two limiting cases. The frequency spread of the axion PSD is controlled by its effective quality factor $Q_a \sim 10^6$. If the axion is narrow compared to the signal mode's bandwidth ($m_a/Q_a \ll \omega_1/Q_1$), we can evaluate the integral of Eq. (2.19) by treating the axion PSD as a delta function. Instead, if the axion is broad compared to the signal bandwidth ($m_a/Q_a \gg \omega_1/Q_1$), we can evaluate the integral using the narrow width approximation for the Breit–Wigner response of the signal mode. The result is

$$P_{\rm sig} \simeq \frac{1}{4} \left(g_{a\gamma\gamma}\, \eta_{10}\, B_0\right)^2 \rho_{\rm DM}\, V \times \begin{cases} Q_1/\omega_1 & \frac{m_a}{Q_a} \ll \frac{\omega_1}{Q_1} \\ \pi Q_a/m_a & \frac{m_a}{Q_a} \gg \frac{\omega_1}{Q_1}\,, \end{cases} \tag{2.24}$$

which matches the parametric estimate of Eq. (2.9). Here we use the normalization

$$\langle a(t)^2 \rangle = \frac{1}{(2\pi)^2} \int d\omega\; S_a(\omega) = \frac{\rho_{\rm DM}}{m_a^2}\,, \tag{2.25}$$

and take $S_a(\omega)$ to be governed by a virialized Maxwellian velocity distribution [133].

For large axion masses, the axion is broad, and the signal power in Eq. (2.24) is suppressed by m_a^{-1} since only a small fraction of the axion PSD lies within the detector bandwidth. As the axion mass decreases, the signal power increases, saturating when these two bandwidths are comparable, i.e., when the axion coherence time matches the ring-up time of the signal mode, $\tau_a \sim \tau_r$. As discussed in the previous section, this differs from resonant experiments where the readout frequency is comparable to the axion mass, in which case the signal power saturates once $Q_1 \gtrsim Q_a$.

Expanding on the intuition developed in Section 2.2, we now compare more carefully the parametric form of the signal power in Eq. (2.24) to that of static-field experiments designed to resonantly detect axions with masses $m_a \ll$ GHz. For example, near-future LC resonators plan on using magnetic fields of size $B_{\rm LC} \sim 4$ T, while the magnetic fields for our setup can be no larger than roughly 0.2 T, to preserve the superconducting properties of the cavity. However, this is compensated by the much larger quality factors attainable by SRF cavities. To see this, note that a static-field LC resonator is required to operate in the quasistatic limit once $m_a \ll V^{-1/3}$. In this case, as discussed in Section 2.2,

the parametric form of the signal power is

$$P_{\rm sig}^{\rm (LC)} \sim (g_{a\gamma\gamma} B_{\rm LC})^2 \, \rho_{\rm DM} \, V^{5/3} \min(Q_{\rm LC}, Q_a) \, m_a \ . \tag{2.26}$$

The factor of m_a in Eq. (2.26) stands in contrast to Eq. (2.24), and appears because the signal frequency in such an experiment is comparable to the axion mass. This is not the case for the setup discussed here because the signal frequency is always fixed to be $\omega_0 + m_a \sim \omega_1 \sim$ GHz even for $m_a \ll$ GHz. Comparing Eqs. (2.24) and (2.26), we have

$$\frac{P_{\rm sig}}{P_{\rm sig}^{\rm (LC)}} \sim \left(\frac{0.2 \text{ T}}{4 \text{ T}}\right)^2 \times \begin{cases} (Q_1/Q_a)^2 \, \frac{(\omega_1/Q_1)}{(m_a/Q_a)} & \frac{m_a}{Q_a} \ll \frac{\omega_1}{Q_1} \\ (\omega_1/m_a)^2 & \frac{m_a}{Q_a} \gg \frac{\omega_1}{Q_1} \, , \end{cases} \tag{2.27}$$

where we took the cavity and LC resonator to be of comparable size, fixed $\omega_1 V^{1/3} \sim 1$ for the cavity setup, and set $Q_{\rm LC} \sim Q_a$. Eq. (2.27) shows that a frequency conversion setup using an SRF cavity has a parametric advantage in signal power when $m_a \ll \omega_1$, which is the regime shown in Figure 2.2. For a broad axion, $m_a \lesssim \omega_1/20$ is already enough to overcome the weaker magnetic field, while for a narrow axion the larger quality factors achievable in SRF cavities more than suffice to compensate at any axion mass.

Of course, this does not suffice to establish a comparably enhanced sensitivity, since noise sources can vary drastically across different experimental setups. We investigate these noise sources in detail in Section 2.5. Realistic values for the relevant cavity parameters are discussed in more detail in the next section.

2.4 A Cavity Concept

In this section, we discuss the choice of cavity geometry and pump and signal modes, as well as the quality factors attainable in SRF cavities. We also outline possible methods for tuning the mode splitting $\omega_1 - \omega_0$, loading the cavity, and reading out the signal.

As mentioned in Section 2.3, the peak magnetic field in an SRF cavity will be smaller than in a conventional RF cavity, and this must be compensated by a larger quality factor. In multi-cell elliptical cavities operating at GHz frequencies designed for accelerating charged particle beams, intrinsic quality factors of $Q_{\rm int} \simeq 4 \times 10^{10}$ (and in one case as high as $Q_{\rm int} \gtrsim 2 \times 10^{11}$) have been achieved [134, 135], a factor of over 10^6 greater than what the same geometry would display in warm copper. However, we are not restricted to geometries useful for particle acceleration. Quality factors of $Q_{\rm int} \sim 10^5$ are commonly achieved in overmoded non-superconducting RF cavities with non-accelerator geometries [136, 137, 138]. This suggests that SRF counterparts can be constructed with quality factors as large as $Q_{\rm int} \sim 10^{12}$.[11]

[11] The power dissipation of a cavity with the parameters of Fig. 2.2 would be $P_{\rm in} \sim 10^4 \times (10^{10}/Q_{\rm int})$ W. As such,

We now consider the choice of cavity geometry, where the goal is to find a cavity design with two nearly degenerate modes and an $\mathcal{O}(1)$ geometric overlap factor η_{10}, as defined in Eq. (2.21). Rectangular, cylindrical, and spherical cavities can be treated analytically straightforwardly; realistic cavities are often variations on these shapes. We do not consider spherical cavities, as they typically do not have pairs of nearly degenerate modes.[12] Furthermore, it is difficult to manufacture rectangular cavities with the required large quality factors. We hence focus on cylindrical cavities.

An ordinary cylindrical cavity supports transverse electric (TE_{mnp}) and transverse magnetic (TM_{mnp}) modes, indexed by integers m, n, and p, as described in Appendix 2.8. Because the axion carries no spin, and we have neglected its spatial gradients, it can only mediate transitions between modes with the same m. Furthermore, since the axion is a pseudoscalar, it must change the parity of p. Finally, axions cannot mediate transitions between pairs of TM modes.

A simple option would be to use transitions between the two polarizations of a single TE mode, after splitting them in frequency by perturbing the cavity. However, this cannot work because the axion transition must change the parity of p. Instead, since the frequencies of the modes each depend differently on the cavity radius R and length L, two modes could be arranged to be nearly degenerate by manufacturing the cavity with an appropriate aspect ratio L/R. As discussed further in Appendix 2.8, overlap factors of $\eta_{10} \simeq 0.5$ can then be achieved for the transitions $\mathrm{TM}_{0,n+1,0} \leftrightarrow \mathrm{TE}_{0n1}$. For example, for a cavity loaded in the TM_{030} mode, the loaded mode frequency is $\omega_0 = 2\pi\,\mathrm{GHz}$ if the cylinder has radius $R \simeq 0.4\,\mathrm{m}$. The TE_{021} signal mode is degenerate if the length is $L \simeq 0.25\,\mathrm{m}$, and a frequency difference of $m_a \sim$ GHz is attained if $L \simeq 0.21\,\mathrm{m}$. Thus, many orders of magnitude in axion mass can be scanned by tuning the length through a relatively small range.

Larger overlap factors of $\eta_{10} \simeq 0.8$ can be achieved by corrugating the outer wall with ridges. Similarly, using orthogonally oriented ridges on the end-walls of a square cross-section cavity to align the electric and magnetic fields of cross-polarized $\mathrm{TE}_{10p}/\mathrm{TE}_{01p}$ modes can also provide a large overlap factor, limited by how large/overmoded the cavity is. To further improve the quality factor, one can do the same with the cross-polarized HE_{11p} hybrid modes in a cylindrical cavity with outer wall corrugations. This final approach is mathematically developed in Appendix 2.8.

We now turn to physical mechanisms for tuning the frequency difference $\omega_1 - \omega_0$. Small changes in the cavity length can be achieved by applying pressure on the end-walls with a piezoelectric device. Concretely, the smallest scan steps we consider in Section 2.6 are of order 0.1 Hz, which corresponds to changes in length of order 0.1 nm. This tuning mechanism can deform a meter-long cavity by a few millimeters at most, leading to a scannable range of axion masses of about $\sim$ MHz. Larger changes in the cavity length can be achieved with mechanically retractable fins, as shown in Figure 2.1(a). For non-corrugated cylindrical cavities, these fins effectively serve to change the length L of the cavity,

operating SRF cavities with intrinsic quality factors significantly lower than 10^{10} is not practical due to power and cooling demands.

[12] It might be possible to use spherical cavities with the poles cut off, where the only modes that can be supported are nearly degenerate high harmonics. Alternatively, one could couple two spherical cavities with a small tunable aperture as in Refs. [132, 130, 131].

while for corrugated cylindrical cavities, they change the length seen by only one of the hybrid mode polarizations.

Using fins, one can cover the full parameter space shown in Figure 2.2 with a single cavity. However, introducing such sharp features into the cavity increases the peak surface fields, and hence has the potential to degrade the quality factor and lead to enhancement of field emission, as discussed in Section 2.5.4.

Since detailed numeric simulations of the cavity are required to understand these effects, we defer further discussion to future work. As such, the reach shown in Figure 2.2 should be interpreted as indicating the potential of our general approach. However, we note that even an uncorrugated cylindrical cavity tuned solely with piezoelectric devices can probe a wide range of motivated parameter space, over orders of magnitude in axion mass.

Finally, loading and readout can be achieved either through coaxial antennae fed into the cavity or with waveguides. For concreteness, we will employ the term "waveguide" when discussing the loading/readout architecture. When we discuss the reach of the proposed approach in Section 2.6, we will explore the optimization of the readout architecture. The language of waveguides lends itself well to this discussion, but the conclusions we reach do not depend on what specific instrument is used to extract the signal from the cavity.

To summarize, as reference cavity parameters we consider $V \sim \mathrm{m}^3$ sized cylindrical SRF cavities operating at frequencies of $\omega/2\pi \sim$ GHz, with typical magnetic fields of $B \sim 0.2$ T, and intrinsic quality factors of $Q_{\mathrm{int}} \gtrsim 10^9$. The level of frequency stability of modes planned for similar SRF cavities [139] suggests that scanning step sizes of ~ 0.1 Hz $- 1$ Hz are achievable. We therefore limit our analysis to frequency steps of 0.1 Hz and above, and do not consider axion masses corresponding to frequencies below 1 Hz, where the effects of such a frequency instability become more dramatic. Furthermore, we do not consider the possibility of large frequency separations between the pump and signal mode, since this would involve accounting for intermediate modes. We therefore restrict our analysis to $m_a \lesssim$ GHz.[13]

2.5 Noise Sources

In this section, we describe the expected dominant noise sources for our setup, shown schematically in Figure 2.3. Some of these noise sources, such as amplifier and thermal noise, are common to axion DM experiments using static background magnetic fields [6, 7, 108, 9, 10, 12, 13, 18]. The remaining contributions, however, are particular to our setup. These include phase noise from the master oscillator that drives the pump mode, mechanical vibrations of the cavity walls, and field emission, commonly known in the accelerator community as "dark current."

The relative sizes of the noise sources, as a function of axion mass, are shown in Figure 2.4.

[13] An initial exploration of the use of higher harmonics of a loaded cavity was conducted in Ref. [127].

Thermal noise in the cavity, and amplifier noise in the readout system are both independent of m_a. Of the two sources, thermal noise in the cavity dominates, and plays the most important role at the largest axion masses that we consider. At smaller axion masses, two other sources of noise become relevant: frequency instability of the resonant modes from mechanical vibrations and power leakage from the pump to the signal mode. These both grow as the axion mass is decreased. As we discuss in the following, they are also both strongly sensitive to the quality factor of the cavity. Increasing the quality factor, other than increasing the signal power, decreases these two sources of noise. In Figure 2.4, the sharp feature evident in the mechanical noise power is due to our assumptions, motivated by the experimental characterization of similar cavities performed in Ref. [130]; we assume that there exists a spectrum of mechanical resonances above a kHz, each maximally coupled to the pump and signal modes of the cavity.

Before turning to a more detailed description of each of these noise sources, it is useful to distinguish the two contributions to the quality factor Q_1 of the signal mode,

$$\frac{1}{Q_1} = \frac{1}{Q_{\rm int}} + \frac{1}{Q_{\rm cpl}}\,, \tag{2.28}$$

where $Q_{\rm int}$ depends only on losses intrinsic to the cavity (such as the residual resistance of the walls) and $Q_{\rm cpl}$ is determined by the rate at which power is transmitted to the readout. Critical coupling occurs when the two losses are equal, $Q_{\rm int} = Q_{\rm cpl}$, but we will see in Section 2.6 that it is optimal to strongly overcouple, $Q_1 \simeq Q_{\rm cpl} \ll Q_{\rm int}$, even though this degrades the total signal power. The readout is set to predominantly couple to the signal mode, as discussed further in Section 2.5.2, so that the pump mode's quality factor is not affected, $Q_0 \simeq Q_{\rm int}$. The PSDs derived in this section represent the total noise power delivered to the cavity and to the readout apparatus in the signal mode.

2.5.1 Thermal and Amplifier Noise

Thermal emission of radio waves from the the cavity walls constitutes an irreducible noise source. If the cavity is cooled to a temperature T, then the PSD of this thermal noise is

$$S_{\rm th}(\omega) = \frac{Q_1}{Q_{\rm int}} \frac{4\pi T\,(\omega\,\omega_1/Q_1)^2}{(\omega^2-\omega_1^2)^2 + (\omega\,\omega_1/Q_1)^2}\,. \tag{2.29}$$

Here, the prefactor of 4π stems from our use of two-sided PSDs and the convention of Eq. (2.13), and the factor of $Q_1/Q_{\rm int}$ arises because the coupling to the readout does not source thermal noise; it is only the cavity walls that are at temperature T. This corresponds to an average total noise power of

$$P_{\rm th} \simeq \frac{T\,\omega_1}{Q_{\rm int}}\,. \tag{2.30}$$

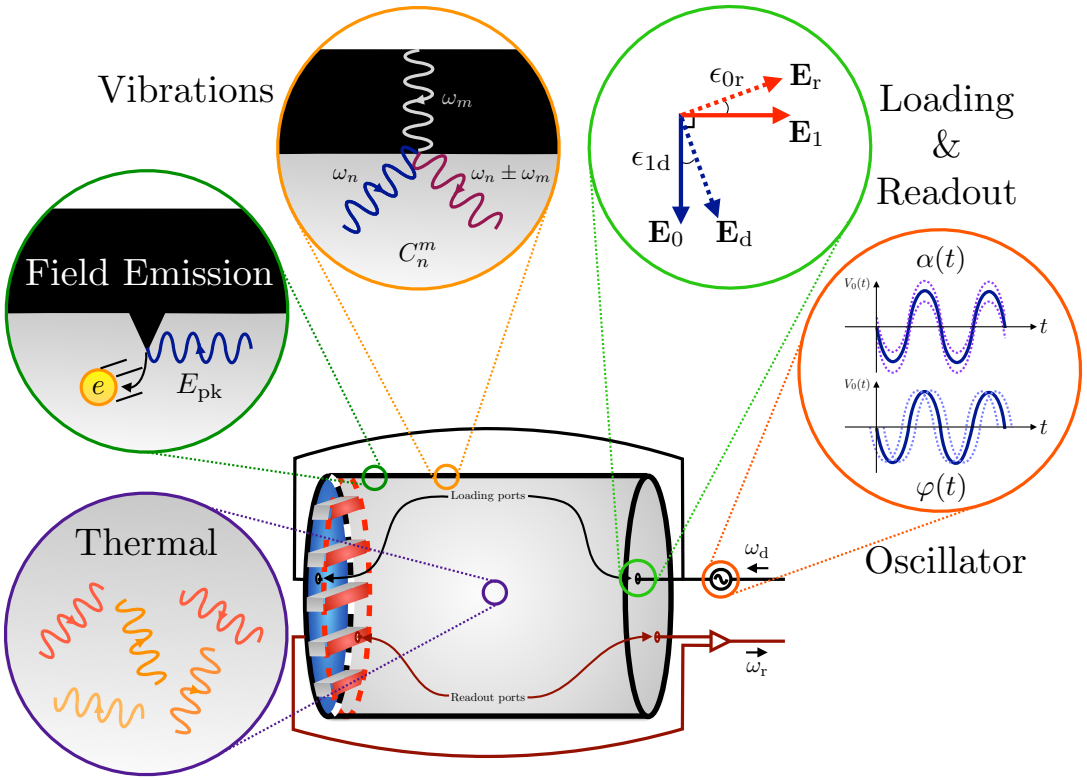

Figure 2.3: A diagram depicting the main expected sources of noise specific to our detection strategy. In counterclockwise order are depictions of individual noise sources: thermal emission, discussed in Section 2.5.1; the effects of oscillator phase noise, as discussed in Section 2.5.2; the precision of the geometric coupling of the loading and readout waveguides, relevant to several noise sources; vibrations of the cavity walls, discussed in Section 2.5.3; and field emission, discussed in Section 2.5.4. Not shown is amplifier noise, discussed in Section 2.5.1.

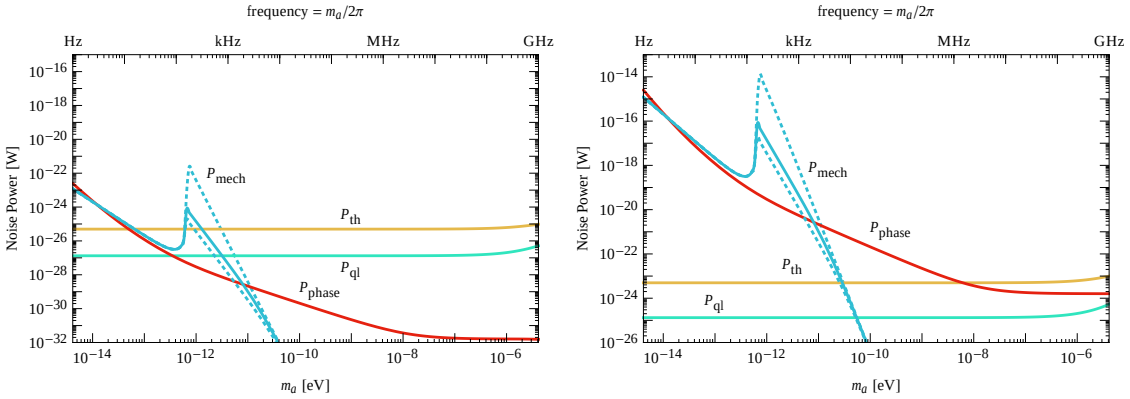

(a) $\epsilon_{1\rm d} = 10^{-7}$, $Q_{\rm int} = 10^{12}$ (b) $\epsilon_{1\rm d} = 10^{-5}$, $Q_{\rm int} = 10^{10}$

Figure 2.4: Comparisons of total power in thermal (yellow), amplifier (cyan), oscillator phase (red), and mechanical vibration (blue) noise, shown as a function of the axion mass m_a. The cavity parameters match the (a) lower and (b) upper curves in Figure 2.2. The figure shows the total power delivered to the readout architecture assuming critical coupling, and thus has appropriate factors of $Q_n/Q_{\rm cpl}$ included as discussed in Section 2.6. The estimated size of mechanical noise depends on the degree of degeneracy between the axion mass and the resonant frequency of mechanical modes of the cavity. The solid line corresponds to the same model incorporated into the reach shown in Figures 2.2 and 2.5, while the dashed lines serve to bracket the variation in such noise, depending on the scan/instrumental strategy employed (see Section 2.5.3 for discussion).

Driven SRF cavities can be efficiently cooled using a superfluid helium bath to a temperature of $T = 1.8\,\mathrm{K}$. This temperature is below the superfluid transition at 2.2 K, which mitigates vibrational noise from the bubbling of gaseous helium. Dissipation of the pump mode increases the temperature of the cavity walls slightly above that of the helium bath, but we neglect this since the typical temperature change is small, of order 0.1 K [140]. For reference, a 1 m^3 cavity operating at GHz with $B_0 \sim 0.2$ T dissipates $P_{\rm loss} \sim 10$ W $-$ 1 kW for $Q_{\rm int} \sim 10^{12} - 10^{10}$.

The signal is to be read out with an amplifier coupled to the resonant cavity. We assume that amplifier noise can be reduced to its standard quantum limit, resulting in one photon of power per unit bandwidth [141, 142]. One half of this power is due to quantum zero-point fluctuations, while the other half accounts for the backaction and imprecision noise associated with the amplifier [143]. The corresponding noise power can be described as a spectrally flat PSD of the form

$$S_{\rm ql}(\omega) = \pi\omega_1\,. \tag{2.31}$$

This assumption is equivalent to that made for other experiments targeting similar axion parameter space [115] and has been achieved in practice at GHz frequencies [9]. For context, at critical coupling, amplifier noise is smaller than thermal noise by a factor of the thermal occupation number, $n_{\rm occ} = T/\omega_1 \sim 100$.

Overcoupling the cavity to the readout can enhance the reach of a thermal noise limited search [115]. Intuitively, this is possible since a quantum-limited readout has an effective noise temperature given by a single photon of noise per unit bandwidth ($T_{\rm eff} \sim \omega_1 \sim 10$ mK $\ll 1.8\,$K), and so overcoupling lowers the effective noise temperature of the system. Similar statements can be made when other noise sources dominate. We discuss these aspects in more detail in Section 2.6 and Appendix 2.10.

2.5.2 Oscillator Phase Noise

The pump mode is excited by driving a waveguide at frequency ω_0 with an external oscillator. The loading waveguide possesses a geometric coupling to the pump mode $\epsilon_{0\rm d} \simeq 1$ and is adjusted to have a small coupling to the signal mode, $\epsilon_{1\rm d} \ll 1$. Similarly, the signal is detected through a readout waveguide, which is adjusted to have a small coupling to the pump mode, $\epsilon_{0\rm r} \ll 1$. Since minimizing the unwanted geometric couplings $\varepsilon_{1\rm d}$ and $\varepsilon_{0\rm r}$ requires precisely controlling the geometry of the two waveguides, we take $\varepsilon_{1\rm d} \simeq \varepsilon_{0\rm r}$. The mechanical precision required to achieve a certain rejection value is discussed further in Appendix 2.9.

The oscillator is centered around the frequency ω_0, but is broadened due to fluctuations in the amplitude and phase of its output voltage, which can be parametrized as

$$V_{\rm osc}(t) = V_0\,(1+\alpha(t))\cos(\omega_0 t + \varphi(t))\,. \tag{2.32}$$

The PSD of the amplitude noise $S_\alpha(\omega)$ typically has flat (white) and $1/\omega$ components, the latter due to so-called "flicker noise." The PSD of the phase noise $S_\varphi(\omega)$ has additional $1/\omega^2$ and $1/\omega^3$ components due to the Leeson effect, whose effects dominate over amplitude noise for the small frequency splittings that we consider [144, 145]. The component of $V_{\rm osc}(t)$ at frequency ω_1 can be inadvertently read out as signal through the coupling $\epsilon_{1\rm d}$ or $\epsilon_{0\rm r}$.

Oscillator manufacturers typically report the one-sideband noise power per unit bandwidth, relative to the carrier power. From this we extract the phase noise PSD $S_\varphi(\omega)$. We fit the reported spectrum of a low-noise commercially available oscillator [146] to the functional form

$$S_\varphi(\omega) = \sum_{n=0}^{3} b_n\,\omega^{-n}\,, \tag{2.33}$$

yielding the values

$$b_0 = 10^{-16}\ {\rm Hz}^{-1}\ ,\ b_1 = 10^{-9}\ ,\ b_2 = 10^{-6}\ {\rm Hz}\ ,\ b_3 = 10^{-5}\ {\rm Hz}^2\ . \tag{2.34}$$

Defining the total power input to the cavity as

$$P_{\rm in} = \frac{\omega_0}{Q_0}\,B_0^2 V\,, \tag{2.35}$$

the PSD due to oscillator phase noise is given by

$$S_{\rm phase}(\omega) \simeq \frac{1}{2}\,\varepsilon_{\rm 1d}^2\, S_\varphi(\omega-\omega_0)\,\frac{(\omega\,\omega_1/Q_1)^2}{(\omega^2-\omega_1^2)^2+(\omega\,\omega_1/Q_1)^2}\,\frac{\omega_0 Q_1}{\omega_1 Q_0}\,P_{\rm in}\,. \tag{2.36}$$

Note that because the width ω_0/Q_0 of the pump mode is much smaller than the axion mass $m_a = \omega_1 - \omega_0$ for all parameters we consider, the noise due to the coupling $\epsilon_{0\rm r}$ is suppressed by the Breit–Wigner tail of the pump mode, $(\omega_0/m_a Q_0)^2 \ll 1$, and is hence negligible. Taking $S_\varphi(\omega)$ to be spectrally flat within the signal mode bandwidth, which is a good approximation for all parameters shown in Figure 2.2, the above PSD corresponds to an average total noise power of

$$P_{\rm phase} \simeq \frac{\varepsilon_{\rm 1d}^2\, S_\varphi(m_a)}{16\pi}\,\frac{\omega_0}{Q_0}\,P_{\rm in}\,. \tag{2.37}$$

Projected sensitivities are shown in Figure 2.2 for $\varepsilon_{\rm 1d} = 10^{-5}$, 10^{-7}. Geometric rejections at the level of $\mathcal{O}(10^{-7})$ have been experimentally demonstrated in Refs. [130, 132] for a different signal and pump mode geometry. As discussed in greater detail in Appendix 2.9, achieving $\epsilon_{\rm 1d} = 10^{-7}$ in our setup requires controlling the cavity components at the few nm level, which is a level of precision that is already envisioned for other applications [139]. For such small rejection factors, $\epsilon_{\rm 1d}$ scales linearly with this distance scale. As shown in Figure 2.4, we find that phase noise is subdominant compared to thermal noise for the largest axion masses that we consider, while it dominates at smaller masses.

2.5.3 Mechanical Vibration Noise

Mechanical oscillations of the cavity boundaries lead to time-dependent shifts in the resonant modes and their corresponding frequencies. Such perturbations can impede the ability to reliably scan over the axion mass range and may also induce transitions between the pump and signal modes, thus constituting a potential background to the axion-induced signal. Various forces can contribute to mechanical noise such as thermal excitations of the cavity, external vibrations from the cryogenic cooling system or seismic activity, and radiation pressure due to the electromagnetic energy stored in the loaded mode. Of these sources, the last is negligible, because it does not source significant vibrations at frequency $\mathcal{O}(m_a)$. Instead, its dominant effect is to introduce a static shift in the cavity mode frequencies, known in the accelerator community as "Lorentz force detuning," which we may simply absorb into the definitions of ω_0 and ω_1.[14] Thermal effects are irreducible but, as we will argue below, subdominant, while power from external sources can be significantly attenuated through active feedback or isolation of the suspended cavity from its immediate surroundings.

To estimate both thermal and vibrational effects, we follow the discussion in Ref. [131]. The

[14] Note that precise knowledge of the central pump and signal mode frequencies is necessary to conduct a search for the axion-induced transition. This can be achieved by active monitoring. Maintaining the stability of mode frequencies within their bandwidth has been demonstrated in SRF cavities over timescales of a few minutes longer than our longest integration time [147].

displacement of the cavity wall from its equilibrium position, denoted as $\boldsymbol{u}(\mathbf{x}, t)$, can be decomposed as a sum over the various dimensionless mechanical normal modes of the cavity, $\boldsymbol{\xi}_\alpha(\mathbf{x})$,

$$\boldsymbol{u}(\mathbf{x}, t) = q_\alpha(t)\, \boldsymbol{\xi}_\alpha(\mathbf{x}) \ , \tag{2.38}$$

where the expansion coefficients are given by the time-dependent generalized coordinates, $q_\alpha(t)$, and a sum over the integer α is implied. The mode vectors are normalized such that

$$\int d^3\mathbf{x}\ \rho(\mathbf{x})\ (\boldsymbol{\xi}_\alpha \cdot \boldsymbol{\xi}_\beta) = M\, \delta_{\alpha\beta} \ , \tag{2.39}$$

where ρ and M are the mass density and total mass of the cavity, respectively. In the following, we focus on an individual mechanical resonance, labeled by $\alpha = m$. The noise power from multiple resonances can be summed, but in most cases only the nearest resonance will be relevant. The response of the generalized coordinate of the cavity boundary is described by the PSD,

$$S_{q_m}(\omega) \simeq \frac{1}{M^2}\ \frac{S_{f_m}(\omega)}{(\omega^2 - \omega_m^2)^2 + (\omega_m \omega / Q_m)^2} \ , \tag{2.40}$$

where ω_m is the resonant frequency of the excited mechanical mode, Q_m is the mechanical quality factor, and f_m is the force projected onto mode $\alpha = m$. In our estimates, we adopt $Q_m = 10^3$ as a representative value [132]. The force term on the right-hand side of Eq. (2.40) contains contributions from radiation pressure, thermal fluctuations, and other environmental sources.

The force generated from thermal fluctuations is negligible compared to seismic or cryogenic noise for realistic attenuation capabilities. For the cavity parameters we consider, thermal vibrations source $S_{f_m^{\rm th}}(\omega) \sim 10^{-23}\ \mathrm{N}^2/\mathrm{Hz} \times (M/\mathrm{kg})\,(T/\mathrm{K})\,(\omega_m/\mathrm{kHz})\,\left(10^3/Q_m\right)$, while, e.g., the authors of Ref. [132] directly measured the *unattenuated* force PSD for a similar resonant cavity design and found values spanning from $\mathcal{O}(10^{-7})\ \mathrm{N}^2/\mathrm{Hz} - \mathcal{O}(10^{-3})\ \mathrm{N}^2/\mathrm{Hz}$ within the measured frequency range of $10\ \mathrm{Hz} - 10\ \mathrm{kHz}$, stemming from vibrations of the surrounding environment. For realistic attenuation factors, the latter vibrational sources are dominant.

Rather than directly reporting an attenuated external force PSD, experiments frequently characterize mechanical noise by the RMS wall displacement $q_{\rm rms}$ induced by these forces. For example, near-term light-shining-through-wall type experiments at FNAL plan on controlling wall displacements of loaded cavities to within sub-nanometer precision through the use of piezo-actuator tuners [139]. To infer a force PSD from this level of vibration, we note that Eq. (2.40) implies an RMS displacement of the m'th normal mode

$$\langle q_m^2 \rangle \simeq \frac{S_{f_m}(\omega_m)\, Q_m}{4\pi\, M^2\, \omega_m^3} \sim 10^6\ \mathrm{nm}^2 \times \left(\frac{S_{f_m}(\omega_m)}{10^{-4}\ \mathrm{N}^2\ \mathrm{Hz}^{-1}}\right) \left(\frac{Q_m}{10^3}\right) \left(\frac{M}{\mathrm{kg}}\right)^{-2} \left(\frac{\omega_m}{\mathrm{kHz}}\right)^{-3} \ . \tag{2.41}$$

The scaling with ω_m implies that, for an approximately flat $S_{f_m}(\omega)$, $\langle q_m^2 \rangle$ is largest for the lowest-frequency mechanical mode. Thus, we normalize the attenuated force PSD to

$$S_{f_m} \simeq 4\pi\, M^2\, \omega_{\rm min}^3\, q_{\rm rms}^2 / Q_m \ , \tag{2.42}$$

where $q_{\rm rms} \sim 0.1$ nm and $\omega_{\rm min} \sim$ kHz is the lowest-lying mechanical resonance of the cavity. This estimate of $\omega_{\rm min}$ is motivated by the measurements of a similar apparatus to search for gravitational waves, which showed a growing number of mechanical resonances above $\omega \sim 0.5$ kHz [130]. Hence, we will assume that externally sourced vibrations are controlled to $\langle q_m^2 \rangle \sim (0.1\ {\rm nm})^2$, which from Eq. (2.41) implies an attenuation ability of $\mathcal{O}(10^{-8})$. Note that even assuming a considerably worse control of the cavity walls, $q_{\rm rms} \sim 10^2\ \mu$m, the estimated sensitivity at large axion masses, and in particular the ability to probe the QCD axion, is not appreciably affected, as shown in Figure 2.5.

These mechanical vibrations couple to the electromagnetic cavity modes by, e.g., shifting their resonant frequencies,

$$\delta\omega_n(t) \simeq -\frac{1}{2}\, q_m(t)\, C_n^m\, \omega_n \ , \tag{2.43}$$

where the coupling coefficients, C_n^m, are given in terms of the electromagnetic modes,[15]

$$C_n^m = \frac{\int d\mathbf{S} \cdot \boldsymbol{\xi}_m(\mathbf{x})\ \left(|\mathbf{B}_n(\mathbf{x})|^2 - |\mathbf{E}_n(\mathbf{x})|^2\right)}{\int d^3\mathbf{x}\ |\mathbf{E}_n(\mathbf{x})|^2} \ . \tag{2.44}$$

In the numerator of Eq. (2.44), the integral is performed over the surface boundary of the deformed cavity. Note that the size of the coupling coefficient C_n^m, and hence also the frequency shift of Eq. (2.43), depends on the specific nature of the mechanical and electromagnetic resonances of the unperturbed cavity. We will pessimistically assume maximum overlap between the mechanical and electromagnetic modes, in which case the coupling coefficient is parametrically of size $C_n^m \sim V^{-1/3}$, where V is the geometric volume of the cavity.

The shift in the cavity mode frequencies in Eq. (2.43) results in a modification of the equation of motion for a mode (labeled n) driven by an external field $\mathbf{D}(t, \mathbf{r})$,

$$\left[\partial_t^2 + \frac{\omega_n}{Q_n}\, \partial_t + (\omega_n + \delta\omega_n)^2\right] \mathbf{B}_n(t, \mathbf{r}) = \omega_n^2\, \mathbf{D}(t, \mathbf{r}) \ . \tag{2.45}$$

When the time-dependent shifts in the cavity mode frequencies are small, we can perturbatively solve the above equation to find the noise PSD due to vibrations of the cavity walls, $S_{\rm mech}(\omega)$. To

[15] We have assumed that the off-diagonal generalizations of the coupling coefficient involving pairs of distinct electromagnetic modes vanish to leading order in the cavity perturbation. We have checked that this is satisfied for various nearly-degenerate modes of cylindrical cavities, which have orthogonal $\mathbf{E}$ and $\mathbf{B}$ fields at every point in space. If this is not the case, additional source terms in the coupled electromagnetic-mechanical equations of motion should be included. See Ref. [131] for additional details.

leading order in $\delta\omega_n^2/\omega_n^2 \ll 1$, we find

$$S_{\rm mech}(\omega) = \sum_{n=0,1} S_{\rm mech}^{(n)}(\omega) \tag{2.46}$$

$$\simeq \frac{\varepsilon_{1d}^2}{4}\frac{\omega_0}{Q_0} P_{\rm in} \sum_{n=0,1} \frac{\left(S_{q_m}(\omega-\omega_0)/V^{2/3}\right)(\omega_n/Q_n)\,\omega_n^4\,\omega^2}{\left[(\omega^2-\omega_n^2)^2+(\omega\,\omega_n/Q_n)^2\right]\left[(\omega_0^2-\omega_n^2)^2+(\omega_0\,\omega_n/Q_n)^2\right]}\,, \tag{2.47}$$

where the sum is over the pump ($n = 0$) and signal ($n = 1$) modes. To understand Eq. (2.47) parametrically, we note that for $m_a \simeq \omega_m$ and $\omega_m/Q_m \ll \omega_n/Q_n$, evaluating $S_{\rm mech}(\omega)$ near the positive frequency resonance ($\omega \simeq \omega_1$) and applying Eqs. (2.40) and (2.41) yields

$$S_{\rm mech}(\omega_1+\Delta\omega) \simeq \frac{\pi}{2}\frac{\varepsilon_{1d}^2\,Q_m}{1+(\Delta\omega/\Delta\omega_m)^2}\frac{\omega_1^2\omega_{\rm min}^3}{m_a^6}\frac{q_{\rm rms}^2}{V^{2/3}}P_{\rm in}\,, \tag{2.48}$$

where we defined the width of the mechanical mode $\Delta\omega_m \equiv \omega_m/2Q_m$.

In the coupled superconducting cavity setup of Ref. [130], direct probes of the designed apparatus revealed the presence of mechanical resonances above $\omega_{\rm min} \sim$ kHz, separated in frequency by $\mathcal{O}(100)$ Hz. For $m_a < \omega_{\rm min}$, mechanical noise is driven by the tail of the lowest-frequency resonance. In this regime, the scaling of mechanical noise is dominated by the cavity's response to an off-resonance driving force, as expected from the form of Eqs. (2.40) and (2.47). Therefore, the noise power scales as roughly $1/m_a^2$. As shown in Figure 2.4, mechanical noise is significant in this mass range and is roughly comparable to oscillator phase noise.

The behavior of mechanical noise in the vicinity of resonances is more subtle, and so merits further discussion. Eqs. (2.40) and (2.47) imply that the power in mechanical noise is maximized for $\omega_m \simeq \omega_1 - \omega_0$. Thus, in a scan over ω_1, the mechanical noise PSD has a forest of local maxima around each resonance $\omega_0 + \omega_m$, with minima in between. In Figure 2.3, we bound the total power in mechanical noise for $m_a > \omega_{\rm min}$ by considering two cases: where the axion mass is situated at or near a local maximum of the noise PSD ($m_a \simeq \omega_m$ for some mechanical resonance m), or at a local minimum (m_a at the midpoint between two adjacent resonances, i.e., assuming a typical separation of ~ 100 Hz between mechanical resonances, at 50 Hz separation from each). The total mechanical noise powers obtained in these two extreme cases, illustrated by dashed curves in Figure 2.3, define an envelope for the mechanical noise power at each scan step. The envelope spans 3 orders of magnitude in noise power, due to the sharpness of the mechanical resonances, but for the same reason, the noise power only approaches the upper envelope in narrow regions of size $\Delta\omega_m$ about each resonance.

For a more representative characterization of the mechanical noise near resonances, we note that in a scan over the range of candidate axion masses between any two resonances, the median noise PSD is that obtained at 25 Hz separation from the nearest mechanical resonance. The total mechanical noise power at this separation is indicated by the solid blue curve in Figure 2.3, and this characteristic noise power is used in deriving the axion sensitivity curves. In a single scan, half of

candidate axion masses are expected to have noise above this line (and hence weaker sensitivity) and half below (and hence stronger sensitivity). It may also be possible to fill these narrow gaps in sensitivity by using two cavities with slight mechanical variations, so that their mechanical resonance frequencies are slightly offset. In this case, each candidate axion mass will be well-separated from the mechanical resonances of at least one of the two cavities.

Near-resonance mechanical noise is only expected to dominate over about one decade in axion mass near angular frequencies of 1 kHz $-$ 10 kHz. At lower frequencies there are no nearby resonances, and mechanical noise falls off rapidly at higher frequencies. These two effects lead to a peak-like structure near $m_a = 1$ kHz in Figure 2.4, and corresponding dips in the reach shown in Figures 2.2 and 2.5. The strength and position of this feature should be appropriately rescaled by $\omega_{\rm min}$ for cavities with higher- or lower-lying resonances.

For $m_a \ll$ MHz, where mechanical noise is important, the integral of Eq. (2.47) over the signal bandwidth is analytically tractable for the pessimistic case of a mechanical resonance very closely spaced to $\omega_1 - \omega_0 \simeq m_a$. Taking the mechanical resonance to be narrower than the cavity bandwidth and further approximating $Q_0 \simeq Q_1$ and $m_a \ll \omega_0$, the average total noise power in mechanical noise is

$$P_{\rm mech} \simeq \frac{\varepsilon_{1d}^2}{16} \frac{\omega_0^2\, \omega_{\rm min}^3}{m_a^5} \frac{q_{\rm rms}^2}{V^{2/3}} P_{\rm in}\,. \tag{2.49}$$

We emphasize that the mechanical noise estimates presented above are most likely overly pessimistic. In particular, we assumed that for every axion mass $\gtrsim$ kHz there is a corresponding resonant mechanical mode that is maximally coupled to the electromagnetic properties of the cavity. In this sense, a dedicated design strategy could potentially significantly mitigate noise from mechanical vibrations.

2.5.4 Field Emission

At high surface electric fields, electrons are emitted from imperfections on the walls of the SRF cavity. The released electrons accelerate to relativistic speeds, absorbing energy from the cavity field, and typically are reabsorbed into the wall within less than one oscillation cycle of the cavity. They emit radiation in three different stages: as they accelerate inside the cavity and emit synchrotron radiation; as they encounter the dielectric mismatch between the interior and wall of the cavity, leading to transition radiation; and as they encounter the nuclear electric fields of the wall material, leading to Bremsstrahlung radiation.

In this section, we crudely approximate the noise due to each process. First, we note that for an electron of energy γm_e, all three processes produce radiation in a small solid angle $1/\gamma^2$ around the electron momentum, spread roughly uniformly over a frequency range much broader than the signal mode bandwidth. Hence, only a small fraction of the power absorbed by the emitted electrons is deposited in the signal mode.

The energy absorbed by a single electron as it traverses a cavity of length $L \sim 1/\omega_0 \sim 1\,\mathrm{m}$ and average electric field of strength $E_0 \sim cB_0 = 60\,\mathrm{MV/m}$ is roughly $U_{\mathrm{abs}} \sim eE_0L$, corresponding to a Lorentz factor of $\gamma \sim 100$. This energy is then released through the three processes described above. The energy released as synchrotron radiation and the corresponding frequency range are

$$U_{\mathrm{sync}} \sim \frac{e^4\gamma^2 E_0^2 L}{m_{\mathrm{e}}^2}\,, \quad \Delta\omega_{\mathrm{sync}} \gtrsim \omega_0\,, \tag{2.50}$$

where the frequency range is determined by the short timescale $t_{\mathrm{sync}} \sim 1/\omega_0$ over which the electron is within the cavity. The energy released in transition radiation depends on the plasma frequency of the wall material, which for niobium is $\omega_p \sim 50\,\mathrm{eV}$. The spectrum of the produced radiation is relatively flat, and the total energy released and the corresponding frequency range are [148]

$$U_{\mathrm{trans}} \sim e^2\gamma\omega_p\,, \quad \Delta\omega_{\mathrm{trans}} \sim \gamma\omega_p\,. \tag{2.51}$$

Finally, as the electron travels inside the cavity wall, the remaining energy is released through losses inside the material. Since both U_{sync} and U_{trans} are both much smaller than U_{abs}, almost all the absorbed energy is released inside the wall. We assume that all of the energy is converted into photons via Bremsstrahlung, that all of these photons are released into the body of the cavity, and that the spectrum of the radiation is approximately flat, giving

$$U_{\mathrm{brem}} \sim eE_0L\,, \quad \Delta\omega_{\mathrm{brem}} \sim \gamma m_{\mathrm{e}}\,. \tag{2.52}$$

In reality, the release of energy in the walls is a complex process, which our assumptions model only very crudely. Our first two assumptions are very pessimistic, while our third assumption is optimistic, as a relativistic electron will create showers of softer electrons which release energy within a smaller frequency range. However, in any case, we will find that the noise PSD due to Bremsstrahlung is subdominant by several orders of magnitude.

We can use these results to evaluate the noise PSD, normalized to the total power loss P_{tot} due to field emission. For concreteness, we compare the three contributions to the typical PSD for thermal noise. Accounting for the small geometric overlap factor $1/\gamma^2$, the PSDs are

$$S_i(\omega) \sim P_{\mathrm{tot}}\,\frac{U_i}{U_{\mathrm{abs}}}\,\frac{1}{\gamma^2\Delta\omega_i}\,, \tag{2.53}$$

where P_{tot} is the total power loss due to field emission. Numerically, we have

$$\frac{S(\omega_1)}{4\pi T} \sim \frac{P_{\mathrm{tot}}}{0.1\,\mathrm{W}} \times \begin{cases} 1 & \text{synchrotron} \\ 10^{-6} & \text{transition} \\ 10^{-5} & \text{Bremsstrahlung}\,, \end{cases} \tag{2.54}$$

so that for field emission to be negligible compared to thermal noise, we require $P_{\rm tot} \lesssim 0.1\,\mathrm{W}$. For context, this corresponds to $\mathcal{O}(100)$ electrons emitted per cycle, or about 0.1% of the total energy loss for a cavity with $Q_{\rm int} = 10^{12}$.

In practice, the rate of field emission is set by the shapes of each cavity's particular defects, which determine the local enhancement of the electric field. Since it is a tunneling effect, the electric current due to a given defect has a strong exponential dependence on the field, $I \sim \exp(-1/\beta E)$, where β depends on the geometry of the defect [149]. As such, field emission from a defect is essentially zero for lower fields, then sharply increases at a certain threshold field value. Modern cavity fabrication techniques can produce cavities where field emission is a small source of energy loss (defined as $P_{\rm tot} < 10\,\mathrm{W}$) up to peak surface electric fields beyond $\sim 60\,\mathrm{MV/m}$. Moreover, in many cases, field emission is not even detectable for peak surface fields of this magnitude [150, 140].

Given this background, the relevance of field emission to our setup depends sensitively on the design. For the cylindrical cavity modes discussed in Section 2.4, the peak surface electric fields are several times smaller than the typical fields $E_0 \sim 60\,\mathrm{MV/m}$, making field emission a completely negligible effect. However, the use of retractable fins to tune the frequency difference would create a sharp feature within the cavity and hence a local enhancement of the surface field. As discussed in Section 2.4, we are sensitive to a wide range of motivated parameter space even without the implementation of fins; we defer further discussion of field emission in this setting to a future detailed study of the experimental design. In particular, both field emission and the resulting synchrotron radiation can be simulated more precisely using existing dedicated numeric programs.

Finally, it is worth mentioning other well-known effects associated with SRF cavities. The cavity must be designed and manufactured to manage well-understood problems such as multipacting and thermal breakdown [149, 140]. Another physical effect to consider is nonlinearity in the response of the cavity walls to the pump mode fields, which could produce radiation with frequency at integer multiples of ω_0. However, this is not relevant for our setup because the signal mode frequency ω_1 is not close to any of these multiples; instead we have $\omega_1 \simeq \omega_0$.

2.6 Physics Reach

With our noise estimates in place, we now compute the conceptual reach of our setup. The signal PSD for the readout is slightly modified from that of Eq. (2.20) because the readout receives a fraction $Q_1/Q_{\rm cpl}$ of the power delivered to the cavity, where Q_1 and $Q_{\rm cpl}$ are related by Eq. (2.28). Referring to Eq. (2.23), we therefore make the replacement

$$S_{\rm sig}(\omega) \to \frac{Q_1}{Q_{\rm cpl}}\, S_{\rm sig}(\omega)\,. \tag{2.55}$$

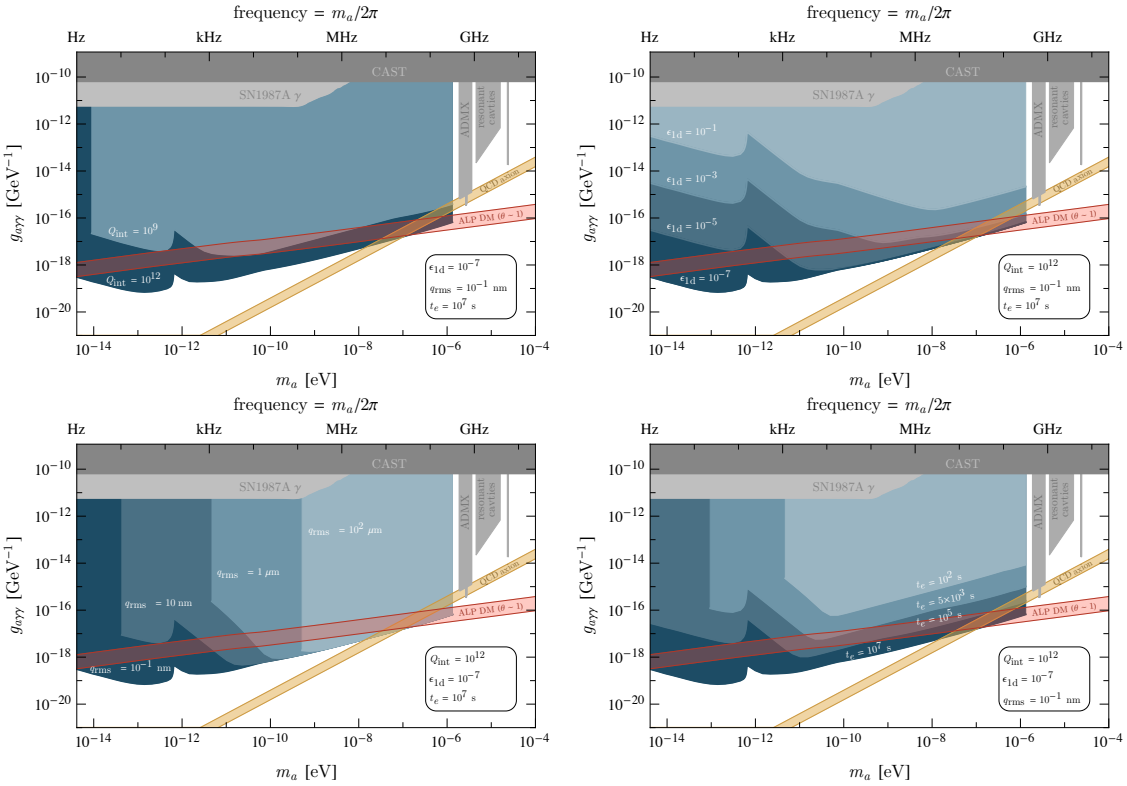

Figure 2.5: The anticipated reach to axion dark matter in the $g_{a\gamma\gamma} - m_a$ plane, for a wide range of experimental parameters. Our baseline parameters are those of the lower curve of Figure 2.2, including $Q_{\rm int} = 10^{12}$, $\varepsilon_{\rm 1d} = 10^{-7}$, $q_{\rm rms} = 10^{-1}$ nm, and $t_e = 10^7$ s. In each panel, we vary one of these four parameters, while keeping the others fixed. All other features of the figures are as explained in Figure 2.2. Throughout, we only consider axion masses for which the integration time for a single scan step $t_{\rm int}$ is larger than the axion coherence time and cavity ring-up time, and axion masses that are greater than the typical frequency shift due to mechanical vibrations.

This is to be compared to the total noise PSD for the readout,

$$S_{\rm noise}(\omega) = S_{\rm ql}(\omega) + \frac{Q_1}{Q_{\rm cpl}}\left(S_{\rm th}(\omega) + S_{\rm phase}(\omega) + S^{(1)}_{\rm mech}(\omega)\right) + \frac{Q_0}{Q_{\rm cpl}}\, S^{(0)}_{\rm mech}(\omega)\,, \tag{2.56}$$

where we do not include field emission noise (see Eq. (2.54)) because it can be kept below thermal noise for cylindrical cavities. Amplifier noise does not receive a factor of $Q_1/Q_{\rm cpl}$ because it is intrinsic to the amplifier itself. The last term in Eq. (2.56) corresponds to the pump mode contribution to mechanical noise (see Eq. (2.47)), which is rescaled by $Q_0/Q_{\rm cpl}$ since it arises from the pump mode readout coupling.

At this point, one can see why it can be advantageous to overcouple: referring to Eqs. (2.29) and (2.36), the signal, thermal noise, and phase noise PSDs are all proportional to $Q_1^2/Q_{\rm cpl}$. Therefore, if either of these noise sources dominates, overcoupling ($Q_{\rm cpl} \simeq Q_1 \ll Q_{\rm int}$) preserves the ratio $S_{\rm sig}(\omega)/S_{\rm noise}(\omega)$ but broadens the frequency range that a scan step is sensitive to, relative to critical coupling ($Q_{\rm cpl} = Q_{\rm int}$).

We now describe the scan optimization. For a scan step with integration time $t_{\rm int}$, the noise power is independent between frequency bins of width $\sim 2\pi/t_{\rm int}$. Each bin thus has an independent SNR, and the bins may be combined by a weighted average. The optimal weighting leads to an overall SNR that is the sum of the SNRs of the bins in quadrature [151]. As in Section 2.3, we assume that $t_{\rm int} > \max(\tau_{\rm r}, \tau_a)$, where $\tau_{\rm r}$ is the ring-up time of the overcoupled signal mode, and hence that the variation of $S_{\rm sig}(\omega)/S_{\rm noise}(\omega)$ is on frequency scales greater than $1/t_{\rm int}$. As a result, the SNR can be approximated as an integral over frequency,

$$({\rm SNR})^2 \simeq t_{\rm int} \int_0^\infty \frac{d\omega}{2\pi} \left(\frac{S_{\rm sig}(\omega)}{S_{\rm noise}(\omega)}\right)^2 , \tag{2.57}$$

where only positive frequencies are included, since the signal and noise PSDs are symmetric in ω.

We assume that a scan is performed uniformly in $\log m_a$, allocating a time t_e for each e-fold in axion mass. It is optimal to scan in steps as wide as possible, as time must be spent waiting for the signal to ring up during each step. We take the width $\Delta\omega_{\rm sc}$ of a single scan step to be set by the range of axion masses near $\omega_1 - \omega_0$ within which the expected SNR, as given by Eq. (2.57), is within an $\mathcal{O}(1)$ factor of the maximal value. Parametrically, this implies

$$\Delta\omega_{\rm sc} \sim \max(m_a/Q_a\,,\, \omega_1/Q_1)\,. \tag{2.58}$$

This step size in turn sets the integration time allowed for each scan step to be

$$t_{\rm int} \simeq t_e\, \frac{\Delta\omega_{\rm sc}}{m_a}\,. \tag{2.59}$$

For each scan step, we numerically optimize the SNR as given by Eq. (2.57) with respect to the

coupling $Q_{\rm cpl}$, subject to the constraint $t_{\rm int} > \max(\tau_{\rm r}, \tau_a)$, and determine the reach by demanding SNR $\gtrsim 1$. The largest $t_{\rm int}$ values we consider are $\mathcal{O}(100)$ s. The stability of frequencies within their bandwidths on timescales of a few minutes has been demonstrated in an SRF cavity in Ref. [147]. As discussed in Section 2.3, we model the axion PSD as following a virialized Maxwellian distribution.

For concreteness, consider the case where thermal noise dominates and the next most important contribution is amplifier noise; this occurs at the largest axion masses shown in Figures 2.2, 2.4, and 2.5. As discussed further in Appendix 2.10, Eq. (2.57) reduces to the usual Dicke radiometer equation [152], and it is optimal to overcouple until the thermal noise is reduced to the quantum noise floor. This requires setting $Q_{\rm cpl} \sim Q_{\rm int}/n_{\rm occ}$ where $n_{\rm occ} \sim T/\omega_1$ is the thermal occupation number, which leads to an enhancement of the SNR by a factor of $n_{\rm occ}^{1/2}$ relative to critical coupling. In this case, the SNR is then, parametrically,

$$\text{SNR} \sim \frac{\rho_{\rm DM}\, V}{m_a\, \omega_1} \left(g_{a\gamma\gamma}\, \eta_{10}\, B_0\right)^2 \left(\frac{Q_a\, Q_{\rm int}\, t_e}{T}\right)^{1/2} . \tag{2.60}$$

For comparison, a similar analysis applied to a static-field LC resonator yields

$$\text{SNR}^{(\rm LC)} \sim \rho_{\rm DM}\, V^{5/3} \left(g_{a\gamma\gamma}\, B_{\rm LC}\right)^2 \left(\frac{Q_a\, Q_{\rm LC}\, t_e}{T_{\rm LC}}\right)^{1/2} . \tag{2.61}$$

Our setup benefits from a large intrinsic quality factor $Q_{\rm int}$ because it reduces dissipation in the cavity and hence thermal noise. As a result, for both our setup and LC resonators, the SNR continues to increase with $Q_{\rm int}$ even after the signal power saturates, in agreement with the conclusions of Ref. [151]. However, for a fixed operational temperature and e-fold time, it is not useful to increase the intrinsic quality factor to arbitrarily large values, as there will be insufficient time to fully ring up the signal. For our choice of $t_e \sim 10^7$ s and $T \sim$ K, this occurs when $Q_{\rm int} \sim 10^{13}$. We also note that the SNR for our setup in Eq. (2.60) is in principle valid for $m_a \gtrsim$ GHz. However, in this regime we have no parametric advantage over existing cavity haloscopes, and accordingly our reach falls off rapidly due to the factor of $\omega_1 \simeq \omega_0 + m_a$ in the denominator.

The optimized reach is shown in Figure 2.2 for two baselines choices of experimental parameters and in Figure 2.5 for a larger set of variations. In both figures, we also show existing exclusions from cavity haloscopes [7, 8, 9, 10, 12, 13, 14], helioscopes [4, 153, 154, 155], and observations of SN1987A [16, 17]. We highlight parameter space that is motivated by the QCD axion as a solution to the strong CP problem, corresponding to a range bounded by the DFSZ [102, 103] and KSVZ [104, 105, 106] models. We also highlight regions of parameter space where an axion-like particle with temperature-independent mass m_a acquires a cosmological abundance from the misalignment mechanism that is in agreement with the observed DM energy density. This occurs if the initial field amplitude at the onset of oscillation is $a_i \sim (T_{\rm eq}^2 m_{\rm pl}^3/m_a)^{1/4}$, where $T_{\rm eq} \sim$ eV is the temperature at matter-radiation equality and $m_{\rm pl}$ is the Planck mass. Defining the initial

misalignment angle as $\theta_i \equiv a_i/f_a$ and relating the axion decay constant to its photon coupling by $g_{a\gamma\gamma} \sim \alpha_{\rm em}/2\pi f_a$, we find

$$g_{a\gamma\gamma} \sim \frac{\alpha_{\rm em}}{2\pi}\left(\frac{m_a}{m_{\rm pl}^3\, T_{\rm eq}^2}\right)^{1/4}\theta_i \sim 10^{-16}\ {\rm GeV}^{-1}\left(\frac{m_a}{\mu{\rm eV}}\right)^{1/4}\theta_i\,. \tag{2.62}$$

This relation, along with the parametric expectation $\theta_i \sim 1$, provides a cosmologically motivated target for axion-like particles.[16]

The projected reach covers unexplored parameter space relevant for the QCD axion for $10^{-8}\,{\rm eV} \lesssim m_a \lesssim 10^{-6}\,{\rm eV}$ and for axion-like particles as light as $m_a \sim 10^{-14}\,{\rm eV}$. The m_a dependence of the projected sensitivity can be understood as follows. Consider the upper curve of Figure 2.2, which displays all of the parametric regimes. At large axion masses, thermal noise dominates and the reach in coupling grows as $1/\sqrt{m_a}$ when m_a is decreased, as shown in Eq. (2.60). For $m_a \lesssim 10^{-10}$ eV, oscillator phase noise becomes the dominant background. The reach changes slope, degrading at smaller axion masses because the signal frequency is closer to the pump mode frequency, where the pump mode power is concentrated. At even smaller axion masses, mechanical vibrations become the dominant source of noise, accounting for the change in slope of the reach curve around $m_a \sim 10^{-11}$ eV. This is due to the rapid increase of the mechanical noise power, as shown in Eq. (2.49). Near $m_a \simeq {\rm kHz} \simeq 10^{-12}$ eV, mechanical noise decreases, as discussed in Section 2.5.3, because of the absence of mechanical resonances below 1 kHz. This result is in agreement with the experimental characterization of similar cavities performed in Ref. [130].

This general description also applies to the four panels of Figure 2.5, which are intended to demonstrate the robustness of our approach. The mass dependence of the reach is qualitatively similar, except that not all of the noise regimes are always realized. For instance, in the lower left panel, oscillator phase noise never dominates over mechanical noise if $q_{\rm rms}$ is large. Figure 2.5 shows that, as long as a large intrinsic quality factor is maintained, our approach is still sensitive to the QCD axion, even if one degrades the geometric rejection factor by 10^4, shortens the e-fold time by 10^2, or increases the amplitude of the wall vibrations by 10^6. In all cases, our approach also still has the potential to cover a wide range of parameter space motivated by axion-like particle DM.

In Figures 2.2 and 2.5, the projected sensitivity of our setup is not shown for $m_a \lesssim$ Hz; this corresponds to the level of frequency (and frequency splitting) control with current technology [139]. As discussed in Sections 2.4 and 2.5.3, this corresponds to controlling the displacement of cavity walls at the ~ 0.1 nm level, allowing for scanning steps as small as $\sim 0.1\ {\rm Hz} - 1\ {\rm Hz}$. Furthermore, our calculation is not valid at these small masses where the axion oscillates less than once per ring-up time. We also refrain from considering axion masses less than $\omega_1\,(q_{\rm rms}/V^{1/3})$, since sizable

[16] Additional dynamics or interactions in the early Universe can allow for axion-like particles to be viable DM candidates in a much larger range of $g_{a\gamma\gamma} - m_a$, as discussed in, e.g., Refs. [156, 157, 158]. Note that for the QCD axion, the temperature-dependence of the axion mass leads to the correct relic abundance being obtained for $m_a \sim 10^{-6}$ eV [159, 160].

mechanical displacements of the cavity walls may impede the ability to scan over such axion masses in a controlled manner.

Finally, we note that in deriving our result for the signal PSD in Eq. (2.23), we treated the oscillator, and hence the pump mode magnetic field, as monochromatic. Since the axion effective current in Eq. (2.12) scales as $J_{\rm eff} \propto B\,\partial_t a$, the oscillator width is negligible so long as it is smaller than the axion width m_a/Q_a. In practice, the oscillator width is quantified by the Allan variance [144]. The phase noise discussed in Section 2.5.2 is better suited to describing the tails of the spectrum. From the manufacturer data sheet of a commercially available oscillator in Ref. [146], we conclude that the pump mode width is negligible for $m_a \gtrsim$ kHz. In a setup where the oscillator can be efficiently coupled to a precise reference clock (e.g., NIST [161]), the pump mode width is negligible in all of the parameter space we consider.

2.7 Outlook

In this chapter, we have proposed an approach to leverage the properties of SRF cavities to detect low-mass axions, with sensitivity to significant new parameter space spanning eight orders of magnitude in axion mass. As shown in Eq. (2.10) and confirmed in Eq. (2.60), our frequency conversion approach is parametrically enhanced compared to static-field LC resonators because of the larger electromotive forces attained (see Eq. (2.5)). In addition, the insights of Ref. [151], which shows that the sensitivity is optimized for a strongly overcoupled readout ($Q_1 \ll Q_{\rm int}$), allow us to take advantage of the extremely large intrinsic quality factors of SRF cavities within a reasonable scanning time.

Estimating the sensitivity of our approach required careful consideration of several noise sources. Aside from thermal noise, which can be treated relatively straightforwardly, we have pinned all of our noise estimates to quantities measured in real apparatuses. As such, we are indebted to the decades of work done on the development of quantum noise limited amplifiers, SRF cavity fabrication and testing, low phase noise oscillators, and previous precision experiments targeting both axions and gravitational waves. Ultimately, we find that for our reference parameters thermal noise is expected to dominate over most of the mass range, with vibrational noise and oscillator phase noise becoming more important at smaller masses.

We have left the detailed design of the experimental apparatus to future work. As mentioned in Sections 2.4 and 2.5.4, there may be a tradeoff between maximizing the scanning range of a single cavity, and maintaining large quality factors and suppressing field emission. However, we note that even a simple cylindrical cavity design without tuning fins can potentially cover six orders of magnitude in axion mass.

In principle, our approach is also sensitive to sub-Hz axion masses. In fact, as discussed in Section 2.3, the signal power is not parametrically suppressed even when the axion does not undergo a full oscillation within a resonator ring-up time. This leads to the intriguing possibility of probing

axion-like particles with frequencies down to mHz or even lower. In this regime, finer details involving the stabilization of the cavity modes and the width of the oscillator become relevant, and we defer a detailed analysis to future work.

Elaborations on our basic approach could be used to further enhance the sensitivity. For example, one could use correlations between two signal modes above and below that of the pump mode ($\omega_\pm \simeq \omega_0 \pm m_a$) to help distinguish the signal from noise, or use several signal modes simultaneously to accelerate the scanning. When mechanical noise dominates, two cavities with distinct mechanical resonant frequencies could be used to avoid gaps in the reach. Furthermore, variations on our approach could be sensitive to other models of ultralight bosonic dark matter, such as dilaton-like scalars that couple to the mechanical modes of the cavity. By leveraging technologies developed and proven over the past few decades, our proposal is potentially sensitive to symmetry breaking scales of up to $f_a \sim 10^{16}\,\mathrm{GeV}$, and thereby some of the highest fundamental energy scales in nature.

Note added: While this study was ongoing, we became aware of Ref. [162]*, which discusses similar ideas for axion detection.*

2.8 Appendix: Cavity Geometry and Overlap Factor

Cylindrical Cavities

The normal modes of a cylindrical cavity are grouped into TE and TM modes. We begin by reviewing facts about these modes, following the treatment in Ref. [148]. The TM modes are defined by the vanishing of the transverse electric field $\mathbf{E}_T$ at $z = 0$ and $z = L$, where L is the height of the cylinder. Thus the z component of a TM mode is defined by

$$E_z = \psi(r, \varphi) \cos\left(\frac{p\pi z}{L}\right) , \tag{2.63}$$

for a nonnegative integer p. The function ψ vanishes at the boundaries and obeys a transverse wave equation, and hence has solutions of the form

$$\psi(r, \varphi) = E_0 J_m(\gamma_{mn} r) e^{im\varphi} , \tag{2.64}$$

where $\gamma_{mn} = x_{mn}/R$, with x_{mn} being the nth zero of the mth order Bessel function $J_m(x)$, and R being the cylinder radius. The transverse electric and magnetic field components of a TM mode are

then given by

$$\mathbf{E}_T = -\frac{p\pi}{L\gamma_{mn}^2}\sin\left(\frac{p\pi z}{L}\right)\boldsymbol{\nabla}_T\psi(r,\varphi)\,, \tag{2.65}$$

$$\mathbf{B}_T = \frac{i\epsilon\mu\omega_{mnp}}{\gamma_{mn}^2}\cos\left(\frac{p\pi z}{L}\right)\,\hat{\mathbf{z}}\times\boldsymbol{\nabla}_T\psi(r,\varphi)\,, \tag{2.66}$$

where $\boldsymbol{\nabla}_T$ is the transverse part of the gradient, and $\mu\epsilon\omega_{mnp}^2 = \gamma_{mn}^2 + (p\pi/L)^2$ defines the frequency of the TM_{mnp} mode.

For TE modes, the boundary condition $B_z = 0$ at $z = 0$ and $z = L$ impose

$$B_z = \phi(r,\varphi)\sin\left(\frac{p\pi z}{L}\right)\,, \tag{2.67}$$

for a positive integer p. The function ϕ now obeys the boundary condition $\partial H_z/\partial r|_{r=R} = 0$. Here, the solutions to the transverse wave equation are

$$\phi(r,\varphi) = \mu B_0 J_m(\gamma'_{mn}r)e^{im\varphi}\,, \tag{2.68}$$

where $\gamma'_{mn} = x'_{mn}/R$, with x'_{mn} being the nth root of $J'_m(x)$. The transverse electric and magnetic field components of a TE mode are then given by

$$\mathbf{E}_T = -\frac{i\omega_{mnp}}{\mu\gamma'^{\,2}_{mn}}\sin\left(\frac{p\pi z}{L}\right)\,\hat{\mathbf{z}}\times\boldsymbol{\nabla}_T\phi(r,\varphi)\,, \tag{2.69}$$

$$\mathbf{B}_T = \frac{p\pi}{L\gamma'^{\,2}_{mn}}\cos\left(\frac{p\pi z}{L}\right)\boldsymbol{\nabla}_T\phi(r,\varphi)\,, \tag{2.70}$$

and $\omega_{mnp}^2 = \gamma'^2_{mn} + (p\pi/L)^2$ defines the frequency of the TE_{mnp} mode.

Overlap Factors for Cylindrical Cavities

In this section, we compute the normalized overlap factors defined in Eq. (2.21) for transitions between cylindrical cavity modes. From this point on, we set $\epsilon = \mu = 1$ for brevity.

We begin by deriving the selection rules quoted in Section 2.4. For a geometric overlap factor between two modes indexed by (m_0, n_0, p_0) and (m_1, n_1, p_1), the integral over z gives a factor of

$$\int_0^L \cos\left(\frac{p_0\pi z}{L}\right)\sin\left(\frac{p_1\pi z}{L}\right)dz = \frac{Lp_1}{\pi(p_1^2-p_0^2)}(1+(-1)^{p_0+p_1+1}) = \frac{Lp_1}{\pi(p_1^2-p_0^2)}\times\begin{cases}2 & p_1+p_0 \text{ odd}\\ 0 & p_1+p_0 \text{ even}\end{cases}\,, \tag{2.71}$$

while the integral over φ gives a factor of

$$\int_0^{2\pi} e^{-im_0\varphi} e^{im_1\varphi}\, d\varphi = \begin{cases} 2\pi & m_0 = m_1 \\ 0 & m_0 \neq m_1 \end{cases} . \tag{2.72}$$

Therefore, a nonzero geometric overlap factor is only possible if the selection rules $m_0 = m_1 = m$ and $p_0 + p_1$ odd are obeyed. Furthermore, TM $\leftrightarrow$ TM mode transitions always have a zero overlap integral, because for two TM modes,

$$\begin{aligned} \int_V \mathbf{E}^*_{mn_1p_1} \cdot \mathbf{B}_{mn_0p_0} &\propto \int_0^R dr\, r \left(\boldsymbol{\nabla}_T \psi^*_{mn_1p_1}(r,\varphi)\right) \cdot \left(\hat{\mathbf{z}} \times \boldsymbol{\nabla}_T \psi_{mn_0p_0}(r,\varphi)\right) \\ &\propto \int_0^R dr \left(\partial_r J_m(\gamma_{mn_1} r)\right) J_m(\gamma_{mn_0} r) + J_m(\gamma_{mn_1} r) \partial_r \left(J_m(\gamma_{mn_0} r)\right) \\ &\propto \int_0^R dr\, \partial_r \left(J_m(\gamma_{mn_1} r) J_m(\gamma_{mn_0} r)\right) \\ &= J_m(\gamma_{mn_1} R) J_m(\gamma_{mn_0} R) \\ &= 0 \end{aligned}$$

where the last line follows from the definition of γ_{mn}.

For $\mathrm{TE}_{m_1n_1p_1} \leftrightarrow \mathrm{TM}_{m_0n_0p_0}$ transitions, the overlap integral can be nonzero. Assuming the selection rules are obeyed, the overlap integral is

$$\begin{aligned} \int_V (\mathbf{E}^*_1)_{\mathrm{TE}} \cdot (\mathbf{B}_0)_{\mathrm{TM}} = B_1 E_0 &\left(\frac{\omega_{mn_1p_1}\omega_{mn_0p_0}}{(\gamma'_{mn_1})^2(\gamma_{mn_0})^2}\right)\left(\frac{4Lp_1}{p_1^2 - p_0^2}\right) \\ &\times \int_0^R r\, dr \left[\partial_r J_m(\gamma'_{mn_1} r)\partial_r J_m(\gamma_{mn_0} r) + \frac{m^2}{r^2} J_m(\gamma'_{mn_1} r) J_m(\gamma_{mn_0} r)\right] . \end{aligned} \tag{2.73}$$

The volume integral $\int_V (\mathbf{B}^*_1)_{\mathrm{TE}} \cdot (\mathbf{E}_0)_{\mathrm{TM}}$ yields the same result, as expected. For $\mathrm{TE}_{m_1n_1p_1} \leftrightarrow \mathrm{TE}_{m_0n_0p_0}$ transitions, the overlap integral can also be nonzero. The same selection rules apply, with the additional requirement $m > 0$. The overlap integral can then be written compactly as

$$\int_V (\mathbf{E}^*_1)_{\mathrm{TE}} \cdot (\mathbf{B}_0)_{\mathrm{TE}} = B_1 B_0 \left(\frac{\omega_{mn_1p_1}\, m\, p_0}{(\gamma'_{mn_1})^2(\gamma'_{mn_0})^2}\right)\left(\frac{8\pi p_1}{p_1^2 - p_0^2}\right)\left[J_m(\gamma'_{mn_1} R) J_m(\gamma'_{mn_0} R)\right] . \tag{2.74}$$

To obtain the normalized overlap factor η_{10} defined in Eq. (2.21), one must also compute the norms

of the modes,

$$\int_V (\mathbf{E}_1^* \cdot \mathbf{E}_1)_{\mathrm{TE}} = \pi L B_1^2 \; \frac{\omega_{mn_1p_1}^2}{(\gamma'_{mn_1})^4} \int_0^R r\,dr \left[\left(\partial_r J_m(\gamma'_{mn_1} r)\right)^2 + \frac{m^2}{r^2} \left(J_m(\gamma'_{mn_1} r)\right)^2 \right], \tag{2.75}$$

$$\int_V (\mathbf{B}_0^* \cdot \mathbf{B}_0)_{\mathrm{TE}} = \pi L B_0^2 \, \frac{(p_0\pi/L)^2}{(\gamma'_{mn_0})^4} \int_0^R r\,dr \left[\left(\partial_r J_m(\gamma'_{mn_0} r)\right)^2 + \left(\frac{m^2}{r^2} + \frac{(\gamma'_{mn_0})^4}{(p_0\pi/L)^2} \right) \left(J_m(\gamma'_{mn_0} r)\right)^2 \right], \tag{2.76}$$

$$\int_V (\mathbf{B}_1^* \cdot \mathbf{B}_1)_{\mathrm{TM}} = \pi L E_0^2 \; \frac{\omega_{mn_0p_0}^2}{(\gamma_{mn_1})^4} \int_0^R r\,dr \left[\left(\partial_r J_m(\gamma_{mn_0} r)\right)^2 + \frac{m^2}{r^2} \left(J_m(\gamma_{mn_0} r)\right)^2 \right]. \tag{2.77}$$

We can now write relatively compact expressions for the overlap factors,

$$\begin{aligned} \eta_{\mathrm{TE}\leftrightarrow\mathrm{TM}} = \frac{4\,p_1}{\pi(p_1^2 - p_0^2)} & \int_0^R r\,dr \left[\partial_r J_m(\gamma'_{mn_1} r) \partial_r J_m(\gamma_{mn_0} r) + \frac{m^2}{r^2} J_m(\gamma'_{mn_1} r) J_m(\gamma_{mn_0} r) \right] \\ & \times \left(\int_0^R r\,dr \left[\left(\partial_r J_m(\gamma'_{mn_1} r)\right)^2 + \frac{m^2}{r^2} \left(J_m(\gamma'_{mn_1} r)\right)^2 \right] \right)^{-1/2} \\ & \times \left(\int_0^R r\,dr \left[\left(\partial_r J_m(\gamma_{mn_0} r)\right)^2 + \frac{m^2}{r^2} \left(J_m(\gamma_{mn_0} r)\right)^2 \right] \right)^{-1/2} \end{aligned} \tag{2.78}$$

and

$$\begin{aligned} \eta_{\mathrm{TE}\leftrightarrow\mathrm{TE}} = \frac{8\,m\,p_1}{\pi(p_1^2 - p_0^2)} & J_m(\gamma'_{mn_1} R) J_m(\gamma'_{mn_0} R) \\ & \times \left(\int_0^R r\,dr \left[\left(\partial_r J_m(\gamma'_{mn_1} r)\right)^2 + \frac{m^2}{r^2} \left(J_m(\gamma'_{mn_1} r)\right)^2 \right] \right)^{-1/2} \\ & \times \left(\int_0^R r\,dr \left[\left(\partial_r J_m(\gamma'_{mn_0} r)\right)^2 + \left(\frac{m^2}{r^2} + \frac{(\gamma'_{mn_0})^4}{(p_0\pi/L)^2} \right) \left(J_m(\gamma'_{mn_0} r)\right)^2 \right] \right)^{-1/2}. \end{aligned} \tag{2.79}$$

Clearly, we wish to maximize p_1 while keeping $p_1^2 - p_0^2$ as small as possible. Therefore, good choices might include $(p_0, p_1) = (0, 1)$ or $(1, 2)$, depending on whether the relevant frequencies have a degenerate solution to perturb around.

Pairs of Degenerate Modes

The axion-induced transitions we are interested in observing would be between nearly degenerate modes. Therefore, it is useful to have an analytic result for the cavity length to radius ratio that

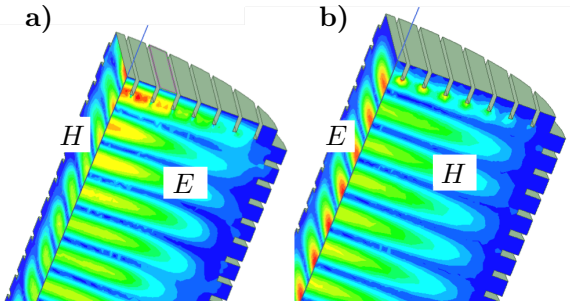

Figure 2.6: Cavity with corrugated end- and side-walls, $R = 3\lambda$. Shown are density plots of the E and H fields as labeled. **a)** Fields for mode with electric field polarized perpendicular to end-wall vanes. **b)** Fields for mode with electric field polarized parallel to end-wall vanes.

would be required to achieve degeneracy. For $\mathrm{TM}_{mn_0p_0} \leftrightarrow \mathrm{TE}_{mn_1p_1}$ transitions, we find that

$$\left(\frac{L}{R}\right)^2 = \frac{\pi\left(p_1^2 - p_0^2\right)}{x_{mn_0}^2 - x'^2_{mn_1}}\,, \tag{2.80}$$

indicating that for there to be a real solution for L/R, then for $p_1 > p_0$ we require $x'_{mn_1} < x_{mn_0}$, while for $p_1 < p_0$ we require $x'_{mn_1} > x_{mn_0}$. A similar analysis can be performed for $\mathrm{TE}_{mn_0p_0} \leftrightarrow \mathrm{TE}_{mn_1p_1}$ transitions, with the same result up to a replacement of $x_{mn_0} \to x'_{mn_0}$. Tuning the length to radius ratio will then allow for axion mass to be scanned. A discussion of how tuning could be performed in practice can be found in Section 2.4.

Corrugated Cylinders

When the outer wall of a cylindrical guide can be characterized by a constant impedance $Z = E_\varphi/H_z$ and $Y = H_\varphi/E_z$, then the waveguide modes are typically hybrid, having both electric and magnetic fields transverse to the longitudinal axis z [163],

$$E_\varphi = -\frac{k_0}{k_\perp}\left(m\frac{k_z}{k_0}\frac{J_m(k_\perp r)}{k_\perp r} + \Lambda J'_m(k_\perp r)\right)\sin m\varphi\,, \tag{2.81}$$

$$E_r = \frac{k_0}{k_\perp}\left(\frac{k_z}{k_0}J'_m(k_\perp r) + m\Lambda\frac{J_m(k_\perp r)}{k_\perp r}\right)\cos m\varphi\,, \tag{2.82}$$

$$H_\varphi = \frac{k_0}{\eta_0 k_\perp}\left(J'_m(k_\perp r) + m\frac{k_z}{k_0}\Lambda\frac{J_m(k_\perp r)}{k_\perp r}\right)\cos m\varphi\,, \tag{2.83}$$

$$H_r = \frac{k_0}{\eta_0 k_\perp}\left(m\frac{J_m(k_\perp r)}{k_\perp r} + \frac{k_z}{k_0}\Lambda J'_m(k_\perp r)\right)\sin m\varphi\,, \tag{2.84}$$

where k_0 and k_z are the free space and longitudinal propagation constants respectively, $k_\perp = \gamma/R$ is the transverse propagation constant where γ is a Bessel root, η_0 is the wave impedance of the medium

filling the guide and Λ is a hybrid factor relating the TE to TM fields. Imposing the boundary condition $Z = E_\varphi/H_z$ and $Y = H_\varphi/E_z$ at $r = R$ yields an equation for the hybrid factor

$$\Lambda = -i\left(\eta_0 Y - \frac{Z}{\eta_0}\right)\frac{k_\perp^2 R}{2mk_z} \pm \left[1 - \left(\left(\eta_0 Y - \frac{Z}{\eta_0}\right)\frac{k_\perp^2 R}{2mk_z}\right)^2\right]^{1/2}. \tag{2.85}$$

The two solutions correspond to the two types of hybrid modes, HE_{mnp} and EH_{mnp}. The most interesting case for our approach occurs when $\eta_0 Y = Z/\eta_0 \ll k_0 R$, yielding $\Lambda = \pm 1$. This limit can be obtained by using a corrugated waveguide surface and is referred to as the balanced hybrid modes. The lower order modes for this case are characterized by significantly reduced wall losses compared to the smooth wall modes. In addition, some of these modes have high degree of field polarization. The dominant balanced hybrid mode is the HE_{11p}, and has losses approximately 2.5 times lower than the lowest loss cylindrical mode, TE_{01p}, and very low cross polar fields. For a guide radius large compared to wavelength $k_z/k_0 \simeq 1$, the radial dependence of the electric and magnetic fields simplifies to $J_0(k_\perp r)$ with $\gamma = x_{10}$. For this dependence the transverse field components go to zero at the wall which explains the low attenuation. The attenuation factor α for the HE_{11p} mode is given by

$$\alpha \simeq \frac{\gamma^2}{R^3 k_0^2}\left(\frac{\omega\epsilon}{2\sigma}\right)^{1/2}, \tag{2.86}$$

where it can be seen that attenuation decreases as $1/R^3$.

The design of the detection cavity can take advantage of both of the special properties (low loss and high polarization) of the HE_{11p} mode. The low wall losses allow generation of a very high Q_{int} cavity and the low cross-polarization coupling allows the pump and signal mode to be identical but of opposite polarization so the coupling between them is minimized.

To achieve a high geometric overlap factor between the pump and signal modes, we again take advantage of the high polarization of the mode by introducing a polarization-dependent reflection at the cavity end walls. This can be achieved by using corrugations on the end walls as shown in Figure 2.6. A mode with electric field polarized parallel to the corrugation vanes will be reflected at the vane edge while the mode with electric field polarized perpendicular to the vane edge will propagate into the vane section which allows for spatial alignment of the electric and magnetic fields of the two modes.

2.9 Appendix: Geometric Rejection

The ability to discriminate between the pump and signal modes can be achieved by ensuring that the input (output) waveguide couples only to the pump (signal) mode to a high degree of precision.

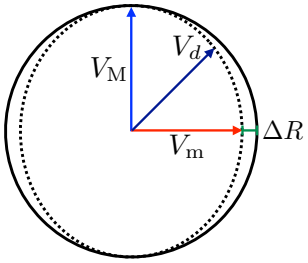

Figure 2.7: Ellipticity of the cavity can lead to signal and pump mode contamination. Shown here are the major axis voltage V_{M} and minor axis voltage V_{m}, and a drive voltage V_{d}, subject to a wall deformation ΔR.

These couplings can be parametrized by geometric overlap factors, defined as

$$\epsilon_{ij} = \frac{\int_V \tilde{\mathbf{E}}_i^* \cdot \tilde{\mathbf{E}}_j}{\sqrt{\int_V |\tilde{\mathbf{E}}_i|^2}\sqrt{\int_V |\tilde{\mathbf{E}}_j|^2}}\,, \tag{2.87}$$

where the $\tilde{\mathbf{E}}_i$ denote the spatial part of the cavity normal modes as defined in Section 2.3. In practice, the undesired couplings between the pump and output mode, $\epsilon_{0\mathrm{r}}$, and the signal and input mode, $\epsilon_{1\mathrm{d}}$, will be nonzero, as it is not possible to perfectly control the geometry of the various components. Below we discuss how ensuring $\epsilon_{0\mathrm{r}} \simeq \epsilon_{1\mathrm{d}} \ll 1$ can be achieved, and the required precision of the geometry of the cavity setup.

Coupling to the two orthogonal pump and detection modes in the cavity can be done through rectangular waveguides placed in the center of the two end walls rotated 90° relative to each other. However, if there is an angular misalignment $\Delta\theta$ there will be coupling between the modes at a level proportional to the angular misalignment. For an amplitude discrimination between modes $i = 0, 1$ and drive/readout $j = \mathrm{d}, \mathrm{r}$ of $\epsilon_{ij} \lesssim 10^{-n}$, then $\Delta\theta \lesssim 10^{-n}$. For a guide height h, this would require the rotational displacement to be $\delta < h\,\Delta\theta/2$. Assuming a frequency $f_0 = 1$ GHz, $h = \lambda/3$ and a desired power discrimination of 140 dB ($\epsilon_{ij} = 10^{-7}$), the rotational displacement error must be $\delta < 5$ nm.

Another source of coupling of the signal and pump modes can come from small deformations of the guide resulting in ellipticity of the guide cross section, as shown in Figure 2.7. Consider the idealized case in which the applied drive signal has a polarization midway between the major and minor axis of the elliptical guide, labeled M and m, such that it may be decomposed into the two orthogonal modes of equal amplitude. Since the propagation constant along the two elliptical axes have a slightly different value $\Delta\beta$ as a result of the radius deformation, the drive signal amplitude $V_{\mathrm{d}}(z)$ in terms of the two orthogonal modes of the elliptical guide will vary as

$$V_{\mathrm{d}}(z) = \frac{1}{\sqrt{2}}\left(V_{\mathrm{M}} + V_{\mathrm{m}} e^{-i\Delta\beta z}\right), \quad V_{\mathrm{M}} = V_{\mathrm{m}} = V_{\mathrm{d}}(0)\,. \tag{2.88}$$

This shift in relative phase between the two orthogonal modes will couple the drive mode to the readout mode as

$$V_{\rm r}(z) = \frac{1}{\sqrt{2}}\left(V_{\rm M} - V_{\rm m}e^{-i\Delta\beta z}\right) = \frac{V_{\rm d}(0)}{2}\left(1 - e^{-i\Delta\beta z}\right) . \tag{2.89}$$

The axial propagation constant of a guided mode is given by

$$\beta = \frac{\omega}{\left(1 - (k_\perp/\omega)^2\right)^{1/2}} . \tag{2.90}$$

The amplitude of the readout voltage at $z = L$ relative to the input drive voltage at $z = 0$ is

$$\frac{V_{\rm r}(L)}{V_{\rm d}(0)} \simeq \frac{L}{2}\frac{d\beta}{dR}\Delta R = \frac{-\gamma^2 L\,\Delta R}{2\omega R^3\left(1 - (k_\perp/\omega)^2\right)^{3/2}} . \tag{2.91}$$

Evaluating this expression for $f_0 = 1$ GHz, $2R = L = 5\lambda$ and a desired power discrimination of 140 dB ($\epsilon_{1\rm d} = \epsilon_{0\rm r} = 10^{-7}$) we find $\Delta R \lesssim 0.2$ μm.

2.10 Appendix: Parametric Optimization of Coupling

In this section, we show analytically that overcoupling the readout can parametrically enhance the reach of our search. Our conclusions match those of Refs. [151, 115], which provide a detailed and enlightening explanation of axion search optimization in general. We will only aim for parametric estimates, as our reach is found by numerically optimizing (2.57). For simplicity, we begin by considering only thermal and amplifier noise, and take the loading to be monochromatic.

We define the dimensionless coupling strength $\xi = Q_{\rm int}/Q_{\rm cpl}$, giving signal and noise PSDs of

$$\begin{aligned} S_{\rm sig}(\omega_1 + \Delta\omega) &\propto \frac{\xi}{(1+\xi)^2}\frac{S_a(\omega_1 - \omega_0 + \Delta\omega)}{1 + (\Delta\omega/\Delta\omega_r)^2} , \\ S_{\rm noise}(\omega_1 + \Delta\omega) &\propto \frac{4\xi}{(1+\xi)^2}\frac{1}{1 + (\Delta\omega/\Delta\omega_r)^2} + \frac{1}{n_{\rm occ}} , \end{aligned} \tag{2.92}$$

where we have absorbed constants to display only the dependence on ξ and ω, and expanded the PSDs near the positive frequency resonance $\omega \simeq \omega_1$.

In all cases we will consider, the integrand of Eq. (2.57) will be roughly constant within an interval $\omega_{\rm max} \pm \Delta\omega_s$, where we call $\Delta\omega_s$ the sensitivity width, and quickly falls off outside it. In this case, evaluating the integral roughly gives

$$\mathrm{SNR}(\xi) \approx \frac{S_{\rm sig}(\omega_{\rm max})}{S_{\rm noise}(\omega_{\rm max})}\sqrt{\frac{t_{\rm int}\Delta\omega_s}{2\pi}} \tag{2.93}$$

which is the familiar Dicke radiometer equation. Directly applying Eq. (2.92), we have

$$\frac{S_{\text{sig}}(\omega_1+\Delta\omega)}{S_{\text{noise}}(\omega_1+\Delta\omega)} \propto \frac{1}{1+1/n_{\text{eff}}} \frac{S_a(\omega_1-\omega_0+\Delta\omega)}{1+(\Delta\omega/\Delta\omega_r)^2/(1+n_{\text{eff}})} \tag{2.94}$$

where n_{eff} describes the ratio of thermal to amplifier noise,

$$n_{\text{eff}} = \frac{4\xi}{(1+\xi)^2}\, n_{\text{occ}} \tag{2.95}$$

and $n_{\text{occ}} \gg 1$.

We now optimize the coupling ξ. When the axion is broad, the sensitivity width is determined by the width of the Breit–Wigner in (2.94),

$$\Delta\omega_s = \Delta\omega_r \sqrt{1+n_{\text{eff}}} \propto (1+\xi)\sqrt{1+n_{\text{eff}}} \tag{2.96}$$

where the second step follows because $\Delta\omega_r \propto 1/Q_1$. The maximum SNR depends on ξ as

$$\frac{S_{\text{sig}}(\omega_{\text{max}})}{S_{\text{noise}}(\omega_{\text{max}})} \propto \frac{1}{1+1/n_{\text{eff}}}. \tag{2.97}$$

Finally, the scan step affects the SNR through the integration time, $t_{\text{int}} \propto \Delta\omega_{\text{sc}}$, as in Eq. (2.59), but in the broad axion case, $\Delta\omega_{\text{sc}} = \Delta\omega_a$ is independent of ξ. Therefore, the figure of merit to be maximized is

$$\text{SNR}(\xi) \propto F(\xi) = \frac{\sqrt{(1+\xi)\sqrt{1+n_{\text{eff}}}}}{1+1/n_{\text{eff}}}. \tag{2.98}$$

We have normalized the figure of merit so that a critically coupled readout that naively detects only the total power within the resonator width (i.e. taking $\xi = 1$ and artificially setting $\Delta\omega_s = \Delta\omega_r$) has $F \sim 1$.

For a narrow axion, the roles of the scan step $\Delta\omega_{\text{sc}}$ and sensitivity width $\Delta\omega_s$ are flipped: it is now the sensitivity width that is determined by the axion width, and the scan step that is determined by the width of the Breit–Wigner. As a result, the SNR has the same parametric dependence on ξ, so we can roughly handle both cases at once.

For $\xi \approx 1$, we have $n_{\text{eff}} \gg 1$, and (2.98) reduces to

$$F(\xi) \approx \sqrt{(1+\xi)\sqrt{n_{\text{eff}}}} = (4\xi n_{\text{occ}})^{1/4} \tag{2.99}$$

which makes it clear that overcoupling is advantageous. For $\xi \gg 1$, we can expand again to find

$$F(\xi) \approx \frac{\sqrt{\xi\sqrt{1+4n_{\text{occ}}/\xi}}}{1+\xi/4n_{\text{occ}}} = \frac{(4\xi n_{\text{occ}})^{1/4}}{(1+\xi/4n_{\text{occ}})^{3/4}} \tag{2.100}$$

which is maximized when $\xi \sim n_{\rm occ}$, at which point $F(\xi) \sim \sqrt{n_{\rm occ}}$, justifying the claims made in Section 2.6. As anticipated, the optimum is achieved when the thermal noise hits the quantum noise floor, $n_{\rm eff} \sim 1$.

We now make some remarks on this result. First, our conclusions are not specific to thermal noise. Referring to Eq. (2.92), we see that they hold for any source of noise which has a Breit–Wigner shape and the same dependence on the coupling ξ. In particular, this is true for oscillator phase noise. As such, the SNR gain from overcoupling is $\sqrt{n_{\rm occ}} \sim 10$ for high axion masses, where thermal noise dominates, and grows further at low axion masses, where oscillator phase noise becomes larger than thermal noise.

Second, if the amplifier were instead at the same physical temperature as the cavity, the thermal noise would not be reduced by overcoupling. Assuming thermal noise dominates, the figure of merit is

$$\mathrm{SNR}(\xi) \propto F(\xi) = \frac{\xi}{(1+\xi)^2}\sqrt{1+\xi} \tag{2.101}$$

where the first factor is due to the PSD ratio, and the second is from the dependence on $\sqrt{t_{int}\Delta\omega_s}$. This quantity is maximized at $\xi = 2$, in accordance with standard results.

Third, we have assumed throughout that $t_{\rm int} > \max(\tau_{\rm r}, \tau_a)$, so that steady state solutions apply. A smaller integration time can be described by multiplying all time-dependent functions by a windowing function of width $t_{\rm int}$, smearing their Fourier transforms over the width $1/t_{\rm int}$. For example, in the broad axion case, the total signal power is penalized as

$$P_s \sim \begin{cases} t^2/\tau_{\rm r}\tau_a & t \ll \tau_a, \\ t/\tau_{\rm r} & \tau_a \ll t \ll \tau_{\rm r}, \\ 1 & \tau_{\rm r} \ll t. \end{cases} \tag{2.102}$$

This signal power is also smeared over a larger frequency range, so detecting it requires taking in more noise, further reducing the SNR. For $t_{\rm int} \lesssim \tau_a$, we also encounter a qualitatively new problem which is statistical in nature [164, 165]. The axion DM field is generically expected to be a Gaussian random field, which implies that its amplitude of oscillation fluctuates by an $\mathcal{O}(1)$ factor over the timescale τ_a. (We suppressed this in the qualitative discussion following Eq. (2.2) for simplicity.) As a result, the axion signal power has large statistical fluctuations, and the possibility of a downward fluctuation significantly weakens the reach; the simple criterion $\mathrm{SNR} \gtrsim 1$ is no longer a good estimate.

These subtleties introduce significant complications, so we have simply imposed $t_{\rm int} > \max(\tau_{\rm r}, \tau_a)$ as a constraint. As a result, if t_e is sufficiently short (as in the lower right panel of Figure 2.5), the readout is overcoupled beyond the optimal value to allow the scan to complete in time.

Finally, we note one more feature of our optimization: the sensitivity width $\Delta\omega_s$ can be parametrically larger than the resonator width $\Delta\omega_r$. For example, for critical coupling and a broad axion, we have $\Delta\omega_s \sim \sqrt{n_{\rm occ}}\,\Delta\omega_r$. A critically coupled experiment which naively looks only at the

power within the resonator width thus parametrically underestimates its potential SNR by a factor of $F(\xi = 1) \sim n_{\mathrm{occ}}^{1/4}$. The intuition here is that the signal and thermal noise PSDs fall off resonance with exactly the same Breit–Wigner tail, so bins far beyond the resonator width can still have high SNR. However, this point is not relevant to our final result, because once the coupling is optimized, we have $\Delta\omega_s \sim \Delta\omega_r$ again.

Chapter 3

Heterodyne Broadband Detection

This chapter is based on *Heterodyne Broadband Detection of Axion Dark Matter*, by A. Berlin, R. T. D'Agnolo, S. A. R. Ellis, K. Zhou, Phys. Rev. D 104, L111701 (2021).

Abstract

We propose a new broadband search strategy for ultralight axion dark matter that interacts with electromagnetism. An oscillating axion field induces transitions between two quasi-degenerate resonant modes of a superconducting cavity. In two broadband runs optimized for high and low masses, this setup can probe unexplored parameter space for axion-like particles covering fifteen orders of magnitude in mass, including astrophysically long-ranged fuzzy dark matter.

3.1 Introduction

Evidence for dark matter (DM) has been accumulating for almost ninety years [166] and its microscopic nature remains one of the most important open questions in physics. Among the many DM candidates proposed in the literature, light pseudoscalar bosons with sub-eV masses have garnered considerable appeal since they generically appear in string compactifications [97, 98, 99] and have a simple and predictive cosmological history. Furthermore, in certain regions of parameter space they can solve the strong CP [93, 94, 95, 96, 100, 101, 102] or electroweak hierarchy problem [167, 168, 169]. In the "fuzzy" mass limit ($m_{\rm DM} \sim 10^{-22}$ eV), light bosonic DM may also play a role in resolving long-standing tensions between observations and simulations of galactic structure [170, 171, 172]. In this chapter, we present a new detection strategy for these DM candidates, which we refer to as axions.

Axion DM generically couples to electromagnetism through the interaction

$$-\mathcal{L} \supset \frac{1}{4}\, g_{a\gamma\gamma}\, a\, F_{\mu\nu}\tilde{F}^{\mu\nu} \supset \frac{1}{2}\, \mathbf{J}_{\rm eff} \cdot \mathbf{A}\,, \tag{3.1}$$

where a is the axion field and $\mathbf{A}$ is the vector potential. In the presence of a background magnetic field $\mathbf{B}$, the axion sources an effective current density

$$\mathbf{J}_{\rm eff} \simeq g_{a\gamma\gamma}\, \partial_t a\, \mathbf{B}\,. \tag{3.2}$$

The interaction of Eq. 3.1 forms the basis of several experimental approaches to axion detection [4, 5, 6, 7, 9, 11, 10, 12, 13, 18, 108, 109, 110, 173, 174, 123]. For instance, the time variation of $\mathbf{J}_{\rm eff}$ may be used to drive a resonant detector [107, 175]. Such experiments exploit the coherence properties of the axion DM field, which we model as a classical Gaussian random field within the galaxy, with an average local density $\rho_{\rm DM} \simeq 0.4$ GeV/cm^3 and oscillating with angular frequency approximately equal to the axion mass m_a. Velocity dispersion from virialization within the galaxy leads to a spectral broadening of the axion, with a characteristic width of $\Delta\omega_a \sim m_a/Q_a$, where $Q_a \sim 10^6$.

In setups applying static magnetic fields, $\mathbf{J}_{\rm eff}$ oscillates with the same frequency as the axion field. Microwave cavities resonantly matched to the axion field can be built for $m_a \sim \mu$eV [11], but for lower axion masses, the required cavity volume becomes impractically large. Resonant detection of lighter axions is possible in static-field setups if the resonant frequency and volume of the detector are independent, such as for lumped-element LC circuits [113, 114, 115]. However, their sensitivity to low mass axions is suppressed by $\partial_t J_{\rm eff} \propto m_a$.

Recently, we have proposed a new approach for axion DM detection, which uses frequency conversion to retain the advantages of resonant cavities while avoiding this suppression at low masses [176] (see also Refs. [127, 177, 178]).[1] A cavity is prepared by driving a "pump mode" with frequency $\omega_0 \sim$ GHz, so that the axion can resonantly drive power into a "signal mode" of nearly

[1] Resonant and broadband heterodyne setups based on optical interferometry have previously been proposed, but their sensitivity is limited by laser shot noise [179, 180, 181].

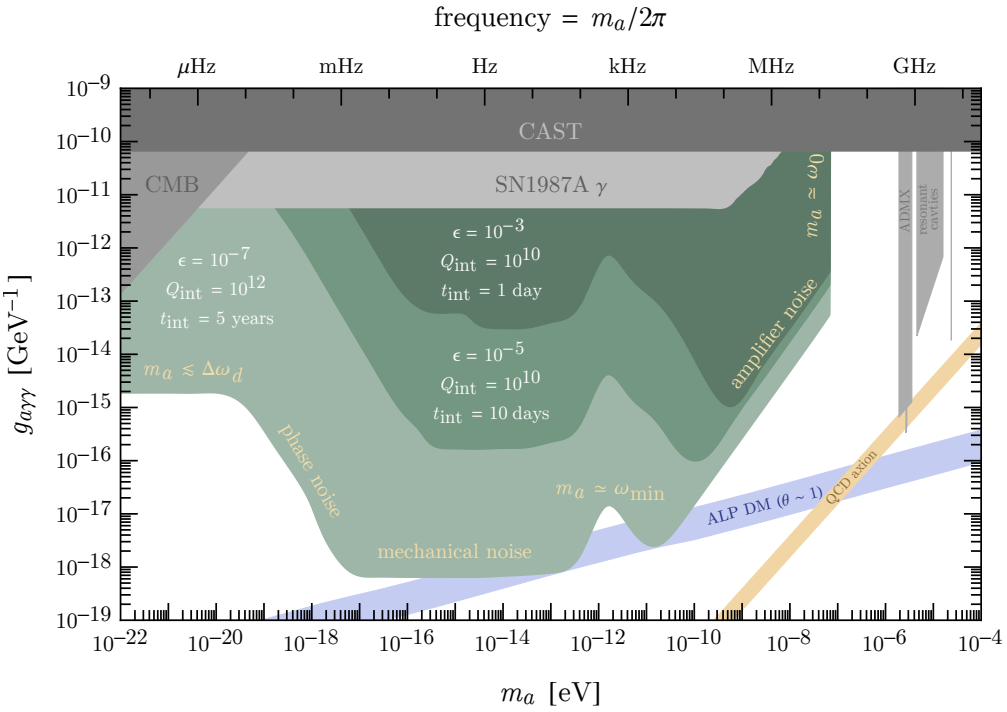

Figure 3.1: In shaded green, the projected 90% C.L. reach of our setup to axion dark matter for several values of leakage noise suppression ε, intrinsic quality factor $Q_{\rm int}$, and integration time $t_{\rm int}$. For each set of parameters, we show the envelope of two or three distinct experimental runs, as discussed in the main text. We assume pump and signal mode frequencies $\omega_0 = \omega_1 = 100$ MHz, a cavity volume $V_{\rm cav} = \text{m}^3$, a magnetic field strength $B_0 = 0.2$ T, a mode overlap form factor $\eta_a = 1$, a drive oscillator width $\Delta\omega_d = 0.1$ mHz, and an attenuated RMS cavity wall displacement $q_{\rm rms} = 0.1$ nm. Further variations are shown in the appendix. Existing constraints [4, 5, 6, 7, 8, 9, 10, 11, 12, 13, 14, 15, 16, 17, 18] are shown in grey. The orange band denotes parameter space motivated by the strong CP problem. Along the blue band, axions are produced through the misalignment mechanism at a level consistent with the observed dark matter density [19], assuming a temperature independent mass, $\mathcal{O}(1)$ initial misalignment angle, and coupling $g_{a\gamma\gamma} = \alpha_{\rm em}/(2\pi f_a)$. (For larger couplings, axions produced in the same way would make up a subcomponent of dark matter. However, since $J_{\rm eff} \propto g_{a\gamma\gamma}\sqrt{\rho_a} \propto g_{a\gamma\gamma} f_a$, our setup is equally sensitive to such subcomponents.)

degenerate frequency $\omega_1 \simeq \omega_0 \pm m_a$ and distinct spatial geometry. A scan over possible axion masses is performed by slightly perturbing the cavity geometry, thereby modulating the frequency splitting $\omega_1 - \omega_0$. Compared to a static-field LC circuit of comparable volume and noise, the signal-to-noise ratio of this "heterodyne" approach is parametrically enhanced by ω_1/m_a. It also benefits from the very large intrinsic quality factors $Q_{\rm int} \gtrsim 2 \times 10^{11}$ achievable in superconducting radio frequency (SRF) cavities [134, 135], which far exceed the quality factors achievable in static-field detectors targeting small axion masses.

In this chapter, we consider a broadband search where the signal and pump modes are fixed to be degenerate within their bandwidth, the feasibility of which is currently being investigated by the DarkSRF collaboration [182]. For the lowest axion masses, $m_a \lesssim \omega_0/Q_{\rm int} \sim 10^{-17}$ eV, the signal power is resonantly enhanced. For higher axion masses, the signal is off-resonance, but so are the dominant sources of noise in the cavity, thereby allowing this setup to explore new parameter space for axions as heavy as $m_a \sim 10^{-7}$ eV, as shown in Fig. 3.1. This broadband approach is thus sensitive to a wide range of axion masses without the need to scan over frequency splittings. It is also the first approach that could directly detect electromagnetically-coupled axion DM at the lowest viable DM masses $m_a \sim 10^{-22}$ eV, which correspond to a de Broglie wavelength the size of dwarf galaxies and a coherence time ten times longer than recorded human history. In this chapter, we will show parametric estimates that illustrate its potential; detailed calculations of signal and noise are given in Ref. [176] and the appendix.

3.2 Detection Strategy

The basic principle of our setup is shown in Fig. 3.2. The effective current, given by Eq. 3.2, oscillates at frequency $\omega_{\rm sig} \simeq \omega_0 \pm m_a$. Since it is parallel to $\mathbf{B}_0$, it drives power into the signal mode with strength parametrized by the form factor

$$\eta_a = \frac{|\int_{V_{\rm cav}} \mathbf{E}_1^*(x) \cdot \mathbf{B}_0(x)|}{\left(\int_{V_{\rm cav}} |\mathbf{E}_1(x)|^2 \int_{V_{\rm cav}} |\mathbf{B}_0(x)|^2\right)^{1/2}} \leq 1 \,, \tag{3.3}$$

where $\mathbf{E}_1$ is the signal mode electric field and $V_{\rm cav}$ is the volume of the cavity. We will be agnostic to the cavity geometry, taking $\omega_0 = \omega_1 \sim (1\,{\rm m})^{-1} \sim 100\,{\rm MHz}$, but as a concrete example, $\eta_a \sim \mathcal{O}(1)$ for the $\rm TE_{011}$ and $\rm TM_{020}$ modes of a cylindrical cavity, which are degenerate in frequency for a length-to-radius ratio of $L/R \simeq 0.8$ [176, 178].

We assume the frequencies of the pump and signal can be held fixed and degenerate within the signal mode bandwidth. However, the assumption of degeneracy only affects the reach at very low masses ($m_a \lesssim \omega_1/Q_1$). Furthermore, as shown in the appendix, even a frequency splitting 10^3 times larger than the bandwidth allows new ultralight axion parameter space to be probed. The fundamental reason our setup can probe such low axion masses is that the signal strength depends

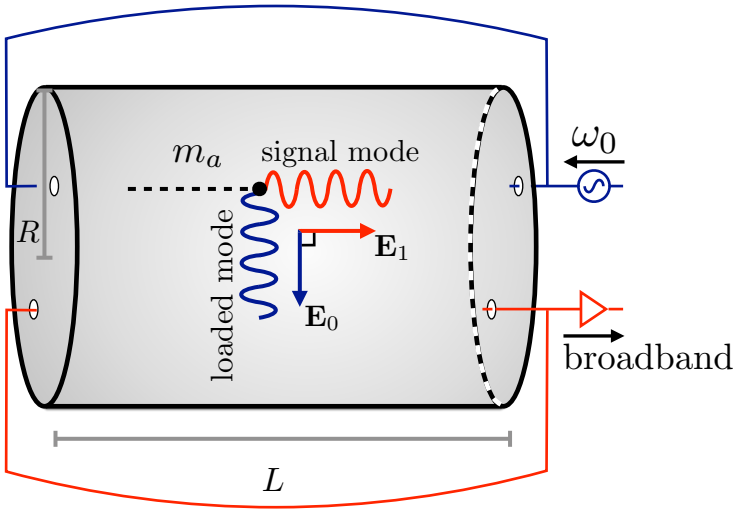

Figure 3.2: A schematic depiction of our setup. An SRF cavity is designed to have two degenerate modes of frequency ω_0. It is prepared by driving a loading waveguide, predominantly coupled to the pump mode, with an external oscillator of frequency ω_0. In the presence of axion DM, the pump mode magnetic field $\mathbf{B}_0$ sources an effective current that drives power into the signal mode. A wide range of axion masses can be simultaneously probed by broadband readout, via a readout waveguide predominantly coupled to the signal mode.

on $\partial_t J_{\rm eff} \simeq g_{a\gamma\gamma}\, \partial_t a\, \partial_t^2 B \propto m_a\, a \propto \sqrt{\rho_{\rm DM}}$. For a fixed axion field *amplitude*, this vanishes as $m_a \to 0$, as required by general principles, but it is independent of m_a for fixed axion energy density.

When the sensitivities of a broadband and scanning approach overlap, the latter is stronger with a similar cavity [176], as expected on general grounds [151]. The two approaches have the same sensitivity only when m_a is smaller than the resonator bandwidth and the broadband setup functions as a resonant experiment. However, a broadband setup is simpler to operate due to its fixed geometry, and could be used as a stepping stone towards a scanning one. Moreover, it can probe a wide range of parameter space in a short integration time.

3.3 Overview of Signal and Noise

The frequency spread $\Delta\omega_{\rm sig}$ of $\mathbf{J}_{\rm eff}$ (and hence of our signal) depends on the width $\Delta\omega_a$ of the axion field and the width $\Delta\omega_d$ of the oscillator driving the pump mode, $\Delta\omega_{\rm sig} \sim \max(\Delta\omega_a, \Delta\omega_d)$. For concreteness, we take the power spectral density (PSD) of the central peak of the oscillator to be flat with a width $\Delta\omega_d \simeq 0.1$ mHz, comparable to a commercially available oscillator [146]. This is narrower than the signal mode width $\Delta\omega_r = \omega_0/Q_1$ for all parameters we consider. Since it can be beneficial to overcouple the readout, the loaded quality factor Q_1 of the signal mode can be much lower than the intrinsic quality factor $Q_{\rm int}$, though the pump mode quality factor Q_0 remains

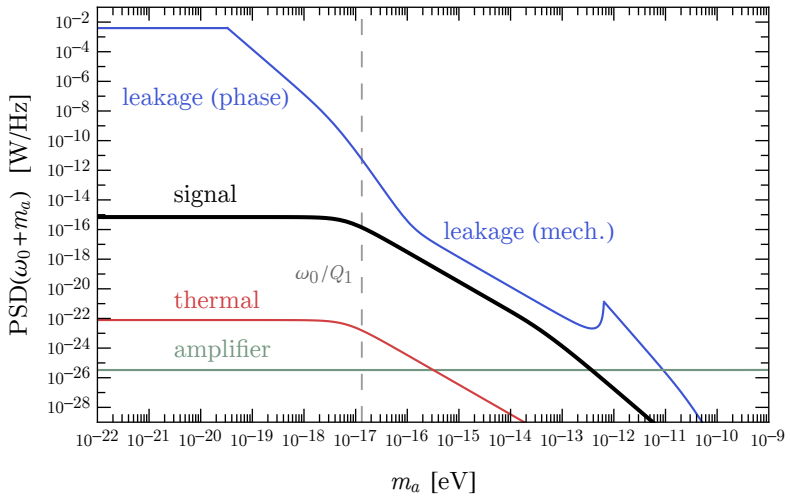

Figure 3.3: The signal and noise PSDs evaluated at $\omega_{\rm sig}$ as a function of the axion mass m_a, at critical coupling. The vertical dashed line denotes the bandwidth $\Delta\omega_r$ of the signal mode. We use a fixed, fiducial value of $g_{a\gamma\gamma}$, below our projected sensitivity, to allow the reader to easily compare the slopes of signal and noise. We show leakage noise (blue), thermal fluctuations of the electromagnetic field in the cavity at $T = 1.8$ K (red), and quantum-limited amplifier noise (green). Mechanical vibrations dominate the leakage noise for high m_a. The parameters are those of the second-lowest curve in Fig. 3.1.

comparable to $Q_{\rm int}$.

The average signal power delivered to the cavity is

$$P_{\rm sig} \sim \frac{(g_{a\gamma\gamma}\,\eta_a\,B_0)^2\,\rho_{\rm DM}V_{\rm cav}}{\max\left(\Delta\omega_r, \Delta\omega_a\right)}\,\min\left[1,\,\left(\frac{\Delta\omega_r}{m_a}\right)^2\right]\,, \tag{3.4}$$

where B_0 is the characteristic amplitude of the pump mode magnetic field. The final factor in Eq. 3.4 accounts for the suppression that occurs when the axion drives the signal mode off-resonance ($m_a \gtrsim \Delta\omega_r$). Given the signal power and noise PSD $S_n(\omega)$, the reach is determined by the signal-to-noise ratio [152]

$$\mathrm{SNR} \sim \frac{P_{\rm sig}}{S_n(\omega_{\rm sig})}\,\sqrt{\frac{t_{\rm int}}{\Delta\omega_{\rm sig}}}\,, \tag{3.5}$$

where $t_{\rm int}$ is the total integration time. Eq. 3.5 is valid when $t_{\rm int} \gtrsim 1/\Delta\omega_{\rm sig}$, which holds for all parameters we consider. A detailed derivation of the signal power and of the test statistic that Eq. 3.5 approximates is given in the appendix.

For most of the axion masses we consider, the dominant noise source is power in the oscillator or pump mode "leaking" into the readout waveguide. For instance, geometric imperfections can lead to small cross-couplings $\varepsilon \ll 1$ between the loading architecture and signal mode (and similarly

between the readout and pump mode), resulting in leakage noise power proportional to ε^2. Leakage noise was previously encountered in the gravitational wave experiment MAGO, which looked for transitions between nearly degenerate symmetric and antisymmetric mode combinations of two identical SRF cavities coupled by a small tunable aperture [130, 131, 132]. The collaboration achieved a noise suppression of $\varepsilon \sim 10^{-7}$ using magic-tees and a variable phase shifter coupled to an active feedback loop [183]. In our setup, the two modes can additionally be chosen to be locally orthogonal, $\mathbf{E}_0 \cdot \mathbf{E}_1 = \mathbf{B}_0 \cdot \mathbf{B}_1 = 0$, with distinct spatial profiles, which could allow for further noise suppression by, e.g., loading/reading out the pump/signal mode near a node of the other mode [178], or by correlating readout measurements across multiple regions of the cavity. However, we conservatively consider $\epsilon \geq 10^{-7}$.

As shown in Fig. 3.3, leakage noise is largest when $m_a \lesssim \Delta\omega_d$, while for higher axion masses it falls off according to the tail of the pump mode PSD, which is determined by oscillator "phase noise" and mechanical vibrations of the cavity [176]. For the highest axion masses we consider, readout amplifier noise dominates. This explains the main qualitative features of Fig. 3.1. Since slightly different setups are optimal in each mass regime (with the exact crossover points depending on the experimental parameters), we organize the following discussion by axion mass.

Low mass axions

When the axion mass is smaller than the oscillator width ($m_a \lesssim 10^{-19}$ eV), the signal overlaps in frequency with the central peak of the oscillator. Both the signal and noise are spread over a bandwidth $\Delta\omega_{\rm sig} \sim \Delta\omega_d$, giving a leakage noise PSD of

$$S_{\rm leak}(\omega_{\rm sig}) \sim \varepsilon^2 \, P_{\rm in}/\Delta\omega_d \ , \tag{3.6}$$

where $P_{\rm in} \sim (\omega_0/Q_{\rm int})\, B_0^2\, V_{\rm cav}$ is the power stored in the cavity. Assuming the readout waveguide is critically coupled to the signal mode ($Q_1 = Q_{\rm int}/2$), which maximizes the sensitivity, Eq. 3.5 gives

$$\text{SNR} \sim \rho_{\rm DM} \left(\frac{g_{a\gamma\gamma}\, Q_{\rm int}}{\omega_0\, \varepsilon}\right)^2 \sqrt{t_{\rm int}\, \Delta\omega_d} \tag{3.7}$$

and hence a reach $g_{a\gamma\gamma} \propto \epsilon/Q_{\rm int}$, independent of m_a.[2]

Since leakage noise dominates, parameters such as B_0, $V_{\rm cav}$, and the cavity temperature do not directly affect the sensitivity. The same is true for external sources of low frequency noise, such as vibrations of the ground or the cooling apparatus. Relative displacements of the cavity walls are suppressed by the rigidity of the cavity and further controlled by actively monitoring the mode frequencies and cross-coupling ϵ. In the appendix, we conservatively estimate the effect of vibrational

[2]The reach is slightly penalized when $\Delta\omega_a \lesssim 1/t_{\rm int}$, as described in the appendix. Furthermore, we do not consider very low axion masses $m_a \lesssim 1/t_{\rm int}$, as the reach is strongly suppressed by the unknown instantaneous phase of the axion.

noise to be subdominant by many orders of magnitude in this mass range, in contrast to precision interferometric experiments where such noise can be dominant.

The signal and noise overlap in frequency, but can be distinguished by their distinct spatial profiles and spectral tails. There are several other effects to consider. Since $m_a \lesssim \Delta\omega_r$ in this regime, the axion field oscillates less than once per ring-up time of the cavity. Hence, the instantaneous signal power tracks the oscillations of $(\partial_t a)^2$, with angular frequency $2m_a$. Furthermore, $J_{\rm eff} \propto B_0$ drives the signal mode on resonance, leading to a signal mode magnetic field $\pi/2$ out of phase with leakage noise. In addition, fluctuations in leakage noise due to fluctuations in the pump mode field can be monitored and ideally subtracted out. Thus, the parameter ϵ in Eq. 3.7 should be regarded as including the ability to distinguish between signal and leakage noise using these additional handles, though here we conservatively take $\epsilon \geq 10^{-7}$.

High mass axions

Here, leakage and thermal noise are negligible due to the off-resonance suppression $(\Delta\omega_r/m_a)^2$. Since the axion is wider than the oscillator, the signal width is $\Delta\omega_{\rm sig} \sim \Delta\omega_a$. As in static broadband axion searches in this mass range [114, 174], amplifier noise dominates, such that

$$\mathrm{SNR} \sim \rho_{\rm DM} V_{\rm cav} \frac{\Delta\omega_r}{S_{\rm amp}(\omega_{\rm sig})} \Big(\frac{g_{a\gamma\gamma}\, B_0}{m_a}\Big)^2 \sqrt{\frac{t_{\rm int}}{\Delta\omega_a}}\ , \tag{3.8}$$

where for a quantum-limited amplifier, $S_{\rm amp}(\omega) \sim \hbar\omega$. We cut off the reach in Fig. 3.1 at $m_a \simeq \omega_0$, above which higher harmonics of the cavity must be considered [127], as well as potential nonlinear response of the cavity walls [184].

The reach scales as $g_{a\gamma\gamma} \propto m_a^{5/4}/\Delta\omega_r^{1/2}$, assuming $\Delta\omega_r \gtrsim \Delta\omega_a$. Thus, when amplifier noise dominates, lowering Q_1 by overcoupling the signal mode to the readout is beneficial, as it reduces the off-resonance suppression of the signal without increasing the noise. The reach shown in Fig. 3.1 can be attained from a critically coupled run targeting low masses and an overcoupled run targeting high masses.[3] For the latter run, we assume a quantum-limited amplifier, and take $Q_1 \sim 10^5$, which is a typical loaded quality factor of SRF cavities in accelerators [140].

Intermediate mass axions

For the bulk of the parameter space shown in Fig. 3.1, the reach is dictated by the high frequency tail of the leakage noise. In most of this range, the oscillator is wider than the axion, so the signal width is $\Delta\omega_{\rm sig} \sim \Delta\omega_d$.

In the lower end of this mass range, the main contribution to the leakage noise tail is from

[3] The lowest curve in Fig. 3.1 requires a third run with intermediate overcoupling, specifically targeting intermediate mass axions.

oscillator phase noise [176], which for $m_a \gtrsim \Delta\omega_r$ is of the form

$$S_{\rm leak}(\omega_{\rm sig}) \sim \varepsilon^2 \, P_{\rm in} \left(\frac{\Delta\omega_r}{m_a}\right)^2 S_\varphi(m_a) \ , \tag{3.9}$$

where the phase noise PSD $S_\varphi(\omega)$ is parametrized by [144]

$$S_\varphi(\omega) = \sum_{n=0}^{3} c_n \, \omega^{-n} \ , \tag{3.10}$$

and the c_n are fit to a commercially available oscillator [146]. For m_a slightly higher than $\Delta\omega_d$, the cubic term in $S_\varphi(\omega)$ dominates, resulting in $S_{\rm leak}(\omega_{\rm sig}) \propto 1/m_a^5$ and a rapid improvement in the reach at higher axion masses.

In the upper end of this mass range, the main noise contribution instead arises from displacements of the cavity walls, where mechanical vibrations at frequency m_a contribute to pump mode power at $\omega_{\rm sig}$ [176]. On the basis of previous measurements in a MAGO prototype [130], we take the external mechanical force PSD to be spectrally flat, and the mechanical modes to have a quality factor $Q_m \sim 10^3$. As described in the appendix, the contribution of the lowest-lying mechanical resonance at $\omega_{\rm min} \sim$ kHz dominates for $m_a \lesssim \omega_{\rm min}$, such that

$$S_{\rm leak}(\omega_{\rm sig}) \sim \varepsilon^2 \, P_{\rm in} \left(\frac{\Delta\omega_r}{m_a}\right)^2 \frac{\delta^2 \, Q_{\rm int}^2}{\omega_{\rm min} \, Q_m} \ , \tag{3.11}$$

where $\delta \ll 1$ is the fractional displacement of the cavity walls. For $\Delta\omega_a \lesssim \Delta\omega_r \lesssim m_a$, $P_{\rm sig} \propto 1/m_a^2$, and thus the sensitivity in this region is independent of the axion mass. For frequencies above $\omega_{\rm min}$, we assume a forest of evenly spaced mechanical modes exists. To estimate δ, we note that the DarkSRF collaboration has recently demonstrated the ability to control the resonant frequency of a driven cavity to one part in $Q_{\rm int} \gtrsim 10^{10}$, corresponding to sub-nm displacements of the cavity walls [139, 182]. This has been demonstrated on minute timescales, and a near-future run is expected to prolong this to $\mathcal{O}(1)$ week. Thus, we fix the typical RMS cavity wall displacement to $q_{\rm rms} = 0.1$ nm, corresponding to $\delta \sim 10^{-10}$ for a meter-sized cavity. This is larger than the displacement due to environmental seismic noise [185], reflecting the expectation that vibrations will primarily arise from the apparatus itself (e.g., the helium pump).

Deformations of the cavity walls can also directly transfer power between the pump and signal modes. This "mode mixing" is parametrized by a dimensionless mechanical form factor $\eta_{\rm mix}$, with $S_{\rm mix} \sim (\eta_{\rm mix}/\epsilon)^2 \, S_{\rm leak}$. The form factor $\eta_{\rm mix}$ vanishes for a perfectly cylindrical cavity, which implies its value is set by cavity deformations [186, 131]. Since ϵ parametrizes the precision to which we can control slow deformations of the cavity and waveguide geometry, we expect $\eta_{\rm mix} \sim \epsilon$, such that mode mixing is at most comparable to mechanical leakage noise.

3.4 Discussion

We have proposed a heterodyne approach to search for ultralight axion dark matter through its coupling to electromagnetism, which applies recent developments in the manufacturing and control of SRF cavities. Due to the decreasing signal power and increasing strength of readout noise at low frequencies, traditional static-field haloscopes have limited reach to axions lighter than a kHz $\sim 10^{-12}$ eV [173, 174]. In contrast, our setup is sensitive to much lighter axions, including the entire allowed mass range for fuzzy dark matter, $m_a \geq \mathcal{O}(10^{-21})$ eV [187, 188, 189, 190, 191, 192], thereby complementing ultralight axion searches that use non-electromagnetic couplings [193, 194, 195, 196]. It is also sensitive to axions as heavy as 10^{-7} eV, including those motivated by string theory [197] and the misalignment mechanism. Finally, the broadband nature of this approach implies that a network of such detectors would be sensitive to axion-induced transients, due to miniclusters or topological defects [198, 199].

Our projections rely on noise estimates anchored to experimental findings, such as those obtained fifteen years ago by the MAGO collaboration [130, 131, 132]. More recently, there has been renewed interest in the SRF community to apply their technological advances to new physics searches, leading to the recent results of the DarkSRF collaboration [182] that show the feasibility of our proposed approach. The promising sensitivity of SRF cavities to weakly coupled physics, demonstrated in this chapter, motivates in situ measurements of mode mixing and leakage noise, in order to further investigate the potential of these ideas. Future developments, some of which are already envisioned by the DarkSRF collaboration, can further extend our reach, improving the capacity to probe some of the most motivated dark matter candidates.

3.5 Appendix: Detailed Analysis

In this appendix, we derive the experimental sensitivity of our proposed approach in detail. We begin by deriving the signal and noise PSDs. We then discuss the statistical procedure used to estimate the reach, which involves subtleties for integration times shorter than the axion coherence time.

3.5.1 Definitions and Conventions

Throughout, we use the conventions of Ref. [176]. In particular, the Fourier transform of a function $f(t)$ is denoted as $f(\omega)$, where

$$f(t) = \frac{1}{2\pi} \int d\omega \; e^{i\omega t} f(\omega) \; , \;\; f(\omega) = \int dt \; e^{-i\omega t} f(t) \, . \tag{3.12}$$

The two-sided PSD of f, denoted as $S_f(\omega)$, is defined to be

$$\langle f(\omega) f^*(\omega') \rangle = S_f(\omega) \, \delta(\omega - \omega') \; , \tag{3.13}$$

where the brackets correspond to an ensemble average. The steady state time-averaged power is then given by

$$\langle f(t)^2 \rangle = \frac{1}{(2\pi)^2} \int d\omega \; S_f(\omega) \; , \tag{3.14}$$

where all integrals over t or ω are taken from $-\infty$ to ∞, unless specified otherwise.

The fields in the pump ($i = 0$) and signal ($i = 1$) modes behave as damped driven harmonic oscillators. Therefore, we will find it convenient to treat them as independent RLC circuits of resonant frequency $\omega_i = 1/\sqrt{L_i C_i}$ and quality factor $Q_i = \sqrt{L_i/C_i}\,/R_i \propto 1/R_i$. This is not a physical statement, but merely a mathematical analogy between two systems obeying the same equations. Furthermore, we often approximate $\omega_1 \simeq \omega_0$, unless the difference $\omega_1 - \omega_0$ is important, in which case we leave the expression generalized to $\omega_1 \neq \omega_0$.

It is also useful to recall the distinction between the intrinsic and loaded quality factors of a cavity mode. The quality factors of the pump and signal modes are denoted by Q_0 and Q_1, respectively, and Q_1 is determined by both the intrinsic energy loss of the cavity $Q_{\rm int} \simeq Q_0 \gtrsim 10^{10}$ and the coupling to the readout $Q_{\rm cpl}$,

$$\frac{1}{Q_1} = \frac{1}{Q_{\rm int}} + \frac{1}{Q_{\rm cpl}} \; . \tag{3.15}$$

In the RLC circuit analogy, this corresponds to the addition of resistances in series, $R_1 = R_{\rm int} + R_{\rm cpl}$. As discussed in the main body, it can be beneficial to overcouple, such that $Q_1 \simeq Q_{\rm cpl} \ll Q_{\rm int}$. For simplicity, we begin by deriving the noise and signal PSDs corresponding to the *total* power delivered to the cavity. However, the sensitivity of the apparatus depends only on the power delivered to the readout, and when discussing overcoupling, we will explicitly show how the PSDs must be modified to account for this.

The total noise PSD S_n receives contributions from leakage noise, mechanical mode mixing, thermal noise, and amplifier noise,

$$S_n(\omega) = S_{\rm leak}(\omega) + S_{\rm mix}(\omega) + S_{\rm th}(\omega) + S_{\rm amp}(\omega) \, . \tag{3.16}$$

Leakage noise from the oscillator is the dominant noise source at low axion masses and is parametrized as

$$S_{\rm leak}(\omega) = \varepsilon^2 \, P_{\rm in} \left(S_{b_0}(\omega) + \frac{Q_1}{Q_0} \, S_{b_1}(\omega) \right) \equiv S^{(0)}_{\rm leak}(\omega) + S^{(1)}_{\rm leak}(\omega) \; , \tag{3.17}$$

where

$$P_{\rm in} \equiv (\omega_0/Q_0) \, B_0^2 \, V_{\rm cav} \tag{3.18}$$

is the power stored in the cavity and the b_i are defined below. Both terms in Eq. 3.17 are suppressed by $\epsilon \ll 1$, which parametrizes the cross-coupling between the pump mode and readout waveguide, and the coupling between the signal mode and the loading waveguide, which are of the same order.

We define the characteristic amplitude of the pump and signal mode magnetic fields as

$$B_i \equiv \sqrt{\frac{1}{V_{\rm cav}} \int_{V_{\rm cav}} |\mathbf{B}_i(x)|^2} \,, \tag{3.19}$$

where $\mathbf{B}_i(x)$ is the time-independent part of the magnetic field

$$\mathbf{B}_i(x,t) = \mathbf{B}_i(x)\, b_i(t) \,, \tag{3.20}$$

and $b_i(t)$ is the dimensionless time-dependent coefficient. For instance, for a monochromatic source exciting mode i, $b_i(t) = \cos\omega_i t$ and $S_{b_i}(\omega) = \pi^2 \Big(\delta(\omega-\omega_i) + \delta(\omega+\omega_i)\Big)$. More generally, phase noise of the oscillator and mechanical vibrations contribute to $S_{b_i}(\omega)$ such that

$$S_{b_i}(\omega) = \pi^2 \Big(\delta(\omega-\omega_i) + \delta(\omega+\omega_i)\Big) + S_{b_i}^{(\rm phase)} + S_{b_i}^{(\rm mech)} \,, \tag{3.21}$$

where $S_{b_i}^{(\rm phase)}$ and $S_{b_i}^{(\rm mech)}$ are given by Eqs. (3.29) and (3.40), respectively.

3.5.2 Leakage Noise and Signal

Oscillator Phase Noise

We model the oscillator as a voltage V_d that drives the equivalent RLC circuits of the pump and signal modes. In particular, a noisy oscillator is parametrized as a driving voltage with a time-dependent phase $\varphi(t)$,

$$V_d(t) = V_d \, \cos\left(\omega_0 t + \varphi(t)\right) \,, \tag{3.22}$$

where the voltage amplitude is fixed to the power delivered to the pump mode,

$$V_d^2/R_0 = P_{\rm in} \,. \tag{3.23}$$

When the amplitude of the phase is small ($\varphi(t) \ll 1$), the above form can be expanded as

$$V_d(t) \simeq V_d \left(\cos\omega_0 t - \varphi(t) \sin\omega_0 t\right) \,. \tag{3.24}$$

This implies that the PSD of the drive voltage is

$$S_{V_d}(\omega) \simeq R_0\, P_{\rm in} \left[\pi^2 \Big(\delta(\omega-\omega_0) + \delta(\omega+\omega_0)\Big) + \frac{1}{4}\Big(S_\varphi(\omega-\omega_0) + S_\varphi(\omega+\omega_0)\Big)\right] \,. \tag{3.25}$$

As we discuss below, $S_\varphi(\omega)$ is peaked near $\omega \simeq 0$ (see Eq. 3.31). Therefore, for a frequency ω of fixed sign, only one of $S_\varphi(\omega \mp \omega_0)$ dominates in the expression above. By convention, we focus on $\omega \simeq \omega_0 > 0$, such that $S_\varphi(\omega-\omega_0) \gg S_\varphi(\omega+\omega_0)$. Also using that $S_\varphi(\omega) = S_\varphi(-\omega) = S_\varphi(|\omega|)$, we

then have

$$S_{V_d}(\omega) \simeq R_0\, P_{\rm in} \left[\pi^2 \left(\delta(\omega-\omega_0)+\delta(\omega+\omega_0)\right) + \frac{1}{4}\, S_\varphi(|\omega-\omega_0|)\right] . \tag{3.26}$$

Above, the first two terms involving delta functions are simply the PSD of a perfectly monochromatic drive. The inclusion of S_φ accounts for so-called "phase noise" of an imperfect oscillator.

The power delivered to the $i^{\rm th}$ mode is determined by the voltage V_i across the resistor R_i, which obeys Kirchoff's voltage law,

$$\ddot{V}_i(t) + \frac{\omega_i}{Q_i}\,\dot{V}_i(t) + \omega_i^2\, V_i(t) = \frac{\omega_i}{Q_i}\,\dot{V}_d(t)\,. \tag{3.27}$$

In the above equation, we have not included the fact that the oscillator's coupling to the $i=1$ signal mode is suppressed by ε. For convenience, we have instead included this factor in Eq. 3.17, so that the derivation of $S^{(i)}_{\rm leak}$ is identical for $i=0$ and $i=1$. Fourier transforming and solving for the PSD of V_i gives the cavity response function,

$$S_{V_i}(\omega) = \frac{(\omega\,\omega_i/Q_i)^2}{(\omega^2-\omega_i^2)^2 + (\omega\,\omega_i/Q_i)^2}\; S_{V_d}(\omega)\ . \tag{3.28}$$

To change variables from V_i to b_i, we equate the total power, $S_{V_i}(\omega)/R_i = (Q_i/Q_0)\, P_{\rm in}\, S_{b_i}(\omega)$, giving

$$S^{(\rm phase)}_{b_i}(\omega) \simeq \frac{1}{4}\; \frac{(\omega\,\omega_0/Q_i)^2}{(\omega^2-\omega_i^2)^2 + (\omega\,\omega_0/Q_i)^2}\; S_\varphi(|\omega-\omega_0|)\ , \tag{3.29}$$

where we approximated $\omega_0/Q_i \simeq \omega_1/Q_i$.

To incorporate the small, but finite, width of the external oscillator ($\Delta\omega_d \lesssim$ mHz), we replace the delta functions in Eq. 3.21 by

$$\delta(\omega) \simeq \frac{\Theta(\Delta\omega_d/2-|\omega|)}{\Delta\omega_d}\ , \tag{3.30}$$

where Θ is the Heaviside step function. For simplicity, we make the approximation $\Delta\omega_d \ll \omega_0/Q_{\rm int}$ throughout our calculations, since this holds for all parameters we consider. As in Ref. [176], for the phase noise PSD $S_\varphi(\omega)$, we fit the reported spectrum of a commercially available oscillator [146] to the form

$$S_\varphi(\omega) = \sum_{n=0}^{3} c_n\, \omega^{-n}\,. \tag{3.31}$$

We find that the coefficients

$$c_0 \sim 10^{-15}\ {\rm Hz}^{-1}\ ,\ c_1 \sim 10^{-11}\ ,\ c_2 \sim 10^{-10}\ {\rm Hz}\ ,\ c_3 \sim 10^{-8}\ {\rm Hz}^2\ , \tag{3.32}$$

provide a good fit for $\omega_0 \sim 100$ MHz. We fix the overall normalization by demanding that the phase

noise term of Eq. 3.29 smoothly matches on to the the central peak of $S_{b_i}(\omega)$ near $\omega \simeq \omega_0$ when using Eq. 3.30 and $\Delta\omega_d \simeq 0.1$ mHz.

Mechanical Leakage Noise

An additional contribution to S_{b_i} arises from small mechanical vibrations of the cavity walls, which lead to time-dependent shifts of the resonant frequencies. These frequency wobbles affect the mode PSDs by enhancing the power in the high frequency tail. We incorporate this effect by continuing with the analogy to an RLC circuit. If the resonant frequency squared of an equivalent RLC circuit has a small fractional time variation $\Delta(t)$, Kirchoff's voltage law becomes

$$\ddot{V}_i(t) + \frac{\omega_i}{Q_i}\,\dot{V}_i(t) + \omega_i^2 V_i(t) = \frac{\omega_i}{Q_i}\,\dot{V}_d(t) - \omega_i^2\,\Delta(t)\,V_i(t)\,. \tag{3.33}$$

Solving this equation to first order in Δ yields

$$S_{V_i}(\omega) \simeq \frac{(\omega\,\omega_i/Q_i)^2}{(\omega^2-\omega_i^2)^2 + (\omega\,\omega_i/Q_i)^2}\left(S_{V_d}(\omega) + \frac{\omega_i^4}{(2\pi)^2}\int d\omega'\,\frac{S_\Delta(\omega-\omega')\,S_{V_d}(\omega')}{(\omega'^{\,2}-\omega_i^2)^2 + (\omega'\,\omega_i/Q_i)^2}\right)\,. \tag{3.34}$$

Relative to Eq. 3.28, the second term incorporates perturbative corrections from mechanical vibrations. Substituting the leading order piece of $S_{V_d}(\omega)$ from Eq. 3.26 into the ω' integral of Eq. 3.34 and converting from V_i to b_i again yields the mechanical vibration contribution to the unit-normalized mode PSD,

$$S_{b_i}^{(\mathrm{mech})}(\omega) \simeq \frac{1}{4}\,\frac{(\omega\,\omega_0/Q_i)^2}{(\omega^2-\omega_i^2)^2 + (\omega\,\omega_0/Q_i)^2}\,\frac{\omega_0^4}{(\omega_0^2-\omega_i^2)^2 + (\omega_0^2/Q_i)^2}\,\big(S_\Delta(\omega-\omega_0)+S_\Delta(\omega+\omega_0)\big)\,. \tag{3.35}$$

When the modes are degenerate, the second Breit–Wigner factor above simplifies, giving

$$S_{b_i}^{(\mathrm{mech})}(\omega) \simeq \frac{1}{4}\,\frac{(\omega\,\omega_0)^2}{(\omega^2-\omega_i^2)^2 + (\omega\,\omega_0/Q_i)^2}\,\big(S_\Delta(\omega-\omega_0)+S_\Delta(\omega+\omega_0)\big)\,. \tag{3.36}$$

For brevity, we will use this form below, though the more general form Eq. 3.35 is useful when considering what happens when the modes are not exactly degenerate.

The PSD of the frequency wobble $S_\Delta(\omega)$ can be computed using cavity perturbation theory, which treats the small displacement of the cavity walls as an expansion parameter. We will assume that for each axion mass, a single mechanical resonance, labeled by "m," dominates the mechanical vibrations. To first order in cavity perturbation theory, $\Delta(t) \simeq -q_m(t)\,C_i^m$, where the displacement of the cavity walls, projected onto the spatial profile of the mechanical resonance, is parametrized by the generalized coordinate q_m, and the coupling coefficient C_i^m quantifies the mechanical overlap of the electromagnetic cavity modes ($i = 0, 1$) with the m^{th} vibrational mode of the cavity walls [131, 176]. Parametrically, fractional length variations are comparable to the fractional frequency variations they induce, so $|C_i^m| \sim V_{\mathrm{cav}}^{-1/3}$ for maximally coupled mechanical and electromagnetic modes.

The amplitude of the wall displacement q_m is determined by the generalized force f_m, such that

$$S_{q_m}(\omega) = \frac{S_{f_m}(\omega)/M_{\rm cav}^2}{(\omega^2 - \omega_m^2)^2 + (\omega\,\omega_m/Q_m)^2} \ , \tag{3.37}$$

where $M_{\rm cav}$ is the mass of the cavity, ω_m is the frequency of the mechanical resonance, and Q_m is its corresponding mechanical quality factor. Here, f_m should be regarded as the remaining force that couples to the cavity after vibrational attenuation is employed. Since $S_\Delta = |C_i^m|^2\, S_{q_m}$,

$$S_\Delta(\omega \pm \omega_0) = \frac{|C_i^m|^2\, S_{f_m}(\omega \pm \omega_0)/M_{\rm cav}^2}{\big((\omega \pm \omega_0)^2 - \omega_m^2\big)^2 + \big((\omega \pm \omega_0)\,\omega_m/Q_m\big)^2} \ . \tag{3.38}$$

The PSD of the generalized force f_m is peaked towards smaller ω [132], which implies that for frequencies near $\omega \simeq \omega_0$ the $S_\Delta(\omega - \omega_0)$ term dominates over the $S_\Delta(\omega + \omega_0)$ term in Eq. 3.36. As in Ref. [176], we determine the size of the force PSD by fixing the RMS cavity wall displacement $q_{\rm rms} \simeq 0.1$ nm, consistent with DarkSRF [182], and assume that it is dominated by the lowest-lying mechanical resonance of the cavity, with corresponding frequency $\omega_{\rm min}$:

$$S_{f_m}(\omega_{\rm min}) \simeq 4\pi\, M_{\rm cav}^2\, \omega_{\rm min}^3\, q_{\rm rms}^2/Q_m \simeq 10^{-13}\ {\rm N}^2\ {\rm Hz}^{-1} \times \left(\frac{M_{\rm cav}}{1\ {\rm kg}}\right)^2 \left(\frac{\omega_{\rm min}}{1\ {\rm kHz}}\right)^3 \left(\frac{q_{\rm rms}}{0.1\,{\rm nm}}\right)^2 \left(\frac{10^3}{Q_m}\right) . \tag{3.39}$$

In the following discussion, we take $\omega_{\rm min} = 1$ kHz and $Q_m = 10^3$, which are representative of the SRF cavities fabricated for the MAGO experiment [130, 132]. For maximally coupled mechanical and electromagnetic modes, Eqs. (3.36), (3.38), and (3.39) imply that

$$S_{b_i}^{(\rm mech)}(\omega) \simeq \frac{(\omega\,\omega_0)^2}{(\omega^2 - \omega_i^2)^2 + (\omega\,\omega_0/Q_i)^2}\ \frac{\pi\,\omega_{\rm min}^3\,\delta^2/Q_m}{((\omega - \omega_0)^2 - \omega_m^2)^2 + ((\omega - \omega_0)\,\omega_m/Q_m)^2} \ , \tag{3.40}$$

where we defined the fractional cavity wall displacement $\delta \equiv q_{\rm rms}/V_{\rm cav}^{1/3}$. For our baseline estimates, we take $q_{\rm rms} = 0.1$ nm, corresponding to $\delta \sim 10^{-10}$ for a meter-sized cavity.

In the SRF cavity setup of Ref. [130], direct measurements found a forest of mechanical resonances above $\omega_{\rm min}$, approximately separated by 100 Hz. For each axion mass m_a above $\omega_{\rm min}$, mechanical noise is most severe if there exists a resonance at the axion mass, $\omega_m \simeq m_a$, and is least severe if the nearest resonance is separated by 50 Hz. We thus estimate the median noise PSD for each value of m_a by taking the nearest mechanical resonance to be separated by 25 Hz,

$$\omega_m(m_a) \simeq \max\left(\omega_{\rm min}, m_a + 25\,{\rm Hz}\right) . \tag{3.41}$$

See Sec. VC of Ref. [176] for a more detailed discussion regarding this point.

To estimate $S_{f_m}(\omega)$ at lower frequencies, we assume that the attenuated $S_{f_m}(\omega)$ that enters our calculations is flat, i.e., $S_{f_m}(\omega) \simeq S_{f_m}(\omega_{\rm min})$, though the precise spectral shape will depend

on the details of the vibration attenuation mechanism. This estimate is consistent with measured *unattenuated* acceleration PSDs from seismic activity at frequencies as low as 10 μHz [200, 201]. Thus, given the implementation of even modest seismic isolation, our estimate for the low frequency force PSD is quite possibly pessimistic.

The effects of vibrations at very low frequencies, $\omega \lesssim \Delta\omega_r$, are resonantly enhanced by the Breit–Wigner factor in Eq. 3.36. This can cause our perturbative calculation to break down even though δ is small. To ensure this is not an issue, we demand that $S_{b_i}^{(\mathrm{mech})}$ in Eq. 3.40 is smaller than the leading order terms in Eq. 3.21. Approximating the delta functions as in Eq. 3.30, this condition holds at low frequencies if

$$\delta \lesssim \left(\frac{Q_m\ \omega_{\mathrm{min}}}{Q_i^2\ \Delta\omega_d}\right)^{1/2} \sim 10^{-7} \times \left(\frac{10^{12}}{Q_i}\right)\ , \tag{3.42}$$

which is easily satisfied. In fact, the sensitivity of our setup is even robust to δ near the perturbative limit, as shown in the lower-left panel of Fig. 3.5, corresponding to vibrational forces many orders of magnitude greater than seismic noise.

It is worth comparing this situation to that faced by interferometric experiments, where seismic noise is an important limiting factor at low frequencies. Such experiments precisely measure the distance between multiple objects, which are typically freely hung and are independently subject to seismic vibrations. By contrast, our approach takes place entirely within a single rigid cavity. Only the *relative* motion between the cavity walls is relevant for noise, and this is many orders of magnitude smaller than the RMS motion of the ground itself. However, throughout this section, we have used Eq. 3.37, which assumes that the mechanical response of the cavity is elastic. Nonelastic deformations can lead to slow drifts of the cavity frequencies, which is addressed in a dedicated section below.

Signal Power

We calculate the signal PSD using the drive mode PSD $S_{b_0}(\omega)$ derived above. From Eq. (19) of Ref. [176], the general form for the signal PSD is

$$S_{\mathrm{sig}}(\omega) = \frac{1}{(2\pi)^2}\,\frac{\omega_0}{Q_1}\,\left(g_{a\gamma\gamma}\,\eta_a\,B_0\right)^2\,V_{\mathrm{cav}}\,\frac{\omega^2\int d\omega'\ I_a(\omega,\omega')}{(\omega^2-\omega_1^2)^2+(\omega\,\omega_0/Q_1)^2}\ , \tag{3.43}$$

where the axion form factor η_a is defined as in Eq. (4) in the main body and

$$I_a(\omega,\omega') \equiv (\omega-\omega')^2\,S_a(\omega-\omega')\,S_{b_0}(\omega')\ . \tag{3.44}$$

Above, $S_a(\omega)$ is the PSD of the axion field, and $S_{b_0}(\omega)$ includes contributions from Eqs. (3.29) and (3.40), as in Eq. 3.21. For the axion PSD, we use a simplified form that neglects effects from solar

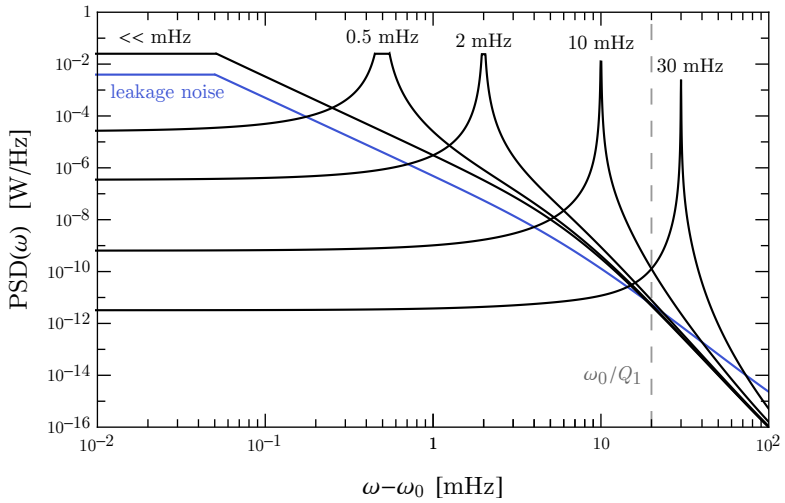

Figure 3.4: The signal (black) and leakage noise (blue) PSDs as a function of $\omega - \omega_0$, for a fixed value of $g_{a\gamma\gamma}$ and various choices of the axion mass (black labels), at critical coupling. The signal PSD peaks at $\omega_{\rm sig}$ and the vertical dashed line denotes the bandwidth $\Delta\omega_r$ of the signal mode. The parameters are those of the second-lowest curve in Fig. 1 in the main body. The signal curve of Fig. 2 of the main body is constructed by taking the maxima of the signal PSDs shown here, as m_a varies.

and terrestrial motion,

$$S_a(\omega) = \Theta(|\omega| - m_a)\, \frac{2\pi^2\, \rho_{\rm DM}}{m_a^3\, \sigma_v^2}\, e^{-(|\omega|-m_a)/(m_a\, \sigma_v^2)}\ , \tag{3.45}$$

where the dispersion velocity is $\sigma_v \simeq 9 \times 10^{-4}$. This is consistent with the normalization $\langle a^2 \rangle = \rho_{\rm DM}/m_a^2$. Examples of the signal PSD, compared to the total leakage noise PSD, are shown in Fig. 3.4 for various values of m_a.

When there is a large hierarchy between the widths of the external oscillator and the axion field, Eq. 3.43 can be simplified by analytically evaluating the ω' integral involving $I_a(\omega, \omega')$. For instance, when the axion is much narrower, $\Delta\omega_a \ll \Delta\omega_d$, we use

$$S_a(\omega) \simeq (2\pi)^2\, \frac{\rho_{\rm DM}}{2m_a^2} \Big(\delta(\omega - m_a) + \delta(\omega + m_a)\Big) \tag{3.46}$$

in Eq. 3.43. Instead, if the oscillator is narrower, $\Delta\omega_d \ll \Delta\omega_a$, then we use

$$S_{b_0}(\omega) \simeq \pi^2 \Big(\delta(\omega - \omega_0) + \delta(\omega + \omega_0)\Big)\ . \tag{3.47}$$

In these limits, the signal PSD simplifies to

$$S_{\rm sig}(\omega) \simeq \frac{1}{2}\,\frac{\omega_0}{Q_1}\,\left(g_{a\gamma\gamma}\,\eta_a\,B_0\right)^2\,V_{\rm cav}\times\begin{cases}\rho_{\rm DM}\,\frac{\omega^2\left(S_{b_0}(\omega-m_a)+S_{b_0}(\omega+m_a)\right)}{(\omega^2-\omega_1^2)^2+(\omega\,\omega_0/Q_1)^2} & \Delta\omega_a \ll \Delta\omega_d\,,\\ \frac{1}{2}\,\frac{\omega^2\left((\omega-\omega_0)^2\,S_a(\omega-\omega_0)+(\omega+\omega_0)^2\,S_a(\omega+\omega_0)\right)}{(\omega^2-\omega_1^2)^2+(\omega\,\omega_0/Q_1)^2} & \Delta\omega_d \ll \Delta\omega_a\,.\end{cases} \tag{3.48}$$

The expression for the signal power in Eq. (5) of the main body can be obtained by approximating the narrowest piece of Eq. 3.48 ($S_a(\omega)$ of width $\Delta\omega_a$, $S_{b_0}(\omega)$ of width $\Delta\omega_d$, or the cavity resonance of width $\Delta\omega_r$) in the expression above as a delta function and integrating over ω.

3.5.3 Additional Noise Sources

Mechanical Noise from Mode Mixing

In the previous section, we showed that mechanical vibrations contribute to leakage noise by affecting how the external oscillator loads power into the high frequency tail of the pump and signal mode PSDs. In addition, deformations of the cavity can lead to "mode mixing," thus allowing for *direct* power transfer between the two modes of interest.

To describe this effect, we use the cavity perturbation theory results of Refs. [186, 131]. For a single mechanical resonance, labeled by "m," to leading order in the fractional displacement of the cavity wall δ, the equation of motion governing the time-evolution of the signal mode is

$$\ddot{V}_1(t) + \frac{\omega_1}{Q_1}\,\dot{V}_1(t) + \omega_1^2\,V_1(t) = \omega_1^2\,\eta_{\rm mix}\,\delta(t)\,V_0(t)\,, \tag{3.49}$$

where we again have used the analogy to an RLC circuit. The dimensionless mechanical form factor $\eta_{\rm mix}$ is

$$\eta_{\rm mix} \propto \int d\mathbf{S}\cdot\boldsymbol{\xi}_m(x)\,\left(\mathbf{E}_0(x)\cdot\mathbf{E}_1(x) - \mathbf{B}_0(x)\cdot\mathbf{B}_1(x)\right)\,, \tag{3.50}$$

where the integral is performed over the surface of the cavity and the spatial profile of the mechanical mode is characterized by the normalized mode vector $\boldsymbol{\xi}_m$. For a perfectly cylindrical cavity, the pump and signal modes considered in this chapter are locally orthogonal, and so $\eta_{\rm mix} = 0$. However, in reality the cavity cannot be manufactured perfectly, and its shape continues to change throughout the experiment due to low frequency deformations sourced by, e.g., seismic noise or fluctuations in the ambient temperature.

We parametrize these static and slowly varying deviations from a cylindrical shape with a fractional displacement $\delta_s(t)$, which has support only on frequencies much less than $\omega_{\rm min} \sim$ kHz. Now, $\eta_{\rm mix}(t) \sim \delta_s(t)$ and the perturbative correction to S_{V_1} from mode mixing in Eq. 3.49 is precisely

the same as that of leakage noise in Eq. 3.33, except that the driving term is proportional to $\eta_{\rm mix}\,\delta(t)\,V_0(t)$ rather than $C_1^m\,q_m(t)\,V_1(t) \sim \delta(t)\,V_1(t)$.[4] Thus, by following the same logic as was used to derive Eq. 3.40, the noise PSD $S_{\rm mix}$ from mode mixing is parametrically

$$\frac{S_{\rm mix}(\omega)}{\varepsilon^2\,P_{\rm in}\;S_{b_1}^{(\rm mech)}(\omega)} \sim \left(\frac{\eta_{\rm mix}}{\varepsilon}\right)^2 \sim \left(\frac{\delta_s}{\epsilon}\right)^2 , \tag{3.51}$$

where we have normalized by the mechanical contribution to leakage noise in Eq. 3.17.

Both δ_s and ϵ parametrize the ability to control the geometry of the experiment and hence are treated together in Ref. [131]. Specifically, ϵ reflects the precision to which the loading and readout waveguide modes can be matched to the pump and signal modes, while δ_s reflects the precision to which the pump and signal modes can be matched to the ideal cylindrical ones. Both would be monitored and controlled by appropriate active feedback mechanisms. Thus, it is reasonable to estimate $\delta_s \sim \epsilon$ in the worst case, making mode mixing merely an $\mathcal{O}(1)$ correction to our existing treatment of mechanical leakage noise. In fact, since the cavity is larger than the waveguides, it would likely be possible to control it to a greater relative precision, $\delta_s \lesssim \epsilon$, in which case mode mixing is negligible. We thus do not include it in our sensitivity projections.

Cavity Frequency Drift

In the previous section, we discussed how low frequency deformations of the cavity can lead to mixing between modes in the presence of higher frequency wall vibrations. Low frequency deformations alone do not lead to significant mode mixing, because the field in each mode adiabatically follows its slowly changing spatial profile. However, they can significantly affect the mode frequencies and the cross-coupling ϵ. In the main body, we have addressed how ϵ must be actively monitored and controlled, as was already done in the MAGO experiment. In this section, we focus on the effect of mode frequency drift, which must be controlled similarly.

Frequency drift manifests as an additional contribution to $\Delta(t)$ in Eq. 3.33, which we write as $\Delta_s(t)$ in analogy to the slow deformations of the cavity walls $\delta_s(t)$. Unlike the elastic deformations considered for mechanical leakage noise, $\Delta_s(t)$ cannot be estimated from first principles, because it depends on technical details such as the cavity's hysteresis upon thermal expansion and contraction. However, since we are assuming the signal and pump modes can be held degenerate within their bandwidth, the RMS of the drift is bounded by

$$\Delta_s^{\rm rms} = \frac{1}{2\pi}\left(\int d\omega\; S_{\Delta_s}(\omega)\right)^{1/2} \lesssim \frac{1}{Q_i} . \tag{3.52}$$

[4] Alternatively, one could include the next order term on the RHS of Eq. 3.49 as $\eta_{\rm mix}\,\delta(t) \to \eta_{\rm mix}\,\delta(t) + \tilde{\eta}_{\rm mix}\,\delta^2(t)$ where $\tilde{\eta}_{\rm mix}$ is an $\mathcal{O}(1)$ form factor that does not vanish even for locally orthogonal modes. Then, upon decomposing $\delta(t)$ in terms of slow and fast components as $\delta(t) = \delta_s(t) + \delta_f(t)$, including the cross term $\delta_s\delta_f$ is equivalent to simply including this contribution as $\eta_{\rm mix} \sim \delta_s$, as we have done here.

The effect of cavity frequency drift is maximized if $S_{\Delta_s}(\omega)$ is entirely supported at $|\omega| \ll \Delta\omega_d, \Delta\omega_r$, in which case the integral in Eq. 3.34 can be performed to give

$$S_{V_i}(\omega) \simeq \frac{(\omega\,\omega_i/Q_i)^2}{(\omega^2-\omega_i^2)^2+(\omega\,\omega_i/Q_i)^2}\; S_{V_d}(\omega)\; \left(1+(Q_i\,\Delta_s^{\rm rms})^2\right)\;. \tag{3.53}$$

Thus, perturbation theory breaks down entirely if Eq. 3.52 is no longer satisfied. In this case, however, we can still understand the effect of Δ_s on physical grounds: since the frequency drift is slow, the oscillations of the modes adiabatically follow it, implying that the pump mode and signal power will be spread over the frequency width $\Delta_s^{\rm rms}\,\omega_i$. This can be shown more precisely using the WKB approximation.[5] Therefore, in the worst case scenario if $\Delta_s^{\rm rms} \simeq 1/Q_i$, the power will at most be spread over the resonator width $\Delta\omega_r$. This can be mimicked by replacing $\Delta\omega_d \to \Delta\omega_r$, as this also spreads out the pump mode and signal over frequency; we show the effect of this on the reach in the upper curve of the lower-right panel of Fig. 3.5 below.

We emphasize that as long as the pump and signal modes can be held degenerate, this is a maximally pessimistic assumption. First, $S_{\Delta_s}(\omega)$ may have some of its support at frequencies $|\omega| \gtrsim \Delta\omega_r$, leading to an off-resonance suppression. For instance, if $S_{\Delta_s}(\omega)$ is flat up to frequency $\Delta\omega_s \gg \Delta\omega_r$, then perturbation theory does not break down instead until $\Delta_s^{\rm rms} \gtrsim \sqrt{\Delta\omega_r/\Delta\omega_s}/Q_i$. Furthermore, if $\Delta_s(t)$ is directly measured by the active feedback system that stabilizes the modes, it can be "deconvolved" almost entirely from the signal. As long as this can be done to a frequency precision of at least $\Delta\omega_d$, low frequency noise does not affect the estimated reach.

Again, we may compare this situation to that faced by interferometers, whose physical dimensions also drift. The fundamental reason that one can monitor the mode frequencies in our approach and subtract out its variations, but not do the same for an interferometer, is that typically the interferometer itself is the most sensitive ruler in the experiment. In our setup, one needs to only measure the signal and pump mode frequencies to fractional precision $\Delta\omega_d/\omega_0$, and atomic clocks exceed this by many orders of magnitude.

As mentioned in the main body, the DarkSRF collaboration has already demonstrated frequency stabilization near that required by our most aggressive parameters. In addition, experimental tests of Lorentz invariance have stabilized cryogenic sapphire microwave oscillators to substantially greater precisions for $\mathcal{O}$(month) timescales [202, 203, 204]. For our approach, even if a continuous run of length $t_{\rm int}$ is infeasible, e.g., if the cavity must be periodically recalibrated, an equivalent sensitivity can be attained by stitching together many shorter runs. Similarly, rare transient events that disrupt the experiment can be removed from the data stream.

[5] For the special case of "monochromatic" frequency wobble of amplitude $\delta\omega$ and frequency ω_Δ, where $V_i(t) \sim \exp(i\omega_i t)\exp(i(\delta\omega/\omega_\Delta)\cos(\omega_\Delta t))$, this can also be shown exactly using the Jacobi–Anger expansion. The $J_n(\delta\omega/\omega_\Delta)e^{i(\omega_i+n\omega_\Delta)t}$ terms have most of their weight for $|n| \sim \delta\omega/\omega_\Delta$, leading to the expected frequency spread of $\delta\omega$.

Thermal and Amplifier Noise

We adopt the same conventions as in Ref. [176] to describe noise arising from thermal fluctuations of the cavity modes and the quantum-limited amplifier in the readout. For completeness, we derive the thermal noise PSD for the signal mode by applying the equipartition theorem to the equivalent RLC circuit. Thermal fluctuations of the signal mode can be modeled as sourced by the resistor, which drives the entire circuit with voltage $V_{\rm th}$. Since the PSD of this noisy driving voltage is flat within the resonance width, we apply the narrow-width approximation to Eq. 3.28, giving

$$S_{V_1} \simeq \frac{\pi\omega_1}{2Q_1}\left(\delta(\omega-\omega_1)+\delta(\omega+\omega_1)\right) S_{V_{\rm th}}(\omega)\ . \tag{3.54}$$

Integrating over ω thus leads to an average voltage across the resistor R_1 of

$$\langle V_1^2\rangle \simeq \frac{\omega_1}{4\pi\, Q_1}\, S_{V_{\rm th}}(\omega_1)\ . \tag{3.55}$$

By the equipartition theorem, the temperature of the circuit T can be related to the energy stored in the inductor L_1, $T/2 \simeq L_1\,\langle I^2\rangle/2$, where I is the current in the circuit. Since the voltage across the equivalent resistor of the signal mode is $V_1 = I\,R_1$, we have $\langle V_1^2\rangle \simeq T\,R_1^2/L_1$. Equating this to Eq. 3.55 and using $Q_i = \omega_i L_i/R_i$, we find $S_{V_{\rm th}} \simeq 4\pi T\,R_1$.

However, only part of the resistance R_1 is due to the intrinsic dissipation $R_{\rm int}$ of the circuit, and only this part necessarily sources thermal fluctuations. If the signal readout is connected to a cold load, so that it does not send thermal noise back to the cavity, then for the signal mode we actually have $S_{V_{\rm th}} \simeq 4\pi T\,R_{\rm int}$. Eq. 3.28 then implies that the thermal noise PSD is

$$S_{\rm th}(\omega) = \frac{S_{V_1}(\omega)}{R_1} = \frac{Q_1}{Q_{\rm int}}\ \frac{4\pi T\,(\omega\,\omega_0/Q_1)^2}{(\omega^2-\omega_1^2)^2+(\omega\,\omega_0/Q_1)^2}\ , \tag{3.56}$$

where we used $R_{\rm int}/R_1 = Q_1/Q_{\rm int}$.

The readout waveguide is attached to an amplifier, which sources its own noise. The lower bound on such noise is dictated by the standard quantum limit, arising from zero-point fluctuations and backaction/imprecision noise. The corresponding PSD is spectrally flat [143],

$$S_{\rm amp}(\omega) = \pi\,\omega_1\,. \tag{3.57}$$

We assume that amplifier noise is quantum-limited, which has been achieved in resonant cavity setups [9] and is often assumed for future projections of other axion experiments, such as DM Radio [115].

3.5.4 Expected Sensitivity

Coupling Optimization

Overcoupling the cavity to the readout corresponds to $Q_{\rm cpl} \ll Q_{\rm int}$. As discussed in Refs. [151, 115, 176], this is optimal for thermal noise limited resonant experiments, even though critical coupling maximizes the signal power, because it decreases *both* the signal power and thermal noise in a way that allows a parametrically faster scan rate. Although these considerations do not apply to our broadband setup, it also benefits from overcoupling for the much simpler reason that it prevents an off-resonance signal from being overwhelmed by amplifier noise. In the limit where amplifier noise dominates, $Q_{\rm cpl}$ should be as small as possible.

For completeness, we now precisely describe how the signal and noise are affected by the value of $Q_{\rm cpl}$. Recall that in the RLC analogy, the signal mode circuit has a resistor $R_1 = R_{\rm int} + R_{\rm cpl}$. When we computed the signal PSD, the thermal noise PSD, and the part of the leakage noise $S^{(1)}_{\rm leak}$ corresponding to the loading waveguide coupling to the signal mode, we computed the total power dissipated across *both* resistors. Thus, the fraction of power sent to the readout is smaller by a factor of $R_{\rm cpl}/R_1 = Q_1/Q_{\rm cpl}$, and all of these PSDs should be rescaled by this amount. Amplifier noise is not affected, since it is intrinsic to the amplifier itself. Finally, consider the part of the leakage noise $S^{(0)}_{\rm leak}$ corresponding to the readout waveguide coupling to the pump mode. In the RLC analogy, the pump mode circuit has a resistor $R_0 = R_{\rm int} + \mathcal{O}(\epsilon^2)\, R_{\rm cpl}$. Therefore, the fraction of power read out as leakage noise is proportional to $R_{\rm cpl}/R_{\rm int} = Q_{\rm int}/Q_{\rm cpl}$, and $S^{(0)}_{\rm leak}$ should be rescaled by this factor.

As described in the main body, we do not consider loaded quality factors lower than $Q_1 \sim 10^5$. One might worry that such a strong coupling to the signal mode might degrade the quality factor of the pump mode. Thus, we impose as a constraint that the power loss in the pump mode due to the readout is negligible, $\epsilon^2 R_{\rm cpl} \ll R_{\rm int}$, which implies

$$Q_{\rm cpl} \gtrsim \max\left[\varepsilon^2\, Q_{\rm int}, 10^5\right] . \tag{3.58}$$

The constraint $Q_{\rm cpl} \gtrsim \varepsilon^2\, Q_{\rm int}$ is unimportant for almost all parameters we consider, except for the most conservative ones in the top-right panel of Fig. 3.5. Critical coupling is optimal for the lowest axion masses, while overcoupling as much as possible is optimal for the highest axion masses. For each intermediate axion mass, a different intermediate coupling is optimal, because overcoupling increases the strength of leakage noise. However, we find numerically that essentially all of the reach shown in Fig. 1 of the main body can be obtained using only a critically coupled run and a maximally overcoupled run. A small remaining slice of parameter space at small couplings and intermediate axion masses can be covered using a third run with $Q_{\rm cpl} \sim 10^7$.

Statistics for Expected Exclusion

In this section, we roughly describe the statistics of a broadband low mass axion search, in order to compute the expected exclusion. One notable result of this analysis is that the sensitivity decreases for $t_{\rm int} \lesssim \tau_a$, where $\tau_a \sim Q_a/m_a$ is the axion coherence time; as derived below, for an integration time $t_{\rm int} = 1$ day or 5 years, the 90% C.L. reach in $g_{a\gamma\gamma}$ is suppressed by approximately a factor of 2 for $m_a \lesssim 10^{-15}$ eV or $m_a \lesssim 10^{-18}$ eV, respectively. A Bayesian approach to the same problem is given in Ref. [165]. A similar frequentist approach is given in Ref. [205], though it focuses on the case $t_{\rm int} \gg \tau_a$.

For concreteness, we neglect unvirialized components of the axion field, as well as any enhanced structure in the axion field that could arise, e.g., from strong axion self-interactions or parametric resonance effects [206, 207, 208, 209, 210, 211]. In the absence of such effects, in the Milky Way the axion can be described as a collection of classical plane waves with independent phases. An experiment with total integration time $t_{\rm int}$ can only resolve frequency bins of width $\Delta\omega \sim 1/t_{\rm int}$. Each bin contains macroscopically many axions; for instance, for $t_{\rm int} \gtrsim \tau_a$,

$$\Delta N_a \simeq \frac{\rho_{\rm DM} V_{\rm cav}}{m_a} \frac{\tau_a}{t_{\rm int}} \simeq 10^{25} \left(\frac{10^{-14}\ \text{eV}}{m_a}\right)^2 \left(\frac{5\ \text{years}}{t_{\rm int}}\right) \left(\frac{V_{\rm cav}}{\text{m}^3}\right) , \tag{3.59}$$

so the central limit theorem applies to the amplitude in each bin. Specifically, suppose we measure $a(t)$ for a time $t_{\rm int}$ and perform a discrete Fourier transform (DFT), yielding the complex amplitude $\tilde{a}_i$ for the frequency bin centered at ω_i. Then the real and imaginary parts of $\tilde{a}_i$ are independent Gaussian random variables with zero mean,[6] so the axion field can be treated as a Gaussian random field. For the rest of this section we will use a PSD normalization suited for these DFT elements, rather than the continuous normalization of Eq. 3.13. For example, for the axion field we define

$$\langle \tilde{a}_i \tilde{a}_j^* \rangle = \delta_{ij}\, S_a(\omega_i) , \tag{3.60}$$

where $S_a(\omega_i)$ is the *discrete* PSD. As illustrated in Ref. [165], a typical realization of $a(t)$ is approximately monochromatic on timescales $t_{\rm int} \lesssim \tau_a$, but fluctuates in amplitude on timescales τ_a with respect to the RMS value $\sqrt{\langle a(t)^2 \rangle} = \sqrt{\rho_{\rm DM}}/m_a$. For $t_{\rm int} \lesssim \tau_a$, the amplitude is approximately fixed for the duration of the experiment, and the possibility of observing a downward amplitude fluctuation is responsible for weakening the projected sensitivity.

For simplicity, we will specialize to axion detection experiments using static fields, and return to our heterodyne approach later. For a static field experiment, the frequency components of the signal $s(t)$ are simply those of the axion field multiplied by a frequency-dependent filtering. Therefore, the signal can also be treated as a Gaussian random field. The experiment measures a data stream $d(t) = s(t) + n(t)$, where the noise $n(t)$ is independent of the signal. For the noise sources that we

[6] Under the standard DFT, the amplitudes $\tilde{a}_i$ in neighboring bins will actually be slightly correlated. We neglect this small effect below.

consider, $n(t)$ is also a Gaussian stationary random variable with zero mean. Thus, the likelihood of observing the data is

$$L[\tilde{d}] = \prod_i \frac{e^{-|\tilde{d}_i|^2/(S_s(\omega_i)+S_n(\omega_i))}}{\pi(S_s(\omega_i)+S_n(\omega_i))} \tag{3.61}$$

where the frequency bins have width $\Delta\omega = 2\pi/t_{\rm int}$. We note that this result has been previously derived in Ref. [205].

We assume for simplicity of notation that the data is taken in a single continuous run, but this is not necessary, as distinct runs can be stitched together. In fact, given a fixed integration time $t_{\rm int}$, this can actually be advantageous. As long as $t_{\rm exp} \gg \tau_a$, where $t_{\rm exp}$ is the total duration of the experiment, the reach will not be penalized by the effect discussed above because the distinct runs during the experiment will sample different amplitudes for the axion field. In addition, Eq. 3.61 implicitly assumes that the axion oscillates many times during the experiment, $t_{\rm exp} \gg 1/m_a$. For $t_{\rm exp} \lesssim 1/m_a$, the likelihood additionally depends on the instantaneous phase of the axion field, which leads to an additional $\mathcal{O}(1)$ suppression of the reach; we will not consider this case below.

The average signal and noise PSDs $S_s(\omega_i)$ and $S_n(\omega_i)$ also depend on nuisance parameters $\theta_{s,n}$ that we imagine are measured with calibration runs. For the purposes of placing an exclusion on $g_{a\gamma\gamma}$, it is convenient to define

$$g_{a\gamma\gamma}^2\, \lambda_{s,i}(\theta_s) \equiv S_s(\omega_i, \theta_s)\,, \quad \lambda_{n,i}(\theta_n) \equiv S_n(\omega_i, \theta_n) \tag{3.62}$$

so that the likelihood takes the form

$$L(g_{a\gamma\gamma}, \theta_s, \theta_n) = \prod_i \frac{e^{-|\tilde{d}_i|^2/(g_{a\gamma\gamma}^2\lambda_{s,i}(\theta_s)+\lambda_{n,i}(\theta_n))}}{\pi(g_{a\gamma\gamma}^2\,\lambda_{s,i}(\theta_s)+\lambda_{n,i}(\theta_n))}\; L_{\rm aux}(\theta_s, \theta_n)\,, \tag{3.63}$$

where $L_{\rm aux}$ contains the results of calibration measurements and is not necessarily Gaussian. These measurements are independent of the data that we take during our physics run, so the two probabilities multiply.

Let $\hat{g}_{a\gamma\gamma}$ be the maximum likelihood estimator for $g_{a\gamma\gamma}$. The incompatibility of the coupling value $g_{a\gamma\gamma}$ with the data can be quantified by the test statistic [212]

$$q(g_{a\gamma\gamma}) = -2\,\log\left(\frac{L(g_{a\gamma\gamma}, \hat{\hat{\theta}}_s, \hat{\hat{\theta}}_n)}{L(\hat{g}_{a\gamma\gamma}, \hat{\theta}_s, \hat{\theta}_n)}\right)\,\Theta(g_{a\gamma\gamma}^2 - \hat{g}_{a\gamma\gamma}^2)\,, \tag{3.64}$$

where $\hat{g}_{a\gamma\gamma}$ and $\hat{\theta}_{s,n}$ are unconditional maximum-likelihood estimators and $\hat{\hat{\theta}}_{s,n}$ are conditional maximum-likelihood estimators for fixed $g_{a\gamma\gamma}$. The step function reflects the fact that we should not be able to exclude couplings smaller than the best-fit value. Below, we will assume $L_{\rm aux}(\hat{\theta}_s, \hat{\theta}_n) \simeq L_{\rm aux}(\hat{\hat{\theta}}_s, \hat{\hat{\theta}}_n)$, so the nuisance parameters play little role.

When the integration time is much longer than the axion coherence time, $t_{\rm int} \gg \tau_a$, the axion

signal is spread over many bins, and asymptotic theorems apply. In particular, Wilks' theorem [213] implies that the distribution of $q(g_{a\gamma\gamma})$ for fixed $g_{a\gamma\gamma}$ is a half chi-squared distribution with one degree of freedom, implying that the 90% and 95% C.L. upper bounds are

$$q_{90\%} = 1.64, \quad q_{95\%} = 2.71. \tag{3.65}$$

Assuming that no axion exists, the exclusion that can be set varies from trial to trial. We use the approach illustrated in Ref. [212], where it is shown that the median exclusion is achieved by the so-called Asimov dataset, in which each of the $|\tilde{d}_i|^2$ are set to the mean value achieved in a background-only dataset, i.e., $|\tilde{d}_i|^2 \to \lambda_{n,i}$. In this case, $\hat{g}^2_{a\gamma\gamma} = 0$. Using this in Eq. 3.64 and approximating $g^2_{a\gamma\gamma}\,\lambda_{s,i} \ll \lambda_{n,i}$ for all $g_{a\gamma\gamma}$ near the sensitivity threshold (valid because the signal is spread over many bins) gives

$$q(g_{a\gamma\gamma}) \simeq \sum_i \left(\frac{g^2_{a\gamma\gamma}\,\lambda_{s,i}(\hat{\hat{\theta}}_s)}{\lambda_{n,i}(\hat{\hat{\theta}}_n)} \right)^2 , \tag{3.66}$$

where we assumed $\lambda_n(\hat{\theta}_n) \simeq \lambda_n(\hat{\hat{\theta}}_n)$. This is closely related to the signal-to-noise ratio (SNR) used to estimate the reach in many axion experiments (see, e.g., Ref. [176]), as can be shown by approximating the sum in the above expression as an integral,

$$q(g_{a\gamma\gamma}) \simeq \frac{t_{\rm int}}{2\pi} \int_0^\infty d\omega \left(\frac{S_s(\omega)}{S_n(\omega)} \right)^2 = {\rm SNR}^2 \, . \tag{3.67}$$

Since this result involves a ratio of PSDs, it also holds for the continuous PSD normalization of Eq. 3.13. Here, negative frequency bins were not included since they are not independent of the positive frequency bins. Combining this with Eq. 3.65 implies that the median 90% or 95% expected exclusion corresponds to an SNR of

$${\rm SNR}(t_{\rm int} \gg \tau_a) \gtrsim \begin{cases} 1.3 & 90\% \text{ C.L.} \\ 1.6 & 95\% \text{ C.L.} \, , \end{cases} \tag{3.68}$$

which roughly matches the SNR $\gtrsim 1$ prescription commonly adopted in the axion literature (see, e.g., Refs. [214, 114]).

In the short integration time limit $t_{\rm int} \ll \tau_a$, the axion signal cannot be resolved, and hence lies in a single frequency bin.[7] In the following we omit for simplicity the explicit dependence on nuisance parameters and $L_{\rm aux}$. We continue to assume negligible systematic errors: $\lambda_n(\hat{\theta}_n) \simeq \lambda_n(\hat{\hat{\theta}}_n)$ and

[7] More precisely, the axion signal could straddle two frequency bins; we neglect this small effect.

$L_{\rm aux}(\hat{\theta}_s, \hat{\theta}_n) \simeq L_{\rm aux}(\hat{\hat{\theta}}_s, \hat{\hat{\theta}}_n)$. Dropping the i subscript and defining $S \equiv |\tilde{d}_i|^2$, we have

$$L(g^2_{a\gamma\gamma}) = \frac{e^{-S/(g^2_{a\gamma\gamma}\,\lambda_s + \lambda_n)}}{g^2_{a\gamma\gamma}\,\lambda_s + \lambda_n} \ . \tag{3.69}$$

In this case, Wilks' theorem does not apply, but the calculation of the test statistic is analytically tractable. In particular, $\hat{g}^2_{a\gamma\gamma}$ can be found by analytically maximizing the likelihood, giving

$$\hat{g}^2_{a\gamma\gamma} = \begin{cases} (S - \lambda_n)/\lambda_s & S \geq \lambda_n \\ 0 & S < \lambda_n \end{cases} \tag{3.70}$$

where the second line is a consequence of $g^2_{a\gamma\gamma} > 0$. The test statistic then takes the explicit form

$$q(g^2_{a\gamma\gamma}, S) = 2 \times \begin{cases} 0 & g^2_{a\gamma\gamma}\,\lambda_s + \lambda_n < S \\ \frac{S}{g^2_{a\gamma\gamma}\,\lambda_s + \lambda_n} - 1 + \log \frac{g^2_{a\gamma\gamma}\,\lambda_s + \lambda_n}{S} & \lambda_n \leq S \leq g^2_{a\gamma\gamma}\,\lambda_s + \lambda_n \\ \frac{S}{g^2_{a\gamma\gamma}\,\lambda_s + \lambda_n} - \frac{S}{\lambda_n} + \log \frac{g^2_{a\gamma\gamma}\,\lambda_s + \lambda_n}{\lambda_n} & S < \lambda_n \ . \end{cases} \tag{3.71}$$

At fixed $g^2_{a\gamma\gamma}$, $q(g^2_{a\gamma\gamma}, S)$ is a monotonically decreasing function of S. Thus, to compute the upper bound q_α on q corresponding to a given C.L. α, we can find the value S_α such that the probability for $S \leq S_\alpha$ is $P(S \leq S_\alpha) = 1 - \alpha$ in order to obtain $q_\alpha(g^2_{a\gamma\gamma}) = q(g^2_{a\gamma\gamma}, S_\alpha(g^2_{a\gamma\gamma}))$. Using the known distribution of S in Eq. 3.69 for a given axion coupling $g^2_{a\gamma\gamma}$, we have

$$\int_0^{S_\alpha(g^2_{a\gamma\gamma})} dS \ \frac{e^{-S/(g^2_{a\gamma\gamma}\,\lambda_s + \lambda_n)}}{g^2_{a\gamma\gamma}\lambda_s + \lambda_n} = 1 - \alpha \ . \tag{3.72}$$

Solving for S_α then yields

$$S_\alpha(g^2_{a\gamma\gamma}) = |\log \alpha| \, (g^2_{a\gamma\gamma}\,\lambda_s + \lambda_n) \ . \tag{3.73}$$

Therefore, in the event that there is no axion signal, the median expected exclusion for an experiment at $(100 \times \alpha)\%$ C.L. is determined by solving [212]

$$q_\alpha(g^2_{a\gamma\gamma}) = q\big(g^2_{a\gamma\gamma}, S_{0.5}(0)\big) \ . \tag{3.74}$$

Once again identifying $q(g^2_{a\gamma\gamma}) \simeq \mathrm{SNR}^2$, we find that the median expected 90% or 95% limit on $g_{a\gamma\gamma}$ corresponds to

$$\mathrm{SNR}(t_{\rm int} \ll \tau_a) \gtrsim \begin{cases} 5.6 & 90\% \text{ C.L.} \\ 12.5 & 95\% \text{ C.L.} \end{cases} \tag{3.75}$$

Since the SNR is proportional to $g^2_{a\gamma\gamma}$, the higher threshold in Eq. 3.75 compared to Eq. 3.68 corresponds to weakening the 90%–95% C.L. sensitivity projections for $g_{a\gamma\gamma}$ by a factor of 2–3 when

$t_{\rm int} \lesssim \tau_a$.

For comparison, Ref. [165] instead found a weakening of ~ 4 for the 95% C.L. $g_{a\gamma\gamma}$ projections, using a Monte Carlo estimate for the test statistic sampling distribution. That work also found a weakening factor of ~ 10 at 95% C.L. using a Bayesian approach with a flat prior on $g_{a\gamma\gamma}$. However, a flat prior in $\log g_{a\gamma\gamma}$ is also reasonable on subjective grounds, as evidenced by the common use of logarithmic scales in plots like Fig. 1 in the main body. The logarithmic prior penalizes smaller values of $g_{a\gamma\gamma}$ much less, and thus the weakening of the sensitivity for $t_{\rm int} \lesssim \tau_a$ is more mild. Similarly, a flat prior in $g_{a\gamma\gamma}^2$ would also be reasonable since the signal is proportional to it, but this penalizes smaller values of $g_{a\gamma\gamma}$ to a greater degree, enhancing the sensitivity suppression. Since the conclusions of the Bayesian approach vary significantly between reasonable priors, we adopt the frequentist approach described above.

In the above analysis, we have mainly sought to explain analytically why the reach is weakened for $t_{\rm int} \lesssim \tau_a$. Since this effect arises solely from the fluctuations of the axion field amplitude, we expect that a similar penalty factor should apply for our heterodyne approach. However, showing this analytically would be notationally complex, because the axion Fourier components are spread out by, e.g., the width of the driver $\Delta\omega_d$, which simultaneously affects the noise. Thus, we defer a more detailed numerical calculation of the projected sensitivity to future work. To estimate our reach here, we use Eqs. (3.67), (3.68), and (3.75), along with the following small modification: for a static field experiment, bins at positive and negative frequencies $\pm\omega$ are redundant because the data stream is real-valued. For a heterodyne experiment, bins at $\omega_0 \pm \omega$ are redundant for the same reason, so Eq. 3.67 should only integrate over positive frequencies above ω_0. The sole exception is when amplifier noise dominates, since its contributions at frequencies $\omega_0 \pm m_a$ are independent of each other.

3.5.5 Variations of Experimental Parameters

To demonstrate the robustness of the approach, in Figs. 3.5 and 3.6 we show the expected reach for experimental parameters which are orders of magnitude worse than the state of the art.

- In the upper-left panel, we vary the intrinsic quality factor $Q_{\rm int}$. Lowering $Q_{\rm int}$ only has an adverse effect at the lowest axion masses; for higher axion masses there is no effect because the signal mode is taken to be strongly overcoupled in this mass range.

- In the upper-right panel, we vary the leakage noise suppression ϵ. Even for $\epsilon = 10^{-3}$ (four orders of magnitude above that measured by MAGO), corresponding to straightforward millimeter-level control of the cavity geometry, substantial new parameter space can be covered.

- In the lower-left panel, we increase the attenuated displacement of the cavity walls by four orders of magnitude. Increasing $q_{\rm rms}$ lowers the reach at intermediate masses, where mechanical noise dominates, but leaves the sensitivity to other axion masses unchanged.

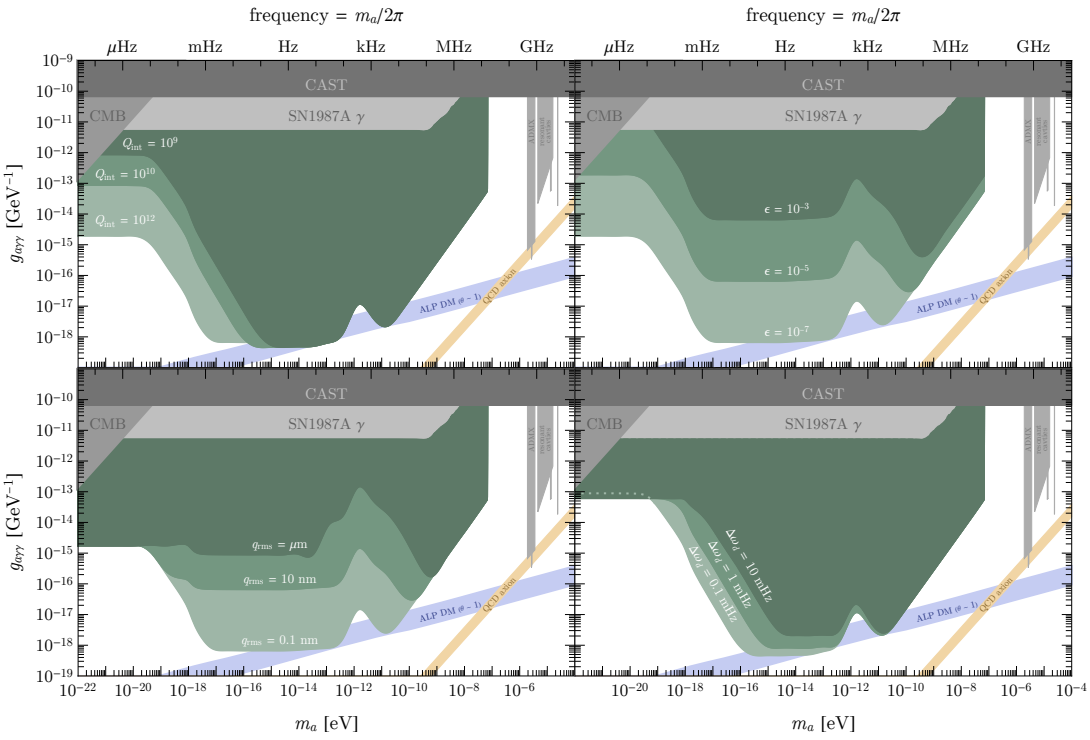

Figure 3.5: The projected 90% C.L. reach of our setup for a wider range of experimental parameters. The benchmark parameters are those of the lowest curve of Fig. 1 in the main body, except for the lower-right panel, where we take $Q_{\rm int} = 10^{10}$. For all panels, we assume an integration time $t_{\rm int} = 5$ years. The green dotted line in this panel shows the reach for $\Delta\omega_d = 0.1$ mHz, demonstrating the small effect of $\Delta\omega_d$ on the sensitivity to small axion masses.

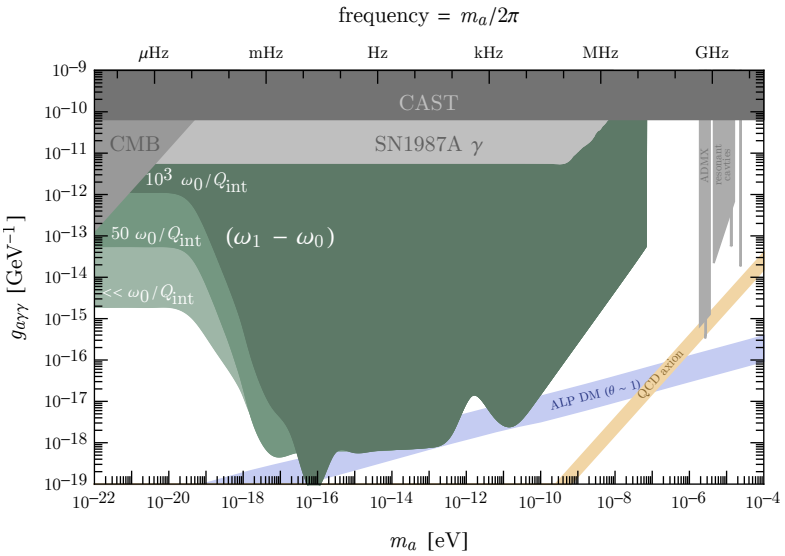

Figure 3.6: The projected 90% C.L. reach of our setup, assuming experimental benchmarks as in Fig. 3.5. We vary the frequency splitting $\omega_1 - \omega_0$ between the pump and signal modes, relaxing the assumption of degeneracy within the bandwidth made in the main body of this chapter.

- In the lower-right panel we increase $\Delta\omega_d$. As discussed in the appendix, this mimics the effect of increased low frequency noise in the form of slow drifts of the resonant frequencies over the range $\omega_0 \pm \Delta\omega_d$. Since we have assumed that the pump and signal modes can be held degenerate (equivalent to $\Delta\omega_d \lesssim \Delta\omega_r$), we have decreased the quality factor to $Q_{\rm int} = 10^{10}$ for this panel. Increasing $\Delta\omega_d$ has little effect at low axion masses because the signal and noise already overlap completely in frequency. However, for intermediate masses, larger $\Delta\omega_d$ decreases the sensitivity since it broadens the signal compared to the dominant noise source. At higher axion masses, there is no effect because $\Delta\omega_a \gtrsim \Delta\omega_d$.

- In Fig. 3.6 we relax the assumption that the pump and signal mode are degenerate within their bandwidth. Although the reach is degraded for $m_a \lesssim \omega_1/Q_1$, new parameter space in this region can still be probed for splittings up to $\omega_1 - \omega_0 \simeq 10^3 \times \omega_1/Q_1$. In addition, the reach at higher masses, near $m_a \simeq \omega_1 - \omega_0$ is resonantly enhanced. Hence, Fig. 3.6 shows that this approach can probe orders of magnitude of unexplored parameter space even if the frequency splitting is much larger than the bandwidth.

Chapter 4

Polarization Haloscopes

This chapter is based on *Discovering QCD-Coupled Axion Dark Matter with Polarization Haloscopes*, by A. Berlin, K. Zhou, Phys. Rev. D 108, 035038 (2023).

Abstract

In the presence of QCD axion dark matter, atoms acquire time-dependent electric dipole moments. This effect gives rise to an oscillating current in a nuclear spin-polarized dielectric, which can resonantly excite an electromagnetic mode of a microwave cavity. We show that with existing technology such a "polarization haloscope" can explore orders of magnitude of new parameter space for QCD-coupled axions. If any cavity haloscope detects a signal from the axion-photon coupling, an upgraded polarization haloscope has the unique ability to test whether it arises from the QCD axion.

4.1 Introduction

The QCD axion is a long-standing, well-motivated dark matter candidate [93, 94, 95, 96, 100, 101, 102] that can also explain why the neutron's electric dipole moment (EDM) is at least 10^{10} times smaller than generically expected [215]. It is a pseudoscalar field a defined by its coupling to gluons

$$\mathcal{L} \supset \theta_a \frac{\alpha_s}{8\pi} G^{\mu\nu}\tilde{G}_{\mu\nu} \ , \tag{4.1}$$

where $\theta_a \equiv a/f_a$ and f_a is the axion decay constant. At temperatures below the QCD phase transition, this coupling generates a potential and mass for the axion [216]

$$m_a = 5.7 \ \mu\text{eV} \times (10^{12} \ \text{GeV}/f_a) \ . \tag{4.2}$$

Over cosmological time, the axion field relaxes towards the minimum of its potential at the parity ($\mathcal{P}$) and time-reversal ($\mathcal{T}$) conserving point $\theta_a = 0$ where the neutron EDM vanishes. Assuming a standard cosmological history and an $\mathcal{O}(1)$ initial misalignment angle, the residual energy in the axion field accounts for the present density of cold dark matter for $m_a \sim (0.5 - 50)\,\mu$eV [160]. In this case, the local axion field has macroscopic mode occupancy and can thus be described by a classical expectation value,

$$\theta_a \simeq \frac{\sqrt{2\rho_{\text{DM}}}}{m_a f_a} \cos m_a t \ \simeq \ 4.3 \times 10^{-19} \cos m_a t \ , \tag{4.3}$$

oscillating with frequency $m_a/2\pi \sim (0.1 - 10)$ GHz, where $\rho_{\text{DM}} \simeq 0.4$ GeV/cm^3 is the local dark matter density.

The direct signatures of QCD axion dark matter are nuclear effects, such as the oscillating neutron EDM [217],

$$d_n \simeq \left(2.4 \times 10^{-3} \ e \ \text{fm}\right) \theta_a \ . \tag{4.4}$$

Detecting such a small signal is very difficult, but has been addressed by several recent proposals. In some cases, static EDM experiments may be repurposed to constrain slowly oscillating EDMs [218, 219, 220]. Other potential detection avenues involve nuclear magnetic resonance [116, 20, 221], spin precession in storage rings [222, 223, 224, 21, 225, 226], atomic and molecular spectroscopy [227, 228], and mechanical oscillations in piezoelectric materials [46]. However, none of these probes are sensitive at the GHz frequencies motivated by standard misalignment production of axion dark matter.

Currently, the most stringent laboratory constraints on axion dark matter at GHz frequencies come from cavity haloscopes [107, 229], which rely on the axion's coupling to photons, $\mathcal{L} \supset g_{a\gamma\gamma} a F^{\mu\nu}\tilde{F}_{\mu\nu}/4$. In these experiments, axion dark matter produces an effective current $\mathbf{J}_{a\gamma\gamma} = g_{a\gamma\gamma}\mathbf{B}\partial_t a$ inside a microwave cavity with background magnetic field $\mathbf{B}$, which can resonantly excite a mode of angular frequency m_a. While there are many other recent proposals to search for the axion (see

Refs. [45, 230, 231] for reviews), the cavity haloscope concept is currently the most well-developed, with many collaborations reporting new results [232, 233, 234, 9, 235, 236, 237, 238, 239, 240, 241, 242, 243, 244, 245, 246, 247, 14, 248] and some operating near or beyond the standard quantum limit [234, 235, 236, 241]. These experiments are well-motivated, as the axion-gluon coupling of Eq. (4.1) is known to induce an axion-photon coupling. However, their relation is indirect: the coefficient $g_{a\gamma\gamma}$ can vary by orders of magnitude within simple models [249, 250, 251, 252], and an axion with an electromagnetic coupling is not necessarily the QCD axion. Definitively discovering or excluding the QCD axion thus requires confronting the axion-gluon coupling directly.

In this chapter, we present the first method to probe the axion-gluon coupling at GHz frequencies. In the presence of axion dark matter, atoms have oscillating EDMs of magnitude d_A directed along their nuclear spin [253], analogous to the neutron EDM in Eq. 4.4. A dielectric thus carries a polarization density $P_{\rm EDM} \sim n_A\, d_A$, where n_A is the density of nuclear spin-polarized atoms. A time-varying polarization induces a physical electromagnetic current $\mathbf{J}_{\rm EDM} = \partial_t \mathbf{P}_{\rm EDM}$, which can be resonantly amplified by placing the dielectric in a microwave cavity with a mode of angular frequency m_a. We call this system, depicted in Fig. 4.1, a polarization haloscope.

To quickly estimate its potential, we may compare the current in a polarization haloscope to that produced in a typical cavity haloscope. For the benchmark DFSZ model, where $g_{a\gamma\gamma} \simeq 0.87 \times 10^{-3}/f_a$ [104, 103], the ratio is

$$\frac{J_{\rm EDM}}{J_{a\gamma\gamma}} \simeq 10^{-3} \times \frac{d_A}{d_n} \left(\frac{n_A}{5\times 10^{22}\ \text{cm}^{-3}}\right) \left(\frac{8\ \text{T}}{B}\right) , \tag{4.5}$$

which suggests that the signal in a cavity haloscope is larger. Furthermore, $J_{\rm EDM}$ is more difficult to calculate, as it depends sensitively on nuclear, atomic, and material properties. For these reasons, the polarization haloscope idea was briefly raised and discarded thirty years ago [254]. However, the rapid recent progress in cavity haloscopes motivates a thorough analysis of its potential. In section 4.2 we show that $d_A \sim d_n$ can be achieved for certain atoms. We then consider the factors necessary to develop an effective polarization haloscope, such as cavity design (section 4.3), material choice (section 4.4), and nuclear spin polarization (section 4.5). We estimate experimental sensitivity in section 4.6 and conclude in section 4.7, laying out a path towards reaching the QCD axion.

4.2 Axion-induced EDMs

The dominant nuclear contribution to the EDM of an atom with atomic number Z arises from the $\mathcal{P},\mathcal{T}$-violating piece of the effective nuclear electric potential [255, 256, 257, 258, 259, 260]

$$\phi_N^{(\rm eff)}(\mathbf{x}) = \left(1 + \frac{1}{Ze}\,\mathbf{d}_N \cdot \nabla\right) \phi_N(\mathbf{x}) \ , \tag{4.6}$$

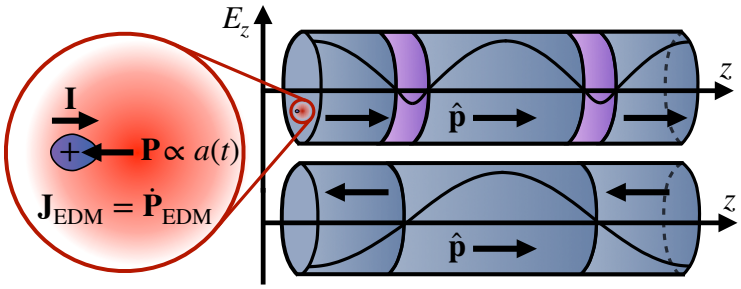

Figure 4.1: Atoms carry EDMs proportional to the axion field (left), aligned with the nuclear spin $\mathbf{I}$. The axion's time variation thus produces a current $\mathbf{J}_{\rm EDM}$ in a nuclear spin-polarized dielectric, whose effect can be amplified in a resonant cavity. For higher axion masses, the geometric overlap factor in Eq. (4.19) can be maximized using layers of inert dielectric (top) or alternating spin polarization (bottom).

which includes the usual electric potential ϕ_N of the nucleus and the response of the atomic electrons to the nuclear EDM $\mathbf{d}_N$. The leading $\mathcal{P},\mathcal{T}$-violating term in a multipole expansion of $\phi_N^{(\rm eff)}$ is the dipole, but it simply vanishes, in accordance with Schiff's theorem [261] which states that the nuclear EDM is efficiently screened by the atomic electrons. The next $\mathcal{P},\mathcal{T}$-violating term is the octupole. Its traceless part corresponds to an electric octupole moment, whose effects are suppressed by the centrifugal barrier near the nucleus [255]. The traceful part yields the dominant contribution to the atomic EDM and is described by the Schiff moment [256],

$$\mathbf{S} = \frac{1}{10}\int d^3\mathbf{x}\;\rho_N(\mathbf{x})\,r^2\left(\mathbf{x} - \frac{5}{3}\frac{\mathbf{d}_N}{Ze}\right)\,, \tag{4.7}$$

where ρ_N is the nuclear charge density; $\mathbf{S}$ sources a $\mathcal{P},\mathcal{T}$-violating electric field that polarizes the atomic electrons, perturbing the electronic Hamiltonian by

$$V_S = -\sum_{i=1}^{Z} e\,\mathbf{S}\cdot\nabla\delta^3(\mathbf{x}_i)\,, \tag{4.8}$$

where the nucleus is at the origin. The interaction V_S mixes opposite parity states, which to first order in perturbation theory gives rise to a non-vanishing atomic EDM, parallel to the nuclear spin $\mathbf{I}$, of the form

$$\mathbf{d}_A \simeq \sum_n \frac{\langle n|V_S|0\rangle\,\langle 0|\mathbf{D}|n\rangle}{E_n - E_0} + \text{h.c.}\,, \tag{4.9}$$

where $|n\rangle$ are atomic states of energy E_n and $\mathbf{D} = -\sum_{i=1}^{Z} e\,\mathbf{x}_i$ is the atomic EDM operator. The result scales as $d_A \propto Z^2 S$, with a moderate relativistic enhancement for the heaviest nuclei. Scaling

numeric results for ^{225}Ra from Refs. [262, 263, 264, 265] yields

$$d_A \simeq -\big(0.27 \times 10^{-3}\ e\ \text{fm}\big)\ \langle S_z\rangle/(e\ \text{fm}^3) \tag{4.10}$$

for ^{161}Dy, with values within 20% for the other nuclei we will consider below. Here, $\langle S_z\rangle$ is the lab-frame expectation value of the Schiff moment directed along the nuclear spin for a maximally-polarized nucleus, $M = I$ [259].

In perturbation theory, the Schiff moment is

$$\langle S_z\rangle \simeq \sum_n \frac{\langle n|V_{\mathcal{PT}}|0\rangle\,\langle 0|S_z|n\rangle}{E_n - E_0} + \text{h.c.}\ , \tag{4.11}$$

where $|n\rangle$ are nuclear states of energy E_n and $V_{\mathcal{PT}} \propto \theta_a$ is the axion's $\mathcal{P},\mathcal{T}$-violating modification to the pion-mediated internucleon interaction. For a typical spherical nucleus with mass number A and radius $R_0 \simeq (1.2\ \text{fm})\,A^{1/3}$, we expect [256, 255]

$$\langle n|V_{\mathcal{PT}}|0\rangle \sim (10^{-2}\,\theta_a/m_n\,R_0)\ (A/m_\pi^2\,R_0^3)\ , \tag{4.12}$$

$$\langle 0|S_z|n\rangle \sim eR_0^3\ , \tag{4.13}$$

$$E_n - E_0 \sim A/m_\pi^2 R_0^3\ , \tag{4.14}$$

which yields the parametric estimate

$$\langle S_z\rangle \sim 10^{-2}\,\frac{eR_0^2}{m_n}\,\theta_a \sim (0.1 \times e\ \text{fm}^3)\,\theta_a\left(\frac{A}{10^2}\right)^{\frac{2}{3}}\ , \tag{4.15}$$

in agreement with detailed calculations [256, 255, 266, 267, 268, 269, 270, 46].

This yields only a small atomic EDM, $d_A \ll d_n$, but for nonspherical nuclei there can be a large intrinsic Schiff moment S_{int} in the body-fixed frame. Evaluating Eq. 4.7 gives $S_{\text{int}} \propto \beta_2\beta_3\,ZeR_0^3$, where β_2 and β_3 parametrize the quadrupole and octupole deformation of the nuclear radius. The lab-frame Schiff moment is then determined by averaging over nuclear orientations, $\langle S_z\rangle = S_{\text{int}}\langle\hat{n}_z\rangle$ where $\hat{\mathbf{n}}$ is the nuclear axis. A nonzero $\langle\hat{n}_z\rangle$ requires $\mathcal{P}$-violation and is thus proportional to θ_a. It can be calculated perturbatively with an expression analogous to Eq. 4.11, the main difference being that octupole deformations imply states with small energy gaps, $E_n - E_0 \sim 50$ keV. For significantly octupole-deformed nuclei, $\beta_2 \sim \beta_3 \sim \mathcal{O}(0.1)$, various numeric factors cancel, leaving [266, 267, 268, 269, 270]

$$\langle S_z\rangle \sim 10^{-2}\,\frac{ZeR_0^2}{m_n}\,\theta_a\ , \tag{4.16}$$

which is crucially enhanced by Z relative to Eq. 4.15. Applying Eq. 4.10, we find that for these

	^{161}Dy	^{153}Eu	^{155}Gd
estimated $\langle S_z \rangle$ (e fm^3 θ_a) [271]	4.3	1.0	1.2
estimated $\lvert d_A \rvert$ (10^{-3} e fm θ_a)	1.2	0.25	0.3
natural abundance [272]	19%	52%	15%
metal price (\$/ton) [273]	300 k	30 k	30 k
$T\, df_p/dB\vert_{B=0}$ (mK/T) [272]	0.08	0.26	0.05

Table 4.1: Stable nuclei with large axion-induced Schiff moments $\langle S_z \rangle$ and atomic EDMs d_A, and their natural abundance and price. We use the last row (equal to $|\gamma|\,(I+1)/3$ where γ is the gyromagnetic ratio [1]) to determine the fractional nuclear spin polarization f_p at a temperature T in a magnetic field B.

nuclei,

$$|d_A| \sim \left(\text{few} \times 10^{-3}\right)\, e \text{ fm} \times \theta_a \left(\frac{Z}{10^2}\right)^3 \left(\frac{A}{10^2}\right)^{\frac{2}{3}} , \tag{4.17}$$

which, as anticipated above, is comparable to d_n.

Most octupole-deformed nuclei are short-lived and thus infeasible to gather in the macroscopic quantities required. Of the nuclei highlighted in Refs. [265, 271, 274], we identify ^{161}Dy, ^{153}Eu, and ^{155}Gd as the most promising. They are absolutely stable and, as indicated in Table 4.1, are inexpensive and expected to possess fairly large axion-induced Schiff moments and atomic EDMs. However, the existence of octupole deformation in these nuclei is not completely settled [275]. This chapter motivates further experimental study. Even if none of these nuclei are octupole deformed, it may still be possible to achieve comparable EDMs via magnetic quadrupole moments, which are enhanced by well-established nuclear quadrupole deformations [271].

4.3 Cavity Excitation

The axion field oscillates with a phase offset and amplitude varying over the coherence time $\tau_a \sim Q_a/m_a$, where $Q_a \sim 10^6$. For all axion masses we consider, spatial gradients of the axion field are negligible. The cavity response is therefore very similar to that of a conventional haloscope, with $\mathbf{J}_{a\gamma\gamma}$ replaced by $\mathbf{J}_{\text{EDM}} \simeq m_a\, n_A\, \mathbf{d}_A$. In our case, there is also an associated physical charge density $\rho_{\text{EDM}} = -\nabla \cdot \mathbf{P}_{\text{EDM}}$ in the cavity, which produces small electric fields, but it is not of interest because it cannot excite resonant modes [276, 277, 278].

We suppose a portion V_p of the volume V of the cavity is filled with dielectric of fractional nuclear spin polarization f_p along the $\hat{\mathbf{p}}$ direction, so that $n_A = f_p\, n_0$ where n_0 is the number density of relevant nuclei. Adapting a standard result [279], the power deposited to the i^{th} mode of the cavity on resonance, $m_a \simeq \omega_i$, is

$$P_{\text{sig}} \simeq m_a\, (f_p\, n_0\, d_A)^2\, (V/\bar{\epsilon})\, \eta_i^2\, \min(Q_a, Q_i) , \tag{4.18}$$

where d_A is now the time-independent amplitude of the atomic EDM, Q_i is the quality factor of the mode, and the last factor accounts for the spectral width of the axion. The typical dielectric permittivity inside the cavity is $\bar{\epsilon}$, and the geometric overlap factor is

$$\eta_i = \frac{\left| \int_{V_p} d^3\mathbf{x}\ \mathbf{E}_i \cdot \hat{\mathbf{p}} \right|}{\sqrt{V \int_V d^3\mathbf{x}\ (\epsilon/\bar{\epsilon})\, E_i^2}}\ . \tag{4.19}$$

This definition is chosen so that $\eta_i \sim 1$ when the cavity is completely filled with dielectric polarized along $\hat{\mathbf{p}}$ parallel to the electric field $\mathbf{E}_i$ of the cavity mode. Below, we suppress mode subscripts to simplify notation.

To probe the lowest possible axion masses, a cylindrical cavity can be completely filled with a dielectric with $\hat{\mathbf{p}}$ along the cylinder's axis, which yields $\eta \simeq 0.83$ for the TM_{010} mode. In Fig. 4.1, we show two concrete ways to guarantee $\mathcal{O}(1)$ geometric overlap for heavier axions coupled to higher resonant modes of the cavity. First, one can insert layers of another dielectric. For example, rutile caries a negligible axion-induced current, and hence does not contribute to V_p. Since it has a very high permittivity at cryogenic temperatures, $\epsilon \gtrsim 10^4$ [280], thin layers would suffice to preserve a large overlap factor. Alternatively, the cavity can be filled with dielectric whose spin polarization alternates in direction. In either case, the mode frequency can be coarsely tuned by changing the number of layers, and finely tuned by introducing gaps and moving the dielectric layers or endcaps along the cylinder's axis.

Such layered structures have been proposed, prototyped, operated, and tuned for haloscopes targeting the axion-photon coupling [281, 282, 283, 284, 285, 286, 287, 288]. Axions can also be effectively coupled to higher-order modes by loading cavities with dielectric wedges or cylindrical shells [289, 290, 279, 291, 292, 293]. At high axion masses, scanning can become impeded by mode crowding. Many innovative approaches have been considered to avoid this issue, such as open resonators [286, 287], phase-matched, coupled, or sub-divided cavities [294, 295, 296, 297, 298, 299, 300, 246, 301, 302, 238, 303], rod or wire metamaterials [117, 304, 305], and thin-shell geometries [306, 307]. Most of these ideas can be adapted to polarization haloscopes, though some tuning mechanisms must be adjusted. For concreteness, we take $\eta = 1$, assume a cylindrical cavity with aspect ratio $L/R = 5$, and require the intermediate layers in Fig. 4.1 be at least 1 cm thick, so that there is a reasonable number to tune. This determines the mass range probed in Fig. 4.2.

4.4 Material Properties

To maximize the signal strength, we consider dielectric materials with a high density of the nuclei in Table 4.1. Unlike other approaches that require the material to be ferroelectric [116] or piezoelectric [46], we only require the material to be insulating at low temperatures.

Some semiconducting or insulating candidate materials are nitrides XN [308], oxides XO, and

sesquioxides X_2O_3 for $X = Dy, Eu, Gd$. Though many alternatives exist, these materials are simple and well-studied, and most are commercially available. For a prototype setup, we consider EuN where the abundance of ^{153}Eu is 52% (see Table 4.1). Following other proposals [46, 116], we assume complete isotope separation for a full-scale experiment, using DyN where the dysprosium is entirely ^{161}Dy. In both cases, the number density of rare earth atoms is 3×10^{22} cm^{-3} [309, 310].

The structure of the material also directly affects the strength of the signal. The most important effect, displayed in Eq. 4.18, is that dielectrics shield electric fields, reducing the signal power by a factor of the permittivity $\bar{\epsilon}$. For our projections we take $\bar{\epsilon} \simeq 7$, based on the static permittivity of DyN [311]. This choice is conservative, as permittivity decreases at higher frequencies.

In addition, the effective atomic EDM may be modified within a crystal, where atomic orbitals are deformed. This effect is quantified by the "electroaxionic" tensor defined in Ref. [46], and calculating the tensor components requires a dedicated relativistic many-body calculation for each material. In $PbTiO_3$, two groups found suppressions of 25% [312] and 50% [313], but with comparably large uncertainties. Thus, for this initial study we simply take d_A to be the value for an isolated atom.

The other key material property is the dielectric loss tangent $\tan\delta$. For a cavity entirely filled with dielectric, the quality factor Q of a mode obeys $1/Q = 1/Q_c + \tan\delta$, where Q_c is the quality factor due to cavity wall losses. Thus, to realize a desired Q, one must have $\tan\delta \lesssim 1/Q$.

At room temperature, dielectrics display high losses due to thermal phonons. However, these "intrinsic" losses fall steeply with temperature [314], and are negligible at the cryogenic temperatures of polarization haloscopes. Instead, extrinsic losses due to defects and impurities dominate [315, 316] and depend on crystal quality. Very low losses have been measured [317, 318, 319, 320], at the level of 10^{-9} for sapphire and 10^{-8} for rutile and YAG.

These are all centrosymmetric crystals, and thereby avoid additional loss mechanisms that would appear in more complex crystals, e.g. through acoustic phonons in piezoelectrics [314] or domain wall motion in ferroelectrics [321]. The candidate materials we have listed above are all simple centrosymmetric crystals. However, their dielectric losses are unknown, and dedicated cryogenic measurements in high-quality crystals are needed. These should be carried out at low electric field amplitudes, because high field amplitudes can mask losses due to two-level systems [322, 323, 324].

4.5 Nuclear Spin Polarization

The current in a polarization haloscope is proportional to the fractional nuclear spin polarization f_p, which is $\mathcal{O}(1\%)$ in thermal equilibrium in typical cavity haloscope conditions (see Table 4.1). However, for both polarization haloscopes and other approaches [116, 46] an $\mathcal{O}(1)$ polarization is required for optimal sensitivity. Below we describe two potential approaches to realize this.

First, one could simply subject the dielectric to a high magnetic field $B \gtrsim 10$ T and ultra-low temperature. At $T = 2$ mK, as achieved by specialized dilution fridges [325, 326], ^{153}Eu nuclei

possess an $\mathcal{O}(1)$ equilibrium polarization. For this technique, the key unknown is the time needed to thermalize the spins. At such high B/T, theoretical estimates suggest that it is prohibitively long [327, 328], but measured spin-lattice relaxation times are much shorter than predicted [329, 330], which could be explained by exotic relaxation mechanisms [331, 332, 333]. Relaxation times might be further reduced by the electric quadrupole moments of the nuclei we consider, which couple more strongly to the lattice than magnetic dipole moments [334], or by the addition of relaxation agents [335, 336].

Another option is frozen spin dynamic nuclear polarization (DNP), in which electrons are polarized in a few-Tesla field at $T \sim 1$ K, and their polarization is transferred to the nuclear spins by applying ~ 1 W/kg of microwave power. This method achieves almost complete proton spin polarization and has been extended to heavier nuclei for NMR studies [337, 338, 339, 340]. It requires the sample to contain a concentration $\sim 10^{-3}$ of paramagnetic centers, produced by chemical doping or ionizing radiation. To "freeze" the nuclear spins, the microwave field is removed and the sample is further cooled to slow relaxation.

This approach has been used for decades to polarize targets for particle physics experiments [341, 342]; notably, the Spin Muon Collaboration at CERN produced frozen spin targets of liter scale [343]. Currently, frozen spin DNP is primarily developed in nuclear physics experiments [344, 345, 346, 347, 348, 349]. The resulting spin polarization is robust, with spin-lattice relaxation times of nearly a year observed in practice [350]. For polarization haloscopes, the next step is to see how this approach can be scaled to larger volumes, while maintaining low dielectric losses.

4.6 Projected Sensitivity

The signal-to-noise ratio is given by the Dicke radiometer equation [351],

$$\mathrm{SNR} \simeq \frac{P_{\mathrm{sig}}}{T_n} \sqrt{\frac{t_{\mathrm{int}}}{\Delta\nu_s}} \,, \tag{4.20}$$

where t_{int} is the time spent probing each axion mass, and $\Delta\nu_s = m_a/(2\pi \max(Q, Q_a))$ is the signal bandwidth. The noise temperature $T_n = T + T_{\mathrm{amp}}$ receives comparable contributions from thermal noise, determined by the physical temperature T, and amplifier noise. Following Ref. [46], we find that noise due to external vibrations or spin fluctuations is vastly subdominant at the GHz frequencies of interest, even with the inclusion of paramagnetic centers as required for DNP. Note that Q is the quality factor of the cavity mode with dielectric losses included; thus, thermal noise automatically includes both the noise from electrons in the cavity walls and dielectric noise, by the fluctuation-dissipation theorem.

In Fig. 4.2, we show the projected sensitivity (corresponding to SNR ≥ 2) for three experimental setups. The two blue shaded regions indicate scanning setups which take frequency steps of size

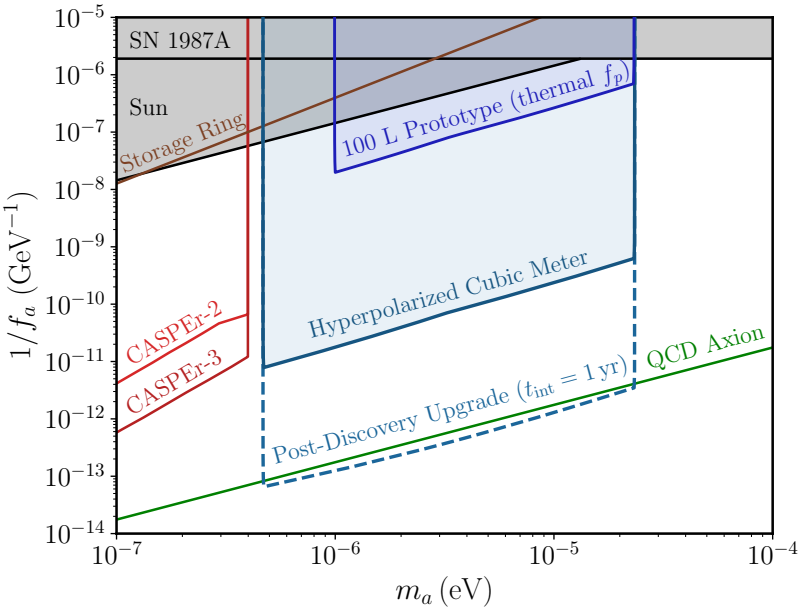

Figure 4.2: The projected sensitivity for three benchmark polarization haloscopes (see text for details). The blue shaded regions indicate the reach of scanning setups, while the dashed blue line shows the reach for an experiment which targets a single candidate QCD axion mass. We also show the ultimate projected sensitivity of CASPEr-Electric [20] and storage ring [21] experiments, as well as existing constraints from the cooling of Supernova 1987A [22] and Solar fusion processes [23]. Note that these existing constraints are strictly stronger than those derived from Big Bang nucleosynthesis [24] (not shown).

$m_a/\min(Q, Q_a)$ with a uniform $t_{\rm int}$, so that one e-fold in axion mass is scanned in one year. Following existing haloscope experiments, we assume an operating temperature of $T = 40$ mK [239] and an amplifier operating at the quantum limit, $T_{\rm amp} \simeq m_a$. When thermal noise dominates, we assume the cavity is optimally overcoupled to the readout, which modestly improves the SNR by a factor of $\sqrt{T/T_{\rm amp}}$ [176].

The "prototype" projection, shown in dark blue, is modeled on the ADMX haloscope [234] and assumes a volume $V = 100$ L, quality factor $Q = 10^5$, and magnetic field $B = 8$ T, which produces a thermal spin polarization $f_p \simeq 5\%$ for ^{153}Eu. This benchmark shows that new parameter space can be explored with minimal investment. (However, this parameter space may be in tension with the stability of white dwarfs [352].)

The light blue projection considers a cubic meter cavity with $Q = 10^6$ and complete spin polarization, $f_p = 1$. Such an experiment would require a large dilution fridge, like those developed for other precision experiments [353, 354, 355, 356, 357], and several tons of dielectric material. In other words, it would require investment comparable to ongoing WIMP dark matter searches [358, 359]. Though it does not reach the canonical QCD axion line defined by Eq. (4.2), it could probe orders of

magnitude of unexplored parameter space, including non-minimal, mildly tuned QCD axion models which solve the strong CP problem with exponentially smaller $m_a f_a$ [360, 361].

If ADMX, CAPP, or any other GHz-frequency haloscope [362, 363, 364, 365, 366] detects a signal consistent with axion dark matter, a "post-discovery" setup, shown in dashed blue, can probe the same mass. Since it sits at a single frequency, the SNR is enhanced by $Q_a^{1/2} \sim 10^3$ for $t_{\rm int} = 1$ yr, as compared to a scanning experiment. We assume noise is reduced, relative to the cuber meter setup, by cooling to 10 mK and reducing amplifier noise by 3 dB using demonstrated vacuum squeezing techniques [236]. We also assume a quality factor of $Q = 10^8$. To achieve this quality factor one needs a material with $\tan\delta \lesssim 10^{-8}$, which has been measured for a number of compounds. As for wall losses, one can achieve $Q_c \gg 10^8$ with a superconducting cavity, since polarization haloscopes do not require large static magnetic fields. Alternatively, the mode profile can be shaped with dielectrics, a technique which has achieved $Q \sim 10^7$ in a liter-scale copper cavity [292]. With these enhancements, a polarization haloscope has the unique ability to probe the minimal QCD axion.

4.7 Discussion

The QCD axion is an exceptional dark matter candidate, which arises automatically in theories which solve other problems of the Standard Model, with a simple and predictive production mechanism. The minimal QCD axion also has the unique advantage of possessing a defining coupling to the Standard Model, which provides a sharp target for laboratory searches.

A polarization haloscope naturally targets higher frequencies than nuclear magnetic resonance experiments [116]. Both approaches detect the electromagnetic fields generated by spin polarized nuclei, but polarization haloscopes do not involve changes in the spin direction and hence do not require long spin coherence times. One could also target kHz to MHz frequencies with our approach by replacing the magnetic field in an LC circuit haloscope [113, 214, 114] with a polarized dielectric.

We have laid out a path towards definitively probing the QCD axion with polarization haloscopes. No fundamentally new technologies are required, but many uncertainties remain. Precisely computing the signal requires expertise in theoretical nuclear, atomic, and solid state physics, while the cavity design and the selection and polarization of the material require experimental investigation. Together, such efforts may enable the next definitive search for dark matter.

Chapter 5

Axion-Fermion Couplings

This chapter is based on *Axion Dark Matter Detection by Superconducting Resonant Frequency Conversion*, by A. Berlin, R. T. D'Agnolo, S. A. R. Ellis, C. Nantista, J. Neilson, P. Schuster, S. Tantawi, N. Toro, K. Zhou, JHEP 07, 088 (2020).

Abstract

In the presence of axion dark matter, fermion spins experience an "axion wind" torque and an "axioelectric" force. We investigate new experimental probes of these effects and find that magnetized analogs of multilayer dielectric haloscopes can explore orders of magnitude of new parameter space for the axion-electron coupling. We also revisit the calculation of axion absorption into in-medium excitations, showing that axioelectric absorption is screened in spin-polarized targets, and axion wind absorption can be characterized in terms of a magnetic energy loss function. Finally, our detailed theoretical treatment allows us to critically examine recent claims in the literature. We find that axioelectric corrections to electronic energy levels are smaller than previously estimated and that the purported electron electric dipole moment due to a constant axion field is entirely spurious.

Conventions and Notation

We use a mostly-negative spacetime metric and natural units, $\hbar = c = k_B = 1$, with rationalized Heaviside–Lorentz units for electromagnetic fields (i.e., SI units with $\varepsilon_0 = \mu_0 = 1$). Instead of the chiral representation, we use the Dirac representation for the gamma matrices,

$$\gamma^0 = \begin{pmatrix} 1 & 0 \\ 0 & -1 \end{pmatrix} \quad , \quad \gamma^i = \begin{pmatrix} 0 & \sigma^i \\ -\sigma^i & 0 \end{pmatrix} \quad , \quad \gamma^5 = \begin{pmatrix} 0 & 1 \\ 1 & 0 \end{pmatrix} \ , \tag{5.1}$$

where the σ^i are the usual Pauli matrices. All states are normalized nonrelativistically, and all operators are in the Schrödinger picture unless specified otherwise. In Secs. 5.3 and 5.4, we work with complex axion and electromagnetic fields which oscillate with positive frequency, proportional to $e^{-i\omega t}$, such that only the real part is physically meaningful.

5.1 Introduction

Axions are among the most well-motivated extensions to the Standard Model, generically arising as pseudo-Goldstone remnants of new approximate global symmetries broken at some high scale and in theories involving compactified extra dimensions [97, 98, 367]. They are also motivated from a bottom-up perspective, as their existence could explain both the microscopic origin of dark matter [101, 100, 102] and the absence of CP violation in the strong interactions [93, 96, 95, 102].

If axions account for the local dark matter density $\rho_{\rm DM} \simeq 0.4$ GeV/cm^3, their occupancy per quantum mode is large for axion masses $m_a \lesssim$ few $\times$ 10 eV. In this case, the axion behaves as a nonrelativistic classical field, oscillating with an angular frequency set by its mass, $a(t) \simeq (\sqrt{2\rho_{\rm DM}}/m_a) \cos m_a t$. This behavior is coherent over macroscopic timescales $(m_a v_{\rm DM}^2)^{-1} \sim 1\ \mu\text{s} \times (\text{meV}/m_a)$ and is uniform over length scales $(m_a v_{\rm DM})^{-1} \sim 10\ \text{cm} \times (\text{meV}/m_a)$, where $v_{\rm DM} \sim 10^{-3}$ is the characteristic velocity of dark matter in the Galaxy. Axions generically couple to Standard Model currents via shift-symmetric higher-dimensional operators suppressed by a symmetry-breaking scale Λ, i.e., $\mathcal{L} \sim (\partial_\mu a)\, J^\mu_{\rm SM}/\Lambda$. Most ongoing and proposed experiments search for coherent signals arising from the axion's coupling to photons via the Chern–Simons current [45, 230, 231, 368].

Comparatively much less attention has been paid to the axion's coupling to color neutral fermions f,

$$\mathcal{L} \supset g_{af}\, (\partial_\mu a)\, \overline{\Psi} \gamma^\mu \gamma^5 \Psi \ . \tag{5.2}$$

Concretely, f can be an electron or nucleon, with mass m_f and charge q_f, Ψ is its corresponding Dirac field, and g_{af} is a dimensionful coupling inversely proportional to the symmetry-breaking scale.[1] Independent of the axion's Galactic abundance, such interactions induce spin-dependent "dipole–dipole" forces between fermions [369, 370], which can be searched for by experiments involving

[1] Some works quantify the coupling in terms of $G_{af} = 2 g_{af}$ or use a dimensionless coupling $\tilde{g}_{af} = 2 m_f\, g_{af}$.

electrons [371, 26, 372, 373, 374], nucleons [375, 376, 377, 378], or both [379, 380]. Stronger probes are possible in the presence of axion dark matter. For low-energy experiments, its physical effects are most directly seen in terms of the nonrelativistic single-particle Hamiltonian,

$$H \supset -g_{af}\,(\nabla a)\cdot\boldsymbol{\sigma} - \frac{g_{af}}{m_f}\,\dot{a}\,\boldsymbol{\sigma}\cdot\boldsymbol{\pi}\ , \tag{5.3}$$

where $\boldsymbol{\pi} \equiv \mathbf{p} - q_f\,\mathbf{A}$ is the fermion's mechanical momentum, defined in terms of the canonical momentum $\mathbf{p} = -i\nabla$ and electromagnetic vector potential $\mathbf{A}$. The first and second terms of Eq. 5.3 are called the "axion wind" and "axioelectric" terms, respectively, and give rise to a variety of spin-dependent effects.

The axion wind causes spins to precess about the axion gradient, like the effect of an effective magnetic field $\mathbf{B}_{\text{eff}}$ on a magnetic dipole moment. Various experimental techniques have been developed and proposed to search for this anomalous torque. For instance, spin-polarized torsion pendulums [25, 48] or precision magnetometers, such as comagnetometers and nuclear magnetic resonance setups [381, 48, 382, 20, 218, 383, 384, 27, 28, 385, 386, 221, 387, 388, 389, 390, 391, 392, 393, 394], can search for axions of mass $m_a \ll \mu$eV. Other recent proposals involve searching for spin precession in superfluid helium [395, 396, 397], nitrogen vacancy centers [50], and storage rings [398, 399, 400, 49, 401]. At higher axion masses, axion absorption can induce spin-flip transitions in atoms [53, 402, 403, 404] or excite in-medium magnons [405, 406]. In the μeV $-$ meV mass range, several experiments [407, 408, 409, 410, 411, 29, 30, 31, 32, 52, 51] search for magnon absorption by placing a magnetic sample in a cavity, thereby mixing the magnon with a cavity mode so that it can be read out as a photon. These efforts, which we term "ferromagnetic haloscopes," leverage existing expertise in cavity magnonics. However, other methods to probe the axion-electron coupling in this mass range have been unexplored.

The axioelectric term acts like an effective electric field $\mathbf{E}_{\text{eff}}$ directed along the spin and hence produces a time-varying force. In analogy to the photoelectric effect, this force can ionize atoms by the "axioelectric effect" [412, 413, 414, 415], which is used to search for, e.g., the absorption of high-energy solar axions [416, 417, 418, 419, 36]. More recent works have considered absorption of less energetic dark matter axions of mass $m_a \lesssim 10$ eV, which can produce electronic excitations in molecules [57] and solids [54, 56, 420, 421, 55] or single phonons in spin-polarized materials [58].

The physical effects of the axioelectric term in the ultralight regime ($m_a \ll 1$ eV) are much less well-understood. While the ability for this oscillating force to generate currents in spin-polarized targets was briefly considered in Refs. [133, 422, 423], the prospects for detecting such effects were never carefully analyzed. Furthermore, some recent studies have investigated axioelectric-induced modifications to electronic energy levels [46, 424, 425], but the sizes of these shifts were only very roughly estimated. Finally, there have been many recent independent claims that the axion-electron coupling generates an electron electric dipole moment (EDM) [426, 47, 427, 428, 429] proportional to the axion field value. This would seem to violate the shift symmetry of the axion field and, if

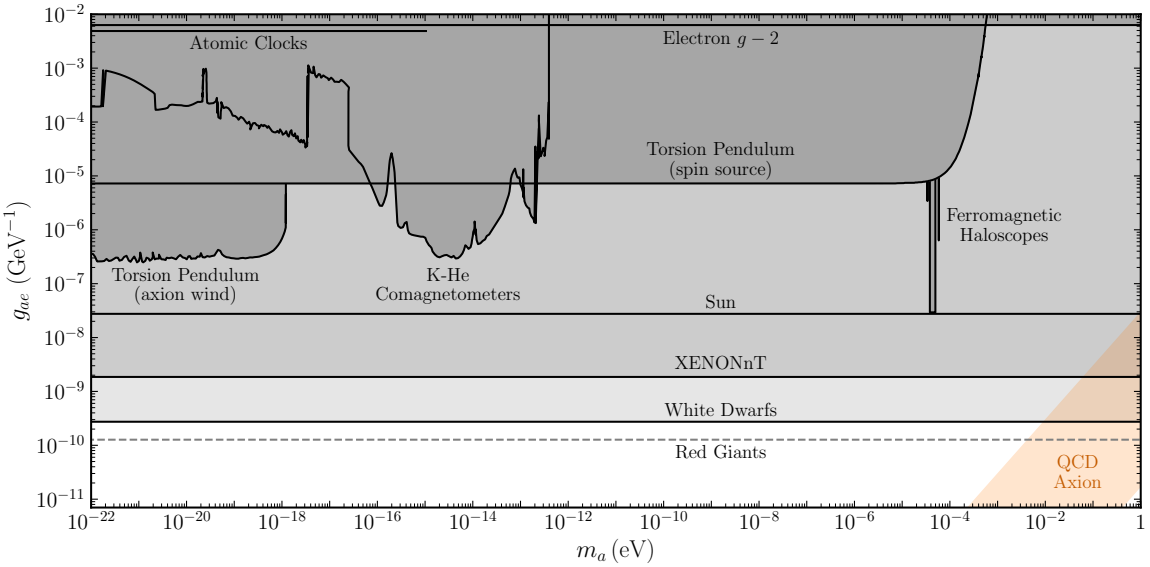

Figure 5.1: Existing constraints on the axion-electron coupling. Laboratory constraints are from torsion pendulums [25, 26], atomic clocks [27], comagnetometers [28], ferromagnetic haloscopes [29, 30, 31, 32], and electron $g-2$ measurements [33, 34] (using the 2σ uncertainty of the latest measurement [35]). Astrophysical constraints are from XENONnT solar axion searches [36] and from considerations of additional energy loss from the Sun [37], white dwarfs [38], and red giants [39]. However, the red giant bound may be significantly weakened when uncertainties in stellar parameters are accounted for [40]. Furthermore, all of these astrophysical constraints are relaxed in axion models with environment-dependent couplings [41]. Bounds derived from supernova 1987A [42, 43] and Big Bang nucleosynthesis [43, 44] are about two orders of magnitude weaker than the solar bound and not shown here for clarity. The orange band corresponds to QCD axion models, reviewed in, e.g., Ref. [45].

true, would imply sensitivity up to twenty orders of magnitude stronger than existing astrophysical bounds. Thus, the physics of the axioelectric term is currently far from clear.

In this chapter, we provide a firm foundation for the study of axion-fermion couplings, with an emphasis on new probes of the axion-electron coupling g_{ae}. Existing constraints on this coupling are reviewed in Fig. 5.1, while the projected sensitivities of future experiments are shown in Fig. 5.2. We begin in Sec. 5.2.1 by reviewing the derivation of the nonrelativistic Hamiltonian of Eq. 5.3. In Sec. 5.2.2, we compute the associated classical torques and forces in an axion background and show how the leading effects can be expressed in terms of effective spin-coupled electromagnetic fields $\mathbf{E}_{\text{eff}}$ and $\mathbf{B}_{\text{eff}}$. In Sec. 5.2.3, we consider the use of spin-polarized mechanical resonators to detect these effects.

In Sec. 5.3, we show how $\mathbf{E}_{\text{eff}}$ and $\mathbf{B}_{\text{eff}}$ give rise to polarization and magnetization currents, respectively, in electron spin-polarized (magnetic) media. To detect these currents, we consider multilayer setups like those used by dielectric haloscopes to search for the axion-photon coupling

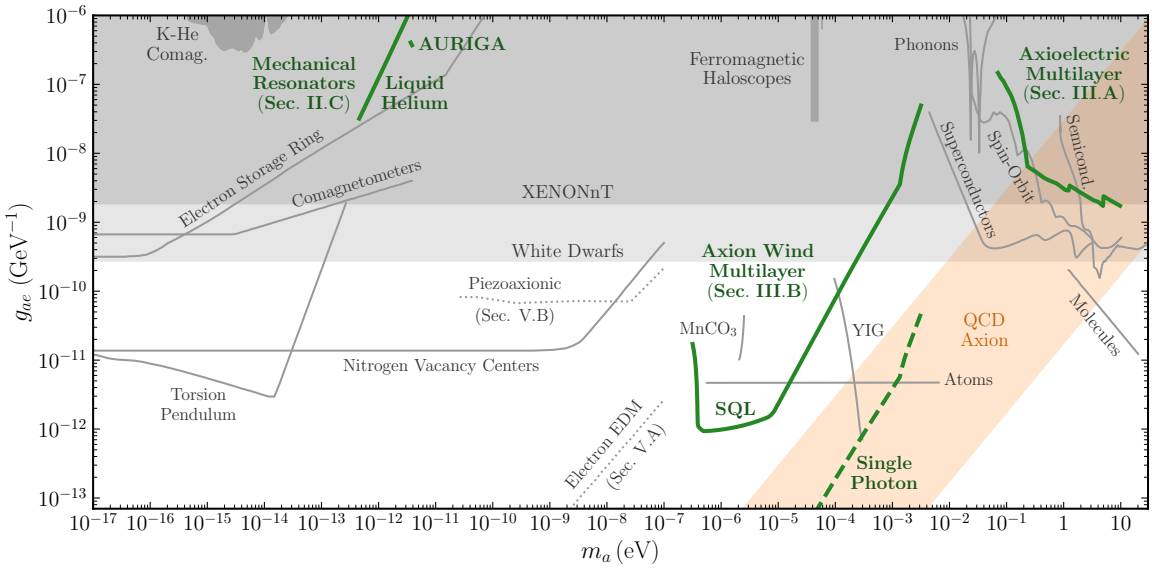

Figure 5.2: Proposed searches for the axion-electron coupling, with existing limits (shaded gray) as in Fig. 5.1. The new directions we explore are shown in solid green, and discussed in the corresponding sections. Dotted gray projections [46, 47] should be revised, as discussed in Sec. 5.5. As solid gray lines, we show projections from torsion pendulums [48], comagnetometers [28], an electron storage ring [49], nitrogen vacancy centers [50], ferromagnetic haloscopes using $MnCO_3$ [51] and YIG [52], and absorption into electronic excitations in atoms [53], superconductors [54], spin-orbit coupled materials [55], semiconductors [56], and molecules [57], as well as into phonon excitations in $FeBr_2$ [58]. For each proposal, we show the most optimistic projection, though the difficulty of experimentally realizing each one varies significantly.

at microwave [430, 431, 432] and optical [118, 433, 434, 435] frequencies, where the signal appears as emitted electromagnetic radiation. As shown in Sec. 5.3.1, such a system can reach QCD axion sensitivity at optical frequencies, where the polarization current dominates. At microwave frequencies, the magnetization current instead dominates. In this case, a multilayer setup can explore orders of magnitude beyond astrophysical bounds, as shown in Sec. 5.3.2.

In Sec. 5.4, we revisit axion absorption into in-medium excitations. For dark photons and axions, such results are often determined by the "energy loss function" $\mathrm{Im}(-1/\varepsilon)$ [436, 437, 438, 439, 440], which has recently been applied to dark photons [438] and photon-coupled axions [440]. In Sec. 5.4.1, we use a classical argument to show that in spin-polarized media, the absorption rate into magnons via the axion wind term is determined by $\mathrm{Im}(-1/\mu)$, the magnetic analogue of the energy loss function. As for the axioelectric term, previous calculations have shown that the absorption rate into electronic excitations scales with $\mathrm{Im}(\varepsilon)$ in unpolarized targets. In Sec. 5.4.2, we show that in spin-polarized targets, it is instead proportional to the usual energy loss function $\mathrm{Im}(-1/\varepsilon)$ and is thus generically screened.

In Sec. 5.5, we critically examine recent claims about the physical effects of the axioelectric term. We show that any apparent EDM proportional to the axion field value is spurious, with no corresponding observable effect, and that energy level shifts from the axioelectric term are smaller than previously estimated. We conclude in Sec. 5.6 by discussing directions for future investigation. The appendices are referred to throughout the text.

5.2 The Nonrelativistic Limit

In this section, we review the physical effects of fermion-coupled axion dark matter. We begin by deriving the nonrelativistic Hamiltonian in Sec. 5.2.1. It is then used in Sec. 5.2.2 to compute the torques and forces on a fermion, showing that the leading effects are simply described by effective spin-coupled magnetic and electric fields $\mathbf{B}_{\mathrm{eff}}$ and $\mathbf{E}_{\mathrm{eff}}$, respectively. In Sec. 5.2.3, we consider the sensitivity of spin-polarized mechanical resonators to these fields.

5.2.1 Deriving the Nonrelativistic Hamiltonian

We first motivate the nonrelativistic Hamiltonian in Eq. 5.3 by considering the classical limit of the axial vector current. As shown in Appendix 5.7, in a classical single-particle state, the spatial integral of its expectation value is essentially the fermion's spin four-vector s^μ, equal to $(0, \hat{\mathbf{s}})^\mu$ in its rest frame, where $\hat{\mathbf{s}}$ is the unit vector aligned with its spin. Thus, to first order in the fermion's velocity $\mathbf{v}$, we have

$$\int d^3\mathbf{x}\ \langle \overline{\Psi}\gamma^\mu\gamma^5\Psi\rangle \simeq (\mathbf{v}\cdot\hat{\mathbf{s}}\ ,\ \hat{\mathbf{s}})^\mu\ , \tag{5.4}$$

If we approximate $\partial_\mu a$ as spatially uniform, we can use Eq. 5.4 to evaluate the spatial integral of Eq. 5.2, giving the particle Lagrangian

$$L \supset g_{af}\,(\nabla a)\cdot\hat{\mathbf{s}} + g_{af}\,\dot{a}\,\mathbf{v}\cdot\hat{\mathbf{s}}\ . \tag{5.5}$$

The nonrelativistic Hamiltonian is given by $H = \mathbf{v}\cdot\mathbf{p} - L$, where the canonical momentum is

$$\mathbf{p} = \partial L/\partial\mathbf{v} = m_f\,\mathbf{v} + q_f\,\mathbf{A} + g_{af}\,\dot{a}\,\hat{\mathbf{s}}\ . \tag{5.6}$$

Identifying $\mathbf{p} \to -i\nabla$ and $\hat{\mathbf{s}} \to \boldsymbol{\sigma}$ in the Hamiltonian recovers Eq. 5.3. The first term in Eq. 5.5 couples to the spin like an effective magnetic field $\mathbf{B}_{\text{eff}} = (g_{af}/\mu_f)\,(\nabla a)$ with $\mu_f = q_f/2m_f$, while the second is of the form $L \supset q_f\,\mathbf{A}_{\text{eff}}\cdot\mathbf{v}$ with an effective vector potential $\mathbf{A}_{\text{eff}} = (g_{af}/q_f)\,\dot{a}\,\hat{\mathbf{s}}$. The axion field thus exerts a torque on spins and a spin-dependent force,

$$\boldsymbol{\tau} = \mu_f\,(\hat{\mathbf{s}}\times\mathbf{B}_{\text{eff}}) = \ g_{af}\,(\hat{\mathbf{s}}\times\nabla a) \tag{5.7}$$

$$\mathbf{F} = q_f\,\mathbf{E}_{\text{eff}} = -g_{af}\,\frac{d}{dt}\big(\dot{a}\,\hat{\mathbf{s}}\big)\ , \tag{5.8}$$

where $\mathbf{E}_{\text{eff}} = -d\mathbf{A}_{\text{eff}}/dt$ is an effective spin-coupled electric field. Though this derivation is merely heuristic, it does capture the axion's leading physical effects.

In order to systematically extract the full set of physical effects, we take the nonrelativistic limit of the fermion's equation of motion, using the same procedure that is used to derive the Pauli Hamiltonian from the Dirac equation. Starting from Eq. 5.2, the equation of motion for Ψ is

$$\left(i\partial\!\!\!/ - m_f - q_f\,A\!\!\!/ + g_{af}\,(\partial\!\!\!/ a)\,\gamma^5\right)\Psi = 0\ . \tag{5.9}$$

In relativistic quantum mechanics, Ψ is the four-component wavefunction of a state with a single particle or antiparticle, and Eq. 5.9 governs the evolution of the wavefunction. Specifically, the positive-frequency solutions of Eq. 5.9 represent the wavefunctions of particles, while negative-frequency solutions represent antiparticles. To reduce to the low-energy nonrelativistic theory, we "integrate out" the antiparticle component using the Pauli elimination method. To make this separation manifest, we divide Ψ into upper and lower two-component wavefunctions,

$$\Psi = e^{-im_f t}\begin{pmatrix}\psi\\ \tilde{\psi}\end{pmatrix}\ , \tag{5.10}$$

where the rapid time-dependence of the positive-frequency solution has been factored out. The wavefunctions ψ and $\tilde{\psi}$ dominate for nonrelativistic particle and antiparticle states, respectively. In

terms of ψ and $\tilde{\psi}$, Eq. 5.9 is

$$\left(i\partial_t - q_f\,\phi + g_{af}\,(\nabla a)\cdot\boldsymbol{\sigma}\right)\psi = \left(\boldsymbol{\pi}\cdot\boldsymbol{\sigma} - g_{af}\,\dot{a}\right)\tilde{\psi} \tag{5.11}$$

$$\left(2m_f + i\partial_t - q_f\,\phi + g_{af}\,(\nabla a)\cdot\boldsymbol{\sigma}\right)\tilde{\psi} = \left(\boldsymbol{\pi}\cdot\boldsymbol{\sigma} - g_{af}\,\dot{a}\right)\psi\ . \tag{5.12}$$

As anticipated, $\tilde{\psi}$ is suppressed by $\sim 1/m_f$ compared to ψ for nonrelativistic particle states. Thus, to economically describe a nonrelativistic particle, we can solve Eq. 5.12 to leading order in the nonrelativistic expansion,

$$\tilde{\psi} \simeq \frac{1}{2m_f}\left(\boldsymbol{\pi}\cdot\boldsymbol{\sigma} - g_{af}\,\dot{a}\right)\psi\ , \tag{5.13}$$

and then use this to eliminate $\tilde{\psi}$ from the equation of motion for ψ in Eq. 5.11. The result is

$$\left(i\partial_t - q_f\,\phi + g_{af}\,(\nabla a)\cdot\boldsymbol{\sigma}\right)\psi \simeq \left(\frac{1}{2m_f}\,|\boldsymbol{\pi}\cdot\boldsymbol{\sigma}|^2 - \frac{g_{af}\,\dot{a}}{m_f}\,\boldsymbol{\pi}\cdot\boldsymbol{\sigma} + \frac{ig_{af}}{2m_f}\,(\nabla\dot{a})\cdot\boldsymbol{\sigma}\right)\psi\ , \tag{5.14}$$

to leading order in the coupling g_{af}. The nonrelativistic Hamiltonian can then be identified by $i\partial_t\psi = H\psi$, which gives

$$H \simeq \frac{\boldsymbol{\pi}^2}{2m_f} + q_f\,\phi - \frac{q_f}{2m_f}\,\mathbf{B}\cdot\boldsymbol{\sigma} - g_{af}\,(\nabla a)\cdot\boldsymbol{\sigma} - \frac{g_{af}}{2m_f}\,\{\dot{a}, \boldsymbol{\pi}\cdot\boldsymbol{\sigma}\}\ , \tag{5.15}$$

where we used the identity $|\boldsymbol{\pi}\cdot\boldsymbol{\sigma}|^2 = \boldsymbol{\pi}^2 - q_f\,\mathbf{B}\cdot\boldsymbol{\sigma}$. The first three terms in Eq. 5.15 form the usual Pauli Hamiltonian, and the axion-dependent terms are in agreement with Ref. [428] (which instead used the Foldy–Wouthuysen method [441] to decouple the antiparticle component). Expanding the anticommutator in the final term yields $\{\dot{a}, \boldsymbol{\pi}\cdot\boldsymbol{\sigma}\} = 2\dot{a}\,\boldsymbol{\pi}\cdot\boldsymbol{\sigma} - i(\nabla\dot{a})\cdot\boldsymbol{\sigma}$, where the first term corresponds to the axioelectric term in Eq. 5.3. Note that the second term is not determined by our heuristic classical argument; however, it is less phenomenologically interesting since it is qualitatively similar to the axion wind, but subdominant for $m_a \ll m_f$.

5.2.2 Torques and Forces

The Hamiltonian of Eq. 5.15 implies that the axion field imparts spin torques and forces on fermions. To show this, we will use Ehrenfest's theorem, $d\langle\mathcal{O}\rangle/dt = \langle\partial_t\mathcal{O}\rangle + i\,\langle\,[H,\mathcal{O}]\,\rangle$, which governs the time evolution of the expectation value of any observable $\mathcal{O}$. For example, it implies that the velocity operator $\mathbf{v} \equiv i[H,\mathbf{x}]$ satisfies $\langle\mathbf{v}\rangle = d\,\langle\mathbf{x}\rangle\,/dt$. In the presence of an axion background, this is

$$\mathbf{v} = \frac{1}{m_f}\,(\boldsymbol{\pi} - g_{af}\,\dot{a}\,\boldsymbol{\sigma})\ , \tag{5.16}$$

which is just the quantum analogue of Eq. 5.6. Next, the expectation value of the spin operator $\mathbf{S} = \boldsymbol{\sigma}/2$ evolves as

$$\frac{d}{dt}\langle \mathbf{S} \rangle = \langle\, 2\,\mu_f\, \mathbf{S} \times \mathbf{B} + 2\, g_{af}\, \mathbf{S} \times (\nabla a + \{\dot{a}, \mathbf{v}\}/2)\,\rangle \ . \tag{5.17}$$

Discarding subdominant contributions proportional to $\nabla\dot{a}$ or g_{af}^2, we find that the axion field imparts the same spin torque as an effective magnetic field

$$\mathbf{B}_{\text{eff}} \simeq \frac{g_{af}}{\mu_f}\left(\nabla a + \dot{a}\,\langle \mathbf{v} \rangle\right) . \tag{5.18}$$

Above, the first term proportional to ∇a is the usual axion wind effect, while the additional term proportional to $\dot{a}$ follows from Galilean invariance; it represents the additional contribution to the axion gradient in the frame of a moving fermion. Note that this new term is subdominant when the fermion velocity is much smaller than the dark matter velocity, which applies to most laboratory experiments.

Evaluating the force from the axion field is somewhat more involved, as it requires taking the time derivative of Eq. 5.16. Using Eq. 5.17 to simplify the result, we find

$$\begin{aligned}\mathbf{F} \equiv m_f \frac{d}{dt}\langle \mathbf{v} \rangle \simeq \Big\langle q_f\, \mathbf{E} + \frac{q_f}{2}\,(\mathbf{v} \times \mathbf{B} - \mathbf{B} \times \mathbf{v}) + \mu_f\, \nabla(\boldsymbol{\sigma} \cdot \mathbf{B})\Big\rangle \\ - g_{af}\frac{d}{dt}\langle \dot{a}\,\boldsymbol{\sigma} \rangle + g_{af}\Big\langle \nabla(\boldsymbol{\sigma} \cdot \nabla a) + \frac{1}{2}\{\boldsymbol{\sigma} \cdot \mathbf{v},\, (\nabla \dot{a})\} - \frac{1}{2}\,(\mathbf{v} \cdot \nabla\dot{a} + \nabla\dot{a} \cdot \mathbf{v})\,\boldsymbol{\sigma}\Big\rangle \ ,\end{aligned} \tag{5.19}$$

where the first line is the usual electromagnetic force on a minimally-coupled spin-1/2 particle, and the second line contains axion-induced effects. Since the gradient of an axion dark matter field is suppressed by its small velocity, the first term in the second line dominates. It is equivalent to an effective electric field aligned with the spin,

$$\mathbf{E}_{\text{eff}} \simeq -\frac{g_{af}}{q_f}\frac{d}{dt}\left(\dot{a}\,\langle \boldsymbol{\sigma} \rangle\right) \ , \tag{5.20}$$

which is consistent with our classical result in Eq. 5.8, since $\langle \boldsymbol{\sigma} \rangle = \hat{\mathbf{s}}$, and agrees with Ref. [422].

Since $\mathbf{E}_{\text{eff}}$ and $\mathbf{B}_{\text{eff}}$ can cause charges to move and dipole moments to precess, respectively, they indirectly give rise to electromagnetic signals, which we will consider in Sec. 5.3. However, first we consider their most direct effects, which are oscillating mechanical forces and torques in spin-polarized materials.

5.2.3 Mechanical Signals

From Eq. 5.20, we see that when a material is electron or nuclear spin-polarized and its spins precess at angular frequency $\omega_{\rm spin}$, then its spins experience an oscillating axioelectric force with angular frequency $\omega_{\rm sig} \simeq m_a \pm \omega_{\rm spin}$, whose magnitude is proportional to $\omega_{\rm sig}$. For concreteness, we focus on electron-coupled axions and static electron spins, $\omega_{\rm spin} = 0$. In an insulating material, where the electrons are not free to move relative to the nuclei, forces on the electrons cause the material to accelerate as a whole. Thus, two nearby test masses of opposite electron spin polarization will experience an oscillating relative acceleration of magnitude

$$\Delta a_{ae} \simeq \frac{2 f_s \, g_{ae} \, \omega_{\rm sig} \sqrt{\rho_{\rm DM}}}{m_N} \, , \tag{5.21}$$

where m_N is the mass per atom and f_s is the number of polarized electron spins per atom.

At ultralow frequencies, $\omega_{\rm sig} \lesssim 10$ Hz, the axioelectric acceleration is very difficult to detect because it is suppressed by $\omega_{\rm sig}/m_N$. Using Refs. [442, 443, 444], we have recast the sensitivity of future torsion pendulums, atom interferometers, and gravitational wave detectors, assuming they can be modified to have $f_s \simeq 1$. In each case we find that the ideal sensitivity is well below that of existing astrophysical bounds and too weak to appear in Fig. 5.2.

Oscillating accelerations at kHz $-$ GHz frequencies can be detected with mechanical resonators. To analyze this case, we recast the results of Refs. [445, 446, 447], which consider how dilaton dark matter modifies the equilibrium length of solid objects, leading to a differential acceleration across the object. Each of these setups can in principle be converted to a probe of the axioelectric force by, e.g., spin polarizing its two halves in opposite directions. Equating the resulting accelerations (under the assumption that $f_s \simeq 1$ can be realized and that the relevant $\mathcal{O}(1)$ mechanical form factors are comparable) yields the curves labeled "Liquid Helium" and "AURIGA" in Fig. 5.2. Though they are more promising, they are still much weaker than existing astrophysical bounds.

The axion wind's spin torque can lead to stronger mechanical effects. In a material where the orientation of electron spins is fixed relative to the atomic lattice, such as a hard ferromagnet, spin torques are converted to torques on the lattice. For an object of length scale L, this corresponds to a characteristic linear acceleration

$$\Delta a_{\rm wind} \sim \frac{f_s \, g_{ae} \, \nabla a}{m_N L} \sim \frac{v_{\rm DM}}{m_a L} \, \Delta a_{ae} \, . \tag{5.22}$$

The axion wind's mechanical effect was already considered for torsion pendulums in Ref. [48], but, in principle, it could also excite "toroidal" (shearing) modes in mechanical resonators. For the resonators considered in Ref. [447], $\Delta a_{\rm wind}$ is enhanced over Δa_{ae} by several orders of magnitude. However, a detailed analysis of this signature is beyond the scope of this chapter.

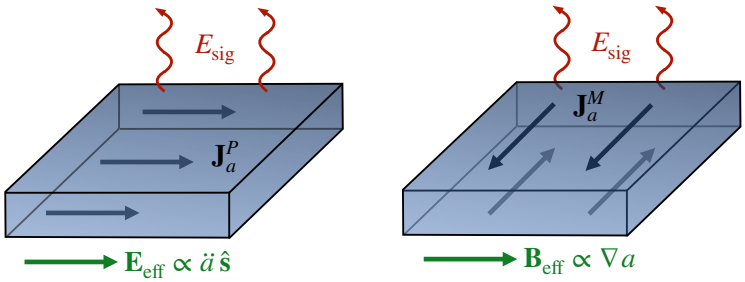

Figure 5.3: Schematic representation of the axion-induced electromagnetic signals considered in Sec. 5.3. **Left**: The axioelectric term's effective electric field $\mathbf{E}_{\rm eff}$ induces a bulk polarization current $\mathbf{J}_a^P$ in a spin-polarized material. **Right**: The axion wind term's effective magnetic field $\mathbf{B}_{\rm eff}$ induces a surface magnetization current $\mathbf{J}_a^M$.

5.3 Electromagnetic Signals

Unlike the axion-photon coupling, the axion-fermion coupling does not directly source electromagnetic fields. This is immediately apparent from both of the Lagrangian forms of the interaction, either in terms of relativistic fields (Eq. 5.2) or nonrelativistic particles (Eq. 5.5), which are independent of the vector potential. Although the Hamiltonian form of the axioelectric term $H \supset -(g_{af}/m_f)\,\dot{a}\,(\mathbf{p} - q_f\,\mathbf{A})\cdot\boldsymbol{\sigma}$ does naively appear to contain a direct coupling between the axion field and the vector potential, it is straightforward to verify that the electromagnetic Heisenberg equations of motion (calculated using Eq. 5.15) do not involve axion-dependent source terms.

Regardless, the effective fields $\mathbf{E}_{\rm eff}$ and $\mathbf{B}_{\rm eff}$ indirectly source real electromagnetic fields through their effect on the motion of charges. For concreteness, we focus here on the axion-electron coupling g_{ae}. In this case, the axioelectric field $\mathbf{E}_{\rm eff}$ drives polarization currents in spin-ordered material, while the axion wind field $\mathbf{B}_{\rm eff}$ induces magnetization currents on the boundary of any material with nonzero magnetic susceptibility. These currents in turn source electromagnetic radiation, as depicted in Fig. 5.3. Thus, dark matter experiments employing photon readout of dielectric stacks [430, 431, 118, 432, 434, 433] can be sensitive to the axion-electron coupling if they are modified to use appropriate materials.

To begin making this more precise, consider a linear medium with permittivity ε and permeability μ. Since the effective fields act on electrons but do *not* satisfy Maxwell's equations, we find it conceptually useful to split the induced polarization and magnetization into a standard and axion-induced part,

$$\mathbf{P} = \mathbf{P}_0 + \mathbf{P}_a = (\varepsilon - 1)\,\mathbf{E} + (\varepsilon_\sigma - 1)\,\mathbf{E}_{\rm eff} \tag{5.23}$$

$$\mathbf{M} = \mathbf{M}_0 + \mathbf{M}_a = (1 - \mu^{-1})\,\mathbf{B} + (1 - \mu^{-1})\,\mathbf{B}_{\rm eff}\ . \tag{5.24}$$

Here, $\mathbf{P}_0$ and $\mathbf{M}_0$ are induced by electromagnetic fields exactly as in ordinary electrodynamics, while

$\mathbf{P}_a$ and $\mathbf{M}_a$ are induced by the axion field. Note that in Eq. 5.23 we have defined ε_σ, the permittivity due to the spin-polarized electrons in the sample (where $\varepsilon_\sigma = 1$ for an unpolarized sample). This will be more properly defined later in Eqs. 5.55 and 5.86. We similarly decompose the in-medium current as $\mathbf{J} = \mathbf{J}_0 + \mathbf{J}_a$, where $\mathbf{J}_0 = \partial_t \mathbf{P}_0 + \nabla \times \mathbf{M}_0$, as usual, and $\mathbf{J}_a = \partial_t \mathbf{P}_a + \nabla \times \mathbf{M}_a$. While the case of an insulating medium may be more familiar, these equations can also be applied to conductors, which can be described by a permittivity with $\mathrm{Im}(\varepsilon) = \sigma/\omega$, where σ is the conductivity and ω is the angular frequency. Since $\mathbf{J}_0$ includes both the usual free and bound currents, only the axion-induced current $\mathbf{J}_a$ appears as a source in the in-medium Maxwell's equations. For instance, Ampère's law reads

$$\nabla \times (\mu^{-1}\,\mathbf{B}) = \mathbf{J}_a + \varepsilon\,\partial_t \mathbf{E}\ . \tag{5.25}$$

Combining this with Faraday's law, which is unchanged, yields the inhomogeneous wave equation

$$\nabla \times \nabla \times \mathbf{E} + n^2\,\partial_t^2 \mathbf{E} = -\mu\,\partial_t \mathbf{J}_a\ , \tag{5.26}$$

where $n = \sqrt{\varepsilon\mu}$ is the refractive index. This is the key result we will need in Secs. 5.3.1 and 5.3.2.

Explicitly, the axion-induced current contains two pieces,

$$\mathbf{J}_a = \mathbf{J}_a^P + \mathbf{J}_a^M = (\varepsilon_\sigma - 1)\,\partial_t \mathbf{E}_{\rm eff} + \nabla \times \left((1-\mu^{-1})\,\mathbf{B}_{\rm eff}\right)\ , \tag{5.27}$$

each of which can produce electromagnetic signals. The axion-induced polarization current $\mathbf{J}_a^P$ only exists in spin-polarized materials, such as ferromagnets, or paramagnets in an external magnetic field. The magnetization current $\mathbf{J}_a^M$ exists on the surface of any finite material with $\mu \neq 1$, though it tends to be most significant in spin-polarized materials. From Eqs. 5.18 and 5.20 we see that for static spins ($d\langle\boldsymbol{\sigma}\rangle/dt = 0$), $\mathbf{E}_{\rm eff}$ depends on a second derivative of the axion field while $\mathbf{B}_{\rm eff}$ depends on only a first derivative. We therefore expect the axioelectric induced current $\mathbf{J}_a^P$ to dominate for large axion masses and the axion wind induced current $\mathbf{J}_a^M$ to dominate at smaller masses. In the following subsections, we consider these two currents in turn.

5.3.1 Axioelectric Polarization Currents

Let us first consider the polarization current $\mathbf{J}_a^P$ resulting from the axioelectric field $\mathbf{E}_{\rm eff}$, by specializing to a monochromatic spatially uniform axion dark matter field $a \propto e^{-im_a t}$. To build intuition, we begin with the example of an infinite uniformly spin-polarized medium. In this case, we can ignore the curl in Eq. 5.26, which then gives

$$\mathbf{E} = \frac{1-\varepsilon_\sigma}{\varepsilon}\,\mathbf{E}_{\rm eff}\ . \tag{5.28}$$

The total current is then

$$\mathbf{J} = (\varepsilon - 1)\,\partial_t \mathbf{E} + (\varepsilon_\sigma - 1)\,\partial_t \mathbf{E}_{\rm eff} = \frac{\varepsilon_\sigma - 1}{\varepsilon}\,\partial_t \mathbf{E}_{\rm eff} = \frac{\mathbf{J}_a^P}{\varepsilon}\ . \tag{5.29}$$

This equation encompasses all of the results of Ref. [422]; in particular, it shows that for large ε, which occurs in conductors with $\sigma \gg m_a$, the axion-induced current is significantly screened. On the other hand, it was not previously realized that the current can be resonantly enhanced when ε approaches zero, which occurs when the axion mass matches that of a quasiparticle that mixes with the photon, such as a plasmon or phonon [448, 117, 449, 405, 450, 451, 452, 440]. However, the frequencies of such resonances are often not easily tunable.

In any case, dielectric haloscope and dish antenna experiments do not measure the current inside a medium, but rather the propagating radiation produced outside of it. The simplest setup which produces such radiation is an infinite slab of material of thickness d placed in vacuum, carrying a uniform spin polarization lying in the slab's plane, as shown in the left panel of Fig. 5.3. Within the slab, the axion induces an electric field as in Eq. 5.28. However, if this was the total electric field, then the component of the electric field tangential to the plane $\mathbf{E}_\parallel$ would be discontinuous at the slab's boundaries. Instead, the continuity of $\mathbf{E}_\parallel$ is restored by including plane wave solutions of Eq. 5.26, which propagate outward from the slab; such fields also exist within the slab, though they are exponentially damped on the scale of the skin depth $1/(\mathrm{Im}(n)\,m_a)$. In other words, the slab's finite thickness breaks translational invariance, providing the momentum mismatch required to generate photons.

As shown in Appendix 5.8, enforcing continuity of $\mathbf{E}_\parallel$ and $\mathbf{B}_\parallel/\mu$ yields a signal amplitude

$$E_{\rm sig} = \left| \frac{J_a^P/m_a}{\varepsilon + i\,n\,\cot\left(n\,m_a\,d/2\right)} \right| \tag{5.30}$$

for the outgoing radiation field. For real ε and μ, the amplitude is maximized for $d \simeq \pi/(n\,m_a)$, in which case $E_{\rm sig} = J_a^P/(m_a\,\varepsilon)$. Note that photon-coupled axions or kinetically-mixed dark photons also produce such signals, but through different physical mechanisms; for photon-coupled axions the fields are sourced by effective currents which exist wherever a background magnetic field B_0 is present, while for electron-coupled axions they are from real currents, which exist only within the slab. Despite these differences, the boundary conditions in these various model-examples have the same form, such that the expression in Eq. 5.30 holds in all three cases [431, 118] if one formally substitutes

$$J_a^P \to \sqrt{\rho_{\rm DM}} \times \begin{cases} (\varepsilon_\sigma - 1)\,g_{ae}\,m_a^2/e & \text{(electron-coupled axion)} \\ (\varepsilon - 1)\,g_{a\gamma\gamma}\,B_0 & \text{(photon-coupled axion)} \\ (\varepsilon - 1)\,\kappa\,m_{A'} & \text{(kinetically-mixed dark photon)}\ . \end{cases} \tag{5.31}$$

In the second line, $g_{a\gamma\gamma}$ is the axion-photon coupling, and in the third line, κ and $m_{A'}$ are the kinetic mixing parameter and mass of the dark photon field, which we assume is polarized tangential to the slab (although a real experiment would have to average over its varying orientation [453, 454]).

To compare these signals, we must estimate ε_σ, the permittivity due to the spin-polarized electrons. Consider a material in which the electrons in the outermost partially-filled shell are completely spin-polarized. Those spin-polarized electrons contribute to ε_σ, and at low frequencies $\omega \lesssim 10$ eV, below the characteristic scale of electronic excitations, they are also the ones that primarily contribute to ε. Therefore, in general we expect $\varepsilon_\sigma \sim \varepsilon$ up to an $\mathcal{O}(1)$ factor. This argument is discussed in more detail in Sec. 5.4.2, and for this initial study we simply take $\varepsilon_\sigma = \varepsilon$.

Under this assumption, Eq. 5.31 allows us to map between couplings which yield signals of equivalent strength,

$$g_{ae} \;\leftrightarrow\; g_{a\gamma\gamma}\,(e\,B_0/m_a^2) \;\leftrightarrow\; \kappa\,(e/m_a)\;. \tag{5.32}$$

As discussed in Appendix 5.8, this mapping is general, holding for an arbitrary series of spin-polarized layers. It can thus be used to recast the sensitivity of dielectric haloscopes, provided they are modified to incorporate spin-polarized media. The strongest sensitivity for this type of experiment is achieved at large axion masses, at which the optical dielectric haloscopes LAMPOST and MuDHI operate. Since LAMPOST has published projections [118], we recast them in Fig. 5.2 to yield the curve labeled "Axioelectric Multilayer," which shows that such a setup could have sensitivity comparable to existing solar limits, corresponding to couplings motivated by the QCD axion.

5.3.2 Axion Wind Magnetization Currents

Next, we turn to the magnetization current $\mathbf{J}_a^M$ of Eq. 5.27. This term results from the axion wind effective magnetic field $\mathbf{B}_{\text{eff}} \propto \nabla a$, which is nonzero due to the solar system's motion through the dark matter halo, i.e., $\nabla a \sim m_a\,\mathbf{v}_{\text{DM}}\,a$ with $v_{\text{DM}} \sim 10^{-3}$ the velocity of the dark matter wind. First, note that $\mathbf{J}_a^M$ vanishes in an infinite medium with a uniform and scalar permeability μ, since from Eqs. 5.18 and 5.27 we have in this case that $\mathbf{J}_a^M \propto \nabla \times \mathbf{B}_{\text{eff}} \propto \nabla \times \nabla a = 0$. Thus, for scalar μ, the simplest nontrivial situation is a planar slab of material of finite thickness, where the discontinuity of the magnetization at the slab's boundaries leads to surface magnetization currents, shown on the right in Fig. 5.3.

Such a signal arises in any finite medium with nonzero magnetic susceptibility $\chi_m = \mu - 1$, but in practice χ_m is small unless the medium is magnetically ordered, in which case χ_m is a nontrivial tensor. Furthermore, since the axion field oscillates in time and the medium can be placed in a tunable magnetic field, we must also consider how χ_m depends on frequency and external field.

Magnetization Dynamics

The form of χ_m can be derived from the well-understood theory of classical magnetization dynamics. Here we review the relevant results, following standard introductory treatments [455, 456, 457, 458]. The starting point is the Landau–Lifshitz equation, which governs the time evolution of a medium's magnetization density $\mathbf{M}$,

$$\frac{d\mathbf{M}}{dt} = \gamma\, \mathbf{M} \times \mathbf{H} + \frac{\alpha\, \gamma}{|\mathbf{M}|}\, \mathbf{M} \times (\mathbf{M} \times \mathbf{H}) \,, \tag{5.33}$$

where $\mathbf{H} = \mathbf{B} - \mathbf{M}$ is the auxiliary magnetic field, α is a small dimensionless damping parameter due to internal losses, and γ is the in-medium gyromagnetic ratio, approximately equal to the electron's gyromagnetic ratio $\gamma_e \simeq -e/m_e$.

For concreteness, consider a medium prepared with high magnetization density $\mathbf{M}_0 = M_0\, \hat{\mathbf{z}}$, aligned with a large applied magnetic field $\mathbf{B}_0 = B_0\, \hat{\mathbf{z}} = \mathbf{H}_0 + \mathbf{M}_0$. We are interested in the magnetization's response to the small axion effective magnetic field $B_{\rm eff} \ll B_0$, which contributes small corrections $\mathbf{M} = \mathbf{M}_0 + \Delta\mathbf{M}$ and $\mathbf{H} = \mathbf{H}_0 + \Delta\mathbf{H}$. Defining $\Delta\mathbf{M} = \chi_m\, \Delta\mathbf{H}$, we can solve Eq. 5.33 for χ_m in frequency space by linearizing in the small components. This yields

$$\chi_m \simeq -\frac{\omega_M}{\omega^2 - (1+\alpha^2)\,\omega_H^2 + 2i\alpha\,\omega\,\omega_H} \begin{pmatrix} (1+\alpha^2)\,\omega_H - i\alpha\,\omega & -i\omega & 0 \\ i\omega & (1+\alpha^2)\,\omega_H - i\alpha\,\omega & 0 \\ 0 & 0 & 0 \end{pmatrix} \,, \tag{5.34}$$

which in the absence of damping ($\alpha = 0$) is known as the Polder tensor. In the presence of damping, the width of the resonant response is controlled by the magnetic quality factor $Q \equiv 1/(2\alpha)$. Here, we have introduced the angular frequencies $\omega_M \equiv |\gamma|\, M_0$ and $\omega_H \equiv |\gamma|\, H_0$, and we also define $\omega_B \equiv |\gamma| B_0 = \omega_H + \omega_M$. Note that the maximum realistic value of the external field, $B_0 = 10$ T, corresponds to $\omega_B \sim 1$ meV, such that for larger frequencies the susceptibility is necessarily strongly suppressed. As a result, $\mu \simeq 1$ at optical frequencies, which is why we were able to neglect the tensorial nature of μ in Sec. 5.3.1.

It is convenient to diagonalize Eq. 5.34 by describing the transverse components with circular polarizations, defined as $M_\pm \equiv (M_x \pm iM_y)/\sqrt{2}$, $H_\pm \equiv (H_x \pm iH_y)/\sqrt{2}$, and similarly for the other fields. In this basis, the magnetic susceptibility is $\chi_m \simeq \mathrm{diag}(\chi_+, \chi_-, 0)$, where the diagonal elements are given by

$$\chi_\pm = \frac{\pm\omega_M + i\omega_M/2Q}{\omega \pm \omega_H + i\omega_H/2Q} \,. \tag{5.35}$$

Note that for positive frequencies, only χ_- can be resonantly enhanced. In other words, if the material is driven by a positive frequency linearly polarized magnetic field (which contains equal magnitude plus and minus circular polarization components), then on resonance its magnetization preferentially rotates in one direction. This predominantly leads to clockwise circularly polarized

radiation propagating along the direction of $\mathbf{B}_0$, and counterclockwise circularly polarized light propagating in the opposite direction.

Form Factor for a Single Slab

Let us now return to the case of a single planar slab of finite thickness d, extending infinitely along the xy-plane. For simplicity, we suppose that ∇a is uniform and also lies in the xy-plane. The slab is placed inside a strong external magnetic field $\mathbf{B}_0 = B_0\,\hat{\mathbf{z}}$, which fully magnetizes it along the z-direction, normal to the slab's surface. Note that since $\mathbf{B}\cdot\hat{\mathbf{z}}$ is continuous across the slab's boundaries, the z-component of the magnetic field inside the slab is also equal to B_0. We can compute the outgoing radiation produced by a single slab using the same method as in Sec. 5.3.1, provided we work in a basis of circular polarizations and account for the discontinuity of $(\mu^{-1}\,\mathbf{B})\times\hat{\mathbf{z}}$ at the slab boundaries due to the axion-induced magnetization surface currents. As shown in Appendix 5.8, the resulting amplitudes of the outgoing radiation components have magnitude $|E^{\pm}_{\rm sig}| = \mathcal{F}_{\pm}\,B_{\rm eff}/\sqrt{2}$, where

$$\mathcal{F}_{\pm} = \left|\frac{\chi_{\pm}}{\mu_{\pm} + i n_{\pm}\,\cot\left(n_{\pm}\,m_a\,d/2\right)}\right|\,, \tag{5.36}$$

is a dimensionless form factor and $n_{\pm} = \sqrt{\varepsilon\mu_{\pm}}$ is the polarization-dependent refractive index. Comparing Eqs. 5.30 and 5.36, we see that if $\mathcal{F}_{\pm}$ is $\mathcal{O}(1)$, then the radiation amplitude due to the axion wind is larger than that due to the axioelectric effect for all $m_a \lesssim m_e\,v_{\rm DM} \sim$ keV. However, a multilayer experiment would become impractically large for $m_a \ll 1$ μeV and, as mentioned above, the magnetic susceptibility is suppressed for $m_a \gtrsim 1$ meV. Thus, the approach described in this section is most useful for targeting axions at microwave frequencies, in a setup analogous to the MADMAX dielectric haloscope that we refer to as a "magnetized multilayer" [430, 431, 432].

The external field strength B_0 can easily be tuned in the laboratory; it affects ω_B and ω_H, and thereby the susceptibility $\chi_{\pm}$ and related quantities. We now consider how it should be chosen to maximize the form factor $\mathcal{F}_{\pm}$ for a given axion mass. For concreteness, we focus on the "minus" polarization, which has permeability

$$\mu_{-} = \frac{m_a - \omega_B + i\omega_B/2Q}{m_a - \omega_H + i\omega_H/2Q}\,. \tag{5.37}$$

Fig. 5.4 shows the value of $\mathcal{F}_{-}$ as a function of ω_B, for an axion mass of $m_a = 100$ μeV and slabs of various thickness d. For thin slabs, the form factor approaches a peak value of $\mathcal{F}_{-} \simeq 1$ when $\omega_H = m_a$. On the other hand, for much thicker slabs, there is a second, parametrically higher peak when ω_B is close to but slightly below m_a.

These results can be understood by carefully considering limiting cases of Eq. 5.36 for fixed m_a. First, in the thin slab regime, $|n_{-}m_a d| \ll 1$, the cotangent in Eq. 5.36 is large and can be expanded as $\cot x \simeq 1/x$. The form factor has a resonant peak about $\omega_H = m_a$, where the numerator $\chi_{-} \simeq \mu_{-}$

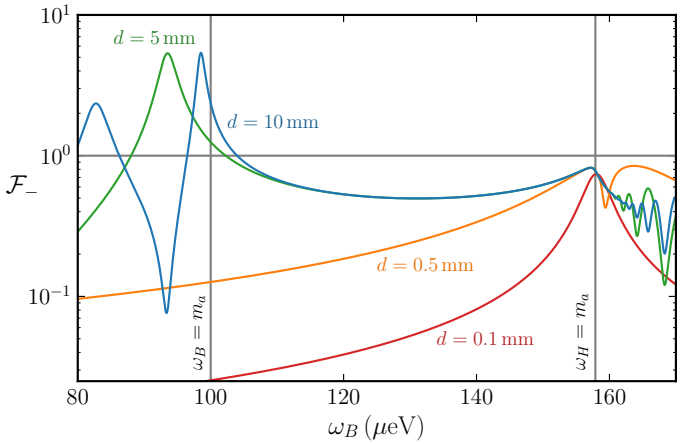

Figure 5.4: The form factor $\mathcal{F}_-$ (Eq. 5.36) for slabs of varying thickness d as a function of $\omega_B = |\gamma|B_0$, for a fixed axion mass of $m_a = 100$ μeV and the material properties listed in Table 5.1. While the form factor always has a peak near $\omega_H = m_a$, it has a higher peak near $\omega_B = m_a$ for thick slabs.

becomes large. Near this peak, we have

$$\mathcal{F}_- \simeq \left| \frac{\omega_M \, m_a \, d/2}{m_a - \omega_H + i\omega_H/2Q_{\mathrm{eff}}} \right| , \tag{5.38}$$

where we took $Q \gg 1$ and defined an effective quality factor

$$\frac{1}{Q_{\mathrm{eff}}} = \frac{1}{Q} + \omega_M \, d \, . \tag{5.39}$$

These results are physically sensible. First, the resonant frequency ω_H is the usual Kittel frequency (i.e., the lowest, zero-momentum magnon frequency) for a thin slab in an orthogonal magnetic field. Next, the second term in Eq. 5.39 describes radiation damping due to the emission of electromagnetic waves. This damping ensures $\mathcal{F}_- \leq 1$ on resonance, regardless of the value of Q, while increasing d simply broadens the width of the resonant response. Thus, for thin slabs in the regime $Q\,\omega_M\,d \gtrsim 1$, increasing the slab thickness can increase the scanning rate of an experiment, but not the peak signal power.

Radiation damping is a familiar concern in ferromagnetic resonance studies [459, 460, 461, 462] and is one of the main reasons that ferromagnetic haloscope experiments enclose their spin-polarized sample in a microwave cavity. Note, however, that Eqs. 5.38 and 5.39 apply only to thin slabs; qualitatively different behavior can occur in the thick slab limit $|n_- m_a d| \gtrsim 1$. In this case the cotangent $\cot(n_- m_a d/2)$ is not necessarily large, but is instead generically $\mathcal{O}(1)$. From Eq. 5.37, when the quality factor is high and the axion mass matches the Kittel frequency of an infinite medium, $m_a = \omega_B$, the permeability is small and approximately imaginary, $\mu_- \simeq i m_a/(2\,Q\,\omega_M)$, so

that $|\mu_-| \ll |n_-|$. Then

$$\mathcal{F}_- \simeq \frac{1}{|\mu_- + i n_- \cot(n_- m_a d/2)|} \simeq \frac{1}{|\cot(n_- m_a d/2)|} \sqrt{\frac{2\,Q\,\omega_M}{m_a\,\varepsilon}}\,, \tag{5.40}$$

so that the form factor can be much greater than one if Q is sufficiently large. This enhancement is possible because for thick slabs, radiation is not merely a source of energy loss. Instead, it couples the magnon and photon degrees of freedom within the slab, forming a propagating hybrid "magnon-polariton" mode.

As shown in Fig. 5.4, we find numerically that the highest form factors occur when ω_B is shifted slightly below the axion mass, $\omega_B = m_a - \Delta\omega$ with $\Delta\omega > 0$, even though this increases $|\mu_-|$. This result also has a simple physical interpretation. For concreteness, suppose that $\Delta\omega$ is nonzero and Q is very high, which implies that μ_- is small and approximately real. In this case, the slab acts as an effective cavity due to the discontinuity of n_- at its boundaries. When $n_- m_a d = \pi$, the in-medium wavelength of the magnon-polariton mode matches the slab's thickness, so that $\cot(n_- m_a d/2)$ vanishes, leading to a greatly enhanced form factor. This phenomenon is familiar from other axion searches using quasiparticle resonances [117, 451, 450, 452, 449] and remains approximately true even at finite Q.

Signal-to-Noise Ratio for a Multilayer Setup

Now that we have discussed the outgoing radiation from a single magnetized layer, we turn to the signal for many layers. Optimizing the response of a general multilayer experiment is analytically intractable. Therefore, for concreteness, we focus on a "transparent mode" setup, where N slabs, each of area A and thickness $d = \pi/(\mathrm{Re}(n_-)\, m_a)$, are separated by vacuum gaps of thickness π/m_a [463, 431]. For such multilayers, an emitted electromagnetic wave accumulates a phase of 2π upon traveling from one slab to the next, so that the total signal amplitude emitted from the $+z$ side of the stack is ideally $N E^-_{\mathrm{sig}}$.[2] In this case, the time-averaged signal power emitted from each end of the stack is therefore

$$P_{\mathrm{sig}} = \frac{1}{2}\, N^2\, |E^-_{\mathrm{sig}}|^2\; A = \frac{1}{4}\, \mathcal{F}_-^2\, N^2\, |B^2_{\mathrm{eff}}|\, A\,. \tag{5.41}$$

As in the MADMAX experiment [431], this power can be focused with a horn antenna onto a pickup circuit, which is coupled to an amplifier. We demand that the total thickness $L = Nd$ of the slabs be no larger than the characteristic screening length $1/(\mathrm{Im}(n_-)\, m_a)$. This implies that the maximum number of layers is

$$N = \frac{\mathrm{Re}(n_-)}{\pi\, \mathrm{Im}(n_-)}\,. \tag{5.42}$$

[2] Radiation of the "plus" circular polarization is also emitted from this side, but its amplitude is negligible, since generically $\mathcal{F}_+$ will not be resonantly enhanced and its contributions from the different slabs will not interfere constructively. Thus, from this point onward we will only consider the "minus" polarization.

Finally, the signal-to-noise ratio is given by the Dicke radiometer equation [351],

$$\mathrm{SNR} = \frac{P_{\mathrm{sig}}}{T_n}\sqrt{\frac{t_{\mathrm{int}}}{\Delta\nu_a}}\,, \tag{5.43}$$

where T_n is the noise temperature, t_{int} is the integration time, and $\Delta\nu_a \simeq m_a/(2\pi Q_a)$ is the axion bandwidth, where $Q_a \sim 1/v_{\mathrm{DM}}^2 \sim 10^6$ is the effective axion quality factor. The integration time is set by $t_{\mathrm{int}} = (\Delta\omega_s/m_a)\, t_e$, where t_e is the total time to scan one e-fold in axion masses and $\Delta\omega_s$ is the sensitivity bandwidth (i.e., the spread in axion masses for which the signal power is near its maximal value for a fixed multilayer geometry and applied field).

To estimate the sensitivity bandwidth, we consider what happens when the axion mass is shifted by a small amount δ from the optimal value, such that $m_a = \omega_B + \Delta\omega + \delta$. When $\delta = 0$, radiation accumulates a phase of 2π upon propagating from one slab to the next, for a total of $2\pi N$ through the entire stack. When $\delta \neq 0$, the wave frequency is shifted, which changes the phase by a fractional amount $\sim \delta/m_a$. Demanding that the total change in phase is less than $\mathcal{O}(1)$ (so that the radiation from each slab still constructively interferes) then yields the constraint $\delta \lesssim m_a/N$, as in standard dielectric haloscope experiments [431]. However, in our case there is another constraint: changing the axion mass also changes the wavelength of the radiation within the slab, by a fractional amount $\Delta(\mathrm{Re}(n))\,/\,\mathrm{Re}(n) \simeq \delta/(2\,\Delta\omega)$, and this quantity must also be less than $\sim 1/N$. This yields the stronger condition $\delta \lesssim 2\,\Delta\omega/N$ and therefore fixes the sensitivity bandwidth to

$$\Delta\omega_s = 2\,\Delta\omega/N\ . \tag{5.44}$$

Note that because $P_{\mathrm{sig}} \propto N^2$ and $\Delta\omega_s \propto 1/N$, the setup obeys the so-called "area law," $\int d\omega\, P_{\mathrm{sig}}(\omega) \propto N$. This is a very general feature of axion dark matter experiments [464, 465] that was first observed for dielectric haloscopes [431].

Given the above discussion, one can determine the signal-to-noise ratio in terms of $\Delta\omega = m_a - \omega_B$ and fixed parameters. Since the applied magnetic field can be tuned experimentally, we numerically optimize the sensitivity with respect to $\Delta\omega$. Qualitatively, moving away from $\omega_B = m_a$ by increasing $\Delta\omega$ increases $\mathrm{Re}(\mu_-)$ (which decreases the thickness of each slab) and decreases $\mathrm{Im}(\mu_-)/\mathrm{Re}(\mu_-)$ (which increases the maximum number of layers). On the other hand, the increasing separation between the Kittel frequency and the axion frequency eventually begins to suppress the form factor. In the absence of other constraints, the optimal value of $\Delta\omega$ is set by a trade-off between these effects.

In Appendix 5.10, we show analytically that for real ε and sufficiently high Q, the optimized signal power scales as

$$P_{\mathrm{sig}} \sim \left(\frac{Q\,\omega_M}{m_a}\right)^2 |B_{\mathrm{eff}}^2|\, A\ . \tag{5.45}$$

The enhancement with ω_M is simply due to the fact that a higher magnetization improves the form factor. The unusual quadratic scaling with Q is also simple to understand; a larger quality

Parameters	Description	Variable	Value	
Material	Saturation magnetization	M_S	0.5 T	
	Magnetic quality factor	Q	10^2	
	Permittivity	ε	15	
Expt.	Slab area	A	1 m^2	
	e-fold scanning time	t_e	1 year	
	Maximum number of layers	$N_{\max}$	80	
	Maximum total material thickness	$L_{\max}$	5 m	
	Maximum applied B field	$B_{\max}$	10 T	
Noise			HEMT	SQL
	Physical temperature	T	4 K	40 mK
	Amplifier noise temperature	$T_{\rm amp}$	$1\text{ K}\left(\frac{m_a}{2\pi\times 4\text{ GHz}}\right)$	m_a

Table 5.1: Material, experimental, and noise parameters assumed when optimizing the experimental setup (Fig. 5.5) and computing the sensitivity (Fig. 5.6) for a polycrystalline spinel ferrite multilayer. The dielectric loss tangent is negligible in these materials, $\tan\delta_\varepsilon \lesssim 10^{-4}$, and so the permittivity can be approximated as real. For HEMT and SQL amplifiers, the physical temperatures correspond to cryostat and dilution fridge cooling, respectively. The total noise temperature used in Eq. 5.43 is $T_n = T + T_{\rm amp}$.

factor reduces $\mathrm{Im}(\mu_-)$, and thereby improves both the resonant enhancement in the form factor and increases the maximum possible number of layers. As a result, Eq. 5.45 can be reexpressed as $P_{\rm sig} \propto Q\,V$, where V is the total volume of the experiment, as in other resonant setups.

We caution that in our discussion below, we will focus on a material for which Q is too small for the approximations used to derive Eq. 5.45 to accurately apply. We also note that Eq. 5.45 cannot be applied at sufficiently small axion masses, where the signal power will be further constrained by an upper limit on the total slab thickness. Regardless, Eq. 5.45 does display the correct qualitative dependence of the signal power on material properties.

Material Properties and Experimental Parameters

The best materials are those with high saturation magnetization M_S, which sets the maximum possible value of M_0, and large magnetic quality factor Q. In addition, the permittivity ε must be approximately real, as a large imaginary component would lower the screening length. In particular, magnetic alloys cannot be used, as they have $\mathrm{Im}(\varepsilon) = \sigma/\omega$ for a large conductivity σ. For such materials, the screening length (i.e., the skin depth) would be well below the thickness of a single slab at the microwave frequencies considered here.

We therefore choose to focus on ferrites, which have negligible conductivity and are widely commercially available. The properties of these materials are well known, and discussed in detail in

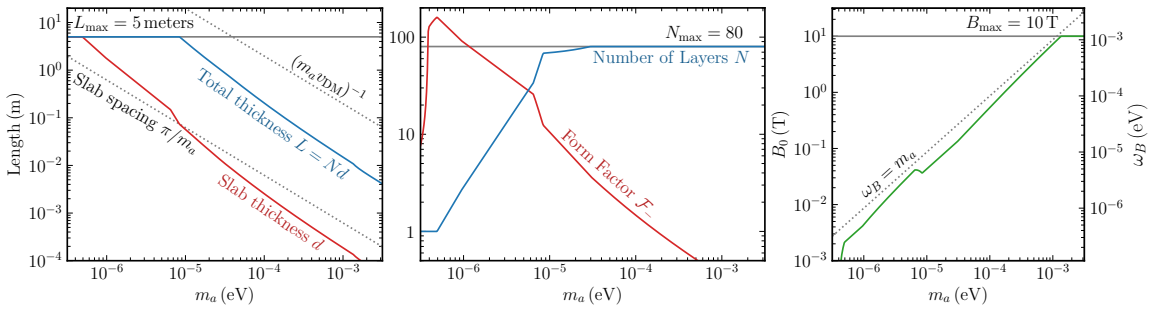

Figure 5.5: Numerically optimized values of the slab thickness and total thickness (left panel), form factor and number of layers (middle panel), and applied external magnetic field (right panel), as a function of the axion mass. The middle panel shows that the signal power, proportional to $\mathcal{F}_-^2 N^2$, is predominantly enhanced by the form factor at small m_a and the number of layers at large m_a. The other panels show that a large total volume is only required at small m_a, and a strong external field is only required at large m_a.

Appendix 5.10. To date, ferromagnetic haloscope experiments have exclusively used single crystal yttrium iron garnet (YIG), as it has the highest known quality factor $Q \sim 10^4$. However, YIG crystals are extraordinarily difficult to grow [466], and currently YIG spheres and films can only be produced individually at ~ 1 mm scales. By contrast, polycrystalline spinel ferrites are mass-produced and can be purchased at a per-kilogram cost over five orders of magnitude lower than YIG. Though they have a relatively low quality factor $Q \sim 10^2$, they possess a saturation magnetization M_S twice as large as that of YIG.

Thus, we will focus on polycrystalline spinel ferrites, since an experiment employing them can benefit tremendously by the increased detector volume. The benchmark values we assume are shown in Table 5.1 and discussed further in Appendix 5.10. We assume the material is fully magnetized, so that $M_0 = M_S$. As for the other experimental parameters, we adopt a slab area $A = 1$ m^2 and e-fold scanning time $t_e = 1$ yr, similar to the MADMAX experiment. We allow a maximum external magnetic field of $B_{\max} = 10$ T, require that the number of layers does not exceed $N_{\max} = 80$, and cap the total thickness $L = Nd$ of the slabs at $L_{\max} = 5$ m.

Experimental Sensitivity

For each axion mass, we numerically optimize the signal-to-noise ratio by varying ω_B, which in turn determines the form factor $\mathcal{F}_-$, number of layers N, slab thickness d, and sensitivity bandwidth $\Delta\omega_s$. The results of the optimization are shown in Fig. 5.5, which shows how the setup qualitatively changes as the axion mass is varied.

At small axion masses, $m_a \lesssim 10^{-5}$ eV, the length of the setup is large, but it only requires a weak applied magnetic field. In this regime, the number of layers is suppressed due to the constraint $L \leq L_{\max}$, and the sensitivity boost primarily comes from operating at small μ_-, corresponding to

a large form factor. Note that this implies the thickness of a single slab is much greater than the spacing between slabs, so that L is approximately the total length of the multilayer setup. In this regime, the experiment most closely resembles axion searches using tunable quasiparticle resonances, such as TOORAD [448, 451] and ALPHA [117, 449, 450].

Increasing the axion mass increases the minimum value of $|\mu_-|$ and therefore decreases the maximum possible form factor. Thus, at large axion masses the sensitivity boost primarily comes from having a large number of layers and is limited by the constraint $N \leq N_{\max}$. For polycrystalline ferrite, one can only use this many layers if the setup is operated well away from the resonance. Numerically, we find $\Delta\omega \gtrsim \omega_M$ in this regime, so that n_- does not have sharp frequency dependence, and the experiment most closely resembles the microwave dielectric haloscope MADMAX. Also note that for $m_a \gtrsim 10^{-3}$ eV, our constraint $B_{\max} = 10$ T limits the size of B_0, preventing resonant enhancement of the form factor entirely. For axion masses near this upper limit, the required magnetic field is large, but the total length of the setup is small, i.e., $\lesssim 1$ cm.

For the parameter values we have chosen, the analytic approximation for the signal power in Eq. 5.45 is only accurate in a narrow mass range centered near $m_a \sim 10^{-5}$ eV. For larger axion masses, we find numerically that the optimized signal power is an $\mathcal{O}(1)$ factor larger. In Appendix 5.10, we also carry out the same computation for single crystal YIG, which we show has a sufficiently high Q for the analytic results to work accurately. For YIG, the reach is slightly stronger, but the results are qualitatively very similar.

The numeric values of d and L shown in the left-panel of Fig. 5.5 allow us to confirm that certain corrections to our results are indeed negligible. First, we have treated ∇a as spatially uniform. This mathematical assumption corresponds to the physical requirement that radiation from different slabs interferes constructively, $L \ll (m_a\, v_{\rm DM})^{-1}$, which is indeed true here. Note that at large axion masses we have $\sqrt{A} \gtrsim (m_a\, v_{\rm DM})^{-1}$, but this is acceptable since there is no requirement that radiation from different parts of the same slab be emitted in phase. Second, we remind the reader that we have only considered surface magnetization currents. In the beginning of this subsection, we noted that for scalar μ, the volume magnetization current vanishes. However, it is in general nonzero for the tensorial μ considered here, albeit suppressed by an additional gradient of the axion field. Thus, the relative effect of the volume magnetization current is $\sim d\, m_a\, v_{\rm DM} \ll 1$, which is completely negligible.

Finally, the total noise temperature can be decomposed as $T_n = T_{\rm th} + T_{\rm amp} + \Delta T$, where $T_{\rm th}$ is due to thermal noise, $T_{\rm amp}$ is the effective noise temperature of the amplifier, and ΔT is due to additional, reducible noise sources. By the fluctuation-dissipation theorem, thermal noise is sourced from any part of the system that dissipates energy. This includes thermal radiation sourced from the charges in the walls of the magnet and the thermally fluctuating spins in the multilayer, and Johnson–Nyquist noise sourced from the resistance in the pickup circuit. However, when the entire system is at the same physical temperature T, these contributions sum to $T_{\rm th} = T$ independently of the details of the setup. As for the additional noise ΔT, it receives contributions from, e.g.,

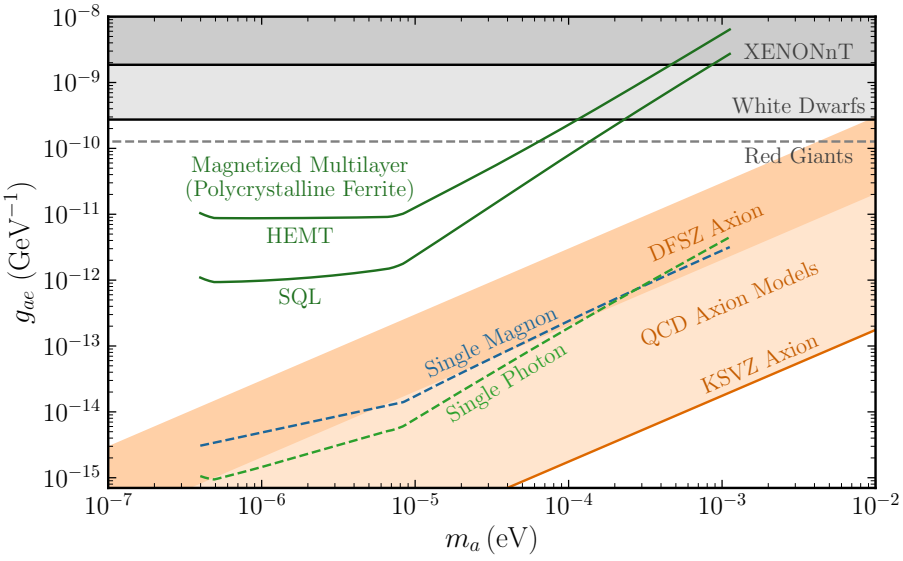

Figure 5.6: In solid green, we show the projected sensitivity at SNR = 2 to the axion-electron coupling of a magnetized multilayer experiment based on detecting the radiation generated by the axion wind induced magnetization current, with layers made of polycrystalline ferrite and either HEMT or SQL amplifiers. All parameters assumed for the projections are listed in Table 5.1. We cut off these reach curves at large axion masses when the required applied magnetic field exceeds $B_{\rm max} = 10$ T and at small axion masses when the optimal thickness of a single layer exceeds $L_{\rm max} = 5$ m. In dashed green and dashed blue, we show the maximum possible reach given noise-free detection of single photon and magnon quanta, respectively (see Sec. 5.3.2 for more details). Astrophysical bounds are as in Fig. 5.1, and the band for DFSZ axions and loop-induced couplings for KSVZ axions are summarized in, e.g., Ref. [45].

nonthermalized magnetic impurities, vibrations of the multilayer or magnet, and Barkhausen noise due to the relaxation of domain walls. However, these effects fall off rapidly above $\sim$ kHz frequencies, and we expect they are subdominant at the GHz to THz frequencies and long integration times relevant in this chapter [467, 468, 469, 470, 471, 472]. Thus, for this initial study we neglect ΔT.

In Fig. 5.6, we show the experimental sensitivity for various noise benchmarks, with corresponding noise parameters shown explicitly in Table 5.1. For the line labeled "HEMT," we have inferred an amplifier noise temperature $T_{\rm amp}$ from manufacturer datasheets [473]. We also show a "standard quantum limit" (SQL) benchmark with a lower physical temperature and a quantum limited amplifier. In this case quantum noise is important, and the fluctuation-dissipation theorem implies that it arises from a variety of sources, including quantum fluctuations in the pickup circuit voltage, and spin-projection noise arising from the uncertainty in the transverse component of the multilayer magnetization [474]. The details of the setup determine which of these effects contributes more to the quantum noise seen by the amplifier, but the SQL itself always corresponds to taking $T_{\rm amp} = m_a$, independent of these details. The detailed contributions of individual sources to the quantum noise

do not affect this result, but may be important for detailed optimization of the detector, which we defer to future work.

For concreteness, we set a sensitivity threshold by taking SNR = 2, though we note that this does not have a definite statistical interpretation, as various $\mathcal{O}(1)$ factors have been dropped throughout our analysis. Finally, the dashed line labeled "Single Photon" indicates a theoretical upper limit on sensitivity; it shows axion couplings for which $P_{\rm sig}\, t_{\rm int} = m_a$, corresponding to an average of a single photon emitted within the integration time [475].

To illustrate the effect of the multilayer geometry, we can compare the photon power absorption rate $P_{\rm sig}$ in an optimized multilayer to the magnon power absorption rate $P_{\rm mag}$ in a uniform medium. As shown in Sec. 5.4.2 and Appendix 5.9, $P_{\rm mag}$ is maximized when $\omega_B = m_a$. When normalized to the same volume V of material, we have

$$\frac{P_{\rm mag}}{P_{\rm sig}} = \frac{2\,Q\,\omega_M\,L}{(N\,\mathcal{F}_-)^2}\ . \tag{5.46}$$

For a setup employing direct readout of magnons, the sensitivity bandwidth is simply the ferromagnetic linewidth $\Delta\omega_s \simeq m_a/Q$, which fixes the integration time as $t_{\rm int}^{\rm mag} = t_e/Q$. Setting $P_{\rm mag}\, t_{\rm int}^{\rm mag} = m_a$ gives the line labeled as "Single Magnon" in Fig. 5.6. This represents the strongest possible sensitivity of an experiment of equal volume but trivial bulk geometry. The fact that the single magnon sensitivity is weaker than the single photon sensitivity shows that the magnon-polariton mode in an optimized multilayer effectively couples more strongly to the axion field than an infinite-medium magnon mode. Moreover, since these magnon-polaritons propagate out of the multilayer in the form of electromagnetic radiation, it is much easier to detect them precisely.

Comments on Experimental Realization

We conclude this section with some additional comments on the experimental realization of such a "magnetized multilayer" experiment. First, unlike the planned MADMAX experiment, the external magnetic field here can significantly affect the medium's properties, allowing strong sensitivity to a very wide range of axion masses. Due to this wide mass range, the experimental implementation is qualitatively different at each end. Referring to Fig. 5.5, at small masses ($m_a \lesssim 10^{-5}$ eV) one requires a large amount of material, but only a few layers and a weak external field. At larger masses ($m_a \sim 10^{-3}$ eV), a strong external field is required, but the entire stack is only a few centimeters long.

Unlike many axion experiments, our concept never requires a magnetic field that is simultaneously strong and large in volume, thus avoiding the need for expensive magnets; however, we do require the magnetic field to be highly uniform. Also note that while MADMAX requires tangential magnetic fields and thus a custom dipole magnet, we require a magnetic field normal to the slabs' surfaces. These can be produced by solenoidal magnets, which are more common and less expensive. In addition,

while the signal in multilayer setups can be calibrated indirectly using reciprocity theorems [476, 477], in our case an electron-coupled axion acts almost exactly like an oscillating transverse magnetic field, so the response can also be calibrated by simply applying a real transverse magnetic field.

Since the sensitivity bandwidth $\Delta\omega_s$ is small, our setup must be tuned to scan across a substantial range of possible axion masses. As we have noted below Eq. 5.43, a magnetized multilayer setup has a somewhat smaller $\Delta\omega_s$ compared to a standard dielectric haloscope since the permeability varies with frequency. However, this is compensated by the fact that there are two independent tuning mechanisms. For fine adjustments, one can alter the refractive index of the material by changing the applied magnetic field, which can be done quickly and precisely. For coarse adjustments, one may instead adjust the spacing between the slabs, as planned for MADMAX [430]. This two-stage strategy ensures that the amount of mechanical tuning required for our setup is never greater, even in the regime $Q \gg N$.

There are a number of experimental details that we have neglected in this chapter, all of which could be addressed in a more detailed analysis, along the lines of Refs. [478, 479]. For simplicity, we have only considered transparent mode setups. These setups are analytically tractable, and as discussed below Eq. 5.40 correspond to near-optimal form factors. However, other multilayer geometries may be more flexible and effective in a real experiment; determining this will require a detailed numeric optimization. Furthermore, we have treated the system as essentially one-dimensional, neglecting finite size effects, and assumed the slab thickness and spacing is perfectly uniform. Finally, we have approximated ∇a as spatially constant and have taken it to lie along the plane of the slabs. In reality, the direction of ∇a is anti-aligned with the Galactic motion of the solar system and thus sweeps over various directions throughout a sidereal day, incurring an $\mathcal{O}(1)$ penalty to the average signal power. However, the signal also exhibits a predictable modulation, which can help disentangle it from background. It is also important to understand the material properties in detail. As discussed in Appendix 5.10, magnetic losses at the relevant cryogenic, low-power conditions are somewhat uncertain and should be measured experimentally. Ideally, the permeability itself could be measured as a function of frequency and applied field, as it entirely determines the relevant response. We have also neglected the small magnetic anisotropy fields generated inside spinel ferrites, which slightly affect the relationship between B_0 and ω_B. Finally, other materials, such as hexagonal ferrites, could also yield good sensitivity at low cost. We defer investigation of these questions to future work.

5.4 Absorption Into In-Medium Excitations

Absorption of electron-coupled axion dark matter produces a variety of in-medium excitations. In analogy to the photoelectric effect, absorption through the axioelectric term gives rise to electronic excitations. This process has been well-studied for non-spin-ordered targets, such as noble liquids [413,

415, 414, 417, 420], semiconductors [420, 56, 421, 480], and spin-orbit coupled materials [55], which target axions of mass $m_a \gtrsim 10$ eV, 1 eV, and 1 meV, respectively.[3] In spin-polarized targets, electron-coupled axion dark matter can generate a wider range of excitations, such as meV-scale phonons [58] and magnons [405, 52], electronic transitions between Zeeman-split levels [53], and "nuclear magnons" in materials with strong hyperfine interactions [51].

In this section, we extend the results for two of these excitation channels. In Sec. 5.4.1, we revisit the calculation of axion dark matter absorption into magnons. We derive the absorption rate using the constitutive relations of classical electromagnetism, and show that it is determined by a magnetic energy loss function, complementing previous quantum mechanical derivations [52, 405]. In Sec. 5.4.2, we compute the axioelectric absorption rate in spin-polarized targets in two complementary ways, and show that the result is parametrically different than in non-spin-polarized targets.

5.4.1 Classical Estimate of Absorption into Magnons

Spin-ordered targets support collective spin excitations known as magnons. Similar to phonons, the energy scale of magnons is typically $\sim (1-100)$ meV, making them useful in the search for scattering of sub-GeV dark matter [406, 481], especially in models preferentially coupling to the electron spin. These excitations have also been studied in the context of axion dark matter, since the wind coupling allows an axion to be absorbed into a magnon [407, 409, 52, 405]. Pioneering work focused on the absorption of an axion into the lowest magnon mode, sometimes referred to as the "Kittel mode," which can be tuned with an applied magnetic field [407, 409, 52]. However, gapped magnon modes exist in any spin-ordered target with more than one magnetic ion in the unit cell and therefore can be used even in the absence of an external magnetic field.[4] A general formalism to understand such axion interactions with spin-ordered targets, with and without an external magnetic field, was developed in Ref. [405].

The axion absorption rate into magnons is typically computed (at least partially) quantum mechanically. In particular, the dynamics of the spins are assumed to be governed by a Heisenberg-like Hamiltonian. This Hamiltonian is diagonalized, which defines the magnon eigensystem, and then coupled to the axion wind. This approach works for any spin-ordered target, and the absorption rate depends on the model parameters of the Heisenberg-like Hamiltonian, which are usually determined from a first-principles calculation. While this provides a starting point to understand general dark matter interactions with spin, it introduces some uncertainty since the model parameters may be difficult to measure directly. Therefore, it is useful to understand if specific calculations may be written in terms of experimentally measurable properties, within the kinematic regime appropriate for the incoming dark matter. Such an approach has been used for axioelectric absorption, and more recently

[3] For $m_a \gtrsim 1$ meV, the axion-electron coupling also induces $a + e \to e +$ phonon transitions in non-spin-ordered superconductors [54, 421].

[4] While the existence of gapped magnon modes makes the axion absorption process kinematically viable, the usefulness of these modes is limited in simple magnets by selection rules. See Ref. [405] for more details.

developed for light dark matter coupling via a kinetically-mixed dark photon [437, 436, 438, 439], as well as for the absorption of electromagnetically-coupled axion dark matter in magnetized media [440]. Both of these dark matter interaction rates have been related to the "energy loss function" $\mathrm{Im}(-1/\varepsilon)$. Here, we show that an analogous classical derivation can be used to derive the axion absorption rate into magnons for a uniform bulk material in terms of a "magnetic energy loss function" $\mathrm{Im}\,(-1/\mu)$, where μ is the target permeability.

Generally, the axion dark matter absorption rate per unit target mass is determined by the imaginary component of the axion field's angular frequency ω [482, 483, 440],

$$R \simeq \frac{\rho_{\rm DM}}{\rho_{\rm T}} \frac{\mathrm{Im}\left(-\omega^2\right)}{m_a^2} \ , \tag{5.47}$$

where $\rho_{\rm T}$ is the mass density of the target. The axion frequency can be evaluated by solving the axion's classical equation of motion,

$$\left(\partial^2 + m_a^2\right) a = -g_{ae}\, \partial_\mu \left(\overline{\Psi}\gamma^\mu\gamma^5\Psi\right) \ . \tag{5.48}$$

Thus, the absorption rate is related to the imaginary component of the source term $g_{ae}\,\partial_\mu\left(\overline{\Psi}\gamma^\mu\gamma^5\Psi\right)$. Classically, this source term is the sum of the contributions from each individual electron in the target, which we define as its "expectation value,"

$$g_{ae}\left\langle \partial_\mu \left(\overline{\Psi}\gamma^\mu\gamma^5\Psi\right)\right\rangle \simeq \frac{g_{ae}}{e} \sum_i \left((\partial_t \mathbf{J}_i)\cdot\hat{\mathbf{s}}_i\right) + \frac{g_{ae}}{\mu_B}\nabla\cdot\mathbf{M} \ , \tag{5.49}$$

where the classical expectation value of the electron axial current $\overline{\Psi}\gamma^\mu\gamma^5\Psi$ was evaluated using the single-particle classical mapping of Eq. 5.101. In the first term of Eq. 5.49, the subscript i indexes the individual electrons, such that $\mathbf{J}_i \equiv e\,\mathbf{v}_i/V$ is the single particle current density with V the target volume, and $\hat{\mathbf{s}}_i$ is the direction of the electron spin. In the second term, μ_B is the Bohr magneton and $\mathbf{M} = \sum_i \mathbf{M}_i$ is the total magnetization density of the target.[5] The first term is dominant for electronic excitations via the axioelectric effect and will be considered in detail in Sec. 5.4.2. The second term governs absorption via the axion wind and will be the focus here.

As stated in Eqs. 5.18 and 5.24, the axion wind electron coupling produces an effective magnetic field $\mathbf{B}_{\rm eff}$ which induces a magnetization $\mathbf{M}_a = (1-\mu^{-1})\,\mathbf{B}_{\rm eff}$. This magnetization contributes to the second term of Eq. 5.49, which becomes

$$\frac{g_{ae}}{\mu_B}\nabla\cdot\mathbf{M} = -\left(\frac{g_{ae}\, m_a\, v_{\rm DM}}{\mu_B}\right)^2 \left(1 - \hat{\mathbf{q}}\cdot\mu^{-1}\cdot\hat{\mathbf{q}}\right) a \ , \tag{5.50}$$

[5] Since $\mathbf{M}$ enters the axion absorption rate and the usual constitutive relationships of electromagnetism in the same way, we can perform a trivial sum rather than explicitly writing down the contributions from each electron in Eq. 5.49. However, this is not the case for the first term in Eq. 5.49, and care must be taken in understanding the individual electronic response.

where $\hat{\mathbf{q}}$ is the unit vector aligned with the axion gradient. To determine the absorption rate R in Eq. 5.47, we substitute Eq. 5.50 into Eq. 5.48, Fourier transform, and evaluate the imaginary component of the axion frequency, which yields

$$R \simeq \left(\frac{g_{ae}\, v_{\rm DM}}{\mu_B}\right)^2 \frac{\rho_{\rm DM}}{\rho_{\rm T}}\; \hat{\mathbf{q}} \cdot \mathrm{Im}\left(-\mu^{-1}\right) \cdot \hat{\mathbf{q}}\;. \tag{5.51}$$

The last factor in Eq. 5.51, related to the imaginary part of the permeability, is the magnetic analogue of the so-called "energy loss function," previously identified within the context of dark matter scattering and absorption [436, 437, 438, 439, 440]. This implies a direct connection between μ and the magnon eigensystem derived previously in Ref. [405], which is worth exploring more generally. Along these lines, we thus anticipate that μ also dictates the dark matter-magnon scattering rate, originally derived in Ref. [406], exploration of which we leave to future work.

While, μ is experimentally measurable in principle, data is typically fit to the Landau–Lifshitz model of Eq. 5.34 (see Appendix 5.10 for details). This model only accounts for the Kittel mode resonance. In particular, absorption into the Kittel mode is controlled by $1/\mu_-$, since $\hat{\mathbf{q}} \cdot \mu^{-1} \cdot \hat{\mathbf{q}} \simeq |\hat{\mathbf{e}}_- \cdot \hat{\mathbf{q}}|^2/\mu_-$ for $m_a \simeq \omega_B$, where $\hat{\mathbf{e}}_-$ is the unit vector of the minus circular polarization. From Eq. 5.35, the magnetic energy loss function for μ_- is given by

$$\mathrm{Im}\left(\frac{-1}{\mu_-}\right) = \frac{m_a\, \omega_M/2Q}{(m_a - \omega_B)^2 + (\omega_B/2Q)^2}\;. \tag{5.52}$$

When $m_a \simeq \omega_B$ and $\hat{\mathbf{q}}$ is perpendicular to the background magnetization, Eq. 5.51 reduces to

$$R \simeq 2\,(g_{ae}\, v_{\rm DM})^2\, \frac{\rho_{\rm DM}}{\rho_{\rm T}}\, \frac{Q\, n_{\rm spin}}{m_a}\;, \tag{5.53}$$

where we defined the spin density $n_{\rm spin} = M_0/\mu_B$. This parametrically matches the magnon absorption rate computed in Ref. [405]. Another classical derivation of this result is presented in Appendix 5.9, which shows that it can be associated to the work done by rotating the magnetic dipoles in the material against the field $\mathbf{B} + \mathbf{B}_{\rm eff}$. While we have neglected boundary conditions throughout this section, it is also possible to include finite volume effects as was done in Ref. [484].

5.4.2 Absorption into Electronic Excitations

In this section, we show that the axioelectric absorption rate into electronic excitations is given by

$$R \simeq \left(\frac{g_{ae}\, m_a}{e}\right)^2 \frac{\rho_{\rm DM}}{\rho_{\rm T}} \times \begin{cases} 3\ \mathrm{Im}\left[\,\varepsilon(m_a)\,\right] & \text{(unpolarized target)} \\ \mathrm{Im}\left[\dfrac{-1}{\varepsilon(m_a)}\right] & \text{(polarized target, spin splitting} \gg m_a\text{)}\;, \end{cases} \tag{5.54}$$

where $\varepsilon(m_a)$ is the permittivity (i.e., dielectric function) evaluated at energy $\omega = m_a$ and zero momentum-transfer, appropriate for nonrelativistic dark matter. The first line of Eq. 5.54 has been derived previously in, e.g., Refs. [413, 56, 421]. The second line is a new result and applies to completely spin-polarized targets with a large energy splitting between electron spin states.

The key difference between the two cases in Eq. 5.54 is that $R \propto 1/|\varepsilon(m_a)|^2$ in polarized targets and thus is typically suppressed.[6] This has a simple physical interpretation. The axioelectric force drives each electron along the direction of its spin. In a spin-polarized target, each electron is thus driven in the same direction, generating a coherent electromagnetic field which backreacts on the electrons, screening the axion's effect. By contrast, in an unpolarized target the electrons respond incoherently, and their motion does not produce any net electromagnetic effects.

Though this screening reduces the signal rate, it can be useful for background rejection, since counting experiments are currently limited by large dark counts [485]. More specifically, the act of comparing polarized and unpolarized targets allows the dark count rate to be directly measured and separated from a potential signal. Ideally, a signal then only needs to overcome *fluctuations* in the background rate to become detectable, allowing the sensitivity to increase with larger exposure (which is not the case when background systematics dominate).

Below we derive Eq. 5.54 in two complementary ways. In Sec. 5.4.2, we use the constitutive relationships of classical electrodynamics, as was done in Sec. 5.4.1. In Sec. 5.4.2, we compute the absorption rate quantum mechanically in terms of self-energy diagrams using the formalism of Refs. [483, 421, 55, 486]. This more rigorous derivation produces correct $\mathcal{O}(1)$ factors, and allows us to generalize the second line of Eq. 5.54 to arbitrary spin splitting in Eq. 5.83.

Classical Derivation

The axioelectric absorption rate into electronic excitations is dominantly controlled by the first term in Eq. 5.49. In order to evaluate this term, we must determine the current density of each electron $\mathbf{J}_i$. We do this by using the classical electronic equation of motion, $m_e\,\ddot{\mathbf{x}}_i = \mathbf{F}_i$, where $\mathbf{x}_i$ and $\mathbf{F}_i$ are the position of and total force acting on the i^{th} electron, respectively. The internal forces are packaged into their contribution to the electric susceptibility χ_{ei}, defined such that in the presence of some external electric field $\mathbf{E}$, the equation of motion becomes $\mathbf{J}_i = \chi_{ei}\,\partial_t\mathbf{E}$. This form also makes it clear that χ_{ei} are related to the dielectric function as $\sum_i \chi_{ei} = \varepsilon - 1$, since this gives the usual constitutive relation $\sum_i \mathbf{J}_i = (\varepsilon - 1)\,\partial_t\mathbf{E}$. Note that in writing this, we have assumed that the target medium is sufficiently large (i.e., larger than the decay length in medium) so that boundary conditions can be neglected [450, 449].

In the presence of the axion field, we must also account for the effective electric of Eq. 5.20 in the electron's equation of motion, such that $\mathbf{J}_i = \chi_{ei}\left(\partial_t\mathbf{E} + (\partial_t E_{\text{eff}})\,\hat{\mathbf{s}}_i\right)$. Here, the electric field $\mathbf{E}$ incorporates the backreaction from any coherent motion of charges induced by the axion field. From

[6] However, it can be enhanced when $|\varepsilon(m_a)| \ll 1$, corresponding to m_a close to an in-medium resonance.

the long-wavelength limit of Ampère's law (or alternatively Eq. 5.26), this field is $\partial_t \mathbf{E} \simeq -\mathbf{J}_a^P/\varepsilon$, where $\mathbf{J}_a^P = (\partial_t E_{\rm eff}) \sum_i \chi_{ei}\, \hat{\mathbf{s}}_i$ is the total polarization current induced by the axioelectric term, as in Eq. 5.27. As an aside, note that by comparing this form of $\mathbf{J}_a^P$ to that given previously in Eq. 5.27, we arrive at a concrete expression for the spin-polarized contribution to the permittivity, denoted as ε_σ in Sec. 5.3. In particular, for a material with a net polarization along the $\hat{\mathbf{s}}$ direction, we have

$$\varepsilon_\sigma \equiv 1 + \sum_i \chi_{ei}\, \hat{\mathbf{s}}_i \cdot \hat{\mathbf{s}} \leq \varepsilon \ , \tag{5.55}$$

so that $\varepsilon_\sigma \simeq \varepsilon$ for a fully spin-polarized medium.

Now, using the result for the backreaction field $\mathbf{E}$ in the expression for $\mathbf{J}_i$, we have that the single-particle current is

$$\mathbf{J}_i \simeq \chi_{ei}\, (\partial_t E_{\rm eff}) \left(\hat{\mathbf{s}}_i - \frac{1}{\varepsilon} \sum_j \chi_{ej}\, \hat{\mathbf{s}}_j \right) = \chi_{ei}\, (\partial_t E_{\rm eff}) \times \begin{cases} \hat{\mathbf{s}}_i & \text{(unpolarized target)} \\ \hat{\mathbf{s}}/\varepsilon & \text{(polarized target)} \ , \end{cases} \tag{5.56}$$

where in the first equality, the first term is from the direct axion interaction with the $i^{\rm th}$ electron, and the second term is due to the electric backreaction from the collective motion of many electrons. In the second equality, we used that if electron spins of the same χ_{ei} are oppositely paired, as in an unpolarized target, then $\sum_i \chi_{ei}\, \hat{\mathbf{s}}_i = 0$, and if the target is instead completely spin-polarized, then $\hat{\mathbf{s}}_i = \hat{\mathbf{s}}$ and $\sum_i \chi_{ei}\, \hat{\mathbf{s}}_i = (\varepsilon - 1)\, \hat{\mathbf{s}}$. From Eq. 5.56, we then have that the first term on the right-hand side of Eq. 5.49 is

$$\sum_i (\partial_t \mathbf{J}_i) \cdot \hat{\mathbf{s}}_i = (\varepsilon - 1)\, \partial_t^2 E_{\rm eff} \times \begin{cases} 1 & \text{(unpolarized target)} \\ 1/\varepsilon & \text{(polarized target)} \ , \end{cases} \tag{5.57}$$

where the second line is in agreement with Eq. 5.29. From this point, the absorption rate R can again be computed using Eq. 5.47. The quantity $\mathrm{Im}(-\omega^2)$ is determined by substituting Eq. 5.57 in Eq. 5.49, and then using Eq. 5.48. This recovers the main result of Eq. 5.54, but without the factor of three for unpolarized targets.

This mismatch occurs because the classical picture provides an incomplete description of quantum spins. More precisely, the other classical arguments in this chapter gave correct numeric factors because they were linear in quantum operators and therefore were guaranteed to match quantum results in expectation by the Ehrenfest theorem. By contrast, since $\mathbf{J}_i \propto \hat{\mathbf{s}}_i$ for unpolarized targets, the classical treatment gives an answer proportional to $\hat{\mathbf{s}}_i \cdot \hat{\mathbf{s}}_i = 1$, while the analogous quantum mechanical treatment would give $\langle \boldsymbol{\sigma}_i \cdot \boldsymbol{\sigma}_i \rangle = 3$. For the polarized case, there is no such discrepancy because the mean spin polarization $\hat{\mathbf{s}}$ is inherently a classical vector and is treated as such in a fully quantum calculation. Finally, we note that an alternative classical derivation of the axioelectric absorption rate for a spin-polarized target is presented in Appendix 5.9, which shows that it can be

associated to the work done by the force on the electrons, proportional to $\mathbf{E} + \mathbf{E}_{\rm eff}$.

Matrix Element Calculation

While the derivation in Sec. 5.4.2, which is based on classical electrodynamics, elucidates some of the underlying physics, a quantum mechanical derivation makes direct contact with electronic states in the system and is therefore necessary for first-principles calculations. Moreover, it provides a general framework to understand any dark matter absorption rate into electronic excitations, which can then be simplified further by including assumptions about the target. The tradeoff is that this derivation is more technically involved than in Sec. 5.4.2. Below, we will use the self-energy formalism recently applied to dark matter absorption in Refs. [483, 487, 488, 489, 421, 55, 486] and refer the reader to Refs. [16, 421] for an introduction. We will adopt absorption kinematics throughout, i.e., that the dark matter is nonrelativistic with $\nabla a \ll \dot{a}$ (or, in other words, that the momentum k satisfies $k \ll \omega$).

To calculate the absorption rate R, we note that the presence of interactions mixes the free axion and photon dispersion relations. In the language of self-energies, the mixed dispersion relation of an interacting photon with polarization λ in Lorenz gauge and an axion is given by (see, for example, Ref. [483])

$$\begin{pmatrix} \omega^2 - k^2 - \Pi^\lambda_{AA} & -\Pi^\lambda_{aA} \\ -\Pi^\lambda_{Aa} & \omega^2 - k^2 - m_a^2 - \Pi_{aa} \end{pmatrix} \begin{pmatrix} A_\lambda \\ a \end{pmatrix} = 0 \ , \tag{5.58}$$

where Π_{aa} is the axion self-energy, $\Pi^\lambda_{aA} = -e^\lambda_\mu \, \Pi^\mu_{aA}$ is the mixed axion-photon self-energy projected onto the photon polarization vector e^λ_μ, and $\Pi^\lambda_{AA} = -e^\lambda_\mu \, \Pi^{\mu\nu}_{AA} \, e^\lambda_\nu$ is the photon self-energy. In the absence of the axion, the photon self-energy simply maps onto the normal dispersion relation for the photon, i.e., $n^2_\lambda \, \omega^2 = k^2$ where n_λ is the refractive index for the λ polarization, giving $\Pi^\lambda_{AA} = \omega^2 \, (1 - n^2_\lambda)$. The fields a and A refer to the free axion and photon states, respectively (i.e., the states defined in the absence of interactions between the axion and the photon).

To understand what an "axion" or "photon" looks like inside a medium, we must diagonalize the mixed dispersion relations in Eq. 5.58, which determines the axion-like and photon-like propagation eigenstates (sometimes also referred to as mass eigenstates). Due to the small axion coupling, the propagation states mostly correspond to the free axion and photon eigenstates, albeit with small admixtures of the opposing interaction states. At lowest nontrivial order (quadratic) in the coupling, we find the dispersion relations

$$\omega^2_\lambda \simeq k^2 + \begin{cases} \Pi^\lambda_{AA} - \dfrac{\Pi^\lambda_{aA} \, \Pi^\lambda_{Aa}}{m_a^2 - \Pi^\lambda_{AA}} & \text{(photon-like)} \\ m_a^2 + \Pi_{aa} + \displaystyle\sum_\lambda \dfrac{\Pi^\lambda_{aA} \, \Pi^\lambda_{Aa}}{m_a^2 - \Pi^\lambda_{AA}} & \text{(axion-like)} \ . \end{cases} \tag{5.59}$$

Analogous to the classical computation of the previous section, we must evaluate the imaginary component of the frequency for the propagating axion-like state in order to find the energy absorbed from the axion. Such a procedure gives, for any axion interaction and target electronic structure, the absorption rate

$$R \simeq -\frac{\rho_{\rm DM}}{\rho_{\rm T}\, m_a^2}\, {\rm Im}\left(\Pi_{aa} + \sum_\lambda \frac{\Pi^\lambda_{aA}\,\Pi^\lambda_{Aa}}{m_a^2 - \Pi^\lambda_{AA}}\right) . \tag{5.60}$$

At the onset, Eq. 5.60 can be simplified if we assume that the target is isotropic. In this limit, the photon self-energy is independent of polarization, $\Pi^\lambda_{AA} = \Pi_{AA}$, and the sum over the photon states can be removed using the completeness relation, $\sum_\lambda e^\lambda_\mu\, e^\lambda_\nu = -g^{\mu\nu}$. This reduces Eq. 5.60 to

$$R \simeq -\frac{\rho_{\rm DM}}{\rho_{\rm T} m_a^2}\, {\rm Im}\left(\Pi_{aa} + \frac{\Pi^i_{aA}\Pi^i_{Aa}}{m_a^2 - \Pi_{AA}}\right) . \tag{5.61}$$

These self-energies can then be computed diagrammatically using the relevant interactions present in the nonrelativistic Lagrangian [421] (ignoring subdominant terms dependent on the axion momentum),

$$\mathcal{L}_{\rm NR} \supset -i\frac{e}{m_e}\mathbf{A}\cdot\psi^\dagger\,\nabla\,\psi + \frac{e^2}{2m_e}\mathbf{A}^2\psi^\dagger\psi - ig_{ae}\,\frac{\dot a}{m_e}\,\psi^\dagger\,\boldsymbol{\sigma}\cdot\nabla\,\psi + g_{ae}\frac{e\dot a}{m_e}\mathbf{A}\cdot\psi^\dagger\,\boldsymbol{\sigma}\,\psi\,, \tag{5.62}$$

where the first two terms are contributions from nonrelativistic QED, and the last two are from the axioelectric interaction, $\mathcal{L} \supset g_{ae}\,\dot a\psi^\dagger\,\boldsymbol{\pi}\cdot\boldsymbol{\sigma}\,\psi/m_e$. The self-energies in Eq. 5.61 are given diagrammatically by

Π_{aa} : a (k^μ) (5.63)

Π_{aA} : a (k^μ) A + a (k^μ) A (5.64)

Π_{AA} : A (k^μ) A + A (k^μ) A . (5.65)

Following the formalism in Ref. [421] these diagrams evaluate to

$$\Pi_{aa} = g_{ae}^2 \frac{\omega^2}{m_e^2} \bar{\Pi}_{\boldsymbol{\sigma}\cdot\mathbf{p},\boldsymbol{\sigma}\cdot\mathbf{p}} \tag{5.66}$$

$$\Pi_{aA}^i = -ie\, g_{ae} \frac{\omega}{m_e} \left(\bar{\Pi}_{\sigma^i} - \frac{1}{m_e} \bar{\Pi}_{\boldsymbol{\sigma}\cdot\mathbf{p},p^i} \right) \tag{5.67}$$

$$\Pi_{AA} = -\frac{e^2}{m_e} \left(\bar{\Pi}_1 - \frac{1}{3m_e} \bar{\Pi}_{p^i,p^i} \right) , \tag{5.68}$$

using the Feynman rules determined by the nonrelativistic Lagrangian in Eq. (5.62), and noting that $\Pi_{Aa}^i = -\Pi_{aA}^i$. The quantities $\bar{\Pi}$ contain all the information about the target electronic structure and for operators $\mathcal{O}$ (such as momentum "p^i" or identity "1" operators) are defined as

$$\bar{\Pi}_{\mathcal{O}_1,\mathcal{O}_2} = -\frac{1}{V} \sum_{I\,I'} \frac{f_I - f_{I'}}{\omega - \Delta\omega_{II'} + i\,\delta_{II'}} \langle I|\mathcal{O}_1|I'\rangle \langle I'|\mathcal{O}_2|I\rangle \tag{5.69}$$

$$\bar{\Pi}_{\mathcal{O}} = -\frac{1}{V} \sum_{I} f_I \langle I|\mathcal{O}|I\rangle , \tag{5.70}$$

where I and I' index the electronic states $|I\rangle$ with energy ω_I, $\Delta\omega_{II'} = \omega_{I'} - \omega_I$, $\delta_{II'} = \delta\ \mathrm{sign}(\omega_{I'} - \omega_I)$ with δ the width of the electronic states, and V is the target volume. The filling fraction satisfies $f_I = 1$ if a state is occupied and $f_I = 0$ otherwise.

We will focus on targets where the states can be indexed by a band number b and spin quantum number $s \in \{\uparrow,\downarrow\}$, such that a state label is given by $I = \{b, s\}$. This is possible when spin is a good quantum number and allows the state to be split into spatial and spin degrees of freedom, i.e., $|I\rangle = |b\rangle \otimes |s\rangle$. We will find it useful to introduce self-energies with a spin index, such that Eq. 5.69 generalizes to

$$\bar{\Pi}_{\mathcal{O}_1,\mathcal{O}_2}^{ss'} = -\frac{1}{V} \sum_{b\,b'} \frac{f_{b\,s} - f_{b'\,s'}}{\omega - \Delta\omega_{bs\,b's'} + i\delta_{bs\,b's'}} \langle b,s|\mathcal{O}_1|b',s'\rangle \langle b',s'|\mathcal{O}_2|b,s\rangle \tag{5.71}$$

$$\bar{\Pi}_{\mathcal{O}}^{s} = -\frac{1}{V} \sum_{b} f_{b,s} \langle b,s|\mathcal{O}|b,s\rangle . \tag{5.72}$$

If the target is spatially isotropic, i.e., $\bar{\Pi}_{p^i,p^j}^{ss'} = \bar{\Pi}_{p^i,p^i}^{ss'} \delta^{ij}/3$, the self-energies in Eq. 5.68 can be simplified further, to

$$\Pi_{aa} = g_{ae}^2 \frac{\omega^2}{m_e^2} \left(\frac{1}{3} \left(\bar{\Pi}_{p^i,p^i}^{\uparrow\uparrow} + \bar{\Pi}_{p^i,p^i}^{\downarrow\downarrow} \right) + \frac{2}{3} \left(\bar{\Pi}_{p^i,p^i}^{\downarrow\uparrow} + \bar{\Pi}_{p^i,p^i}^{\uparrow\downarrow} \right) \right) \tag{5.73}$$

$$\Pi_{aA}^i = -ie\, g_{ae} \frac{\omega}{m_e} \hat{s}^i \left(\bar{\Pi}_1^{\uparrow} - \bar{\Pi}_1^{\downarrow} - \frac{1}{3m_e} \left(\bar{\Pi}_{p^i,p^i}^{\uparrow\uparrow} - \bar{\Pi}_{p^i,p^i}^{\downarrow\downarrow} \right) \right) \tag{5.74}$$

$$\Pi_{AA} = -\frac{e^2}{m_e} \left(\bar{\Pi}_1^{\uparrow} + \bar{\Pi}_1^{\downarrow} - \frac{1}{3m_e} \left(\bar{\Pi}_{p^i,p^i}^{\uparrow\uparrow} + \bar{\Pi}_{p^i,p^i}^{\downarrow\downarrow} \right) \right) , \tag{5.75}$$

where $\hat{s}^i = \langle s| \sigma^i |s\rangle$ is the expectation value of spin (as used in, e.g., Eq. 5.20). Note that since $\bar{\Pi}_1^s$ is simply the expectation value of the identity operator, it is straightforwardly evaluated as $\bar{\Pi}_1^s = -N_e^s/V$, where N_e^s is the number of electrons in spin state s.

Before computing the absorption rate in a spin-polarized target, we reproduce the standard result for a target with no spin polarization. In the absence of a net spin polarization, $f_{bs} = f_b$ (i.e., if a spin-up state is filled, then so is the corresponding spin-down state). Furthermore, we assume that the energy levels are spin independent, $\omega_{bs} \simeq \omega_b$. For a target satisfying these assumptions, we have $\bar{\Pi}^{ss'}_{\mathcal{O}_1,\mathcal{O}_2} = \bar{\Pi}_{\mathcal{O}_1,\mathcal{O}_2}$, and therefore Eqs. 5.73–5.75 simplify to

$$\Pi_{aa} = 2g_{ae}^2 \frac{\omega^2}{m_e^2} \bar{\Pi}_{p^i,p^i} \tag{5.76}$$

$$\Pi^i_{aA} = 0 \tag{5.77}$$

$$\Pi_{AA} = -\frac{2e^2}{m_e}\left(\bar{\Pi}_1 - \frac{1}{3m_e}\bar{\Pi}_{p^i,p^i}\right) . \tag{5.78}$$

Notice that since $\Pi^i_{aA} = 0$, there will be no mixing or screening effects; the photon and axion do not directly interact, which leaves the propagation eigenstates simply as the free states (this reflects the absence of any electromagnetic backreaction that screens the signal in unpolarized targets, as discussed in the classical derivation above). Substituting these self-energies into Eq. 5.61 gives

$$R = -\frac{\rho_{\rm DM}}{\rho_{\rm T}} \frac{2g_{ae}^2}{m_e^2} \,\mathrm{Im}\left(\bar{\Pi}_{p^i,p^i}\right) = -\frac{\rho_{\rm DM}}{\rho_{\rm T}} \frac{3g_{ae}^2}{e^2} \,\mathrm{Im}\left(\Pi_{AA}\right) = \frac{\rho_{\rm DM}}{\rho_{\rm T}} \frac{3g_{ae}^2 m_a^2}{e^2} \,\mathrm{Im}\left(\,\varepsilon(m_a)\,\right) , \tag{5.79}$$

where in the last step we used $\Pi_{AA}(\omega) \simeq \omega^2\left(1 - \varepsilon(\omega)\right)$ for $k \ll \omega$, in agreement with the first case of Eq. 5.54.

A similar calculation can be performed to determine the absorption rate for a target that is "super-polarized," e.g., one where all the electrons are polarized in the spin-up $\uparrow$ state. In this case, $f_{b,\downarrow} = 0$, for all b, and $f_{b,\uparrow} = 1$ when $\omega_{b\uparrow} < 0$ (corresponding to the electrons below the Fermi surface). In this limit, some of the self-energies simplify, such as $\bar{\Pi}^{\downarrow}_{\mathcal{O}} = 0$ and $\bar{\Pi}^{\downarrow\downarrow}_{\mathcal{O}_1,\mathcal{O}_2} = 0$. Additionally, the contribution from $\bar{\Pi}^{\downarrow\uparrow}_{p^i,p^i}$ to $\mathrm{Im}\left(\Pi_{aa}\right)$ is negligible in the small width limit, since there are no allowed $\downarrow$ to $\uparrow$ transitions in a spin-up super-polarized target. Therefore, in this case, the self-energies in Eqs. 5.73–5.75 reduce to

$$\Pi_{aa} = g_{ae}^2 \frac{\omega^2}{3m_e^2}\left(\bar{\Pi}^{\uparrow\uparrow}_{p^i,p^i} + 2\,\bar{\Pi}^{\uparrow\downarrow}_{p^i,p^i}\right) \tag{5.80}$$

$$\Pi^i_{aA} = -ie\, g_{ae} \frac{\omega}{m_e} \hat{s}^i \left(\bar{\Pi}^{\uparrow}_1 - \frac{1}{3m_e}\bar{\Pi}^{\uparrow\uparrow}_{p^i,p^i}\right) \tag{5.81}$$

$$\Pi_{AA} = -\frac{e^2}{m_e}\left(\bar{\Pi}^{\uparrow}_1 - \frac{1}{3m_e}\bar{\Pi}^{\uparrow\uparrow}_{p^i,p^i}\right) . \tag{5.82}$$

Unlike the unpolarized case, the polarized spins do induce a mixing between the axion and the photon

(consistent with the expectation of screening generated by an electrical backreaction, as discussed in the classical derivation above). These self-energies can be simplified further by noticing that $\Pi^i_{aA} = -ig_{ae}\, m_a\, \hat{s}^i\, \Pi_{AA}/e$, which can be used in the second term of Eq. 5.60. Additionally, note that $\mathrm{Im}\,(\Pi_{aa})$ has two contributions in Eq. 5.80. The first term corresponds to where the spin is fixed as $\uparrow$ which incorporates the classical force described in Sec. 5.2.2. The second term instead corresponds to a spin-flip transition, which does not have a classical analogue. The first term can be simply related to the self-energy of the photon Π_{AA} which is consistent with the picture of the axioelectric effect as a spin-coupled effective electric field (i.e., when all spins are polarized one can simply relate charges and spins and so electrons should have a similar effect on both the axion and photon). However, this statement does not hold for the spin-flip term. The absorption rate is then given by

$$R \simeq g_{ae}^2\, \frac{\rho_{\rm DM}}{\rho_{\rm T}} \left(\frac{m_a^2}{e^2}\, \mathrm{Im}\left(\frac{-1}{\varepsilon(m_a)} \right) + \frac{2}{3m_e^2}\, \mathrm{Im}\left(-\bar{\Pi}^{\uparrow\downarrow}_{p^i,p^i} \right) \right) , \tag{5.83}$$

where the first term matches the result in Sec. 5.4.2, as expected. Since the second term includes spin-flip transitions, it is natural that it could not be incorporated in the classical derivation. Furthermore, in the limit of large spin splitting, when the spin-flip transitions are kinematically unavailable, $\mathrm{Im}\left(-\bar{\Pi}^{\uparrow\downarrow}_{p^i,p^i}\right) \to 0$, and the absorption rate reduces to Eq. 5.54. Note that the dependence on $\mathrm{Im}(-1/\varepsilon)$ comes about due to the mixing of the axion with the photon and gives the same functional form as a direct electromagnetically-coupled axion. Thus, while the couplings are different in either case, the resulting physics is similar in the spin-polarized limit. In fact, we can also rederive the form of the axion-induced E-field by considering the basis that diagonalizes the dispersion relation of Eq. 5.58 to leading order, which we will label as $(\tilde{A}, \tilde{a})$. To convert from propagation basis to the interaction (A, a) basis, we can use the rotation matrix

$$\begin{pmatrix} A \\ a \end{pmatrix} \simeq \begin{pmatrix} 1 & \frac{\Pi_{aA}}{\Pi_{AA}-m_a^2} \\ \frac{-\Pi_{aA}}{\Pi_{AA}-m_a^2} & 1 \end{pmatrix} \begin{pmatrix} \tilde{A} \\ \tilde{a} \end{pmatrix} . \tag{5.84}$$

From this matrix, and noting that at lowest nontrivial order the magnitudes of a and $\tilde{a}$ are the same, we see that axion-photon mixing induces an E-field in an infinite medium of the form

$$E^i \simeq i\omega A^i \simeq i\omega\, \frac{\Pi^i_{aA}}{\Pi_{AA} - m_a^2}\, \tilde{a} \simeq -i\, \frac{\Pi^i_{aA}}{\varepsilon}\, \frac{a}{\omega} . \tag{5.85}$$

An alternative definition of the spin-polarized contribution to the permittivity ε_σ can then be obtained by equating Eqs. 5.85 and 5.28,

$$\varepsilon_\sigma \equiv 1 + \frac{e^2}{\omega^2\, m_e} \left(\bar{\Pi}^{\uparrow}_1 - \bar{\Pi}^{\downarrow}_1 - \frac{1}{3m_e} \left(\bar{\Pi}^{\uparrow\uparrow}_{p^i,p^i} - \bar{\Pi}^{\downarrow\downarrow}_{p^i,p^i} \right) \right) . \tag{5.86}$$

For "super-polarized" spins, we can use $\Pi^i_{aA} = -i\, g_{ae}\, m_a\, \hat{s}^i\, \Pi_{AA}/e$ to explicitly show that $\varepsilon_\sigma = \varepsilon$;

conversely, if the spins are unpolarized, then $\varepsilon_\sigma = 1$, as mentioned previously. Note that this form for ε_σ is analogous to the classical sum over spin weighted susceptibilities in Eq. 5.55 where the contributions to spin-up and spin-down states are added electron by electron.

While the derivation incorporates the entirety of electronic states, further simplifications can be made when the core electrons are much more tightly bound than the valence electrons, as in typical solids. In this case, the core electrons' contributions to the self-energies are negligible, due to their suppressed electron propagator in Eq. 5.69. This can be understood physically from the dielectric function, which encodes the target electronic response to an impinging electric field. If the core electrons are very tightly bound, then they respond less efficiently to an electric field. If the electronic response can be approximated by only including the least bound electrons, then only these electrons need to be spin-polarized for the "super-polarized" approximation discussed previously to hold. This is a much weaker, and more realistic, condition than requiring every electron to be spin-polarized.

5.5 Dipole Moments and Energy Shifts

In this section, we discuss two cases in which simple parametric estimates can yield misleading results. In Sec. 5.5.1, we show how one can use field redefinitions to work in a Hamiltonian lacking manifest axion shift symmetry. This leads to apparent electric dipole moment effects, which are actually spurious. In Sec. 5.5.2, we show that the axioelectric atomic energy level shift is smaller than the naive expectation.

5.5.1 Spurious Electric Dipole Moments

The axion-fermion coupling in Eq. 5.2 has an approximately equivalent nonderivative form, which has been the subject of some recent confusion. Let us first review how the nonderivative coupling is derived. In the original Lagrangian,

$$\mathcal{L} \supset \overline{\Psi}(i\partial\!\!\!/ - m_f)\Psi + g_{af}\,(\partial_\mu a)\,\overline{\Psi}\gamma^\mu\gamma^5\Psi \ , \tag{5.87}$$

one can perform a chiral redefinition of the fermion field, $\Psi \to e^{-ig_{af}a\gamma^5}\Psi$. This yields

$$\mathcal{L} \supset \overline{\Psi}(i\partial\!\!\!/ - e^{2ig_{af}a\gamma^5}m_f)\Psi - \frac{q_f^2}{8\pi^2}\,g_{af}\,a\,F_{\mu\nu}\,\tilde{F}^{\mu\nu} \ , \tag{5.88}$$

where the derivative coupling has been rotated away. The last term in Eq. 5.88, which arises due to the chiral anomaly, shifts the axion-photon coupling; it affects computations of loop-induced processes but will be irrelevant to the physical signatures considered in this chapter. Since these two Lagrangians are related by a field definition, they must yield precisely the same S-matrix elements and thus the same physical predictions [490, 491]. While it may naively appear that Eq. 5.88 implies

the presence of physical effects even for time- and space-indendent axion fields, $a(x,t) = a_0$, this cannot be the case, as the derivative coupling in Eq. 5.87 would simply vanish exactly.

Truncating the exponential in Eq. 5.88 at $\mathcal{O}(g_{af})$ and dropping the anomaly term yields a nonderivative interaction

$$\mathcal{L} \supset -2\, m_f\, g_{af}\, a\, \overline{\Psi} i\gamma^5 \Psi \ . \tag{5.89}$$

As shown in Appendix 5.11, it results in an alternative low-energy Hamiltonian for the fermion of the form

$$H_{\rm alt} \simeq \frac{\boldsymbol{\pi}^2}{2m_f} + q_f\, \phi - \frac{q_f}{2m_f}\, \mathbf{B}\cdot\boldsymbol{\sigma} - g_{af}\, (\nabla a)\cdot\boldsymbol{\sigma} - \frac{g_{af}}{4m_f}\, \{\dot{a}, \boldsymbol{\pi}\cdot\boldsymbol{\sigma}\} + \frac{q_f\, g_{af}}{2m_f}\, a\, \mathbf{E}\cdot\boldsymbol{\sigma} \ . \tag{5.90}$$

Compared to the original Hamiltonian of Eq. 5.15, Eq. 5.90 has an axioelectric term with coefficient smaller by a factor of two, as well as a "nonrelativistic EDM" term proportional to a that seems to violate the axion's shift symmetry.

The resolution of this paradox is that the two Hamiltonians describe exactly the same physics, but differ in their labeling of position states. To see this explicitly, note that the chiral field redefinition of Ψ modifies the nonrelativistic field ψ, defined in Eq. 5.10, by a momentum-dependent phase factor,

$$\psi \to \psi - i g_{af}\, a\, \tilde{\psi} \simeq \exp\left(-\frac{i g_{af}\, a\, \boldsymbol{\sigma}\cdot\boldsymbol{\pi}}{2m_f}\right)\psi, \tag{5.91}$$

where we used Eq. 5.13. This implies a shift of the particle's coordinate position by $\Delta\mathbf{x} = g_{af}\, a\, \boldsymbol{\sigma}/2m_f$. While the original Hamiltonian in Eq. 5.15 describes the fermion using a position operator that coincides with its center of charge, in the alternative Hamiltonian of Eq. 5.90 it is displaced from the center of charge by $\Delta\mathbf{x}$, thereby leading to an EDM of $\mathbf{d} = -q\,\Delta\mathbf{x}$. In other words, the apparent dependence on a is purely an artifact of the description. As we discuss in detail in Appendix 5.11, the physical equivalence of these Hamiltonians is completely general and occurs because they can be related by a unitary transformation generated by the Hermitian operator $S \propto \{a, \boldsymbol{\sigma}\cdot\boldsymbol{\pi}\}$. While calculations of experimental observables using the alternative Hamiltonian may contain a-dependent intermediate quantities, they must drop out of the final result.

In particular, electron EDM experiments measure the coefficient d of the full relativistic EDM operator $(d/2)\, \overline{\Psi}\gamma^5\sigma^{\mu\nu}\Psi\, F_{\mu\nu}$, where $\sigma^{\mu\nu} \equiv [\gamma^\mu, \gamma^\nu]/2$, which reduces to $-d\,\boldsymbol{\sigma}\cdot\mathbf{E}$ in the nonrelativistic limit [492]. Several recent works [426, 47, 427] have claimed extremely strong limits on g_{ae} by implicitly assuming that these EDM experiments constrain the coefficient of $\boldsymbol{\sigma}\cdot\mathbf{E}$, which carries an a-dependent contribution in Eq. 5.90. This is incorrect, because the operator $-d\,\boldsymbol{\sigma}\cdot\mathbf{E}$ produces no $\mathcal{O}(d)$ energy level shift by Schiff's theorem [261]. Instead, the signal from a true EDM arises entirely from its relativistic effects, which are not shared by the apparent EDM induced by an axion field. As discussed in detail in Appendix 5.11, for a constant axion field, the apparent axion-induced EDM is spurious, and thereby does not shift energy levels or give rise to any other physical effects. These

cancellations, which seem mysterious at the Hamiltonian level, arise from the axion's non-manifest shift symmetry.

On the other hand, a time-varying axion field can lead to physical effects in EDM experiments, but they are suppressed at low m_a by the small ratio of the axion mass to typical atomic energy scales. These effects are most straightforward to calculate with the derivative coupling, since the nonrelativistic EDM term lacks an explicit axion time derivative. Ref. [493] found that for nonrelativistic electrons bound in an atom, the leading energy shift linear in the external electric field is suppressed by $\mathcal{O}(m_a^2/\mathrm{Ry}^2)$, where the Rydberg constant $\mathrm{Ry} = \alpha^2 m_e/2$ gives the scale of electronic energy levels. As a result, the sensitivity of EDM searches to the axion-electron coupling is much weaker than existing astrophysical bounds. By contrast, two recent works [428, 429] missed this suppression factor, thereby overestimating the sensitivity of EDM experiments by many orders of magnitude. As explained further in Appendix 5.11, such overestimates can be avoided by taking care to compute the relevant physical observables for each experiment.

5.5.2 Suppressed Shifts of Electronic Energy Levels

The axion-electron coupling also shifts electronic energy levels in the absence of external fields. The leading-order contributions to these shifts are from the axion wind, $H_{\mathrm{wind}} = -g_{ae}\,(\nabla a)\cdot\boldsymbol{\sigma}$, and axioelectric, $H_{\mathrm{ae}} = -(g_{ae}/m_e)\,\dot{a}\,\boldsymbol{\pi}\cdot\boldsymbol{\sigma}$, terms in the nonrelativistic Hamiltonian of Eq. 5.15. Thus, to first order in perturbation theory, a naive estimate for the energy level shifts to an electronic state is $\Delta E_{\mathrm{wind}} \simeq \langle\psi|\,H_{\mathrm{wind}}\,|\psi\rangle \sim g_{ae}\,|\nabla a|$ and $\Delta E_{\mathrm{ae}} \simeq \langle\psi|\,H_{\mathrm{ae}}\,|\psi\rangle \sim g_{ae}\,\dot{a}\,v_e$, where $v_e \sim Z_{\mathrm{eff}}\,\alpha$ is the characteristic electron velocity bound to an ion with effective charge Z_{eff}.

The above estimate for the axion wind energy level shift is parametrically correct and is used to infer the reach of atomic clock experiments. However, we illustrate here that the effect of the axioelectric term is parametrically overestimated. To understand why, consider the leading-order terms in the nonrelativistic electron Hamiltonian, $H_0 = \boldsymbol{\pi}^2/2m_e + V(\mathbf{x})$, where the spin-independent potential $V(\mathbf{x})$ includes, e.g., the electrostatic potential energy. For electronic states governed by this Hamiltonian, $\boldsymbol{\pi} = im_e\,[H_0, \mathbf{x}]$ and thus

$$\Delta E_{\mathrm{ae}} = \langle\psi|H_{\mathrm{ae}}|\psi\rangle = -\frac{g_{ae}}{m_e}\,\dot{a}\,\langle\psi|\,\boldsymbol{\pi}\cdot\boldsymbol{\sigma}\,|\psi\rangle = ig_{ae}\,\dot{a}\,\langle\psi|\,\mathbf{x}\cdot[H_0,\boldsymbol{\sigma}]\,|\psi\rangle = 0\ , \tag{5.92}$$

such that the naive leading-order energy level shift from the axioelectric term vanishes, where in the last equality we used that H_0 commutes with the spin operator, by definition. ΔE_{ae} can be intuitively understood as the work done by the axion effective electric field. To see this, note that in the Heisenberg picture and using the Heisenberg equation of motion for the spin operator, ΔE_{ae} can be rewritten as $\Delta E_{\mathrm{ae}} = -e\,\langle\mathbf{x}_H\cdot\hat{\mathbf{E}}_{\mathrm{eff}}\rangle$, where $\hat{\mathbf{E}}_{\mathrm{eff}} \equiv -(g_{ae}/e)\,\dot{a}\,\dot{\boldsymbol{\sigma}}_H$, in analogy with Eq. 5.20. Hence, if the spin orientation is fixed, then Eq. 5.92 holds.

Instead, any energy level shift from the axioelectric term must arise from higher-order contributions

to H_0 that break the derivation in Eq. 5.92. For example, the relativistic kinetic energy correction shifts $[H_0, \mathbf{x}]$ so that it is no longer proportional to $\boldsymbol{\pi}$, while the electrons' spin-orbit or spin-spin interactions contribute to $[H_0, \boldsymbol{\sigma}]$. All of these terms are suppressed by v_e^2 relative to H_0, leading to the parametric estimate $\Delta E_{\rm ae} \sim g_{ae}\, \dot{a}\, v_e^3$, which is smaller than the naive estimate by a factor of $\alpha^2 \sim 10^{-4}$ for electrons with $Z_{\rm eff} \sim 1$. For light elements, this suppresses the projected reach in Ref. [46], which used the naive estimate discussed previously; however, it can be alleviated for very heavy atoms, with $Z \gg 1$. Future calculations of this energy shift, such as those relevant for Ref. [424], must be careful to account for these suppressions, as well as including any contributions from the vector potential $e\,\mathbf{A}$ when computing $\langle\psi|\boldsymbol{\pi}\cdot\boldsymbol{\sigma}|\psi\rangle$.

5.6 Outlook

The direct coupling of axion dark matter to Standard Model fermions leads to new experimental signatures. We have provided a firm theoretical foundation in Sec. 5.2 that clarifies the nature of these signatures, thereby resolving some existing disagreements in the literature in Sec. 5.5. We have also identified several new experimental strategies, focusing predominantly on the axion-electron coupling. Among these, the magnetized multilayer experiment discussed in Sec. 5.3.2 appears to be the most promising. Like previous ferromagnetic haloscope concepts, it relies on detecting the radiation emitted from the magnetization current induced by the axion wind torque on electron spins. The enhanced sensitivity of our setup comes from a combination of various factors: the use of inexpensive polycrystalline ferrite materials enables a much larger detector volume and a multilayer geometry enhances the effective coupling to the axion field. As a result, orders of magnitude of new parameter space can be explored with existing technology, for axion masses ranging from μeV to meV.

If nearly background-free single photon detectors are developed, they would enable magnetized multilayers to fully explore the DFSZ QCD axion model space when the abundance is set by the well-motivated post-inflationary misalignment mechanism [494, 495, 496, 497, 498, 499, 500, 501]. Single photon detection for frequencies in the $(1 - 100)$ μeV range has recently seen promising advances using, e.g., Rydberg atoms and superconducting qubits, though both technologies are relatively new and not background free [502, 503]. For higher frequencies, near a meV, transition edge sensors and kinetic inductance detectors can be used but currently suffer from large dark counts [504].

In future work, we will explore further refinements in determining the sensitivity of a magnetized multilayer haloscope. This includes a detailed numerical analysis that explores optimal tuning and effects from the axion wind's $\mathcal{O}(1)$ daily modulation. More generally, enhancing the axion's effective coupling to collective excitations in a multilayer geometry by operating slightly off resonance may also prove useful for other experiments, such as TOORAD [451].

We also plan on further exploring the findings of Sec. 5.4.1, which showed that the axion absorption

rate into spin excitations can be inferred directly from measurements of the magnetic energy loss function $\mathrm{Im}(-1/\mu)$, circumventing the need for a detailed microscopic model of magnetic materials. In particular, it would be interesting to expand this result to more general spin-coupled absorption and scattering of particles, which would simplify the formalism needed for dark matter searches, by connecting the signal rate directly to experimentally measurable parameters.

Although we have focused almost exclusively on the axion-electron coupling throughout most of this chapter, many of our results also translate to the axion-nucleon coupling. In particular, the mechanical resonators mentioned in Sec. 5.2.3 would be sensitive to comparable values of the axion-nucleon coupling, albeit only if $\mathcal{O}(1)$ nuclear spin-polarization can be achieved. Furthermore, the magnetization current discussed in Sec. 5.3.2 also exists for nucleon couplings, but is suppressed by the small magnitude of nuclear magnetic dipole moments. However, both of these issues may be alleviated in materials with strong hyperfine interactions between nuclear and electronic spins [51].

There are also a number of experimental concepts we have not considered in detail. In Sec. 5.2.3, we discussed how the axion wind may excite toroidal modes in mechanical resonators, which could lead to competitive sensitivity in the kHz $-$ MHz frequency range not covered by existing torsion pendulums or electromagnetic experiments. Developing this idea further would require considering the quality factors of such modes, the form factors for coupling to them, and mechanisms to read out their excitations. Finally, we note that if electron spins are made to precess at an angular frequency $\omega_{\rm spin} \gg m_a$, then both the mechanical and magnetization current signatures can be upconverted to a higher frequency $\omega_{\rm sig} \simeq m_a + \omega_{\rm spin}$. Such a "heterodyne" approach has been applied to cavity experiments for photon-coupled axions [176, 178, 123, 505], enabling sensitivity to axion masses parametrically smaller than the cavity's mode frequencies, but at the cost of introducing additional noise sources, which must be carefully analyzed.

The axion-fermion coupling leads to a rich variety of experimental signatures, which have previously been underexplored. Going forward, we hope that this work serves as a firm foundation for new ideas and future efforts.

5.7 Appendix: Reducing the Axial Current

Here, we show two ways to take the nonrelativistic limit of the axial vector current $\overline{\Psi}\gamma^\mu\gamma^5\Psi$. The fastest is to treat Ψ as a relativistic wavefunction and decompose it into two-component spinors, as in Eq. 5.10, which gives

$$\overline{\Psi}\gamma^\mu\gamma^5\Psi = \left(\psi^\dagger\tilde{\psi} + \tilde{\psi}^\dagger\psi \ , \ \psi^\dagger\boldsymbol{\sigma}\psi + \tilde{\psi}^\dagger\boldsymbol{\sigma}\tilde{\psi} \right)^\mu \ . \tag{5.93}$$

Now, note that Eqs. 5.13 and 5.16 imply $\tilde{\psi} \simeq (1/2)\,\mathbf{v}\cdot\boldsymbol{\sigma}\,\psi$ to leading order in g_{af}. Using this in Eq. 5.93 then yields

$$\overline{\Psi}\gamma^\mu\gamma^5\Psi \simeq \psi^\dagger \left(\mathbf{v}\cdot\boldsymbol{\sigma} \ , \ \boldsymbol{\sigma} \right)^\mu \psi + \mathcal{O}(v^2) + \mathcal{O}(g_{af}) \ . \tag{5.94}$$

Integrating Eq. 5.94 over space then yields Eq. 5.4, the axial current for a single particle.

Another method, which works for multi-particle states, is to treat Ψ as a quantized field with free mode expansion

$$\Psi(\mathbf{x}) = \int \frac{d^3\mathbf{p}}{(2\pi)^3} \sum_s \left(a^s_{\mathbf{p}}\, u_s(\mathbf{p})\, e^{i\mathbf{p}\cdot\mathbf{x}} + b^s_{\mathbf{p}}\, v_s(\mathbf{p})\, e^{-i\mathbf{p}\cdot\mathbf{x}} \right) , \tag{5.95}$$

where states with momentum $\mathbf{p}$ and spin s are described by $|\mathbf{p}, s\rangle = a^{s\,\dagger}_{\mathbf{p}} |0\rangle$ with $\langle \mathbf{p}, r|\mathbf{q}, s\rangle = (2\pi)^3\, \delta^{(3)}(\mathbf{p}-\mathbf{q})\, \delta^{rs}$. In Eq. 5.95, the coefficient of the particle annihilation operator $a^s_{\mathbf{p}}$ is a positive-frequency mode-function which can be obtained by solving the free Dirac equation, yielding

$$u_s(\mathbf{p}) = \sqrt{\frac{E+m_f}{2E}} \begin{pmatrix} \xi_s \\ \dfrac{\mathbf{p}\cdot\boldsymbol{\sigma}}{E+m_f}\, \xi_s \end{pmatrix} , \tag{5.96}$$

where E is the energy, ξ_s is a two-component spinor, and we used the nonrelativistic normalization $u^\dagger_s(\mathbf{p}) u_s(\mathbf{p}) = 1$.

We restrict to single particle states in the presence of an axion field with approximately constant uniform $\partial_\mu a$. In this case, we can take the classical limit by computing diagonal matrix elements of the axial vector current. As a warm up, let's first evaluate the matrix element for the vector current $\overline{\Psi}\gamma^\mu\Psi$. Its spatial components have expectation values

$$\langle \mathbf{p}, s|\, \overline{\Psi}\gamma^i \Psi\, |\mathbf{p}, s\rangle = \overline{u}_s(\mathbf{p})\gamma^i u_s(\mathbf{p}) = \frac{1}{E}\, \xi^\dagger_s \left(\sigma^i\, \mathbf{p}\cdot\boldsymbol{\sigma}\right) \xi_s = v^i , \tag{5.97}$$

where $\mathbf{v}$ is the velocity and we used the form of the mode-functions in Eq. 5.96. The expectation value of the temporal component is simply 1, by our normalization convention. By superposing plane waves, one can construct one-particle wavepackets of spatial spread r momentarily centered around a location $\mathbf{x}_0$, provided that $r \gg 1/m$. In such a normalized state, the expectation value of the vector current is thus approximately

$$\langle \overline{\Psi}\gamma^\mu\Psi\rangle \simeq (1, \mathbf{v})^\mu\ \delta^{(3)}(\mathbf{x}-\mathbf{x}_0) \tag{5.98}$$

for small r, which is a classical particle's number current, as expected. Similarly, for the axial vector current,

$$\langle \mathbf{p}, s|\, \overline{\Psi}\gamma^0\gamma^5\Psi\, |\mathbf{p}, s\rangle = \overline{u}_s(\mathbf{p})\gamma^0\gamma^5 u_s(\mathbf{p}) = \frac{1}{E}\, \xi^\dagger_s\, \mathbf{p}\cdot\boldsymbol{\sigma}\, \xi_s = \mathbf{v}\cdot\hat{\mathbf{s}} , \tag{5.99}$$

where $\hat{\mathbf{s}}$ is the unit normalized spin vector, and

$$\langle \mathbf{p}, s|\, \overline{\Psi}\gamma^i\gamma^5\Psi\, |\mathbf{p}, s\rangle = \overline{u}_s(\mathbf{p})\gamma^i\gamma^5 u_s(\mathbf{p}) = \sqrt{1-v^2}\ s_i + \frac{v_i\, \mathbf{v}\cdot\hat{\mathbf{s}}}{1+\sqrt{1-v^2}} . \tag{5.100}$$

Thus, in a normalized one-particle wavepacket state, the axial vector current is

$$\langle \overline{\Psi}\gamma^\mu\gamma^5\Psi\rangle = \left(\mathbf{v}\cdot\hat{\mathbf{s}}\,,\, \hat{\mathbf{s}} + \mathcal{O}(v^2)\right)^\mu\ \delta^{(3)}(\mathbf{x}-\mathbf{x}_0) , \tag{5.101}$$

which recovers Eq. 5.4. Note that this derivation implicitly treats $\partial_\mu a$ as constant because it only considers diagonal momentum-space matrix elements; thus, it does not yield the $\nabla \dot{a}$ term in the full Hamiltonian Eq. 5.15. Finally, note that the four-vectors in Eqs. 5.98 and 5.101 are not Lorentz covariant, because they multiply a noncovariant delta function; however, they are related by a factor of γ to the familiar four-velocity u^μ and spin four-vector s^μ [506, 507].

5.8 Appendix: Radiation From Slabs and Multilayers

In this appendix, we derive the results quoted in Sec. 5.3 for radiation emitted from single slabs. We then discuss how these results are extended to calculations for multilayer setups.

Polarization Currents

First, we derive the amplitude of the radiation field outside of a single infinite slab of thickness d, with boundaries located at $z = \pm d/2$. As discussed in Sec. 5.3.1, at the high frequencies relevant for the axioelectric polarization current, we can neglect the tensorial nature of μ. For concreteness, suppose the slab's spin polarization lies along $\hat{\mathbf{x}}$. Solving Eq. 5.26 for the electric field within each region gives

$$E_x = e^{-im_a t} \times \begin{cases} E_{\rm sig}\, e^{-im_a z} & z < -d/2 \\ E_{\rm in} \cos(n m_a z) + J_a^P/(im_a \varepsilon) & -d/2 < z < d/2 \\ E_{\rm sig}\, e^{im_a z} & z > d/2\ , \end{cases} \tag{5.102}$$

where $E_{\rm sig}$ and $E_{\rm in}$ are complex amplitudes and we used the fact that the polarization current, and hence the field, is symmetric about $d = 0$. Imposing continuity of E_x at $z = d/2$, we have

$$E_{\rm in}\, \cos(n m_a d/2) + \frac{J_a^P}{im_a\, \varepsilon} = E_{\rm sig}\, e^{im_a d/2}\ . \tag{5.103}$$

Furthermore, since there is no axion-induced surface current in this case, B_y/μ is also continuous at the boundary, such that Faraday's law yields

$$\frac{in}{\mu}\, E_{\rm in}\, \sin(n m_a d/2) = E_{\rm sig}\, e^{im_a d/2}\ . \tag{5.104}$$

Solving this system of equations, we arrive at Eq. 5.30.

In a situation involving many interfaces, such as a multilayer dielectric haloscope, it is not practical to directly solve for E_x in each region by simultaneously imposing all of the boundary conditions. Instead, the solution can be built up by considering the outgoing radiation generated at each interface. Each of these waves then propagates through the rest of the stack, as in ordinary electrodynamics. Thus, let us continue by considering an interface at $z = 0$ between two mediums with scalar permittivities $\varepsilon_{1,2}$ and permeabilities $\mu_{1,2}$, assuming uniform spin polarization along $\hat{\mathbf{x}}$.

For the axioelectric polarization current, the resulting electric field is

$$E_x = e^{-im_a t} \times \begin{cases} E_1^\gamma \, e^{-in_1 m_a z} + E_1^a & z < 0 \\ E_2^\gamma \, e^{in_2 m_a z} + E_2^a & z > 0 \ , \end{cases} \tag{5.105}$$

where $E_i^a = J_{a,i}^P/(im_a\varepsilon_i)$. Imposing continuity of $\mathbf{E}_\parallel$ and $\mathbf{B}_\parallel/\mu$, we have

$$E_1^\gamma + E_1^a = E_2^\gamma + E_2^a \, , \tag{5.106}$$

$$(-n_1/\mu_1)\, E_1^\gamma = (n_2/\mu_2)\, E_2^\gamma \ , \tag{5.107}$$

whose solution is

$$E_1^\gamma = -E_2^\gamma = (E_2^a - E_1^a)\ \frac{\varepsilon_2 n_1}{\varepsilon_1 n_2 + \varepsilon_2 n_1} \ . \tag{5.108}$$

If both media are maximally spin-polarized, with $\varepsilon_{\sigma,i} = \varepsilon_i$, then the difference of E_i^a above simplifies to

$$E_2^a - E_1^a = \left(\frac{\varepsilon_{\sigma,1} - 1}{\varepsilon_1} - \frac{\varepsilon_{\sigma,2} - 1}{\varepsilon_2}\right) E_{\text{eff}} = \left(\frac{1}{\varepsilon_2} - \frac{1}{\varepsilon_1}\right) E_{\text{eff}} \ . \tag{5.109}$$

In this case, Eq. 5.108 exactly matches the analogous result for the axion-photon coupling in, e.g., Sec. 3.1 of Ref. [431], after making the replacment $g_{a\gamma\gamma}\, a\, B_0 \to -E_{\text{eff}}$. Thus, in Sec. 5.3.1 we may directly recast results from conventional dielectric haloscope calculations, as stated in Eq. 5.32.

More generally, the layers can have different degrees of spin polarization, which leads to more flexibility than in a conventional dielectric haloscope. If ε_2 is large, then $E_2^a - E_1^a$ is maximized when $\varepsilon_1 = 1$. As such, the most aggressive forecast for the LAMPOST optical dielectric haloscope in Ref. [118] assumed vacuum gaps between layers. These are mechanically challenging at optical wavelengths and thus have been avoided by current LAMPOST and MuDHI prototypes. However, here we can achieve the same enhancement in $E_2^a - E_1^a$ with arbitrary ε_1 by simply not spin-polarizing that medium, such that $\varepsilon_{\sigma,1} = 1$. This case does not directly map onto a conventional dielectric haloscope, but we expect it yields a similar signal enhancement without the need for vacuum gaps.

Magnetization Currents

For the axion wind induced magnetization current, we assume that ∇a is uniform and lies in the slab's plane. As discussed in Sec. 5.3.2, we can treat the circular polarizations of the generated electric field separately. These polarizations have amplitudes

$$E^\pm = e^{-im_a t} \times \begin{cases} -E_{\text{sig}}^\pm \, e^{-im_a z} & z < -d/2, \\ E_{\text{in}}^\pm \, \sin(n m_a z) & -d/2 < z < d/2, \\ E_{\text{sig}}^\pm \, e^{im_a z} & z > d/2 \ , \end{cases} \tag{5.110}$$

where we used the fact that the magnetization current, and hence the field, is antisymmetric about $d = 0$. At $z = d/2$, $E^\pm$ is continuous while $B^\pm/\mu_\pm$ jumps by $M_a^\pm$, giving

$$E_{\rm in}^\pm \sin(n_\pm m_a d/2) = E_{\rm sig}^\pm \, e^{i m_a d/2} \tag{5.111}$$

$$-\frac{i n_\pm}{\mu_\pm} E_{\rm in}^\pm \cos(n_\pm m_a d/2) = E_{\rm sig}^\pm \, e^{i m_a d/2} + M_a^\pm \ . \tag{5.112}$$

Solving these equations and using the definition of $\mathbf{M}_a$ in Eq. 5.24, along with $B_{\rm eff}^\pm = B_{\rm eff}/\sqrt{2}$, then yields Eq. 5.36.

Once again, to understand a general multilayer, we first consider the radiation emitted from a single interface at $z = 0$. In this case, the radiation is due to a surface current $\mathbf{K}_a = \mathbf{M}_{a,1}^\parallel - \mathbf{M}_{a,2}^\parallel$ at the boundary. The radiation field is

$$E^\pm = e^{-i m_a t} \times \begin{cases} E_1^\pm \, e^{-i n_1 m_a z} & z < 0 \\ E_2^\pm \, e^{i n_2 m_a z} & z > 0 \ . \end{cases} \tag{5.113}$$

The relevant boundary conditions,

$$E_1^\pm = E_2^\pm, \tag{5.114}$$

$$(-n_1/\mu_1) E_1^\pm = (n_2/\mu_2) E_2^\pm + K_a^\pm \ , \tag{5.115}$$

determine $E_{1,2}^\pm$ to be

$$E_1^\pm = E_2^\pm = K_a^\pm \, \frac{\mu_1 \, \mu_2}{\mu_1 \, n_2 + \mu_2 \, n_1} \ . \tag{5.116}$$

Note that this is a completely different structure compared to the analogous result in Eq. 5.108, and hence has no simple mapping to a conventional dielectric haloscope.

5.9 Appendix: Power Absorption in Classical Electrodynamics

The power absorbed from the axion field in a spin-polarized medium, through either the axioelectric or axion wind terms, can be computed classically by considering the work done on the electrons. Similar arguments have been used for photon-coupled axions [117, 452, 449] and dark photons [489]. For electron-coupled axions, one must take care to account for the work done by both the real electromagnetic fields $\mathbf{E}$ and $\mathbf{B}$ and the effective fields $\mathbf{E}_{\rm eff}$ and $\mathbf{B}_{\rm eff}$.

First, consider absorption through the axioelectric term in an infinite medium with $\varepsilon_\sigma \simeq \varepsilon$. Both $\mathbf{E}$ and $\mathbf{E}_{\rm eff}$ do work on the electrons, since the net force is proportional to their sum. Applying Eq. 5.28 gives $\mathbf{E} + \mathbf{E}_{\rm eff} \simeq \mathbf{E}_{\rm eff}/\varepsilon$, and combining Eqs. 5.27 and 5.29 gives a total current density

$\mathbf{J} = (\varepsilon - 1)\,\partial_t \mathbf{E}_{\rm eff}/\varepsilon$. The time-averaged power dissipated in the medium per unit volume is then given by a generalized form of Ohm's law,

$$\frac{P}{V} = \frac{1}{2}\,\mathrm{Re}\big((\mathbf{E} + \mathbf{E}_{\rm eff}) \cdot \mathbf{J}^*\big) \simeq \frac{m_a}{2}\,|E_{\rm eff}^2|\;\mathrm{Im}\left(\frac{-1}{\varepsilon}\right)\,, \tag{5.117}$$

where the factor of $1/2$ accounts for the time average.

Next, consider absorption through the axion wind term in an infinite medium with a constant background magnetization $\mathbf{M}_0$ and magnetic field $\mathbf{B}$. In this case, the work done is associated with the rotation of magnetic dipoles in the presence of $\mathbf{B}$ and $\mathbf{B}_{\rm eff}$. Accounting for both of these fields gives

$$\frac{P}{V} = \frac{1}{2}\,\mathrm{Re}\big((\mathbf{H} + \mathbf{H}_{\rm eff}) \cdot (\partial_t \mathbf{M})^*\big) = \frac{1}{2}\,\mathrm{Re}\Big(\big(\mathbf{B} + \mathbf{B}_{\rm eff} - \mathbf{M}_0 - \mathbf{M}_a\big) \cdot \big(\partial_t(\mathbf{M}_0 + \mathbf{M}_a)\big)^*\Big)\,. \tag{5.118}$$

Since $\mathbf{M}_0$ is constant and the induced magnetization $\mathbf{M}_a$ is orthogonal to $\mathbf{M}_0$ and $\mathbf{B}$, the expression above reduces to

$$\frac{P}{V} = \frac{1}{2}\,\mathrm{Re}\big((\mathbf{B}_{\rm eff} - \mathbf{M}_a) \cdot (\partial_t \mathbf{M}_a)^*\big) = \frac{m_a}{2}\,|B_{\rm eff}^2|\;\mathrm{Im}\left(-\hat{\mathbf{q}}^T \mu^{-1} \hat{\mathbf{q}}\right)\,, \tag{5.119}$$

where we applied Eq. 5.23, used the fact that μ is Hermitian, and defined $\hat{\mathbf{q}}$ as the unit vector pointing along the axion gradient. The dominant contribution to the power comes from the resonantly amplified "minus" circular polarization. Its permeability, given in Eq. 5.37, corresponds to

$$\mathrm{Im}\left(\frac{-1}{\mu_-}\right) = \frac{m_a\,\omega_M/2Q}{(m_a - \omega_B)^2 + (\omega_B/2Q)^2}\,. \tag{5.120}$$

The power absorption rate is maximized when the axion frequency matches the infinite-medium Kittel frequency, $m_a \simeq \omega_B$, and $\hat{\mathbf{q}}$ is perpendicular to the background magnetization. In this case, we have

$$\frac{P}{V} = \frac{1}{2}\,|B_{\rm eff}^2|\,Q\,\omega_M\,. \tag{5.121}$$

Alternatively, if one averages over all directions of $\hat{\mathbf{q}}$, then the power is reduced by a factor of $2/3$.

The results above for the power density P/V match those of Sec. 5.4 after rescaling to a rate per unit target mass, $R = (P/V)/(\rho_T\, m_a)$, and substituting in the definitions of the effective fields. In particular, Eq. 5.117 corresponds to the second line of Eq. 5.54 after substituting $|E_{\rm eff}^2|/2 = (g_{ae}\, m_a/e)^2\,\rho_{\rm DM}$, and Eq. 5.119 reduces to Eq. 5.51 after substituting $|B_{\rm eff}^2|/2 = (g_{ae}\, v_{\rm DM}/\mu_B)^2\,\rho_{\rm DM}$.

Though the derivations here assumed infinite media, they also apply to finite media, provided that the characteristic size of the medium is much larger than the screening length and boundary conditions are unimportant. Moreover, these calculations can be straightforwardly generalized for arbitrary geometries, provided one accounts for how the boundary conditions affect the real electromagnetic fields, as was done in Ref. [449]. On the other hand, since in-medium fields and currents are always

macroscopically averaged, these arguments cannot be applied to unpolarized media, where those quantities would simply vanish. For the unpolarized case, one must instead use the methods of Sec. 5.4.

5.10 Appendix: Analysis of Ferrite Multilayers

In this appendix, we justify the choices of ferrite material properties listed in Table 5.1, discuss analytic estimates of the signal power in a multilayer setup, and present numeric results for single crystal YIG.

Properties of Ferrite Materials

Ferrite materials are well-studied [508, 509, 510, 511], and here we present some of their measured properties. First, for polycrystalline spinel ferrites, we infer the saturation magnetization and microwave permittivity ε from a commercial datasheet [146]. This datasheet also gives the microwave permittivity of YIG, which is comparable to that of the spinel ferrites. The saturation magnetization of YIG significantly increases when it is cooled. In particular, at cryogenic temperatures it is $M_S = 0.25$ T [512], half that of spinel ferrite.

Ferrites can be fabricated with small dielectric losses, $\tan\delta_\varepsilon = \mathrm{Im}(\varepsilon)/\mathrm{Re}(\varepsilon) \lesssim 10^{-4}$, which are largely due to the presence of divalent Fe ions or other impurities [508]. Thus, magnetic losses dominate for all materials we consider here. The magnetic quality factor Q is the most difficult parameter to infer; for simplicity, we first focus on Q for single crystal YIG.

The quality factor of undoped single crystal YIG spheres has been directly measured at room temperature and ranges from $Q \sim (0.7-1.8)\times 10^4$ at microwave frequencies [513, 514, 515]. However, for YIG, Q has a complex dependence on temperature. It is generally inferred from the linewidth of the ferromagnetic resonance, $\Delta H \simeq H/Q$. As the temperature is reduced, the linewidth is observed to initially reduce, but then sharply increase below $T \sim 100$ K [516, 517, 512]. These trends are understood theoretically to be arising from the reduced density of thermal phonons and the increased effect of fast-relaxing rare earth ions, respectively [510]. At even lower temperatures, $T \lesssim 10$ K, the linewidth reduces again as the effects of rare earth ions freezes out. However, recent measurements down to $T = 30$ mK have found that the linewidth increases again due to coupling to two-level systems [518, 519]. Remarkably, the linewidth at such low temperatures is comparable to that at room temperature, even though the loss mechanisms are completely different. Given this ambiguity, in our discussion below, we adopt an intermediate value of $Q \sim 10^4$ for single crystal YIG.

In polycrystalline materials, the resonance linewidth is much larger. For instance, Ref. [146] found that $\Delta H \lesssim 200$ Oe for a millimeter wave ferrite. Taking this number at face value and assuming that this material is accurately described by Eq. 5.33 then yields $Q \sim 20$. However, in reality the linewidth for polycrystalline materials is mostly due to inhomogeneities in the material's microscopic structure

and, thus, cannot be used to infer the damping away from resonance [520, 521, 522]. Instead, one must measure the frequency-dependent "effective linewidth" $\Delta H_{\rm eff}$, which determines the parameter Q appearing in Eq. 5.37. Away from resonance, $\Delta H_{\rm eff}$ is much smaller than ΔH for polycrystalline materials and can even approach the value of ΔH for single crystals [523]. For instance, Ref. [508] quotes a linewidth of $\Delta H_{\rm eff} = 4$ Oe for lithium ferrites, corresponding to $Q \sim 10^3$. However, given the many other uncertainties, we adopt a conservative intermediate value of $Q \sim 10^2$ for polycrystalline spinel ferrite.

In both cases, a detailed estimate of the experimental sensitivity requires dedicated measurements in appropriate conditions. Since magnetic losses depend on the geometry of the sample and applied field, such measurements should use thin slab samples with an orthogonal applied field. They must also be performed at cryogenic temperatures and low input power, well away from resonance.

Analytic Estimates

As noted in Sec. 5.3.2, the quality factor of polycrystalline spinel ferrite is too low to derive accurate, simple analytic expressions. However, for single crystal YIG, analytic approximations provide an excellent description of the numeric result. In deriving them below, we assume that ε is a real $\mathcal{O}(1)$ number and $\Delta\omega \ll m_a, \omega_M$. We also assume that the setup is operated many linewidths away from the resonance, $\Delta\omega \gg m_a/Q$, which increases the screening length and allows the use of many layers. These approximations are consistent provided that $Q \gg 1$ and $Q\,\omega_M/m_a \gg 1$, which are satisfied, for both polycrystalline ferrite and YIG, for all masses we consider.

In this regime, the transparent mode slab thickness is

$$d \simeq \frac{\pi}{m_a}\sqrt{\frac{\omega_m}{\varepsilon\,\Delta\omega}}\,, \tag{5.122}$$

which is much larger than the vacuum gaps between slabs. The sensitivity bandwidth is

$$\Delta\omega_s \simeq \frac{\pi}{2}\frac{m_a}{Q}\,, \tag{5.123}$$

which scales with Q just as in typical resonant experiments. The number of layers grows with $\Delta\omega$,

$$N \simeq \frac{4Q}{\pi}\frac{\Delta\omega}{m_a}\,, \tag{5.124}$$

which is large when $\Delta\omega \gg m_a/Q$, as anticipated. Finally, the form factor has nontrivial dependence on $\Delta\omega$, even though we have fixed $\mathrm{Re}(n_-)m_a d = \pi$, because the argument of the cotangent in Eq. 5.36 has an imaginary part. In particular, the form factor is approximately

$$\mathcal{F}_- \simeq \left|\frac{1}{\mu - in\tan(i/2N)}\right| \simeq \left|\frac{1}{\mu + n/2N}\right| \simeq \left|\frac{\Delta\omega}{\omega_M} + \frac{\pi\sqrt{\varepsilon}}{8Q}\frac{m_a}{\sqrt{\omega_M\,\Delta\omega}}\right|^{-1}\,, \tag{5.125}$$

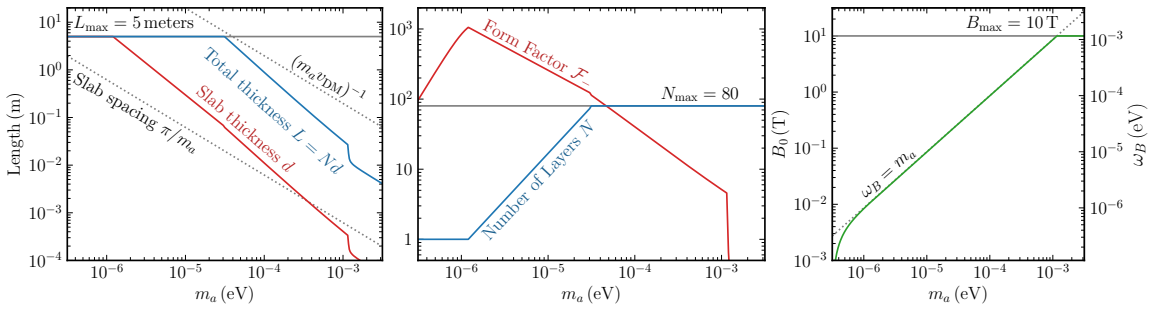

Figure 5.7: Analogue of Fig. 5.5, but for single crystal YIG.

so that increasing $\Delta\omega$ decreases the cotangent term, leading to a peak in $\mathcal{F}_-$ at nonzero $\Delta\omega$.

The signal power is determined by the product $N\,\mathcal{F}_-$, which monotonically increases with $\Delta\omega$ until it saturates at $N\,\mathcal{F}_- \sim (4/\pi)\,(Q\,\omega_M/m_a)$ at frequency separations $\Delta\omega \gtrsim \Delta\omega_0 \equiv (m_a\,\sqrt{\varepsilon\,\omega_M}/Q)^{2/3}$. In this regime, N and $\mathcal{F}_-$ are inversely proportional, yielding a simple estimate for the signal power,

$$P_{\rm sig} \simeq \frac{4}{\pi^2}\left(\frac{Q\,\omega_M}{m_a}\right)^2 |B_{\rm eff}^2|\,A\ . \tag{5.126}$$

Now, we can perform some cross-checks. First, note that for a fixed $\Delta\omega$, the total volume of the slabs scales as $V = N\,A\,d \propto Q$, so that Eq. 5.126 can be rewritten as $P_{\rm sig} \propto Q\,V$ as generically expected. Second, Eq. 5.126 was derived without considering the limits on the number of layers and total slab length, both of which increase with $\Delta\omega$. Demanding that these limits do not take effect until the maximum signal power is reached at $\Delta\omega \gtrsim \Delta\omega_0$ implies

$$N_{\max} \gtrsim \left(\frac{Q\,\omega_M}{m_a}\right)^{1/3} \tag{5.127}$$

$$m_a L_{\max} \gtrsim \left(\frac{Q\,\omega_M}{m_a}\right)^{2/3}\ , \tag{5.128}$$

where we have dropped numeric factors. For both materials, Eq. 5.127 is true for all masses we consider, and Eq. 5.128 is true only in the upper half of the mass range. For lower masses, the signal power is limited by the constraint on L.

Finally, for self-consistency we must ensure that the optimal $\Delta\omega$ is not too large for our approximations to break down. Since it is favorable to increase $\Delta\omega$ whenever our approximations hold, its value is dictated by either $N_{\max}$ or $L_{\max}$. When the limit comes from the former, $N = N_{\max}$, demanding that $\Delta\omega \ll \omega_M, m_a$ yields the condition

$$Q \gg N_{\max}, (m_a/\omega_M)N_{\max}\ . \tag{5.129}$$

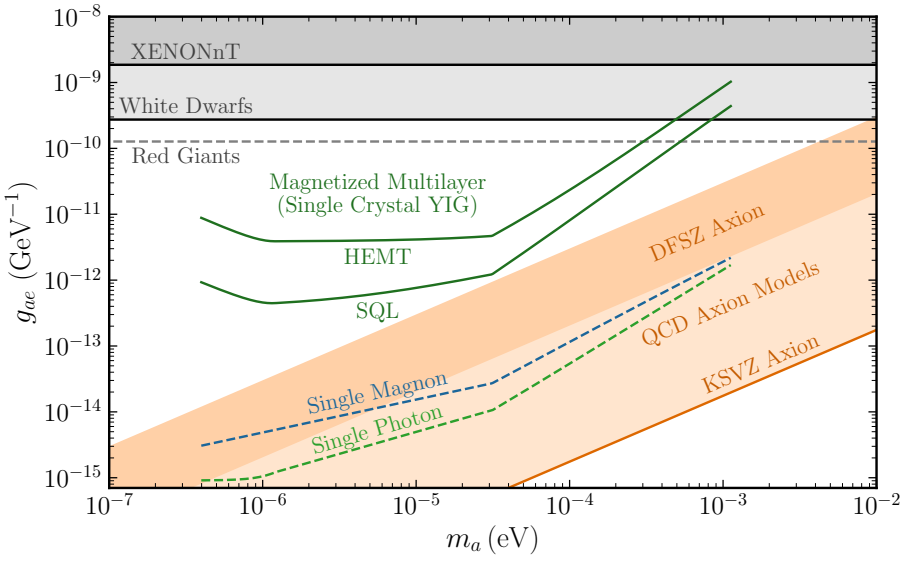

Figure 5.8: Analogue of Fig. 5.6, but for single crystal YIG. We assume material parameters $M_S = 0.25$ T, $Q = 10^4$, and $\varepsilon = 15$, while all other parameters are as in Table 5.1.

For single crystal YIG, this is satisfied for the entire mass range we consider, but for polycrystalline ferrite it is not satisfied at all; in the latter case a signal power higher than Eq. 5.126 is possible.

Sensitivity with Single Crystal YIG

For the sake of comparision, we compute the sensitivity for single crystal YIG, corresponding to $M_S = 0.25$ T, $Q = 10^4$, and $\varepsilon = 15$, using the same procedure as in Sec. 5.3.2. Some intermediate quantities from the numeric calculation are shown in Fig. 5.7. They are qualitatively similar to the corresponding results for polycrystaline ferrite, but they match the analytic results quite closely for $m_a \gtrsim 3 \times 10^{-5}\,\mathrm{eV}$, where the multilayer is not limited by $L_{\max}$.

The resulting sensitivity for a YIG multilayer setup is shown in Fig. 5.8. Numerically, it is only slightly greater than the result in Fig. 5.6 for polycrystalline ferrite. Though the signal power is enhanced by Q^2, this improvement is partially cancelled by the decrease in ω_M and in the sensitivity bandwidth. In addition, the signal power for polycrystalline ferrite is somewhat greater than the approximate analytic result in Eq. 5.126. Overall, for a magnetized multilayer setup, using single crystal YIG provides only a small sensitivity enhancement at a greatly increased cost.

5.11 Appendix: Equivalence of the Nonderivative Coupling

The axion-fermion coupling has equivalent derivative and nonderivative forms, which we denote with subscripts d and n, respectively. For brevity, we will drop all other subscripts in this appendix,

replacing q_f, m_f, and g_{af} with q, m, and g, respectively. In this chapter, we have focused mostly on the derivative form of the coupling,

$$\mathcal{L}_d = g\,(\partial_\mu a)\,\overline{\Psi}\gamma^\mu\gamma^5\Psi\ . \tag{5.130}$$

In Sec. 5.5.1, we discussed how this coupling is equivalent at $\mathcal{O}(g)$ via a field redefinition to a nonderivative form

$$\mathcal{L}_n = -2m\,ga\,\overline{\Psi}i\gamma^5\Psi\ , \tag{5.131}$$

where we neglected the axion-photon coupling generated by the chiral anomaly. In this appendix, we explain how these couplings are equivalent at the level of their nonrelativistic Hamiltonians. In Sec. 5.2.1, we showed that, up to higher-order terms in $1/m$, the derivative coupling $\mathcal{L}_d$ corresponds to

$$H_d = H_0 - g\,(\nabla a)\cdot\boldsymbol{\sigma} - \frac{g}{2m}\,\{\dot{a}, \boldsymbol{\pi}\cdot\boldsymbol{\sigma}\}\ , \tag{5.132}$$

where H_0 is the usual Pauli Hamiltonian. In Appendix 5.11.1, we will show that $\mathcal{L}_n$ instead corresponds to

$$H_n = H_0 - g\,(\nabla a)\cdot\boldsymbol{\sigma} - \frac{g}{4m}\,\{\dot{a}, \boldsymbol{\pi}\cdot\boldsymbol{\sigma}\} + \frac{q\,g}{2m}\,a\,\mathbf{E}\cdot\boldsymbol{\sigma}\ , \tag{5.133}$$

to the same order in $1/m$. In Appendix 5.11.2, we show that H_d and H_n are related by a unitary transformation and thereby physically equivalent. These results are consistent with those in recent works.

The two Hamiltonians superficially do not appear to be physically equivalent, which has led to substantial recent confusion. First, H_d and H_n do not have the same coefficient for the axioelectric term. In Appendix 5.11.3, we show that the axioelectric term encodes measurable relative acceleration effects. As a result, when one considers a multi-particle Hamiltonian, H_n necessarily contains complicated additional terms which precisely compensate for the smaller coefficient of its axioelectric term. Second, for constant a, H_n contains a term of the form $d\,\boldsymbol{\sigma}\cdot\mathbf{E}$ with $d \propto q\,a$, which appears to violate the axion's underlying shift symmetry. In Appendix 5.11.4, we explain why this "nonrelativistic EDM" term has no $\mathcal{O}(a)$ physical effects in the nonrelativistic limit. The essential reason is that such a term is just an artifact of choosing to describe an ordinary charged particle with a shifted position operator. Of course, as we discuss in Appendix 5.11.5, true EDMs do have physical effects, but those effects arise solely through their higher-order and relativistic corrections. By contrast, this axion-induced spurious EDM does not share these corrections and therefore does not produce a signal proportional to a in any EDM experiment, reflecting the axion's underlying shift symmetry.

5.11.1 Deriving The Nonderivative Hamiltonian

To derive H_n, we use the Pauli elimination method, as in Sec. 5.2.1. For $\mathcal{L}_n$, the fermion's equation of motion is

$$(i\partial\!\!\!/ - m - q\,A\!\!\!/ - 2im\,ga\,\gamma^5)\,\Psi = 0\ , \tag{5.134}$$

which in terms of two-component fields is

$$(i\partial_t - q\phi)\,\psi = (\boldsymbol{\pi}\cdot\boldsymbol{\sigma} + 2im\,ga)\,\tilde{\psi} \tag{5.135}$$

$$(i\partial_t + 2m - q\phi)\,\tilde{\psi} = (\boldsymbol{\pi}\cdot\boldsymbol{\sigma} - 2im\,ga)\,\psi\ . \tag{5.136}$$

In these equations, the axion coupling always appears with the fermion mass m, so we must work to higher order in the nonrelativistic expansion to capture the desired $\mathcal{O}(g/m)$ terms in the Hamiltonian. To do so, we write $\tilde{\psi}$ as

$$\tilde{\psi} = \frac{1}{2m}(\boldsymbol{\pi}\cdot\boldsymbol{\sigma} - 2im\,ga)\,\psi - \frac{i\partial_t - q\phi}{2m}\,\tilde{\psi} \tag{5.137}$$

$$= \frac{1}{2m}\left(1 - \frac{i\partial_t - q\phi}{2m}\right)(\boldsymbol{\pi}\cdot\boldsymbol{\sigma} - 2im\,ga)\,\psi + \mathcal{O}(1/m^3)\ , \tag{5.138}$$

where we iterated Eq. 5.137 to reach Eq. 5.138. Substituting this back into Eq. 5.135 yields

$$(i\partial_t - q\phi)\,\psi \simeq \frac{1}{2m}\,(\boldsymbol{\pi}\cdot\boldsymbol{\sigma} + 2im\,ga)\left(1 - \frac{i\partial_t - q\phi}{2m}\right)(\boldsymbol{\pi}\cdot\boldsymbol{\sigma} - 2im\,ga)\,\psi\ , \tag{5.139}$$

which is accurate up to $\mathcal{O}(1/m^3)$ terms. Note that this power counting argument treats the momentum as $\mathcal{O}(1)$, so that an expansion in $1/m$ is also an expansion in velocity.

At this point, we can read off a fiducial Hamiltonian $\bar{H}_n$ by defining $i\partial_t\psi = \bar{H}_n\psi$. As shown in Refs. [524, 525], the g-independent terms at $\mathcal{O}(1/m^2)$ will contain the usual fine-structure corrections to the Pauli Hamiltonian. We are instead interested in the $\mathcal{O}(g/m)$ terms, which can arise from either the first or last factor in Eq. 5.139. The contribution from the first factor of Eq. 5.139 is

$$\bar{H}_n \supset iga\left(1 - \frac{i\partial_t - q\phi}{2m}\right)\boldsymbol{\pi}\cdot\boldsymbol{\sigma} \simeq iga\,\boldsymbol{\pi}\cdot\boldsymbol{\sigma} - \frac{ga}{2m}\,q\dot{\mathbf{A}}\cdot\boldsymbol{\sigma}\ , \tag{5.140}$$

where we used the fact that $(i\partial_t - q\phi)\,\psi = \mathcal{O}(1/m)$ and can thus be neglected. The last factor of Eq. 5.139 gives

$$\bar{H}_n \supset \boldsymbol{\pi}\cdot\boldsymbol{\sigma}\left(1 - \frac{i\partial_t - q\phi}{2m}\right)(-iga) \tag{5.141}$$

$$\simeq -iga\,\boldsymbol{\pi}\cdot\boldsymbol{\sigma} - g\,(\nabla a)\cdot\boldsymbol{\sigma} - \frac{ga}{2m}\,q(\nabla\phi)\cdot\boldsymbol{\sigma} + \frac{ig}{2m}\,(\nabla\dot{a})\cdot\boldsymbol{\sigma} - \frac{g\dot{a}}{2m}\,\boldsymbol{\pi}\cdot\boldsymbol{\sigma}\ . \tag{5.142}$$

Combining the two yields the $\mathcal{O}(g/m)$ part of the Hamiltonian,

$$\bar{H}_n \supset -g\,(\nabla a)\cdot\boldsymbol{\sigma} + \frac{ga}{2m}\,q\mathbf{E}\cdot\boldsymbol{\sigma} + \frac{ig}{2m}\,(\nabla\dot{a})\cdot\boldsymbol{\sigma} - \frac{g\dot{a}}{2m}\,\boldsymbol{\pi}\cdot\boldsymbol{\sigma}\ . \tag{5.143}$$

However, this Hamiltonian is not physically appropriate, as it is not Hermitian. The reason is that the equations of motion preserve the norm of the full four-component wavefunction Ψ, which is

$$\int d^3\mathbf{x}\,\Psi^\dagger\Psi = \int d^3\mathbf{x}\,\psi^\dagger\psi + \tilde{\psi}^{\,\dagger}\tilde{\psi} \simeq \int d^3\mathbf{x}\,\psi^\dagger\left(1 + \frac{(\boldsymbol{\pi}\cdot\boldsymbol{\sigma})^2}{4m^2} - \frac{g\,(\nabla a)\cdot\boldsymbol{\sigma}}{2m}\right)\psi\ , \tag{5.144}$$

where we used Eq. 5.138 and again dropped $\mathcal{O}(1/m^3)$ terms. We thus define a renormalized two-component wavefunction whose norm is preserved,

$$\psi_{\rm nr} \simeq M\,\psi \equiv \left(1 + \frac{(\boldsymbol{\pi}\cdot\boldsymbol{\sigma})^2}{8m^2} - \frac{g\,(\nabla a)\cdot\boldsymbol{\sigma}}{4m}\right)\psi\ , \tag{5.145}$$

which defines the rescaling coefficient M. This subtlety was irrelevant for the derivation of H_d in Sec. 5.2.1, since there the contributions to M started at $\mathcal{O}(g/m^2)$. The physical Hamiltonian is then identified using $i\partial_t\psi_{\rm nr} = H_n\psi_{\rm nr}$, giving

$$H_n \simeq \bar{H}_n + [M, \bar{H}_n] + i\partial_t M\ . \tag{5.146}$$

As discussed in Refs. [524, 525], these M-dependent correction terms are essential for reproducing fine-structure corrections; to give a more recent application, such a field renormalization is also required to derive correct results in heavy quark effective theory [526, 527]. For our purposes, we are interested in the g-dependent correction term, $i\partial_t M \supset -ig\,(\nabla\dot{a})\cdot\boldsymbol{\sigma}/4m$. Including this term, we arrive at the claimed result Eq. 5.133, which matches the one found in Ref. [428] using the methods of Foldy–Wouthuysen transformations. The Pauli elimination method was also used in Refs. [426, 427, 429], yielding the same EDM term, though only Ref. [429] kept track of the full Hamiltonian.

5.11.2 Equivalence of the Hamiltonians

Truncating the Interaction

Before we explain why H_d and H_n are equivalent, let us first dispatch a red herring. It is tempting to conclude that the mismatch arises from truncating the exponential at $\mathcal{O}(g)$ in the full nonderivative form of the interaction in Eq. 5.88, resulting in $\mathcal{L}_n$. Historically, this was the resolution to a related puzzle which arose in the study of pion-nucleon interactions, which have "pseudovector" and "pseudoscalar" forms closely analogous to $\mathcal{L}_d$ and $\mathcal{L}_n$, respectively. In terms of our axion-based language, Dyson claimed that the couplings were equivalent on the basis of the axion wind terms

being the same [528]. However, the two couplings give different amplitudes at $\mathcal{O}(g^2)$ [529], and it was quickly realized that the couplings were only equivalent up to additional interaction terms of $\mathcal{O}(g^2)$ [530, 531, 532]. To give a more recent example, for axions produced in supernova, both axion-nucleon and pion-nucleon interactions are relevant. Both interactions can be rotated to the nonderivative form, but in that case the cross-term $(g\,m/f_\pi)\,\bar{N}a\,\pi N$ must be kept to compute a correct axion bremsstrahlung rate [533, 534, 535].

By contrast, in our case there is nothing wrong with truncating at $\mathcal{O}(g)$. We are focusing on axion dark matter searches, where all relevant amplitudes are $\mathcal{O}(g)$, since $\mathcal{O}(g^2)$ and higher effects are negligible. Furthermore, the mismatch between the Hamiltonians starts at $\mathcal{O}(g)$, so it cannot be resolved by considering higher-order terms.

Incidentally, we note that $\mathcal{L}_n$ is often derived by applying integration by parts to $\mathcal{L}_d$, and then "simplifying" with the free Dirac equation. This is not exact, but it yields the correct result because applying the equations of motion preserves S-matrix elements up to the addition of higher-order terms that are negligible here [536].

Unitary Equivalence

To relate the two Hamiltonians, we note that any quantum theory can be reparametrized by applying a unitary transformation to the states. In particular, for any Hermitian operator S, we can define "primed" states by $|\psi'\rangle = e^{iS}\,|\psi\rangle$. If the original states evolve as $i\partial_t\,|\psi\rangle = H\,|\psi\rangle$, the primed states evolve as $i\partial_t\,|\psi'\rangle = H'\,|\psi'\rangle$, where

$$H' = e^{iS}\,(H - i\partial_t)\,e^{-iS} = H + i[S, H] - \partial_t S + \mathcal{O}(S^2)\ . \tag{5.147}$$

In particular, suppose we start with the derivative Hamiltonian, $H = H_d$, and choose

$$S = -\beta\,\frac{g}{4m}\,\{a, \boldsymbol{\pi}\cdot\boldsymbol{\sigma}\}\ , \tag{5.148}$$

where β is a dimensionless parameter. Working to $\mathcal{O}(g/m)$, the primed Hamiltonian is then

$$H' \simeq H_d + \beta\,\frac{g}{4m}\,\{\dot{a}, \boldsymbol{\pi}\cdot\boldsymbol{\sigma}\} + \beta\,\frac{q\,g}{2m}\,a\,\boldsymbol{\sigma}\cdot\mathbf{E}\ . \tag{5.149}$$

For $\beta = 1$, we recover the nonderivative Hamiltonian H_n. Evidently, this transformation is the nonrelativistic Hamiltonian analogue of the field redefinition used to convert $\mathcal{L}_d$ to $\mathcal{L}_n$. Of course, the fact that the Hamiltonian can be transformed in appearance does not imply that experimental results are ambiguous. If an experiment measures an observable A in the original picture, then in the primed picture it measures a primed observable A' with the same matrix elements, $\langle\psi|\,A\,|\psi\rangle = \langle\psi'|\,A'\,|\psi'\rangle$, which implies that operators transform correspondingly as

$$A' = e^{iS}\,A\,e^{-iS} = A + i[S, A] + \mathcal{O}(S^2)\ . \tag{5.150}$$

Since matrix elements match by construction, experimental results are exactly the same in either picture.

This insight was crucial to resolve an old controversy in the theory of pion-nucleon interactions. In our language, Refs. [537, 538] pointed out that the coefficient of the axioelectric term could be modified by a unitary transformation. This led to confusion, with some claiming that pion absorption amplitudes were ambiguous. However, in Ref. [539], it was pointed out that such a transformation also generates an additional term involving the nuclear potential (the analogue of the EDM term above), and that when this is properly accounted for, all physical results are unchanged.

A similar lesson can be drawn from the relativistic quantum mechanics of spin-1/2 particles, where a unitary transformation can be used to map the Dirac representation to the Foldy–Wouthuysen representation [441]. In the latter representation, the so-called "Zitterbewegung" (or jittering) of the fermion's position and spin is eliminated, but its coupling to electromagnetic fields becomes nonlocal [540, 541]. Despite these radical differences, the two representations are perfectly physically equivalent. Similarly, we will see that all values of β give equivalent physical predictions, but $\beta = 0$ is by far the easiest choice to work with. For any $\beta \neq 0$, proper calculations of physical observables will display "mysterious" cancellations that reflect the non-manifest axion shift symmetry.

5.11.3 The Physical Axioelectric Term

In this section, we set the axion gradient ∇a to zero for simplicity. We also consider only neutral particles, $q = 0$, so that we can discuss the axioelectric term in isolation. In this case, the primed Hamiltonian in Eq. 5.149 is

$$H' \simeq \frac{p^2}{2m} - \left(1 - \frac{\beta}{2}\right) \frac{g\dot{a}}{m} \mathbf{p} \cdot \boldsymbol{\sigma} \ . \tag{5.151}$$

Thus, for neutral particles it appears that one can shift the coefficient of the axioelectric term to an arbitrary value, without any other consequences. On this basis, Ref. [428] concluded that the axioelectric term is unphysical for neutral particles, and should be eliminated by choosing $\beta = 2$.

The problem with this reasoning is that for a single particle, *any* force, whether real or fictitious, can be removed by performing a unitary transformation which maps the laboratory frame to the particle's frame. The difference between the two cases is that real forces can produce relative accelerations between distinct colocated particles, while fictitious forces do not. By this standard, the axioelectric force is real and its effects can be measured experimentally.

To see this explicitly, we must generalize Eq. 5.151 to a Hamiltonian with multiple interacting particles. One simple way to do this is to consider a Lagrangian with two neutral fermion fields Ψ_1 and Ψ_2 of mass m, with interactions

$$\mathcal{L}_d^{(12)} = g\,(\partial_\mu a)\,\left(\overline{\Psi}_1 \gamma^\mu \gamma^5 \Psi_1 + \overline{\Psi}_2 \gamma^\mu \gamma^5 \Psi_2\right) + c\,\overline{\Psi}_1 \Psi_1 \overline{\Psi}_2 \Psi_2 \ , \tag{5.152}$$

where c is a coupling constant for the contact interaction. Following the same procedure as in

Sec. 5.2.1 yields

$$i\partial_t \psi_1 \simeq \left(\frac{p_1^2}{2m} - \frac{g\dot{a}}{m}\,\mathbf{p}_1\cdot\boldsymbol{\sigma}_1 - c\,\overline{\Psi}_2\Psi_2\right)\psi_1 \ , \tag{5.153}$$

where a similar equation holds for ψ_2. In the limit where there is a single nonrelativistic well-localized particle of each type, we can simplify the bilinears as in Appendix 5.7, giving a Hamiltonian

$$H \simeq \frac{p_1^2}{2m} + \frac{p_2^2}{2m} - c\,\delta^{(3)}(\mathbf{x}_1-\mathbf{x}_2) - \frac{g\dot{a}}{m}\left(\mathbf{p}_1\cdot\boldsymbol{\sigma}_1 + \mathbf{p}_2\cdot\boldsymbol{\sigma}_2\right) . \tag{5.154}$$

Finally, applying the unitary transformation generated by Eq. 5.148 to each particle yields

$$H' \simeq \frac{p_1^2}{2m} + \frac{p_2^2}{2m} - c\,\delta^{(3)}(\mathbf{x}_1-\mathbf{x}_2) - \left(1-\frac{\beta}{2}\right)\frac{g\dot{a}}{m}\left(\mathbf{p}_1\cdot\boldsymbol{\sigma}_1 + \mathbf{p}_2\cdot\boldsymbol{\sigma}_2\right) + \frac{\beta}{2}\,\frac{ga\,c}{m}\left(\boldsymbol{\sigma}_1-\boldsymbol{\sigma}_2\right)\cdot\nabla_1\delta^{(3)}(\mathbf{x}_1-\mathbf{x}_2) \ . \tag{5.155}$$

For the unprimed Hamiltonian in Eq. 5.154, the axioelectric term produces a measurable relative acceleration effect. For example, if the particles begin in their lowest bound state, with different spin directions, then a time-varying axion field can induce a transition to an excited state. On the other hand, for the primed Hamiltonian in Eq. 5.155 with $\beta = 2$, the axioelectric term is indeed rotated away, but it is replaced with a new term which induces precisely the same transitions. Similar reasoning would hold for any interaction between a particle and a measurement apparatus. One is free to work with H', but for $\beta \neq 0$ it will always contain complicated additional terms which encode the physical effect of the axioelectric force.

One might argue that the final term in Eq. 5.155 is only present because we chose to start with the derivative form of the interaction. Indeed, if we had started with

$$\mathcal{L}_n^{(12)} = -2m\,ga\,\left(\overline{\Psi}_1 i\gamma^5\Psi_1 + \overline{\Psi}_2 i\gamma^5\Psi_2\right) + c\,\overline{\Psi}_1\Psi_1\overline{\Psi}_2\Psi_2 \ , \tag{5.156}$$

then the corresponding nonrelativistic Hamiltonian would be Eq. 5.155 with $\beta = 1$ but without the final term. However, Eq. 5.156 is not an appropriate choice of Lagrangian because it violates the shift symmetry of the axion. The correct way to derive $\mathcal{L}_n^{(12)}$ is to start from Eq. 5.152 and apply a chiral field redefinition, which instead yields

$$\mathcal{L}_n^{(12)} = -2m\,ga\,\left(\overline{\Psi}_1 i\gamma^5\Psi_1 + \overline{\Psi}_2 i\gamma^5\Psi_2\right) + c\,\overline{\Psi}_1 e^{2iga\gamma^5}\Psi_1\,\overline{\Psi}_2 e^{2iga\gamma^5}\Psi_2 \ . \tag{5.157}$$

It is straightforward to check that the nonrelativistic Hamiltonian corresponding to this Lagrangian is indeed given by Eq. 5.155 with $\beta = 1$. In other words, regardless of what Lagrangian we start from, the axioelectric force is most directly described by taking $\beta = 0$.

5.11.4 The Unphysical Nonrelativistic EDM Term

In this section, we instead set the axion gradient ∇a and time derivative $\dot{a}$ to zero for simplicity, so that we can discuss the nonrelativistic EDM term in isolation. In this case, the primed Hamiltonian in Eq. 5.149 is

$$H'(\mathbf{x}, \mathbf{p}) \simeq \frac{(\mathbf{p} - q\,\mathbf{A})^2}{2m} + q\,\phi - \frac{q}{2m}\,\mathbf{B}\cdot\boldsymbol{\sigma} - d\,\mathbf{E}\cdot\boldsymbol{\sigma}\ , \tag{5.158}$$

where $d \equiv -\beta q\, g a/(2m)$, and all of the external fields above are evaluated at $\mathbf{x}$. The final term in Eq. 5.158 is indeed the nonrelativistic limit of the contribution of a true EDM to the Hamiltonian density, $\mathcal{H}_{\rm EDM} = (d/2)\,\overline{\Psi}\gamma^5\sigma^{\mu\nu}\Psi\,F_{\mu\nu}$. However, perhaps surprisingly, the term $-d\,\mathbf{E}\cdot\boldsymbol{\sigma}$ in isolation has no $\mathcal{O}(d)$ physical effects in the nonrelativistic limit, so that Eq. 5.158 does not directly imply physical effects proportional to the axion field.

Energy Levels of Bound Electrons

The simplest and most general way to see this is to note that H' is unitarily equivalent to H_d, which has no nonrelativistic EDM term. Crucially, unlike the axioelectric term in Appendix 5.11.3, the Hamiltonian without the nonrelativistic EDM term does not contain any other $\mathcal{O}(d)$ terms, so its effect can truly be removed without consequence. This remains true even when interparticle Coulomb interactions are included.

In particular, EDMs are often measured through the energy level shifts they induce in atoms placed in an external, constant electric field. If the atoms are described nonrelativistically, with only pairwise Coulomb interactions, then a nonrelativistic EDM term can be eliminated at $\mathcal{O}(d)$ by a unitary transformation generated by $S \propto \boldsymbol{\pi}\cdot\boldsymbol{\sigma}$. Since this S is time-independent, Eq. 5.147 implies that it preserves energy levels. We thus conclude that nonrelativistic EDMs do not have any $\mathcal{O}(d)$ effects on atomic energy levels, which is simply the famous statement of Schiff's theorem [261].

Shifting the Position Operator

While the physical equivalence of H_n and H_d decisively rules out an $\mathcal{O}(d)$ EDM, it is unintuitive that the $-d\,\mathbf{E}\cdot\boldsymbol{\sigma}$ term is unphysical for charged particles. This is because such a term seems to suggest the generation of electric dipole radiation and spin precession in an electric field. Indeed, the neutron EDM *can* be measured using the latter effect [542]. However, the situation for charged particles is fundamentally different. The reason is that a particle of charge q can always be artificially described by a position operator shifted relative to the usual one by $\Delta\mathbf{x}$, which introduces an electric dipole moment $\mathbf{d} = q\,\Delta\mathbf{x}$. This is the fundamental reason an EDM term appears in Eq. 5.158, and it implies that the same physical effects can be described without it.

To make this statement more precise, consider the position operator $\mathbf{x}$ in the unprimed Hamiltonian, which has no EDM term. As usual, the acceleration of the particle is proportional to $\mathbf{E}(\mathbf{x})$, its static Coulomb field is centered at $\mathbf{x}$, and when the particle accelerates, the electric dipole radiation it

produces is governed by $d^2\mathbf{x}/dt^2$. In light of these facts, we say that $\mathbf{x}$ is the particle's "center of charge" $\mathbf{x}_q$. However, after a unitary transformation to H', Eq. 5.150 implies that the center of charge becomes

$$\mathbf{x}'_q = \mathbf{x} + (d/q)\,\boldsymbol{\sigma} + \mathcal{O}(d^2)\ , \tag{5.159}$$

which is shifted from $\mathbf{x}$ precisely as anticipated in the previous paragraph. By construction, the center of charge evolves the same way in both pictures, so that any effect of the apparent EDM can be equivalently explained without it.

For example, suppose a free electron is placed in a uniform magnetic field $\mathbf{B}_0$, so that the spin precesses at the Larmor frequency $\omega_L = qB_0/m$. If the particle is at rest under the unprimed Hamiltonian, $d\mathbf{x}/dt = 0$, then $d\mathbf{x}_q/dt = 0$, which implies that no electric dipole radiation is produced. When we consider the same situation under the primed Hamiltonian, the particle has a precessing EDM, but simultaneously orbits in a circle of radius d/q in the opposite direction at the cyclotron frequency $\omega_c = qB_0/m$. These two effects compensate each other, so that $d\mathbf{x}'_q/dt = 0$ and, again, no electric dipole radiation is produced. Conversely, if the particle were at rest under the primed Hamiltonian, electric dipole radiation would be produced, but it would be equivalently described under the unprimed Hamiltonian as a consequence of the particle's circular motion.

EDM-Induced Spin Precession

Similarly, it naively seems possible to unambiguously identify the EDM through its effect on spin precession, but this is also impossible. To illustrate this point we will consider two more thought experiments.

First, Ref. [426] proposed an approach which is analogous to certain searches for the neutron EDM. Its authors claimed that if an electron was placed in a uniform electric field, the EDM would cause its spin to precess, resulting in an observable transverse magnetic field from its magnetic dipole moment. This led Ref. [47] to project very strong experimental sensitivity for atomic magnetometers, shown in Fig. 5.2. However, this idea has a fundamental problem. If the electron was free, it would immediately accelerate out of the experimental apparatus. If it was instead bound in a nonrelativistic atom, it would experience zero average electric field and hence undergo no spin precession [543].

Therefore, the experiment proposed in Ref. [426] cannot work as stated. For a free electron, we could instead allow the electron to fly away, but subsequently measure its spin dynamically. Concretely, suppose a free electron is prepared at rest with vertical spin, and then experiences a uniform horizontal electric field. After passing through this field it encounters a Stern–Gerlach apparatus, i.e., a vertical but nonuniform magnetic field, where the field gradient deflects the electron according to its spin. This appears, in principle, to be a way to measure the EDM-induced spin precession without requiring it to be bound.

The problem with this idea is that the unprimed Hamiltonian, with no EDM, yields the same deflection. In this picture, the electron's location is shifted by $(d/q)\,\boldsymbol{\sigma}$, so it flies through the

Stern–Gerlach apparatus off center, yielding an additional $q\mathbf{v} \times \mathbf{B}$ Lorentz force. It is straightforward to show that the center of charge behaves the same way to $\mathcal{O}(d)$ in both pictures. Once again, the apparent EDM effect can be equivalently explained without an EDM.

5.11.5 True EDMs and Spurious EDMs

There are many experiments, reviewed in Refs. [544, 545], which are sensitive to constant electron EDMs. Unfortunately, the shift symmetry of the axion implies that a constant axion field cannot produce a signal in any of them. Here, we explain how a number of these experiments work and elaborate on why they cannot measure an axion signal.

Scattering and Spin Precession of Free Electrons

A true electron EDM affects the relativistic scattering of electrons on nuclei [546, 547, 548]. True EDMs can also cause spin precession when a particle moves at relativistic speeds through a *magnetic* field; this was used in the first searches for the electron and muon EDM [549, 550, 551, 552] and today is relevant in storage ring experiments. Crucially, both of these signatures do not follow from the nonrelativistic EDM term, but rather come from relativistic corrections present in the true EDM's full Hamiltonian density, $\mathcal{H}_{\text{EDM}} = (d/2)\,\overline{\Psi}\gamma^5\sigma^{\mu\nu}\Psi\,F_{\mu\nu}$.

Since the axion contributes a nonrelativistic EDM term of $\mathcal{O}(ga/m)$, such corrections would first appear in the Hamiltonian at $\mathcal{O}(ga/m^2)$. However, Ref. [428] computed the Hamiltonian out to this order and showed that the $\mathcal{O}(ga/m^2)$ terms actually exactly vanish for a constant uniform axion field.[7] In other words, while a true EDM and a constant axion field modify the Hamiltonian in the same way at leading order in the nonrelativistic expansion, the axion does not induce the relativistic corrections that make true EDMs observable for free particles.

Energy Levels of Bound Electrons

The most sensitive modern electron EDM experiments measure shifts of atomic or molecular energy levels. As we have discussed in Appendix 5.11.4, Schiff's theorem states that $\mathcal{O}(d)$ shifts of atomic energy levels vanish in the nonrelativistic limit. Therefore, to find a nonzero effect one must either work to $\mathcal{O}(d^2)$ [553, 554] or account for relativistic effects such as length contraction, in whose presence there are $\mathcal{O}(dv^2)$ energy level shifts [555, 556, 557].

Recalling that our expansion in $1/m$ is equivalent to an expansion in v, these facts naively suggest that a constant axion field shifts energy levels at $\mathcal{O}(g^2a^2/m^2)$ and at $\mathcal{O}(ga/m^3)$, respectively. The problem with this reasoning is, again, that a constant axion field does not enter the Hamiltonian in the same way as a true EDM. The two have the same nonrelativistic limit, but differ in their relativistic and higher-order corrections. In order to compute these purported axion-induced energy level shifts

[7] Note that Ref. [428] uses a different convention for the coupling; in their variables the nonrelativistic EDM term is $\mathcal{O}(1/m^2)$ and the leading relativistic corrections to it are $\mathcal{O}(1/m^3)$.

consistently, one must expand the Hamiltonian to $\mathcal{O}(g^2a^2/m^2)$ and $\mathcal{O}(ga/m^3)$, respectively. This produces additional terms which completely cancel off any energy level shift. Although such a lengthy computation has not been explicitly demonstrated in the literature, such a cancellation *must* occur to all orders due to the underlying shift symmetry of the axion. These "mysterious" cancellations are the hallmark of a non-manifest symmetry and are one of the reasons it is often easier to work with manifest symmetries.

Recasting EDM Experiments

In an EDM experiment of measurement time τ, Ref. [427] asserted that the axion-induced nonrelativistic EDM term acts like a constant true EDM when $m_a\tau \ll 1$, thereby claiming a bound on the axion-electron coupling many orders of magnitude stronger than existing bounds. However, this is incorrect; as we have just discussed, the signal from a true EDM arises from relativistic corrections which are not shared by the spurious axion EDM.

On the other hand, when the axion field has nontrivial time dependence, a term proportional to $a(t)\,\boldsymbol{\sigma}\cdot\mathbf{E}$ can produce observable effects, such as shifts in electronic energy levels. However, such shifts are generally suppressed by powers of m_a/Ry, where $\mathrm{Ry} = \alpha^2 m_e/2$ is the scale of electronic energy levels. For example, Ref. [493] showed that the energy level shift for bound electrons, linear in the external electric field, is suppressed by $(m_a/\mathrm{Ry})^2$.

Recently, Refs. [428, 429] noted that for *free* electrons, axion-induced effects are suppressed by powers of $m_a\tau$. For example, Ref. [429] computed the time evolution operator for a free particle, from $t = 0$ to $t = \tau$, and noted that it depended on the quantity

$$\frac{1}{\tau}\int_0^\tau dt\; d_{\mathrm{eff}}(t) \equiv \frac{1}{\tau}\int_0^\tau dt\; (d(t) - d(\tau))\;, \tag{5.160}$$

where d_{eff} is an "effective" EDM. The left-hand side has a simple physical interpretation given by Eq. 5.159; for a free particle at rest in the primed picture, it is simply q times the difference of the center of charge's final location and its average location. Eq. 5.160 is indeed suppressed for $m_a\tau \ll 1$, and unsuppressed for $m_a\tau \gtrsim 1$. However, Refs. [428, 429] assumed without justification that the signal in a *bound* electron EDM experiment is not suppressed when $m_a\tau \gtrsim 1$, even though it is governed by completely different observables. Thus, for $m_a\tau \sim 1$ these works overestimate the signal strength for bound electrons by powers of $\mathrm{Ry}\cdot\tau \gg 1$.

Color Charged Fermions

Throughout this chapter, we have exclusively considered the case where Ψ is a color neutral fermion. The story is somewhat different when Ψ is a quark field, since the chiral field redefinition leading to the nonderivative coupling $\mathcal{L}_n$ also produces a term proportional to $a\,G_{\mu\nu}\tilde{G}^{\mu\nu}$. Both

this term and $\mathcal{L}_n$ can produce true hadronic EDMs for a constant axion field a. If one starts with only a derivative coupling, then their contributions will cancel, in accordance with the fact that the derivative coupling $\mathcal{L}_d$ itself vanishes for constant a. But in a generic QCD axion model, there will be true hadronic EDMs induced, which can be probed by both existing EDM experiments and in dedicated experiments which resonantly amplify the effect at nonzero m_a [381]. For a recent review of such efforts, see Ref. [558].

Chapter 6

Stellar Shocks From Dark Asteroids

This chapter is based on *Stellar Shocks From Dark Matter Asteroid Impacts*, by A. Das, S. A. R. Ellis, P. Schuster, K. Zhou, Phys. Rev. Lett. 128, 021101 (2022).

Abstract

Macroscopic dark matter is almost unconstrained over a wide "asteroid-like" mass range, where it could scatter on baryonic matter with geometric cross section. We show that when such an object travels through a star, it produces shock waves which reach the stellar surface, leading to a distinctive transient optical, UV and X-ray emission. This signature can be searched for on a variety of stellar types and locations. In a dense globular cluster, such events occur far more often than flare backgrounds, and an existing UV telescope could probe orders of magnitude in dark matter mass in one week of dedicated observation.

6.1 Introduction

Astronomical and cosmological observations have provided all evidence for dark matter (DM) thus far. Stars, substellar objects, and stellar remnants therefore comprise natural venues for probing the nature of DM. The capture of particle DM is well-studied, and can result in signatures ranging from heating [559, 560, 561, 562] and modifications of stellar structure [563, 564], to outright destruction by the formation of a black hole [565, 566, 567]. DM candidates light enough to be produced thermally in stars, such as the axion, can also be constrained by stellar cooling rates [568].

However, DM could also be in the form of objects of macroscopic mass and size, a possibility which is consistent with all cosmological constraints [569, 570, 571]. While macroscopic DM arises in many theoretical scenarios, it is difficult to detect terrestrially primarily because such objects are rare, given the low local DM density. As $M_{\rm DM}$ increases, experimental searches require either large detection volumes or long integration times. For example, for $M_{\rm DM} \lesssim 10^5\,{\rm kg}$, limits on macroscopic DM passing near the Earth can be set with tabletop experiments, calorimeters, and gravitational wave detectors [572, 573], or searches for fast-moving meteors [574, 575, 576] and seismic waves [577, 578]. However, for $M_{\rm DM} \gtrsim 10^{-20} M_\odot$, corresponding to a heavy asteroid, macroscopic DM would not have collided with Earth since the advent of human civilization, and setting constraints requires speculative appeals to geologic history [579, 580]. Unambiguously probing the mass range $10^{-20} M_\odot \lesssim M_{\rm DM} \lesssim 10^{-11} M_\odot$ of "dark asteroids" will therefore require looking to the stars.

In this chapter, we point out that because dark asteroids move supersonically in stars, dissipation through any non-gravitational interaction will generate shock waves. This allows the dissipated energy to quickly propagate to the stellar surface, where it is released in the form of a transient, thermal ultraviolet (UV) emission. Crucially, such events are correlated with the local DM density, but uncorrelated with the underlying activity of the star. Next-generation survey telescopes would detect such events without requiring a dedicated search, while existing telescopes could find them by monitoring regions of high DM density. This would constitute a DM direct detection experiment on astronomical scales, with the stars as the detector volume.

A detailed overview of models that produce dark asteroids is beyond the scope of this chapter, but the reader can keep several scenarios in mind. Self-interactions in the dark sector allow models as simple as asymmetric DM [581] to build up composite objects of high multiplicity in the early universe [582, 583], and support compact structures [584, 585, 586]. Additionally introducing a lighter, oppositely-charged particle allows dark atoms to form, providing an alternative cooling mechanism which can generate large DM structures [587], while charging the DM under a non-Abelian gauge group naturally allows dark nucleosynthesis [588, 589]. An even richer dark sector, which could result from mirroring part or all of the Standard Model, allows the formation of mirror stars [590, 591, 592, 593]. Phase transitions in the dark sector can also produce large dark objects, for both bosonic and fermionic DM [594, 595, 596, 597], with the density determined by the temperature of the phase transition.

For concreteness, we will introduce our signature by assuming that all DM is in the form of spherical dark asteroids with the same mass $M_{\rm DM}$ and radius $R_{\rm DM}$. We further assume that they scatter baryons elastically with geometric cross section $\sigma = \pi R_{\rm DM}^2$, enter the star head-on, and do not disintegrate while passing through the star. In the final section, we discuss how these properties can arise and how the signature changes when they are relaxed.

6.2 Stellar Collisions

We compute stellar profiles with MESA [598, 599, 600, 601, 602], assuming solar metallicity and the settings recommended by MIST [603], and match them at the photosphere to atmospheric profiles computed with PHOENIX [604]. When a dark asteroid enters a star of mass $M_\star$ and radius $R_\star$, it will be traveling at roughly the escape velocity $v_{\rm esc} = \sqrt{2GM_\star/R_\star}$, and is therefore hypersonic, with Mach number Ma ~ 100. It is accelerated inward by gravity, and dissipates energy due to a drag force $\rho\sigma v^2 c_d/2$, where $c_d \simeq 1$ for a supersonic sphere [605]. For most of the parameters we consider, the dark asteroid remains hypersonic until it either dissipates most of its energy to drag, or reaches the hot stellar core.

Describing the resulting production and propagation of shock waves is a complex hydrodynamic problem. However, it can be decomposed into simpler problems each solvable by controlled approximations, as shown in more detail in the Supplemental Material. First, because the dark asteroid is hypersonic, Ma $\gg 1$, its passage can be treated as an instantaneous deposition of energy $F_{\rm dr}$ per unit length, which creates a cylindrical blast wave. Numeric blast wave solutions are known, and are used to model meteors traversing the Earth's atmosphere [606, 607]. The shock wave becomes weak after it travels a characteristic radial distance $R_0 = \sqrt{2F_{\rm dr}/p} \sim {\rm Ma}\, R_{\rm DM}$, and asymptotically approaches an N-wave profile, a weak shock solution characterized by a pressure discontinuity Δp and length L. Following Ref. [606], we match a blast wave onto an N-wave profile at distance $10R_0$, where the shock strength is $\Delta p/p = 0.06$, the length is $L = 2.8R_0$, and roughly half of the original energy remains in the shock wave.

To treat the propagation to the stellar surface, we use standard results from weak shock theory [608, 609]. In particular, the propagation of a weak shock wave through a slowly varying medium can be described by geometric acoustics. Because the speed of sound decreases with distance from the center of the star, the ray paths refract radially outward. We propagate each piece of the shock front along such a ray. For an acoustic wave, if the wavefront area evolves as $A(s)$ along a ray, then the pressure amplitude varies as $\Delta p \propto \sqrt{\rho c_s/A(s)}$, while the period L/c_s remains constant. The discontinuities of an N-wave cause additional dissipation: when the shock wave travels a length L, there is a fractional increase in L, and a fractional decrease in shock strength and total energy, of order $\Delta p/p$.

Finally, as each piece of the shock front approaches the stellar surface, the decreasing density and pressure cause a rapid increase in the shock strength. For the DM masses and radii of interest here,

the shock becomes strong, $\Delta p/p \gtrsim 1$, below the photosphere, at optical depths up to $\sim 10^2$. Analytic solutions exist to describe the arrival of a strong shock wave at the edge of a star [610]. To roughly approximate these results, we assume that once the shock wave becomes strong, its remaining energy heats the stellar material above it to a uniform temperature T_f, which sets the typical frequency band of emission. This is reasonable because convection in the shocked region near the stellar surface will effectively smooth out temperature gradients. The timescale for energy release is then dictated by the rate of blackbody radiation from the surface, and is typically on the order of hundreds of seconds.

This treatment is compatible with previous work on shock waves in stars. In massive stars just prior to core collapse, convection can excite acoustic waves [611] which then steepen into weak shocks, which dissipate in the same way as they travel outward [612, 613]. Refs. [614, 615] considered the strengthening of a shock wave near the surface of a star; consistent with this chapter, we find that our shocks are insufficiently energetic to eject mass, as they emerge with a typical speed $\sqrt{k_B T_f/m_p} \ll v_{\rm esc}$.

In Fig. 6.1, we show the total shock energy released from the surface of a Sun-like star, and the typical final temperature T_f. The qualitative features of this plot can be readily understood. For higher $R_{\rm DM}$, the dark asteroid stops near the stellar surface, and a small portion of the surface is heated to a high temperature. As $R_{\rm DM}$ decreases, the shock waves are primarily produced deeper in the star, with a shorter wavelength. This increases the dissipation they experience as they propagate out to the surface, decreasing the energy released. At the smallest radii, drag is insufficient to prevent the dark asteroid from passing through the entire star, so that only part of its energy is deposited, leading to a rapid fall-off in signal energy.

Since a strong shock has $\Delta T/T \sim 1$, the temperature T_f roughly tracks the local temperature at the depth where the weak shock becomes strong again; as a result, it is relatively insensitive to $M_{\rm DM}$ and $R_{\rm DM}$, and typically peaks in the far UV. At lower densities, T_f rapidly rises because the dark asteroid stops so close to the surface that the shock never becomes weak. At the very lowest densities shown, the dark asteroid stops above the photosphere. In this extreme case, the emission spectrum is not necessarily thermal, and depends on the detailed physics of the resulting plasma. We do not study this regime because it is in tension with cosmological constraints, but we expect photons to be released at up to X-ray energies, $\epsilon \sim m_p v_{\rm esc}^2 \sim 10^4\,{\rm eV}$.

Similar results apply to other star types, and are shown in the Supplemental Material. The main difference is that for equal $M_{\rm DM}$ and $R_{\rm DM}$, the signal energy is higher for more compact objects, such as red and brown dwarfs, because their density profiles rise more steeply with depth, causing the dark asteroid's energy to be deposited closer to the surface. Conversely, the signal energy is significantly lower for giant stars, because of their extended envelopes.

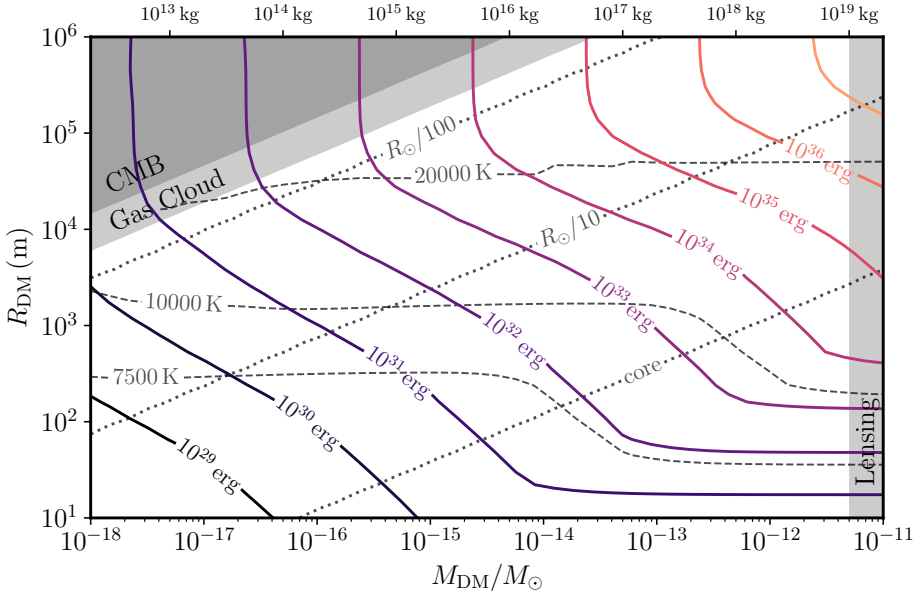

Figure 6.1: Contours of energy release (solid), characteristic temperature (dashed), and penetration depth (dotted) for a dark asteroid impact on a Sun-like star. We show bounds from the CMB limit on DM-baryon scattering [59], heating of cold gas clouds [60] (though see also Ref. [61]), and microlensing [62] (though see also Refs. [63, 64, 65]). We do not show constraints from femtolensing of gamma-ray bursts [66], which are weakened by finite source size effects [67].

6.3 Observational Prospects

Dark asteroids are expected to produce rare transients on all types of stars, with a frequency dependent on the stellar and local DM parameters. For a star moving with a DM halo, averaging over a Maxwellian velocity distribution for the DM yields a collision rate [616]

$$\Gamma = \sqrt{\frac{8}{3\pi}} \frac{\rho_{\rm DM} v_d}{M_{\rm DM}} \pi R_\star^2 \left(1 + \frac{3v_{\rm esc}^2}{2v_d^2}\right) \tag{6.1}$$

where v_d is the velocity dispersion. The final term accounts for the focusing effect of gravitational attraction. In all cases we will consider, $v_{\rm esc} \gg v_d$, giving

$$\Gamma \simeq (4 \times 10^{-5}\,{\rm yr}^{-1}) \frac{M_\star}{M_\odot} \frac{R_\star}{R_\odot} \frac{10^{-15} M_\odot}{M_{\rm DM}} \frac{\rho_{\rm DM}}{0.4\,{\rm GeV/cm}^3} \frac{270\,{\rm km/s}}{v_d}. \tag{6.2}$$

As shown in the inset of figure 6.2, we expect a brief X-ray emission as the dark asteroid passes through the stellar atmosphere, followed by a gradual optical and UV emission as the shock wave produced inside reaches the surface of the star. Since most of the energy emerges in the UV, and cooler stars emit relatively little in this band, it is easiest to search for these events as UV transients.

The light curve would also have a long tail as the violently heated patch of the stellar surface gradually cools, which could be targeted for follow-up optical observation. Note that we have treated all collisions as head-on, though the high degree of gravitational focusing implies that most collisions are glancing. Our calculation is thus maximally conservative, because it gives the shock waves the longest possible path to the surface. Accounting for the impact parameters would increase the signal strength and temperature, and could also increase visibility to X-ray telescopes.

Upcoming transient surveys could detect dark asteroid collisions on nearby stars without requiring a dedicated search. Among star types, K dwarfs are promising targets, as they have significantly larger masses and radii than M dwarfs, but also have a higher number density and negligible UV emission compared to hotter stars. As a concrete example, we consider ULTRASAT [617], a proposed wide-field UV transient explorer designed to detect distant supernova shock breakouts, which will also monitor many nearby stars. We compute the maximum distance from which ULTRASAT could observe dark asteroid collisions at SNR ≥ 5, conservatively counting only impacts on K dwarfs, and approximate the star density as uniform out to 1 kpc from the Earth. The observable region of parameter space is cut off at high $R_{\rm DM}$ because the signal temperature becomes too high, at low $R_{\rm DM}$ and $M_{\rm DM}$ because the signal energy becomes too low, and at high $M_{\rm DM}$ because the events become too rare.

A similar region could be probed by the upcoming LSST survey [618], but estimating the event rate is more difficult because of LSST's complex observing strategy and multiple filters. In addition, since LSST would be able to see events at a significantly larger distance $d \gtrsim$ kpc, a more detailed model of the galactic stellar and DM densities would be required, along with estimates of UV extinction. Exoplanet searches such as TESS [619] and the planned PLATO mission [620] have exceptionally large fields of view, but observe in the red, which reduces the sensitivity because of stellar variability and shot noise. However, these instruments could effectively detect transients on cool red dwarfs or brown dwarfs, which thereby probes lower $R_{\rm DM}$, as shown in the Supplemental Material.

Because the local DM density is low, a potential obstacle for any local search is the background from stellar superflares, which occupy a similar temperature and energy range. Observations from Kepler [621, 622] and TESS [623] find no superflares on the vast majority of FGK dwarfs, and almost none on those that are not rotating rapidly, which allows highly active stars to be excluded from observation. However, for any individual event, it would be difficult to rule out the possibility of a superflare without further information. For example, follow-up observations could determine the detailed light curve, which could fall off more slowly for dark asteroid impacts because the energy emerges from within the star rather than from its atmosphere. Simultaneous observation with other instruments could rule out flares using spectral information, as they are expected to have a significant radio and X-ray component.

An alternative strategy is to perform a focused search in a region where the impact rate per star

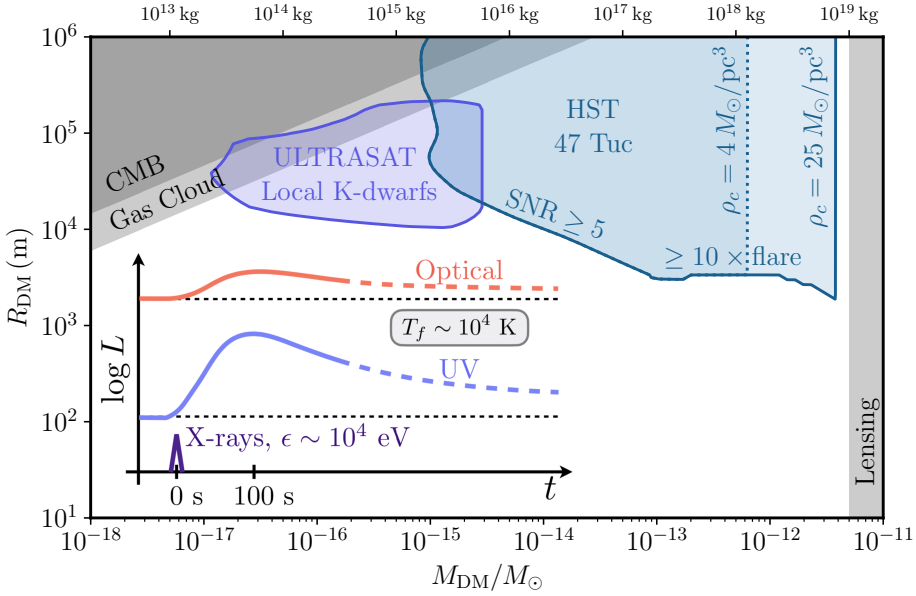

Figure 6.2: Contour plot showing observability. We shade regions where impacts on K dwarfs within 1 kpc would be seen by ULTRASAT, and impacts on Sun-like stars in 47 Tuc would be seen by HST, at least once per year and week of observation on average, respectively. In both cases, we demand SNR ≥ 5. For 47 Tuc, we show two possible values of the core DM density, as discussed in the main text, and require the rate of dark asteroid impacts to exceed superflares of similar energy by at least an order of magnitude. A schematic light curve for three frequency bands is shown in the inset.

is significantly higher. As a concrete example, we consider 47 Tuc (NGC 104), a well-studied nearby ($d \sim 4\,\mathrm{kpc}$) globular cluster which has a dense core and negligible UV dust extinction [624].

While the DM content of globular clusters today is not known [625, 626], they are thought to have formed in large DM subhalos [627, 628], with computational studies suggesting an initial DM mass of about 260 times the stellar mass [629]. Tidal stripping and DM thermalization are expected to have reduced the DM content of the globular cluster since formation [630], with $\sim$1% remaining today [631]. We assume this formation history holds for 47 Tuc, and model the DM distribution with an NFW profile [632]. Gravitational interactions transfer kinetic energy to the dark asteroids and lighter stars, which we account for by coring the DM profile [633] and taking a relatively heavy benchmark star of solar mass.

From the above procedure, detailed in the Supplemental Material, we infer a core DM density $\rho_{\rm DM} \simeq 4\,M_\odot/\mathrm{pc}^3$. Since the velocity dispersion is $v_d \simeq 12\,\mathrm{km/s}$, the collision rate per star is almost 4 orders of magnitude higher than in the local region, even though DM is still a vastly subdominant component of the core. For most of the parameters we consider, the event rate exceeds the rate of superflares of comparable energy on Sun-like stars [622] by orders of magnitude. Yet our estimate is conservative, as a recent analysis with similar assumptions [559] found a core DM density

$\rho_{\rm DM} \simeq 25\,M_\odot/{\rm pc}^3$ [634]. Furthermore, we neglect adiabatic contraction of the DM halo [635, 636], which would significantly increase the core density, and we do not consider the possibility of a DM cusp due to an intermediate-mass black hole [637, 638], within which the DM density would be enhanced by orders of magnitude.

To monitor 47 Tuc, we consider the Wide Field Camera 3 instrument on the Hubble Space Telescope (HST), using the F225W filter. This instrument's field of view is sufficient to capture most of the DM core, and the UV filter alleviates stellar crowding [639]. In Fig. 6.2, we show the region where at least one event with SNR ≥ 5 is expected in one week of continuous observation. HST has in fact already monitored 47 Tuc for over a week to search for exoplanets [640], though these optical and infrared observations are less useful for our purposes due to stellar backgrounds. Since the event rate scales as $1/M_{\rm DM}$, new parameter space could be probed with as little as one hour of dedicated UV observation.

6.4 Discussion

For concreteness, we have focused on specific assumptions and experimental searches, but our results also apply more generally. For instance, we have taken elastic scattering as a generic benchmark, but specific models can give rise to nonelastic interactions, such as catalyzing proton decay, annihilating with ordinary matter, or absorbing part of the dissipated energy. We have also assumed a geometric cross section for baryon scattering because it is the result of any sufficiently strong interaction that is not long-ranged, but the dark asteroid can be partly transparent to baryons, or interact by a long-range force, yielding a smaller or larger cross section respectively. These effects can be accounted for by simply scaling the energy deposited per length, $F_{\rm dr}$, as long as $R_0 \gtrsim R_{\rm DM}$.

The assumption of geometric cross section implies relatively strong DM interactions with the SM, and it is interesting to see how this can be compatible with existing constraints. As shown in Fig. 6.1, cosmological constraints are relatively weak, essentially because dark asteroids would be extremely rare, and the constraint from DM self-interaction in the Bullet cluster is orders of magnitude weaker. Strong DM constituent interactions with the SM could be accommodated if, for example, the dark asteroid was composed of "dark atoms" comprised of oppositely charged particles bound by a dark $U(1)$. If the constituent has $m_{\rm DM} \lesssim 100$ MeV, and less than 1% is unbound, terrestrial constraints require that the DM-nucleon cross section not exceed $\sigma_{\rm SI} \lesssim 10^{-29}$ cm^2 [641, 642]. A dark asteroid of density g/cm^3 containing 100 MeV constituents with this SM interaction strength would have a mean free path of $\sim$100 m, so that the assumption of opacity holds for the regions of interest of Fig. 6.2.

Our rough estimates of the collision rate and signal energy could be refined in many ways. We have taken all dark asteroids to have the same mass $M_{\rm DM}$, though a realistic production mechanism would lead to a range of masses. This would not necessarily harm prospects for a local search, as

impacts of heavier dark asteroids could be seen from further away. Dark asteroids could pass through a star but lose sufficient energy to be captured, ensuring subsequent collisions. This enhancement of the event rate occurs for a wide range of $M_{\rm DM}$ because most collisions are glancing, and leads to the intriguing possibility of followup detection. Finally, our treatment of the shock propagation and convective energy transport near the surface could be improved with detailed analytic arguments or numerics, which would also yield the detailed shape of the light curve.

Collision events have been investigated in related contexts, though the results are qualitatively different. Primordial black holes passing through stars deposit a small amount of energy through dynamical friction, but the result is too weak to observe [643, 644]. Dark asteroids could also trigger supernova in white dwarfs by depositing energy in their interiors [645, 646]. The survival of white dwarfs therefore implies a strong constraint on macroscopic DM due to the long effective integration time, but it only applies to dark asteroids of roughly nuclear density, which can penetrate the white dwarf's crust.

Within the Standard Model, the closest analogue to a dark asteroid impact would be a comet impact [647]. However, comets are expected to be rare outside of planetary systems, with the interstellar comet density bounded orders of magnitude below the DM density [648]. Comets are also "rubble piles" which fall apart before even reaching the stellar surface, leading to a qualitatively different signature. By contrast, in simple dark sector models the binding energy of a dark asteroid may easily exceed its kinetic energy, which is only about $(v_d/c)^2 \sim 10^{-6}$ of its total mass energy, implying that ablation is a small effect.

Many additional directions could be explored in future work. For instance, the high DM density at the galactic center would make it ideal for a focused search, though one would have to model its distinct stellar populations and use a sightline with low extinction. Globular clusters besides 47 Tuc could be promising, especially if new nearby clusters are found, or confirmed to contain an intermediate-mass black hole. Milky Way satellite galaxies are more distant but are known to host a high DM density, and could likely be used to probe higher $M_{\rm DM}$. At the opposite end of the mass range, impacts on the Sun are expected to occur annually for $M_{\rm DM} \lesssim 10^{-19} M_\odot$, and would be energetic enough to be easily detected by solar observatories. It would be interesting to see if the resolution of these instruments permits such impacts to be distinguished from solar flares. In many of these cases, it may be possible to find impact events in a reanalysis of archival data.

The possibility of detecting dark asteroid impacts in nearby stars provides an interesting target for UV transient searches with small satellites [649, 650, 651], while more powerful instruments would be well-suited for focused searches. These observations are enabled by the rapid advance of time-domain astronomy, which we have shown provides an unusual route to discovering the nature of dark matter.

6.5 Appendix: Supplemental Calculations

6.5.1 Details of Shock Calculation

In this section, we give further details on the shock wave calculation described in the main body, which is depicted in Fig. 6.3. The initial cylindrical blast wave has been calculated numerically [652], and following Ref. [606], its shock strength can be fit as

$$\frac{\Delta p}{p} \simeq \frac{2\gamma}{\gamma+1}\frac{0.4503}{(1+4.803x^3)^{3/8}-1} \tag{6.3}$$

where $x = r/R_0$, and we set $\gamma = 5/3$. For $x = 10$, the shock wave profile closely approximates an N-wave. The paths of the shock rays for the N-wave are calculated by applying the principle of least time to the sound speed profile $c(r)$ computed by MESA.

To propagate the N-wave, we use the formulation of Ref. [609], which states that the pressure profile can be written as

$$\Delta p(\ell, t) = B(\ell)\, g(\psi) \tag{6.4}$$

where ℓ is the arc length along a shock ray. Here, the scaling $B(\ell) \propto \sqrt{\rho c/A(\ell)}$ accounts for energy conservation as the local density, sound speed, and shock front area $A(\ell)$ change, and $B(0) = 1$. The pressure profile is a function of

$$\psi = t - \tau(\ell) + g(\psi)\mathcal{A}(\ell) \tag{6.5}$$

where τ is the travel time, $d\tau = d\ell/c$. In the absence of nonlinear effects, $\psi = t - \tau$, indicating that the wave maintains its temporal profile. The shock age $\mathcal{A}$ accounts for the nonlinearity of the wave, with $d\mathcal{A} = (\beta B/\rho c^3)\, d\ell$ and $\beta = (\gamma+1)/2$. The pressure profile for an N-wave with initial pressure amplitude Δp_0 is

$$g(t) = \begin{cases} -\Delta p_0\, t/T_0 & -T_0 \le t \le T_0 \\ 0 & \text{otherwise} \end{cases} \tag{6.6}$$

where $L_0 = 2cT_0$. Plugging this into the previous results, the pressure amplitude Δp, length L, and total shock wave energy E evolve as $\Delta p = \epsilon B\, \Delta p_0$, $L = L_0/\epsilon$, and $E = \epsilon E_0$, where

$$\epsilon(\ell) = \frac{1}{\sqrt{1 + (\Delta p_0/T_0)\mathcal{A}(\ell)}}. \tag{6.7}$$

Dissipation by photon diffusion is also present, but it is subdominant for all of the parameter space probed in Fig. 2 of the main body.

To calculate the total energy release, we discretize the dark asteroid's trajectory. For each segment, we match to an N-wave, which determines Δp_0 and T_0. This determines the initial N-wave energy

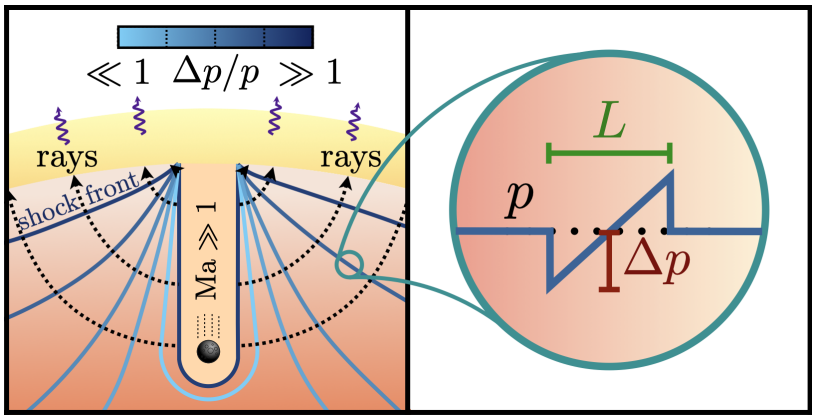

Figure 6.3: Depiction of the phases of shock propagation (left). A cylindrical blast wave solution is matched to an N-wave (right) when the shock become weak. The N-wave is propagated along acoustic rays, and becomes strong and deposits its energy near the surface.

for the segment,

$$E_0 \simeq \frac{2}{3}\frac{(\Delta p_0)^2}{\rho c^2}(AT_0 c) \tag{6.8}$$

which is approximately half the energy dissipated by the dark asteroid in that segment. We then integrate $\epsilon(\ell)$ along each shock ray until the shock becomes strong again. To calculate the final temperature of each piece of the surface, we take the remaining energy ϵE_0 of the shock wave and assume it uniformly heats the patch of the surface above it, calculating the heat capacity using the MESA profile. The typical final temperature T_f is defined by an energy-weighted median.

Two main features of this formalism determine the qualitative behavior of Fig. 1 of the main body. First, the fractional energy dissipation when the shock wave travels a length L is $(\Delta p/p)(\beta/\gamma)$, as can be shown by expanding Eq. (6.7). (This is equivalent to Eq. (15) of Ref. [613] up to a factor of 2, which arises because Ref. [613] considers a train of N-waves, while we consider only a single N-wave.) Therefore, there is a significant loss of energy when the shock originates from deep inside the star, cutting off sensitivity to low $R_{\rm DM}$. Second, the typical initial length L_0 is not $R_{\rm DM}$, as might naively be expected, but the much larger $R_0 \sim \mathrm{Ma}\, R_{\rm DM}$. This allows a significant fraction of the energy to escape, even though we consider $R_{\rm DM}$ much smaller than stellar scales.

For very low $R_{\rm DM}$, shock dissipation is very effective, so the shock remains weak all the way to the photosphere, and continues traveling outward through the stellar atmosphere. The total energy release is highly suppressed, as indicated at the bottom of Fig. 1 of the main body, but T_f can be much higher due to the high temperatures of the chromosphere and corona. The detection prospects would thus be quite different from the UV signals primarily considered in this chapter.

For the opposite limit of large $R_{\rm DM}$ and low dark asteroid densities, the dark asteroid stops very close to the surface, and the stellar profile changes significantly on the scale R_0, rendering the

cylindrical blast wave solution inapplicable for large x. In these cases, we match at $x = 2$ when possible (which we have checked yields almost identical results, in general, to matching at $x = 10$). However, when the shock starts so close to the surface that it never becomes weak, our calculation breaks down entirely, and we simply assume that all the energy escapes, leading to the vertical contours at the top of Fig. 1 of the main body. To very roughly estimate T_f in this case, we assume the volume along the shock rays is heated to a uniform temperature.

To illustrate these points, we show results for brown dwarfs and red giants in Fig. 6.4. In red giants, the shock waves lose the vast majority of their energy and remain weak all the way to the surface, where the emission is at temperature $T_f \sim T_\star$. This makes it difficult to observe dark asteroid impacts, even though the rate per star is high. For brown dwarfs, the energy released is high even for very low $R_{\rm DM}$, but the stellar density profile rises so rapidly that the caveat mentioned in the previous paragraph applies to a wide range $R_{\rm DM} \gtrsim 1\,{\rm km}$. To get a reliable estimate of T_f in this regime, it may be useful to compare to detailed hydrodynamic studies of comets [653] and rocky planets [654] impacting Jupiter.

6.5.2 Modeling of 47 Tuc

To find the collision rate between dark asteroids and stars in 47 Tuc, we must estimate the distribution of both species. For the stellar matter, we fit the surface density data reported by Ref. [655] to a 2D King model [656],

$$\Sigma(r) = k\left(\frac{1}{\sqrt{1+(r/r_{\rm c})^2}} - \frac{1}{\sqrt{1+(r_{\rm t}/r_{\rm c})^2}}\right)^2, \tag{6.9}$$

where the core radius $r_{\rm c}$ and tidal radius $r_{\rm t}$ are as reported in Ref [655]. Our best fit to the surface density in the GC core yields $k \simeq 6\times 10^4\ M_\odot/{\rm pc}^2$, and the resulting model agrees to within 30% everywhere within $r < 30$ pc, which is sufficiently accurate for our estimates. Assuming the GC is spherically symmetric, we use the Abel transform,

$$\rho_\star(r) = -\frac{1}{\pi}\int_r^\infty \frac{d\Sigma(y)}{dy}\frac{dy}{\sqrt{y^2-r^2}}, \tag{6.10}$$

to obtain the 3D stellar density profile shown in Fig. 6.5.

To model the DM density profile, we assume the globular cluster formed in a DM-rich halo with initial total DM mass $M_{\rm DM,tot} \simeq 260 M_{\star,\rm GC} = 2\times 10^8 M_\odot$, as inferred from Ref. [629]. We model this formation halo with an NFW profile [632],

$$\rho_{\rm NFW}(r) = \frac{\rho_0}{\left(\frac{r}{a}\right)\left(1+\frac{r}{a}\right)^2}, \tag{6.11}$$

where a is the scale radius. Here, the reference density is defined in terms of the concentration

parameter c as

$$\rho_0 = \frac{M_{\rm DM,tot}}{4\pi a^3}\left(\ln(1+c) - \frac{c}{1+c}\right)^{-1}. \tag{6.12}$$

We infer the values of a and c using the estimated age of 47 Tuc of 11.5 ± 0.4 Gyr [657, 658], corresponding to a formation redshift $z_f \simeq 3.0 \pm 0.5$ in a ΛCDM cosmological history. To do this, we set $M_{\rm DM,tot}$ to the halo's virial mass

$$M_{200} = (200\rho_c(z_f))\,\frac{4}{3}\pi r_{200}^3, \tag{6.13}$$

defined as the mass corresponding to an average halo density 200 times the critical density of the universe at formation, $\rho_c(z) = 3H(z)^2/8\pi G$. In a Λ-CDM universe, $H(z) = H_0\sqrt{\Omega_m(1+z)^3+\Omega_\Lambda}$, where $H_0 \simeq 67.4$ km/s/Mpc today and $\Omega_m = 1-\Omega_\Lambda \simeq 0.315$ [659], from which we obtain $r_{200} = 4600 \pm 600$ pc. The scale radius a is equal to r_{200}/c.

Finally, to compute c, we use the semi-analytic results of Ref. [660] (which are consistent with the more recent analyses in Refs. [661, 662] for our halo mass), which yield $c(z, M_{200}) = 5.8 \pm 0.7$. We therefore choose the parameters $c = 5.8$ and $a = 790\,$pc for the profile shown in Fig. 6.5. Note that the z_f dependence in c and r_{200} roughly cancels, imply little uncertainty in a. Therefore, our results are relatively insensitive to uncertainties in the age of 47 Tuc.

After the globular cluster's formation, the DM is heated through gravitational interactions with stars, which cores the DM profile. Given a typical DM energy $E \sim M_{\rm DM}v_{\rm rms}^2$, the rate of change of DM energy due to these interactions is [633]

$$\frac{dE}{dt} \simeq \frac{8(6\pi)^{1/2}G^2\rho_\star M_{\rm DM}\ln\Lambda}{\left(v_{\rm rms}^2 + v_{\star,\rm rms}^2\right)^{3/2}}(E_\star - E), \tag{6.14}$$

where $\ln\Lambda \sim \ln(0.4N_\star)$ is the Coulomb logarithm [663] and $N_\star$ is the number of stars in the core of the globular cluster, $v_{\star,\rm rms}$ is the rms speed of the stars, and E_* is the average stellar kinetic energy. Assuming $v_{\rm rms} \sim v_{\star,\rm rms}$ and noting that $E_\star \gg E$, the typical heating timescale is

$$t_{\rm heat} = \left|\frac{1}{E}\frac{dE}{dt}\right|^{-1} \sim \frac{0.0814 v_{\rm rms}^3}{G^2 M_\star \rho_\star \ln\Lambda}. \tag{6.15}$$

Setting $t_{\rm heat}$ to the estimated age of 47 Tuc, $M_\star$ to a solar mass $M_\odot$, and $v_{\rm rms}$ to the measured velocity dispersion $v_0 = 12.3$ km/s [655] yields $\rho_\star \simeq 86\,M_\odot/{\rm pc}^3$. We therefore assume the DM profile is cored when the stellar density exceeds this value, which corresponds to coring the NFW profile obtained above at $r_{\rm heat} \simeq 5.6$ pc.

As a check that our procedure yields sensible results, integrating the cored NFW profile out to the tidal radius of 47 Tuc gives a total DM mass of $1.9 \times 10^6 M_\odot$, which is roughly consistent with the results of the Jeans equation solution models of Ref. [626] for NGC 2419. It should be noted,

however, that 47 Tuc, owing to its greater proximity to the galactic center than NGC 2419, might have experienced greater stripping of its DM halo.

6.5.3 Event Rate and Telescope Sensitivity

We estimate the observable event rate for a search on nearby stars as

$$\Gamma_{\rm tot} \simeq \frac{1}{2}\left(\frac{4}{3}\pi d_{\rm max}^3\right)\frac{\Omega}{4\pi}\, n_\star \Gamma \tag{6.16}$$

where $d_{\rm max}$ is the maximum distance at which the events can be observed, $n_\star$ is the stellar density, and Ω is the angular field of view. The factor of $1/2$ is because impact events can only be seen from one side of the star. We consider K dwarfs with benchmark $M_\star = 0.7 M_\odot$ and $R_\star = 0.75 R_\odot$, and following Ref. [664], we estimate the local density of K dwarfs to be $n_\star = 0.0135\,{\rm pc}^{-3}$ on the basis of a local census.

The currently planned field of view of ULTRASAT [665] is $\Omega = 200\,{\rm deg}^2$. To find the maximum distance, we assume the signal energy is released isotropically, so that the observed flux at a distance d is

$$F \simeq \frac{E_{\rm sig}}{t_{\rm exp}}\frac{2}{4\pi d^2} \tag{6.17}$$

where the factor of 2 is again because events are only visible from the hemisphere of impact, and the timescale is $t_{\rm exp} = \max(t_{\rm typ}, 300\,{\rm s})$, to account for ULTRASAT's cadence. We then calculate the AB magnitude of the events in the ULTRASAT band 220–280 nm, assuming a blackbody spectrum of temperature T_f. For the events we consider, star noise is subdominant, and the limiting magnitude for detection at SNR ≥ 5 given a total exposure time 900 s is 22.3. We scale this sensitivity to a time $t_{\rm exp}$ and use it to determine $d_{\rm max}$, which we cap at 1 kpc.

For a search in 47 Tuc, the event rate is

$$\Gamma_{\rm tot} \simeq \int_0^{r_{\rm max}} dr\,(4\pi r^2) n_\star \Gamma. \tag{6.18}$$

Because of mass segregation, we take the stars in the core to be Sun-like, $M_* = M_\odot$ and $R_* = R_\odot$. Since the distance to 47 Tuc is $d = 4\,{\rm kpc}$, we integrate out to $r_{\rm max} = 2.5\,{\rm pc}$, accounting for the field of view of the WFC3 instrument of HST. We calculate the AB magnitude of the events in the same way as for ULTRASAT, using the F225W filter, which is most sensitive to wavelengths 210–260 nm. We infer a sensitivity threshold over a timescale $t_{\rm exp} = \max(t_{\rm typ}, 300\,{\rm s})$ using the measured sensitivity, at SNR = 5, to sources of magnitude 26.3 in an exposure time 5400 s [666].

Note that because the signal energy varies over orders of magnitude over the parameter space, the region probed is relatively insensitive to order one factors. For instance, taking a higher threshold, such as SNR ≥ 10, or removing the factors of 2 discussed above, would not qualitatively change Fig. 2 of the main body.

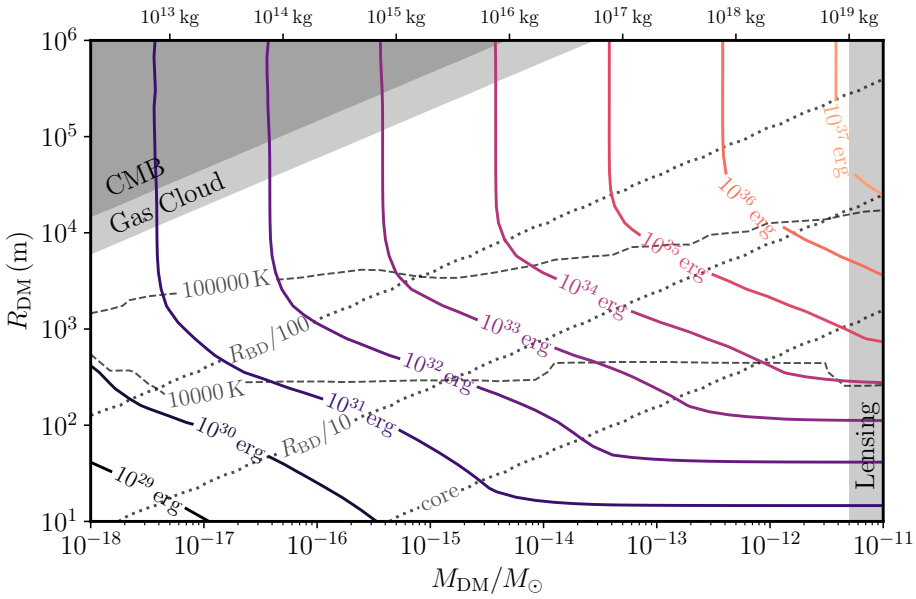

(a) Brown dwarf of mass $0.065 M_\odot$

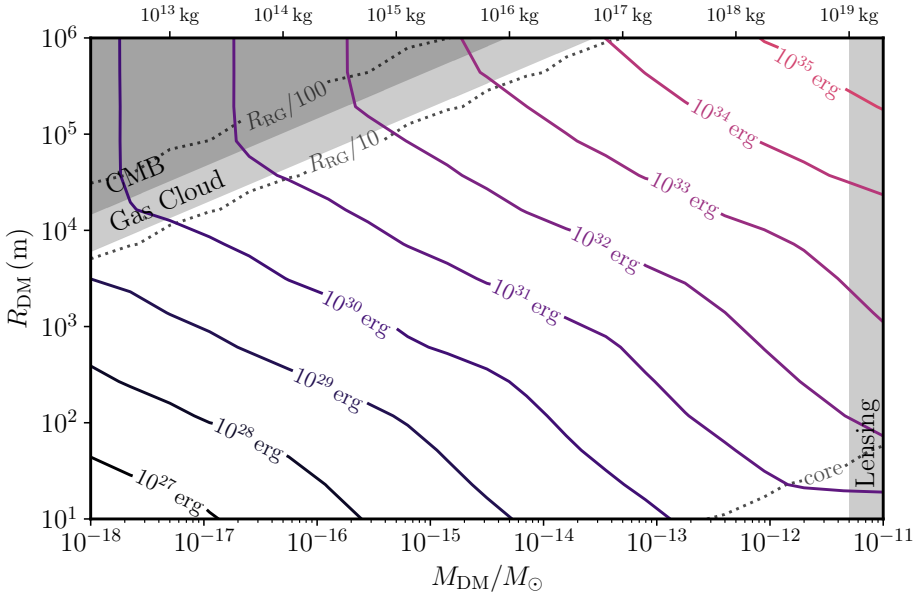

(b) Red giant of mass $M_\odot$

Figure 6.4: Analogues of Fig. 1 of the main body for other star types. The differences in signal energy at the lowest dark asteroid density are due to the differences in escape velocity at the surface. Shock dissipation is less severe for brown dwarfs, because dark asteroids are stopped more quickly. It is much more severe for red giants, because even low density dark asteroids can penetrate to a substantial depth.

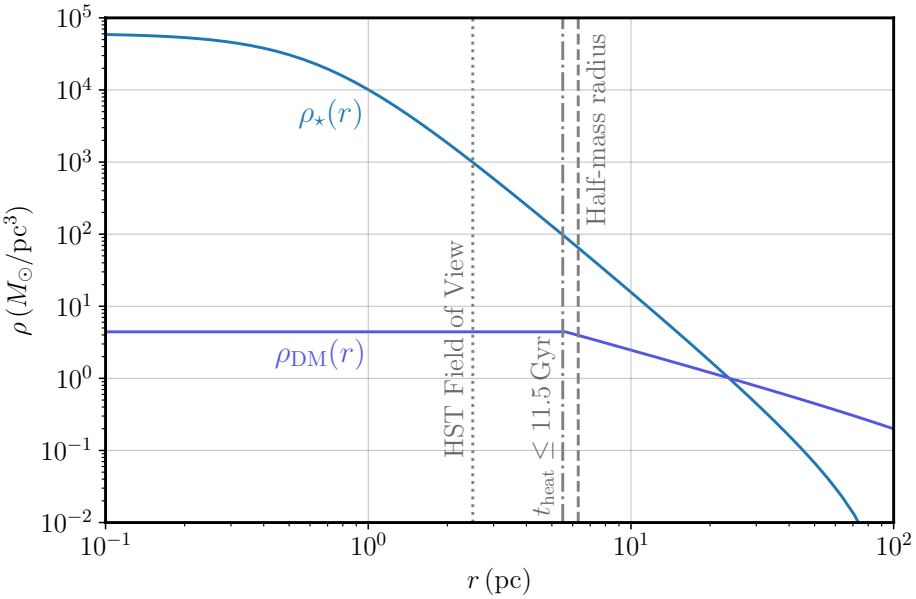

Figure 6.5: Our modeled stellar and DM density profiles for 47 Tuc. We also show the field of view of HST, which encompasses the entire stellar core, but only part of the DM core.

Chapter 7

Invisible Vector Meson Decays

This chapter is based on *Probing Invisible Vector Meson Decays with the NA64 and LDMX Experiments*, by P. Schuster, N. Toro, K. Zhou, Phys. Rev. D 105, 035036 (2022).

Abstract

Electron beam fixed target experiments such as NA64 and LDMX use missing energy-momentum to detect the production of dark matter and other long-lived states. The most studied production mechanism is dark Bremsstrahlung through a vector mediator. In this chapter, we explore a complementary source of missing energy-momentum signals: Bremsstrahlung photons can convert to hard vector mesons in exclusive photoproduction processes, which then decay to dark matter or other invisible particles, such as neutrinos. We find that existing NA64 data can improve the leading constraints on invisible light vector meson decays, while a future run of LDMX could improve them by up to 5 orders of magnitude. For the examples of a dark photon and a $U(1)_B$ gauge boson mediator, accounting for meson decays substantially enhances these experiments' sensitivity, especially to thermal relic dark matter of mass $m_\chi \gtrsim 0.1\,\mathrm{GeV}$.

	$\mathrm{Br}(V, M \to \mathrm{inv})$	$\mathrm{Br}(V, M \to \nu\bar{\nu})$	$\mathrm{Br}(V, M \to \gamma + X_{\mathrm{inv}})$	$\mathrm{Br}(V, M \to \gamma\nu\bar{\nu})$
ρ^0	–	2.4×10^{-13} [3]	–	unknown
ω	$< 7 \times 10^{-5}$ [685]	2.8×10^{-13} [3]	–	unknown
ϕ	$< 1.7 \times 10^{-4}$ [685]	1.7×10^{-11} [3]	–	unknown
$J/\psi(1S)$	$< 7 \times 10^{-4}$ [687]	2.7×10^{-8} [690]	$< 1.7 \times 10^{-6}$ [691]	7×10^{-11} [692]
$\Upsilon(1S)$	$< 3 \times 10^{-4}$ [688]	1.0×10^{-5} [690]	$< 4.5 \times 10^{-6}$ [693]	2.5×10^{-9} [681]
π^0	$< 4.4 \times 10^{-9}$ [689]	see caption	$< 1.9 \times 10^{-7}$ [74]	2×10^{-18} [694]
η	$< 1.0 \times 10^{-4}$ [686]	see caption	$\lesssim 5 \times 10^{-4}$ [695]	$\sim 2 \times 10^{-15}$ [694]
η'	$< 6 \times 10^{-4}$ [686]	see caption	$\lesssim 2 \times 10^{-6}$ [695]	$\sim 2 \times 10^{-14}$ [694]

Table 7.1: Summary table for invisible and radiative decays of flavorless vector mesons V and pseudoscalar mesons M. Most experimental bounds are as in Ref. [2], except for invisible π^0 decay and radiative η and η' decay. The experimental bounds on invisible decays tag decays of a heavier meson and search for missing mass corresponding to the given meson, while those for radiative decays search for missing mass from an invisibly decaying X. In the Standard Model, these processes occur through decays to neutrinos. Note that for the pseudoscalar mesons, decays to two neutrinos are proportional to m_ν^2 because of helicity suppression. Thus, decays to four neutrinos may dominate, but they are also extremely rare [3], being suppressed by $(G_F m_M^2)^4$.

7.1 Introduction

Light dark matter (DM) in the sub-GeV mass range has received a surge of interest over the last decade, triggered by its potential to explain several direct and indirect detection anomalies [667, 668, 669], and more generally by its viability as a WIMP-like thermal relic in simple dark sector models. Such models generically predict meson decays with missing energy, and several works explored flavor violating decays of B mesons, D mesons, and kaons [670, 671, 672], and invisible and radiative decays of light flavorless mesons [673, 670] and heavy quarkonia [674, 675, 676, 677]. More recently, invisible and radiative decays of light flavorless mesons [678, 679] and heavy quarkonia [680, 681, 682, 683, 684] into DM have been reconsidered from an effective field theory perspective.

Motivated by these predictions and others, flavor factories have set limits on invisible meson decay, as we show in Table 7.1. Invisible decays of the light mesons ω, ϕ, η, and η' have been searched for at BES [685, 686], and the leading constraints on the invisible decay of heavy quarkonia J/ψ and Υ have been set at BaBar [687, 688]. Recently, NA62 [689] has set a stringent limit on invisible decays of π^0 mesons.

In this chapter, we describe a new method for detecting invisible meson decay. Existing searches tag the invisibly decaying meson by producing it through the decay of a heavier meson. By contrast, missing energy/momentum experiments such as NA64 [696, 697] and LDMX [698, 699] are sensitive to *any* process in which a beam electron transfers most of its energy to invisible particles, leading to a missing energy signal with no accompanying penetrating particles. The exclusive production and invisible decay of an energetic meson contributes to this inclusive missing energy signal. As a

result, such experiments may be used to simultaneously set limits on the invisible branching ratios of all kinematically accessible mesons, potentially strengthening existing constraints by orders of magnitude. These electron beam experiments are conventionally interpreted as probes of the DM coupling to electrons, but as we will see, their sensitivity to invisible meson decays also offers a powerful probe of the DM or light mediator couplings to quarks.

We will consider dark sector models where the DM particle χ interacts with a vector mediator A' which in turn interacts weakly with quarks, focusing on the well-motivated examples of a kinetically mixed dark photon [700, 701] and a $U(1)_B$ gauge boson [702, 703, 704, 705]. (For reviews of dark sectors and dark photons, see Refs. [706, 707, 708, 709].) Such models can be probed by the invisible decays of flavorless vector mesons. This signature is particularly promising because photons impinging on nuclei can efficiently convert into these mesons, through exclusive forward photoproduction reactions that transfer little energy to the recoiling nucleus or nucleon. Our work thus complements Ref. [710], which focuses on invisible decays of light pseudoscalar mesons.

A simple estimate demonstrates the potential of our approach. At NA64 or LDMX, the sequence of events that leads to a missing energy/momentum signal from invisible vector meson decay is shown in Fig. 7.1. The expected yield of the vector meson V through exclusive photoproduction is $N_V = N_e f_{\rm brem} p_V$, where N_e is the number of electrons on target, $f_{\rm brem}$ is the fraction that produce a hard Bremsstrahlung photon, and p_V is the probability the photon undergoes an exclusive photoproduction process.

Most photons initiate an electromagnetic shower through a photon-conversion process, with cross section $\sigma_{\gamma N \to e^+e^- N} \simeq 7 m_N / 9 X_0$, where m_N is the mass of the nucleus and X_0 is the radiation length. The photoproduction cross section is $\sigma_{\gamma N \to V N} = f^V_{\rm nuc} A \sigma^V_0$, where σ^V_0 is the cross section for exclusive photoproduction on a single nucleon, and $f^V_{\rm nuc}$ is an order-one correction factor. Thus,

$$p_V \simeq \frac{9}{7} \frac{\sigma^V_0 X_0 f^V_{\rm nuc}}{m_p} = 10^{-5} \frac{X_0}{12.86\ {\rm g/cm^2}} \frac{\sigma^V_0}{1\ \mu{\rm b}} \frac{f^V_{\rm nuc}}{1.0} \tag{7.1}$$

where we have normalized to the radiation length for copper. Typically σ^V_0 is on the order of 1 μb, so that given the LDMX Phase II design parameters $N_e = 10^{16}$ and $f_{\rm brem} = 0.03$, we expect meson yields on the order of 10^9 to 10^{10}. This leads to the strong projected bounds on invisible vector meson decay shown in Fig. 7.2. As we will see, at high $m_{A'}$, the corresponding sensitivity to dark sector models exceeds that due to A' Bremsstrahlung, largely because the latter is parametrically suppressed by $(m_e/m_{A'})^2$.

The rest of the chapter is structured as follows. In section 7.2, we describe in greater detail how invisible meson decay can give rise to missing energy/momentum signals at NA64 and LDMX. In section 7.3, we estimate the exclusive photoproduction yields of the relevant vector mesons, reserving details for the appendix. We calculate the invisible branching ratios in the dark photon and $U(1)_B$ models in section 7.4, and show the resulting projected constraints in section 7.5. We conclude by

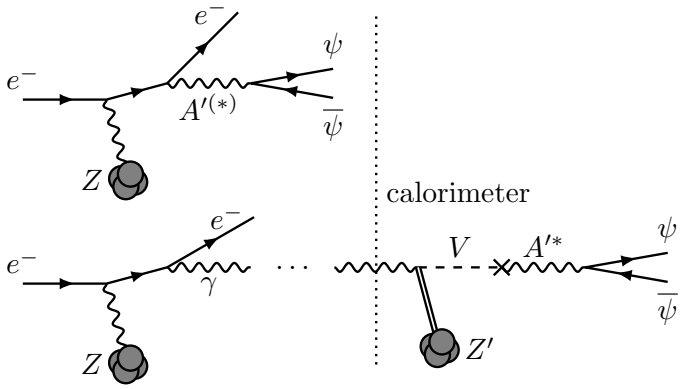

Figure 7.1: Schematic depiction of the DM signal at LDMX from A' Bremsstrahlung (top) and invisible vector meson decay (bottom). In the former, DM is produced through an on- or off-shell A' in the target. In the latter, a hard photon is produced in the target, and converts to a vector meson V in an exclusive photoproduction process in the calorimeter. The vector meson then decays invisibly to DM via mixing with the A'.

discussing potential future directions, such as experimental studies and applications to neutrino physics, in section 7.6.

7.2 Missing Energy/Momentum Experiments

Fixed target experiments have emerged as a powerful probe of light dark sectors [711, 712, 713]. In this chapter, we focus on the missing energy approach [714], exemplified by NA64, and the missing momentum approach [715], exemplified by the proposed LDMX experiment. In both cases, individual electrons from a low-intensity electron beam are tagged and directed at a target. Dark matter production through A' Bremsstrahlung, shown at the top of Fig. 7.1, leads to an observed final state consisting solely of a much lower-energy (and transversely deflected) recoil electron, with the rest of the energy carried by the produced DM particles, which pass through the detector without interacting. These events are identifiable with order-one efficiency by measuring the electron's energy loss with downstream tracking and/or calorimeters, together with the absence of other detected particles that could have carried the energy away. Missing energy/momentum experiments must measure the detector response to one electron at a time, which limits their event yield. Nonetheless, they can match or exceed the sensitivity of much higher-luminosity beam dump experiments to weakly coupled light DM, as beam dumps are only sensitive to the small fraction of DM production events where the DM rescatters in a downstream detector.

In the missing energy approach, the target is the front of the electromagnetic calorimeter itself. By contrast, in the missing momentum approach, DM production occurs in a thin target separated from the electromagnetic calorimeter, allowing the electron to be subsequently deflected and tracked

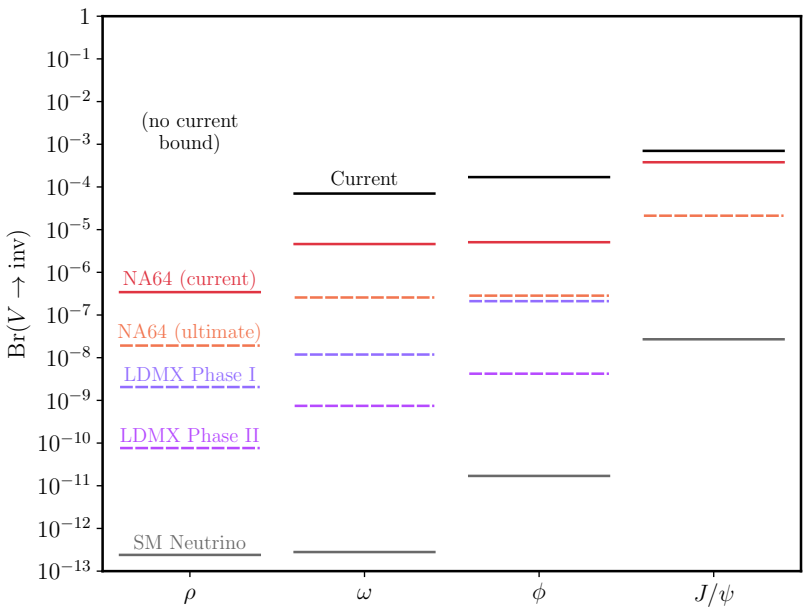

Figure 7.2: Bounds on invisible meson decay, summarizing information from Tables 7.1 and 7.3. We show the best current bound, our projected 90% C.L. exclusions for four experimental benchmarks (assuming zero background events), and the invisible branching ratio within the SM due to decays to neutrinos.

downstream of the target. This enables a higher degree of background rejection, as well as in situ background measurements that would lend credence to any claimed discovery.

In both experimental approaches, electrons often produce hard Bremsstrahlung photons in the target which carry away the majority of their energy, and such events must be rejected extremely reliably. A key potential source of background is the case where the hard photon initiates a hadronic shower through an exclusive photoproduction process, such as $\gamma p \to \pi^+ n$ or $\gamma N \to N K_S K_L$. Reliably rejecting these photonuclear reactions is an important design driver for the downstream electromagnetic and hadronic calorimeters, which has been studied in detail for LDMX in Refs. [698, 699].

The main point of this chapter is that the exclusive photoproduction of vector mesons, $\gamma N \to V N$, can also be an important source of *real* missing energy/momentum signals. These vector mesons carry almost all of the original photon's energy, and decay well before directly interacting with any other nuclei in the calorimeters. If they decay to invisible final states such as DM, as shown at the bottom of Fig. 7.1, then the entire process leaves no trace of the original photon besides the recoil energy of the nucleus or nucleon. Therefore, it is crucial to understand the efficiency with which these recoils survive vetoes used by NA64 and LDMX to reject Standard Model backgrounds. While this is ultimately an experimental question, we will argue below that these survival probabilities should be of order one.

As discussed in the following section, meson production proceeds through both coherent and incoherent processes. Coherent production involves scattering off an entire nucleus, and is peaked at very low momentum transfer $q \lesssim 1/r_{\rm nuc}$. Even for a light target nucleus such as silicon, this corresponds to recoil kinetic energies below 100 keV. Such energy depositions are unobservably small, especially given the likelihood that the nucleus would never even reach active material of the calorimeter. Thus, coherent meson photoproduction produces an unambiguous missing energy signal. It accounts for most of the light meson yield at NA64, and about half of the meson yield at LDMX. However, it is form factor suppressed for heavy mesons, such as ϕ mesons at LDMX and J/ψ's at NA64.

In these cases, incoherent production dominates; it leads to recoils off individual nucleons, with characteristic momentum transfer ~ 500 MeV. Therefore, the nucleons receive a typical kinetic energy ~ 100 MeV, and recoil at wide angles of 50° to 70° from the beamline. These energies are near the sensitivity limits of the detectors.

For example, a proton with 50 MeV kinetic energy at these angles would stop within one tungsten absorber layer of the LDMX ECal, and thus could be completely undetectable. By contrast, a 200 MeV proton could travel through 5 to 10 layers and leave a short track, similar to those LDMX has proposed to use to reject short-lived charged kaon backgrounds [699]. These higher-energy proton recoils may also be vetoed by NA64's selections on the lateral and longitudinal shape of the electromagnetic shower [714]. When the scattered nucleon is a neutron, it would miss the NA64 HCal completely due to the wide production angle and so is presumably undetectable, but the veto efficiency of the LDMX side HCal for wide-angle, low-energy neutrons is marginal (e.g. see Fig. 50 of Ref. [698]).

Properly determining the signal efficiency for incoherent meson production is thus an experimental question that requires detailed simulation and, preferably, in situ performance measurements. Nucleons with recoil energies below 50 MeV are virtually assured to appear as missing energy, while those with recoil energies up to 200 MeV would survive vetoes with an order one probability. For this chapter, we therefore take a kinetic energy cutoff of 100 MeV for both protons and neutrons at NA64 and LDMX. However, as discussed below, our results are generally not qualitatively sensitive to the choice of cutoff.

We note that at LDMX, the p_T distribution of missing-energy events from meson photoproduction and invisible decay matches that of ordinary Bremsstrahlung, not the higher-p_T spectrum expected from A' Bremsstrahlung. Therefore, electron p_T does not offer any additional discriminating power between the meson-induced signal and Bremsstrahlung-initiated background. This does not impact our sensitivity analysis, which is based on LDMX projections that assume sub-single-event backgrounds *before* any additional electron p_T requirements. However, it does limit the toolkit available for distinguishing a meson-induced signal from mismodeled backgrounds.

We will numerically estimate meson yields for four experimental benchmarks, described in

Table 7.3. First, we consider both existing NA64 data using a 100 GeV beam, and the results of a future run with roughly 20 times more electrons [87] at similar energies. At NA64, an event is potentially identified as signal if more than half of the energy is missing. On the basis of the thick target Bremsstrahlung results of Ref. [716], we estimate that a fraction $f_{\rm brem} \approx 0.5$ of the electrons result in a hard photon carrying at least this much energy, and since the Bremsstrahlung spectrum is roughly flat, we take a typical photon energy of 75 GeV. For LDMX, we consider the two nominal stages of running described in Ref. [698], assuming a thin, 10% radiation length tungsten target. For the 4 GeV "Phase I" benchmark, the trigger requires the electron to lose more than 2.8 GeV of its energy, which occurs via Bremsstrahlung to a fraction $f_{\rm brem} \approx 0.03$ of the electrons, resulting in photons with typical energy 3.5 GeV. For the 8 GeV "Phase II" benchmark, we double these energy numbers.

7.3 Vector Meson Photoproduction

Our next task is to refine our estimate of the exclusive photoproduction yield N_V. Proton beam dumps face a similar problem, as in their case, pseudoscalar meson decay is an important source of DM. Typically, the reach of a proton beam dump experiment is estimated using Monte Carlo simulations (e.g. see Refs. [717, 718, 719]), which are tuned to match data at the $\sim 25\%$ level. However, this approach is unnecessary for our purposes. Particle transport Monte Carlo programs such as Geant4 [720] excel at modeling the complex secondary interactions that occur for typical photons. This level of modeling is not required for our study, where photons only undergo a single, exclusive photoproduction process, and the vector mesons produced in these reactions decay well before interacting with any matter in the downstream detector.

In fact, a simulation-based approach is also inadequate, as neither Geant's hadronic models nor particle physics Monte Carlos such as Pythia [721] include careful modeling of exclusive photoproduction processes. Pythia's parton-based modeling is designed for the deep-inelastic regime, while our reactions of interest are in the diffractive regime. Meanwhile, Geant4 [722] does not include short-lived resonances in its hadronic models, but rather treats reactions such as $\gamma p \to \rho p$ as a component of, e.g., $\gamma p \to \pi^+\pi^- p$. More specialized programs such as GiBUU [723] do propagate the light vector mesons through nuclei, but no semiclassical procedure can adequately describe coherent photoproduction, which often accounts for most of the meson yield. For heavy nuclei and high photon energies, neglecting coherent photoproduction underestimates the yield by up to an order of magnitude.

Therefore, we will focus on estimating the yield transparently from a combination of theory and experimental measurements. Of course, to study more experimentally subtle questions, such as the probability of vetoing a recoiling nucleon from incoherent photoproduction, the models discussed below would need to be embedded into a Monte Carlo program with appropriate systematic uncertainties.

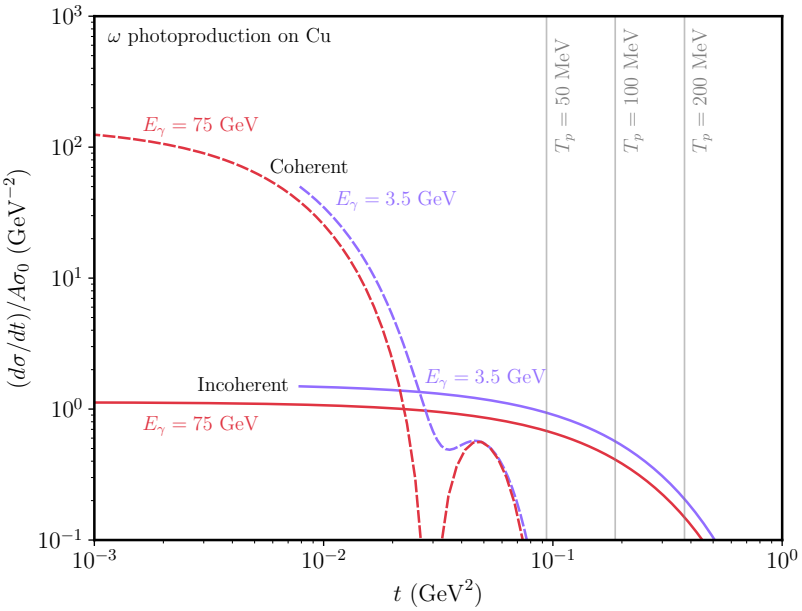

Figure 7.3: Differential cross sections for coherent (dashed) and incoherent (solid) ω photoproduction. We also show contours of nucleon recoil energy for the incoherent process.

To begin, we refine Eq. (7.1) to account for the fact that the calorimeters are comprised of layers containing different nuclei. Weighting by the photon survival probability yields

$$p_V = \int_0^\infty \exp\left(-\int_0^x \frac{7\rho(x')}{9X_0(x')}\,dx'\right) \frac{\rho(x)\sigma_0^V}{m_p}\, f_{\rm nuc}^V(x)\,dx. \tag{7.2}$$

For both NA64 and LDMX, this integral is largely determined by the composition of the front of the electromagnetic calorimeters. At NA64, most of the mesons are photoproduced in the lead absorber layers, with most of the remainder from carbon in the plastic scintillator [697]. For LDMX, about half of the mesons are photoproduced from carbon, silicon, and oxygen in the preshower, while most of the rest are photoproduced in the tungsten absorber layers [724]. Note that in general, p_V is higher for materials with lighter nuclei, because the radiation length scales as $X_0 \sim A/Z^2$, due to coherent scattering off the Z protons.

The per-nucleon exclusive photoproduction cross section σ_0^V has been thoroughly measured for all relevant mesons in the entire energy range of interest. We extract the light vector meson cross sections in Table 7.3 from the theoretical fit of Ref. [725]. For the ϕ meson, Pomeron exchange is the dominant contribution, explaining the characteristic slow rise in cross section with energy. For the ρ and ω mesons, exchanges of light mesons such as the $f_2(1270)$ and π^0 dominate for low energies, while Pomeron exchange takes over at high energies, explaining why the cross section remains fairly high at NA64 energies.

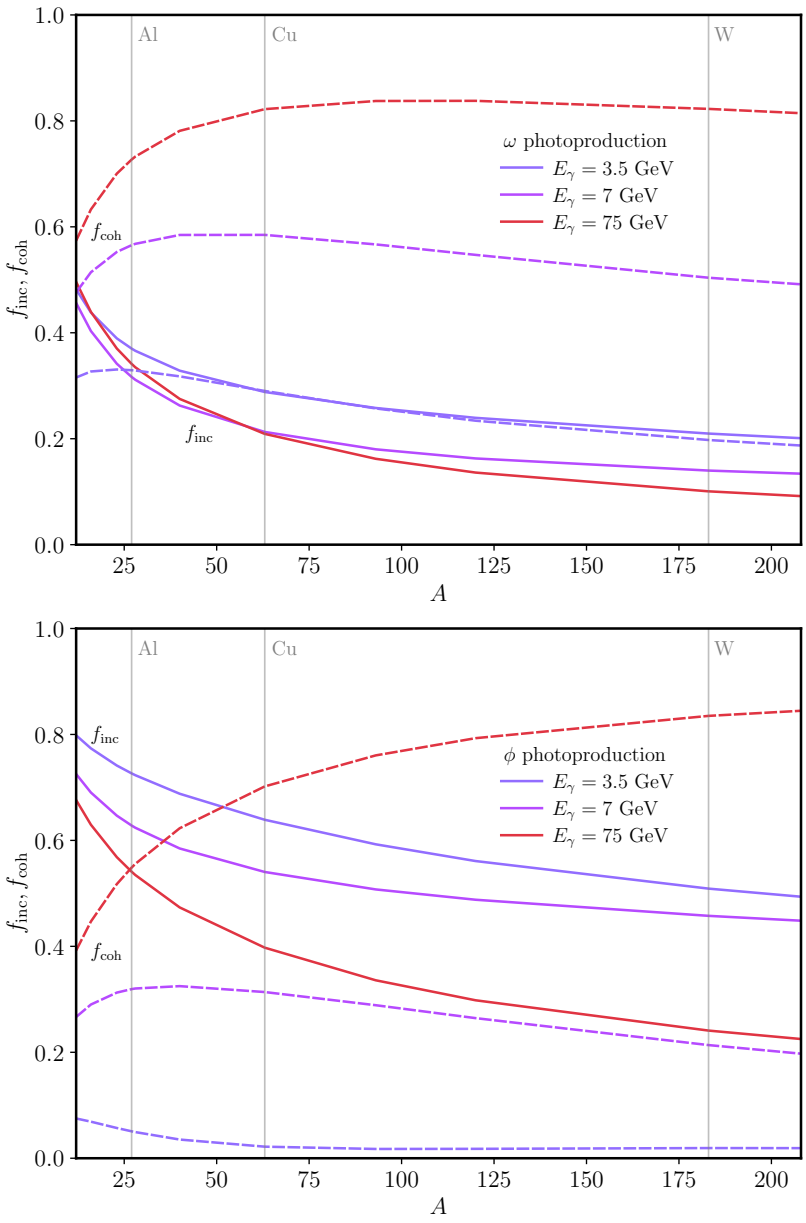

Figure 7.4: Contributions to meson yield from incoherent (solid) and coherent (dashed) processes, as a function of the nucleon number A, for typical photon energies at LDMX and NA64. We show results for ω (left) and ϕ (right) photoproduction; results for ρ are similar to those for ω. Coherent production is suppressed for the ϕ meson at low photon energies, due to its higher mass.

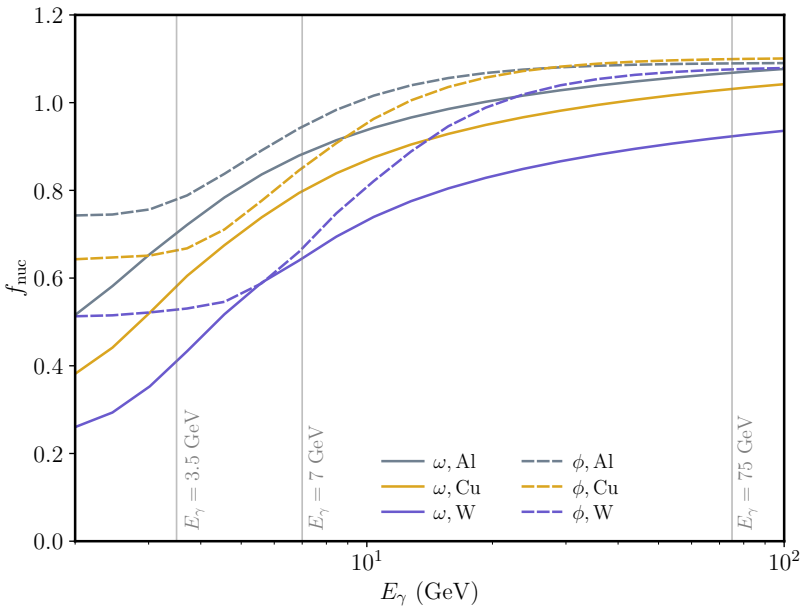

Figure 7.5: Measure of total meson yield for the ω and ϕ for three benchmark nuclei, as a function of the photon energy E_γ.

	N_e	E_e	E_γ	f_{brem}	$\sigma_0^\rho(\mu\text{b})$	$\sigma_0^\omega(\mu\text{b})$	$\sigma_0^\phi(\mu\text{b})$	N_ρ	N_ω	N_ϕ
NA64 (cur.)	2.8×10^{11}	100 GeV	75 GeV	0.5	9	0.8	0.7	7×10^6	5×10^5	5×10^5
NA64 (ult.)	5×10^{12}	100 GeV	75 GeV	0.5	9	0.8	0.7	1.2×10^8	9×10^6	8×10^6
LDMX I	4×10^{14}	4 GeV	3.5 GeV	0.03	23	5	0.4	1.1×10^9	1.9×10^8	1.1×10^7
LDMX II	10^{16}	8 GeV	7 GeV	0.03	16	1.9	0.5	3×10^{10}	3×10^9	5×10^8

Table 7.2: Total electrons on target N_e, electron energy E_e, and estimated fraction f_{brem} of electrons that yield hard Bremsstrahlung photons (with typical energy E_γ), for our four benchmarks, as discussed in section 7.2. We also show the per-nucleon exclusive light vector meson photoproduction cross sections and the estimated total meson yields, calculated as described in section 7.3. The estimated number $N_{J/\psi}$ of J/ψ mesons produced at NA64, not shown in the table, is 6×10^3 (current) and 1.1×10^5 (ultimate).

Naively, the cross section for nuclei is simply the incoherent sum $A\sigma_0^V$, but the computation of the correction factor $f_{\rm nuc}$ is nontrivial. To proceed, we must note that mesons can be exclusively photoproduced through two distinct processes. In the coherent process, the nucleus remains in its ground state and recoils as a whole, leaving it with negligible kinetic energy; it is peaked at very low momentum transfer, with a scale set by the radius of the nucleus. In the incoherent process, the meson recoils off an individual nucleon, and the characteristic momentum transfers are somewhat higher, being set by Pomeron physics. These qualitative features are shown in Fig. 7.3.

We separate the contributions of these processes by defining $f_{\rm inc,coh} = \sigma_{\rm inc,coh}/A\sigma_0$, where $f_{\rm nuc} = f_{\rm inc} + f_{\rm coh}$. Naively, the cross section for the incoherent process scales as A, but it is suppressed by absorptive final state interactions. In the limit of a very large, opaque nucleus, the effective number of nucleons participating is determined by the geometric cross section of the nucleus, $A_{\rm eff} \sim r_{\rm nuc}^2 \sim A^{2/3}$, leading to the rough scaling $f_{\rm inc} \sim A^{-1/3}$. It is further suppressed by nuclear shadowing, a destructive interference effect most important at high photon energies.

In the coherent process, the photoproduction amplitude is coherently summed over the nucleons, leading to a forward differential cross section $d\sigma_{\rm coh}/dt|_{\theta=0}$ that naively scales as A^2. The coherent peak extends up to $t \sim 1/r_{\rm nuc}^2 \sim A^{-2/3}$, implying a rough scaling $f_{\rm coh} \sim A^{1/3}$, though it is also suppressed for heavy nuclei by absorptive final state interactions. In contrast to the incoherent process, the coherent cross section increases at higher photon energies, because a lower longitudinal momentum transfer $q_\parallel \approx m_V^2/E_\gamma$ is required to produce the meson, leading to constructive interference across the entire nucleus. These qualitative features are shown in Fig. 7.4.

The coherent and incoherent cross sections on nuclei can be measured separately, since coherent production is peaked at very low momentum transfer. For the light vector mesons, the coherent cross sections have been thoroughly measured decades ago, for a wide variety of nuclei and photon energies, and a standard Glauber optical model fits the data; we estimate that the theoretical uncertainty is at most 25%. The subleading incoherent cross section is less well-measured, and the data is more ambiguous; here we estimate an uncertainty of up to 50%. Further details on the theoretical modeling and experimental measurements may be found in the appendix, but for the purposes of estimating the reach, the conclusion is simply that $f_{\rm nuc}$ is close to one for most energies and nuclei we consider, as shown in Fig. 7.5. We compute the entries in Table 7.3 by additionally requiring that the nucleon recoil energy be less than 100 MeV for the incoherent process, which decreases the incoherent yield by up to 50%. However, as shown in the appendix, our results are not strongly dependent on the precise choice of cutoff; it is usually the uncertainty on the coherent and incoherent cross sections that dominates.

We may also consider heavier vector mesons, and the most promising example is J/ψ photoproduction at NA64. Following HERA data [726], we estimate a per-nucleon elastic photoproduction cross section of $\sigma_0^{J/\psi} = 15$ nb at NA64 energies. Photoproduction of J/ψ on nuclear targets may also be described by optical models, which have been recently refined within the leading twist

$f_{V,X}$ (MeV)	ρ	ω	ϕ
$\bar{u}\gamma^\mu u$	157	136	8
$\bar{d}\gamma^\mu d$	-148	142	8
$\bar{s}\gamma^\mu s$	0	-10	233
J^μ_{EM}	154	46	-75
J^μ_B	2.8	89	83

Table 7.3: Form factors describing the coupling of a light vector meson V to a current X.

approximation to treat ultraperipheral ion collisions at the LHC (e.g. see Ref. [727]). Fortunately, it is much more straightforward to treat the lower center-of-mass energies at NA64, $W_{\gamma p} \sim 10$ GeV. In this case, the high longitudinal momentum transfer strongly suppresses coherent photoproduction and nuclear shadowing in incoherent photoproduction. Furthermore, final state interactions are relatively unimportant because the J/ψ-nucleon cross section is several times smaller than for the light vector mesons [728]. We may thus estimate $f_{\text{coh}} \approx 0$, $f_{\text{inc}} \approx 1$, with accuracy comparable to our other yield estimates.

NA64 can also produce Υ mesons, but the cross sections at its energies are orders of magnitude smaller than for J/ψ, making it uncompetitive with the current BaBar constraint. Meanwhile, at LDMX energies, Υ production and incoherent J/ψ production are kinematically forbidden. Coherent J/ψ production is kinematically allowed, but our optical models are not necessarily trustworthy in this very high momentum transfer regime; in any case, they predict a very strong suppression. We thus consider only J/ψ production at NA64, yielding the final column of Table 7.3.

7.4 Invisible Branching Ratios

Given the meson yields shown in Table 7.3, LDMX and NA64 can place a 90% C.L. limit $\text{Br}(V \to \text{inv}) \leq 2.3/N_V$ on the invisible branching ratio of each relevant meson, assuming zero background events and neglecting theoretical uncertainty, yielding the results shown in Fig. 7.2. We expect that current NA64 data could already set a strong limit on the invisible decays of the ρ meson, improve the bounds for ω and ϕ by about an order of magnitude, and improve the J/ψ bound by roughly a factor of 2. Of course, actually setting such limits would require a more detailed analysis of theoretical uncertainties and experimental efficiencies, since our projections consider only statistical uncertainty.

Future NA64 data will improve on all of these results by roughly a factor of 20. In particular, the resulting limit on J/ψ invisible decay would be competitive with the projected limit $\text{Br}(J/\psi \to \text{inv}) \leq 3 \times 10^{-5}$ from a future run of BES III [729]. LDMX could further improve on the light meson results by orders of magnitude, highlighting the potential of missing energy/momentum experiments as precision probes of meson physics.

To constrain specific dark sector models, we must compute the expected invisible branching ratio

of each meson. For concreteness, we focus on dark sectors with pseudo-Dirac fermion DM, and a vector mediator with interactions

$$\mathcal{L} \supset \epsilon e A'_\mu J^\mu_X + g_D\, A'_\mu \bar{\chi}\gamma^\mu \chi \tag{7.3}$$

where ϵ is the kinetic mixing parameter, and $J^\mu_X = \sum_q c_q \bar{q}\gamma^\mu q$ stands for the electromagnetic current $J^\mu_{\rm EM}$ ($c_q = Q_q$) or the baryon current J^μ_B ($c_q = 1/3$). For the $U(1)_B$ model, we also assume a loop-suppressed kinetic mixing $\epsilon e/(4\pi)^2$ with the photon. This does not affect the meson decay signature, but is relevant for computing the reach from A' Bremsstrahlung and the thermal relic target below the two-pion threshold. For the dark sector parameters, we take benchmarks $\alpha_D = g_D^2/4\pi = 0.5$ and $m_{A'}/m_\chi = 3$.

To compute the invisible branching ratios for light vector mesons, we first find the relevant form factors, defined by $\langle 0|J^\mu_X|V(\epsilon)\rangle = i m_V f_{V,X}\epsilon^\mu$. From the results of Appendix C of Ref. [730], which accounts for ϕ-ω and ρ-ω mixing, we infer the first three rows of Table 7.3, giving the couplings $f_{V,q}$ to light quark currents $\bar{q}\gamma^\mu q$. Note that $f_{\rho,s}$ vanishes because we are ignoring the small effect of ρ-ϕ mixing, but this does not qualitatively affect the results. Next, we straightforwardly infer the bottom two rows of Table 7.3. Here, $f_{\omega,\rm EM}$ is suppressed due to a partial cancellation between the u and d components, while $f_{\rho,B}$ is strongly suppressed, because it is only nonzero due to mixing effects.

The amplitude for an on-shell vector meson V to decay to $\chi\bar{\chi}$ through a virtual A' is

$$\mathcal{M} = \frac{\eta^{\mu\nu} - q^\mu q^\nu/m^2_{A'}}{q^2 - m^2_{A'}}\,(g_D\epsilon e)(\bar{u}(p)\gamma_\nu v(p'))(m_V f_{V,X}\epsilon_\mu) \tag{7.4}$$

where q^μ is the meson's momentum. Squaring and summing over final spins and averaging over initial meson polarizations ϵ^μ gives the decay rate

$$\Gamma_{V\to\chi\bar{\chi}} = \frac{\alpha_D(\epsilon e)^2 f^2_{V,X}}{3}\frac{(m^2_V + 2m^2_\chi)\sqrt{m^2_V - 4m^2_\chi}}{(m^2_{A'} - m^2_V)^2 + \Gamma^2_{A'}m^2_{A'}} \tag{7.5}$$

in the frame of the meson. The resonant peak is cut off by the width $\Gamma_{A'}$ of the A' due to decay to DM, where for our dark sector model,

$$\frac{\Gamma_{A'}}{m_{A'}} = \frac{\alpha_D}{3}\sqrt{1 - 4m^2_\chi/m^2_{A'}}\,(1 + 2m^2_\chi/m^2_{A'}). \tag{7.6}$$

for on-shell A'. (These results can equivalently be derived by considering mixing with the A' in the vector meson dominance framework, e.g. see Ref. [83].) The expected number of missing energy events via production of V is then $N_V\Gamma_{V\to\chi\bar{\chi}}/\Gamma_V$.

However, in the above derivation, we have implicitly applied the narrow width approximation for the vector meson V by taking it to be on-shell. A more accurate expression is obtained by averaging Eq. (7.5) over the spectral density of photoproduced V's, or equivalently, by treating both V and A'

as intermediate states in the full $\gamma N \to \chi\bar{\chi}N$ process. In particular, when $\Gamma_{A'} \ll \Gamma_V$ but the two resonances overlap, $|m_{A'} - m_V| \lesssim \Gamma_V$, it is more accurate to apply the narrow width approximation to the A'. Assuming a Breit–Wigner lineshape for both resonances, the resulting correction is equivalent to multiplying Eq. (7.5) by $\Gamma_V/\Gamma_{A'}$ and replacing $\Gamma_{A'}$ with Γ_V in the denominator. We apply this correction when showing results for the ρ meson, which is about twice as wide as the A' for nearby masses, resulting in a flattening and broadening of the resonant peaks.

When the masses are widely separated, $|m_{A'} - m_V| \gg \Gamma_{A'}, \Gamma_V$, the situation is more subtle. Here, the spectral density has two distinct contributions. The contribution at $q^2 \approx m_V^2$ corresponds to the standard result from on-shell V's, while the additional contribution at $q^2 \approx m_{A'}^2$ corresponds to production of far off-shell vector mesons that mix with a nearly on-shell A'. The contribution of this second peak can be comparable or even greater, especially when $\alpha_D \ll 1$. It cannot be interpreted in terms of an invisible branching ratio of the ρ, but it does enhance the signal rate. However, properly evaluating this contribution would require a more detailed treatment of the momentum-dependence of the photon-ρ Pomeron vertex, the final-state phase space, and the spectral shape of the ρ. Therefore, we conservatively neglect it in this initial study.

Finally, for the $J/\psi(1S)$, we compute the invisible decay width by comparing it to the decay width to e^+e^-, as in Ref. [731]. Because the quarks carry spin 1, the quark spinor bilinear $\bar{u}\gamma^\mu v$ is purely spatial, which implies that the longitudinal term in the A' propagator does not contribute to the amplitude. As a result, the two decay widths are identical up to constants and kinematic factors, giving

$$\frac{\mathrm{Br}(J/\psi \to \chi\bar{\chi})}{\mathrm{Br}(J/\psi \to e^+e^-)} = \frac{\alpha_D}{\alpha_e}\left(\frac{c_c\epsilon}{Q_c}\right)^2 \frac{m_V(m_V^2 + 2m_\chi^2)\sqrt{m_V^2 - 4m_\chi^2}}{(m_{A'}^2 - m_V^2)^2 + \Gamma_{A'}^2 m_{A'}^2} \tag{7.7}$$

where we used $m_e \ll m_V = m_{J/\psi}$. In the limit $m_\chi, m_{A'} \ll m_V$, the final factor reduces to unity, leaving the expected ratio of couplings.

7.5 Projected Reach

For a specific dark sector model, the expected number of signal events is $N_{\mathrm{sig}} = \sum_V N_V \mathrm{Br}(V \to \mathrm{inv})$, and if no signal and background events are seen, a 90% C.L. limit may be set on the model by imposing $N_{\mathrm{sig}} < 2.3$. In Fig. 7.6, we show the current and projected constraints on the dark photon model from individual mesons. As indicated in the left panel, current constraints on the invisible decays of J/ψ and the light vector mesons are not competitive with the leading experimental bounds. However, as shown in the right panel, missing energy experiments can improve the latter constraints by up to 5 orders of magnitude, in the case of LDMX Phase II. When combined with the projected improved measurements of J/ψ and Υ invisible decays, we find that meson decays alone can probe a substantial portion of the thermal freeze-out "target" region of couplings for $m_\chi \gtrsim 0.1$ GeV.

In Fig. 7.7, we show the same results for a $U(1)_B$ gauge boson mediator. In this case, most

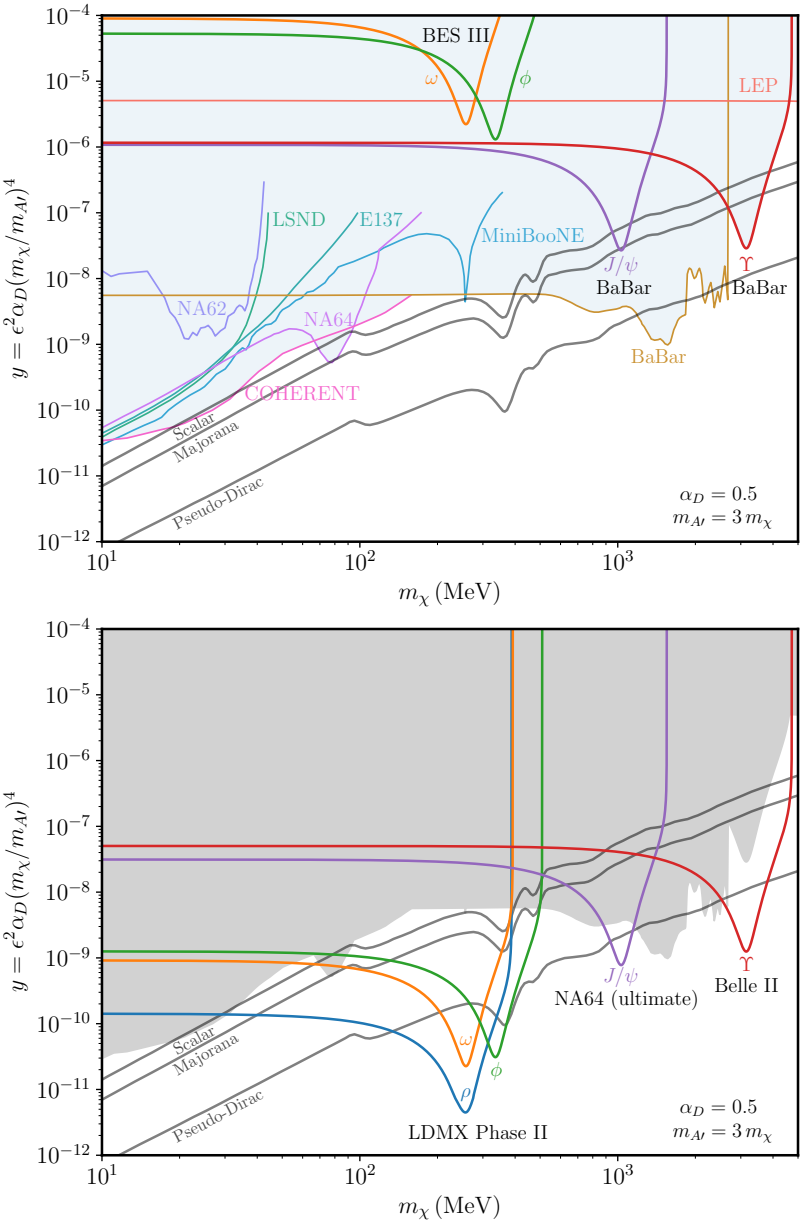

Figure 7.6: Constraints on the dark photon model with fermionic DM. At left, we show existing constraints from current bounds on invisible vector meson decays, as well as those from the beam dumps LSND [68, 69], E137 [70, 71], MiniBooNE [72], and COHERENT [73], radiative pion decay at NA62 [74], the missing energy experiment NA64 [75, 76], production in e^+e^- collisions at BaBar [77], and precision measurements of the Z^0 mass at LEP [78]. At right, we show the strongest projected 90% C.L. exclusions from invisible decays of each meson alone. For the light vector mesons and J/ψ, these constraints will come from LDMX and NA64, respectively, assuming zero background events. For the Υ, we take the projected limit $\mathrm{Br}(\Upsilon \to \mathrm{inv}) < 1.3 \times 10^{-5}$ from Belle II [79].

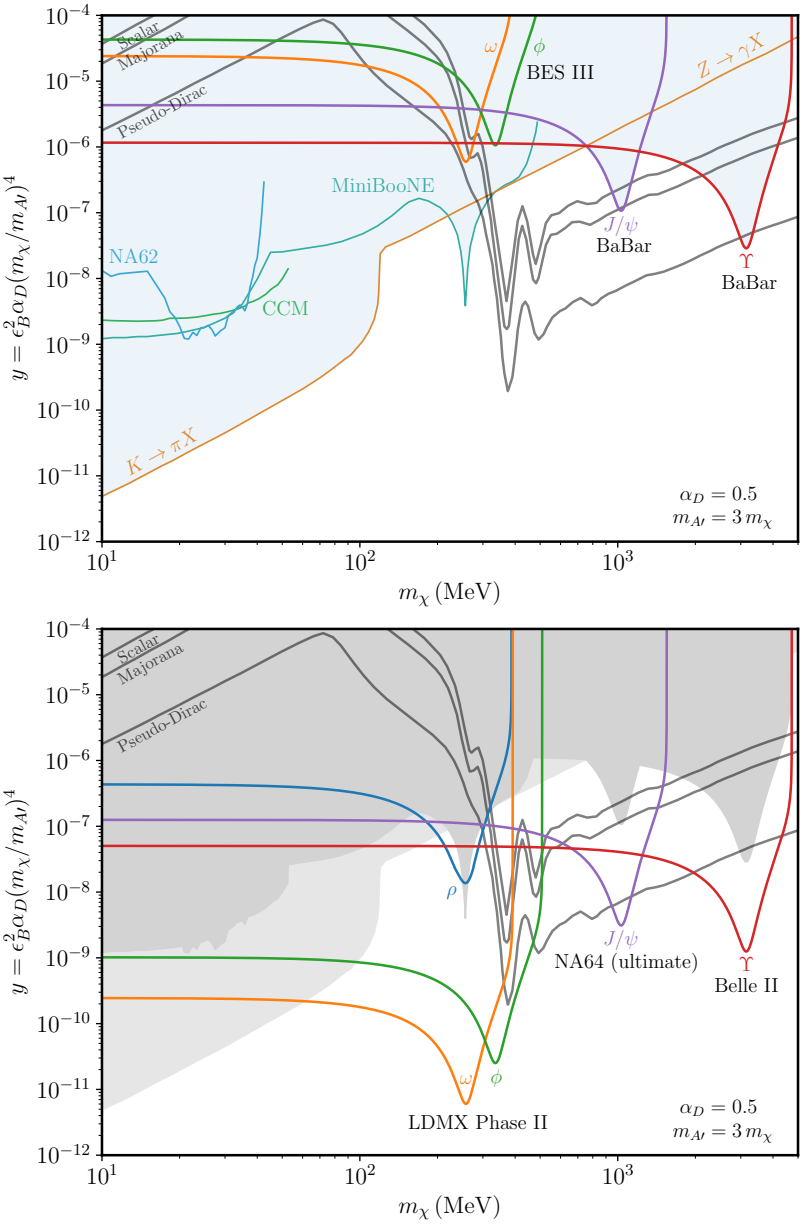

Figure 7.7: Same as Fig. 7.6, but in the $U(1)_B$ model. In this case, the leading existing constraints are from CCM [80, 81] (rescaled to $m_{A'}/m_\chi = 3$ using Ref. [82]), NA62 [74] (recast for a $U(1)_B$ gauge boson using Ref. [83]), MiniBooNE [72] (rescaled to $\alpha_D = 0.5$), and rare processes $K \to \pi X$ and $Z \to \gamma X$, which have $1/m_{A'}^2$ enhanced rates due to the $U(1)_B$ anomaly [84, 85]. These latter constraints are shaded more lightly at right, since they may be removed by coupling to a nonanomalous current such as $B - 3L_\tau$. Thermal relic curves assume a loop-suppressed kinetic mixing with the photon, and are computed as in Ref. [86].

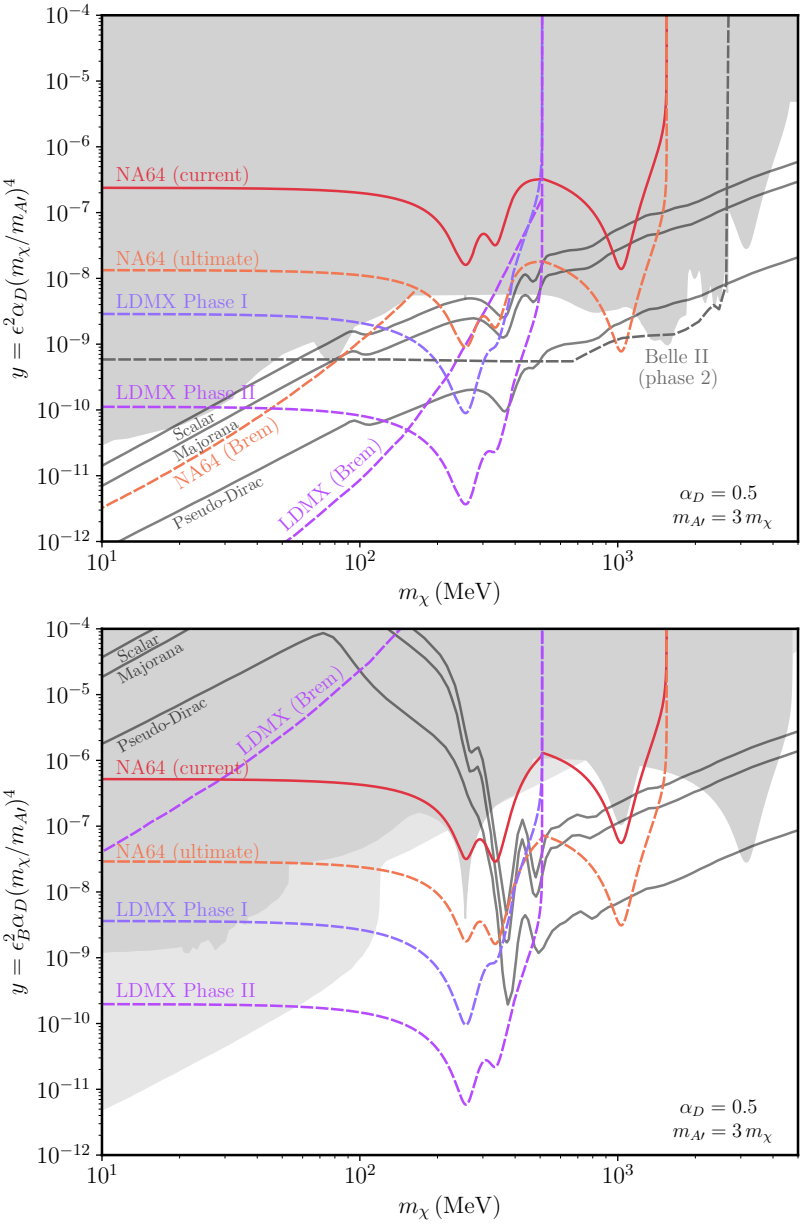

Figure 7.8: Projected 90% C.L. exclusions for the four experimental benchmarks described in Table 7.3, assuming zero background events, in the dark photon (left) and $U(1)_B$ (right) models, both with fermionic DM. For comparison, we also show projections for Belle II [79], and for A' Bremsstrahlung at LDMX Phase II [86] and a future run of NA64 [87]. For projections from proton beam experiments, see Ref. [88].

constraints on dark photons do not apply, because they depend on the dark photon's coupling to electrons. Instead the strongest constraints for most masses come from precision measurements of rare processes, which are enhanced due to the $U(1)_B$ anomaly, though invisible Υ decay remains the strongest constraint at high masses. Despite these strong existing bounds, the projected future reach from meson decay probes new parameter space for $m_\chi \gtrsim 0.1$ GeV, and covers almost the entirety of the thermal freeze-out region. The sensitivity to invisible ρ meson decay is suppressed by a small form factor, as noted above, but this is compensated by increased sensitivity to invisible ω decays.

Referring to Table 7.1, invisible decays to neutrinos in the Standard Model remain a negligible background for the light vector mesons, even at LDMX Phase II. However, they imply that any future meson decay experiment will only be able to probe 2 to 3 orders of magnitude beyond LDMX Phase II, before running into a "neutrino floor" that slows further progress. For the J/ψ, this floor is a few orders of magnitude beyond the NA64 (ultimate) projections, while Belle II will nearly reach the Υ floor. Conversely, by searching for invisible meson decays, LDMX and NA64 will also be sensitive to neutrino-quark interactions from physics beyond the Standard Model. As we discuss in section 7.6.3, they could provide the leading bounds on several effective operators that are otherwise difficult to probe with upcoming neutrino experiments.

In Fig. 7.8, we show the constraints on dark sectors for our four experimental benchmarks. The main qualitative feature is that in all cases, meson decay improves the reach of these experiments for $m_{A'} \gtrsim 0.5$ GeV. In this regime, the reach due to A' Bremsstrahlung is weak, due to the $(m_e/m_{A'})^2$ suppression of the Bremsstrahlung cross section, and the fact that the higher momentum transfer begins to resolve heavy nuclei. In the case of NA64, meson decay does not currently probe new parameter space. However, it will allow future runs of NA64 to probe the thermal freeze-out region at masses around the resonances $m_{A'} \approx m_V$, up to an order of magnitude higher in mass than through A' Bremsstrahlung alone. Meson decay also extends the reach of LDMX upward in mass, by roughly a factor of 2. We note that the reach from Belle II is highly complementary: when combined with LDMX, the thermal freeze-out region from MeV to GeV masses will be well explored.

For the $U(1)_B$ model, meson decay dramatically improves the reach of both NA64 and LDMX, since the A' Bremsstrahlung channel is penalized by the loop-suppressed coupling to electrons. Typically, these experiments are viewed as probing mediator couplings to electrons, while proton beam experiments probe couplings to quarks. The meson decay signature discussed here shows that electron beam experiments can have competitive sensitivity to quark couplings.

The constraints we show fall sharply at threshold, $2m_\chi = m_V$, but in fact, heavier dark matter can be produced in these experiments through the decays of heavier mesons, such as the resonances $\omega(1420)$ and $\rho(1450)$ of the light vector mesons. The main obstacle to predicting this sensitivity is the lack of data on photoproduction cross sections for these resonances. We expect the sensitivity to be lower, due to the larger width of the resonances, but potentially still high enough to probe new parameter space. Similarly, for the J/ψ, one can consider production of excited charmonium states

such as $\psi(2S)$.

It is also interesting to consider how the reach due to meson decay depends on the dark sector parameters ϵ, α_D, m_χ, and $m_{A'}$. First, both the thermal annihilation cross section and the invisible meson decay rate are proportional to $\epsilon^2\alpha_D$, which implies that for a fixed mass ratio $R = m_{A'}/m_\chi$, both of these curves are roughly independent of α_D on a y vs. m_χ plot. Therefore, invisible meson decay maintains its relative sensitivity to the thermal freeze-out region for lower α_D, though the reach due to A' Bremsstrahlung improves. (However, as mentioned in Section 7.4, the invisible decay rate might actually be enhanced at lower α_D because of the contribution of off-shell vector mesons mixing with on-shell A'.)

The effect of changing the mass ratio R is shown in Fig. 7.9. For low $m_{A'}$, increasing R rapidly improves the reach in y of both A' Bremsstrahlung and meson decay, because $y \propto 1/R^4$, while in this regime the A' Bremsstrahlung rate is proportional to $1/R^2$, and the invisible meson decay rate is independent of R. Increasing R allows invisible meson decay to probe very high mediator masses, $m_{A'} \gg m_V$, even though the mixing with the vector meson is lowered. In this regime A' Bremsstrahlung would be strongly suppressed because of the high momentum transfer required to produce the A', but invisible meson decay is not, as the momentum transfer is set by m_V rather than $m_{A'}$.

Because invisible meson decay proceeds through off-shell mediators, it also occurs in the "forbidden" regime $R < 2$, where an on-shell A' cannot decay to DM. In this case, there may be complementary constraints from visible A' decay, and there is still a predictive thermal target for sufficiently high $m_{A'}$ and α_D [86]. However, the potential to reach these targets through the meson decay signature is weaker because of the scaling with R mentioned in the previous paragraph.

7.6 Future Directions

7.6.1 Additional Meson Decays

We have focused on the invisible decay of vector mesons as a probe of dark sectors with vector mediators, but there are numerous potential extensions. First, missing energy experiments will also set leading, but weaker limits on the invisible decay of pseudoscalar mesons. NA62 has set a strong bound on invisible π^0 decay, which seems difficult to improve upon, but the bounds on invisible η and η' decay are quite weak. Since these mesons have a different spin from the photon, they cannot be photoproduced by Pomeron exchange. Instead, their exclusive photoproduction is described by Reggeon exchange, leading to cross sections that rapidly fall with energy [732, 733]. This suppresses the yield of these mesons at NA64, though both NA64 and LDMX should still be able to significantly improve bounds for η and η'.

In a similar vein, it could be interesting to investigate the invisible decay of scalar mesons ($J^{PC} = 0^{++}$), such as the $f_0(980)$ and $a_0(980)$, as these provide complementary information to the

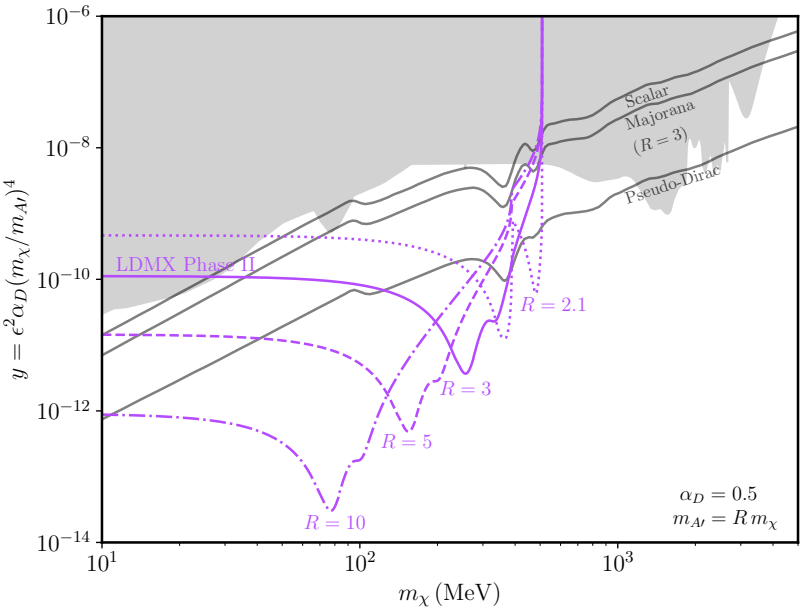

Figure 7.9: Projected 90% C.L. exclusions from invisible vector meson decay at LDMX Phase II in the dark photon model, for several choices of the mass ratio $R = m_{A'}/m_\chi$. Thermal targets are shown for $R = 3$, and are roughly independent of the mass ratio except when $R - 2$ is small.

invisible decay of vector mesons. However, there is currently little data on the photoproduction of these mesons, with the first measurements only made comparatively recently [734, 735].

The invisible decay of neutral kaons has never been measured, and both NA64 and LDMX should be able to set strong bounds, without requiring a kaon beam. We note, however, that there are several complications that suppress the potential sensitivity. First, as for η and η', the exclusive photoproduction cross sections for K_S and K_L fall rapidly with energy. Due to conservation of strangeness, kaon photoproduction converts a nucleon to a hyperon. This implies a minimum energy deposition in the calorimeters of about 200 MeV when the hyperon decays; determining the associated veto efficiency requires further detector study. Finally, the K_L is sufficiently long-lived that there is a substantial penalty from demanding that it decay before interacting with the calorimeters.

Mesons can also undergo radiative decays, into a photon plus missing energy. For both LDMX and NA64, the signal efficiency for such a process is penalized because the photon must carry sufficiently little energy. This is relatively unimportant at NA64, where the photon may carry a substantial fraction of the meson's energy, but at LDMX we require the photon to be soft enough to completely avoid detection in the calorimeters, which requires it to be emitted nearly backwards in the meson's frame. It may be possible to partially circumvent this penalty by allowing a small amount of energy to be detected in the calorimeters, but this could introduce other backgrounds, which would require a more detailed study to evaluate.

mediator coupling	$V \to \chi\bar{\chi}$	$V \to \gamma\chi\bar{\chi}$	$M \to \chi\bar{\chi}$	$M \to \gamma\chi\bar{\chi}$
scalar $\bar{q}q$		✓		
pseudoscalar $\bar{q}\gamma^5 q$		✓	✓	
vector $\bar{q}\gamma^\mu q$	✓			✓
axial vector $\bar{q}\gamma^\mu\gamma^5 q$		✓	✓	

Table 7.4: Quark couplings to mediators that can cause invisible and radiative decays of vector mesons V ($J^{PC} = 1^{--}$) and pseudoscalar mesons M ($J^{PC} = 0^{-+}$).

In particular, missing energy experiments could improve bounds on radiative η and η' decay by orders of magnitude, extending existing constraints associated with radiative π^0 decay to higher A' mass. Constraints on this process could also be set using existing data at BES [736] and KLOE [737], and much stronger future constraints could come from "η-factory" experiments [738], such as the upcoming JEF [739] and proposed REDTOP [740].

7.6.2 Additional Dark Sectors

We have focused on dark sectors with vector mediators because they are probed by invisible vector meson decay, but as indicated in Table 7.4, the other meson decays discussed in the previous section can probe other types of mediators. Here we consider each possibility in turn.

First, we note that vector mediators can also be probed through radiative pseudoscalar meson decays. For the reasons given in the previous subsection, we expect that the associated constraints will be weaker, for the models considered in this chapter, than those from invisible vector meson decays. On the other hand, when $m_{A'} < m_M$, the A' can be produced on-shell in the decay $M \to A'\gamma$, giving an radiative decay rate independent of α_D. It could therefore be a leading constraint in models with $\alpha_D \ll 1$, such as $U(1)_B$ models with $\alpha_D \sim \alpha_B$.

Scalar mediators can be probed by radiative vector meson decays. In the minimal case of a Higgs-mixed scalar, the mediator couples to quarks proportionally to their mass, and thus our signatures are not competitive with collider and B meson constraints [741], which already exclude most of the thermal relic target. On the other hand, it may be possible to probe new parameter space in models where the scalar preferentially couples to light quarks [742, 743, 744].

Axial vector mediators can lead to invisible pseudoscalar and radiative vector meson decay, and in minimal models, they couple universally to up-type and down-type quarks [745]. However, axial vectors are very strongly constrained through the FCNC processes $K \to \pi A'$ and $B \to K A'$, which occur with $1/m_{A'}^2$ enhanced rates due to the vector's coupling to a nonconserved current [85]. This will be the strongest constraint at low $m_{A'}$, but our meson decays may be competitive for A' masses above the $K \to \pi A'$ threshold. A similar story applies for pseudoscalar mediators [746], as they behave like the longitudinal components of light axial vectors.

Our results could also be generalized by changing the type of DM considered. We have focused on

pseudo-Dirac DM because it is a simple option consistent with all cosmological constraints. It is also a conservative choice, since its thermal freeze-out region is the most difficult to probe. However, we do not expect any of our results to qualitatively depend on this choice. The coupling of the mediator to quarks crucially determines which meson decays are allowed because the initial meson states have definite P and C. But since the DM is generally produced at least semi-relativistically, it does not necessarily exit in the s-wave, which implies that the particular coupling of the mediator to DM is not as important. Therefore, we expect similar results to apply for scalar and Majorana DM, except that the falloff of the sensitivity near threshold, $m_V \approx 2m_\chi$, may differ. For this reason, we have not shown constraints from DM direct detection, which depend sensitively on the type of DM.

Finally, new physics that explicitly violates flavor could give rise to invisible or radiative neutral kaon decays [747, 748], but this must compete with stringent existing flavor constraints, such as from K^+ decays. For instance, in a sterile neutrino model, these constraints imply $\mathrm{Br}(K_L \to \nu\nu) \lesssim 10^{-10}$ [749], which could possibly be probed by dedicated searches, but is likely out of reach of the strategy described in this chapter. On a related note, one can consider models where the dark sector particles carry baryon number, which can then lead to baryon decays with missing energy [750], such as the invisible decay of neutral hyperons [751]. At NA64, this can appear as a missing energy signal if the hyperon is produced by, e.g. $\gamma p \to K^+\Lambda$ at large momentum transfer, so that it carries most of the photon's energy. However, the dark sector particle masses must fall within a narrow window so that the analogous nucleon decays are kinematically forbidden, to avoid much stronger constraints on proton and neutron decays, and there are again potentially strong but model-dependent flavor constraints.

7.6.3 Neutrino Constraints

Independent of dark matter, the signatures discussed here can be used to test any model that enhances meson decays with neutrinos in the final state. For example, a new gauge boson that couples to both quarks and neutrinos can mediate invisible vector meson decay or radiative pseudoscalar meson decay. Assuming the quarks and neutrinos have comparable charges, the latter process is likely more sensitive since it is suppressed by only g^2, where g is the gauge coupling, while the former is suppressed by g^4.

Many of the strongest constraints on new light gauge bosons, such as electron beam dump experiments, rely on the coupling to electrons. Thus, light gauge bosons that couple to a combination of B, L_μ, and L_τ [752, 753, 754, 755] are subject to fewer constraints. As a concrete example, a light $B - 3L_\tau$ gauge boson would be nonanomalous, assuming the introduction of a right-handed neutrino, and predominantly decay invisibly to τ neutrinos. The leading direct constraints on such a particle are largely from measurements of radiative pseudoscalar decays [756], which, as mentioned in section 7.6.1, could be significantly improved upon by missing energy experiments.

However, there are also much stronger indirect constraints on such gauge bosons, due to constraints

on neutrino non-standard interactions from measurements of neutrino oscillations [757, 758]. Therefore it may be more interesting to take a more model-independent, effective field theory point of view. As shown in Ref. [759], a number of four-fermion operators involving strange quarks or tau neutrinos are unconstrained by measurements of neutrino oscillations or the CEνNS process. For these operators, the best existing constraints come from the relatively weak bounds on invisible vector meson decay, and the potential 5 order of magnitude improvement of these bounds at LDMX would resolve this blind spot.

7.6.4 Experimental Prospects

The potential of the invisible meson decay signal immediately suggests several avenues of further study, to refine our rough estimates. As a first step, Monte Carlo simulations could be used to compute the flux and spectrum of Bremsstrahlung photons, account for the detailed composition of the front of the calorimeters where photoproduction dominantly occurs, and to better understand the detector (non-)response at NA64 and LDMX to the recoil energy left behind. The optical models used for the meson yields, which we estimate have uncertainties ranging from 25% to 50%, could be substantially improved by dedicated photoproduction measurements on nuclei at the relevant energies. Ideally, however, one would additionally perform in situ measurements to assess the meson yield and experimental efficiency, such as by "removing" tracks from meson production and decay in real events. At LDMX, it may also be possible to measure mesons produced in the target itself.

Meson production could also be considered as an explicit factor in the LDMX experimental design. For example, because of the A/Z^2 scaling of the photoproduction probability p_V, the meson yield could be significantly enhanced using a preshower primarily composed of light elements. However, this would also increase photonuclear backgrounds, presenting a tradeoff against the reach from A' Bremsstrahlung. In addition, since mesons can also be photoproduced in the target itself, the meson yield could be enhanced by, e.g. replacing the tungsten target with a thicker titanium target.

Further study of vector meson production and decay is highly motivated for a number of experiments. At electron beam dumps such as E137 or the proposed ILC beam dump [760], the exclusive photoproduction processes described here account for only a small fraction of the mesons produced. However, these mesons are highly energetic, leading to forward boosted dark matter that is more likely to hit a distant detector; it would thus be interesting to consider whether this effect could extend the beam dumps' reach. At NA64, there is already an opportunity to claim leading constraints on the invisible decays of ρ, ω, ϕ, and J/ψ, if the experimental and theoretical uncertainties can be accurately quantified. Finally, at future runs of NA64 and at LDMX, exploring this signature is essential to assessing the ultimate sensitivity to dark matter.

7.7 Appendix: Optical Model for Meson Photoproduction

As discussed in section 7.3, exclusive photoproduction includes both a coherent process, where the nucleus remains in the ground state and recoils as a whole, and an incoherent process, representing the effect of photoproduction off individual nucleons. Both of these processes are well described by a Glauber optical model. Such models have a long history; we will follow the notation of the most comprehensive review [761], but its results do not differ significantly from the first theoretical expressions written over fifty years ago, e.g. see Ref. [762]. First, the coherent differential cross section for photoproduction of a vector meson V is

$$\frac{d\sigma_c}{dt} = \frac{d\sigma_0}{dt}\bigg|_{\theta=0} \left| \int d^2b\, dz\, e^{i(\mathbf{q}_T\cdot\mathbf{b}+q_\parallel z)} n(b,z) \exp\left(-\frac{\sigma_V}{2}(1-i\alpha_V)\int_z^\infty dz'\, n(b,z')\right)\right|^2 \tag{7.8}$$

where $(d\sigma_0/dt)|_{\theta=0}$ is the forward differential cross section for photoproduction of V off a single nucleon, $n(b,z)$ is the nucleon number density, $\mathbf{q}_T$ and $q_\parallel$ are the transverse and longitudinal momentum transfer, σ_V is the scattering cross section of V on nucleons, and α_V is the ratio of the real to the imaginary part of the V-nucleon scattering amplitude. The first exponential factor represents the difference in phases due to photoproduction at different points in the nucleus, while the final factor accounts for absorption as the meson leaves the nucleus.

These absorptive final state interactions have a significant effect, as shown in Fig. 7.10. Of course, in reality, final state interactions actually produce other particles, and Monte Carlo simulations indicate that a substantial fraction of the inclusive meson yield arises from "sidefeeding", i.e. production in these secondary reactions [723]. However, for missing energy experiments we require a hard vector meson to carry the vast majority of the photon energy, so we are primarily interested in exclusive meson production; it is thus reasonable to treat the final state interactions as purely absorptive.

The coherent cross section is dominated at very low momentum transfer, $|t| \ll m_p^2$, and in this regime $t \approx -(q_\parallel^2 + q_T^2)$, where $q_\parallel \approx m_V^2/2E_\gamma$ is the minimum momentum transfer. In the high energy limit $q_\parallel r_{\rm nuc} \ll 1$, the coherent peak extends to $q_T \sim 1/r_{\rm nuc}$, leading to the narrow coherent peaks shown in Fig. 7.11. For heavy nuclei at few-GeV energies, we have $q_\parallel r_{\rm nuc} \gtrsim 1$, which leads to the suppressed coherent cross sections shown in Fig. 7.4.

It is interesting to compare these results to the cross section for A' Bremsstrahlung, which can be estimated in the Weizsäcker–Williams approximation (e.g. see Ref. [711]). The integral in Eq. (7.8) effectively defines a form factor qualitatively similar to the elastic nuclear form factor in A' Bremsstrahlung, with both falling off for $t \gtrsim 1/r_{\rm nuc}^2$. However, A' Bremsstrahlung is a $2 \to 3$ process with an intermediate virtual photon, leading to a differential cross section additionally weighted by $(t - t_{\rm min})/t^2$ which softens the dependence on $r_{\rm nuc}$. This is responsible for the Z^2 scaling of A' Bremsstrahlung at low $m_{A'}$, in contrast to the rough $A^{4/3}$ scaling for coherent photoproduction.

Because $t_{\rm min} \sim (m_{A'}^2/2E_e)^2$ for A' Bremsstrahlung, the falloff in A' Bremsstrahlung for high $m_{A'}$ is similar to the falloff in coherent photoproduction for high m_V. However, the absorptive

term in Eq. (7.8) implies that not all nucleons in a heavy nucleus effectively contribute to coherent photoproduction. This effectively lowers the nuclear radius by an order-one factor, which is the reason the meson decay signature reaches somewhat higher in $m_{A'}$ than A' Bremsstrahlung before being significantly form factor suppressed. For example, at LDMX Phase II, the finite beam energy suppresses coherent ϕ photoproduction by a factor of ~ 4, but it suppresses A' Bremsstrahlung at $m_{A'} = m_\phi$ by over two orders of magnitude.

Next, the incoherent differential cross section is

$$\frac{d\sigma_i}{dt} = \frac{d\sigma_0}{dt} \int d^2b\, dz\, n(b,z) \exp\left(-\sigma_V \int_z^\infty dz'\, n(b,z')\right) \times \left|1 - \int_{-\infty}^z dz''\, n(b,z'') \frac{\sigma_V}{2}(1 - i\alpha_V) e^{iq_\parallel (z''-z)} \exp\left(-\frac{\sigma_V}{2}(1-i\alpha_V) \int_{z''}^z dz'''\, n(b,z''')\right)\right|^2 . \quad (7.9)$$

Here, the first factor accounts for absorption, while the final factor is a "shadowing" correction accounting for destructive interference between photoproduction at z, and photoproduction at z'' followed by scattering at z. (This equation has a misprint in Ref. [761], which we have corrected.) Both of these effects are comparably important for heavy nuclei, as shown in Fig. 7.10. Because shadowing is a coherent effect, it becomes more important at high energies, leading to the decrease of $f_{\rm inc}$ with increasing energy shown in Fig. 7.4. Measurements of the angular distribution $d\sigma_0/dt$ are well-described by exponentials $e^{-B|t|}$, and following the most recent measurements, we take $B = 6.4$ GeV^{-2} for ρ [763], $B = 5.4$ GeV^{-2} for ω [764], and $B = 3.0$ GeV^{-2} for ϕ [765, 766]. For the J/ψ, we take $B = 4.7$ GeV^{-2} as measured by HERA [726]. These quantities determine the differential cross section at high momentum transfer, shown in Fig. 7.11.

As discussed in section 7.2, we demand a nucleon recoil energy $T_p \leq 100$ MeV for incoherent photoproduction, but the precise veto efficiency is somewhat uncertain. However, because the LDMX and NA64 calorimeters are dominantly comprised of heavy nuclei, where coherent photoproduction generally dominates, the choice of cutoff does not qualitatively affect our results. Varying the cutoff by a factor of 2 affects the light meson yields at NA64 by less than 5%, while at LDMX it affects the ρ and ω yields at the 10% level. Coherent photoproduction is suppressed for ϕ at LDMX and J/ψ at NA64, where the choice of cutoff leads to a uncertainty of up to 50%.

For the parameters σ_V and α_V, we adopt the values of Model I of Ref. [761], which were motivated by quark model estimates and chosen to adequately describe coherent photoproduction data. The results do not depend strongly on the nuclear density model, but we use a Woods–Saxon distribution [767],

$$n(r) \propto \frac{1}{1 + e^{(r-c)/a}} \quad (7.10)$$

where $c = 1.12\, A^{1/3}$ fm and $a = 0.545$ fm. We fix the total single nucleon photoproduction cross sections σ_0 to data, as described in section 7.3.

Because coherent production is so sharply forward peaked, the coherent and incoherent channels

may be measured separately by placing restrictions on t. As reviewed in Ref. [761], coherent ρ and ω photoproduction have been thoroughly measured for a variety of nuclei and photon energies, and are well-described by optical models to within an uncertainty of at most 25%. Coherent ϕ photoproduction is less well-measured; the data can still be fit, but with a larger uncertainty in α_ϕ and σ_ϕ.

There is much less data available for incoherent photoproduction, particularly at high photon energies, and the data that exists is more ambiguous. At the time of writing of Ref. [761], the data for incoherent ρ photoproduction was sufficient to confirm the existence of a shadowing effect, but not enough to investigate it in detail. We have chosen to implement the simplest version of it, but theoretically reasonable modifications of Eq. (7.9) could change the cross section by as much as 50%, while still fitting the data comparably well.

More recently, a number of experiments have measured incoherent photoproduction on nuclei, motivated by anomalous results for ϕ mesons at SPring-8 [768] (for a recent review, see Ref. [769]). The measurements indicate a steep falloff of f_{inc} with increasing A for low photon energies, corresponding to an absorption cross section σ_ϕ dramatically above the quark model expectation. Several theoretical works have proposed explanations based on "in-medium" modifications of the ϕ meson width, while Ref. [770] considers the alternative of ω to ϕ transitions. Currently, these puzzling results do not seem to have a canonical explanation, and different experiments are not fully in agreement; thus, we regard our estimate of ϕ production at LDMX Phase I to be uncertain within a factor of 2. Fortunately, these in-medium effects should become less important at the higher energies of LDMX Phase II and NA64, where incoherent photoproduction is in any case subdominant.

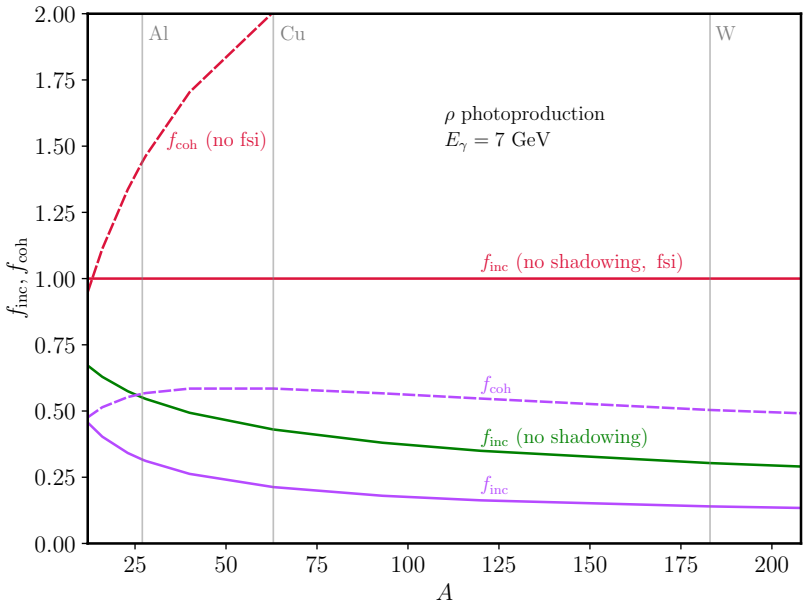

Figure 7.10: Illustration of the effects of parts of Eqs. (7.8) and (7.9), with full results in purple. Shadowing and absorptive final state interactions play comparable roles in reducing the incoherent cross section. Without final state interactions, the coherent cross section would be much larger, with $f_{\rm coh} \sim A^{1/3}$.

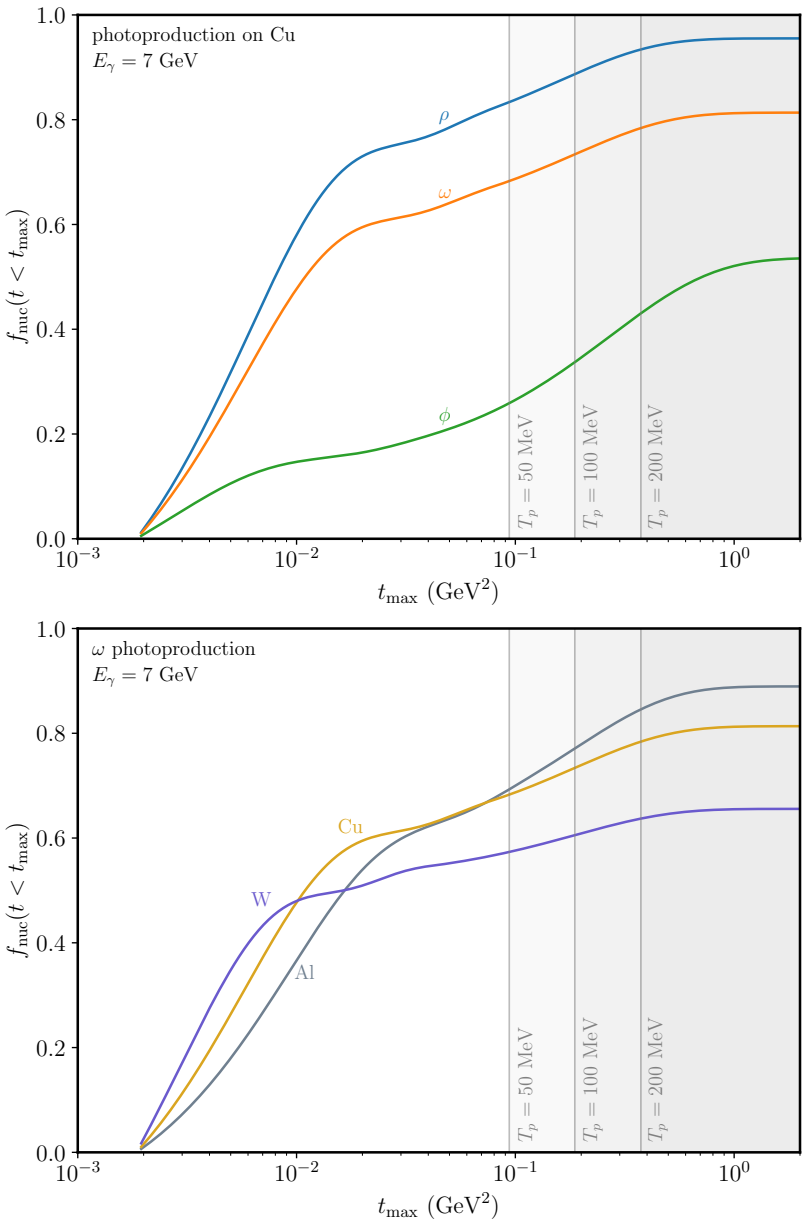

Figure 7.11: Illustration of the integrated differential cross section for meson production, for several different mesons (left) and nuclei (right), at LDMX Phase II energies. Coherent production is sharply peaked at low t, especially for heavier nuclei. Incoherent production extends significantly higher in t, and we show vertical contours of the associated nucleon recoil energy.

Chapter 8

Continuous Spin Fields

This chapter is based on *Interactions of Particles with "Continuous Spin" Fields*, by P. Schuster, N. Toro, K. Zhou, JHEP 04, 010 (2023)

Abstract

Powerful general arguments allow only a few families of long-range interactions, exemplified by gauge field theories of electromagnetism and gravity. However, all of these arguments presuppose that massless fields have zero spin scale (Casimir invariant) and hence exactly boost invariant helicity. This misses the most general behavior compatible with Lorentz symmetry. We present a Lagrangian formalism describing interactions of matter particles with bosonic "continuous spin" fields with arbitrary spin scale ρ. Remarkably, physical observables are well approximated by familiar theories at frequencies larger than ρ, with calculable deviations at low frequencies and long distances. For example, we predict specific ρ-dependent modifications to the Lorentz force law and the Larmor formula, which lay the foundation for experimental tests of the photon's spin scale. We also reproduce known soft radiation emission amplitudes for nonzero ρ. The particles' effective matter currents are not fully localized to their worldlines when $\rho \neq 0$, which motivates investigation of manifestly local completions of our theory. Our results also motivate the development of continuous spin analogues of gravity and non-Abelian gauge theories. Given the correspondence with familiar gauge theory in the small ρ limit, we conjecture that continuous spin particles may in fact mediate known long-range forces, with testable consequences.

8.1 Motivation and Overview

Relativity and quantum mechanics imply that long-range forces are mediated by massless particles, which were first classified by Wigner [771]. Powerful restrictions on their interactions have been derived from the covariance of amplitudes for soft radiation emission [772, 773, 774], as well as the consistency of coupling to perturbative general relativity [775] and gauge theories, e.g. see Refs. [776, 777, 778]. These results underlie the common belief that familiar gauge theories and general relativity encompass the full range of possibilities for long-distance physics in nature.

However, these arguments ignored the most general type of massless particle in Wigner's classification, a "continuous spin" particle (CSP) with nonzero spin Casimir $W^2 = -\rho^2$, where we call ρ the spin scale. The bosonic CSP has an infinite tower of integer helicity states. Just as with ordinary massive particles, the helicity states are mixed under Lorentz transformations by an amount controlled by the spin scale. As $\rho \to 0$ one smoothly recovers the familiar massless states with Lorentz invariant helicity.

Recent results suggest that this limiting behavior applies well beyond kinematics. In Refs. [779, 780], the arguments of Ref. [772] were first extended to bosonic CSPs, yielding well-behaved soft factors. Furthermore, Lorentz covariance and unitarity imply the soft factors are scalar-like, vector-like, or tensor-like. In each case, for $\rho \ll \omega$ the soft factors reduce to those for minimally coupled massless scalars, photons, and gravitons respectively, with the other helicities decoupling. This "helicity correspondence" raises the intriguing possibility that the massless particles in our universe may in fact be CSPs, with deviations from familiar theories in the deep infrared.

More recently, Ref. [781] constructed the first gauge field theory for a bosonic CSP, which reduces as $\rho \to 0$ to a sum of free actions for each integer helicity, e.g. a Maxwell action for $h = \pm 1$ and a Fierz–Pauli action for $h = \pm 2$. (For reviews and discussion, see Refs. [782, 783, 784, 785].) This continuous spin field action was quickly generalized to lower dimensions [786] and the fermionic [787] and supersymmetric [788, 789] cases, illustrating the robustness of its approach of encoding spin as orientation in an auxiliary "vector superspace." Other formalisms, including constrained metric-like, frame-like, and BRST [790, 791] formulations, have also been used to construct actions for fermionic [792, 793] and supersymmetric [794, 795, 796, 797] continuous spin fields, as well as those in higher-dimensional [798, 799, 800] and (A)dS [801, 802, 803, 804, 805, 806] spaces. Relations between these formulations and the vector superspace formulation are discussed in Refs. [782, 799, 788].

The key outstanding physical question is to understand how continuous spin fields couple to matter. Interactions of continuous spin fields with matter fields were studied in Refs. [807, 808, 809, 810], but they were gauge invariant only to leading order, like the Berends–Burgers–van Dam currents for higher spin fields [811]. Furthermore, the currents that could reduce to minimal couplings as $\rho \to 0$ do not exist for matter fields of equal mass. All of the other currents are nonminimal: they correspond to higher-dimension operators such as charge radii, with vanishing soft factors. While they are a valuable first step, they are less interesting phenomenologically as they do not capture the

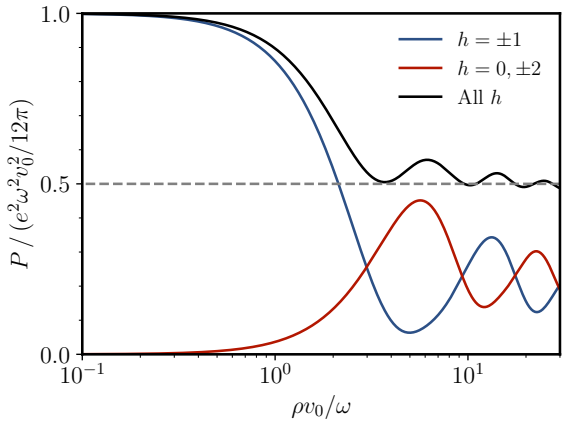

Figure 8.1: Power radiated by an nonrelativistic oscillating charged particle, normalized to the ordinary Larmor result, for a photon with spin scale ρ. We show power emitted into the ordinary helicities $h = \pm 1$, the "nearest neighbor" helicities $h = 0, \pm 2$, and the total in all integer helicities.

leading, inverse-square forces we observe.

In this chapter, we aim to resolve both of these problems, putting the study of matter interactions on a firm footing. We depart from previous work by coupling the continuous spin field to a spinless matter particle with worldline $z^\mu(\tau)$, via the action

$$S = -m\int d\tau + \frac{1}{2}\int d^4x\,[d^4\eta]\,\left(\delta'(\eta^2+1)(\partial_x\Psi)^2 + \frac{1}{2}\,\delta(\eta^2+1)(\Delta\Psi)^2\right) + \int d^4x\,[d^4\eta]\,\delta'(\eta^2+1)\,\Psi(\eta,x)\int d\tau\, j(\eta, x - z(\tau), \dot{z}(\tau)). \tag{8.1}$$

The first line contains the free gauge field action of Ref. [781], which is integrated over a bosonic superspace (x^μ, η^μ), and depends on ρ via the operator $\Delta = \partial_x \cdot \partial_\eta + \rho$. The final term couples the field to a current sourced by the matter particle. The interaction is exactly gauge invariant when j satisfies the local continuity condition $\Delta j = 0$ up to total τ-derivatives. We classify all solutions to this equation as scalar-like, vector-like, or non-minimal, where the first two families reduce to minimal scalar or vector couplings as $\rho \to 0$.

For each choice of j, we can use the action (8.1) to compute various observables. "Integrating out" the field Ψ by solving its equations of motion yields an effective action for the matter particles, which contains static and velocity-dependent potentials. Evaluating the action for a given Ψ yields the force on a matter particle in a background field, while evaluating it for a given $z^\mu(\tau)$ yields the field produced by a moving particle. Remarkably, we find that observables involving only null modes of the field, such as radiation emission and forces in a radiation background, are universal. That is, for all scalar-like or vector-like currents the results depend only on ρ, and not on the details of the current.

Universality allows us to predict specific deviations from familiar results in electromagnetism. For example, if the photon is a CSP, the force per charge on a particle with any vector-like current in an $h = \pm 1$ plane wave background with angular frequency ω is

$$\frac{\mathbf{F}}{e} = (\mathbf{E} + \mathbf{v} \times \mathbf{B}) - \frac{\rho^2}{4\omega^2} \left((\mathbf{E} \cdot \mathbf{v}_\perp)\mathbf{v}_\perp + \mathbf{E}\, v_\perp^2/2 \right) + \dots \tag{8.2}$$

where $\mathbf{v}_\perp = \mathbf{v} - (\mathbf{v} \cdot \hat{\mathbf{k}})\hat{\mathbf{k}}$ is the particle's velocity transverse to the direction of propagation $\hat{\mathbf{k}}$. The force can be written exactly in terms of Bessel functions, and is well-behaved for arbitrary ρ/ω. As another example, if such a particle performs nonrelativistic sinusoidal motion with characteristic velocity v_0 and frequency ω, the total power it emits into radiation modes is

$$P = \frac{e^2\omega^2 v_0^2}{12\pi} \left(1 - \frac{9}{80} \frac{\rho^2 v_0^2}{\omega^2} + \dots \right) \tag{8.3}$$

where the leading term matches the standard Larmor formula, and the first correction includes radiation emitted into helicities $h = 0, \pm 2$ and a reduction of radiation emitted into $h = \pm 1$. As shown in Fig. 8.1, we can compute the power for arbitrary $\rho v_0/\omega$, and it always remains finite, even in the limit $\rho v_0 \gg \omega$ where radiation is produced with many helicities.

The force between two particles is not universal, depending on the details of the current, but still obeys helicity correspondence. For example, we will show that some simple vector-like currents predict no deviations from Coulomb's law, while others predict corrections at long distances. The underlying reason that many equally "minimal" currents exist is that these currents are not fully localized to the particle's worldline. We expect this feature can be removed in a more fundamental description involving additional "intermediate" fields. Exploring such descriptions is a key next step, and might in turn identify certain preferred currents. However, with our present theory we can already recover manifestly causal particle dynamics assuming appropriate boundary conditions for j.

Another key next step would be the formulation of continuous spin fields with non-Abelian symmetry, which are necessary to consistently describe tensor-like currents, or to embed a CSP photon within the Standard Model. Such developments would be exciting because of the possible relevance of continuous spin to outstanding problems in fundamental physics. In particular, the enhanced gauge symmetry of a continuous spin field could shed light on the cosmological constant and hierarchy problems, while the presence of weakly coupled "partner" polarizations and modifications to long-range force laws may have bearing on dark matter and cosmic acceleration. Currently these applications are only speculative, but the results derived here already make it possible to probe the spin scale of the photon experimentally.

Remarkably, observable consequences of nonzero ρ have never been considered before this work, besides the pioneering attempt of Ref. [812] to identify neutrinos with fermionic CSPs. The underlying reason is that continuous spin physics has been shrouded in confusion since its inception. It is often assumed that the infinite number of polarization states would render physical observables divergent,

but the helicity correspondence implies that almost all of these states decouple. Thus, real experiments will measure finite values for, e.g. Casimir forces and the heat capacity of the vacuum. All helicities are emitted in Hawking radiation, but the total power remains finite because of the falling greybody factors for high helicity modes. Finally, as we have already stated above, forces remain finite despite being mediated by an infinite number of helicity states, and radiation emission is finite even in the $\rho \to \infty$ limit where all helicities are produced.

Confusion has also stemmed from field-theoretic "no-go" results. Several authors showed in the 1970s that it was impossible to construct Lorentz invariant, local theories of gauge invariant fields that created and annihilated CSPs [813, 814, 815, 816, 817]. However, under such restrictive assumptions it would also be impossible to construct electromagnetism, which requires a gauge potential, or general relativity, which in addition has no local gauge invariant operators. There are also plentiful no-go theorems concerning interactions of "higher spin" fields with $|h| > 2$ [818]. These theorems indeed imply we cannot write currents which reduce to minimal couplings of higher spin fields in the $\rho \to 0$ limit, but they do not pose any obstruction to the existence of scalar-like or vector-like currents.

The chapter is organized as follows. In section 8.2, we review the kinematics of CSPs and the action for the bosonic continuous spin field. In section 8.3, we couple this field to a current sourced by a matter particle and identify families of scalar-like and vector-like currents. In section 8.4 we investigate the localization of simple currents in spacetime, and show how appropriate choices of current yield manifestly causal dynamics. In section 8.5, we compute static and velocity-dependent forces between a pair of matter particles, as well as the force on a matter particle in a radiation background, which is universal. In section 8.6, we find the universal radiation emitted from an accelerating particle in arbitrary motion, and use the special case of an abruptly kicked particle to recover the soft factors found in Refs. [779, 780]. Finally, in section 8.7 we discuss future directions and speculative applications. Detailed derivations are collected in appendices, which are referenced throughout the text.

Conventions

We work in natural units, $\hbar = c = \epsilon_0 = 1$. We denote the Minkowski metric by $g_{\mu\nu}$, and use a $(+---)$ metric signature. Fourier transforms obey $f(k) = \int d^4x\, e^{ik\cdot x} f(x)$, so that a spacetime derivative $\partial^\mu = \partial^\mu_x$ becomes $-ik^\mu$. Vector superspace coordinates are naturally defined with raised indices, so that $\eta^\mu = (\eta^0, \boldsymbol{\eta})$, and similarly we write $k^\mu = (\omega, \mathbf{k})$ and $x^\mu = (t, \mathbf{r})$. Vector superspace derivatives are always written as ∂^μ_η, with the η explicit.

When manipulating tensors, symmetrizations and antisymmetrizations of n indices are defined without factors of $1/n!$, complete contractions of symmetric tensors are denoted by a dot, and a prime denotes a contraction with the metric, i.e. a trace. For example, for a totally symmetric rank 3 tensor $S^{\mu\nu\rho}$, we have $S^{(\mu\nu\rho)} = 6S^{\mu\nu\rho}$, $S \cdot S = S^{\mu\nu\rho} S_{\mu\nu\rho}$, and $S'^\mu = g_{\nu\rho} S^{\mu\nu\rho}$. Two primes denotes

a double trace, i.e. a contraction with two copies of the metric.

For a null four-vector k^μ, we will often introduce a basis of null complex frame vectors $(k^\mu, q^\mu, \epsilon_+^\mu, \epsilon_-^\mu)$, where $\epsilon_+^* = \epsilon_-$, and the only nonzero inner products are $\epsilon_+ \cdot \epsilon_- = -2$ and $q \cdot k = 1$. (This normalization differs from Refs. [779, 780] but matches Ref. [781].) This implies

$$g_{\mu\nu} = (k_\mu q_\nu + q_\mu k_\nu) - \frac{1}{2}(\epsilon_{+,\mu}\epsilon_{-,\nu} + \epsilon_{-,\mu}\epsilon_{+,\nu}). \tag{8.4}$$

We define the Levi–Civita symbol to obey $\epsilon^{0123} = 1$, and fix the handedness of the basis by demanding $\epsilon^{\mu\nu\rho\sigma} = k^{[\mu} q^\nu \epsilon_+^\rho \epsilon_-^{\sigma]}/2i$. As a concrete example, if $k^\mu = (\omega, 0, 0, \omega)$, we can choose

$$q^\mu = (1/2\omega, 0, 0, -1/2\omega), \qquad \epsilon_\pm^\mu = (0, 1, \pm i, 0). \tag{8.5}$$

8.2 The Free Theory

In this section, we set up the theory of a free bosonic continuous spin field. We begin in subsection 8.2.1 by reviewing the continuous spin states that such a field must create and annihilate. In subsection 8.2.2 we write down the action and immediately specialize to $\rho = 0$, where familiar gauge theories are recovered as special cases. Finally, in subsection 8.2.3 we consider nonzero ρ and discuss the resulting qualitative changes.

8.2.1 Continuous Spin States in Context

In a relativistic quantum theory, states transform under translations P^μ and rotations and boosts $J^{\mu\nu}$, which generate the connected Poincare group. The state space of an elementary particle is an irreducible unitary representation of this group. For any such particle, we can always diagonalize translations to yield states obeying $P^\mu|k,\sigma\rangle = k^\mu|k,\sigma\rangle$, where k^μ is the particle's four-momentum and σ denotes its internal "polarization" state. The nontrivial physical content of each representation is given by the action of "little group" transformations [771], which keep the four-momentum constant but may change the internal state. In general, the little group is generated by the elements of the Pauli–Lubanski vector $W^\mu = \frac{1}{2}\epsilon^{\mu\nu\rho\sigma} J_{\nu\rho} P_\sigma$, which has three independent components because $k \cdot W\,|k,\sigma\rangle = 0$. Representations are classified by the values of the Casimir invariants $P^2 = m^2$ and $W^2 = -\rho^2$, where m is the mass and we call ρ the spin scale.

For massive particles, with $P^2 > 0$, we can boost the particle's momentum to $k^\mu = (m, 0, 0, 0)$. In this case, the nonzero components of the Pauli–Lubanski vector are the rotation generators $\mathbf{W} = m\mathbf{J}$. The little group is therefore the rotation group $SO(3)$, whose projective representations are characterized by an integer or half-integer spin $S \geq 0$, corresponding to spin scale $\rho = m\sqrt{S(S+1)}$. These are the usual massive spin-s particles, often encountered in the quantum mechanics of atoms and nuclei.

This familiar setting allows us to give the spin scale an intuitive physical meaning. Label the states of a moving particle as $|k,h\rangle$ where the helicity $h=-s,\ldots,s$ is the projection of the spin in the particle's direction of motion, $\mathbf{J}\cdot\hat{\mathbf{k}}$. Then an infinitesimal Lorentz boost by $\mathbf{v}_\perp$ in a transverse direction mixes these states into each other, $U(\mathbf{v}_\perp)\,|k,h\rangle=\sum_{h'}c_{hh'}|k',h'\rangle$ where the mixing coefficients for $h\neq h'$ scale as positive powers of $\rho\,v_\perp/k^0$. In other words, the spin scale characterizes the mixing of helicity states under Lorentz transformations.

We can carry these lessons to the case of massless particles, $P^2=0$, where the little group generators for a general momentum k^μ are

$$R=q\cdot W,\quad T_\pm=\epsilon_\pm\cdot W \tag{8.6}$$

and q and $\epsilon_\pm$ are the frame vectors defined in the conventions. These operators obey the commutation relations $[R,T_\pm]=\pm T_\pm$, with $T_+^\dagger=T_-$, which is the algebra of $\mathrm{ISO}(2)=E(2)$, the isometry group of a plane. (See Ref. [779] for further discussion.) Concretely, if $k^\mu=(\omega,0,0,\omega)$ and we choose the other frame vectors as in (8.5), then $R=\mathbf{J}\cdot\hat{\mathbf{k}}$ is a rotation about the axis of the three-momentum and $T_\pm$ are combinations of transverse boosts and rotations. By diagonalizing the helicity operator R, we can work with states obeying $R\,|k,h\rangle=h\,|k,h\rangle$, just as in the massive case.

Since the helicity operator is not inherently Lorentz invariant, we expect $T_\pm$ to mix helicity states by an amount controlled by the spin scale. Indeed, the commutation relations yield

$$T_\pm\,|k,h\rangle=\rho\,|k,h\pm1\rangle. \tag{8.7}$$

This equation implies that the ladder of helicity states does not end! That is, a single massless particle generically has *infinitely* many polarizations, which is tied to the non-compactness of the little group $E(2)$. To avoid this situation, textbook treatments specialize to $\rho=0$, sometimes implicitly, recovering the familiar irreducible representations which have only a single internal state $|k,h\rangle$ with Lorentz invariant helicity.

By contrast, the "continuous spin" representations are characterized by a nonzero spin scale ρ, which can take on a continuum of real values. Their historical name often leads to the misconception that we are allowing the *helicity* to take on continuous values, but h must always be integer or half-integer to yield a projective representation of the Poincare group. A bosonic continuous spin representation contains states of all integer h, a fermionic continuous spin representation contains all half-integer h, and supersymmetry unifies the two into one multiplet [788]. One can Fourier transform the helicity basis to reach the "angle" basis $|k,\theta\rangle=\sum_h e^{ih\theta}\;|k,h\rangle$, where the little group transformations take a simpler form [779]. Although the angle basis provides a geometric picture for the little group action, we will work primarily in the helicity basis, as it offers the most natural description of physical reactions.

For completeness, we note that the continuous spin representations can also be constructed by

starting with a massive particle representation, and taking the simultaneous limits $m \to 0$ and $S \to \infty$ with mS fixed [819]. However, that description will not be useful here.

From States to Fields

In the nonrelativistic limit, it is straightforward to describe the interactions of atoms and nuclei with arbitrarily high spin. However, while these particles evidently have no trouble interacting in our Lorentz invariant universe, we have a more difficult time describing such processes using the standard tool of relativistic quantum field theory.

The basic problem is that the building blocks of quantum field theory are local fields transforming in representations of the Lorentz group, but these fields must create and annihilate particles transforming in little group representations. Outside of the simplest cases, there will be a mismatch in the number of degrees of freedom. For example, a massive spin 1 particle has 3 polarizations, but is usually described by a vector field $A^\mu(x)$ with 4 components. To remove the extra degree of freedom, one must use a Lagrangian whose equations of motion yield a single constraint, such as $\partial \cdot A = 0$. More generally, a bosonic spin s particle with $2s+1$ degrees of freedom can be described by a symmetric rank s tensor field with $(s+3)(s+2)(s+1)/6$ degrees of freedom, provided one chooses a special Lagrangian which yields an intricate set of constraints. This approach was pioneered by Singh and Hagen for arbitrary spin [820, 821], but to this day it remains challenging to use.

The situation is even more subtle for massless particles. The CPT theorem implies that the helicities of massless particles always come in opposite-sign pairs, where $h = \pm 1$ for the photon and $h = \pm 2$ for the graviton. To describe the two photon polarizations with a four-component vector field one must use a Lagrangian with a built-in redundancy, or "gauge symmetry," so that the two unwanted degrees of freedom decouple or are non-dynamical. Describing the graviton with a symmetric tensor field $h_{\mu\nu}(x)$ requires removing eight degrees of freedom, and hence a more complex gauge symmetry. More generally, gauge field theories for free particles of any helicity were developed by Fang and Fronsdal [822, 823], and involve high-rank symmetric tensors. As with the massive case, manipulating these tensors at high ranks is cumbersome. In addition, the gauge symmetries place increasingly severe constraints on the fields' interactions at higher ranks, as we will discuss in subsection 8.3.1.

8.2.2 Embedding Fields in Vector Superspace

Vector Superspace Actions

We now turn to the problem of constructing a free field which creates and annihilates a single bosonic continuous spin particle, which has all integer helicities. Given the preceding discussion, one can expect such a field theory must involve symmetric tensor fields of arbitrarily high rank, and an accompanying set of gauge symmetries to account for extra degrees of freedom. However,

manipulating all of these fields would be technically painful.

Relatively recently, Ref. [781] introduced the first action for a free bosonic continuous spin field, which is the basis for the treatment of interactions in this chapter. (Predecessors to this result include a covariant equation of motion [824] and an alternative action which propagated a continuum of CSPs [825].) The key is to avoid the complications of high-rank tensors by introducing fields that depend on an auxiliary four-vector coordinate η^μ in addition to the spacetime coordinate x^μ. Lorentz transformations act on this "vector superspace" by $x \to \Lambda x$ and $\eta \to \Lambda\eta$, so that the Poincare generators are

$$P^\mu = i\,\partial_x^\mu, \quad J^{\mu\nu} = i\,(x^{[\mu}\partial_x^{\nu]} + \eta^{[\mu}\partial_\eta^{\nu]}). \tag{8.8}$$

A field $\Psi(\eta, x)$ analytic in η can be decomposed into component symmetric tensor fields of arbitrarily high rank. For example, a direct Taylor expansion would give $\Psi(\eta, x) = \psi^{(0)}(x) + \eta^\mu\psi_\mu^{(1)}(x) + \eta^\mu\eta^\nu\psi_{\mu\nu}^{(2)}(x) + \ldots$, though we will shortly see that a slightly different expansion is more useful.

The action for the field is [781]

$$S[\Psi] = \frac{1}{2}\int d^4x\,[d^4\eta]\,\left(\delta'(\eta^2+1)(\partial_x\Psi)^2 + \frac{1}{2}\,\delta(\eta^2+1)(\Delta\Psi)^2\right) \tag{8.9}$$

where $\Delta = \partial_\eta\cdot\partial_x + \rho$. To explain the notation, the delta function and its derivative imply the action only depends on Ψ and its first η-derivative on the unit hyperboloid $\eta^2+1=0$, and thus remains unchanged under the gauge symmetry $\delta\Psi = (\eta^2+1)^2\chi(\eta,x)$. The field Ψ is defined for all η, but field values far off the unit hyperboloid are pure gauge, with no physical meaning. The regulated integration measure $[d^4\eta]$ permits standard manipulations such as integration by parts. The η integrals in this subsection can be evaluated using

$$\int [d^4\eta]\,\delta(\eta^2+1)\,F(\eta) = \left(1 - \frac{1}{8}\partial_\eta^2 + \frac{1}{192}\partial_\eta^4 - \ldots\right)F(\eta)\Big|_{\eta=0}, \tag{8.10}$$

$$\int [d^4\eta]\,\delta'(\eta^2+1)\,F(\eta) = \left(1 - \frac{1}{4}\partial_\eta^2 + \frac{1}{64}\partial_\eta^4 - \ldots\right)F(\eta)\Big|_{\eta=0}. \tag{8.11}$$

These generating functions are derived in appendix 8.8.1, and all other η-space integration identities needed in this chapter are derived in appendix 8.8.2. The deeper geometric motivation for the action is discussed in appendix 8.8.3 and Ref. [781].

In the rest of this subsection, we will specialize to $\rho = 0$ and show how (8.9) contains the action, equation of motion, and gauge symmetry for familiar massless particles of arbitrary integer helicity. For instance, the derivatives on the right-hand sides of (8.10) and (8.11) will produce tensor contractions between the component fields. The purpose of this exercise is to gradually build facility with η-space computations, and to demonstrate the power of the formalism, which can replace an infinite set of tensor manipulations with a single integral.

Decomposing the Action

We can write the action in terms of uncoupled component tensor fields by defining

$$\Psi(\eta, x) = \sum_{n\geq 0} P_{(n)}(\eta) \cdot \phi^{(n)}(x) \tag{8.12}$$

$$= \phi(x) + \sqrt{2}\,\eta^\mu A_\mu(x) + (2\eta^\mu\eta^\nu - g^{\mu\nu}(\eta^2+1))\,h_{\mu\nu}(x) + \dots. \tag{8.13}$$

where the $\phi^{(n)}$ are symmetric rank n tensors, and the $P_{(n)}$ are the polynomials

$$P_{(n)}^{\mu_1\cdots\mu_n} = 2^{n/2}\left(\eta^{\mu_1}\cdots\eta^{\mu_n} - \frac{1}{4(n-2)!}\,g^{(\mu_1\mu_2}\eta^{\mu_3}\cdots\eta^{\mu_n)}(\eta^2+1)\right). \tag{8.14}$$

It is straightforward to see how the action reduces in simple cases. First, if only $\phi^{(0)} = \phi$ is nonzero, then only the first term of (8.9) is nonzero, giving

$$S[\Psi] = \frac{1}{2}\int d^4x\,[d^4\eta]\,\delta'(\eta^2+1)(\partial_x\phi)^2 = \frac{1}{2}\int d^4x\,(\partial_x\phi)^2 \tag{8.15}$$

which is the action for a massless scalar field. If only $\phi^{(1)}_\mu = A_\mu$ is nonzero, the terms are

$$\frac{1}{2}\int [d^4\eta]\,\delta'(\eta^2+1)\,(\partial_x\Psi)^2 = -\frac{1}{2}\,\partial_\rho A_\mu\,\partial^\rho A^\mu \tag{8.16}$$

$$\frac{1}{2}\int [d^4\eta]\,\frac{1}{2}\delta(\eta^2+1)(\partial_\eta\cdot\partial_x\Psi)^2 = \frac{1}{2}\,(\partial_\mu A^\mu)^2 \tag{8.17}$$

which sum to the canonically normalized Maxwell action,

$$S[\Psi] = -\frac{1}{4}\int d^4x\,F_{\mu\nu}F^{\mu\nu}. \tag{8.18}$$

If both $\phi^{(0)}$ and $\phi^{(1)}$ are nonzero, there is no cross-coupling between them because their product is linear in η, and only even powers of η contribute to the integrals.

Similarly, if only $\phi^{(2)}_{\mu\nu} = h_{\mu\nu}$ is nonzero, one recovers the Fierz–Pauli action, which describes the metric perturbation in linearized gravity. As explained in Ref. [781], one can recover a Fronsdal action for each of the $\phi^{(n)}$, and furthermore there are no cross-couplings between fields of different ranks. This can be efficiently derived using orthogonality theorems for the polynomials $P_{(n)}$ shown in appendix 8.9.1, though it need not be read to follow the main text.

Decomposing the Equation of Motion

By formally varying (8.9) with respect to Ψ, we obtain the equation of motion

$$\delta'(\eta^2+1)\,\partial_x^2\Psi - \frac{1}{2}\,\Delta\,(\delta(\eta^2+1)\,\Delta\Psi) = 0. \tag{8.19}$$

In general, we can integrate this against $P_{(n)}$ to extract the equation of motion for $\phi^{(n)}$.

For example, if we trivially multiply by $P_{(0)} = 1$ and integrate over η, the second term in (8.19) does not contribute because it is a total η derivative. The first term yields

$$0 = \int [d^4\eta]\, \delta'(\eta^2+1)\, \partial_x^2 \Psi \tag{8.20}$$

$$= \int [d^4\eta]\, \delta'(\eta^2+1)\, \left(\partial_x^2 \phi + \sqrt{2}\, \eta^\mu \partial_x^2 A_\mu + (2\eta^\mu \eta^\nu - g^{\mu\nu}(\eta^2+1))\, \partial_x^2 h_{\mu\nu} + \dots\right) \tag{8.21}$$

$$= \partial_x^2 \phi \tag{8.22}$$

as expected. Above, the contribution of A_μ vanished since it is linear in η, and the contribution of $h_{\mu\nu}$ cancels after evaluating the integral. More generally, the decoupling of all other $\phi^{(n)}$ immediately follows from the orthogonality theorems in appendix 8.9.1.

To give one more example, integrating the equation of motion against $P^\mu_{(1)} = \sqrt{2}\,\eta^\mu$ gives

$$0 = \sqrt{2} \int [d^4\eta]\, \delta'(\eta^2+1)\, \eta^\mu\, \partial_x^2 \Psi - \frac{1}{2} \eta^\mu\, \Delta\, (\delta(\eta^2+1)\, \Delta \Psi) \tag{8.23}$$

$$= \sqrt{2} \int [d^4\eta]\, \delta'(\eta^2+1)\, \eta^\mu\, \partial_x^2 \Psi + \frac{1}{2} \partial_x^\mu\, (\delta(\eta^2+1)\, \Delta \Psi) \tag{8.24}$$

$$= -\partial_x^2 A^\mu + \partial_x^\mu \partial \cdot A \tag{8.25}$$

again as expected, where ϕ and $h_{\mu\nu}$ decouple by parity considerations, and again the $\phi^{(n)}$ in general decouple by orthogonality. Of course, with more work we recover the linearized Einstein equations at rank 2, and the Fronsdal equations for general rank n.

Gauge Symmetry

The general gauge symmetry of the action (8.9) is

$$\delta_\epsilon \Psi = D\epsilon(\eta, x) = (\eta \cdot \partial_x - \tfrac{1}{2}(\eta^2+1)\Delta)\epsilon(\eta, x). \tag{8.26}$$

where $\epsilon(\eta, x)$ is an arbitrary function analytic in η. The operator D satisfies two identities which will be used frequently below,

$$\Delta(D\epsilon) = \partial_x^2 \epsilon - \frac{1}{2}(\eta^2+1)\Delta^2 \epsilon, \tag{8.27}$$

$$\delta'(\eta^2+1) D\epsilon = \frac{1}{2} \Delta(\delta(\eta^2+1)\, \epsilon). \tag{8.28}$$

These identities, together with integration by parts, can be used to show the infinitesimal gauge variations of the two terms in the action cancel, as required.

Once again, the single expression (8.26) simultaneously packages the gauge symmetries of all of

the component fields, as can be seen by expanding

$$\epsilon(\eta, x) = \sum_{n\geq 0} P_{(n)}(\eta) \cdot \epsilon^{(n)}(x). \tag{8.29}$$

For example, the contribution of $\epsilon^{(0)}$ is

$$\delta_{\epsilon^{(0)}} \Psi = \eta^\mu \partial_\mu \epsilon^{(0)} \tag{8.30}$$

which is, up to an overall constant, simply the familiar gauge transformation $\delta A_\mu = \partial_\mu \epsilon$ of electromagnetism. Similarly, the contribution of $\epsilon^{(1)}$ is

$$\delta_{\epsilon^{(1)}} \Psi = \frac{1}{\sqrt{2}} \left(2\eta^\mu \eta^\nu - g^{\mu\nu}(\eta^2+1)\right) (\partial_\mu \epsilon^{(1)}_\nu) \tag{8.31}$$

which is essentially the gauge transformation $\delta h_{\mu\nu} = \partial_{(\mu}\xi_{\nu)}$ of linearized gravity. The pattern continues, with $\epsilon^{(n-1)}$ generating the gauge symmetry for $\phi^{(n)}$.

Gauge Fixing and Plane Wave Solutions

In electromagnetism, the Lorenz gauge $\partial_\mu A^\mu = 0$ simplifies the free equation of motion to $\partial^2 A^\mu = 0$. Similarly, in linearized gravity the Lorenz/harmonic gauge $\partial_\mu \bar{h}^{\mu\nu} = 0$ simplifies the equation of motion to $\partial^2 h^{\mu\nu} = 0$, where $\bar{h}^{\mu\nu} = h_{\mu\nu} - \frac{1}{2} h' g_{\mu\nu}$ is the trace-reversed metric perturbation. Both of these gauges are special cases of the "harmonic" gauge

$$\delta(\eta^2+1)\, \Delta\Psi = 0 \tag{8.32}$$

which simplifies the equation of motion (8.19) to $\delta'(\eta^2+1)\, \partial_x^2 \Psi = 0$. Concretely, this implies that in harmonic gauge $\partial_x^2 \Psi$ must be proportional to $(\eta^2+1)^2$.

Such an ambiguity does not appear in electromagnetism and linearized gravity, but does in higher spin theories, where it arises from the freedom in double traces. We can remove it by using some of the residual gauge symmetry to go to "strong harmonic" gauge, where

$$\partial_x^2 \Psi = 0. \tag{8.33}$$

While these gauge conditions will be crucial throughout the chapter, we defer further discussion to the next subsection, where we show that these gauges can be achieved for arbitrary ρ.

The equations above are solved by the null plane waves $\Psi = e^{-ik\cdot x}\, \psi_{h,k}(\eta)$, where k^μ is a null

four-momentum, h is an integer, and

$$\psi_{h,k}(\eta)\Big|_{\rho=0} = \begin{cases} (i\eta\cdot\epsilon_+)^h & h \geq 0 \\ (-i\eta\cdot\epsilon_-)^{-h} & h \leq 0 \end{cases} \tag{8.34}$$

where $\epsilon_\pm^\mu$ are null frame vectors associated with k^μ, defined in the conventions. As shown in Ref. [781], the little group generators act as $R\,\psi_{h,k} = h\,\psi_{h,k}$, which implies h is indeed the helicity, and $T_\pm\,\psi_{h,k} = 0$ up to pure gauge terms, which implies the helicity is Lorentz invariant. More concretely, if we further specify to $\epsilon_\pm^0 = 0$, the modes given above are exactly those of radiation gauge in electromagnetism for $h = \pm 1$, and of transverse traceless gauge in linearized gravity for $h = \pm 2$. As we will show in the next subsection, (8.34) gives a complete basis of physical solutions. This implies that the action (8.9) for $\rho = 0$ indeed contains, for each null momentum, exactly one mode of each integer helicity.

8.2.3 Continuous Spin Fields

Generalizing the previous results to arbitrary spin scale is straightforward, as ρ only appears through the operator $\Delta = \partial_\eta \cdot \partial_x + \rho$. Remarkably, all of our η-space results, including the equation of motion (8.19), gauge symmetry (8.26), identities (8.27) and (8.28), and (strong) harmonic gauge condition (8.32) and (8.33) are unchanged. The null plane wave solutions are now

$$\psi_{h,k}(\eta) = e^{-i\rho\eta\cdot q} \times \begin{cases} (i\eta\cdot\epsilon_+)^h & h \geq 0 \\ (-i\eta\cdot\epsilon_-)^{-h} & h \leq 0 \end{cases} \tag{8.35}$$

where q^μ is another null frame vector. The integer h still represents the helicity, but now we have $T_\pm\,\psi_{h,k} = \rho\,\psi_{(h\pm1),k}$ up to pure gauge terms, so that the parameter ρ indeed corresponds to the spin scale. This was shown explicitly in Ref. [781], though that work used a different phase convention for $T_\pm$, and the phase factor $e^{-i\rho\eta\cdot q}$ was sometimes reversed or dropped.

Again, the solutions (8.35) are a complete basis of physical solutions, in the sense that the general mode expansion for a free bosonic continuous spin field is

$$\Psi(\eta,x) = \int \frac{d^3\mathbf{k}}{(2\pi)^3\,2|\mathbf{k}|} \sum_h \left(a_h(\mathbf{k})\psi_{h,k}(\eta)e^{-ik\cdot x} + \text{c.c.}\right)\Big|_{k^0=|\mathbf{k}|} + D\epsilon \tag{8.36}$$

which is everywhere analytic in η. Here, $D\epsilon$ is a pure gauge term, and $a_h(\mathbf{k})$ is the amplitude of the mode of helicity h and momentum $\mathbf{k}$. These coefficients contain all of the gauge invariant information in the field. By the orthonormality relation (8.268) for helicity modes, they can be extracted by projection,

$$a_h(\mathbf{k}) = 2|\mathbf{k}| \int [d^4\eta]\,\delta'(\eta^2+1)\,\psi^*_{h,k}(\eta)\Psi(\eta,k)\Big|_{k^0=|\mathbf{k}|}. \tag{8.37}$$

To see that the pure gauge term does not contribute to the right-hand side, apply (8.28) and note that the solutions (8.35) satisfy the harmonic gauge condition.

These are the key results we will need going forward; in the remainder of this subsection we prove the assertions made above, and discuss further features of the action.

Tensor Mixing

An important qualitative difference for nonzero ρ is the ubiquitous mixing of tensor components. For example, the action now contains mixing terms and apparent mass terms,

$$S[\Psi] = S[\Psi]\Big|_{\rho=0} + \frac{\rho}{\sqrt{2}}\left(\phi\,(\partial^\mu A_\mu) + A^\mu(\partial_\mu h' - \partial^\nu h_{\mu\nu}) + \ldots\right) + \frac{\rho^2}{4}\left(\phi^2 - \frac{1}{2}A_\mu A^\mu - \phi\,h' + \frac{1}{6}(h')^2 - \frac{1}{3}h_{\mu\nu}h^{\mu\nu} + \ldots\right) \tag{8.38}$$

which makes it hard to see that the physical solutions still represent massless particles. The mixing terms vanish in harmonic gauge, but then the harmonic gauge condition itself mixes tensor ranks, as do the solutions (8.35), which each contain tensors of arbitrarily high rank. Thus, while the tensor expansion is a useful conceptual tool at $\rho = 0$, it is less intuitive at any nonzero ρ, and may be misleading if not used with care.

Achieving (Strong) Harmonic Gauge

To think about gauge fixing, it is useful to separate the null and non-null modes of the field. For the null modes, one has $\partial_x^2\Psi = 0$ by definition, and the equation of motion implies the harmonic gauge condition is automatically satisfied for all fields which are bounded at infinity. The (strong) harmonic gauge conditions are only nontrivial statements about non-null modes, on which ∂_x^2 is invertible.

To see that harmonic gauge can be reached for non-null modes, note that (8.27) implies

$$\delta_\epsilon(\delta(\eta^2+1)\,\Delta\Psi) = \delta(\eta^2+1)\,\partial_x^2\epsilon. \tag{8.39}$$

Since ϵ is arbitrary and ∂_x^2 is invertible on these modes, this freedom can be used to set $\delta(\eta^2+1)\,\Delta\Psi$ to zero. The residual gauge freedom is in the form of ϵ with $\partial_x^2\epsilon = 0$, which only affects null modes, and ϵ proportional to η^2+1. We can use the latter freedom to reach strong harmonic gauge, since for $\epsilon = (\eta^2+1)\beta(\eta,x)$ we have

$$\delta_\epsilon(\partial_x^2\Psi) = -\frac{1}{2}(\eta^2+1)^2\partial_x^2\,\Delta\beta. \tag{8.40}$$

Since $\Delta\beta$ is arbitrary and ∂_x^2 is invertible, we can indeed set $\partial_x^2\Psi$ to zero for non-null modes, which completely eliminates them.

Incidentally, gauge transformations of the form $\epsilon = (\eta^2+1)\beta$ correspond precisely to the gauge symmetries $\delta_\chi \Psi = (\eta^2+1)^2\chi$ first noted below (8.9) for $\chi = -\Delta\beta/2$. The only subtlety of this correspondence is that χ gauge transformations which fall appropriately at infinity may correspond to β which do *not* fall at infinity. For this reason, Ref. [781] and the higher spin literature often introduce ϵ and χ gauge transformations as two separate families, despite their redundancy.

Completeness of Helicity Modes

Working in momentum space, the field $\Psi(\eta, k)$ in strong harmonic gauge is only nonzero for null k^μ. Fixing one such k^μ for consideration, there is a residual gauge transformation $\epsilon(\eta, k)$, and the operator (8.26) that generates gauge transformations is

$$D = -ik\cdot\eta - \frac{1}{2}(\eta^2+1)(-ik\cdot\partial_\eta + \rho)). \tag{8.41}$$

It is convenient to pull out phases, defining $\epsilon = -2ie^{-i\rho\eta\cdot q}\,\tilde{\epsilon}$ and $\Psi = e^{-i\rho\eta\cdot q}\,\tilde{\Psi}$, which simplifies the gauge transformation and the harmonic gauge condition to

$$\delta_\epsilon \tilde{\Psi} = ((\eta^2+1)(k\cdot\partial_\eta) - 2\eta\cdot k)\,\tilde{\epsilon}, \tag{8.42}$$

$$k\cdot\partial_\eta\,\tilde{\Psi} = (\eta^2+1)\,\alpha \tag{8.43}$$

for some arbitrary $\alpha(\eta, k)$. Now, (8.42) implies

$$\delta_\epsilon(k\cdot\partial_\eta\,\tilde{\Psi}) = (\eta^2+1)(k\cdot\partial_\eta)^2\tilde{\epsilon}. \tag{8.44}$$

To understand this, it is useful to think of $\tilde{\epsilon}$ and α as Taylor series in $\eta\cdot k$, $\eta\cdot q$, and $\eta\cdot\epsilon_\pm$. In these variables we have $k\cdot\partial_\eta = \partial_{\eta\cdot q}$, so there is enough freedom in $\tilde{\epsilon}$ to cancel off any α. The residual gauge freedom is in $\tilde{\epsilon} = f + (\eta\cdot q)g$ for f and g independent of $\eta\cdot q$, for which

$$\delta_\epsilon\tilde{\Psi} = -2(\eta\cdot k)f + (1 - \eta\cdot\epsilon_+\,\eta\cdot\epsilon_-)g. \tag{8.45}$$

In other words, we can use all of the remaining gauge freedom to remove any terms in $\tilde{\Psi}$ with powers of $\eta\cdot k$, or powers of both $\eta\cdot\epsilon_+$ and $\eta\cdot\epsilon_-$. After removing such terms we are left with $\tilde{\Psi}$ equal to a sum of monomials in $\eta\cdot\epsilon_+$ or $\eta\cdot\epsilon_-$. This shows that the helicity modes (8.35) are a complete basis of physical solutions.

A New Spacetime Symmetry

As a final remark, the vector superspace used to construct continuous spin fields is a bosonic analogue of the fermionic superspace used in supersymmetric theories. As first noted in Ref. [783], the action (8.9) is invariant under the η-dependent spacetime translation $\delta x^\mu = \omega^{\mu\nu}\eta_\nu$ for antisymmetric

$\omega^{\mu\nu}$, corresponding to the tensorial conserved charge

$$N^{\mu\nu} = i(\eta^\mu \partial_x^\nu - \eta^\nu \partial_x^\mu). \tag{8.46}$$

This symmetry mixes modes of different helicity, even for $\rho = 0$, and it continues to hold when the continuous spin field couples to particles. It would then appear to be a novel extension of spacetime symmetry, which could evade the Coleman–Mandula theorem by virtue of the infinite number of polarization states. While we have not yet found any use for this symmetry, it may be a guide to constructing more complete continuous spin theories.

8.3 Coupling Matter Particles to Fields

We can couple spinless matter particles to fields by introducing currents built from the particle's worldline. This is the most useful way to describe low-energy classical experiments, and for familiar theories it can be readily quantized, yielding a worldline formalism equivalent to perturbative quantum field theory. In subsection 8.3.1 we identify minimal couplings to ordinary fields, and show that almost all non-minimal couplings produce only contact interactions, which do not affect a particle's coupling to radiation. We generalize to continuous spin fields in subsection 8.3.2, where we enumerate an enormous family of potential currents. Again, we find that the vast majority of these currents do not couple to radiation, allowing us to define families of scalar-like and vector-like currents that couple universally to radiation, and reduce to the familiar minimal scalar and vector couplings as $\rho \to 0$.

8.3.1 Review: Coupling to Ordinary Fields

Minimal Couplings to Scalar and Vector Fields

A free matter particle of mass m and worldline $z^\mu(\tau)$ has action

$$S_0 = -m \int \sqrt{\frac{dz^\mu}{d\tau}\frac{dz_\mu}{d\tau}}\, d\tau. \tag{8.47}$$

In this section we take τ to be the proper time, but all results below can be straightforwardly rewritten for general worldline parametrization by replacing $d\tau$ with $\sqrt{\dot{z}^2}\, d\tau$ and $\dot{z}^\mu = dz^\mu/d\tau$ with $\dot{z}^\mu/\sqrt{\dot{z}^2}$. Now, we can couple the particle to a massless real scalar field $\phi(x)$ by

$$S_{\text{int}} = \int d^4x\, \phi(x) J(x) \tag{8.48}$$

which yields an equation of motion $\partial_x^2 \phi = J$ for the field. The current $J(x)$ can be built from $z^\mu(\tau)$ and its derivatives; if we were considering particles with spin, it could also depend on the spin tensor

$S^{\mu\nu}(\tau)$. The minimal coupling corresponds to the simplest possible current,

$$J(x) = g \int d\tau\, \delta^{(4)}(x - z(\tau)) \tag{8.49}$$

which is localized to the worldline, and corresponds to a Yukawa interaction in a field-theoretic description of the matter.

Next, consider the coupling of a particle of charge e to a massless vector field $A_\mu(x)$,

$$S_{\text{int}} = -\int d^4x\, A_\mu(x) J^\mu(x). \tag{8.50}$$

Here the simplest possible current J^μ, obeying worldline locality, translation invariance, and current conservation $\partial_\mu J^\mu = 0$ (which is required for S_{int} to be gauge invariant) is

$$J^\mu(x) = e \int d\tau\, \dot{z}^\mu(\tau)\, \delta^{(4)}(x - z(\tau)), \tag{8.51}$$

which corresponds to a minimal coupling of scalar matter to a vector field. The field's equation of motion is $\partial_x^2 A^\mu = J^\mu$ in Lorenz gauge. The current is conserved because its divergence is a total τ derivative,

$$\partial_\mu J^\mu = e \int d\tau\, (\dot{z}^\mu \partial_\mu)\, \delta^{(4)}(x - z(\tau)) = -e \int d\tau\, \frac{d}{d\tau} \delta^{(4)}(x - z(\tau)) = 0 \tag{8.52}$$

where the integral vanishes because worldlines have no boundaries. This physically corresponds to assuming particles and antiparticles are always produced or destroyed in pairs.

Non-minimal Couplings and Contact Terms

We are most interested in currents for continuous spin fields which reduce to the currents defined above as $\rho \to 0$. However, our formalism also includes currents which reduce to non-minimal couplings, so to build intuition we first review them for scalar and vector fields. We continue to assume the currents are Lorentz covariant and translationally invariant, so that the only dependence on position is through the combination $x^\mu - z^\mu(\tau)$. We further assume the current can be written as a τ integral of a function of $z^\mu(\tau)$ and $\dot{z}^\mu(\tau)$, with no explicit dependence on higher τ derivatives or on τ-nonlocal products.

For a scalar field, the most general current obeying these assumptions can be constructed from (8.49) by acting on the delta function with powers of ∂_x^2 or $\dot{z} \cdot \partial_x$. This general current is most compactly expressed in momentum space,

$$J(k) = \int d\tau\, e^{ik\cdot z(\tau)} f(k^2, k \cdot \dot{z}(\tau)), \tag{8.53}$$

where the minimal coupling (8.49) corresponds to $f(k^2, k \cdot \dot{z}) = g$.

All terms with at least one power of k^2 do not produce any fields away from the particles themselves, and thus correspond to contact interactions. To build intuition, we will derive this basic result for $f = g\,k^2$ in several ways. In this case, the Lagrangian for the field is

$$\mathcal{L} = \frac{1}{2}(\partial_\mu \phi)^2 - J_0(x)\,\partial^2 \phi(x) \tag{8.54}$$

where J_0 is the minimal current (8.49). In terms of the shifted field $\tilde{\phi} = \phi + J_0$, it becomes

$$\mathcal{L} = \frac{1}{2}(\partial_\mu \tilde{\phi})^2 - \frac{1}{2}(\partial_\mu J_0)^2. \tag{8.55}$$

Since J_0 is localized to a particle's worldline, the interaction term is only nonzero when two particles coincide, so it mediates a contact interaction. The shifted field is free, which implies the field ϕ is not affected except for exactly on the particle itself. In particular, this coupling does not affect the radiation produced by an accelerating particle. Conversely, it does not affect the particle's motion in the presence of a free background field, including any radiation field. In general, all of these conclusions hold whenever the function f contains a factor of the differential operator ∂^2 appearing in the field's free equation of motion.

We can also give some of these terms a more direct physical interpretation. For a particle at rest, $\dot{z}^\mu = (1, \mathbf{0})$, the τ integration sets $k^0 = 0$, giving $J(\mathbf{k}) = f(-|\mathbf{k}|^2, 0)$. Thus, for static particles terms with powers of $k \cdot \dot{z}$ have no effect, while those proportional to powers of k^2 describe the particle's static, spherically symmetric spatial profile.

The k^2 term itself corresponds in field theory to an operator analogous to a charge radius. However, we note that, despite the name, the presence of such an operator does not actually imply a particle has a nonzero radius, any more than a dipole moment implies a particle has a specific length. The corresponding current is still localized, in the sense that it only depends on fields in a neighborhood of the worldline. Particles of finite size can be described by (8.53), but only by summing over an infinite series of terms. We highlight this point because the currents introduced in subsection 8.3.2 will, by contrast, be intrinsically delocalized.

Terms with only powers of $k \cdot \dot{z}$ are the only ones that can yield non-contact interactions. To understand them more physically, note that

$$\int d\tau\,(k \cdot \dot{z})^n\, e^{ik\cdot z} = -i \int d\tau\,(k \cdot \dot{z})^{n-1}\,\frac{d}{d\tau}(e^{ik\cdot z}) = i \int d\tau\, e^{ik\cdot z}\frac{d}{d\tau}(k \cdot \dot{z})^{n-1}. \tag{8.56}$$

This implies that a term with a single power of $k \cdot \dot{z}$ has no effect, and a term with two powers of $k \cdot \dot{z}$ implicitly depends on the acceleration $\ddot{z}$. In general, a power of $k \cdot \dot{z}$ can be exchanged for a τ derivative by the above manipulation, so term with more powers of $k \cdot \dot{z}$ depends on higher time derivatives of $\dot{z}$. These terms describe the particle's dynamic response to nontrivial motion. In other words, they characterize the particle's non-rigidity, e.g. distinguishing a rigid charged sphere from a

spherical balloon full of charged jelly. To further build intuition, note that the $n = 2$ case corresponds to a coupling in position space

$$S_{\text{int}} \supset \int d^4x\, d\tau\, (\partial_\mu \partial_\nu \phi(x))\, \dot{z}^\mu \dot{z}^\nu\, \delta^{(4)}(x - z(\tau)), \tag{8.57}$$

which has the enhanced shift symmetry $\delta\phi = c + b_\mu x^\mu$ of a galileon field [826].

The terms highlighted in (8.56) are the only ones that can affect the radiation produced by an accelerating particle, though their effect is suppressed at low accelerations. This conclusion might seem surprising because in general, it is certainly possible for a particle's static structure to impact the radiation it produces, e.g. through dipole and higher moments. However, those terms are not permitted for a spinless particle by rotational symmetry.

In the vector case, gauge invariance imposes the constraint $k_\mu J^\mu(k) = 0$. After suitable subtraction of total τ derivatives, the most general current can be written as

$$J^\mu(k) = \int d\tau\, e^{ik\cdot z} \left(e\, \dot{z}^\mu + f(k^2, k\cdot\dot{z})(\dot{z}^\mu k^2 - k^\mu k\cdot\dot{z}) \right), \tag{8.58}$$

where we have isolated the minimal coupling (8.51) in the first term. Again, terms in f proportional to powers of $k \cdot \dot{z}$ describe the source's non-rigidity, and terms with k^2 describe the source's static spatial profile, though now the constant term represents the charge radius.

In contrast to the scalar case, *all* of the non-minimal vector couplings correspond to contact interactions, because they are proportional to $(k^2\eta^{\mu\nu} - k^\mu k^\nu)\dot{z}_\nu$, and the field's free equation of motion is $(k^2\eta^{\mu\nu} - k^\mu k^\nu)A_\nu = 0$. None of the non-minimal couplings produce any fields away from the particle itself, and they therefore cannot affect the particle's response to free fields, or the radiation it produces. This is essentially a statement of Gauss's law: the vector radiation from a spherically symmetric particle is determined solely by its charge.

Tensor and Higher Spin Fields

Matter particles can also couple to higher rank fields, but such fields introduce additional complications. First, at rank 2, the coupling of a particle to the canonically normalized metric perturbation $h_{\mu\nu}(x)$ in linearized gravity is

$$S_{\text{int}} = \frac{\kappa}{2} \int d^4x\, h_{\mu\nu}(x) T^{\mu\nu}(x) \tag{8.59}$$

where $\kappa = \sqrt{32\pi G}$. The stress-energy tensor of the particle is

$$T^{\mu\nu}(x) = m \int d\tau\, \dot{z}^\mu(\tau)\dot{z}^\nu(\tau)\, \delta^{(4)}(x - z(\tau)) \tag{8.60}$$

and its divergence is

$$\partial_\mu T^{\mu\nu} = m \int d\tau\, \ddot{z}^\nu(\tau)\, \delta^{(4)}(x - z(\tau)). \tag{8.61}$$

This presents two well-known, closely related problems: consistency of the equations of motion, and gauge invariance of the action off-shell.

First, the equation of motion for $h_{\mu\nu}$ in linearized gravity implies $\partial_\mu T^{\mu\nu} = 0$, which is only true for non-accelerating particles. Thus, if we regard $z^\mu(\tau)$ as a given background then we cannot consider nontrivial trajectories, while if we regard $z^\mu(\tau)$ as dynamical then the equations of motion are inconsistent [507]. The resolution is simply the equivalence principle: in (8.59) we must use the total stress-energy tensor, including that of the fields which cause the particle to accelerate. Full consistency requires an infinite series in κ of terms involving $h_{\mu\nu}$, which leads to the nonlinear structure of general relativity [827]. However, it is still possible to compute results to leading order in the coupling κ in the linearized theory.

Second, if we regard $z^\mu(\tau)$ as dynamical, gauge invariance of S_{int} under $\delta h_{\mu\nu} = \partial_{(\mu}\epsilon_{\nu)}$ seems to require $\partial_\mu T^{\mu\nu} = 0$ *identically*, which is not true for general off-shell $z^\mu(\tau)$. The resolution is to recall that the gauge transformation arises from an infinitesimal diffeomorphism symmetry, which also acts on the particle's position by $\delta z^\mu = \kappa\epsilon^\mu$. Including this contribution implies that S_0 also varies under a gauge transformation, rendering the full action gauge invariant to leading order in κ [827]. Achieving full gauge invariance requires generalizing $\delta h_{\mu\nu}$ to an infinite series in κ, which recovers the nonlinear gauge structure of general relativity [828].

These subtleties make it more difficult to generalize (8.60) to continuous spin fields, even at leading order in κ. The consistency problem implies we must include additional terms in the stress-energy tensor, which complicates calculations. The gauge invariance problem is more serious, as it is not clear how the more general continuous spin gauge symmetry (8.26) is supposed to act on z^μ. Furthermore, it is unclear to what degree one can trust results calculated with an action that is only partially gauge invariant.

For these reasons, we defer the study of "tensor-like" continuous spin currents that reduce to (8.60) as $\rho \to 0$ to future work. In this paper, we exclude tensor-like currents by demanding that both z^μ and the action be completely gauge invariant.

As an aside, Ref. [829] considered a minimal coupling to higher spin fields,

$$J^{\mu_1\cdots\mu_n}(x) = m g_n \int d\tau\, \dot{z}^{\mu_1}(\tau)\cdots\dot{z}^{\mu_n}(\tau)\,\delta^{(4)}(x - z(\tau)). \tag{8.62}$$

As for rank 2, the current is conserved when $\ddot{z}^\mu = 0$, and gauge invariance can be restored to leading order in g_n by gauge transforming the worldline, by $\delta z_\mu \propto g_s\, \epsilon^{(n-1)}_{\mu\nu_1\ldots\nu_{n-2}} \dot{z}^{\nu_1}\cdots\dot{z}^{\nu_{n-2}}$. (For a perspective on these transformations, see Refs. [830, 831].) However, we will not consider this further as for $n > 2$ there is no known theory consistent or gauge-invariant to all orders.

8.3.2 Coupling to Continuous Spin Fields

The free continuous spin field can be coupled to a current by

$$S_{\text{int}} = \int d^4x\, [d^4\eta]\, \delta'(\eta^2+1)\, J(\eta,x)\Psi(\eta,x). \tag{8.63}$$

This is a canonical choice, as taking an integral over $\delta(\eta^2+1)$ would just yield a special case of (8.63) by the identity (8.243), while integrating over $\delta''(\eta^2+1)$ or any other distribution would couple generic currents to field values off the first neighborhood of the hyperboloid, which are pure gauge. To gain intuition for (8.63), note that when $\rho = 0$, defining

$$J(\eta,x) = \sum_{n\geq 0} \bar{P}_{(n)}(\eta)\cdot J^{(n)}(x) \tag{8.64}$$

$$= J(x) + \sqrt{2}\,\eta^\mu J_\mu(x) + (2\eta^\mu\eta^\nu + g^{\mu\nu})\,\frac{\kappa\, T_{\mu\nu}(x)}{2} + \dots. \tag{8.65}$$

simultaneously yields the minimal scalar coupling (8.48), vector coupling (8.50), and tensor coupling (8.59). More generally, defining the "dual" polynomials by

$$\bar{P}^{\mu_1\cdots\mu_n}_{(n)} = 2^{n/2}\left(\eta^{\mu_1}\cdots\eta^{\mu_n} + \frac{1}{4(n-1)!}\, g^{(\mu_1\mu_2}\eta^{\mu_3}\cdots\eta^{\mu_n)}\right) \tag{8.66}$$

leads to a sum of canonically coupled currents at each rank,

$$S_{\text{int}} = \int d^4x \sum_{n\geq 0} (-1)^n \phi^{(n)}\cdot J^{(n)} \tag{8.67}$$

as shown in appendix 8.9.1. The current J appears on the right-hand side of the equation of motion (8.19), so the (strong) harmonic gauge conditions (8.32) and (8.33) become

$$\delta(\eta^2+1)\,\Delta\Psi = 0, \qquad \partial_x^2\Psi = J. \tag{8.68}$$

The Continuity Condition

Demanding gauge invariance of S_{int} yields a key constraint on the current,

$$\delta(\eta^2+1)\,\Delta J = 0 \tag{8.69}$$

which we term the continuity condition. Here we assume it holds off-shell, though note that on-shell, it ensures the two conditions in (8.68) are consistent. As shown in appendix 8.9.1, we can reexpress

the continuity condition in terms of tensor components as

$$\left\langle \partial \cdot J_{(n)} + \frac{\rho}{n\sqrt{2}}(J_{(n-1)} + \frac{1}{2}J'_{(n+1)}) \right\rangle = 0 \tag{8.70}$$

for all $n \geq 1$, where the brackets denote a trace subtraction.

To build intuition, we note that the trace subtraction is trivial at lower ranks, so that for $\rho = 0$ we recover the ordinary conservation conditions $\partial \cdot J_{(1)} = 0$ and $\partial \cdot J_{(2)} = 0$, and for higher ranks we recover a "weak" conservation condition $\langle \partial \cdot J_{(n)} \rangle = 0$ familiar in higher spin theory. However, for nonzero ρ the continuity condition mixes tensor ranks, which implies that any current must contain an infinite tower of nonzero $J_{(n)}$.

Concretely, consider the $n = 1$ and $n = 2$ cases of the continuity condition,

$$\partial \cdot J_{(1)} = -\frac{\rho}{\sqrt{2}}\left(J_{(0)} + \frac{1}{2}J'_{(2)}\right), \qquad \partial \cdot J_{(2)} = -\frac{\rho}{2\sqrt{2}}\left(J_{(1)} + \frac{1}{2}J'_{(3)}\right). \tag{8.71}$$

If we wanted to construct a "scalar-like" current whose $\rho \to 0$ limit had only $J_{(0)}$ of the form (8.49), then the first equation implies $J_{(1)}$ must have a *nonconserved*, order ρ contribution, which then implies $J_{(2)}$ must have a nonconserved, order ρ^2 contribution, and so on to arbitrary $J_{(n)}$. Alternatively, to construct a "vector-like" current whose $\rho \to 0$ limit has only the conserved $J_{(1)}$ of the form (8.51), the second equation requires $J_{(2)}$ of order ρ, and so on.

Constructing such a tower of tensors, with appropriate trace subtractions, requires complex combinatorics. Furthermore, the results are physically opaque due to the omnipresent mixing between ranks. For instance, it might seem impossible for $J_{(1)}$ to be nonconserved, given that it couples to A_μ in the $\rho \to 0$ limit, but this is permitted because of the complex mixing (8.38) of A_μ with other tensor components. For these reasons, we find it much more straightforward to construct currents directly in η-space, without using a tensor expansion.

Constructing Currents

We will construct currents from the worldline using the same assumptions we used to find the general scalar current (8.53) and vector current (8.58). Specifically, we assume the current in position space has the form

$$J(\eta, x) = \int d\tau\, j(\eta, x - z(\tau), \dot{z}(\tau)) \tag{8.72}$$

which corresponds in momentum space to

$$J(\eta, k) = \int d\tau\, e^{ik\cdot z} f(\eta, k, \dot{z}) \tag{8.73}$$

where f is the Fourier transform of j. The minimal scalar current (8.49) corresponds to $f(\eta, k, \dot{z}) = g$, and the minimal vector current (8.51) corresponds to $f(\eta, k, \dot{z}) = \sqrt{2}\, e\, \eta \cdot \dot{z}$.

We assume $z^\mu(\tau)$ is gauge invariant; as discussed above, this excludes currents which reduce to minimal tensor or higher spin couplings as $\rho \to 0$. Then gauge invariance of the full action requires the continuity condition (8.69) to hold for arbitrary $z^\mu(\tau)$, which implies

$$(k \cdot \partial_\eta + i\rho) f(\eta, k, \dot{z}) = (\eta^2 + 1)\, \alpha(\eta, k, \dot{z}) \tag{8.74}$$

where α is an arbitrary function analytic in η. Strictly speaking, we are also free to add terms to f proportional to $k \cdot \dot{z}$, with no other $\dot{z}$ dependence, as these are total τ derivative which not contribute to the current; the above equation assumes such terms have been dropped.

We assume f is analytic in η, so that it can only contain positive powers of η, and for nonzero ρ the continuity condition implies that f must have arbitrarily high powers of η. These must be accompanied by arbitrarily high *negative* powers of k, which implies the currents cannot be localized to the worldline. Furthermore, f contains an enormous amount of freedom, even if one fixes the $\rho \to 0$ limit. We will shortly discuss general currents, which are parametrized in appendix 8.9.2, but let us first build intuition through simple examples.

Simple Scalar-Like and Vector-Like Currents

We begin by considering "scalar-like" currents with $\alpha = 0$, which all reduce to (8.49) in the limit $\rho \to 0$. Note that for any vector $V^\mu(k, \dot{z})$, the continuity condition is satisfied by

$$f(\eta, k, \dot{z}) = g\, e^{-i\rho\eta \cdot V / k \cdot V} \tag{8.75}$$

This family contains two illustrative special cases: the "temporal" current

$$J_T(\eta, k) = g \int d\tau\, e^{ik\cdot z}\, e^{-i\rho\eta\cdot\dot{z}/k\cdot\dot{z}} \tag{8.76}$$

which corresponds to $V^\mu = \dot{z}^\mu$, and the "spatial" current

$$J_S(\eta, k) = g \int d\tau\, e^{ik\cdot z}\, \exp\left(-i\rho\, \frac{\eta\cdot k - \eta\cdot\dot{z}\,\dot{z}\cdot k}{k^2 - (k\cdot\dot{z})^2}\right) \tag{8.77}$$

which corresponds to $V^\mu = k^\mu - (k\cdot\dot{z})\dot{z}^\mu$, the linear combination orthogonal to $\dot{z}^\mu$. We can also define vectors which are inhomogeneous in k^μ, such as

$$V^\mu_\pm = k^\mu \pm \beta\rho\dot{z}^\mu \tag{8.78}$$

for a dimensionless parameter β. For real β, we can construct the "inhomogeneous" current

$$J_I(\eta, k) = \frac{g}{2} \int d\tau\, e^{ik\cdot z} \left(e^{-i\rho\eta\cdot V_+/k\cdot V_+} + e^{-i\rho\eta\cdot V_-/k\cdot V_-}\right). \tag{8.79}$$

Above, two terms are required to ensure the position-space current is real, $J(-k) = J(k)^*$. Note that a pure imaginary β would also satisfy the continuity condition, though in that case each term alone would give a real position-space current.

Though many others exist, the temporal current J_T is the simplest for situations involving radiation, the spatial current J_S has the simplest static limit, and the inhomogeneous current J_I is a relatively simple extension of the two. Note that all three have essential singularities at $k\cdot V = 0$. Such isolated essential singularities are a generic feature of solutions to (8.74). However, while finite-order poles in k are pathological, we will see these singularities are benign, leading to well-behaved physical results and only a weak nonlocality.

These scalar-like currents can be straightforwardly generalized to "vector-like" currents, which reduce to (8.51) as $\rho \to 0$. For example, the vector-like temporal current is

$$J_T^V(\eta,k) = \sqrt{2}\,e\int d\tau\; e^{ik\cdot z}\,(\eta\cdot\dot z)\sum_{m=0}^{\infty}\frac{1}{(m+1)!}\left(\frac{-i\rho\,\eta\cdot\dot z}{k\cdot\dot z}\right)^m \tag{8.80}$$

$$= \frac{\sqrt{2}\,e}{\rho}\int d\tau\; e^{ik\cdot z}\,(ik\cdot\dot z)\,(e^{-i\rho\eta\cdot\dot z/k\cdot\dot z}-1). \tag{8.81}$$

We can drop the -1 term because it is a total τ derivative, leaving an integrand which directly satisfies (8.74). This unfortunately makes the current appear to diverge in the $\rho\to 0$ limit, but it is convenient since the result is related to J_T by the simple substitution $g \to (\sqrt{2}\,e/\rho)(ik\cdot\dot z)$. Similarly, we can write a vector-like inhomogeneous current

$$J_I^V(\eta,k) = \frac{e}{\sqrt{2}\,\beta\rho^2}\int d\tau\, e^{ik\cdot z}\left((ik\cdot V_+)\,e^{-i\rho\eta\cdot V_+/k\cdot V_+} - (ik\cdot V_-)\,e^{-i\rho\eta\cdot V_-/k\cdot V_-}\right) \tag{8.82}$$

where analogous total τ derivative terms have been dropped. Finally, writing the vector-like spatial current requires constructing a prefactor which is annihilated by $k\cdot\partial_\eta$ but also reduces to $\eta\cdot\dot z$ in the $\rho\to 0$ limit, again up to total τ derivatives. The result is

$$J_S^V(\eta,k) = \sqrt{2}\,e\int d\tau\, e^{ik\cdot z}\left(\frac{(\eta\cdot\dot z)k^2-(\eta\cdot k)(k\cdot\dot z)}{k^2-(k\cdot\dot z)^2}-\frac{ik\cdot\dot z}{\rho}\right)$$
$$\times\exp\left(-i\rho\,\frac{\eta\cdot k-\eta\cdot\dot z\,\dot z\cdot k}{k^2-(k\cdot\dot z)^2}\right). \tag{8.83}$$

Despite appearances, these currents are all vector-like.

General Currents

Now that we have seen some examples, let us parametrize the general solution for f. The result for $\alpha = 0$ is given by (8.337) in appendix 8.9.2, which is equivalent to

$$f = e^{-i\rho\eta\cdot\dot{z}/k\cdot\dot{z}}\left(g_0(u, k\cdot\dot{z}, k^2) + \left(\eta^2 + 1 - \frac{2\eta\cdot k\,\eta\cdot\dot{z}}{k\cdot\dot{z}} + \frac{(\eta\cdot\dot{z})^2\,k^2}{(k\cdot\dot{z})^2}\right) g_1(u, k\cdot\dot{z}, k^2)\right) \tag{8.84}$$

where $u = \eta\cdot(k - \dot{z}\,k^2/(k\cdot\dot{z}))$. For $\rho = 0$, this expression efficiently packages the minimal scalar and vector currents, and all non-minimal currents. The general scalar current (8.53) corresponds to g_0 independent of u, while the general vector current (8.58) corresponds to g_0 with a prefactor of $(k\cdot\dot{z})u$. The function g_1 is less familiar, but if we take $g_1 \propto (k\cdot\dot{z})^2$, which is the simplest case which avoids negative powers of k, the result includes a nonminimal tensor current. Similarly, taking the simplest $\alpha \propto (k\cdot\dot{z})^3$ and applying (8.338), the result includes a nonminimal current for a rank 3 higher spin field.

The situation is less clear for nonzero ρ, where negative powers of k appear. For instance, the temporal current (8.76) has $g_0 = g$, while the spatial current (8.77) has $g_0 = g\,e^{i\rho u/((k\cdot\dot{z})^2 - k^2)}$. Given how complicated g_0 can be for even the simplest examples, it is not obvious how to usefully define a "scalar-like" current, nor how to extract predictions given the enormous freedom in the general solution.

However, a remarkable simplification occurs when we consider coupling to null modes of the field, with $k^2 = 0$. In this case, the difference of the spatial and temporal currents is

$$J_S - J_T = g\int d\tau\, e^{ik\cdot z} e^{-i\rho\eta\cdot\dot{z}/k\cdot\dot{z}}\left(\exp\left(i\rho\frac{\eta\cdot k}{(k\cdot\dot{z})^2}\right) - 1\right) \tag{8.85}$$

where the factor in parentheses contains only terms proportional to $(\eta\cdot k)^n$ for $n > 0$. Such terms do not contribute to the action in the presence of radiation modes (8.35), because the η integral in this case is proportional to

$$\int [d^4\eta]\,\delta'(\eta^2 + 1)\, e^{i\rho\eta\cdot(q - \dot{z}/k\cdot\dot{z})}(\eta\cdot\epsilon_\pm)^{|h|}\,(\eta\cdot k)^n = 0 \tag{8.86}$$

which vanishes because k is orthogonal to itself, $\epsilon_\pm$, and $q - \dot{z}/k\cdot\dot{z}$. Thus, the spatial and temporal currents couple to radiation in exactly the same way.

This phenomenon turns out to be very general. As shown in appendix 8.9.2, any f, including those corresponding to arbitrary α, can be written in the form

$$f(\eta, k, \dot{z}) = e^{-i\rho\eta\cdot\dot{z}/k\cdot\dot{z}}\,\hat{g}(k\cdot\dot{z}) + (k^2 + D\,\Delta)X(\eta, k, \dot{z}) \tag{8.87}$$

where $\hat{g}(k\cdot\dot{z}) = g_0(0, k\cdot\dot{z}, 0)$, D is the operator (8.41) generating gauge transformations, and X is regular as $k^2 \to 0$. The action (8.63) only depends on the current through the combination

$\delta'(\eta^2+1)J$, and under this delta function the second term simplifies as

$$\delta'(\eta^2+1)(k^2+D\,\Delta)X = \left(\delta'(\eta^2+1)\,k^2 + \frac{1}{2}\,\Delta\,\delta(\eta^2+1)\,\Delta\right)X \tag{8.88}$$

where we used (8.28). The object acting on X is just, up to a sign, the differential operator in the free equation of motion (8.19). Thus, by the same logic as in subsection 8.3.1, these terms do not affect the radiation a particle emits, or its response to a free field background. These key physical observables are determined solely by the single-variable function $\hat{g}$.

We can therefore give sharp definitions of classes of currents based on $\hat{g}$:

- Scalar-like currents have constant $\hat{g}(k\cdot\dot{z}) = g$.
- Vector-like currents have linear $\hat{g}(k\cdot\dot{z}) = (\sqrt{2}\,e/\rho)(ik\cdot\dot{z})$.
- Non-minimal scalar-like currents have $\hat{g} \propto (k\cdot\dot{z})^n$ for $n \geq 2$. They generalize the couplings highlighted by (8.56), which characterize the matter particle's non-rigidity.
- Currents with negative powers of $k\cdot\dot{z}$ are permitted in our analysis but less phenomenologically interesting, because their support is nonlocal even when $\rho = 0$.

This classification is the main result of this subsection, and for the rest of this chapter we will focus on scalar-like and vector-like currents. A continuous spin field coupled by a scalar-like current is of less phenomenological interest because it reduces as $\rho \to 0$ to a massless scalar field, which has not been observed. However, this case is mathematically simpler and will serve as useful preparation for the case of vector-like currents, which can describe infrared modifications of electromagnetism.

We have defined scalar-like and vector-like currents so that they couple to radiation universally. Note, however, that the long-range force between particles is *not* universal. For scalar and vector fields, we found that currents proportional to the equation of motion operator produce contact interactions, which only take effect when particles coincide in space. By contrast, a continuous spin current is generally not localized to a particle's worldline, so the currents of particles can overlap even when the particles themselves are well-separated.

To conclude, we note that while the decompositions above use a "temporal" prefactor $e^{-i\rho\eta\cdot\dot{z}/k\cdot\dot{z}}$, this was an arbitrary choice made for later convenience, and does not single out the temporal current as more fundamental. In addition, it is natural to conjecture that in a more complete description, where all sources of stress-energy could to the continuous spin field with equal strength, one might have tensor-like currents with $\hat{g} \propto (k\cdot\dot{z})^2/\rho^2$, where the terms that diverge as $\rho \to 0$ reduce to total derivatives on-shell. We defer further exploration of this conjecture to future work. Finally, in appendix 8.9.3 we compare our currents to those previously found by working in terms of matter fields.

8.4 Currents and Interactions in Spacetime

The nonlocality of the currents found in section 8.3 motivates investigating the locality and causality properties of our theory. In subsection 8.4.1, we compute the profiles of some simple currents in spacetime, and show that they can be confined to the forward or backward light cone if their essential singularities appear only at real frequencies. In subsection 8.4.2, we give specific requirements on currents and their boundary conditions for the matter particles to have manifestly causal dynamics. This section can be skipped without loss of continuity.

8.4.1 Simple Currents in Spacetime

Currents of Worldline Elements

We first compute the inverse Fourier transforms $j(\eta, x, \dot{z})$ for our simple currents, which gives the spacetime profile of the current from a differential element of the worldline. For simplicity we can work in the frame of such a worldline element, where $\dot{z}^\mu = (1, \mathbf{0})$. The results below are illustrated at left in Fig. 8.2, and derived in appendix 8.9.4.

First, for the scalar-like spatial current, we have

$$j_S(\boldsymbol{\eta}, \mathbf{r}) = g \int \frac{d\omega\, d^3\mathbf{k}}{(2\pi)^4}\, e^{-ik\cdot x} e^{-i\rho\boldsymbol{\eta}\cdot\hat{\mathbf{k}}/|\mathbf{k}|} \tag{8.89}$$

$$= g\,\delta(t)\left(\delta^{(3)}(\mathbf{r}) - \frac{|\rho\boldsymbol{\eta}|(1-\cos\theta)}{8\pi r^2} J_2\left(\sqrt{2|\rho\boldsymbol{\eta}| r(1-\cos\theta)}\right)\right) \tag{8.90}$$

where θ is the angle between $\boldsymbol{\eta}$ and $\mathbf{r}$. Above, the ω integral was trivial, while the $\mathbf{k}$ integral requires handling a benign essential singularity at $\mathbf{k} = 0$. One curious feature of this result is that it is not everywhere analytic in η. Analytic f's can correspond to nonanalytic j's, but there is still no problem with defining η-space integration, as explained in appendix 8.8.3.

The result (8.90) shows that the spatial current of a worldline element is localized in time, but has a part spread over a distance $r \sim 1/\rho$ in space. The delocalized part smoothly goes to zero at large r, and in the $\rho \to 0$ limit it becomes *larger* in spatial extent, but also decouples. By contrast, for the scalar-like temporal current the current is localized in space,

$$j_T(\eta^0, \mathbf{r}, t) = g \int \frac{d\omega\, d^3\mathbf{k}}{(2\pi)^4}\, e^{-ik\cdot x} e^{-i\rho\eta^0/\omega} = g\,\delta^{(3)}(\mathbf{r}) \int \frac{d\omega}{2\pi}\, e^{-i\omega t} e^{-i\rho\eta^0/\omega}. \tag{8.91}$$

The frequency integral now passes through an essential singularity at $\omega = 0$, and thus requires a contour prescription to define. Passing above or below it corresponds to imposing retarded or advanced boundary conditions in position space, respectively. For the former, we find

$$j_T(\eta^0, \mathbf{r}, t) = g\,\delta^{(3)}(\mathbf{r})\left(\delta(t) - \theta(t)\sqrt{\frac{\rho\eta^0}{t}} J_1\left(2\sqrt{\rho\eta^0 t}\right)\right). \tag{8.92}$$

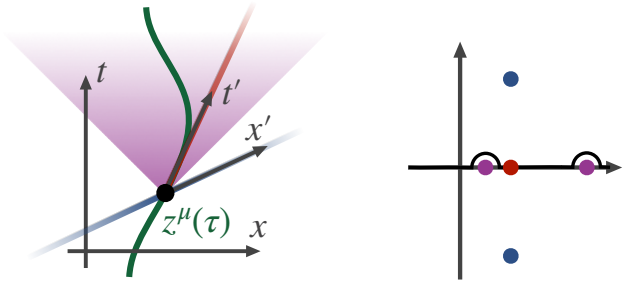

Figure 8.2: **Left:** Localization properties of some simple scalar-like currents. In the rest frame of a worldline element, with coordinates $(\mathbf{x}', t')$, the spatial current (blue) is localized on the spacelike slice $t' = 0$, the retarded temporal current (red) is localized on the timelike ray $\mathbf{x}' = 0$, $t' > 0$, and the retarded inhomogeneous current (purple) is contained on or within the forward light cone. **Right:** Essential singularities in the complex ω plane for the spatial current, temporal current, and the integral in (8.93) for the inhomogeneous current, for a velocity with $\mathbf{k} \cdot \mathbf{v} > 0$. We also show an integration contour corresponding to retarded boundary conditions for the inhomogeneous current.

Concretely, this implies the current of a worldline element at position $\mathbf{r}$ with velocity $\mathbf{v}$ is supported on the forward ray $\mathbf{r} + \mathbf{v}T$ for $T > 0$. It varies on the timescale $t \sim 1/\rho$, and is confined to within the forward light cone.

Finally, for the scalar-like inhomogeneous current we have

$$j_I(\eta, \mathbf{r}, t) = g \,\mathrm{Re} \int \frac{d\omega \, d^3\mathbf{k}}{(2\pi)^4} \, e^{-ik\cdot x} \, \exp\left(-i\rho \frac{\eta^0(\omega + \rho\beta) - \boldsymbol{\eta} \cdot \mathbf{k}}{\omega^2 + \rho\beta\omega - |\mathbf{k}|^2}\right). \tag{8.93}$$

For real β, the integral has two essential singularities at real ω, so a contour prescription is again required to define the current in spacetime. Integrating above both singularities corresponds to retarded boundary conditions, and gives a result confined to $t \geq 0$. While we have not computed the result, we expect it to have a spacetime spread $\sim 1/\rho$ on dimensional grounds, and Lorentz invariance implies it must be confined on or within the forward light cone. Advanced boundary conditions correspond to integrating below both singularities.

The properties above are qualitatively unchanged for the vector-like currents. For example, for the vector-like spatial current, j_S^V is identical to (8.90) but with g replaced with $\sqrt{2}\, e\eta^0$. For the vector-like temporal current (8.81), we have

$$j_T^V(\eta^0, \mathbf{r}, t) = \sqrt{2}\, e\eta^0 \, \delta^{(3)}(\mathbf{r}) \left(\delta(t) - \theta(t) \, \frac{\rho}{t} J_2\left(2\sqrt{\rho\eta^0 t}\right)\right) \tag{8.94}$$

which has the same localization properties as (8.92).

One cannot ascribe too much significance to the expressions above because η-space expressions are unphysical. We must always integrate over η to produce physical observables, and as we will see in later sections, the results are often the same for currents which appear radically different in η-space.

However, we can infer in general that boundary conditions are needed to define any current with essential singularities at real ω, and retarded or advanced boundary conditions can be imposed for any current whose essential singularities are all at real ω. These features suggest that such currents arise more fundamentally through integrating out locally coupled, auxiliary degrees of freedom.

Currents and Fields of Static Particles

We can also build intuition by evaluating the total current for a static particle at rest at the origin, and the accompanying continuous spin field. For ordinary fields, these currents are time-independent and localized at the origin, but the continuity condition forbids such solutions for nonzero ρ, leading to currents that are either delocalized or time-dependent.

For the scalar-like spatial current, trivially integrating (8.90) gives

$$J_S(\boldsymbol{\eta}, \mathbf{r}) = g \left(\delta^{(3)}(\mathbf{r}) - \frac{|\rho\boldsymbol{\eta}|(1-\cos\theta)}{8\pi r^2} J_2\left(\sqrt{2|\rho\boldsymbol{\eta}| r(1-\cos\theta)}\right)\right) \tag{8.95}$$

which is delocalized. The corresponding field, in strong harmonic gauge, is

$$\Psi_S(\boldsymbol{\eta}, \mathbf{r}) = \frac{g}{4\pi r} J_0\left(\sqrt{2|\rho\boldsymbol{\eta}| r(1-\cos\theta)}\right). \tag{8.96}$$

For the scalar-like temporal current, formally integrating (8.92) yields zero for positive η^0, but a divergent result for negative η^0. To make sense of the current, we need to introduce an appropriate infrared regulator. One simple prescription is to turn off the coupling g at early times, replacing it with $g\,\theta(\tau + T)$ for a large positive T. This gives a current

$$J_T(\eta^0, t, \mathbf{r}) = g\,\delta^{(3)}(\mathbf{r})\, J_0\left(2\sqrt{\rho\eta^0(t+T)}\right)\theta(t+T) \tag{8.97}$$

and the corresponding field, in strong harmonic gauge, is an outgoing spherical wave

$$\Psi_T(\eta^0, t, \mathbf{r}) = \frac{g}{4\pi r} J_0\left(2\sqrt{\rho\eta^0(t+T-r)}\right)\theta(t+T-r). \tag{8.98}$$

We recover the familiar scalar solution in the limit $\rho \to 0$ and $T \to \infty$, provided that $\rho T \ll 1$. We could also regulate the solution by allowing the charge to oscillate with a low frequency, or by giving the particle nontrivial motion; expressions for the current for arbitrary particle motion are given in appendix 8.9.4 but are unenlightening.

For the scalar-like inhomogeneous current, there are a variety of contour prescriptions for the frequency integration, but they all give the same current for a static particle. This is reflected by the fact that we can perform the τ integration first, which produces a delta function that eliminates the

frequency integration, yielding

$$J_I(\eta, \mathbf{r}) = g \int \frac{d^3\mathbf{k}}{(2\pi)^3} e^{i\mathbf{k}\cdot\mathbf{r}} e^{-i\rho\boldsymbol{\eta}\cdot\hat{\mathbf{k}}/|\mathbf{k}|} \cos(\eta^0 \beta \rho^2/|\mathbf{k}|^2) \tag{8.99}$$

which reduces to the spatial current for $\beta \to 0$. Such a manipulation would not have been possible for the temporal current, because for a static particle its essential singularity is at $\omega = 0$ itself. Finally, for the vector-like currents the results are qualitatively similar, though there is also an overall prefactor of η^0.

8.4.2 Equations of Motion and Causality

We have just seen that the current j of an element of a particle's worldline is not local, which seems to violate naive causality. Specifically, generalizing the action (8.1) to multiple matter particles with worldlines $z_i^\mu(\tau_i)$ yields the equations of motion

$$\partial_x^2 \Psi(\eta, x) = \sum_i \int d\tau_i \, j(\eta, x - z_i(\tau_i), \dot{z}_i(\tau_i)), \tag{8.100}$$

$$m_i \ddot{z}_i^\mu(\tau_i) = -\int d^4x \, [d^4\eta] \, \delta'(\eta^2 + 1) \, \Psi(\eta, x) \left(\partial_x^\mu + \frac{d}{d\tau_i} \frac{\partial}{\partial \dot{z}_i^\mu}\right) j(\eta, x - z_i(\tau_i), \dot{z}_i(\tau_i)). \tag{8.101}$$

This yields two types of potentially acausal effects. First, if j extends outside the forward lightcone of z_i, then (8.100) implies the field is sourced acasually: there are reference frames where the field at x depend on the motion of particles at times later than x^0. Likewise, if j extends outside the backward lightcone of z_i, then (8.101) implies the particle responds acausally: there are frames where its acceleration depends on field values at times later than z_i^0. These effects are both avoided if j is local, but this is impossible for nonzero ρ.

Manifestly Causal Equations of Motion

There is, however, a straightforward modification of the equations of motion that renders our theory manifestly causal. We have seen that currents whose essential singularities are at real ω, such as the temporal and inhomogeneous currents, admit retarded or advanced boundary conditions, where j is confined within the forward or backward light cone respectively. The theory is manifestly causal if the current has retarded boundary conditions j_R when sourcing the field, and advanced boundary conditions j_A when responding to it, i.e. if

$$\partial_x^2 \Psi(\eta, x) = \sum_i \int d\tau \, j_R(\eta, x - z_i(\tau_i), \dot{z}_i(\tau_i)), \tag{8.102}$$

$$m_i \ddot{z}_i^\mu(\tau_i) = -\int d^4x \, [d^4\eta] \, \delta'(\eta^2 + 1) \, \Psi(\eta, x) \left(\partial_x^\mu + \frac{d}{d\tau_i} \frac{\partial}{\partial \dot{z}_i^\mu}\right) j_A(\eta, x - z_i(\tau_i), \dot{z}_i(\tau_i)). \tag{8.103}$$

Note, however, that these equations of motion still have the unfamiliar property that their exact solution appears to require knowledge of fields and particle trajectories in the infinite past, not just on a Cauchy surface in spacetime.

Such equations of motion do not directly emerge from our action (8.1), which allows only a single choice of current. But it is reasonable to speculate that this action is merely an effective one, which arises from integrating out "intermediate" auxiliary or dynamical fields that interact locally with both the particle and the continuous spin field. In this case, solving the intermediate fields' equations of motion would require a choice of boundary conditions. Inserting such solutions into the full equations of motion would induce precisely the kind of asymmetry in (8.102) and (8.103). Motivated by the form of our currents, we have constructed toy models with similar structure, but we have yet to realize a full Lagrangian model that renders our currents entirely local.

Non-Manifest Causality

We should also take care in dismissing the original equations of motion (8.100) and (8.101) as irreparably acausal. In particular, the gauge field $\Psi(\eta, x)$ has a huge amount of gauge freedom, and indeed no local gauge-invariant observables can be built from the field. Thus, the apparently acausal sourcing of $\Psi(\eta, x)$ could be a gauge artifact. To avoid this ambiguity, we should define causality in terms of the interactions of matter particles: the theory is causal if, when a particle is instantaneously kicked at some point, the kick cannot affect the trajectories of other particles until they enter the future light cone of that point.

One can perform a concrete computation to determine if the theory is causal in this sense, for each choice of current j. We have not yet rigorously studied this question, but we note the answer is not obvious a priori, as apparently acausal effects can vanish after the x and η integrations for certain j. A similar cancellation arises in the quantization of the continuous spin field, where the gauge fixed field operators end up obeying causal commutation relations.

Another possibility is that full consistency requires additional effects absent from (8.1), such as "contact" interactions between extended currents that do not involve a continuous spin field, but which exactly cancel acausal effects. Indeed, this is precisely what occurs in electromagnetism in Coulomb gauge, which contains an instantaneous interparticle potential but yet is causal as a whole.

Further investigation of all of these possibilities represent important directions for future work. For now, one can simply define our theory by the manifestly causal equations of motion. In practical terms, the physical results derived below are not affected either way, as they either consider non-accelerating particles – where retarded and advanced boundary conditions give equal results – or the coupling of particles to radiation, where the results are completely independent of the details of the current.

8.5 Forces on Matter Particles

We can readily calculate the dynamics of matter particles from the action (8.1). In subsection 8.5.1, we consider two particles interacting via the continuous spin field, and compute both the static interaction potential and the leading velocity-dependent corrections for some example currents. In subsection 8.5.2 we compute forces from radiation background fields. These are universal for all scalar-like and vector-like currents, depending only on the spin scale ρ, and we give results for backgrounds with $|h| \leq 2$.

8.5.1 Static and Velocity-Dependent Interaction Potentials

Consider particles with trajectories $z_i^\mu(\tau)$, coupled to a continuous spin field by currents J_i. Each current produces a field Ψ_i which interacts with each other particle j, contributing

$$S_{ij} = \int d^4x\, [d^4\eta]\, \delta'(\eta^2+1)\, \Psi_i(\eta,x) J_j(\eta,x) \tag{8.104}$$

$$= -\int \frac{d^4k}{(2\pi)^4}\, [d^4\eta]\, \delta'(\eta^2+1)\, \frac{J_i(\eta,k)J_j(\eta,-k)}{(\omega+i\epsilon)^2-|\mathbf{k}|^2} \tag{8.105}$$

$$= -\int \frac{d^4k}{(2\pi)^4}\, [d^4\eta]\, \delta'(\eta^2+1)\, d\tau_i\, d\tau_j\, \frac{e^{-ik\cdot(z_i(\tau_i)-z_j(\tau_j))} f(\eta,k,\dot{z}_i) f^*(\eta,k,\dot{z}_j)}{(\omega+i\epsilon)^2-|\mathbf{k}|^2} \tag{8.106}$$

to the action, where we have assumed retarded boundary conditions. Evaluating this generic expression in terms of the particle trajectories allows us to compute both static and velocity-dependent potentials. For simplicity we consider two dynamical particles, where the total interaction action is $S_{\text{int}} = (S_{12}+S_{21})/2$ to avoid double counting. Two useful integrals are

$$\int \frac{d^3\mathbf{k}}{(2\pi)^3} \frac{e^{i\mathbf{k}\cdot\mathbf{r}}}{|\mathbf{k}|^{2+n}} = \frac{1}{(2n)!} \frac{(-r^2)^n}{4\pi r}, \tag{8.107}$$

$$\int \frac{d^3\mathbf{k}}{(2\pi)^3} \frac{(\mathbf{a}\cdot\hat{\mathbf{k}})(\mathbf{b}\cdot\hat{\mathbf{k}})\, e^{i\mathbf{k}\cdot\mathbf{r}}}{|\mathbf{k}|^2} = \frac{\mathbf{a}\cdot\mathbf{b} - (\mathbf{a}\cdot\hat{\mathbf{r}})(\mathbf{b}\cdot\hat{\mathbf{r}})}{8\pi r}. \tag{8.108}$$

The $n=0$ case of (8.107) is standard, and can be used to derive (8.108) using symmetry. For general integer $n>0$, (8.107) can be derived inductively by taking the Laplacian of both sides. Technically, in that case there are also distributional corrections at $r=0$, but this does not affect the computation of long-range forces.

Static Potentials

We warm up by considering static particles, $z_i^\mu(\tau) = (t_i, \mathbf{r}_i)$, interacting by an ordinary scalar field, $f = g$. Then the interaction simplifies to

$$S_{ij} = -g^2 \int \frac{d^4k}{(2\pi)^4} [d^4\eta]\, \delta'(\eta^2+1)\, dt_i\, dt_j\, \frac{e^{-i\omega(t_i-t_j)} e^{i\mathbf{k}\cdot(\mathbf{r}_i-\mathbf{r}_j)}}{(\omega+i\epsilon)^2 - |\mathbf{k}|^2}. \tag{8.109}$$

Performing one time integration and stripping off the other to yield a Lagrangian gives

$$L_{\text{int}} = g^2 \int \frac{d^3\mathbf{k}}{(2\pi)^3} \frac{e^{i\mathbf{k}\cdot(\mathbf{r}_1-\mathbf{r}_2)}}{|\mathbf{k}|^2} = \frac{g^2}{4\pi r} \tag{8.110}$$

for a pair of particles with separation $\mathbf{r} = \mathbf{r}_1 - \mathbf{r}_2$. This is a familiar $1/r^2$ attractive force.

Given our previous results (8.96) and (8.98) for the continuous spin fields of static particles, one might suspect that for nonzero ρ the static potential must be radically different, either deviating from $1/r$ or exhibiting time dependence. However, in the static limit, the ρ-dependent phases in the temporal and spatial scalar-like currents simply cancel out, leading to the exact same result. This is a first hint that continuous spin physics can be simpler than the intermediate η-space expressions suggest.

In general, while the definition of a scalar-like current ensures the potential contains a piece of the form (8.110), there can be deviations at short or long distances. In appendix 8.9.2, we wrote the general solution to the continuity condition for static particles. Using just the $\bar{g}_0$ term in the homogeneous solution (8.349), one can introduce terms in the integrand of (8.110) scaling as $|\mathbf{k}|^n$, which yield contributions to the potential proportional to $1/r^{n+1}$. For positive n, this reflects how ordinary nonminimal couplings can modify forces at short distances. The novelty of continuous spin physics is that the continuity condition motivates solutions with an infinite series of negative n, which modify forces at long distances.

To give one simple example, we consider the inhomogeneous current (8.79), which satisfies the continuity condition for both real and imaginary β. For this current there are cross terms whose phases do not cancel, leading to

$$L_{\text{int}} = \frac{g^2}{4} \int \frac{d^3\mathbf{k}}{(2\pi)^3} \frac{e^{i\mathbf{k}\cdot\mathbf{r}}}{|\mathbf{k}|^2} \int [d^4\eta]\, \delta'(\eta^2+1) \left(2 + e^{2i\eta^0\beta\rho^2/|\mathbf{k}|^2} + e^{-2i\eta^0\beta\rho^2/|\mathbf{k}|^2}\right) \tag{8.111}$$

$$= \frac{g^2}{2} \int \frac{d^3\mathbf{k}}{(2\pi)^3} \frac{e^{i\mathbf{k}\cdot\mathbf{r}}}{|\mathbf{k}|^2} \left(1 + J_0(2i\beta\rho^2/|\mathbf{k}|^2)\right) \tag{8.112}$$

$$= \frac{g^2}{4\pi^2} \frac{1}{r} \int_0^\infty dx\, \frac{\sin x}{x} \left(1 + J_0\left(\frac{2i\beta\rho^2 r^2}{x^2}\right)\right) \tag{8.113}$$

$$= \frac{g^2}{8\pi r} \left(1 + \int_{-\infty}^\infty dx\, \frac{e^{ix}}{\pi i\, x} J_0\left(\frac{2i\beta\rho^2 r^2}{x^2}\right)\right) \tag{8.114}$$

where we applied (8.255), then integrated over $\hat{\mathbf{k}}$ and defined $x = |\mathbf{k}|r$.

While it would be tempting to evaluate the integral by Taylor expanding the Bessel function and applying (8.107) to each term, this would not be legitimate because the integral passes directly through an essential singularity at $x = 0$. However, for imaginary β the Bessel function is rapidly oscillating but bounded near $x = 0$, so the integral can be evaluated analytically. A continuation with the desired symmetry properties can be written in terms of Meijer G-functions,

$$L_{\text{int}} = \frac{g^2}{8\pi r}\left(1 + \frac{1}{\sqrt{2\pi}}\, G^{0,3}_{6,0}\left(\frac{2^{16}}{\beta^4(\rho r)^8}, 2\middle|^{\frac{1}{4}\ \frac{3}{4}\ 1\ \frac{1}{2}\ 1\ 1}\right)\right). \tag{8.115}$$

At real β, the function (8.115) can be Taylor expanded as

$$L_{\text{int}} = \frac{g^2}{4\pi r}\left(1 - \frac{4\sqrt{2\beta}\,\rho r}{\Gamma(1/4)^2} + \frac{\beta^{3/2}\,(\rho r)^3}{12\sqrt{2}\,\Gamma(7/4)^2} + \dots\right) \tag{8.116}$$

The force is always attractive, and at large r, the G-function falls to zero, leaving an asymptotic potential of half the standard strength.

All of these qualitative conclusions hold unchanged for vector-like currents. For an ordinary vector field, one picks up a factor of $(\eta^0)^2$ which causes a sign flip, so that like charges repel. Again, the temporal and spatial currents do not produce any deviations from Coulomb's law, and the inhomogeneous current yields long-distance corrections,

$$L_{\text{int}} = -\frac{e^2}{4\pi r}\int_{-\infty}^{\infty} dx\, \frac{e^{ix}}{\pi i\, x}\, \frac{x^4}{\beta^2(\rho r)^4}\left(J_0\left(\frac{2i\beta\rho^2 r^2}{x^2}\right) - 1\right) \tag{8.117}$$

$$= \frac{e^2}{4\pi r}\left(\frac{1}{\sqrt{2\pi}}\, G^{0,3}_{6,0}\left(\frac{2^{16}}{\beta^4(\rho r)^8}, 2\middle|^{\frac{1}{4}\ \frac{3}{4}\ 1\ \frac{1}{2}\ 2\ 2}\right)\right). \tag{8.118}$$

This result can again be Taylor expanded for real β, giving

$$L_{\text{int}} = -\frac{e^2}{4\pi r}\left(1 - \frac{\sqrt{\beta}\,\rho r}{\sqrt{2}\,\Gamma(9/4)^2} + \dots\right) \tag{8.119}$$

while at large r it oscillates and alternates in sign.

Velocity-Dependent Potentials

We computed static interaction potentials by evaluating the action for static particles, but there are also important velocity-dependent effects. We can include them by evaluating the action for moving but nonaccelerating particles, yielding a velocity-dependent potential. These potentials in turn neglect acceleration-dependent effects, such as radiation reaction, but yield a good description of the dynamics when the acceleration is small.

To aid the reader, we first review the velocity-dependent potential for an ordinary scalar field.

For nonaccelerating particles, the worldline is $x_i^\mu(\tau) = (t_i, \mathbf{r}_i^0 + \mathbf{v}_i t_i)$ where $t_i = \gamma_i \tau$, so

$$S_{ij} = -g^2 \int \frac{d^4k}{(2\pi)^4} \frac{dt_i\, dt_j}{\gamma_i \gamma_j} \frac{e^{-i\omega(t_i - t_j)} e^{i\mathbf{k}\cdot(\mathbf{r}_i^0 - \mathbf{r}_j^0)} e^{i\mathbf{k}\cdot(\mathbf{v}_i t_i - \mathbf{v}_j t_j)}}{(\omega + i\epsilon)^2 - |\mathbf{k}|^2} \tag{8.120}$$

$$= g^2 \int \frac{d^3\mathbf{k}}{(2\pi)^3} \frac{dt_j}{\gamma_i \gamma_j} \frac{e^{i\mathbf{k}\cdot\mathbf{r}_{ij}(t_j)}}{|\mathbf{k}|^2 - (\mathbf{k}\cdot\mathbf{v}_i)^2}. \tag{8.121}$$

where doing the t_i integral set $\omega = \mathbf{k}\cdot\mathbf{v}_i$, and the separation is $\mathbf{r}_{ij}(t) = \mathbf{r}_i^0 + \mathbf{v}_i t - (\mathbf{r}_j^0 + \mathbf{v}_j t)$. Stripping off the t_j integration yields the Lagrangian for particle j in the field of particle i, so that the interaction Lagrangian of two dynamical particles with separation $\mathbf{r}(t)$ is

$$L_{\rm int} = \frac{g^2}{2\gamma_1\gamma_2} \int \frac{d^3\mathbf{k}}{(2\pi)^3} \frac{e^{i\mathbf{k}\cdot\mathbf{r}(t)}}{|\mathbf{k}|^2} \left(\frac{1}{1 - (\hat{\mathbf{k}}\cdot\mathbf{v}_1)^2} + \frac{1}{1 - (\hat{\mathbf{k}}\cdot\mathbf{v}_2)^2} \right) \tag{8.122}$$

$$= \frac{g^2}{4\pi r} \left(1 - \frac{v_1^2}{4} - \frac{v_2^2}{4} - \frac{(\mathbf{v}_1\cdot\hat{\mathbf{r}})^2}{4} - \frac{(\mathbf{v}_2\cdot\hat{\mathbf{r}})^2}{4} + O(v^4) \right) \tag{8.123}$$

where we used (8.108). A similar calculation for a vector field yields the potential

$$L_{\rm int} = -\frac{e^2}{4\pi r} \left(1 - \mathbf{v}_1\cdot\mathbf{v}_2 + \frac{v_1^2}{4} + \frac{v_2^2}{4} - \frac{(\mathbf{v}_1\cdot\hat{\mathbf{r}})^2}{4} - \frac{(\mathbf{v}_2\cdot\hat{\mathbf{r}})^2}{4} + O(v^4) \right) \tag{8.124}$$

which includes magnetic interactions and retardation effects. While it may look unfamiliar, it is equivalent to the textbook Darwin Lagrangian [506]

$$L_{\rm int} = -\frac{e^2}{4\pi r} \left(1 - \frac{\mathbf{v}_1\cdot\mathbf{v}_2 + (\mathbf{v}_1\cdot\hat{\mathbf{r}})(\mathbf{v}_2\cdot\hat{\mathbf{r}})}{2} + O(v^4) \right) \tag{8.125}$$

since, up to accelerations, it differs by the total time derivative of $(e^2/16\pi)(\mathbf{v}_1\cdot\hat{\mathbf{r}} - \mathbf{v}_2\cdot\hat{\mathbf{r}})$.

For nonzero ρ our formalism readily yields expressions for velocity-dependent potentials in momentum space, but evaluating the Fourier transform is complicated by the essential singularity terms. We will therefore consider only the scalar spatial current, where the integrals are simplest. The answer will be a series in the independent dimensionless variables v^2 and $\rho v r$, so to avoid clutter we will neglect terms suppressed by a power of v^2.

Defining $\mathbf{v}_{ij} = \mathbf{v}_j - \mathbf{v}_i$, and letting V_i be the vector defined below (8.77), we have

$$L_{ij} \approx g^2 \int \frac{d^3\mathbf{k}}{(2\pi)^3} \frac{e^{i\mathbf{k}\cdot\mathbf{r}_{ij}(t)}}{|\mathbf{k}|^2} \int [d^4\eta]\, \delta'(\eta^2 + 1)\, e^{-i\rho\eta\cdot V_i/k\cdot V_i} e^{i\rho\eta\cdot V_j/k\cdot V_j} \Big|_{\omega = \mathbf{k}\cdot\mathbf{v}_i} \tag{8.126}$$

$$\approx g^2 \int [d^4\eta]\, \delta'(\eta^2 + 1) \int \frac{d^3\mathbf{k}}{(2\pi)^3} \frac{e^{i\mathbf{k}\cdot\mathbf{r}_{ij}(t)}}{|\mathbf{k}|^2}\, e^{-i\rho\eta^0 \mathbf{k}\cdot\mathbf{v}_{ij}/|\mathbf{k}|^2}. \tag{8.127}$$

where we dropped terms of order v^2 inside the exponent. Next, the $\mathbf{k}$ integral can be evaluated using the same method as used to evaluate (8.353). Defining $x = \rho v_{ij} r_{ij}(1 - \cos\theta)$, where θ is the angle

between $\mathbf{r}_{ij}$ and $\mathbf{v}_{ij}$, we have

$$L_{ij} \approx \frac{g^2}{4\pi r_{ij}} \int [d^4\eta]\, \delta'(\eta^2+1)\, J_0\left(\sqrt{2\eta^0 x}\right) = \frac{g^2}{4\pi r_{ij}}\, I_0(\sqrt{x}) J_0(\sqrt{x}) \tag{8.128}$$

where we performed the η integral by directly using the generating function (8.254). Thus, at leading nontrivial order, the velocity-dependent potential for a pair of matter particles is

$$L_{\rm int} = \frac{g^2}{4\pi r}\left(1 - \frac{\rho^2 r^2}{32}\left(|\mathbf{v}_i - \mathbf{v}_j| - (\mathbf{v}_i - \mathbf{v}_j)\cdot\hat{\mathbf{r}}\right)^2 + O(v^2, (\rho v r)^4)\right). \tag{8.129}$$

For particles moving along a line, the new term has no effect, while for transverse motion it becomes important at long distances, $\rho v r \sim 1$, just like the corrections to static forces.

8.5.2 Forces From Background Radiation Fields

The Interaction Lagrangian

Next, we consider the dynamics of a particle in a free background field Ψ, by evaluating the interaction action (8.63) in terms of the mode expansion coefficients defined in (8.36),

$$S_{\rm int} = \mathrm{Re}\int \frac{d^3\mathbf{k}}{(2\pi)^3\,|\mathbf{k}|}\,[d^4\eta]\,\delta'(\eta^2+1)\sum_h a_h(\mathbf{k})\psi_{h,k}(\eta) J(\eta,k)^*\Big|_{k^0=|\mathbf{k}|} \tag{8.130}$$

where taking the real part adds on the negative frequency part of the field. As explained below (8.87), this action is independent of $X(\eta,k,\dot{z})$, and thus depends only on $\hat{g}(k\cdot\dot{z})$.

For concreteness, we note this can be shown more directly. The k^2X term in (8.87) vanishes since k is null, and the remaining term is of the form $D\xi$. However, the identity (8.28) implies

$$\int [d^4\eta]\,\delta'(\eta^2+1)\,(D\xi)\,\Psi = \frac{1}{2}\int [d^4\eta]\,\Delta(\delta(\eta^2+1)\,\xi)\,\Psi \tag{8.131}$$

and integrating by parts yields an integrand proportional to $\delta(\eta^2+1)\,(\Delta\Psi)$, which vanishes in harmonic gauge. It thus vanishes in any gauge, since the action is gauge invariant.

In any case, we can keep just the $\hat{g}$ term in the current, yielding

$$S_{\rm int} = \mathrm{Re}\sum_h \int d\tau\, \frac{d^3\mathbf{k}}{(2\pi)^3\,|\mathbf{k}|}\,[d^4\eta]\,\delta'(\eta^2+1)\,\hat{g}^*\,a_h(\mathbf{k})e^{-ik\cdot z}\,\psi_{h,k}(\eta)\,e^{i\rho\eta\cdot\dot{z}/k\cdot\dot{z}}\Big|_{k^0=|\mathbf{k}|} \tag{8.132}$$

$$= \mathrm{Re}\sum_h \int d\tau\, \frac{d^3\mathbf{k}}{(2\pi)^3\,|\mathbf{k}|}\,\hat{g}^*\,a_h(\mathbf{k})e^{-ik\cdot z}\left(\frac{\epsilon_+\cdot V}{|\epsilon_+\cdot V|}\right)^h J_h(\sqrt{-V^2})\Big|_{k^0=|\mathbf{k}|} \tag{8.133}$$

where we performed the η integral using (8.273) with $V = \rho((\dot{z}/k\cdot\dot{z}) - q)$. We can make this more physically transparent by specializing to $\epsilon_\pm^0 = 0$ and simplifying using the properties of the null frame

vectors. The result is the Lagrangian

$$L_{\rm int} = {\rm Re}\sum_h \sqrt{1-v^2}\int \frac{d^3\mathbf{k}}{(2\pi)^3\,|\mathbf{k}|}\hat{g}^* a_h(\mathbf{k}) e^{-i(|\mathbf{k}|t-\mathbf{k}\cdot\mathbf{r})}\left(\frac{-\boldsymbol{\epsilon}_+\cdot\mathbf{v}_\perp}{v_\perp}\right)^h J_h\left(\frac{\rho v_\perp}{|\mathbf{k}|-\mathbf{k}\cdot\mathbf{v}}\right) \tag{8.134}$$

whose integral over coordinate time t is the interaction action. Above, $\mathbf{r}(t)$ and $\mathbf{v}(t)$ are the position and velocity of the particle, and $\mathbf{v}_\perp$ is the velocity in the plane transverse to $\hat{\mathbf{k}}$. The action is smooth in $\mathbf{v}$, despite its dependence on the magnitude of $\mathbf{v}_\perp$, because of the phase in front of the Bessel function.

The expression (8.134) is our general result, but for simplicity we will specialize to monochromatic plane waves traveling in the $\hat{\mathbf{k}} = \hat{\mathbf{z}}$ direction, by taking

$$a_h(\mathbf{k}) = \omega_0\,\bar{a}_h\,(2\pi)^3\delta^{(3)}(\mathbf{k}-\omega\hat{\mathbf{z}}). \tag{8.135}$$

The resulting Lagrangians are

$$L^S_{\rm int} = g\sqrt{1-v^2}\,{\rm Re}\sum_h \bar{a}_h e^{-i\omega_0(t-z)}\left(\frac{-v_x-iv_y}{v_\perp}\right)^h J_h\left(\frac{\rho v_\perp}{\omega_0(1-v_z)}\right) \tag{8.136}$$

for any scalar-like current, and

$$L^V_{\rm int} = \frac{\sqrt{2}\,e}{\rho}\,{\rm Re}\sum_h \bar{a}_h e^{-i\omega_0(t-z)}(-i\omega_0(1-v_z))\left(\frac{-v_x-iv_y}{v_\perp}\right)^h J_h\left(\frac{\rho v_\perp}{\omega_0(1-v_z)}\right) \tag{8.137}$$

for any vector-like current, where above z now stands for $\mathbf{r}\cdot\hat{\mathbf{z}}$ and $v_\perp = \sqrt{v_x^2+v_y^2}$.

We will work with three specific backgrounds below. First, we will consider a helicity zero background with $\bar{a}_0 = \phi_0$, which reduces to a scalar field $\phi = \phi_0\cos(\omega_0(t-z))$ as $\rho\to 0$. Next, a background with nonzero $\bar{a}_1$ reduces as $\rho\to 0$ to a circularly polarized electromagnetic wave. For simplicity, we will consider the combination of $h=\pm 1$ backgrounds $\bar{a}_{-1} = -\bar{a}_1 = A_0/\sqrt{2}$, which reduces as $\rho\to 0$ to the linearly polarized wave

$$\mathbf{A} = -A_0\sin(\omega_0(t-z))\,\hat{\mathbf{x}}, \tag{8.138}$$

$$\mathbf{E} = \omega_0 A_0\cos(\omega_0(t-z))\hat{\mathbf{x}}, \tag{8.139}$$

$$\mathbf{B} = \omega_0 A_0\cos(\omega_0(t-z))\hat{\mathbf{y}}. \tag{8.140}$$

By varying the ratio $\bar{a}_1/\bar{a}_{-1}$, we could also produce backgrounds with an arbitrary elliptical polarization. Finally, we consider a helicity ± 2 background with $\bar{a}_2 = \bar{a}_{-2} = h$, which reduces as $\rho\to 0$ to a "plus" polarized gravitational wave, $h_{xx} = -h_{yy} = h\cos(\omega_0(t-z))$.

Extracting the Force

We can straightforwardly compute forces with the Lagrangians above, but there are multiple natural definitions of force. To build intuition, let us first consider particles minimally coupled to scalar, vector, or tensor fields with $\rho = 0$. The equations of motion are

$$(m - g\phi)\ddot{z}^\mu = -g(g^{\mu\nu} - \dot{z}^\mu \dot{z}^\nu)\partial_\nu \phi, \tag{8.141}$$

$$m\ddot{z}^\mu = e\dot{z}_\nu F^{\mu\nu}, \tag{8.142}$$

$$\ddot{z}^\mu = \kappa\, \dot{z}^\nu \dot{z}^\rho (\partial_\nu h_\rho{}^\mu + \partial_\rho h_\nu{}^\mu - \partial^\mu h_{\nu\rho})/2 \tag{8.143}$$

where a dot denotes a derivative with respect to proper time τ, and all fields are evaluated at $z^\mu(\tau)$. These are straightforwardly derived from the interaction actions (8.48), (8.50), and (8.59), which correspond to Lagrangians

$$L_{\text{int}}(\mathbf{r}(t), \mathbf{v}(t)) = \begin{cases} g\,\phi\,\sqrt{1-v^2} & \text{scalar} \\ e\,\mathbf{A}\cdot\mathbf{v} & \text{vector, radiation gauge} \\ (\kappa m/2)\, h^{ij} v_i v_j / \sqrt{1-v^2} & \text{tensor, transverse traceless gauge} \end{cases} . \tag{8.144}$$

All three fields produce qualitatively different effects. While the vector field yields the familiar Lorentz force, a scalar field can affect the particle's inertia, which can even cause singular accelerations when $\phi = m/g$, at which point our entire description of matter as particles breaks down. This effect comes from the v^2 term in the scalar Lagrangian. By contrast, there is no v^2 term for a tensor field in transverse traceless gauge, but in this case the coordinate acceleration of a free particle initially at rest is zero, indicating that the coordinate system itself stretches with the gravitational wave. This is an unnatural way to describe laboratory experiments with rigid detectors, for which we should instead use the proper detector frame, where the tensor field produces an ordinary Newtonian force [828].

For continuous spin backgrounds, we choose to define the force by $\mathbf{F} = d\mathbf{p}/dt$ where $\mathbf{p} = m\mathbf{v}/\sqrt{1-v^2}$ is the unperturbed three-momentum, as this is the most natural quantity for a vector background. The Euler–Lagrange equation yields

$$\mathbf{F} = \frac{\partial L_{\text{int}}}{\partial \mathbf{r}} - \frac{d}{dt}\frac{\partial L_{\text{int}}}{\partial \mathbf{v}} = \frac{\partial L_{\text{int}}}{\partial \mathbf{r}} - \left(\frac{\partial}{\partial t} + \mathbf{v}\cdot\frac{\partial}{\partial \mathbf{r}} + \mathbf{a}\cdot\frac{\partial}{\partial \mathbf{v}}\right)\frac{\partial L_{\text{int}}}{\partial \mathbf{v}}. \tag{8.145}$$

This is only an implicit equation, since $\mathbf{a}$ in the final term is itself determined by the force. In addition, this final term contains the inertia-modifying effects of a scalar field, which can produce singular accelerations. We avoid both of these issues by assuming the particle experiences only a single weak background field. In this case, both $\mathbf{a}$ and L_{int} start at first order in the field, so the last term is second order and can be dropped. (Of course, we are also implicitly ignoring backreaction effects, such as radiation reaction forces.)

Working in Euclidean notation, the resulting forces for scalar, vector, and tensor fields are

$$\mathbf{F} \approx g(\nabla\phi + \mathbf{v}\dot{\phi} - (v^2/2)\nabla\phi + \mathbf{v}(\mathbf{v}\cdot\nabla)\phi + O(v^3)), \tag{8.146}$$

$$\mathbf{F} = e(\mathbf{E} + \mathbf{v}\times\mathbf{B}), \tag{8.147}$$

$$F_i = \kappa m(-\dot{h}_{ij}v_j + v_jv_k(\partial_i h_{jk} - \partial_j h_{ik} - \partial_k h_{ij})/2 + O(v^3)) \tag{8.148}$$

respectively, where a dot now represents a time derivative. As discussed above, this force is not the most natural quantity for a scalar or tensor background, but we can still use it as a starting point to compute corrections at nonzero ρ. We denote the order ρ^n contribution to the force on a particle with a scalar-like or vector-like current by $\mathbf{F}^{S,n}$ and $\mathbf{F}^{V,n}$, respectively.

Scalar-Like Currents

We now warm up by considering a particle with a scalar-like current. First, in the helicity 0 background defined above, the Lagrangian is

$$L^S_{\text{int}} = g\phi_0\cos(\omega_0(t-z))\sqrt{1-v^2}J_0\left(\frac{\rho v_\perp}{\omega_0(1-v_z)}\right). \tag{8.149}$$

The leading term of the Bessel produces the standard force (8.146), which in this case is

$$\mathbf{F}^{S,0}_{h=0} = g\omega_0\phi_0\sin(\omega_0(t-z))(\hat{\mathbf{z}} - \mathbf{v} + O(v^2)). \tag{8.150}$$

More generally, $\hat{\mathbf{z}}$ would be the direction of propagation $\hat{\mathbf{k}}$ of the plane wave, by rotational symmetry. Next, the quadratic term in the Bessel gives the leading correction,

$$\mathbf{F}^{S,2}_{h=0} = -\frac{\rho^2}{2\omega_0^2}\, g\omega_0\phi_0\sin(\omega_0(t-z))(\mathbf{v}_\perp + O(v^2)). \tag{8.151}$$

For the same particle in the helicity ±1 background, the leading term in the Lagrangian is

$$L^S_{\text{int}} = \frac{g\rho}{\sqrt{2}\,\omega_0}A_0\cos(\omega_0(t-z))\frac{\sqrt{1-v^2}}{1-v_z}\,v_x + O(\rho^2) \tag{8.152}$$

which corresponds to a force

$$\mathbf{F}^{S,1}_{|h|=1} = \frac{g\rho}{\sqrt{2}}\,A_0\sin(\omega_0(t-z))(\hat{\mathbf{x}} + 2v_x\hat{\mathbf{z}} + O(v^2)) \tag{8.153}$$

$$= -\frac{g\rho}{\sqrt{2}}\left(\mathbf{A} + 2(\mathbf{v}\cdot\mathbf{A})\hat{\mathbf{k}}\right). \tag{8.154}$$

The two terms here are like an electric and magnetic force respectively, but their relative normalization differs from the usual Lorentz force, and the "magnetic" force instead points along the

direction of propagation of the wave. Furthermore, both forces are $\pi/2$ out of phase with the usual definitions (8.139) and (8.140) of the electric and magnetic fields.

Thus, ρ-dependent corrections to forces generally have novel direction and velocity dependence. For a higher helicity background $h > 1$, the Lagrangian would start at order $\bar{a}_h(\rho v/\omega)^h$, with nontrivial tensor structure in v, and yields a leading force of order $(\rho\bar{a}_h)(\rho v/\omega)^{h-1}$.

Vector-Like Currents

We now turn to the more phenomenologically interesting case of particles with vector-like currents. We first consider the helicity 0 background, where

$$L^V_{\text{int}} = -\frac{\sqrt{2}\, e\, \omega_0}{\rho}\, \phi_0 \sin(\omega_0(t-z))(1-v_z) J_0\left(\frac{\rho v_\perp}{\omega_0(1-v_z)}\right). \tag{8.155}$$

In this case there should be no force when $\rho = 0$, but the Lagrangian instead appears to diverge as $\rho \to 0$, due to the constant term in the Bessel. The resolution is familiar from subsection 8.3.2: the apparently divergent term is a total time derivative, and thus has no physical effect. Discarding this term, the leading correction is from the quadratic term,

$$\mathbf{F}^{V,1}_{h=0} = -\frac{e\rho}{\sqrt{2}}\, \phi_0 \cos(\omega_0(t-z))(\mathbf{v}_\perp + O(v^2)). \tag{8.156}$$

This has the same velocity dependence as (8.151), which is not a coincidence. In the nonrelativistic limit, the leading correction to the force is always purely transverse, due to the dependence of the Bessel functions on $v_\perp$, and for a $h = 0$ background that force must be directly proportional to $\mathbf{v}_\perp$ by rotational symmetry.

Next, for the helicity ± 1 background, we have

$$L^V_{\text{int}} = e\mathbf{A}\cdot\mathbf{v} + \frac{e\rho^2}{8\omega_0^2} A_0 \sin(\omega_0(t-z))(v_x v_\perp^2 + O(v^4)) + O(\rho^4) \tag{8.157}$$

where the first term recovers the Lorentz force law (8.147), and the second term yields

$$\mathbf{F}^{V,2}_{|h|=1} = -\frac{e\rho^2}{4\omega_0} A_0 \cos(\omega_0(t-z)) \left(\frac{3v_x^2 + v_y^2}{2}\,\hat{\mathbf{x}} + v_x v_y\,\hat{\mathbf{y}} + O(v^3)\right) \tag{8.158}$$

$$= -\frac{e\rho^2}{4\omega_0^2}\left((\mathbf{E}\cdot\mathbf{v}_\perp)\mathbf{v}_\perp + \mathbf{E}\, v_\perp^2/2 + O(v^3)\right) \tag{8.159}$$

as quoted in (8.2), where terms involving $\mathbf{B}$ appear at order v^3. While this correction is suppressed by $(\rho v/\omega_0)^2$ relative to the familiar electric force, it has a distinctive direction and velocity dependence which may be detectable. For instance, it includes a term parallel to $\mathbf{v}_\perp$. Note that (8.159) only applies to radiation backgrounds; it does not apply to situations with static electromagnetic fields,

where the force correction is not universal.

Finally, for the helicity ± 2 background, we have

$$L^V_{\text{int}} = \frac{e\rho}{2\sqrt{2}\,\omega}\, h \sin(\omega_0(t-z))\,(v_y^2 - v_x^2 + O(v^3)) \tag{8.160}$$

which corresponds to a force

$$\mathbf{F}^{V,1}_{|h|=2} = \frac{e\rho}{\sqrt{2}}\, h \cos(\omega_0(t-z))(v_x\hat{\mathbf{x}} - v_y\hat{\mathbf{y}} + O(v^2)). \tag{8.161}$$

This has the same velocity dependence as the leading force (8.148) from a gravitational wave, but shifted $\pi/2$ out of phase. More generally, in a higher helicity background $h > 2$, the Lagrangian starts at order $v\bar{a}_h(\rho v/\omega)^{h-1}$ and yields a leading force of order $(\rho v\bar{a}_h)(\rho v/\omega)^{h-2}$.

Discussion

In the above discussion we have restricted to plane wave backgrounds. Generalizing to arbitrary radiation backgrounds, such as wavepackets, is computationally straightforward and may offer a useful perspective on the localization properties of the interactions. We have also neglected inertia-modifying effects, which, e.g. would arise for a particle with a vector-like current in an $h = 0$ background. Searching for such effects would provide information about the amplitude of low-frequency background radiation in all of the helicity modes.

It is also interesting to consider if there is a natural continuous spin counterpart to a uniform static electric or magnetic field. Some care must be taken in defining this for several reasons. First, the enormous gauge redundancy (8.26) and the absence of local gauge-invariant observables obscures what a "uniform field" should mean. Second, the linearly varying potentials of uniform fields in electromagnetism, such as $A^\mu(\mathbf{x}, t) = (Ez, \mathbf{0})$, have no clear continuous spin counterpart that satisfies the free equation of motion (8.19). Third, as we have seen in subsection 8.3.1, the currents of source particles are generically spatially delocalized and thus overlap the probe particle, so requiring that "uniform" fields satisfy a free equation of motion is not even justified. (The temporal current is not spatially delocalized, but it is not time-independent and does not give rise to a static field.)

As a result, free background fields are not a useful concept for describing static forces. One should instead compute these non-universal interparticle forces directly, as we have already done in subsection 8.5.1. There, we saw that the static force law for spatial and temporal currents was exactly $1/r$, so for these currents all *electrostatic* forces are unchanged. We have also seen that the inhomogeneous current has a modified static force law, and that continuous spin fields generically have modified velocity-dependent force laws.

8.6 Radiation Emission From Matter Particles

In this section we investigate the continuous spin radiation emitted by an accelerating particle. First, we review radiation in ordinary scalar and vector fields in subsection 8.6.1. We cover this standard material carefully, in a way that directly generalizes to the nonlocal currents of continuous spin fields in subsection 8.6.2. In subsection 8.6.3 we apply these results to particles in nonrelativistic motion, yielding concrete deviations from the Larmor formula, and show the radiated power is well-behaved for arbitrary accelerations. Along the way, we make contact with previous work by recovering the soft factors for CSP emission, by considering the radiation emitted by an instantaneously kicked particle.

8.6.1 Review: Scalar and Vector Radiation

The Radiation Field and Soft Factors

We first consider the radiation produced in a massless scalar field ϕ by a time-dependent source J. Given retarded boundary conditions, the equation of motion $\partial^2\phi = J$ is solved by

$$\phi(x) = \int d^4y\, G_r(x-y)J(y) \tag{8.162}$$

where G_r is the retarded Green's function. If the source J corresponds to matter particles that eventually stop accelerating, then at late times the field contains outgoing radiation and the static fields of these particles. We can isolate the radiation in a covariant way by defining

$$\phi(x) = \phi_{\text{rad}}(x) + \phi_a(x) \tag{8.163}$$

where $\phi_a(x)$ is the solution with advanced boundary conditions, corresponding to Green's function G_a. The difference $\phi_{\text{rad}}(x)$ contains only radiation, because $\partial_x^2\phi_{\text{rad}} = \partial_x^2(\phi - \phi_a) = 0$, so it has the null plane wave expansion

$$\phi_{\text{rad}}(x) = \int \frac{d^3\mathbf{k}}{(2\pi)^3\, 2|\mathbf{k}|} \left(a(\mathbf{k})e^{-ik\cdot x} + \text{c.c.}\right)\Big|_{k^0=|\mathbf{k}|}. \tag{8.164}$$

On the other hand, in momentum space the retarded propagator corresponds to integrating along a k^0 contour that passes above the poles at $k^0 = \pm|\mathbf{k}|$, while the advanced propagator passes below them. Their difference corresponds to integrating along a contour C that simply encircles both poles clockwise, so

$$\phi_{\text{rad}}(x) = -\int \frac{d^3\mathbf{k}}{(2\pi)^3} \int_C \frac{dk^0}{2\pi} \frac{J(k)e^{-ik\cdot x}}{k^2} \tag{8.165}$$

$$= \int \frac{d^3\mathbf{k}}{(2\pi)^3\, 2|\mathbf{k}|} \left(iJ(k)e^{-ik\cdot x} + \text{c.c.}\right)\Big|_{k^0=|\mathbf{k}|} \tag{8.166}$$

from which we read off $a(\mathbf{k}) = iJ(|\mathbf{k}|, \mathbf{k})$.

For example, if the source is a single particle that receives an instantaneous kick at the origin, then the particle's worldline is

$$z^\mu(\tau) = \begin{cases} (\gamma\tau, \gamma\mathbf{v}\tau) & \tau < 0 \\ (\gamma'\tau, \gamma'\mathbf{v}'\tau) & \tau > 0 \end{cases} . \tag{8.167}$$

Integrating the worldline current (8.49) yields

$$J(\omega, \mathbf{k}) = \frac{ig}{\gamma(\omega - \mathbf{k}\cdot\mathbf{v})} - \frac{ig}{\gamma'(\omega - \mathbf{k}\cdot\mathbf{v}')} \tag{8.168}$$

which corresponds to a radiation amplitude

$$a(\mathbf{k}) = (2mg)\left(\frac{1}{2k\cdot p'} - \frac{1}{2k\cdot p}\right)_{k^0=|\mathbf{k}|} \tag{8.169}$$

where m is the mass of the particle, and p and p' are its initial and final four-momenta.

We can derive essentially the same result in quantum field-theoretic language by taking a matter field Φ of mass m with Yukawa coupling $y\phi^2\Phi$, where matching to the particle theory sets $y = 2mg$. Then in any process with a Φ particle of initial momentum p and final momentum p', the amplitude to emit a soft ϕ particle of momentum k obeys

$$\frac{\mathcal{M}(p \to p' + k)}{\mathcal{M}_0(p \to p')} = (2mg)\left(\frac{1}{2k\cdot p'} - \frac{1}{2k\cdot p}\right) \tag{8.170}$$

where the "soft factors" on the right-hand side can be determined solely using unitarity, locality, and Lorentz invariance [773]. Of course, this matches (8.169) in form. To make the connection more explicit one can consider amplitudes with an arbitrary number of outgoing ϕ particles, yielding a coherent final state for the ϕ field with $\langle a(\mathbf{k})\rangle$ given by (8.169). We thus recover the exact same result for the radiation field in the classical limit of many emissions.

It is straightforward to generalize these results to a massless vector field A^μ. Defining the radiation field A^μ_{rad} analogously, in Lorenz gauge we have

$$A^\mu_{\text{rad}}(x) = \int \frac{d^3\mathbf{k}}{(2\pi)^3\, 2|\mathbf{k}|} \left(iJ^\mu(k)e^{-ik\cdot x} + \text{c.c.}\right)\Big|_{k^0=|\mathbf{k}|} \tag{8.171}$$

and the corresponding plane wave expansion is

$$A^\mu_{\text{rad}}(x) = \int \frac{d^3\mathbf{k}}{(2\pi)^3\, 2|\mathbf{k}|} \left(\sum_{\lambda=\pm} \hat{\epsilon}^\mu_\lambda a_\lambda(\mathbf{k})e^{-ik\cdot x} + \text{c.c.} + \text{gauge}\right)\Big|_{k^0=|\mathbf{k}|} . \tag{8.172}$$

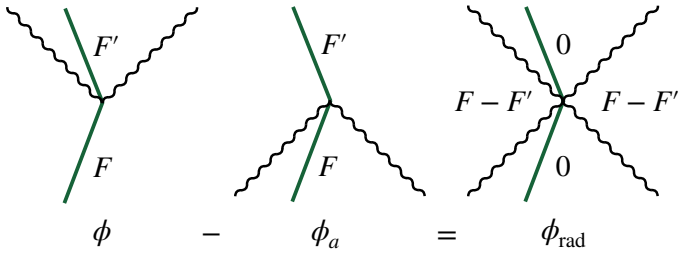

Figure 8.3: The field ϕ of a kicked particle has outgoing radiation on the forward light cone, the final static field F' inside, and the initial static field F outside. Subtracting off the advanced field ϕ_a gives a pure radiation field, which has incoming radiation on the backward light cone, outgoing radiation on the forward light cone, and the difference $F - F'$ outside both light cones.

Here we define $\hat{\epsilon}_\lambda = \epsilon_\lambda/\sqrt{2}$ to reach the usual normalization for helicity ± 1 modes. Now,

$$J^\mu = (k \cdot J)q^\mu + (q \cdot J)k^\mu - (\hat{\epsilon}_- \cdot J)\hat{\epsilon}_+^\mu - (\hat{\epsilon}_+ \cdot J)\hat{\epsilon}_-^\mu \tag{8.173}$$

where the first term is zero by current conservation, and the second term corresponds to the residual gauge freedom in Lorenz gauge. The last two terms yield

$$a_\pm(\mathbf{k}) = (i\hat{\epsilon}_\pm)^* \cdot J(k)\Big|_{k^0=|\mathbf{k}|}. \tag{8.174}$$

Returning to the example of a single kicked particle, coupled to the vector field by (8.51), a derivation analogous to the previous one gives

$$J^\mu(\omega, \mathbf{k}) = \frac{ie\,(\gamma, \gamma\mathbf{v})}{\gamma(\omega - \mathbf{k}\cdot\mathbf{v})} - \frac{ie\,(\gamma', \gamma'\mathbf{v}')}{\gamma'(\omega - \mathbf{k}\cdot\mathbf{v}')} \tag{8.175}$$

which corresponds to a radiation amplitude

$$a_\pm(\mathbf{k}) = e\left(\frac{\hat{\epsilon}_\pm^* \cdot p}{k \cdot p} - \frac{\hat{\epsilon}_\pm^* \cdot p'}{k \cdot p'}\right)_{k^0=|\mathbf{k}|}. \tag{8.176}$$

Of course, this matches the ratio $\mathcal{M}(p \to p' + k)/\mathcal{M}_0(p \to p')$ from field-theoretic soft factors.

Radiated Power

Defining $x^\mu = (t, r\hat{\mathbf{r}})$, we can simplify (8.164) in the far field limit $r \to \infty$ using

$$e^{i\mathbf{k}\cdot\mathbf{r}} = \frac{2\pi e^{i|\mathbf{k}|r}}{i|\mathbf{k}|r}\,\delta^{(2)}(\hat{\mathbf{k}}, \hat{\mathbf{r}}) - \frac{2\pi e^{-i|\mathbf{k}|r}}{i|\mathbf{k}|r}\delta^{(2)}(\hat{\mathbf{k}}, -\hat{\mathbf{r}}) \tag{8.177}$$

which holds since both sides are integrated against smooth functions of $\hat{\mathbf{k}}$ and $\hat{\mathbf{r}}$. This yields

$$\lim_{r\to\infty}\phi_{\rm rad}(x) = \frac{1}{4\pi r}\int_0^\infty \frac{d|\mathbf{k}|}{2\pi}\left(-ia(|\mathbf{k}|\hat{\mathbf{r}})\,e^{-i|\mathbf{k}|(t-r)} + ia(-|\mathbf{k}|\hat{\mathbf{r}})\,e^{-i|\mathbf{k}|(t+r)} + \text{c.c.}\right) \tag{8.178}$$

$$= \frac{1}{4\pi r}\int \frac{d\omega}{2\pi}\left(J(\omega,\omega\hat{\mathbf{r}})\,e^{-i\omega(t-r)} - J(\omega,-\omega\hat{\mathbf{r}})\,e^{-i\omega(t+r)}\right). \tag{8.179}$$

Much of the information in this expression is irrelevant to computing the radiated power. To see this, consider a particle kicked at time $t = 0$, and let F (F') be the static field that would exist if the particle had its initial (final) velocity for all time. The spacetime profile of $\phi_{\rm rad}$ is shown in Fig. 8.3, and contains outgoing radiation (from the first term of (8.179)), incoming radiation (from the second term), and a combination of static fields (from both terms).

Static fields never contribute to radiated power in the far field, since their derivatives are suppressed by $1/r$. The incoming radiation is unphysical and vanishes for $t > 0$, and more generally vanishes at late times for any situation where the particles eventually stop accelerating. Thus, at late times we can compute the radiated power from the physical, outgoing radiation in ϕ by working with only the first term of (8.179). This prescription even works for periodic motion as long as we consider its amplitude to eventually damp as $t \to \infty$, which we will leave implicit below.

To compute the angular distribution of radiated power, we note that in the far field limit, the derivatives in the Poynting vector $T^{0i} = \partial^0\phi\,\partial^i\phi$ effectively only act upon the exponential $e^{-i\omega(t-r)}$, as other contributions are suppressed by $1/r$. Then at late times,

$$\frac{dP(t)}{d\hat{\mathbf{r}}} = \lim_{r\to\infty} r^2\,(\partial^0\phi(x))\,(\partial^r\phi(x)) \tag{8.180}$$

$$= \left|\int \frac{d\omega}{2\pi}\frac{e^{-i\omega(t-r)}}{4\pi}\,\omega J(\omega,\omega\hat{\mathbf{r}})\right|^2. \tag{8.181}$$

Similarly, for a vector field in Lorenz gauge, the radiation field in the far field limit is

$$\lim_{r\to\infty} A^\mu_{\rm rad}(x) = \frac{1}{4\pi r}\int\frac{d\omega}{2\pi}\left(-\sum_{\lambda=\pm}\hat{\epsilon}^\mu_\lambda\,(\hat{\epsilon}^*_\lambda\cdot J(\omega,\omega\hat{\mathbf{r}}))\,e^{-i\omega(t-r)} + \text{incoming} + \text{gauge}\right). \tag{8.182}$$

We may again discard the incoming term at late times, and since the Poynting vector $T^{0r} = -F^{0\mu}F^r{}_\mu$ is gauge invariant, we may also discard the pure gauge term proportional to k^μ. Now, in the far field limit, a derivative $i\partial^\mu$ yields a factor of $k^\mu = (\omega,\omega\hat{\mathbf{r}})$, so

$$\frac{dP(t)}{d\hat{\mathbf{r}}} = \lim_{r\to\infty} r^2\,(k^0A^\mu - k^\mu A^0)(k^rA_\mu - k_\mu A^r) \tag{8.183}$$

$$= \lim_{r\to\infty}\omega^2r^2\,A^\mu A_\mu \tag{8.184}$$

$$= \sum_{\lambda=\pm}\left|\int\frac{d\omega}{2\pi}\frac{e^{-i\omega(t-r)}}{4\pi}\,\omega\,\hat{\epsilon}^*_\lambda\cdot J(\omega,\omega\hat{\mathbf{r}})\right|^2 \tag{8.185}$$

where we arrived at (8.184) using $k^2 = 0$ and $k \cdot \hat{\epsilon}_\pm = 0$. We may also perform the sum over polarizations using $k \cdot J = 0$ to get a compact expression for the total power,

$$\frac{dP(t)}{d\hat{\mathbf{r}}} = -\left| \int \frac{d\omega}{2\pi} \frac{e^{-i\omega(t-r)}}{4\pi} \, \omega J^\mu(\omega, \omega\hat{\mathbf{r}}) \right|^2 . \tag{8.186}$$

As a concrete example, we can again consider a kicked particle. Since the radiation is emitted instantaneously, it is natural to integrate (8.181) over time. We then strip off the remaining frequency integration, pairing positive and negative ω, to find the energy spectrum

$$\frac{dE}{d\omega \, d\hat{\mathbf{r}}} = \frac{\omega^2}{16\pi^3} |J(\omega, \omega\hat{\mathbf{r}})|^2 = \frac{g^2}{16\pi^3} \left(\frac{1}{\gamma(1 - \hat{\mathbf{r}} \cdot \mathbf{v})} - \frac{1}{\gamma'(1 - \hat{\mathbf{r}} \cdot \mathbf{v}')} \right)^2 \tag{8.187}$$

for $\omega \geq 0$. Similarly, integrating the vector result (8.186) yields

$$\frac{dE}{d\omega \, d\hat{\mathbf{r}}} = -\frac{\omega^2}{16\pi^3} |J^\mu(\omega, \omega\hat{\mathbf{r}})|^2 = -\frac{e^2}{16\pi^3} \left(\frac{(1, \mathbf{v})}{1 - \hat{\mathbf{r}} \cdot \mathbf{v}} - \frac{(1, \mathbf{v}')}{1 - \hat{\mathbf{r}} \cdot \mathbf{v}'} \right)^2 \tag{8.188}$$

which is a well-known result (e.g. see Eq. (15.2) of Ref. [506]).

Particles in Periodic Motion

Next, we consider the radiation emitted by a particle undergoing periodic motion with period $T = 2\pi/\omega_0$. In the scalar case, the current and field amplitude have the form

$$J(\omega, \mathbf{k}) = 2\pi \sum_n j_n(\mathbf{k}) \, \delta(\omega - n\omega_0), \qquad a(\mathbf{k}) = 2\pi \sum_n a_n(\hat{\mathbf{k}}) \, \delta(|\mathbf{k}| - n\omega_0) \tag{8.189}$$

where the Fourier components can be extracted by

$$a_n(\hat{\mathbf{r}}) = i j_n(n\omega_0 \hat{\mathbf{r}}) = i \int_0^T \frac{dt}{T} \, e^{in\omega_0 t} J(t, n\omega_0 \hat{\mathbf{r}}). \tag{8.190}$$

The time-averaged power distribution is

$$\frac{d\bar{P}}{d\hat{\mathbf{r}}} = \int_0^T \frac{dt}{T} \frac{dP(t)}{d\hat{\mathbf{r}}} = \frac{1}{8\pi^2} \sum_{n>0} n^2 \omega_0^2 |a_n(\hat{\mathbf{r}})|^2 \tag{8.191}$$

where we paired terms with positive and negative n, and dropped the static $n = 0$ term, which does not contribute to the radiated power. In general, we have

$$a_n(\hat{\mathbf{r}}) = ig \int_0^T \frac{dt}{T} \, e^{in\omega_0(t - \hat{\mathbf{r}} \cdot \mathbf{z}(t))} \sqrt{1 - |\mathbf{v}(t)|^2} \tag{8.192}$$

where the final factor comes from changing variables from τ to t. This shows that the leading contribution to a_n is of order v_0^n, where v_0 is the typical speed, so that in the nonrelativistic limit radiation is predominantly emitted at the fundamental frequency.

For nonrelativistic sinuosidal motion $\mathbf{z}(t) = \ell \cos(\omega_0 t)\, \hat{\mathbf{x}}$ with $v_0 = \omega_0 \ell \ll 1$, we have

$$a_1(\hat{\mathbf{r}}) = ig \int_0^T \frac{dt}{T}\, e^{i\omega_0 t} e^{-iv_0(\hat{\mathbf{r}}\cdot\hat{\mathbf{x}})\cos(\omega_0 t)} \sqrt{1 - v_0^2 \sin^2(\omega_0 t)} = \frac{g v_0}{2}(\hat{\mathbf{r}}\cdot\hat{\mathbf{x}}) + O(v_0^2). \tag{8.193}$$

This radiation is emitted primarily longitudinally, and the total averaged power is

$$\bar{P} = \frac{g^2\omega_0^2 v_0^2}{32\pi^2} \int d\hat{\mathbf{r}}\, (\hat{\mathbf{r}}\cdot\hat{\mathbf{x}})^2 = \frac{g^2 a_0^2}{24\pi} \tag{8.194}$$

where $a_0 = \omega_0 v_0$. This is simply the scalar Larmor formula.

For the vector case, we can define the components $j_n^\mu(\mathbf{k})$ and $a_{\pm,n}(\hat{\mathbf{k}})$ analogously to (8.189), and they are now related by

$$a_{\pm,n}(\hat{\mathbf{r}}) = (i\hat{\epsilon}_\pm)^* \cdot j_n(n\omega_0 \hat{\mathbf{r}}). \tag{8.195}$$

To quickly recover familiar results, we time average the power summed over helicities (8.186),

$$\frac{d\bar{P}}{d\hat{\mathbf{r}}} = -\frac{1}{8\pi^2} \sum_{n>0} n^2\omega_0^2 |j_n^\mu(n\omega_0\hat{\mathbf{r}})|^2. \tag{8.196}$$

The leading contribution to radiation at the n^{th} harmonic is still of order v_0^n, since

$$j_n^\mu(n\omega_0\hat{\mathbf{r}}) = e\int_0^T \frac{dt}{T}\, e^{in\omega_0(t - \hat{\mathbf{r}}\cdot\mathbf{z}(t))}\, (1, \mathbf{v}(t)). \tag{8.197}$$

Again specializing to nonrelativistic sinusoidal motion, we have

$$j_1^\mu(n\omega_0\hat{\mathbf{r}}) = e\int_0^T \frac{dt}{T}\, e^{i\omega_0 t - iv_0(\hat{\mathbf{r}}\cdot\hat{\mathbf{x}})\cos(\omega_0 t)}\, (1, -v_0 \sin(\omega_0 t)\, \hat{\mathbf{x}}) = -\frac{iev_0}{2}(\hat{\mathbf{r}}\cdot\hat{\mathbf{x}}, \hat{\mathbf{x}}) + O(v_0^2). \tag{8.198}$$

Now the radiation is emitted primarily along the transverse direction, and the total is

$$\bar{P} = \frac{e^2\omega_0^2 v_0^2}{32\pi^2} \int d\hat{\mathbf{r}}\, |\hat{\mathbf{r}}\times\hat{\mathbf{x}}|^2 = \frac{e^2\, a_0^2}{12\pi}. \tag{8.199}$$

which is the usual Larmor formula, since $\langle a^2\rangle = a_0^2/2$. We can also recover the polarization content of the radiation by applying (8.195), which shows that the radiation is linearly polarized, along the projection of $\hat{\mathbf{x}}$ in the plane transverse to $\hat{\mathbf{r}}$. Of course, these are all familiar results, but we are now prepared to see how they are modified at nonzero ρ.

8.6.2 Defining Continuous Spin Radiation

The Radiation Field and Soft Factors

Our analysis of continuous spin radiation will closely mirror the previous subsection. We work in strong harmonic gauge, where the equation of motion (8.68) is solved by

$$\Psi(\eta, x) = -\int \frac{d^3\mathbf{k}}{(2\pi)^3} \int_{C_r} \frac{dk^0}{2\pi} \frac{J(\eta, k) e^{-ik\cdot x}}{k^2} \tag{8.200}$$

where the contour C_r passes above the poles at $k^0 = \pm|\mathbf{k}|$. We define Ψ_a with a contour C_a that passes below these poles but is otherwise identical, so that both contours enclose the same essential singularities. Then the difference,

$$\Psi_{\text{rad}}(\eta, x) = \Psi(\eta, x) - \Psi_a(\eta, x) = \int \frac{d^3\mathbf{k}}{(2\pi)^3\, 2|\mathbf{k}|} \left(iJ(\eta, k) e^{-ik\cdot x} + \text{c.c.} \right) \Big|_{k^0=|\mathbf{k}|} \tag{8.201}$$

is a pure radiation field, with support on only null momenta. We have argued in subsection 8.3.2 that the Ψ_{rad} produced by a current depends only on the function $\hat{g}$, and is universal for scalar-like or vector-like currents. This can also be seen directly by plugging the general decomposition (8.87) of the current into the equation above. The $k^2 X$ term vanishes since k is null, and the final term is of the form $D\xi$, which corresponds to a pure gauge field.

The mode expansion of Ψ_{rad} is given by (8.36), and the gauge invariant coefficients can be found by projecting against a helicity wavefunction by (8.37),

$$a_h(\mathbf{k}) = \int [d^4\eta]\, \delta'(\eta^2 + 1)\, i\psi^*_{h,k}(\eta) J(\eta, k) \Big|_{k^0=|\mathbf{k}|}. \tag{8.202}$$

We can now readily derive soft factors by considering a kicked particle with worldline (8.167).

First, for any scalar-like current we have

$$J(\eta, k) = \frac{ig\, e^{-i\rho\eta\cdot p/k\cdot p}}{\gamma(\omega - \mathbf{k}\cdot\mathbf{v})} - \frac{ig\, e^{-i\rho\eta\cdot p'/k\cdot p'}}{\gamma'(\omega - \mathbf{k}\cdot\mathbf{v}')}. \tag{8.203}$$

This corresponds to a radiation amplitude

$$a_h^S(\mathbf{k}) = (2mg) \left(\frac{s_h^S(k, p')}{2k\cdot p'} - \frac{s_h^S(k, p)}{2k\cdot p} \right)_{k^0=|\mathbf{k}|} \tag{8.204}$$

where the scalar-like soft factor is

$$s_h^S(k,p) = \int [d^4\eta]\, \delta'(\eta^2+1)\, \psi^*_{h,k}(\eta) e^{-i\rho\eta\cdot p/k\cdot p} \tag{8.205}$$

$$= \left(\frac{\epsilon_-\cdot p}{|\epsilon_-\cdot p|}\right)^h J_h\left(\rho|\epsilon_-\cdot p/k\cdot p|\right). \tag{8.206}$$

Here we evaluated the integral using (8.273) with $V = \rho(q - p/k\cdot p)$. Up to differences in phase and normalization conventions, this matches the scalar-like CSP soft factors from Ref. [780]. Explicitly, defining $z = \epsilon_-\cdot p/k\cdot p$ for brevity, the leading terms are

$$s_h^S(k,p) = \begin{cases} \frac{1}{8}\rho^2 z^2 & h=2 \\ \frac{1}{2}\rho z & h=1 \\ 1-\frac{1}{4}\rho^2 z^* z & h=0 \\ -\frac{1}{2}\rho z^* & h=-1 \\ \frac{1}{8}\rho^2 (z^*)^2 & h=-2 \end{cases} + O(\rho^3) \tag{8.207}$$

In general, the leading contribution to s_h^S is of order $\rho^{|h|}$, so in the $\rho\to 0$ limit all the soft factors vanish except for $s_0^S = 1$, recovering the result (8.170) for ordinary scalars.

For vector-like currents, the results are identical up to the substitution $g \to (\sqrt{2}\, e/\rho)(ik\cdot\dot{z})$. Then the radiation amplitude is

$$a_h^V(\mathbf{k}) = e\left(\frac{s_h^V(k,p)}{k\cdot p} - \frac{s_h^V(k,p')}{k\cdot p'}\right)_{k^0=|\mathbf{k}|} \tag{8.208}$$

where the vector-like soft factors are

$$s_h^V(k,p) = \frac{\sqrt{2}\, k\cdot p}{i\rho} s_h(k,p). \tag{8.209}$$

This agrees with the vector-like CSP soft factors of Ref. [780], up to differences in conventions. As already noted there, the soft factor for $h=0$ diverges as $1/\rho$, but this contribution cancels between the two terms of (8.208), and more generally it will cancel from the soft emission amplitude for any process by charge conservation. Thus discarding this term, the leading contributions are

$$s_h^V(k,p) = -ik\cdot p \times \begin{cases} \frac{1}{4\sqrt{2}}\rho z^2 & h=2 \\ \frac{1}{\sqrt{2}} z - \frac{1}{8\sqrt{2}}\rho^2 z^2 z^* & h=1 \\ -\frac{1}{2\sqrt{2}}\rho z z^* & h=0 \\ -\frac{1}{\sqrt{2}} z^* + \frac{1}{8\sqrt{2}}\rho^2 (z^*)^2 z & h=-1 \\ \frac{1}{4\sqrt{2}}\rho (z^*)^2 & h=-2 \end{cases} + O(\rho^3) \tag{8.210}$$

In general, the leading physical contribution to s_h^V is of order $\rho^{||h|-1|}$, so in the $\rho \to 0$ limit all the soft factors vanish except for $s_{\pm 1}^V = \mp i \hat{\epsilon}_\pm^* \cdot p$, recovering the result (8.176) for ordinary vectors (up to the phases used to define the helicity basis (8.35)).

We have therefore recovered all the physical results of Ref. [780], up to the tensor-like CSP soft factors, which we defer to future work. The agreement is heartening but unsurprising, since soft factors are highly constrained by symmetries. We now turn to deriving new results.

Extracting the Radiated Power

We can compute the radiated power using the canonical stress-energy tensor [781]

$$T^{\mu\nu} = -g^{\mu\nu}\mathcal{L} + \int [d^4\eta] \, \frac{\partial \mathcal{L}}{\partial(\partial_\mu \Psi)} \, \partial^\nu \Psi \tag{8.211}$$

$$= -g^{\mu\nu}\mathcal{L} + \int [d^4\eta] \, \delta'(\eta^2+1) \, \partial^\mu \Psi \partial^\nu \Psi - \frac{1}{2}\partial_\eta^\mu (\delta(\eta^2+1)\Delta\Psi) \, \partial^\nu \Psi. \tag{8.212}$$

Compared to the examples in section 8.6.1, there is a new subtlety: the stress-energy tensor is not gauge invariant, even after Belinfante improvement terms are added to yield a symmetric tensor $\Theta^{\mu\nu}$. This is not surprising since the same phenomenon already occurs in linearized gravity; it reflects the fact that both general relativity and continuous spin theories do not have local gauge invariant observables. The resolution here is exactly the same as in linearized gravity [828]: for radiation and gauge transformations with typical wavelength λ, the average $\langle \Theta^{\mu\nu} \rangle$ of the stress-energy tensor over a spacetime region of typical size $L \gg \lambda$ is approximately gauge invariant, up to terms suppressed by powers of λ/L. Thus, one can meaningfully describe energy-momentum flow on scales longer than the wavelength.

To see how this works, note that averaging and discarding terms suppressed by λ/L allows us to perform integration by parts, and more generally to discard total derivative terms such as the Belinfante improvement terms, which yields $\langle \Theta^{\mu\nu} \rangle \approx \langle T^{\mu\nu} \rangle$. Furthermore, the variation of $\langle \mathcal{L} \rangle$ approximately vanishes for the same reason that the action (8.9) is gauge invariant. The variations of the remaining terms cancel after using the equation of motion (8.19) and integration by parts, as shown by a tedious but straightforward calculation in appendix 8.9.5.

There is another subtlety which is unique to continuous spin fields. In section 8.6.1, we neglected the initial and final static fields F and F' when computing the radiated power because their derivatives fall off as $1/r^2$. But continuous spin fields have currents which are not localized to the worldline, as discussed in subsection 8.4.1, leading to different behavior at large r. For example, the derivatives of the static field of the spatial current (8.96) do not simply scale as $1/r^2$, but they do fall off faster than $1/r$, and thus do not contribute to radiated power in the far field. We do not know how to prove this in general, partly because our analysis is framed in terms of fields with a high degree of gauge redundancy. For example, the temporal current depends explicitly on a particle's past history, so that even the "static" field (8.98) depends explicitly on time and an early time cutoff.

These features obscure the asymptotic behavior of the field and its derivatives. In lieu of a proof, we make the physically well-motivated conjecture that $\Psi_{\rm rad}(\eta, x)$, which encodes "on-shell" null modes, provides the sole contribution to the far-field power, for all physically sensible currents satisfying the continuity condition.

We can now derive results. Our discussion of gauge invariance implies that we may work in any gauge, as long as we only compute spacetime averaged quantities. We use harmonic gauge, where only the second term of (8.212) contributes to the Poynting vector,

$$T^{0r} = \int d^4\eta\, \delta'(\eta^2+1)\, \partial^0\Psi \partial^r \Psi. \tag{8.213}$$

In analogy with (8.179), the part of $\Psi_{\rm rad}$ containing outgoing radiation in the far field limit is

$$\lim_{r\to\infty} \Psi_{\rm rad}(\eta, x) \supset \frac{1}{4\pi r}\int \frac{d\omega}{2\pi}\sum_h \psi_{h,k}(\eta)\int [d^4\eta']\, \delta'(\eta'^2+1)\, \psi^*_{h,k}(\eta') J(\eta', k) \tag{8.214}$$

where we defined $k = (\omega, \omega\hat{\mathbf{r}})$ for brevity. As discussed above, we use this piece alone to compute the far field radiated power flux, omitting contributions from "static" fields. Following the same steps that led to (8.181) and applying the orthogonality relation (8.264) yields the radiated power in each helicity mode,

$$\frac{dP_h(t)}{d\hat{\mathbf{r}}} = \left| \int \frac{d\omega}{2\pi} \frac{\omega\, e^{i\omega(r-t)}}{4\pi} \int d^4\eta\, \delta'(\eta^2+1)\, \psi^*_{h,k}(\eta) J(\eta, k)\right|^2. \tag{8.215}$$

We can sum over h using the completeness relation (8.282), giving the total

$$\frac{dP(t)}{d\hat{\mathbf{r}}} = \int d^4\eta\, \delta'(\eta^2+1) \left| \int \frac{d\omega}{2\pi} \frac{e^{i\omega(r-t)}}{4\pi}\, \omega J(\eta, k)\right|^2. \tag{8.216}$$

The total radiated power distribution (8.216) is Lorentz invariant, but its distribution in helicity (8.215) is not. This reflects the fact that the helicity of a continuous spin particle is not Lorentz invariant, as mentioned in section 8.2.

To render (8.215) and (8.216) gauge invariant and physically meaningful, it suffices to average in time. This fact follows from the same argument as in the gravitational wave literature [828]: in the limit $r \to \infty$, evaluating the power emitted through any nonzero solid angle automatically involves a large spatial average over the transverse directions. Furthermore, since the power is written in terms of fields that are purely outgoing spherical waves, an average in t is equivalent to an average in r, so no further averaging is needed.

8.6.3 Computing Continuous Spin Radiation

As a first example, we can integrate over all times to find the radiated energy spectrum for a kicked particle. In terms of the radiation amplitudes defined above, we have

$$\frac{dE}{d\omega\, d\hat{\mathbf{r}}} = \sum_h \frac{\omega^2}{16\pi^3} \times \begin{cases} |a_h(\omega\hat{\mathbf{r}})|^2 & \text{scalar-like} \\ |a_h^V(\omega\hat{\mathbf{r}})|^2/2 & \text{vector-like} \end{cases} \tag{8.217}$$

where the factor of $1/2$ is due to the normalization of the frame vectors $\epsilon_\pm^\mu$. As expected, these results reduce to (8.187) and (8.188) as $\rho \to 0$.

Our main interest in this section is on particles in periodic motion, for which we can compute a gauge invariant radiated power by averaging over a period. As in section 8.6.1, the currents and amplitudes satisfy

$$J(\eta, \omega, \mathbf{k}) = 2\pi \sum_n j_n(\eta, \mathbf{k})\delta(\omega - n\omega_0), \qquad a_h(\mathbf{k}) = 2\pi \sum_n a_{h,n}(\hat{\mathbf{k}})\delta(|\mathbf{k}| - n\omega_0) \tag{8.218}$$

and the Fourier components can be extracted by

$$a_{h,n}(\hat{\mathbf{r}}) = i \int [d^4\eta]\, \delta'(\eta^2 + 1)\, \psi^*_{h,k_n}(\eta) j_n(\eta, k_n) \tag{8.219}$$

where we define $k_n = n\omega_0(1, \hat{\mathbf{r}})$. The time-averaged power distribution is

$$\frac{d\bar{P}_{h,n}}{d\hat{\mathbf{r}}} = \frac{n^2\omega_0^2}{8\pi^2} |a_{h,n}(\hat{\mathbf{r}})|^2. \tag{8.220}$$

With this single expression we can compute the universal radiated power, differential in direction $\hat{\mathbf{r}}$, helicity h, and harmonic $n > 0$, for both scalar-like and vector-like currents.

First, for any scalar-like current,

$$a_{h,n}(\hat{\mathbf{r}}) = ig \int_0^T \frac{dt}{T}\, e^{in\omega_0(t - \hat{\mathbf{r}}\cdot\mathbf{z}(t))} \sqrt{1 - |\mathbf{v}(t)|^2} \int [d^4\eta]\, \delta'(\eta^2 + 1)\, \psi^*_{h,k_n}(\eta) e^{-i\rho\eta\cdot\dot{z}(t)/k_n\cdot\dot{z}(t)} \tag{8.221}$$

$$= ig \int_0^T \frac{dt}{T}\, e^{in\omega_0(t - \hat{\mathbf{r}}\cdot\mathbf{z}(t))} \sqrt{1 - |\mathbf{v}(t)|^2} \left(\frac{\epsilon_- \cdot \dot{z}}{|\epsilon_- \cdot \dot{z}|}\right)^h J_h\left(\rho |\epsilon_- \cdot \dot{z}/k_n \cdot \dot{z}|\right) \tag{8.222}$$

where we performed the integral using the same logic as in (8.206). This can be written more transparently by writing $\dot{z} = (1, \mathbf{v}) = (1, v_r\hat{\mathbf{r}} + \mathbf{v}_\perp)$, and choosing frame vectors with $\epsilon_\pm^\mu = (0, \boldsymbol{\epsilon}_\pm)$, so that $\boldsymbol{\epsilon}_\pm \cdot \hat{\mathbf{r}} = 0$ and $|\boldsymbol{\epsilon}_\pm \cdot \mathbf{v}| = v_\perp$. This yields

$$a_{h,n}(\hat{\mathbf{r}}) = ig \int_0^T \frac{dt}{T}\, e^{in\omega_0(t - \hat{\mathbf{r}}\cdot\mathbf{z})} \sqrt{1 - v^2}\, (-\boldsymbol{\epsilon}_- \cdot \hat{\mathbf{v}}_\perp)^h\, J_h\left(\frac{\rho v_\perp}{n\omega_0(1 - v_r)}\right). \tag{8.223}$$

Notice that while the original expression (8.221) had direct dependence on ρ/ω_0, our final result only

depends on the combination $\rho v_0/\omega_0$, which is physically reasonable since this parameter controls the mixing of helicity states under boosts, as discussed in section 8.2.1. Thus, the amplitude can be viewed as a series in the dimensionless variables v_0 and $\rho\ell$, where $\ell = v_0/\omega_0$ is the typical length scale of the particle's path.

We have seen that for nonrelativistic sinusoidal motion, the amplitude (8.193) for ordinary $h = 0$, $n = 1$ scalar radiation begins at order v_0. By contrast, the leading continuous spin corrections begin at *zeroth* order in v_0, and are

$$a_{h,n}(\hat{\mathbf{r}}) = ig \int_0^T \frac{dt}{T}\, e^{in\omega_0 t} \left(-\boldsymbol{\epsilon}_- \cdot \hat{\mathbf{v}}_\perp\right)^h J_h\left(\frac{\rho v_\perp}{n\omega_0}\right) + O(v_0) \tag{8.224}$$

$$= ig \int_0^{2\pi} \frac{d\phi}{2\pi}\, e^{in\phi} \left(-e^{i\alpha}\,\mathrm{sign}(\sin\phi)\right)^h J_h\left(\frac{\rho\ell\sin\theta}{n}\,|\sin\phi|\right) + O(v_0) \tag{8.225}$$

where we changed variables to $\phi = \omega_0 t$, θ is the angle of $\hat{\mathbf{r}}$ to the direction of motion $\hat{\mathbf{x}}$, and the constant phase $e^{i\alpha}$ depends on the phase convention for the polarization vector $\boldsymbol{\epsilon}_-$. Discarding the irrelevant phases by taking the magnitude yields

$$|a_{h,n}(\hat{\mathbf{r}})| = g \left| \int_0^{2\pi} \frac{d\phi}{2\pi}\, e^{in\phi} J_h\left(\frac{\rho\ell\sin\theta}{n}\sin\phi\right)\right| + O(v_0). \tag{8.226}$$

Thus, for nonrelativistic sinuosidal motion the leading contribution to radiation at helicity $h > 0$ has order $(\rho\ell)^h$ and appears at harmonics $n = h, h-2, \ldots$, while higher order terms in $\rho\ell$ can also contribute to higher harmonics.

The resulting radiated power distribution, illustrated at left in Fig. 8.4, is

$$\frac{d\bar{P}_{h,n}}{d\hat{\mathbf{r}}} = \frac{g^2\omega_0^2}{32\pi^2} \times \begin{cases} v_0^2\cos^2\theta\,(1-(\rho\ell\sin\theta)^2/8) & h=0, n=1 \\ (\rho\ell\sin\theta)^2/4 & |h|=1, n=1+\ldots \\ (\rho\ell\sin\theta)^4/1024 & |h|=2, n=2 \end{cases} \tag{8.227}$$

where we show the leading ρ-dependent corrections for a few h and n. Note that the familiar scalar radiation is primarily emitted longitudinally, while the $h \neq 0$ radiation is primarily emitted in the transverse directions, due to the dependence of the amplitude on $\mathbf{v}_\perp$. As expected, the familiar scalar radiation dominates for small $\rho \ll \omega_0$.

It is also interesting to consider how the radiated power behaves in the deep infrared limit $\rho\ell \to \infty$. As shown at left in Fig. 8.5, the radiated power in each helicity and harmonic initially increases monotonically with ρ, then oscillates and decreases. This is a consequence of the rapid oscillation of the Bessel function in (8.226); roughly evaluating the integral with the method of stationary phase, we find that at large $\rho\ell$ the radiated power is distributed democratically among helicities $h \lesssim n$, and dominated by harmonics $n \lesssim \sqrt{\rho\ell}$.

To confirm this behavior numerically, it is easiest to sum the power (8.220) over all helicities

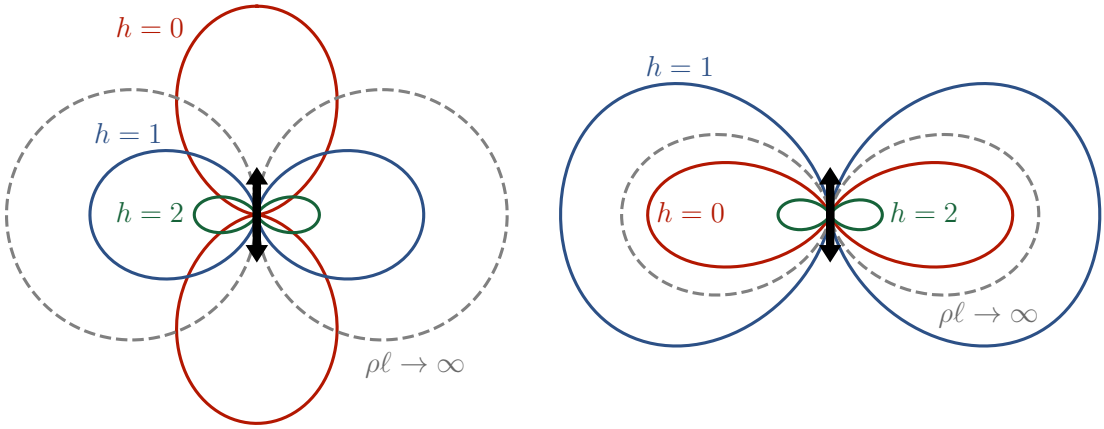

Figure 8.4: Angular distribution of helicity h radiation (not to scale) from a particle in nonrelativistic sinusoidal motion with amplitude ℓ and $\rho\ell \ll 1$, for a scalar-like (left) or vector-like (right) current. The dashed curve shows the total power emission in all helicities in the deep infrared limit $\rho\ell \to \infty$.

using the completeness relation (8.282), which yields

$$\frac{d\bar{P}}{d\hat{\mathbf{r}}} = \frac{g^2\omega_0^2}{8\pi^2}\sum_{n>0} n^2 \int [d^4\eta]\,\delta'(\eta^2+1)\left|\int_0^T \frac{dt}{T}\, e^{in\omega_0(t-\hat{\mathbf{r}}\cdot\mathbf{z}(t))}\sqrt{1-|\mathbf{v}(t)|^2}e^{-i\rho\eta\cdot\dot{z}(t)/k_n\cdot\dot{z}(t)}\right|^2 \tag{8.228}$$

$$= \frac{g^2\omega_0^2}{8\pi^2}\sum_{n>0} n^2 \int [d^4\eta]\,\delta'(\eta^2+1)\left|\int_0^T \frac{dt}{T}\, e^{in\omega_0 t}e^{-i\rho(\eta^0 v_r(t)-\boldsymbol{\eta}\cdot\mathbf{v}(t))/n\omega_0}\right|^2 \tag{8.229}$$

$$= \frac{g^2\omega_0^2}{8\pi^2}\sum_{n>0} n^2 \int_0^T \frac{dt}{T}\int_0^T \frac{dt'}{T}\, e^{in\omega_0(t-t')}\, J_0\left(\frac{\rho|\mathbf{v}_\perp(t)-\mathbf{v}_\perp(t')|}{n\omega_0}\right) \tag{8.230}$$

where we took the nonrelativistic limit, cancelled a phase, and evaluated the η integral using (8.255). In the special case of sinusoidal motion, one can evaluate the integrals in terms of hypergeometric functions, yielding

$$\lim_{\rho\ell\to\infty}\frac{d\bar{P}}{d\hat{\mathbf{r}}} = \frac{g^2\omega_0^2}{8\pi^4}\,\rho\ell\sin\theta. \tag{8.231}$$

This scaling, shown at right in Fig. 8.5, has an important physical consequence. Working in terms of the independent measurable quantities v_0 and a_0, where $a_0 = \omega_0 v_0$ is the typical acceleration, the infrared limit $\rho\ell \gg 1$ is precisely the low acceleration regime $a_0 \ll \rho v_0^2$. Combining (8.194) and (8.231) yields

$$\bar{P} = \begin{cases} g^2 a_0^2/24\pi & a_0 \gg \rho v_0^2 \\ g^2\rho a_0/8\pi^2 & a_0 \ll \rho v_0^2 \end{cases} \tag{8.232}$$

so that the radiated power smoothly goes to zero as the acceleration vanishes, even though radiation

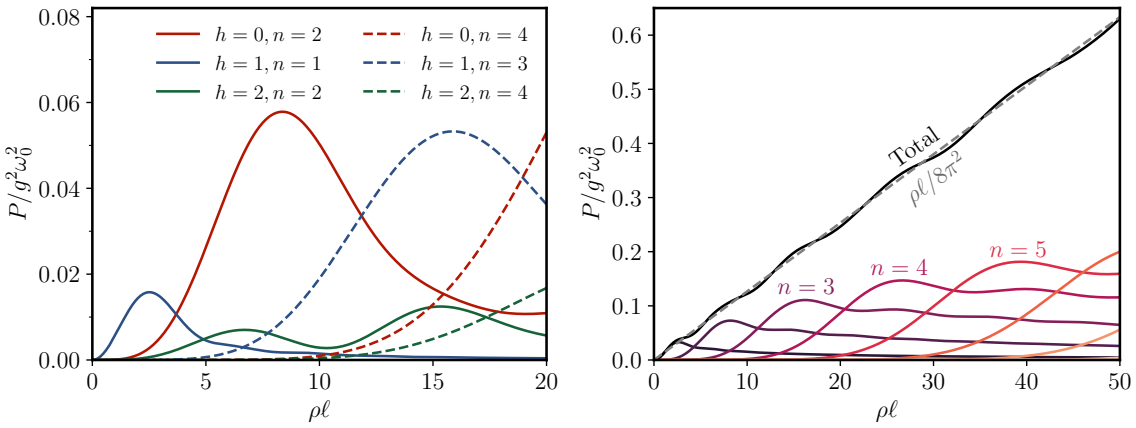

Figure 8.5: Radiation from a particle with a scalar-like current in nonrelativistic sinusoidal motion of amplitude ℓ. The left panel shows the power emitted in each given harmonic and helicity, evaluated with (8.226). It does not show the ordinary, ρ-independent scalar radiation at $h = 0$, $n = 1$, as this is suppressed by v_0^2. The right panel shows the power summed over helicities, evaluated using (8.230). As discussed in the text, it implies the total power is well-behaved in the limit of low accelerations.

is emitted into an unbounded number of helicities. This is a general phenomenon: as shown in appendix 8.9.5, one can extract the scaling of (8.231) from applying a stationary phase approximation to (8.230) for any smooth trajectory. This is another striking example of how continuous spin theories are well-behaved compared to naive expectations.

As in section 8.6.2, we can easily convert our results to vector-like currents by replacing g with $(\sqrt{2}\, e/\rho)(ik \cdot dz/d\tau)$, giving similar results. The analogue of (8.223) is

$$a_{h,n}(\hat{\mathbf{r}}) = -\frac{\sqrt{2}\, env_0}{\rho\ell} \int_0^T \frac{dt}{T}\, e^{in\omega_0(t-\hat{\mathbf{r}}\cdot\mathbf{z})}\, (1-v_r)\, (-\boldsymbol{\epsilon}_- \cdot \hat{\mathbf{v}}_\perp)^h\, J_h\left(\frac{\rho v_\perp}{n\omega_0(1-v_r)}\right). \tag{8.233}$$

The $\rho \to 0$ limit appears to diverge for $h = 0$, due to the constant term in the Bessel function. However, that contribution vanishes since the integrand is a total derivative.

The integral may again be expanded in $\rho\ell$ and v_0. Taking the nonrelativistic limit for sinusoidal motion by removing terms subleading in v_0, as in (8.226), yields

$$|a_{h,n}(\hat{\mathbf{r}})| = \sqrt{2}\, env_0 \left| \frac{1}{\rho\ell} \int_0^{2\pi} \frac{d\phi}{2\pi}\, e^{in\phi} J_h\left(\frac{\rho\ell \sin\theta}{n} \sin\phi\right) + O(v_0) \right|. \tag{8.234}$$

Unlike the scalar-like case, this expression also contains the usual ρ-independent amplitude, since it appears at the same order in v_0 as the leading corrections. The leading contribution to the radiation

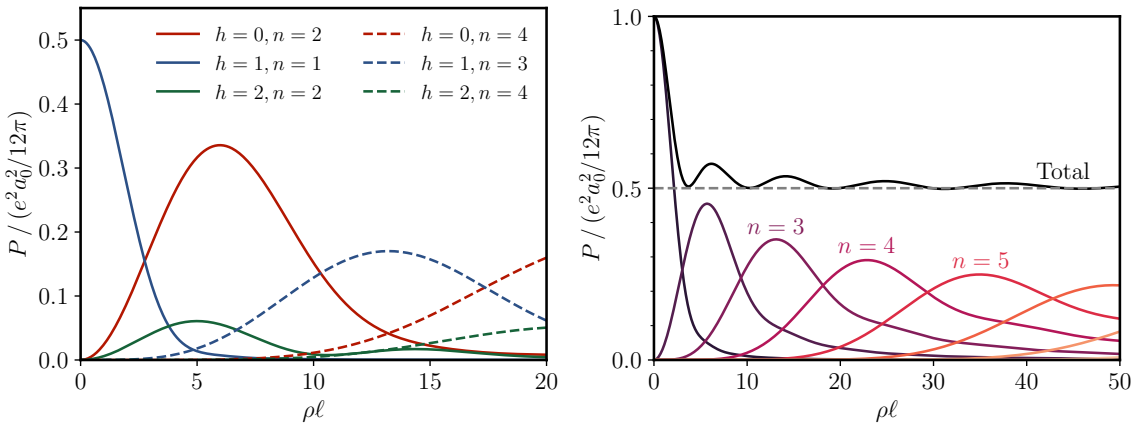

Figure 8.6: Radiation from a particle with a vector-like current in nonrelativistic sinusoidal motion of amplitude ℓ, normalized to the power at $\rho = 0$. We evaluate (8.234) to find the power emitted in each harmonic and helicity (left), and (8.236) to find the power summed over helicities (right).

amplitude at helicity h is of order $v_0(\rho\ell)^{||h|-1|}$, and the radiated power is

$$\frac{d\bar{P}_{h,n}}{d\hat{\mathbf{r}}} = \frac{e^2\omega_0^2 v_0^2}{64\pi^2} \times \begin{cases} \frac{1}{16}(\rho\ell)^2 \sin^4\theta & h = 0, n = 2 \\ \sin^2\theta - \frac{3}{16}(\rho\ell)^2 \sin^4\theta & |h| = 1, n = 1 + \cdots \\ \frac{1}{64}(\rho\ell)^2 \sin^4\theta & |h| = 2, n = 2 \end{cases} \tag{8.235}$$

All the radiation is primarily emitted in the transverse directions, as shown at right in Fig. 8.4. Integrating this equation over angles yields our earlier stated result (8.3).

Numeric results extending to large $\rho\ell$, where high harmonics and many helicities contribute, are shown in Fig. 8.6 and earlier in Fig. 8.1. Again, to find the total power emitted it is easiest to sum over helicities. The analogue of (8.230) is

$$\frac{d\bar{P}}{d\hat{\mathbf{r}}} = \frac{e^2\omega_0^2 v_0^2}{4\pi^2} \sum_{n>0} \frac{n^4}{(\rho\ell)^2} \int_0^T \frac{dt}{T} \int_0^T \frac{dt'}{T}\, e^{in\omega_0(t-t')}\, J_0\left(\frac{\rho|\mathbf{v}_\perp(t) - \mathbf{v}_\perp(t')|}{n\omega_0}\right) \tag{8.236}$$

which can again be evaluated in terms of hypergeometric functions, yielding the simple result

$$\lim_{\rho\ell\to\infty} \frac{d\bar{P}}{d\hat{\mathbf{r}}} = \frac{e^2\omega_0^2 v_0^2}{64\pi^2} \sin^2\theta. \tag{8.237}$$

This is precisely half the radiated power distribution for an ordinary vector field, though the radiation is now distributed over many helicities. Again, for a general smooth motion one can derive the same result, up to a different numeric constant, by applying a stationary phase approximation to (8.236). This again illustrates how continuous spin physics is surprisingly well-behaved, yielding sensible results for arbitrary accelerations.

8.7 Discussion and Future Directions

Is Continuous Spin a Fundamental Feature of Nature?

All observables in the continuous spin theories computed in this chapter reduce to those of familiar theories when $\omega \gg \rho$. This motivates a bold conjecture: all massless degrees of freedom in nature could have continuous spin. One could begin exploring this possibility along two independent directions. First, the Abelian gauge theory of this paper must be generalized to theories with nonzero ρ that reduce as $\rho \to 0$ to non-Abelian gauge theories and general relativity. Second, one must embed the Higgs mechanism within a continuous spin theory, which could initially be pursued in the context of Abelian Higgs models.

Intriguingly, a "continuous spin Standard Model" may provide insight on the gauge hierarchy problem. In familiar theories, a massless scalar field that mediates a $1/r$ potential is unstable against radiative corrections from interactions with other massive degrees of freedom. Continuous spin fields with scalar correspondence behave just like such fields as $\rho \to 0$, but have a gauge symmetry which forbids a mass term, and thus could render a light scalar technically natural. This simple observation strongly motivates developing interacting continuous spin theories to the point where one can compute radiative corrections. The result is not clear a priori; for instance, the gauge symmetry might be anomalous at the quantum level, or supersymmetry might be required. Or perhaps an entirely new mechanism, related to analytic structure in η-space, will play a role. Even if ρ is zero in our universe, such investigations may inspire new resolutions to the hierarchy problem.

Investigating the possibility that the graviton is a CSP requires developing a non-Abelian continuous spin theory with tensor correspondence, i.e. one which reduces to general relativity as $\rho \to 0$. This challenging task is motivated by the cosmological constant problem. In general relativity, a cosmological constant term is allowed by general covariance, and quantum effects are generically expected to produce large corrections to such a term. However, continuous spin fields have a larger gauge symmetry which forbids this term when $\rho = 0$, which could render a small cosmological constant technically natural. A first step toward developing this idea would be to construct currents which reduce to the contribution of vacuum energy to $T_{\mu\nu}$ in the limit $\rho \to 0$. An even more radical possibility is that the cosmological constant is completely forbidden, and the accelerated expansion of the universe instead results from ρ-dependent corrections to the static force law.

Future Theoretical Developments

We highlighted some long-term goals of a continuous spin research programme above; we now list some theoretical developments which can serve as intermediate steps, and may also open new avenues for experimental measurements and detection.

First, in this paper we have focused on spinless matter particles, since these give rise to the leading contributions to long-distance forces and radiation. It would be interesting to see how our

universal decomposition of currents is modified for matter particles with spin. Understanding the role of spin would also enable precision tests using nuclear or electronic spin precession.

Second, we have only computed classical observables in this chapter, but nonzero ρ could also produce distinctive signatures at microscopic scales, such as forbidden atomic transitions through emission of partner polarizations, or modifications to atomic energy levels. As already discussed in Ref. [781], the free continuous spin field is straightforward to quantize, and the mode amplitudes $a_h^*(\mathbf{k})$ and $a_h(\mathbf{k})$ simply become raising and lowering operators for field modes with momentum $\mathbf{k}$ and helicity h. There are well-known techniques for computing quantum amplitudes for matter particles and gauge fields (e.g. see Refs. [832, 833, 834]) which in fact predate [835] the traditional approach using matter fields. These formalisms could be a starting point for computing matter-CSP transition amplitudes from our action (8.1). It is not obvious if such quantized theories will be fully consistent, but the completeness relation (8.282) strongly suggests that correct unitarity cuts will be obtained at least for tree-level CSP-mediated matter scattering.

Third, as already discussed in subsection 8.4.2, it would be interesting to explore causality more thoroughly, as well as local completions of the action involving intermediate fields. This may shed light on the physical interpretation of our delocalized effective currents and might be necessary to properly define and compute radiative corrections.

Fourth, it would be interesting to tie our work to the broader field theory literature. For instance, one could generalize our interacting formalism to supersymmetric continuous spin fields, or investigate its relation to interactions in higher spin theory, which also often require towers of arbitrarily high helicity modes. In addition, while massless CSPs do not appear in the perturbative treatment of the familiar bosonic string [836], it would be interesting to see if they can emerge from other types of string theory.

Fifth, we have focused on the coupling of continuous spin fields to matter particles, and it would also be interesting to consider their coupling to matter fields. As discussed in appendix 8.9.3, existing currents built from matter fields do not obey gauge invariance, do not contain the most relevant minimal couplings, and appear to have vanishing coupling to radiation. We suspect that suitable currents can be built from matter fields, but they must be either nonlocal or involve additional intermediate fields. Understanding this structure is likely a prerequisite to developing non-Abelian continuous spin theories, which require matter-like couplings for the continuous spin field itself.

Finally, since CSPs are known to exist in (A)dS spaces, it would be interesting to study continuous spin fields in curved spacetimes, such as black holes. For a black hole with radius $r_s \ll 1/\rho$, a photon CSP should be equivalent to one particle of each integer helicity, yielding an unambiguous deviation from the ordinary Hawking radiation rate. More spectacularly, since ρ provides a length scale, a continuous spin field might be exponentially amplified around a black hole through the superradiant instability. Alternatively, our formalism could simply be inconsistent in curved spacetime. It might even be that the only fully consistent gravitational theories of interacting CSPs require the graviton

to be a CSP as well.

Towards Experimental Tests of the Photon and Graviton Spin Scale

In the near-term, the formalism explored in this chapter can already be used to devise probes of the photon or graviton spin scale. These phenomenological tests should be largely independent of the ultimate origin of the spin scale.

If the photon has a nonzero spin scale ρ_γ, then the familiar charged particles in nature must couple to it through vector-like currents, leading to distinctive deviations from ordinary electromagnetism. One promising avenue is to try to detect the "nearest neighbor" partner polarizations with $h = 0$ or $|h| = 2$, which can be both produced and detected by antennas and electromagnetic resonators. For example, if an electromagnetic cavity is excited, then it will emit in the partner polarizations, which pass out through its walls and can be detected by a second cavity. The partner polarizations could also be produced deep within the Sun. Anomalous cooling caused by such emission should set a bound on ρ. Even below this bound the partner modes can freely propagate to a "helioscope" detector on Earth, where they would appear as X-rays which penetrate conventional shielding. While we have not yet performed detailed calculations, we can certainly say that $\rho_\gamma \lesssim 10^{-6}\,\text{eV}$ due to the nonobservation of strong deviations from ordinary electromagnetism in microwave/radiofrequency technology and we roughly estimate stellar cooling constraints imply $\rho_\gamma \lesssim 10^{-9}\,\text{eV}$.

Our results strongly suggest that continuous spin fields have well-behaved thermodynamics, and furthermore make it possible to probe ρ_γ-dependent corrections to ordinary thermodynamics. For example, nonzero ρ_γ changes the effective number of light degrees of freedom in the early universe, which might be constrained through precision cosmological measurements, or detected through the cosmic background radiation in the partner polarizations.

In these respects, searches for the photon's partner polarizations bear a strong resemblance to ongoing searches for weakly coupled, ultralight fields, such as axions, dilatons, and dark photons. One crucial difference is that deviations from radiation-induced forces are purely velocity-dependent. Another difference is that all ρ-dependent effects are enhanced in the infrared, with forces from nearest neighbor polarizations suppressed by ρ_γ/ω, which might enhance signals for telescopes sensitive to lower frequency radiation. Very low momentum scales could be probed via long distance modifications of force laws, such as from astrophysical or cosmological magnetic fields, though here the deviations are not universal.

We suspect it is possible to probe the spin scale ρ_g of the graviton within the context of linearized general relativity, by suitably adapting the tensor-like current discussed at the end of subsection 8.3.2. Using the formalism developed in this chapter, it would then be relatively straightforward to compute ρ_g-dependent corrections to gravitational radiation, recover the tensor-like soft factors derived in Ref. [780], and investigate deviations from ordinary gravitational dynamics on galactic and cosmological scales.

We have discussed a broad set of future directions, but it is also likely that the most exciting new ideas are still waiting to be found. This subject is still in its infancy, and we hope this work will serve as a solid foundation for many developments to come.

8.8 Appendix: Vector Superspace Integration

In this section, we define vector superspace integrals of the form

$$\int [d^4\eta]\, \delta(\eta^2+1)\, F(\eta), \qquad \int [d^4\eta]\, \delta'(\eta^2+1)\, F(\eta) \tag{8.238}$$

for arbitrary analytic functions $F(\eta)$, and present two equivalent procedures for evaluating them. These approaches were introduced in Ref. [781], but we include a streamlined summary to make this paper self-contained and provide complementary derivations. We also derive several powerful new identities (8.269), (8.273), and (8.282) used throughout the paper.

Integrals over an ordinary measure $d^4\eta$ diverge, as the hyperboloid $\eta^2+1=0$ has infinite volume. Heuristically, the regulated measure $[d^4\eta]$ is defined by factoring the volume out,

$$d^4\eta = [d^4\eta] \int d^4\eta\, \delta(\eta^2+1). \tag{8.239}$$

While this is merely a formal definition, requiring that the integration results obey sensible constraints, such as Lorentz covariance, fully determines all integrals of the form (8.238). This approach is pursued in App. 8.8.1 and used to write the integrals in terms of generating functions, and derive new identities in App. 8.8.2. Alternatively, the regulated measure can be concretely defined by analytic continuation to Euclidean signature, as shown in App. 8.8.3.

These two formulations are completely equivalent, but complementary. The generating function approach can always be straightforwardly applied, but often produces tedious combinatorics. By contrast, the analytic continuation approach requires more geometric insight to use, but can yield elegant shortcuts. We will show how both approaches can be used to derive the "master identity" (8.269) from which our other new identities follow. Finally, although both approaches use analyticity of the integrand $F(\eta)$, they only require analyticity on an appropriate region, as we show in an example at the end of App. 8.8.3.

8.8.1 Generating Functions

We begin by deriving generating functions for the integrals (8.238) from six basic properties they must satisfy. First, the heuristic definition (8.239) implies the normalization

$$\int [d^4\eta]\, \delta(\eta^2+1) = 1. \tag{8.240}$$

We further require integrals over $\delta(\eta^2+1)$ to respect the delta function and integration by parts identities,

$$\int [d^4\eta]\, \delta(\eta^2+1)(\eta^2+1)F(\eta) = 0, \tag{8.241}$$

$$\int [d^4\eta] \quad \partial_\eta^\mu \left(\delta(\eta^2+1)F(\eta)\right) \quad = 0. \tag{8.242}$$

To relate these to integrals over $\delta'(\eta^2+1)$, we impose the distributional identity

$$\delta'(\eta^2+1)(\eta^2+1) = -\delta(\eta^2+1) \tag{8.243}$$

underneath an η integral. Finally, we assume that integration is linear and the results are Lorentz covariant, in a way we will describe more concretely shortly.

The above properties determine the integrals (8.238) for any analytic function F. To show this, note that by linearity, it suffices to define the integral for each term in the Taylor expansion of F, which in turn follow from integrals of the form

$$\int [d^4\eta]\, \delta(\eta^2+1)\, \eta^{\mu_1}\eta^{\mu_2}\cdots\eta^{\mu_m}. \tag{8.244}$$

By Lorentz symmetry, the result must be a fully symmetric rank-m tensor built from $g^{\mu\nu}$. Thus, it must be zero for odd m, while for even $m = 2n$, we must have

$$\int [d^4\eta]\, \delta(\eta^2+1)\, \eta^{\mu_1}\eta^{\mu_2}\cdots\eta^{\mu_{2n}} = c_n \left(g^{\mu_1\mu_2}\cdots g^{\mu_{2n-1}\mu_{2n}} + \text{perms.}\right) \tag{8.245}$$

where the right-hand side has $(2n)!$ terms. Contracting this with $g_{\mu_1\mu_2}$, the left-hand side is

$$g_{\mu_1\mu_2}\int [d^4\eta]\, \delta(\eta^2+1)\, \eta^{\mu_1}\eta^{\mu_2}\cdots\eta^{\mu_{2n}} = -c_{n-1}(g^{\mu_3\mu_4}\cdots g^{\mu_{2n-1}\mu_{2n}} + \text{perms.}) \tag{8.246}$$

where we used (8.241). The right-hand side has the same tensor structure; to find the numeric coefficient, note there are $2n(2n-2)!$ terms containing $g^{\mu_1\mu_2}$ or $g^{\mu_2\mu_1}$, which each produce a factor of $D = 4$ in the contraction, and the other $(2n)(2n-2)(2n-2)!$ terms yield a product of metric tensors with unit coefficient. Comparing the two sides yields the recursion relation

$$-c_{n-1} = (2n)(4+(2n-2))\, c_n. \tag{8.247}$$

Since $c_0 = 1$, the general solution is

$$c_n = \frac{(-1/4)^n}{n!\,(n+1)!} = \begin{cases} -1/8 & n = 1 \\ 1/192 & n = 2 \end{cases}. \tag{8.248}$$

Both types of η integral can be written economically in terms of generating functions,

$$\int [d^4\eta]\, \delta(\eta^2+1)\, F(\eta) = G\left(\sqrt{\partial_\eta^2}\right) F(\eta)\Big|_{\eta=0} \tag{8.249}$$

$$\int [d^4\eta]\, \delta'(\eta^2+1)\, F(\eta) = G'\left(\sqrt{\partial_\eta^2}\right) F(\eta)\Big|_{\eta=0} \tag{8.250}$$

where we have just shown that

$$G(x) = \sum_{n=0}^{\infty} c_n x^{2n} = \frac{2J_1(x)}{x}. \tag{8.251}$$

To address the other integral, note that the above properties imply

$$\int [d^4\eta]\, \delta'(\eta^2+1) F(\eta) = \int [d^4\eta]\, \delta(\eta^2+1) \left(\frac{1}{2}\,\partial_\eta\cdot\eta - 1\right) F(\eta), \tag{8.252}$$

which is readily verified by integrating the right-hand side by parts and applying (8.243). This result holds for general D, and for $D=4$, the term in parentheses produces a factor of $n+1$ when acting on η^{2n}. Thus, the Taylor series of G' has coefficients

$$d_n = \frac{(-1/4)^n}{(n!)^2} = \begin{cases} -1/4 & n=1 \\ 1/64 & n=2 \end{cases} \tag{8.253}$$

which sums to

$$G'(x) = \sum_{n=0}^{\infty} d_n x^{2n} = J_0(x). \tag{8.254}$$

The appearance of Bessel functions is not surprising from a geometric standpoint, and we can see more directly why they must appear with an alternate derivation. Note that showing (8.254) is equivalent to showing

$$I(V) = \int [d^4\eta]\, \delta'(\eta^2+1)\, e^{i\eta\cdot V} = J_0(\sqrt{-V^2}) \tag{8.255}$$

for any four-vector V, since each factor of ∂_η^2 yields a factor of $-V^2$. Now, by (8.243) we have

$$\partial_V^2 I(V) = \int [d^4\eta]\, \delta'(\eta^2+1)\, (-\eta^2) e^{i\eta\cdot V} \tag{8.256}$$

$$= \int [d^4\eta]\, \delta'(\eta^2+1)\, e^{i\eta\cdot V} + \int [d^4\eta]\, \delta(\eta^2+1)\, e^{i\eta\cdot V}. \tag{8.257}$$

On the other hand, we can use integration by parts (8.242) to show that

$$\partial_V^\mu I(V) = \int [d^4\eta]\, \delta'(\eta^2+1)\, (i\eta^\mu) e^{i\eta\cdot V} \tag{8.258}$$

$$= \frac{i}{2}\int [d^4\eta]\, (\partial_\eta^\mu \delta(\eta^2+1))\, e^{i\eta\cdot V} \tag{8.259}$$

$$= \frac{i}{2}\int [d^4\eta]\, \delta(\eta^2+1)\, (-\partial_\eta^\mu) e^{i\eta\cdot V} \tag{8.260}$$

$$= \frac{1}{2}\int [d^4\eta]\, \delta(\eta^2+1)\, V^\mu e^{i\eta\cdot V}. \tag{8.261}$$

Combining these results yields the differential equation

$$V^2\, \partial_V^2 I(V) = 2\, V\cdot\partial_V I(V) + V^2 I(V). \tag{8.262}$$

Since $I(V)$ is a scalar function of V^μ, it must be solely a function of $x = \sqrt{-V^2}$. In D spacetime dimensions, (8.262) implies $x^2 I''(x) + (D-3)xI'(x) + x^2 I(x) = 0$, which for $D = 4$ is the Bessel differential equation of order zero. The normalization $I(0) = 1$ fixes $I(x) = J_0(x)$.

8.8.2 Useful Identities

With the generating functions in hand, we can prove the concrete identities used in the main text. Most of these identities involve the null frame vectors defined in the conventions. They can be efficiently handled in the generating function approach because (8.4) implies

$$\partial_\eta^2 = 2(q\cdot\partial_\eta)(k\cdot\partial_\eta) - (\epsilon_+\cdot\partial_\eta)(\epsilon_-\cdot\partial_\eta). \tag{8.263}$$

In other words, applying ∂_η^2 produces contractions between the $\eta\cdot q$ and $\eta\cdot k$ components of the integrand, as well as between the $\eta\cdot\epsilon_+$ and $\eta\cdot\epsilon_-$ components.

As a simple example of this, consider the overlaps of the helicity modes,

$$\langle \psi_{h,k}|\psi_{h',k}\rangle \equiv \int [d^4\eta]\, \delta'(\eta^2+1)\, \psi^*_{h,k}(\eta)\psi_{h',k}(\eta) \tag{8.264}$$

$$= \int [d^4\eta]\, \delta'(\eta^2+1)\, (\mp i\eta\cdot\epsilon_\mp)^{|h|}(\pm i\eta\cdot\epsilon_\pm)^{|h'|} \tag{8.265}$$

where the top and bottom signs apply for positive and negative h and h'. When $h \neq h'$, the result must be zero because there are an unequal number of copies of ϵ_+ and ϵ_-. (Similarly, the result would automatically be zero if the conjugation in (8.264) was not present, since the factors of $e^{-i\rho\eta\cdot q}$

would not cancel.) If $h = h'$, then for positive h the norm is

$$\langle \psi_{h,k} | \psi_{h,k} \rangle = d_h \, (\partial_\eta^2)^h \, (\eta \cdot \epsilon_-)^h (\eta \cdot \epsilon_+)^h \Big|_{h=0} \tag{8.266}$$

$$= d_h \, (-1)^h \, (\epsilon_+ \cdot \partial_\eta)^h (\eta \cdot \epsilon_-)^h \, (\epsilon_- \cdot \partial_\eta)^h (\eta \cdot \epsilon_+)^h \Big|_{h=0} \tag{8.267}$$

$$= d_h \, (-1)^h \, ((\epsilon_+ \cdot \epsilon_-)^h \, h!)^2 = 1. \tag{8.268}$$

with an identical result for negative h. This shows the helicity basis is orthonormal.

Using this result, we can derive a powerful "master" identity, which reduces certain vector superspace integrals to integrals over the unit circle in the plane spanned by ϵ_+ and ϵ_-,

$$\int [d^4\eta] \, \delta'(\eta^2 + 1) \, F(\eta) = \int \frac{d\theta}{2\pi} \, F(\eta) \Big|_{\eta = \mathrm{Re}(e^{i\theta} \epsilon_-)} \quad \text{when } \delta(\eta^2 + 1) \, k \cdot \partial_\eta \, F = 0 \tag{8.269}$$

for some null k. The condition above is equivalent to letting

$$k \cdot \partial_\eta \, F = (\eta^2 + 1) \, \beta(\eta) \tag{8.270}$$

for an arbitrary analytic function β.

To prove (8.269) in the special case $\beta = 0$, consider Taylor expanding F in the variables $\eta \cdot k$, $\eta \cdot q$, and $\eta \cdot \epsilon_\pm$. Terms involving $\eta \cdot q$ would contribute to the Taylor expansion of $k \cdot \partial_\eta \, F$, and so must vanish by assumption. But then (8.263) implies that $\eta \cdot k$ terms do not contribute to the left-hand side, since they have to be contracted with $\eta \cdot q$ terms. Only terms of the form $(\eta \cdot \epsilon_+ \, \eta \cdot \epsilon_-)^h$ contribute, with unit coefficients as we have just shown, and this is reproduced by the integral on the right-hand side.

It is possible, but tedious, to verify (8.269) for nonzero β by Taylor expanding both F and β and evaluating the left-hand side using the generating function. Alternatively, consider decomposing $F = F_0 + F_\beta$, where the "homogeneous" solution F_0 satisfies $k \cdot \partial_\eta \, F_0 = 0$. The previous paragraph shows that F_0 obeys the master identity, so it suffices to construct a "particular" solution F_β which does not contribute to either side of (8.269). To do this, let

$$F_\beta(\eta) = \int_0^{\eta \cdot q} dx \, (\eta^2 + 1 + 2(\eta \cdot k)(x - \eta \cdot q)) \, \beta(\eta + (x - \eta \cdot q)k). \tag{8.271}$$

By construction, $k \cdot \partial_\eta$ annihilates the integrand, so that $k \cdot \partial_\eta \, F_\beta = (\eta^2 + 1) \, \beta(\eta)$ from differentiating the integral's upper bound. Now we show that F_β does not contribute to either side of (8.269). On the right-hand side, $\eta \cdot q = 0$ on the unit circle, so the range of the x integral vanishes. The left-hand

side vanishes because its integrand can be rewritten as a total derivative,

$$\int [d^4\eta]\, k\cdot\partial_\eta \left(\delta(\eta^2+1)\int_0^{\eta\cdot q} dx\,(x-\eta\cdot q)\,\beta(\eta+(x-\eta\cdot q)k)\right)=0, \tag{8.272}$$

as can be checked by carrying out the derivative and using (8.243).

As a first application of the master identity, we prove a result which is often useful when evaluating projections against helicity modes,

$$\int [d^4\eta]\,\delta'(\eta^2+1)(i\eta\cdot\epsilon_\pm)^h e^{i\eta\cdot V} = e^{ih\arg(\epsilon_\pm\cdot V)}\,J_h(\sqrt{-V^2}) \text{ when } V\cdot k=0 \tag{8.273}$$

for any nonnegative integer h. Note that the $h=0$ case is simply our earlier result (8.255), and that conjugating the result for the upper sign gives the result for the lower sign. Also note that when applying this identity to helicity modes with negative h, it is often convenient to simplify the final result using $J_{-n}(x)=(-1)^n J_n(x)$.

To prove the result, note that the condition $V\cdot k=0$ implies V can be decomposed as

$$V=(q\cdot V)\,k-\frac{v^*}{2}\,\epsilon_+-\frac{v}{2}\,\epsilon_- \tag{8.274}$$

where $v=\epsilon_+\cdot V$, which in turn implies $|v|^2=-V^2$. Now, applying the master identity to the left-hand side of (8.273) gives

$$\begin{aligned}
\int [d^4\eta]\,\delta'(\eta^2+1)(i\eta\cdot\epsilon_+)^h e^{i\eta\cdot V} &= \int \frac{d\theta}{2\pi}\,(i\eta\cdot\epsilon_+)^h e^{i\eta\cdot V}\Big|_{\eta=\mathrm{Re}(e^{i\theta}\epsilon_-)} && (8.275)\\
&= \int \frac{d\theta}{2\pi}\,e^{ih(\theta-\pi/2)}e^{i|v|\cos(\theta-\arg v)} && (8.276)\\
&= e^{ih\arg v}\int \frac{d\theta}{2\pi}\,e^{ih(\theta-\pi/2)}e^{i|v|\cos\theta} && (8.277)\\
&= e^{ih\arg v}J_h(|v|) && (8.278)
\end{aligned}$$

where we plugged in $\eta=\mathrm{Re}(e^{i\theta}\epsilon_-)=(e^{i\theta}\epsilon_-+e^{-i\theta}\epsilon_+)/2$, shifted θ, and used the integral representation of the Bessel functions. This is the desired result (8.273) for the upper sign.

Of course, we can also show the result by using generating functions to directly evaluate the left-hand side. The first term in (8.274) produces factors of $\eta\cdot k$ which have no factors of $\eta\cdot q$ to

contract with, so it can be dropped. The left-hand side is then

$$\sum_{n=0}^{\infty} \frac{(-1/4)^{n+h}}{(n+h)!^2} (\partial_\eta^2)^{n+h} \, (i\eta \cdot \epsilon_+)^h e^{-(i/2)(\eta\cdot\epsilon_+)v^*} e^{-(i/2)(\eta\cdot\epsilon_-)v} \Big|_{\eta=0} \tag{8.279}$$

$$= \sum_{n=0}^{\infty} \frac{(-1/4)^{n+h}}{(n+h)!^2} \binom{n+h}{h} \left((-2)^h v^h \, h!\right) |v^2|^n \tag{8.280}$$

$$= \left(\frac{v}{|v|}\right)^h \sum_{n=0}^{\infty} \frac{(-1)^n}{n! \, (n+h)!} \left(\frac{|v|}{2}\right)^{2n+h} \tag{8.281}$$

which in the first step, h of the copies of ∂_η^2 acted on an $i\eta \cdot \epsilon_+$ and the first exponential, and the other n copies acted on both exponentials. This is the desired right-hand side.

As another example, we prove the completeness relation for the helicity modes,

$$\sum_h \psi_{h,k}(\eta) \psi^*_{h,k}(\eta') \, \delta'(\eta^2+1) \, \delta'(\eta'^2+1) \simeq \delta^{(4)}(\eta - \eta') \, \delta'(\eta^2+1), \tag{8.282}$$

which holds when both sides are integrated over η and η' against $F(\eta, \eta', k)$ satisfying

$$(ik \cdot \partial_\eta + \rho) F = (\eta^2+1) \, \beta, \tag{8.283}$$

$$(-ik \cdot \partial'_\eta + \rho) F = (\eta'^2+1) \, \beta'. \tag{8.284}$$

A key physical example is $F(\eta, \eta', k) = J(\eta, -k) J'(\eta', k)$ where the currents J and J' satisfy the continuity condition (8.69). In that case, (8.282) implies that the continuous spin propagator between two currents is equivalent to a sum over physical polarizations, as expected by unitarity.

To show the result, first note that the integrated left-hand side of (8.282) is

$$\int [d^4\eta][d^4\eta'] \, \delta'(\eta^2+1) \delta'(\eta'^2+1) \sum_h (e^{i\rho(\eta'-\eta)\cdot q} F(\eta, \eta', k)) (\eta \cdot \epsilon_\pm)^{|h|} (\eta' \cdot \epsilon_\mp)^{|h|} \tag{8.285}$$

where the upper and lower signs apply for positive and negative h. The function in brackets satisfies the condition (8.270) to apply the master identity in both η and η', giving

$$\int \frac{d\theta}{2\pi} \frac{d\theta'}{2\pi} F(\eta, \eta', k) \sum_h (\eta \cdot \epsilon_\pm)^{|h|} (\eta' \cdot \epsilon_\mp)^{|h|} \Big|_{\substack{\eta = \mathrm{Re}(e^{i\theta}\epsilon_-) \\ \eta' = \mathrm{Re}(e^{i\theta'}\epsilon_-)}} = \int \frac{d\theta}{2\pi} F(\eta, \eta, k) \Big|_{\eta = \mathrm{Re}(e^{i\theta}\epsilon_-)} \tag{8.286}$$

as the summation yields a delta function, $\sum_h e^{ih(\theta-\theta')} = 2\pi \, \delta(\theta - \theta')$. On the right-hand side, we have a single integral over $F(\eta, \eta, k)$, and using the master identity gives the same result.

8.8.3 Regulated Measure From Analytic Continuation

In this section, we concretely define the regulated measure $[d^D\eta]$ by analytic continuation. While we have already shown that vector superspace integrals can be determined without specifying a regulator, this new perspective readily generalizes to any spacetime dimension D and provides geometric intuition for the identities proven above.

Specifically, we analytically continue to complex η^0 and rotate the η^0 integration contourclockwise, going up the imaginary axis. The resulting integral is naturally expressed in terms of Wick rotated coordinates $\bar{\eta}^M = (\eta^1, \ldots, \eta^{D-1}, -i\eta^0)$, where $M = 1, \ldots, D$. Euclidean inner products are always implied for barred quantities, e.g. the quantity η^2 analytically continues to $-\bar{\eta}^2$. Integrals over the Minkowskian unit hyperboloid $\eta^2 + 1 = 0$ thus continue to integrals over a Euclidean unit sphere $\bar{\eta}^2 - 1 = 0$. This will yield finite results since the unit sphere has finite area S_{D-1}.

For any analytic function $F(\eta)$, we therefore define

$$\int [d^D\eta]\, \delta(\eta^2 + 1) F(\eta) \equiv \frac{2}{S_{D-1}} \int d^D\bar{\eta}\, \delta(\bar{\eta}^2 - 1) \bar{F}(\bar{\eta}), \tag{8.287}$$

where the prefactor ensures the normalization condition (8.240) is satisfied. Similarly,

$$\int [d^D\eta]\, \delta'(\eta^2 + 1) F(\eta) = -\frac{2}{S_{D-1}} \int d^D\bar{\eta}\, \delta'(\bar{\eta}^2 - 1) \bar{F}(\bar{\eta}), \tag{8.288}$$

where the minus sign appears because $\delta'(-x) = -\delta'(x)$, and ensures consistency with (8.243). This is the same definition as used in Ref. [781], though the analogue of (8.288) in that work does not show the factor of 2. Note that $\bar{F}$ is also defined by analytic continuation, i.e. $\bar{F}(\bar{\eta}) = F(i\bar{\eta}^D, \bar{\eta}^1, \ldots, \bar{\eta}^{D-1}) = F(\eta)$.

Recovering the Generating Functions

As a simple example, we will use analytic continuation to evaluate the integral

$$I(V) = \int [d^D\eta]\, \delta'(\eta^2 + 1) e^{i\eta \cdot V}. \tag{8.289}$$

As explained around (8.255), this is equivalent to finding the generating function G', which together with the property (8.243) determines G and thus all vector superspace integrals. It therefore suffices to evaluate the above integral for $D = 4$ to show the equivalence of analytic continuation to the symmetry-based arguments in appendix 8.8.1.

We define $\bar{V} = (V^1, \ldots, V^{D-1}, -iV^0)$ so the integrand can be written in terms of Euclidean inner

products, $\eta \cdot V = -\bar{\eta} \cdot \bar{V}$. Applying (8.287) and the Euclidean analogue of (8.252) gives

$$I(V) = \frac{2}{S_{D-1}} \int d^D\bar{\eta}\, \delta(1-\bar{\eta}^2)\, \frac{1}{2}(\partial_{\bar{\eta}} \cdot \bar{\eta} - 2) e^{-i\bar{\eta}\cdot\bar{V}} \tag{8.290}$$

$$= \frac{1}{S_{D-1}} \int d^D\bar{\eta}\, \delta(1-\bar{\eta}^2)\, (D - 2 + \bar{\eta} \cdot \partial_{\bar{\eta}}) e^{-i\bar{\eta}\cdot\bar{V}}. \tag{8.291}$$

Note that $\bar{V}$ is complex in general, but it suffices to evaluate (8.291) at real $\bar{V}$ and analytically continue the result. Specializing to $D = 4$, the measure in spherical coordinates is

$$d^4\bar{\eta} = |\bar{\eta}|^3 d|\bar{\eta}|\, \sin^2\theta\, d\theta\, d^2\Omega_2 \tag{8.292}$$

where θ is the angle between $\bar{\eta}$ and V and Ω_2 indicates the remaining angular integral. Then

$$I(V) = \frac{1}{S_3} \int_0^\infty d|\bar{\eta}|\, \delta(1-|\bar{\eta}|^2)\, |\bar{\eta}|^3 \int_0^\pi d\theta\, \sin^2\theta\, (2 - i|\bar{\eta}||\bar{V}|\cos\theta) e^{-i|\bar{\eta}||\bar{V}|\cos\theta} \int d^2\Omega_2 \tag{8.293}$$

$$= \frac{1}{\pi} \int_0^\pi d\theta\, \sin^2\theta\, (2 - i|\bar{V}|\cos\theta) e^{-i|\bar{V}|\cos\theta} \tag{8.294}$$

$$= J_0(|\bar{V}|) \tag{8.295}$$

where we used $S_2 = 4\pi$ and $S_3 = 2\pi^2$. This matches our earlier result (8.255), as $|\bar{V}| = \sqrt{-V^2}$.

The D-dimensional analogue of this result is given in Ref. [781], and can also be derived using spherical coordinates. However, it turns to be simpler to use polyspherical coordinates, even though they employ weaker symmetry properties of the integrand. To do this, group the $\bar{\eta}$ coordinates into a two-dimensional subspace η_L orthogonal to $\bar{V}$ and a $(D-2)$-dimensional subspace $\tilde{\eta}$. Using polar coordinates for η_L, the measure is

$$d^D\bar{\eta} = d^{D-2}\tilde{\eta}\, \frac{d|\eta_L|^2\, d\theta}{2} \tag{8.296}$$

and since $\bar{\eta} \cdot \bar{V} = \tilde{\eta} \cdot \tilde{V}$, the integral (8.291) becomes

$$I(V) = \frac{1}{2S_{D-1}} \int d^{D-2}\tilde{\eta}\, d|\eta_L|^2\, d\theta\, \delta(1-|\tilde{\eta}|^2-|\eta_L|^2)\, (D - 2 + \bar{\eta} \cdot \partial_{\bar{\eta}}) e^{-i\tilde{\eta}\cdot\tilde{V}} \tag{8.297}$$

$$= \frac{\pi}{S_{D-1}} \int_{|\tilde{\eta}|\le 1} d^{D-2}\tilde{\eta}\, (D - 2 + \tilde{\eta} \cdot \partial_{\tilde{\eta}}) e^{-i\tilde{\eta}\cdot\tilde{V}} \tag{8.298}$$

$$= \frac{\pi}{S_{D-1}} \int_{|\tilde{\eta}|\le 1} d^{D-2}\tilde{\eta}\, \partial_{\tilde{\eta}} \cdot (\tilde{\eta}\, e^{-i\tilde{\eta}\cdot\tilde{V}}) \tag{8.299}$$

$$= \frac{\pi}{S_{D-1}} \int_{|\tilde{\eta}|=1} d^{D-3}\Omega_{\tilde{\eta}}\, e^{-i\tilde{V}\cdot\tilde{\eta}} \tag{8.300}$$

where we performed the integral over η_L and used the divergence theorem. The integral thus cleanly reduces to one over a $(D-3)$-dimensional unit sphere. For example, when $D = 4$ the remaining

integral is over a unit circle, $d\Omega_{\bar\eta} = d\theta$, giving

$$I(V) = \frac{1}{2\pi}\int_0^{2\pi} d\theta\, e^{-i|\bar V|\cos\theta} = J_0(|\bar V|) \tag{8.301}$$

in agreement with our previous result.

Generalizing the Master Identity

We now use analytic continuation to generalize the master identity (8.269) to D dimensions, and shed light on its geometric meaning. We consider the integral

$$\int [d^D\eta]\,\delta'(\eta^2+1)F(\eta) = -\frac{2}{S_{D-1}}\int d^D\bar\eta\,\delta'(\bar\eta^2-1)\bar F(\bar\eta) \tag{8.302}$$

where $k\cdot\partial_\eta F = (\eta^2+1)\beta$ for some null k. We first take $\beta = 0$, in which case $\bar k\cdot\partial_{\bar\eta}\bar F = 0$.

The first step is to parallel our earlier derivation, but in Euclidean signature. We decompose $\bar\eta$ into a $(D-2)$-dimensional subspace $\tilde\eta$ which is orthogonal to $\bar k$, and a two-dimensional subspace η_L spanned by $\bar k$ and $\bar q$, which satisfy $\bar k^2 = \bar q^2 = 0$ and $\bar k\cdot\bar q = -1$. (This is possible because $\bar k$ and $\bar q$ are complex Euclidean vectors. And as in Lorentzian signature, there is freedom in the choice of $\bar q$.) The requirement $\bar k\cdot\partial_{\bar\eta}\bar F = 0$ then implies that $\bar F$ cannot depend on $\bar\eta\cdot\bar q$. To handle the $\bar\eta\cdot\bar k$ dependence, we write

$$\bar F(\tilde\eta,\bar\eta\cdot\bar k) = \tilde F(\tilde\eta) + \bar\eta\cdot\bar k\, G(\tilde\eta,\bar\eta\cdot\bar k) \tag{8.303}$$

which is always possible since $\bar F$ is analytic. The second term does not contribute to the integral (8.302). To see this, note that $\bar k\cdot\partial_{\bar\eta}G = 0$, so we may write

$$\int d^D\bar\eta\,\delta'(\bar\eta^2-1)\,\bar\eta\cdot\bar k\,G = \frac{1}{2}\int d^D\bar\eta\,\bar k\cdot\partial_{\bar\eta}\left(\delta(\bar\eta^2-1)G\right). \tag{8.304}$$

The integrand is a total derivative, which vanishes at infinity due to the delta function.

Therefore, only $\tilde F(\tilde\eta)$ contributes to the right-hand side of (8.302). Now, note that in the derivation of (8.300), the only property of the function $e^{-i\bar\eta\cdot\bar V}$ we used was that it did not depend on η_L. Since this is also true of $\tilde F(\tilde\eta)$, we may use the exact same reasoning to show

$$\int [d^D\eta]\,\delta'(\eta^2+1)F(\eta) = \frac{\pi}{S_{D-1}}\int_{|\tilde\eta|=1} d^{D-3}\Omega_{\tilde\eta}\,\tilde F(\tilde\eta). \tag{8.305}$$

Using the recurrence relation $S_{D-1} = 2\pi S_{D-3}/(D-2)$ and analytically continuing the right-hand side back to Lorentzian signature (which is trivial when the $\tilde\eta$ subspace does not contain η^0) yields

$$\int [d^D\eta]\,\delta'(\eta^2+1)\,F(\eta) = \frac{D-2}{2S_{D-3}}\int_{S_{\tilde\eta}} d^{D-3}\Omega_{\tilde\eta}\,F(\eta), \tag{8.306}$$

where $\eta^2 = -1$ and $\eta \cdot k = 0$ on the sphere $S_{\bar{\eta}}$. This is the generalized master identity. For $D = 4$, $S_{\bar{\eta}}$ is a unit circle in the plane spanned by $\epsilon_\pm \cdot \eta$, which recovers (8.269).

The above proof only applies to $\beta = 0$, but our earlier method to generalize the proof to nonzero β, based upon constructing an explicit particular solution, carries over unchanged. Also note that for Lorentz scalar F, the right-hand side of (8.306) is not manifestly Lorentz invariant. However, any Lorentz transformation that fixes k simply maps the sphere $S_{\bar{\eta}}$ to another sphere which satisfies the same condition $\eta \cdot k = 0$, leaving the result unchanged.

Our derivation above sheds light on why a useful identity should exist specifically for a $\delta'(\eta^2+1)F$ integral and a null k. If we had a timelike k, such as $k^\mu = (1, 0, \ldots, 0)$, then we would only have been able to conclude that $\bar{F}$ does not depend on $\bar{\eta}^0$, and performing the $\bar{\eta}^0$ integral leaves an integral over a $(D-1)$-dimensional ball. For null k, we have seen that we can drop dependence on both $\bar{\eta} \cdot \bar{k}$ and $\bar{\eta} \cdot \bar{q}$, leaving an integral over a $(D-2)$-dimensional ball. Finally, $\delta'(\eta^2+1)F$ turns out to be a total derivative, which would not have been true for $\delta(\eta^2+1)F$, reducing the integral to one over a unit $(D-3)$-sphere.

This is an enormous simplification, especially when $D = 4$. It is connected to the observation in Ref. [781] that, to encode spin in a scalar function of η and x, the function must be defined on the first neighborhood of a hyperboloid in η-space. Indeed, the final integral over $S_{\bar{\eta}}$ is an integral over the continuous basis for CSP representations of the massless little group $ISO(D-2)$ in general dimension, e.g. for $D = 4$ it is an integral over the angle basis $|\theta\rangle$ mentioned below (8.7). This is the fundamental reason the action (8.1) may be written solely in terms of integrals over $\delta(\eta^2+1)$ and $\delta'(\eta^2+1)$, without requiring $\delta''(\eta^2+1)$ or higher derivative terms.

A Non-Entire Example

While most expressions we encounter are analytic everywhere in η, we can also encounter expressions with branch cuts, such as the static field (8.96) which depends directly on $|\boldsymbol{\eta}| = \sqrt{\boldsymbol{\eta}^2}$. Integrals of such functions are still well-defined by either the generating functional or analytic continuation approach because they are analytic in an appropriate region. As a simple example, consider the integral

$$I = \int [d^4\eta]\, \delta(\eta^2+1)\, |\boldsymbol{\eta}|. \tag{8.307}$$

The integrand does not have a Taylor expansion about $\eta = 0$ because of the branch cut starting at the surface $\sum_i \eta_i^2 = 0$, which passes thorugh the origin. However, on the support of the delta function the integrand is equivalent to $\sqrt{1+(\eta^0)^2}$, which does have a Taylor expansion. We can thus use the generating function (8.251) to conclude

$$I = \int [d^4\eta]\, \delta(\eta^2+1)\, \sqrt{1+(\eta^0)^2} = -\sum_{n=0}^{\infty} \frac{(2n)!(2n-3)!!}{2^{3n}\,(n!)^2\,(n+1)!} = \frac{8}{3\pi}. \tag{8.308}$$

Alternatively, $|\boldsymbol{\eta}|$ is analytic in η^0, so that by the definition (8.287) we have

$$I = \frac{2}{S_3}\int d^4\bar{\eta}\,\delta(\bar{\eta}^2-1)\,|\bar{\boldsymbol{\eta}}| = \frac{S_2}{S_3}\int_0^\pi \sin^3\theta = \frac{8}{3\pi} \tag{8.309}$$

by analytic continuation. By similar reasoning we can make sense of any integral over $\delta(\eta^2+1)$ of a function of $|\boldsymbol{\eta}|$, and by applying (8.252), any integral over $\delta'(\eta^2+1)$ as well.

We do not have a precise definition of the space of functions $F(\eta)$ for which the integrals (8.238) are well-defined, but this toy example illustrates that the space includes non-entire functions. It may be valuable to define this space more carefully, and in particular to understand whether allowing fields $\Psi(\eta,x)$ non-entire in η would admit physically inequivalent solutions to the free equation of motion (8.19).

8.9 Appendix: Vector Superspace Computations

This appendix collects derivations of more technical results. In App. 8.9.1 we prove the statements made in subsections 8.2.2 and 8.3.2, which relate the continuous spin theory to familiar theories when $\rho = 0$. In App. 8.9.2 we parametrize the set of all worldline currents obeying the continuity condition, and in App. 8.9.3 we compare the results to currents built from matter fields. In App. 8.9.4 we compute the spacetime profiles of some simple currents by evaluating integrals with essential singularities, deriving results quoted in subsection 8.4.1. Finally, in App. 8.9.5 we establish some results for radiation emission quoted in section 8.6.

8.9.1 Tensor Decompositions

Absence of Cross-Couplings of Tensor Fields

In subsection 8.2.2, we claimed that for $\rho = 0$, the action and equation of motion do not contain cross-couplings between distinct tensor fields. To show this, we first recall that gauge symmetry allows us to add terms proportional to $(\eta^2+1)^2$ to the field Ψ. This freedom is sufficient to eliminate the double trace of every tensor component, i.e. $\phi^{(n)}{}'' = 0$ for $n \geq 4$.

For fully symmetric, double-traceless tensors $\phi^{(n)}$ and $\psi^{(m)}$ of rank n and m, we have

$$\int [d^4\eta]\,\delta'(\eta^2+1)\,P_{(n)}\cdot\phi^{(n)}\,P_{(m)}\cdot\psi^{(m)} \propto \delta_{nm} \tag{8.310}$$

$$\int [d^4\eta]\,\delta(\eta^2+1)\,\Delta(P_{(n)}\cdot\phi^{(n)})\,\Delta(P_{(m)}\cdot\psi^{(m)}) \propto \delta_{nm}. \tag{8.311}$$

These show that there are no cross-couplings in the first and second term, respectively, of the action and equation of motion.

Let us first motivate (8.310), taking $n \geq m$ without loss of generality. As shown in appendix 8.8.1,

the η integrations above produce full contractions of the tensors in the integrand. If $n-m$ is odd, the total number of indices is odd, so no full contractions exist. If $n-m \geq 4$, at least two pairs of indices on $\phi^{(n)}$ must be contracted, which produces a double trace which vanishes by assumption. Similar logic applies to (8.311), so in both cases we need only check there is no contribution from $n-m=2$.

Proof of the Orthogonality Theorems

To derive (8.310), note that since the tensors are double-traceless, the only possible contribution when $n = m+2$ is of the form $\phi^{(m+2)'} \cdot \psi^{(m)}$, so we must show its coefficient vanishes. The coefficient is simplest to calculate by rewriting the main results of appendix 8.8.1 as

$$\int [d^4\eta]\, \delta(\eta^2+1)\, \eta^{\mu_1}\eta^{\mu_2}\cdots\eta^{\mu_{2n}} = \tilde{c}_n \left(g^{\mu_1\mu_2}\cdots g^{\mu_{2n-1}\mu_{2n}} + \text{other pairings}\right) \tag{8.312}$$

$$\int [d^4\eta]\, \delta'(\eta^2+1)\, \eta^{\mu_1}\eta^{\mu_2}\cdots\eta^{\mu_{2n}} = \tilde{d}_n \left(g^{\mu_1\mu_2}\cdots g^{\mu_{2n-1}\mu_{2n}} + \text{other pairings}\right) \tag{8.313}$$

where $\tilde{c}_n = (-1/2)^n/(n+1)!$ and $\tilde{d}_n = (-1/2)^n/n!$, and we sum over the $(2n-1)!!$ distinct ways to pair up indices.

Now, we write the integral in (8.310) as a sum of three integrals,

$$2^{(n+m)/2}\phi^{\nu_1\ldots\nu_n}\psi^{\mu_1\ldots\mu_m} \times \Bigg[\int [d^4\eta]\, \delta'(\eta^2+1)\, \eta_{\nu_1}\cdots\eta_{\nu_n}\eta_{\mu_1}\cdots\eta_{\mu_m} \tag{8.314}$$

$$+ \frac{n(n-1)}{4}\, g_{\nu_1\nu_2} \int [d^4\eta]\, \delta(\eta^2+1)\, \eta_{\nu_3}\cdots\eta_{\nu_n}\eta_{\mu_1}\cdots\eta_{\mu_m} \tag{8.315}$$

$$+ \frac{m(m-1)}{4} g_{\mu_1\mu_2} \int [d^4\eta]\, \delta(\eta^2+1)\, \eta_{\nu_1}\cdots\eta_{\nu_n}\eta_{\mu_3}\cdots\eta_{\mu_m} \Bigg] \tag{8.316}$$

where we simplified using (8.241) and (8.243) and removed a redundant symmetrization. The final integral (8.316) cannot produce terms of the form $\phi^{(m+2)'} \cdot \psi^{(m)}$, since it already contains a trace of $\psi^{(m)}$, so we need only consider the first two integrals.

In the first integral (8.314), we count pairings which contract two ν indices, and pair all remaining ν indices with μ indices; this yields a combinatorial factor of $\binom{m+2}{2}\, m!$. The second integral (8.315) already has a trace on $\phi^{(m+2)}$, so we only count pairings where all remaining ν indices go with μ indices; this yields a combinatorial factor of $m!$. The overall coefficient is

$$2^{m+1}\left[\tilde{d}_{m+1}\binom{m+2}{2} m! + \tilde{c}_m \frac{(m+2)(m+1)}{4}\, m!\right] = 0 \tag{8.317}$$

which establishes the result.

It will also shortly prove useful to derive the value of the integral when $m = n$,

$$\int [d^4\eta]\, \delta'(\eta^2+1)\, P_{(n)}\cdot\phi^{(n)}\, P_{(n)}\cdot\psi^{(n)} = (-1)^n \left(\phi^{(n)}\cdot\psi^{(n)} - \frac{n(n-1)}{4}\phi^{(n)'}\cdot\psi^{(n)'}\right) \tag{8.318}$$

The two terms on the right-hand side are the only ones that could have appeared, so we need only compute their coefficients. Only (8.314) can produce $\phi^{(n)}\cdot\psi^{(n)}$ terms, with coefficient $2^n\tilde{d}_n\, n! = (-1)^n$ as desired. By contrast, all three integrals can produce $\phi^{(n)\prime}\cdot\psi^{(n)\prime}$ terms. The relevant combinatorial factor for (8.314) is $\binom{n}{2}^2(n-2)!$, and the combinatorial factor for each of the other two integrals is $\binom{n}{2}(n-2)!$, giving a total coefficient

$$2^n\left[\tilde{d}_n\binom{n}{2}^2(n-2)! + 2\,\tilde{c}_{n-1}\,\frac{n(n-1)}{4}\binom{n}{2}(n-2)!\right] = (-1)^{n-1}\,\frac{n(n-1)}{4} \tag{8.319}$$

as desired. One immediate consequence of (8.318) is that the action (8.9) has canonically normalized kinetic terms for the tensor fields $\phi^{(n)}$. The alternating sign $(-1)^n$ is due to the mostly negative metric, as the physical components of $\phi^{(n)}$ have n spatial indices.

The other orthogonality theorem (8.311) can also be derived with straightforward combinatorics, but there is a faster route. The integral contains terms of the form

$$\Delta(P_{(n)}\cdot\phi^{(n)}) \propto \partial_\eta^\nu\left(\eta^{\mu_1}\cdots\eta^{\mu_n} - \frac{n(n-1)}{4}\eta^{\mu_1}\cdots\eta^{\mu_{n-2}}g^{\mu_{n-1}\mu_n}(\eta^2+1)\right)\partial_\nu\phi^{(n)}_{\mu_1\ldots\mu_n} \tag{8.320}$$

where the η derivative can hit any of the n factors of η in the first term, but must hit the factor of η^2+1 in the second term due to the delta function. The result is

$$n\,\eta^{\mu_1}\cdots\eta^{\mu_{n-1}}(\partial\cdot\phi^{(n)})_{\mu_1\ldots\mu_{n-1}} - \frac{n(n-1)}{2}\eta^{\mu_1}\cdots\eta^{\mu_{n-2}}\eta^\nu\partial_\nu\phi^{(n)\prime}{}_{\mu_1\cdots\mu_{n-2}} \tag{8.321}$$

which, by symmetry, is equal to

$$n\,\eta^{\mu_1}\cdots\eta^{\mu_{n-1}}\left((\partial\cdot\phi^{(n)})_{\mu_1\ldots\mu_{n-1}} - \frac{1}{2}\sum_{k=1}^{n-1}\partial_{\mu_k}\phi^{(n)\prime}{}_{\mu_1\ldots\mu_{k-1}\mu_{k+1}\ldots\mu_{n-1}}\right). \tag{8.322}$$

The quantity in parentheses is traceless. Thus, the integral (8.311) involves contractions of traceless tensors, which can only be nonzero if $m = n$.

Dual Polynomials for the Current Expansion

Now we motivate the "dual" polynomials (8.66) used to define the tensor components $J^{(n)}$ of the current. If we expand $J(\eta,x)$ in the same polynomials as the continuous spin field,

$$J(\eta,x) = \sum_{n\geq 0} P_{(n)}(\eta)\cdot j^{(n)}(x) \tag{8.323}$$

and use the freedom to add terms proportional to $(\eta^2+1)^2$ to the current J to eliminate the double trace of every $j^{(n)}$, then (8.318) immediately implies

$$S_{\text{int}} = \sum_{n\geq 0}(-1)^n \left(\phi^{(n)}\cdot j^{(n)} - \frac{n(n-1)}{4}\phi^{(n)\prime}\cdot j^{(n)\prime}\right) \tag{8.324}$$

The unwanted trace terms for $n \geq 2$ can be removed if we define tensors $J^{(n)}$ by

$$J^{(n)}_{\mu_1\ldots\mu_n} = j^{(n)}_{\mu_1\ldots\mu_n} - \frac{1}{4\,(n-2)!}\, g_{(\mu_1\mu_2} j^{(n)\prime}_{\mu_3\ldots\mu_n)} \tag{8.325}$$

where $J^{(2)}$ is the trace reversal of $j^{(2)}$, and generally $J^{(n)\prime} = (1-n)\, j^{(n)\prime}$ with double traces still vanishing. This produces an interaction (8.67) in canonical form, and is equivalent to expanding the current in the dual polynomials $\bar{P}_{(n)}$ defined in (8.66). For completeness, we note that the $\bar{P}_{(n)}$ obey an orthogonality relation like (8.310), and the analogue of (8.318) is

$$\int [d^4\eta]\, \delta'(\eta^2+1)\, \bar{P}_{(n)}\cdot J^{(n)}\, \bar{P}_{(n)}\cdot K^{(n)} = (-1)^n \left(J^{(n)}\cdot K^{(n)} - \frac{n(n+1)}{4} J^{(n)\prime}\cdot K^{(n)\prime}\right) \tag{8.326}$$

for double-traceless $J^{(n)}$ and $K^{(n)}$.

Conservation and Continuity Conditions

Finally, we derive the tensor form (8.70) of the continuity condition. Note that for a symmetric tensor A of rank n, the trace subtraction is defined for $n \geq 2$ by

$$\langle A^{\mu_1\ldots\mu_n}\rangle = A^{\mu_1\ldots\mu_n} - \frac{1}{4n\,(n-2)!}\, g^{(\mu_1\mu_2} A'^{\mu_3\ldots\mu_n)} \tag{8.327}$$

and has no effect for $n < 2$.

We warm up by considering the case $\rho = 0$, where the result reduces to $\langle\partial\cdot J_{(n)}\rangle = 0$. To derive this result, note that the continuity condition (8.69) expands to

$$0 = \delta(\eta^2+1)\sum_{n\geq 1} 2^{n/2} n\, \eta_{\mu_3}\cdots\eta_{\mu_{n-1}}\left[\eta_{\mu_1}\eta_{\mu_2}(\partial\cdot J_{(n)})^{\mu_1\ldots\mu_{n-1}} + \frac{n-2}{4}(\partial\cdot J'_{(n)})^{\mu_3\ldots\mu_{n-1}}\right] \tag{8.328}$$

$$= \delta(\eta^2+1)\sum_{n\geq 1} 2^{n/2} n\, \eta_{\mu_1}\cdots\eta_{\mu_{n-1}}\langle\partial\cdot J_{(n)}\rangle^{\mu_1\ldots\mu_{n-1}}. \tag{8.329}$$

where the second term in the first line is only nonzero for $n \geq 3$, and we reached the second line by multiplying that term by $-\eta^2$, which is equal to one on the support of the delta function. We can show that each term in the sum individually vanishes by induction. Integrating (8.329) over η immediately produces $\langle\partial\cdot J_{(1)}\rangle = 0$, because all other terms would be proportional to vanishing traces. Next, suppose we have shown $\langle\partial\cdot J_{(n)}\rangle = 0$ for all $n \leq m$. Then if one multiplies (8.329) by

$\eta_{\nu_1} \cdots \eta_{\nu_m}$ before integrating over η, the only term that can contribute is $n = m + 1$, and performing the integration yields $\langle \partial \cdot J_{(m+1)} \rangle = 0$.

For $\rho \neq 0$, a similar calculation to the one above shows the continuity condition is

$$0 = \delta(\eta^2 + 1) \sum_{n \geq 1} 2^{n/2} n \, \eta_{\mu_1} \cdots \eta_{\mu_{n-1}} \left\langle \partial \cdot J_{(n)} + \frac{\rho}{n\sqrt{2}} (J_{(n-1)} + \frac{1}{2} J'_{(n+1)}) \right\rangle^{\mu_1 \cdots \mu_{n-1}} \tag{8.330}$$

and an identical inductive argument shows that each term in the sum vanishes.

8.9.2 General Worldline Currents

In this section we parametrize the general $f(\eta, k, \dot{z})$ obeying the continuity condition (8.74), and derive the general decomposition (8.87). We also give a simpler parametrization specialized to null k, and another suited for static particles.

General Solution for Null Momenta

We warm up by writing the general solution to the continuity condition for only null k. First, note that any solution can be decomposed as

$$f(\eta, k, \dot{z}) = e^{-i\rho\eta \cdot \dot{z}/k \cdot \dot{z}} \left(\tilde{f}_0(\eta, k, \dot{z}) + \tilde{f}_\alpha(\eta, k, \dot{z}) \right) \tag{8.331}$$

where the "homogeneous" solution $\tilde{f}_0$ and the "particular" solution $\tilde{f}_\alpha$ obey

$$k \cdot \partial_\eta \, \tilde{f}_0 = 0, \tag{8.332}$$

$$k \cdot \partial_\eta \, \tilde{f}_\alpha = (\eta^2 + 1) \, \alpha(\eta, k, \dot{z}). \tag{8.333}$$

We have factored the phase of the scalar temporal current (8.76) out of tilded variables, which is not necessary, but yields the most convenient parametrization for radiation problems.

To find the general homogeneous solution for null k, note that its dependence on η can be written solely in terms of the variables $\eta \cdot \dot{z}$, $\eta \cdot k$, and $\eta^2 + 1$. We drop terms with more than one power of $\eta^2 + 1$, as they can never couple to the continuous spin field due to the delta function in (8.63). Since $k \cdot \partial_\eta$ annihilates $\eta \cdot k$, the general solution is parametrized by two analytic functions of $\eta \cdot k$ and the single kinematic variable $k \cdot \dot{z}$,

$$\tilde{f}_0 = g_0(\eta \cdot k, k \cdot \dot{z}) + \left(\eta^2 + 1 - 2 \, \eta \cdot k \, \frac{\eta \cdot \dot{z}}{k \cdot \dot{z}} \right) g_1(\eta \cdot k, k \cdot \dot{z}). \tag{8.334}$$

For null k, we can construct a particular solution using the same trick as in appendix 8.8.2,

$$\tilde{f}_\alpha = \int_0^{\eta \cdot q} dx \, (\eta^2 + 1 - 2 \, \eta \cdot k \, (\eta \cdot q - x)) \, \alpha(\eta - (\eta \cdot q - x)k, k \cdot \dot{z}). \tag{8.335}$$

While many other particular solutions are possible, this one has the special feature that it vanishes when $\eta \cdot q = 0$, i.e. all terms in its Taylor expansion have at least one power of $\eta \cdot q$.

General Solution for Arbitrary Momenta

It is straightforward to extend the above derivation to general k. As before, we may drop terms with more than one power of $\eta^2 + 1$, and the remaining η dependence is through $\eta \cdot \dot{z}$ and $\eta \cdot k$. The general solution still depends on only three functions g_0, g_1, and α, but they can now depend on two independent kinematic variables k^2 and $k \cdot \dot{z}$.

In general, $k \cdot \partial_\eta$ does not annihilate $\eta \cdot k$. However, if we define

$$u = \eta \cdot k - \frac{\eta \cdot \dot{z}}{k \cdot \dot{z}}\, k^2, \qquad v = \frac{\eta \cdot \dot{z}}{k \cdot \dot{z}} \tag{8.336}$$

then $k \cdot \partial_\eta\, u = 0$. In these variables, we have $k \cdot \partial_\eta = \partial_v$, so the homogeneous solution is

$$\tilde{f}_0 = g_0(u, k \cdot \dot{z}, k^2) + \left(\eta^2 + 1 - 2uv - v^2 k^2\right) g_1(u, k \cdot \dot{z}, k^2). \tag{8.337}$$

As for the particular solution, we can no longer use the null frame vector q, but the same role can be played by $\dot{z}/k \cdot \dot{z}$ as it also has unit inner product with k,

$$\tilde{f}_\alpha = \int_0^v dx\, (\eta^2 + 1 - 2u(v - x) - (v^2 - x^2)k^2)\, \alpha(\eta - (v - x)k, k \cdot \dot{z}, k^2). \tag{8.338}$$

These expressions contain the full freedom in the solutions to the continuity condition.

To derive the decomposition (8.87) of the general solution, it suffices to show that

$$f(\eta, k, \dot{z}) = e^{-i\rho\eta \cdot \dot{z}/k \cdot \dot{z}}\, \hat{g}(k \cdot \dot{z}) + k^2 X(\eta, k, \dot{z}) + D\xi(\eta, k, \dot{z}) \tag{8.339}$$

where X and ξ are both regular as $k^2 \to 0$. This is because the continuity condition automatically implies a relation between X and ξ,

$$0 = \delta(\eta^2 + 1)\Delta f = \delta(\eta^2 + 1)(k^2 \Delta X - k^2 \xi) \tag{8.340}$$

where we used the momentum space form of (8.27). Since we have dropped terms in X and ξ with more than one power of $\eta^2 + 1$, this implies $\xi = \Delta X$ and hence (8.87). Equivalently, we can always add terms proportional to $(\eta^2 + 1)^2$ to set $\xi = \Delta X$ for any current.

It is convenient to work entirely in terms of tilded variables, which all have the temporal current's phase factored out. Defining

$$\tilde{D} = \frac{i}{2}(\eta^2 + 1)(k \cdot \partial_\eta) - i\eta \cdot k \tag{8.341}$$

we aim to show that $\tilde{f} = \hat{g} + k^2 \tilde{X} + \tilde{D}\tilde{\xi}$. First, using $-2i\tilde{D}v = \eta^2 + 1 - 2uv - 2v^2 k^2$, we can write

the contributions of g_1 and α as

$$\tilde{f}_0 \supset \tilde{D}(-2ig_1 v) + k^2(g_1 v^2), \tag{8.342}$$

$$\tilde{f}_\alpha = \tilde{D}\int_0^v dx\,(-2i)(v-x)\alpha(\eta-(v-x)k) + k^2\int_0^v dx\,(v-x)^2\alpha(\eta-(v-x)k). \tag{8.343}$$

From these results we can read off $\tilde{X}$ and $\tilde{\xi}$, and also readily confirm the expected result $\tilde{\xi} = \tilde{\Delta}\tilde{X} = (-ik\cdot\partial_\eta)\tilde{X}$, by using $\tilde{\Delta}v = -i$ and $\tilde{\Delta}(\eta-(v-x)k) = 0$.

As for g_0, we can decompose it by separating out terms with powers of u or k^2,

$$g_0(u, k\cdot z, k^2) = \hat{g}(k\cdot\dot{z}) + ug_u(u, k\cdot\dot{z}) + k^2 g_k(u, k\cdot\dot{z}, k^2) \tag{8.344}$$

which we can write in the desired final form as

$$\tilde{f}_0 \supset \hat{g} + (k^2 + \tilde{D}\tilde{\Delta})(g_k - g_u v). \tag{8.345}$$

General Solution for Static Particles

For computations involving static particles, where $\dot{z}^\mu = (1, \mathbf{0})$, a time integration often sets the frequency to zero, so that $k^\mu = (0, \mathbf{k})$ and $k\cdot\dot{z} = 0$. In this case the expressions above are not useful because they factor out a divergent phase, which is tied to the problems with defining a static limit for the temporal current. We instead parametrize the general static solution by factoring out the phase of the static spatial current,

$$f(\eta, \mathbf{k}) = e^{-i\rho\boldsymbol{\eta}\cdot\hat{\mathbf{k}}/|\mathbf{k}|}\left(\bar{f}_0(\eta, \mathbf{k}) + \bar{f}_\alpha(\eta, \mathbf{k})\right) \tag{8.346}$$

so that the homogeneous and particular solutions satisfy

$$\mathbf{k}\cdot\nabla_{\boldsymbol{\eta}}\,\bar{f}_0 = 0, \tag{8.347}$$

$$\mathbf{k}\cdot\nabla_{\boldsymbol{\eta}}\,\bar{f}_\alpha = (\eta^2+1)\,\alpha(\eta, \mathbf{k}). \tag{8.348}$$

To compactly write the general solution, note that the dependence on η can be written in terms of the variables η^0, $\boldsymbol{\eta}\cdot\hat{\mathbf{k}}$, and $|\boldsymbol{\eta}\times\hat{\mathbf{k}}|^2$. In these variables, (8.347) states that the homogeneous solution must be independent of $\boldsymbol{\eta}\cdot\hat{\mathbf{k}}$, and the decoupling of higher powers of η^2+1 implies we do not need to consider terms with more than one power of $|\boldsymbol{\eta}\times\hat{\mathbf{k}}|^2$. Then the general homogeneous solution is simply

$$\bar{f}_0 = \bar{g}_0(\eta^0, |\mathbf{k}|) + |\boldsymbol{\eta}\times\hat{\mathbf{k}}|^2\,\bar{g}_1(\eta^0, |\mathbf{k}|). \tag{8.349}$$

For example, the scalar-like inhomogeneous current (8.79) has $\bar{g}_0 = g\cos(\eta^0\beta\rho^2/|\mathbf{k}|^2)$ and the vector-like spatial current (8.83) has $\bar{g}_0 = \sqrt{2}\,e\eta^0$, with both having zero $\bar{g}_1$. Finally, a particular solution

is

$$\bar{f}_\alpha = \int_0^{\boldsymbol{\eta}\cdot\hat{\mathbf{k}}/|\mathbf{k}|} dx\,(\eta^2+1-(\boldsymbol{\eta}\cdot\hat{\mathbf{k}})(\boldsymbol{\eta}\cdot\hat{\mathbf{k}}-|\mathbf{k}|x))\,\alpha(\eta-(\boldsymbol{\eta}\cdot\hat{\mathbf{k}}-x|\mathbf{k}|),\mathbf{k}). \tag{8.350}$$

8.9.3 Comparison to Currents From Matter Fields

In section 8.3 we coupled continuous spin fields to matter particles and identified the most relevant interactions, which reduce to familiar scalar and vector minimal couplings as $\rho \to 0$. It is interesting to compare to previous work which instead described the matter with fields [807, 809, 808, 810]. The most comprehensive analysis for scalar matter fields is Ref. [810], which gives a current quadratic in matter fields ϕ_1 and ϕ_2 of mass M, parametrized by nonnegative integers n_0, n_1, and n_2, and two real parameters λ_1 and λ_2 related by $\rho = (\lambda_1+\lambda_2)M^2$. For illustration, let us consider the case $n_0 = 2$, $n_1 = n_2 = 0$, which in our conventions is

$$J(\eta,x) = g(\eta\cdot\partial_x)^2(\bar{\phi}_1\bar{\phi}_2) + g(\eta^2+1)\left(2M^2\,\bar{\phi}_1\bar{\phi}_2 - \left(2+\frac{\lambda_1+\lambda_2}{2}\,\eta\cdot\partial_x\right)\partial^\mu\bar{\phi}_1\,\partial_\mu\bar{\phi}_2\right). \tag{8.351}$$

Above, we have defined $\bar{\phi}_i = \phi_i(x+\lambda_i\eta)$, which should be interpreted as a series in λ_i. It is straightforward to show this current obeys the continuity condition for on-shell matter fields, but only to first order in the coupling g, i.e. only when one uses the free equations of motion $(\partial^2+M^2)\bar{\phi}_i = 0$. This feature is shared by all currents previously found, and it is therefore unclear to what degree they can be trusted when computing physical observables.

Furthermore, these currents have no relation to the phenomenologically interesting scalar-like or vector-like currents we have identified. The leading terms in the currents have $n = n_0+n_1+n_2$ derivatives, while a minimal scalar or vector current has 0 or 1 derivative, respectively. Thus, the currents could only be scalar-like or vector-like for $n < 2$, but when $n_0 < 2$ the current contains undefined negative powers of η. As discussed in Refs. [808, 810], if one treats these negative powers as equivalent to zero, then the continuity condition cannot be satisfied even at first order in g for equal mass scalar fields.

One might hope the current (8.351) is somehow a tensor-like current, but this is not the case either. In the limit $\rho, \lambda_i \to 0$ it instead reduces to a combination of a nonminimal current $J = \partial^2(\phi^2)/2$ for a scalar field, and a trivially conserved current $T_{\mu\nu} = (\partial_\mu\partial_\nu - g_{\mu\nu}\partial^2)\phi^2$ for a tensor field. Furthermore, the current in general can be rewritten in the form (8.339),

$$J(\eta,x) = -\partial_x^2\left(\frac{g}{2}(\eta^2+1)\,(\bar{\phi}_1\bar{\phi}_2)\right) + D(g\,\eta\cdot\partial_x(\bar{\phi}_1\bar{\phi}_2)) \tag{8.352}$$

which indeed obeys (8.340). As discussed below (8.87), this implies the current does not affect radiation emission or the response of the matter to a free field background; in our classification it corresponds to the trivial case $\hat{g} = 0$.

It would be interesting to see if the currents in our work, which satisfy the continuity condition

to all orders in g, can be recovered in terms of matter fields by relaxing the assumptions of Ref. [807, 809, 808, 810]. In particular, one could either allow explicitly nonlocal Lagrangians or resolve the nonlocality by introducing appropriate auxiliary fields.

8.9.4 Fields and Currents in Spacetime

The Scalar-Like Spatial Current

To evaluate the scalar-like spatial current in position space, it turns out to be easier to first evaluate the field, which satisfies $\Psi_S(\boldsymbol{\eta}, \mathbf{k}) = J_S(\boldsymbol{\eta}, \mathbf{k})/|\mathbf{k}|^2$ in strong harmonic gauge. Defining $k = |\mathbf{k}|$, expanding $d\mathbf{k} = (k^2\, dk)\, d\hat{\mathbf{k}}$ and performing the $\hat{\mathbf{k}}$ integral gives

$$\Psi_S(\boldsymbol{\eta}, \mathbf{r}) = \frac{g}{2\pi^2} \int_0^\infty dk\, \frac{\sin\left(|\rho\boldsymbol{\eta}/k - k\mathbf{r}|\right)}{|\rho\boldsymbol{\eta}/k - k\mathbf{r}|} \tag{8.353}$$

$$= \frac{g}{2\pi^2 r} \int_0^\infty dx\, \frac{\sin\left(\sqrt{\alpha\left((x - 1/x)^2 + \beta\right)}\right)}{\sqrt{(x - 1/x)^2 + \beta}} \tag{8.354}$$

where we have switched to the dimensionless variable $x = k\sqrt{r/|\rho\boldsymbol{\eta}|}$, defined $\alpha = |\rho\boldsymbol{\eta}|r$ and $\beta = 2(1 - \cos\theta)$, and always use the positive branch of the square root. The remaining integral is difficult to evaluate directly because of the essential singularity at $x = 0$, but we can avoid it by exploiting the symmetry of the integrand. Mapping the integration range $x \in [0, 1]$ to $x \in [1, \infty)$ by sending $x \to 1/x$ gives, for any function f,

$$\int_0^\infty dx\, f((x - 1/x)^2) = \int_1^\infty dx\, \left(1 + \frac{1}{x^2}\right) f((x - 1/x)^2) = \int_0^\infty du\, f(u^2). \tag{8.355}$$

Applying this trick, the static field reduces to

$$\Psi_S(\boldsymbol{\eta}, \mathbf{r}) = \frac{g}{2\pi^2 r} \int_0^\infty du\, \frac{\sin\left(\sqrt{\alpha(u^2 + \beta)}\right)}{\sqrt{u^2 + \beta}} \tag{8.356}$$

$$= \frac{g}{2\pi^2 r} \int_0^\infty dz\, \sin\left(\sqrt{\alpha\beta}\, \cosh z\right) \tag{8.357}$$

$$= \frac{g}{4\pi r} J_0(\sqrt{\alpha\beta}) \tag{8.358}$$

where we let $u = \sqrt{\beta}\cosh z$ and used an integral representation of the Bessel function. This is precisely (8.96), applying $-\nabla^2$ yields (8.95), and removing the time integration yields (8.89).

Temporal Currents

The frequency integral (8.91) for the scalar-like temporal current encloses an essential singularity at $\omega = 0$. While this situation may be unfamiliar, such integrals are well-known in the literature (e.g. see section 4.6 of Ref. [837]) and can be handled straightforwardly because the integrand has a

convergent Laurent series for all $z \neq 0$. The basic identity we will need is

$$\int_C \frac{dz}{2\pi} (iz)^p e^{-ibz} e^{-ia/z} = \left(\frac{a}{b}\right)^{(p+1)/2} J_{p+1}(2\sqrt{ab}) \tag{8.359}$$

where C is a counterclockwise contour encircling the origin, and p is a nonnegative integer. It is derived by simply expanding the integrand in z and applying the residue theorem,

$$\int_C \frac{dz}{2\pi} (iz)^p e^{-ibz} e^{-ia/z} = \int_C \frac{dz}{2\pi} \sum_{n,m\geq 0} (iz)^p \frac{(-ibz)^n}{n!} \frac{(-ia/z)^m}{m!} \tag{8.360}$$

$$= -ia^{p+1} \int_C \frac{dz}{2\pi z} \sum_{n=0}^{\infty} \frac{(-ab)^n}{n!\,(n+p+1)!} \tag{8.361}$$

$$= a^{p+1} \sum_{n=0}^{\infty} \frac{(-ab)^n}{n!\,(n+p+1)!}. \tag{8.362}$$

Note that we would find the same result if any of the $p+1$ initial terms in the Laurent expansion of $e^{-ia/z}$ were removed, because such terms cannot yield simple poles.

Now, to evaluate (8.91) we rewrite the integrand as

$$\int \frac{d\omega}{2\pi} e^{-i\omega t} e^{-i\rho\eta^0/\omega} = \int \frac{d\omega}{2\pi} e^{-i\omega t} + \int \frac{d\omega}{2\pi} e^{-i\omega t} (e^{-i\rho\eta^0/\omega} - 1) \tag{8.363}$$

where the first integral yields $\delta(t)$, and the second falls off at large ω, so that the contour integral can be closed at infinity. We may therefore close the contour in the upper-half plane for $t < 0$, giving zero, and in the lower-half plane for $t > 0$. In the latter case, we can shrink the contour to a clockwise one enclosing the essential singularity and apply (8.359), which yields the result (8.92). Similarly, to derive (8.94) for the vector-like temporal current, write

$$j_T^V(\eta^0, \mathbf{r}, t) = \frac{\sqrt{2}\, e}{\rho} \left(\int \frac{d\omega}{2\pi} \rho\eta^0 e^{-i\omega t} + \int \frac{d\omega}{2\pi} i\omega\, e^{-i\omega t} \left(e^{-i\rho\eta^0/\omega} - (1 - i\rho\eta^0/\omega)\right) \right) \tag{8.364}$$

where the first term produces the delta function and the second can be evaluated using (8.359).

Incidentally, for real a, integrals like (8.359) are well-defined even when the contour passes directly through the essential singularity along the real axis, where the integrand is bounded. When a is positive (negative), the contour can be deformed off the origin in the positive (negative) imaginary direction, and the remaining integral can be evaluated using (8.359).

Currents for Arbitrary Motion

For completeness, we note that it is straightforward to write expressions for the currents of particles in arbitrary motion, once one has evaluated the current of a worldline element at rest. For example, if we expand $k^\mu = k_\ell \dot{z}^\mu(\tau) + k_p^\mu$, where $\dot{z} \cdot k_p = 0$, and do the same for x and z, then the scalar-like

temporal current is

$$J_T(\eta,x) = g\int d\tau \int \frac{d^3k_p}{(2\pi)^3}\, e^{-ik_p\cdot(x_p-z_p)} \int \frac{dk_\ell}{2\pi}\, e^{-i\rho\eta_\ell/(k_\ell+i\epsilon)} e^{-ik_\ell(x_\ell-z_\ell)}. \tag{8.365}$$

By the same reasoning used to derive (8.92) above, we have

$$J_T(\eta,x) = g\int d\tau\, \delta^{(4)}(x-z) - \theta(x_\ell-z_\ell)\,\delta^{(3)}(x_p-z_p)\sqrt{\frac{\rho\eta^0}{x_\ell-z_\ell}}J_1\left(2\sqrt{\rho\eta^0(x_\ell-z_\ell)}\right). \tag{8.366}$$

Performing the τ integral for a static particle with a cutoff $\tau=-T$ yields (8.97). Similarly, the scalar-like spatial current is

$$J_S(\eta,x) = g\int d\tau \int \frac{d^3k_p}{(2\pi)^3}\,\delta(x_\ell-z_\ell)\, e^{-ik_p\cdot(x_p-z_p)} e^{-i\rho k_p\cdot\eta_p/k_p^2} \tag{8.367}$$

where the k_p integral can be evaluated analogously to (8.90). However, while expressions like these make the spacetime support of the current manifest, they are seldom useful for calculating physical quantities, where the momentum space expressions are more convenient.

8.9.5 Radiation Emission Results

Gauge Invariance of the Averaged Stress-Energy Tensor

As discussed in section 8.6.2, it suffices to consider the variations of the second and third terms of $T^{\mu\nu}$ in (8.212) under an infinitesimal gauge transformation $\delta_\epsilon\Psi = D\epsilon$. Since we are implicitly taking a spacetime average, we can freely integrate spacetime derivatives by parts, and we can simplify terms involving the operator D using the identities (8.27) and (8.28).

First, defining $\epsilon^\nu = \partial^\nu\epsilon$ for brevity, the variation of the second term is

$$\delta T^{\mu\nu}_{(a)} = -2\int [d^4\eta]\,\delta'(\eta^2+1)\,\Psi\, D(\partial^\mu\partial^\nu\epsilon) \tag{8.368}$$

$$= -\int [d^4\eta]\,\Psi\,\Delta(\delta(\eta^2+1)\,\partial^\mu\epsilon^\nu) \tag{8.369}$$

$$= -\int [d^4\eta]\,\delta(\eta^2+1)\,(\Delta\Psi)\,\partial^\mu\epsilon^\nu \tag{8.370}$$

where we integrated by parts and used (8.28). The variation of the third term includes

$$\delta T^{\mu\nu}_{(b)} = -\frac{1}{2}\int [d^4\eta]\, \partial^\mu_\eta(\delta(\eta^2+1)\,\Delta D\epsilon)\,\partial^\nu\Psi \tag{8.371}$$

$$= \frac{1}{2}\int [d^4\eta]\, \partial^\mu_\eta(\delta(\eta^2+1)\,\partial_x^2\epsilon^\nu)\,\Psi \tag{8.372}$$

$$= \int [d^4\eta]\, (\partial_x^2\Psi)\left(\frac{1}{2}\delta(\eta^2+1)\,\partial^\mu_\eta\epsilon^\nu + \delta'(\eta^2+1)\,\eta^\mu\epsilon^\nu\right) \tag{8.373}$$

where we integrated by parts and used (8.27). The other part of the third term's variation is

$$\delta T^{\mu\nu}_{(c)} = \frac{1}{2}\int [d^4\eta]\, \delta(\eta^2+1)\,(\Delta\Psi)(\partial^\mu_\eta\partial^\nu D\epsilon) \tag{8.374}$$

$$= \frac{1}{2}\int [d^4\eta]\, \delta(\eta^2+1)\,(\Delta\Psi)\left((\eta\cdot\partial_x)(\partial^\mu_\eta\epsilon^\nu) + (\partial^\mu - \eta^\mu\Delta)\epsilon^\nu\right) \tag{8.375}$$

$$= \int [d^4\eta]\, \delta(\eta^2+1)\,(\Delta\Psi)\left(\frac{1}{2}(\eta\cdot\partial_x)(\partial^\mu_\eta\epsilon^\nu) + \partial^\mu\epsilon^\nu - \frac{1}{2}\Delta\eta^\mu\epsilon^\nu\right) \tag{8.376}$$

where we simply performed the η derivative using the definition of D. The middle term of this expression cancels with $\delta T^{\mu\nu}_{(a)}$. The last term cancels with the last term of $\delta T^{\mu\nu}_{(b)}$ upon using the equation of motion (8.19). Finally, note that multiplying the equation of motion by η^2+1 and simplifying gives the identity

$$\delta(\eta^2+1)\,\partial_x^2\Psi = \delta(\eta^2+1)\,(\eta\cdot\partial_x)\Delta\Psi \tag{8.377}$$

which implies the remaining two terms cancel.

Stationary Phase Approximation for Total Power

Here we extract the scaling behavior of the integral

$$I = \sum_{n>0} n^2 \int_0^T \frac{dt}{T}\int_0^T \frac{dt'}{T}\, e^{in\omega_0(t-t')}\, J_0\left(\frac{\rho|\mathbf{v}_\perp(t)-\mathbf{v}_\perp(t')|}{n\omega_0}\right). \tag{8.378}$$

Consider an arbitrary generic linear motion, meaning that $v_\perp(t) = v_0 f(\omega_0 t)\sin\theta$ where v_0 is the typical speed, and $f(\phi)$ is an order one periodic function with order one derivatives. Defining $x = (\rho v_0/\omega_0)\sin\theta$ and changing variables to the phase sum and difference gives

$$I \sim \sum_{n>0} n^2 \int d\phi' \int d\phi\, e^{in\phi} J_0\left(\frac{x}{n}(f(\phi+\phi'/2) - f(\phi-\phi'/2))\right) \tag{8.379}$$

$$= \int d\phi' \sum_{n>0} n^2 \int d\phi\, e^{in\phi} J_0\left(x g_{\phi'}(\phi)/n\right) \tag{8.380}$$

where $g_{\phi'}(\phi)$ is another order one periodic function. Since x and n are large, the integrand is rapidly oscillating and thus dominated by contributions from points of stationary phase. Using the asymptotic expansion of the Bessel function gives, up to overall phases,

$$I \sim \int d\phi' \sum_{n>0} n^2 \int d\phi \sqrt{\frac{n}{x}}\, e^{i(n\phi + x g_{\phi'}/n)}. \tag{8.381}$$

The integrand has stationary phase when $n + x g'_{\phi'}/n = 0$, which is generically possible only when $n \lesssim \sqrt{x}$, and at such points, the rate of change of phase is $x g''_{\phi'}/n$. Then we have

$$I \sim \int \frac{d\phi'}{\sqrt{g''_{\phi'}}} \int_0^{\sqrt{x}} dn\, n^2\, \frac{n}{x} \sim x \tag{8.382}$$

where the ϕ' integral is of order one because $g''_{\phi'}$ is generically of order one. This recovers the scaling exhibited in (8.231), as well as the rough distribution of the power in harmonics.

Bibliography

[1] K. F. Stupic, Z. I. Cleveland, G. E. Pavlovskaya, and T. Meersmann, "Hyperpolarized 131Xe NMR spectroscopy," *Journal of Magnetic Resonance* **208** (2011) no. 1, 58–69.

[2] **Particle Data Group** Collaboration, P. A. Zyla *et al.*, "Review of Particle Physics," *PTEP* **2020** (2020) no. 8, 083C01.

[3] D.-N. Gao, "Note on invisible decays of light mesons," *Phys. Rev. D* **98** (2018) no. 11, 113006, arXiv:1811.10152 [hep-ph].

[4] **CAST** Collaboration, V. Anastassopoulos *et al.*, "New CAST Limit on the Axion-Photon Interaction," *Nature Phys.* **13** (2017) 584–590, arXiv:1705.02290 [hep-ex].

[5] **ADMX** Collaboration, C. Hagmann *et al.*, "Results from a high sensitivity search for cosmic axions," *Phys. Rev. Lett.* **80** (1998) 2043–2046, arXiv:astro-ph/9801286 [astro-ph].

[6] **ADMX** Collaboration, C. Boutan *et al.*, "Piezoelectrically Tuned Multimode Cavity Search for Axion Dark Matter," *Phys. Rev. Lett.* **121** (2018) no. 26, 261302, arXiv:1901.00920 [hep-ex].

[7] **ADMX** Collaboration, N. Du *et al.*, "A Search for Invisible Axion Dark Matter with the Axion Dark Matter Experiment," *Phys. Rev. Lett.* **120** (2018) no. 15, 151301, arXiv:1804.05750 [hep-ex].

[8] S. J. Asztalos, R. F. Bradley, L. Duffy, C. Hagmann, D. Kinion, D. M. Moltz, L. J. Rosenberg, P. Sikivie, W. Stoeffl, N. S. Sullivan, D. B. Tanner, K. van Bibber, and D. B. Yu, "Improved rf cavity search for halo axions," *Phys. Rev. D* **69** (Jan, 2004) 011101. https://link.aps.org/doi/10.1103/PhysRevD.69.011101.

[9] B. M. Brubaker *et al.*, "First results from a microwave cavity axion search at 24 μeV," *Phys. Rev. Lett.* **118** (2017) no. 6, 061302, arXiv:1610.02580 [astro-ph.CO].

[10] S. DePanfilis, A. C. Melissinos, B. E. Moskowitz, J. T. Rogers, Y. K. Semertzidis, W. U. Wuensch, H. J. Halama, A. G. Prodell, W. B. Fowler, and F. A. Nezrick, "Limits on the

abundance and coupling of cosmic axions at m_a μev," *Phys. Rev. Lett.* **59** (Aug, 1987) 839–842. https://link.aps.org/doi/10.1103/PhysRevLett.59.839.

[11] **ADMX** Collaboration, T. Braine *et al.*, "Extended Search for the Invisible Axion with the Axion Dark Matter Experiment," *Phys. Rev. Lett.* **124** (2020) no. 10, 101303, arXiv:1910.08638 [hep-ex].

[12] W. Wuensch, S. De Panfilis-Wuensch, Y. K. Semertzidis, J. T. Rogers, A. C. Melissinos, H. J. Halama, B. E. Moskowitz, A. G. Prodell, W. B. Fowler, and F. A. Nezrick, "Results of a Laboratory Search for Cosmic Axions and Other Weakly Coupled Light Particles," *Phys. Rev.* **D40** (1989) 3153.

[13] C. Hagmann, P. Sikivie, N. S. Sullivan, and D. B. Tanner, "Results from a search for cosmic axions," *Phys. Rev.* **D42** (1990) 1297–1300.

[14] B. T. McAllister, G. Flower, E. N. Ivanov, M. Goryachev, J. Bourhill, and M. E. Tobar, "The ORGAN Experiment: An axion haloscope above 15 GHz," *Phys. Dark Univ.* **18** (2017) 67–72, arXiv:1706.00209 [physics.ins-det].

[15] M. A. Fedderke, P. W. Graham, and S. Rajendran, "Axion Dark Matter Detection with CMB Polarization," *Phys. Rev.* **D100** (2019) no. 1, 015040, arXiv:1903.02666 [astro-ph.CO].

[16] G. G. Raffelt, *Stars as laboratories for fundamental physics*. 1996. http://wwwth.mpp.mpg.de/members/raffelt/mypapers/199613.pdf.

[17] A. Payez, C. Evoli, T. Fischer, M. Giannotti, A. Mirizzi, and A. Ringwald, "Revisiting the SN1987A gamma-ray limit on ultralight axion-like particles," *JCAP* **1502** (2015) no. 02, 006, arXiv:1410.3747 [astro-ph.HE].

[18] **HAYSTAC** Collaboration, L. Zhong *et al.*, "Results from phase 1 of the HAYSTAC microwave cavity axion experiment," *Phys. Rev.* **D97** (2018) no. 9, 092001, arXiv:1803.03690 [hep-ex].

[19] N. Blinov, M. J. Dolan, P. Draper, and J. Kozaczuk, "Dark matter targets for axionlike particle searches," *Phys. Rev.* **D100** (2019) no. 1, 015049, arXiv:1905.06952 [hep-ph].

[20] D. F. Jackson Kimball *et al.*, "Overview of the Cosmic Axion Spin Precession Experiment (CASPEr)," *Springer Proc. Phys.* **245** (2020) 105–121, arXiv:1711.08999 [physics.ins-det].

[21] O. Kim and Y. K. Semertzidis, "New method of probing an oscillating EDM induced by axionlike dark matter using an rf Wien filter in storage rings," *Phys. Rev. D* **104** (2021) no. 9, 096006, arXiv:2105.06655 [hep-ph].

[22] G. Lucente, L. Mastrototaro, P. Carenza, L. Di Luzio, M. Giannotti, and A. Mirizzi, "Axion signatures from supernova explosions through the nucleon electric-dipole portal," *Phys. Rev. D* **105** (2022) no. 12, 123020, arXiv:2203.15812 [hep-ph].

[23] A. Hook and J. Huang, "Probing axions with neutron star inspirals and other stellar processes," *JHEP* **06** (2018) 036, arXiv:1708.08464 [hep-ph].

[24] K. Blum, R. T. D'Agnolo, M. Lisanti, and B. R. Safdi, "Constraining Axion Dark Matter with Big Bang Nucleosynthesis," *Phys. Lett. B* **737** (2014) 30–33, arXiv:1401.6460 [hep-ph].

[25] W. A. Terrano, E. G. Adelberger, C. A. Hagedorn, and B. R. Heckel, "Constraints on axionlike dark matter with masses down to 10^{-23} eV/c^2," *Phys. Rev. Lett.* **122** (2019) no. 23, 231301, arXiv:1902.04246 [astro-ph.CO].

[26] W. A. Terrano, E. G. Adelberger, J. G. Lee, and B. R. Heckel, "Short-range spin-dependent interactions of electrons: a probe for exotic pseudo-Goldstone bosons," *Phys. Rev. Lett.* **115** (2015) no. 20, 201801, arXiv:1508.02463 [hep-ex].

[27] R. Alonso, D. Blas, and P. Wolf, "Exploring the ultra-light to sub-MeV dark matter window with atomic clocks and co-magnetometers," *JHEP* **07** (2019) 069, arXiv:1810.00889 [hep-ph].

[28] I. M. Bloch, Y. Hochberg, E. Kuflik, and T. Volansky, "Axion-like Relics: New Constraints from Old Comagnetometer Data," *JHEP* **01** (2020) 167, arXiv:1907.03767 [hep-ph].

[29] N. Crescini *et al.*, "Operation of a ferromagnetic axion haloscope at $m_a = 58\,\mu$eV," *Eur. Phys. J. C* **78** (2018) no. 9, 703, arXiv:1806.00310 [hep-ex]. [Erratum: Eur.Phys.J.C 78, 813 (2018)].

[30] **QUAX** Collaboration, N. Crescini *et al.*, "Axion search with a quantum-limited ferromagnetic haloscope," *Phys. Rev. Lett.* **124** (2020) no. 17, 171801, arXiv:2001.08940 [hep-ex].

[31] G. Flower, J. Bourhill, M. Goryachev, and M. E. Tobar, "Broadening frequency range of a ferromagnetic axion haloscope with strongly coupled cavity–magnon polaritons," *Phys. Dark Univ.* **25** (2019) 100306, arXiv:1811.09348 [physics.ins-det].

[32] T. Ikeda, A. Ito, K. Miuchi, J. Soda, H. Kurashige, and Y. Shikano, "Axion search with quantum nondemolition detection of magnons," *Phys. Rev. D* **105** (2022) no. 10, 102004, arXiv:2102.08764 [hep-ex].

[33] H. Yan, G. A. Sun, S. M. Peng, H. Guo, B. Q. Liu, M. Peng, and H. Zheng, "Constraining exotic spin dependent interactions of muons and electrons," *Eur. Phys. J. C* **79** (2019) no. 11, 971.

[34] M. Bauer, M. Neubert, S. Renner, M. Schnubel, and A. Thamm, "Flavor probes of axion-like particles," *JHEP* **09** (2022) 056, arXiv:2110.10698 [hep-ph].

[35] X. Fan, T. G. Myers, B. A. D. Sukra, and G. Gabrielse, "Measurement of the Electron Magnetic Moment," *Phys. Rev. Lett.* **130** (2023) no. 7, 071801, arXiv:2209.13084 [physics.atom-ph].

[36] **XENON** Collaboration, E. Aprile *et al.*, "Search for New Physics in Electronic Recoil Data from XENONnT," *Phys. Rev. Lett.* **129** (2022) no. 16, 161805, arXiv:2207.11330 [hep-ex].

[37] P. Gondolo and G. G. Raffelt, "Solar neutrino limit on axions and keV-mass bosons," *Phys. Rev. D* **79** (2009) 107301, arXiv:0807.2926 [astro-ph].

[38] M. M. Miller Bertolami, B. E. Melendez, L. G. Althaus, and J. Isern, "Revisiting the axion bounds from the Galactic white dwarf luminosity function," *JCAP* **10** (2014) 069, arXiv:1406.7712 [hep-ph].

[39] F. Capozzi and G. Raffelt, "Axion and neutrino bounds improved with new calibrations of the tip of the red-giant branch using geometric distance determinations," *Phys. Rev. D* **102** (2020) no. 8, 083007, arXiv:2007.03694 [astro-ph.SR].

[40] M. T. Dennis and J. Sakstein, "Tip of the Red Giant Branch Bounds on the Axion-Electron Coupling Revisited," arXiv:2305.03113 [hep-ph].

[41] W. DeRocco, P. W. Graham, and S. Rajendran, "Exploring the robustness of stellar cooling constraints on light particles," *Phys. Rev. D* **102** (2020) no. 7, 075015, arXiv:2006.15112 [hep-ph].

[42] G. Lucente and P. Carenza, "Supernova bound on axionlike particles coupled with electrons," *Phys. Rev. D* **104** (2021) no. 10, 103007, arXiv:2107.12393 [hep-ph].

[43] R. Z. Ferreira, M. C. D. Marsh, and E. Müller, "Strong supernovae bounds on ALPs from quantum loops," *JCAP* **11** (2022) 057, arXiv:2205.07896 [hep-ph].

[44] D. Ghosh and D. Sachdeva, "Constraints on Axion-Lepton coupling from Big Bang Nucleosynthesis," *JCAP* **10** (2020) 060, arXiv:2007.01873 [hep-ph].

[45] I. G. Irastorza and J. Redondo, "New experimental approaches in the search for axion-like particles," *Prog. Part. Nucl. Phys.* **102** (2018) 89–159, arXiv:1801.08127 [hep-ph].

[46] A. Arvanitaki, A. Madden, and K. Van Tilburg, "The Piezoaxionic Effect," arXiv:2112.11466 [hep-ph].

[47] P. H. Chu, Y. J. Kim, and I. Savukov, "Comment on "Search for an axion-induced oscillating electric dipole moment for electrons using atomic magnetometers"," arXiv:1904.10543 [hep-ph].

[48] P. W. Graham, D. E. Kaplan, J. Mardon, S. Rajendran, W. A. Terrano, L. Trahms, and T. Wilkason, "Spin Precession Experiments for Light Axionic Dark Matter," *Phys. Rev. D* **97** (2018) no. 5, 055006, arXiv:1709.07852 [hep-ph].

[49] C. Brandenstein, S. Stelzl, E. Gutsmiedl, W. Schott, A. Weiler, and P. Fierlinger, "Towards an electrostatic storage ring for fundamental physics measurements," *EPJ Web Conf.* **282** (2023) 01017, arXiv:2211.08439 [hep-ex].

[50] S. Chigusa, M. Hazumi, E. D. Herbschleb, N. Mizuochi, and K. Nakayama, "Light Dark Matter Search with Nitrogen-Vacancy Centers in Diamonds," arXiv:2302.12756 [hep-ph].

[51] S. Chigusa, T. Moroi, K. Nakayama, and T. Sichanugrist, "Dark matter detection using nuclear magnetization in magnet with hyperfine interaction," *Phys. Rev. D* **108** (2023) no. 9, 095007, arXiv:2307.08577 [hep-ph].

[52] S. Chigusa, T. Moroi, and K. Nakayama, "Detecting light boson dark matter through conversion into a magnon," *Phys. Rev. D* **101** (2020) no. 9, 096013, arXiv:2001.10666 [hep-ph].

[53] P. Sikivie, "Axion Dark Matter Detection using Atomic Transitions," *Phys. Rev. Lett.* **113** (2014) no. 20, 201301, arXiv:1409.2806 [hep-ph]. [Erratum: Phys.Rev.Lett. 125, 029901 (2020)].

[54] Y. Hochberg, T. Lin, and K. M. Zurek, "Detecting Ultralight Bosonic Dark Matter via Absorption in Superconductors," *Phys. Rev. D* **94** (2016) no. 1, 015019, arXiv:1604.06800 [hep-ph].

[55] H.-Y. Chen, A. Mitridate, T. Trickle, Z. Zhang, M. Bernardi, and K. M. Zurek, "Dark matter direct detection in materials with spin-orbit coupling," *Phys. Rev. D* **106** (2022) no. 1, 015024, arXiv:2202.11716 [hep-ph].

[56] Y. Hochberg, T. Lin, and K. M. Zurek, "Absorption of light dark matter in semiconductors," *Phys. Rev. D* **95** (2017) no. 2, 023013, arXiv:1608.01994 [hep-ph].

[57] A. Arvanitaki, S. Dimopoulos, and K. Van Tilburg, "Resonant absorption of bosonic dark matter in molecules," *Phys. Rev. X* **8** (2018) no. 4, 041001, arXiv:1709.05354 [hep-ph].

[58] A. Mitridate, K. Pardo, T. Trickle, and K. M. Zurek, "Effective Field Theory for Dark Matter Absorption on Single Phonons," arXiv:2308.06314 [hep-ph].

[59] C. Dvorkin, K. Blum, and M. Kamionkowski, "Constraining Dark Matter-Baryon Scattering with Linear Cosmology," *Phys. Rev. D* **89** (2014) no. 2, 023519, arXiv:1311.2937 [astro-ph.CO].

[60] A. Bhoonah, J. Bramante, S. Schon, and N. Song, "Detecting Composite Dark Matter with Long Range and Contact Interactions in Gas Clouds," arXiv:2010.07240 [hep-ph].

[61] D. Wadekar and G. R. Farrar, "First astrophysical constraints on dark matter interactions with ordinary matter at low relative velocity," arXiv:1903.12190 [hep-ph].

[62] H. Niikura, M. Takada, N. Yasuda, R. H. Lupton, T. Sumi, S. More, T. Kurita, S. Sugiyama, A. More, M. Oguri, and M. Chiba, "Microlensing constraints on primordial black holes with Subaru/HSC Andromeda observations," *Nature Astronomy* **3** (Apr., 2019) 524–534, arXiv:1701.02151 [astro-ph.CO].

[63] P. Montero-Camacho, X. Fang, G. Vasquez, M. Silva, and C. M. Hirata, "Revisiting constraints on asteroid-mass primordial black holes as dark matter candidates," *JCAP* **08** (2019) 031, arXiv:1906.05950 [astro-ph.CO].

[64] N. Smyth, S. Profumo, S. English, T. Jeltema, K. McKinnon, and P. Guhathakurta, "Updated Constraints on Asteroid-Mass Primordial Black Holes as Dark Matter," *Phys. Rev. D* **101** (2020) no. 6, 063005, arXiv:1910.01285 [astro-ph.CO].

[65] D. Croon, D. McKeen, N. Raj, and Z. Wang, "Subaru-HSC through a different lens: Microlensing by extended dark matter structures," *Phys. Rev. D* **102** (2020) no. 8, 083021, arXiv:2007.12697 [astro-ph.CO].

[66] A. Barnacka, J. F. Glicenstein, and R. Moderski, "New constraints on primordial black holes abundance from femtolensing of gamma-ray bursts," *Phys. Rev. D* **86** (2012) 043001, arXiv:1204.2056 [astro-ph.CO].

[67] A. Katz, J. Kopp, S. Sibiryakov, and W. Xue, "Femtolensing by Dark Matter Revisited," *JCAP* **12** (2018) 005, arXiv:1807.11495 [astro-ph.CO].

[68] **LSND** Collaboration, L. B. Auerbach *et al.*, "Measurement of electron-neutrino electron elastic scattering," *Phys. Rev. D* **63** (2001) 112001, arXiv:hep-ex/0101039.

[69] P. deNiverville, M. Pospelov, and A. Ritz, "Observing a light dark matter beam with neutrino experiments," *Phys. Rev. D* **84** (2011) 075020, arXiv:1107.4580 [hep-ph].

[70] J. D. Bjorken, S. Ecklund, W. R. Nelson, A. Abashian, C. Church, B. Lu, L. W. Mo, T. A. Nunamaker, and P. Rassmann, "Search for Neutral Metastable Penetrating Particles Produced in the SLAC Beam Dump," *Phys. Rev. D* **38** (1988) 3375.

[71] B. Batell, R. Essig, and Z. Surujon, "Strong Constraints on Sub-GeV Dark Sectors from SLAC Beam Dump E137," *Phys. Rev. Lett.* **113** (2014) no. 17, 171802, arXiv:1406.2698 [hep-ph].

[72] **MiniBooNE DM** Collaboration, A. A. Aguilar-Arevalo *et al.*, "Dark Matter Search in Nucleon, Pion, and Electron Channels from a Proton Beam Dump with MiniBooNE," *Phys. Rev. D* **98** (2018) no. 11, 112004, arXiv:1807.06137 [hep-ex].

[73] D. Akimov *et al.*, "First Probe of Sub-GeV Dark Matter Beyond the Cosmological Expectation with the COHERENT CsI Detector at the SNS," arXiv:2110.11453 [hep-ex].

[74] **NA62** Collaboration, E. Cortina Gil *et al.*, "Search for production of an invisible dark photon in π^0 decays," *JHEP* **05** (2019) 182, arXiv:1903.08767 [hep-ex].

[75] D. Banerjee *et al.*, "Dark matter search in missing energy events with NA64," *Phys. Rev. Lett.* **123** (2019) no. 12, 121801, arXiv:1906.00176 [hep-ex].

[76] Y. M. Andreev *et al.*, "Improved exclusion limit for light dark matter from e^+e^- annihilation in NA64," arXiv:2108.04195 [hep-ex].

[77] **BaBar** Collaboration, J. P. Lees *et al.*, "Search for Invisible Decays of a Dark Photon Produced in e^+e^- Collisions at BaBar," *Phys. Rev. Lett.* **119** (2017) no. 13, 131804, arXiv:1702.03327 [hep-ex].

[78] A. Hook, E. Izaguirre, and J. G. Wacker, "Model Independent Bounds on Kinetic Mixing," *Adv. High Energy Phys.* **2011** (2011) 859762, arXiv:1006.0973 [hep-ph].

[79] **Belle-II** Collaboration, W. Altmannshofer *et al.*, "The Belle II Physics Book," *PTEP* **2019** (2019) no. 12, 123C01, arXiv:1808.10567 [hep-ex]. [Erratum: PTEP 2020, 029201 (2020)].

[80] **CCM** Collaboration, A. A. Aguilar-Arevalo *et al.*, "First Dark Matter Search Results From Coherent CAPTAIN-Mills," arXiv:2105.14020 [hep-ex].

[81] A. A. Aguilar-Arevalo *et al.*, "First Leptophobic Dark Matter Search from Coherent CAPTAIN-Mills," arXiv:2109.14146 [hep-ex].

[82] A. Berlin, P. deNiverville, A. Ritz, P. Schuster, and N. Toro, "Sub-GeV dark matter production at fixed-target experiments," *Phys. Rev. D* **102** (2020) no. 9, 095011, arXiv:2003.03379 [hep-ph].

[83] B. Batell, P. deNiverville, D. McKeen, M. Pospelov, and A. Ritz, "Leptophobic Dark Matter at Neutrino Factories," *Phys. Rev. D* **90** (2014) no. 11, 115014, arXiv:1405.7049 [hep-ph].

[84] J. A. Dror, R. Lasenby, and M. Pospelov, "New constraints on light vectors coupled to anomalous currents," *Phys. Rev. Lett.* **119** (2017) no. 14, 141803, arXiv:1705.06726 [hep-ph].

[85] J. A. Dror, R. Lasenby, and M. Pospelov, "Dark forces coupled to nonconserved currents," *Phys. Rev. D* **96** (2017) no. 7, 075036, arXiv:1707.01503 [hep-ph].

[86] A. Berlin, N. Blinov, G. Krnjaic, P. Schuster, and N. Toro, "Dark Matter, Millicharges, Axion and Scalar Particles, Gauge Bosons, and Other New Physics with LDMX," *Phys. Rev. D* **99** (2019) no. 7, 075001, arXiv:1807.01730 [hep-ph].

[87] S. N. Gninenko, N. V. Krasnikov, and V. A. Matveev, "Search for dark sector physics with NA64," *Phys. Part. Nucl.* **51** (2020) no. 5, 829–858, arXiv:2003.07257 [hep-ph].

[88] P. deNiverville, C.-Y. Chen, M. Pospelov, and A. Ritz, "Light dark matter in neutrino beams: production modelling and scattering signatures at MiniBooNE, T2K and SHiP," *Phys. Rev. D* **95** (2017) no. 3, 035006, arXiv:1609.01770 [hep-ph].

[89] B. J. Hunt, *Pursuing power and light: technology and physics from James Watt to Albert Einstein*. JHU Press, 2010.

[90] M. Riordan, "The demise of the superconducting super collider," *Physics in Perspective* **2** (2000) 411–425.

[91] S. Weinberg, "The Quantum Theory of Fields I,".

[92] N. Craig, "Naturalness: past, present, and future," *Eur. Phys. J. C* **83** (2023) no. 9, 825, arXiv:2205.05708 [hep-ph].

[93] R. D. Peccei and H. R. Quinn, "CP Conservation in the Presence of Instantons," *Phys. Rev. Lett.* **38** (1977) 1440–1443. [,328(1977)].

[94] R. D. Peccei and H. R. Quinn, "Constraints Imposed by CP Conservation in the Presence of Instantons," *Phys. Rev.* **D16** (1977) 1791–1797.

[95] S. Weinberg, "A New Light Boson?," *Phys. Rev. Lett.* **40** (1978) 223–226.

[96] F. Wilczek, "Problem of Strong P and T Invariance in the Presence of Instantons," *Phys. Rev. Lett.* **40** (1978) 279–282.

[97] P. Svrcek and E. Witten, "Axions In String Theory," *JHEP* **06** (2006) 051, arXiv:hep-th/0605206 [hep-th].

[98] A. Arvanitaki, S. Dimopoulos, S. Dubovsky, N. Kaloper, and J. March-Russell, "String Axiverse," *Phys. Rev.* **D81** (2010) 123530, arXiv:0905.4720 [hep-th].

[99] M. J. Stott, D. J. E. Marsh, C. Pongkitivanichkul, L. C. Price, and B. S. Acharya, "Spectrum of the axion dark sector," *Phys. Rev.* **D96** (2017) no. 8, 083510, arXiv:1706.03236 [astro-ph.CO].

[100] J. Preskill, M. B. Wise, and F. Wilczek, "Cosmology of the Invisible Axion," *Phys. Lett.* **120B** (1983) 127–132.

[101] L. F. Abbott and P. Sikivie, "A Cosmological Bound on the Invisible Axion," *Phys. Lett.* **B120** (1983) 133–136.

[102] M. Dine and W. Fischler, "The Not So Harmless Axion," *Phys. Lett.* **B120** (1983) 137–141.

[103] M. Dine, W. Fischler, and M. Srednicki, "A Simple Solution to the Strong CP Problem with a Harmless Axion," *Phys. Lett.* **104B** (1981) 199–202.

[104] A. R. Zhitnitsky, "On Possible Suppression of the Axion Hadron Interactions. (In Russian)," *Sov. J. Nucl. Phys.* **31** (1980) 260. [Yad. Fiz.31,497(1980)].

[105] J. E. Kim, "Weak Interaction Singlet and Strong CP Invariance," *Phys. Rev. Lett.* **43** (1979) 103.

[106] M. A. Shifman, A. I. Vainshtein, and V. I. Zakharov, "Can Confinement Ensure Natural CP Invariance of Strong Interactions?," *Nucl. Phys.* **B166** (1980) 493–506.

[107] P. Sikivie, "Experimental Tests of the Invisible Axion," *Phys. Rev. Lett.* **51** (1983) 1415–1417.

[108] B. D. Blout, E. J. Daw, M. P. Decowski, P. T. P. Ho, L. J. Rosenberg, and D. B. Yu, "A Radio telescope search for axions," *Astrophys. J.* **546** (2001) 825–828, arXiv:astro-ph/0006310 [astro-ph].

[109] **H.E.S.S.** Collaboration, A. Abramowski *et al.*, "Constraints on axionlike particles with h.e.s.s. from the irregularity of the pks 2155 − 304 energy spectrum," *Phys. Rev. D* **88** (Nov, 2013) 102003. https://link.aps.org/doi/10.1103/PhysRevD.88.102003.

[110] **The Fermi-LAT** Collaboration, M. Ajello *et al.*, "Search for spectral irregularities due to photon–axionlike-particle oscillations with the fermi large area telescope," *Phys. Rev. Lett.* **116** (Apr, 2016) 161101. https://link.aps.org/doi/10.1103/PhysRevLett.116.161101.

[111] P. Sikivie and Q. Yang, "Bose-Einstein Condensation of Dark Matter Axions," *Phys. Rev. Lett.* **103** (2009) 111301, arXiv:0901.1106 [hep-ph].

[112] S. Davidson, "Axions: Bose Einstein Condensate or Classical Field?," *Astropart. Phys.* **65** (2015) 101–107, arXiv:1405.1139 [hep-ph].

[113] P. Sikivie, N. Sullivan, and D. B. Tanner, "Proposal for Axion Dark Matter Detection Using an LC Circuit," *Phys. Rev. Lett.* **112** (2014) no. 13, 131301, arXiv:1310.8545 [hep-ph].

[114] Y. Kahn, B. R. Safdi, and J. Thaler, "Broadband and Resonant Approaches to Axion Dark Matter Detection," *Phys. Rev. Lett.* **117** (2016) no. 14, 141801, arXiv:1602.01086 [hep-ph].

[115] S. Chaudhuri, K. D. Irwin, P. W. Graham, and J. Mardon, "Optimal Electromagnetic Searches for Axion and Hidden-Photon Dark Matter," arXiv:1904.05806 [hep-ex].

[116] D. Budker, P. W. Graham, M. Ledbetter, S. Rajendran, and A. Sushkov, "Proposal for a Cosmic Axion Spin Precession Experiment (CASPEr)," *Phys. Rev.* **X4** (2014) no. 2, 021030, arXiv:1306.6089 [hep-ph].

[117] M. Lawson, A. J. Millar, M. Pancaldi, E. Vitagliano, and F. Wilczek, "Tunable axion plasma haloscopes," *Phys. Rev. Lett.* **123** (2019) no. 14, 141802, arXiv:1904.11872 [hep-ph].

[118] M. Baryakhtar, J. Huang, and R. Lasenby, "Axion and hidden photon dark matter detection with multilayer optical haloscopes," *Phys. Rev.* **D98** (2018) no. 3, 035006, arXiv:1803.11455 [hep-ph].

[119] **MADMAX Working Group** Collaboration, A. Caldwell, G. Dvali, B. Majorovits, A. Millar, G. Raffelt, J. Redondo, O. Reimann, F. Simon, and F. Steffen, "Dielectric Haloscopes: A New Way to Detect Axion Dark Matter," *Phys. Rev. Lett.* **118** (2017) no. 9, 091801, arXiv:1611.05865 [physics.ins-det].

[120] Z. Bogorad, A. Hook, Y. Kahn, and Y. Soreq, "Probing axionlike particles and the axiverse with superconducting radio-frequency cavities," *Phys. Rev. Lett.* **123** (Jul, 2019) 021801. https://link.aps.org/doi/10.1103/PhysRevLett.123.021801.

[121] R. Janish, V. Narayan, S. Rajendran, and P. Riggins, "Axion production and detection with superconducting rf cavities," *Phys. Rev. D* **100** (Jul, 2019) 015036. https://link.aps.org/doi/10.1103/PhysRevD.100.015036.

[122] M. Goryachev, B. Mcallister, and M. E. Tobar, "Axion Detection with Precision Frequency Metrology," *Phys. Dark Univ.* **26** (2019) 100345, arXiv:1806.07141 [physics.ins-det].

[123] C. A. Thomson, B. T. McAllister, M. Goryachev, E. N. Ivanov, and M. E. Tobar, "Results from UPLOAD-DOWNLOAD: A phase-interferometric axion dark matter search," arXiv:1912.07751 [hep-ex].

[124] A. C. Melissinos, "Search for Cosmic Axions using an Optical Interferometer," *Phys. Rev. Lett.* **102** (2009) 202001, arXiv:0807.1092 [hep-ph].

[125] H. Liu, B. D. Elwood, M. Evans, and J. Thaler, "Searching for Axion Dark Matter with Birefringent Cavities," *Phys. Rev.* **D100** (2019) no. 2, 023548, arXiv:1809.01656 [hep-ph].

[126] D. Martynov and H. Miao, "Quantum-enhanced interferometry for axion searches," arXiv:1911.00429 [physics.ins-det].

[127] P. Sikivie, "Superconducting Radio Frequency Cavities as Axion Dark Matter Detectors," arXiv:1009.0762 [hep-ph].

[128] F. Pegoraro, E. Picasso, and L. A. Radicati, "On the operation of a tunable electromagnetic detector for gravitational waves," *Journal of Physics A: Mathematical and General* **11** (oct, 1978) 1949–1962. https://doi.org/10.1088%2F0305-4470%2F11%2F10%2F013.

[129] C. E. Reece, P. J. Reiner, and A. C. Melissinos, "Observation of 4 x 10**(-17)-cm Harmonic Displacement Using a 10-GHz Superconducting Parametric Converter," *Phys. Lett.* **A104** (1984) 341–344.

[130] P. Bernard, G. Gemme, R. Parodi, and E. Picasso, "A Detector of small harmonic displacements based on two coupled microwave cavities," *Rev. Sci. Instrum.* **72** (2001) 2428–2437, arXiv:gr-qc/0103006 [gr-qc].

[131] P. Bernard, A. Chincarini, G. Gemme, R. Parodi, and E. Picasso, "A Detector of gravitational waves based on coupled microwave cavities," arXiv:gr-qc/0203024 [gr-qc].

[132] R. Ballantini *et al.*, "Microwave apparatus for gravitational waves observation," arXiv:gr-qc/0502054 [gr-qc].

[133] L. Krauss, J. Moody, F. Wilczek, and D. E. Morris, "Calculations for Cosmic Axion Detection," *Phys. Rev. Lett.* **55** (1985) 1797.

[134] A. Romanenko, A. Grassellino, A. C. Crawford, D. A. Sergatskov, and O. Melnychuk, "Ultra-high quality factors in superconducting niobium cavities in ambient magnetic fields up to 190 mG," *Appl. Phys. Lett.* **105** (2014) 234103, arXiv:1410.7877 [physics.acc-ph].

[135] S. Posen, G. Wu, E. Harms, A. Grassellino, O. S. Melnychuk, D. A. Sergatskov, N. Solyak, A. Palczewski, D. Gonnella, and T. Peterson, "Role of magnetic flux expulsion to reach $Q_0 > 3 \times 10^{10}$ in superconducting rf cryomodules," *Phys. Rev. Accel. Beams* **22** (2019) no. 3, 032001, arXiv:1812.03950 [physics.acc-ph]. [Phys. Rev. Accel. Beams22,032001(2019)].

[136] Z. D. Farkas, H. A. Hoag, G. A. Loew, and P. B. Wilson, "SLED: A Method of Doubling SLAC's Energy," in *Proceedings, 9th International Conference on the High-Energy Accelerators (HEACC 1974): Stanford, California, May 2-7, 1974*, p. 576. 1974. http://www-public.slac.stanford.edu/sciDoc/docMeta.aspx?slacPubNumber=SLAC-PUB-1453.

[137] S. Tantawi, M. Shumail, J. Neilson, G. Bowden, C. Chang, E. Hemsing, and M. Dunning, "Experimental Demonstration of a Tunable Microwave Undulator," *Phys. Rev. Lett.* **112** (2014) no. 16, 164802.

[138] J. W. Wang *et al.*, "Development for a supercompact X -band pulse compression system and its application at SLAC," *Phys. Rev. Accel. Beams* **20** (2017) no. 11, 110401.

[139] A. Grassellino, "SRF-based dark matter search: Experiment," 2019. https://indico.fnal.gov/event/19433/session/2/contribution/2/material/slides/0.pdf.

[140] H. Padamsee, *RF Superconductivity: Science, Technology, and Applications*. John Wiley & Sons, 2009.

[141] A. A. Clerk, "Quantum-limited position detection and amplification: A linear response perspective," *Phys. Rev. B* **70** (Dec, 2004) 245306. https://link.aps.org/doi/10.1103/PhysRevB.70.245306.

[142] C. M. Caves, "Quantum limits on noise in linear amplifiers," *Phys. Rev. D* **26** (Oct, 1982) 1817–1839. https://link.aps.org/doi/10.1103/PhysRevD.26.1817.

[143] A. A. Clerk, M. H. Devoret, S. M. Girvin, F. Marquardt, and R. J. Schoelkopf, "Introduction to quantum noise, measurement, and amplification," *Rev. Mod. Phys.* **82** (Apr, 2010) 1155–1208. https://link.aps.org/doi/10.1103/RevModPhys.82.1155.

[144] E. Rubiola, *Phase noise and frequency stability in oscillators*. Cambridge University Press, 2009.

[145] D. M. Pozar, *Microwave engineering; 3rd ed.* Wiley, Hoboken, NJ, 2005. https://cds.cern.ch/record/882338.

[146] Berkeley Nucleonics Corporation, *Model 865-M Wideband Synthesizer Data Sheet*, 5, 2019. https://www.berkeleynucleonics.com/sites/default/files/products/datasheets/865-m_datasheet_5-3-19_v1.04.pdf.

[147] A. Grassellino, "First results of DarkSRF: a dark photon search using SRF cavities," 2020. https://indico.physics.lbl.gov/indico/event/939/contributions/4371/attachments/2162/2812/DarkSRF-Aspen.pdf.

[148] J. D. Jackson, *Classical electrodynamics*. Wiley, New York, NY, 3rd ed., 1999. http://cdsweb.cern.ch/record/490457.

[149] H. Padamsee, J. Knobloch, and T. Hays, *RF superconductivity for accelerators*. John Wiley & Sons, 1998.

[150] J. L. Wiener and H. Padamsee, "Improvements in Field Emission: A Statistical Model for Electropolished Baked Cavities," *Conf. Proc.* **C0806233** (2008) MOPP164.

[151] S. Chaudhuri, K. Irwin, P. W. Graham, and J. Mardon, "Fundamental Limits of Electromagnetic Axion and Hidden-Photon Dark Matter Searches: Part I - The Quantum Limit," arXiv:1803.01627 [hep-ph].

[152] R. H. Dicke, "The Measurement of Thermal Radiation at Microwave Frequencies," *Rev. Sci. Instrum.* **17** (1946) no. 7, 268–275.

[153] **CAST** Collaboration, M. Arik *et al.*, "Search for sub-ev mass solar axions by the cern axion solar telescope with ^{3}He buffer gas," *Phys. Rev. Lett.* **107** (Dec, 2011) 261302. https://link.aps.org/doi/10.1103/PhysRevLett.107.261302.

[154] **CAST** Collaboration, M. Arik *et al.*, "Search for solar axions by the cern axion solar telescope with ^{3}He buffer gas: Closing the hot dark matter gap," *Phys. Rev. Lett.* **112** (Mar, 2014) 091302. https://link.aps.org/doi/10.1103/PhysRevLett.112.091302.

[155] **CAST** Collaboration, M. Arik *et al.*, "New solar axion search using the CERN Axion Solar Telescope with ^{4}He filling," *Phys. Rev.* **D92** (2015) no. 2, 021101, arXiv:1503.00610 [hep-ex].

[156] P. W. Graham and A. Scherlis, "Stochastic axion scenario," *Phys. Rev.* **D98** (2018) no. 3, 035017, arXiv:1805.07362 [hep-ph].

[157] P. Agrawal, G. Marques-Tavares, and W. Xue, "Opening up the QCD axion window," *JHEP* **03** (2018) 049, arXiv:1708.05008 [hep-ph].

[158] M. A. Buen-Abad and J. Fan, "Dynamical axion misalignment with small instantons," *JHEP* **12** (2019) 161, arXiv:1911.05737 [hep-ph].

[159] G. Grilli di Cortona, E. Hardy, J. Pardo Vega, and G. Villadoro, "The QCD axion, precisely," *JHEP* **01** (2016) 034, arXiv:1511.02867 [hep-ph].

[160] S. Borsanyi *et al.*, "Calculation of the axion mass based on high-temperature lattice quantum chromodynamics," *Nature* **539** (2016) no. 7627, 69–71, arXiv:1606.07494 [hep-lat].

[161] T. P. Heavner, E. A. Donley, F. Levi, G. Costanzo, T. E. Parker, J. H. Shirley, N. Ashby, S. Barlow, and S. R. Jefferts, "First accuracy evaluation of NIST-f2," *Metrologia* **51** (may, 2014) 174–182. https://doi.org/10.1088%2F0026-1394%2F51%2F3%2F174.

[162] R. Lasenby, "Microwave Cavity Searches for Low-Frequency Axion Dark Matter," arXiv:1912.11056 [hep-ph].

[163] P. J. B. Clarricoats and P. K. Saha, "Propagation and radiation behaviour of corrugated feeds. part 1: Corrugated-waveguide feed," *Proceedings of the Institution of Electrical Engineers* **118** (Sep., 1971) 1167–1176.

[164] J. W. Foster, N. L. Rodd, and B. R. Safdi, "Revealing the Dark Matter Halo with Axion Direct Detection," *Phys. Rev.* **D97** (2018) no. 12, 123006, arXiv:1711.10489 [astro-ph.CO].

[165] G. P. Centers *et al.*, "Stochastic fluctuations of bosonic dark matter," arXiv:1905.13650 [astro-ph.CO].

[166] F. Zwicky, "Die Rotverschiebung von extragalaktischen Nebeln," *Helv. Phys. Acta* **6** (1933) 110–127.

[167] P. W. Graham, D. E. Kaplan, and S. Rajendran, "Cosmological Relaxation of the Electroweak Scale," *Phys. Rev. Lett.* **115** (2015) no. 22, 221801, arXiv:1504.07551 [hep-ph].

[168] N. Fonseca and E. Morgante, "Relaxion Dark Matter," *Phys. Rev. D* **100** (2019) no. 5, 055010, arXiv:1809.04534 [hep-ph].

[169] A. Banerjee, H. Kim, and G. Perez, "Coherent relaxion dark matter," *Phys. Rev. D* **100** (2019) no. 11, 115026, arXiv:1810.01889 [hep-ph].

[170] J. Goodman, "Repulsive dark matter," *New Astron.* **5** (2000) 103, arXiv:astro-ph/0003018.

[171] W. Hu, R. Barkana, and A. Gruzinov, "Cold and fuzzy dark matter," *Phys. Rev. Lett.* **85** (2000) 1158–1161, arXiv:astro-ph/0003365 [astro-ph].

[172] L. Hui, J. P. Ostriker, S. Tremaine, and E. Witten, "Ultralight scalars as cosmological dark matter," *Phys. Rev.* **D95** (2017) no. 4, 043541, arXiv:1610.08297 [astro-ph.CO].

[173] J. L. Ouellet *et al.*, "First Results from ABRACADABRA-10 cm: A Search for Sub-μeV Axion Dark Matter," *Phys. Rev. Lett.* **122** (2019) no. 12, 121802, arXiv:1810.12257 [hep-ex].

[174] A. V. Gramolin, D. Aybas, D. Johnson, J. Adam, and A. O. Sushkov, "Search for axion-like dark matter with ferromagnets," arXiv:2003.03348 [hep-ex].

[175] P. Sikivie, "Detection Rates for 'Invisible' Axion Searches," *Phys. Rev.* **D32** (1985) 2988. [Erratum: Phys. Rev.D36,974(1987)].

[176] A. Berlin, R. T. D'Agnolo, S. A. R. Ellis, C. Nantista, J. Neilson, P. Schuster, S. Tantawi, N. Toro, and K. Zhou, "Axion Dark Matter Detection by Superconducting Resonant Frequency Conversion," arXiv:1912.11048 [hep-ph].

[177] Z. Bogorad, A. Hook, Y. Kahn, and Y. Soreq, "Probing Axionlike Particles and the Axiverse with Superconducting Radio-Frequency Cavities," *Phys. Rev. Lett.* **123** (2019) no. 2, 021801, arXiv:1902.01418 [hep-ph].

[178] R. Lasenby, "Microwave cavity searches for low-frequency axion dark matter," arXiv:1912.11056 [hep-ph].

[179] W. DeRocco and A. Hook, "Axion interferometry," *Phys. Rev.* **D98** (2018) no. 3, 035021, arXiv:1802.07273 [hep-ph].

[180] I. Obata, T. Fujita, and Y. Michimura, "Optical Ring Cavity Search for Axion Dark Matter," *Phys. Rev. Lett.* **121** (2018) no. 16, 161301, arXiv:1805.11753 [astro-ph.CO].

[181] H. Liu, B. D. Elwood, M. Evans, and J. Thaler, "Searching for Axion Dark Matter with Birefringent Cavities," *Phys. Rev. D* **100** (2019) no. 2, 023548, arXiv:1809.01656 [hep-ph].

[182] A. Grassellino, "SRF-based dark matter search: Experiment," 2020. https://indico.physics.lbl.gov/event/939/contributions/4371/attachments/2162/2915/DarkSRF-Aspen-2.pdf.

[183] P. Bernard, G. Gemme, R. Parodi, and E. Picasso, "The RF control and detection system for PACO the parametric converter detector," arXiv:physics/0004031.

[184] D. Eriksson, G. Brodin, M. Marklund, and L. Stenflo, "A Possibility to measure elastic photon-photon scattering in vacuum," *Phys. Rev.* **A70** (2004) 013808, arXiv:physics/0411054 [physics].

[185] P. R. Saulson, *Fundamentals of Interferometric Gravitational Wave Detectors*. World Scientific, 2nd. ed. ed., 2017.

[186] D. Meidlinger, "A General Perturbation Theory for Cavity Mode Field Patterns," 2009. https://accelconf.web.cern.ch/SRF2009/papers/thppo005.pdf.

[187] E. Armengaud, N. Palanque-Delabrouille, C. Yèche, D. J. Marsh, and J. Baur, "Constraining the mass of light bosonic dark matter using SDSS Lyman-α forest," *Mon. Not. Roy. Astron. Soc.* **471** (2017) no. 4, 4606–4614, arXiv:1703.09126 [astro-ph.CO].

[188] V. Irˇ sič, M. Viel, M. G. Haehnelt, J. S. Bolton, and G. D. Becker, "First constraints on fuzzy dark matter from Lyman-α forest data and hydrodynamical simulations," *Phys. Rev. Lett.* **119** (2017) no. 3, 031302, arXiv:1703.04683 [astro-ph.CO].

[189] M. Nori, R. Murgia, V. Irˇ sič, M. Baldi, and M. Viel, "Lyman α forest and non-linear structure characterization in Fuzzy Dark Matter cosmologies," *Mon. Not. Roy. Astron. Soc.* **482** (2019) no. 3, 3227–3243, arXiv:1809.09619 [astro-ph.CO].

[190] A. Garzilli, O. Ruchayskiy, A. Magalich, and A. Boyarsky, "How warm is too warm? Towards robust Lyman-α forest bounds on warm dark matter," arXiv:1912.09397 [astro-ph.CO].

[191] D. J. Marsh and J. C. Niemeyer, "Strong Constraints on Fuzzy Dark Matter from Ultrafaint Dwarf Galaxy Eridanus II," *Phys. Rev. Lett.* **123** (2019) no. 5, 051103, arXiv:1810.08543 [astro-ph.CO].

[192] K. Schutz, "Subhalo mass function and ultralight bosonic dark matter," *Phys. Rev. D* **101** (2020) no. 12, 123026, arXiv:2001.05503 [astro-ph.CO].

[193] P. W. Graham, D. E. Kaplan, J. Mardon, S. Rajendran, W. A. Terrano, L. Trahms, and T. Wilkason, "Spin precession experiments for light axionic dark matter," *Physical Review D* **97** (2018) no. 5, 055006.

[194] T. Wu, J. W. Blanchard, G. P. Centers, N. L. Figueroa, A. Garcon, P. W. Graham, D. F. J. Kimball, S. Rajendran, Y. V. Stadnik, A. O. Sushkov, *et al.*, "Search for axionlike dark matter with a liquid-state nuclear spin comagnetometer," *Physical review letters* **122** (2019) no. 19, 191302.

[195] W. A. Terrano, E. G. Adelberger, C. A. Hagedorn, and B. R. Heckel, "Constraints on axionlike dark matter with masses down to 10- 23 ev/c 2," *Physical review letters* **122** (2019) no. 23, 231301.

[196] C. Abel, N. J. Ayres, G. Ban, G. Bison, K. Bodek, V. Bondar, M. Daum, M. Fairbairn, V. V. Flambaum, P. Geltenbort, *et al.*, "Search for axionlike dark matter through nuclear spin precession in electric and magnetic fields," *Physical Review X* **7** (2017) no. 4, 041034.

[197] J. Halverson, C. Long, B. Nelson, and G. Salinas, "Towards string theory expectations for photon couplings to axionlike particles," *Phys. Rev. D* **100** (2019) no. 10, 106010, arXiv:1909.05257 [hep-th].

[198] M. Pospelov, S. Pustelny, M. P. Ledbetter, D. F. Jackson Kimball, W. Gawlik, and D. Budker, "Detecting Domain Walls of Axionlike Models Using Terrestrial Experiments," *Phys. Rev. Lett.* **110** (2013) no. 2, 021803, arXiv:1205.6260 [hep-ph].

[199] D. F. Jackson Kimball, D. Budker, J. Eby, M. Pospelov, S. Pustelny, T. Scholtes, Y. V. Stadnik, A. Weis, and A. Wickenbrock, "Searching for axion stars and Q-balls with a terrestrial magnetometer network," *Phys. Rev. D* **97** (2018) no. 4, 043002, arXiv:1710.04323 [physics.atom-ph].

[200] U. S. G. Survey and J. R. Peterson, "Observations and modeling of seismic background noise," tech. rep., 1993. http://pubs.er.usgs.gov/publication/ofr93322.

[201] S. Rosat and J. Hinderer, "Limits of detection of gravimetric signals on earth," *Scientific Reports* **8** (2018) no. 1, 15324. https://doi.org/10.1038/s41598-018-33717-z.

[202] P. Wolf, S. Bize, A. Clairon, A. N. Luiten, G. Santarelli, and M. E. Tobar, "Tests of relativity using a microwave resonator," *Phys. Rev. Lett.* **90** (2003) 060402, arXiv:gr-qc/0210049.

[203] P. L. Stanwix, M. E. Tobar, P. Wolf, M. Susli, C. R. Locke, E. N. Ivanov, J. Winterflood, and F. van Kann, "Test of Lorentz invariance in electrodynamics using rotating cryogenic sapphire microwave oscillators," *Phys. Rev. Lett.* **95** (2005) 040404, arXiv:hep-ph/0506074.

[204] P. L. Stanwix, M. E. Tobar, P. Wolf, C. R. Locke, and E. N. Ivanov, "Improved test of Lorentz invariance in electrodynamics using rotating cryogenic sapphire oscillators," *Phys. Rev. D* **74** (2006) 081101, arXiv:gr-qc/0609072.

[205] J. W. Foster, N. L. Rodd, and B. R. Safdi, "Revealing the Dark Matter Halo with Axion Direct Detection," *Phys. Rev. D* **97** (2018) no. 12, 123006, arXiv:1711.10489 [astro-ph.CO].

[206] A. Arvanitaki, S. Dimopoulos, M. Galanis, L. Lehner, J. O. Thompson, and K. Van Tilburg, "Large-misalignment mechanism for the formation of compact axion structures: Signatures from the QCD axion to fuzzy dark matter," *Phys. Rev. D* **101** (2020) no. 8, 083014, arXiv:1909.11665 [astro-ph.CO].

[207] M. Fairbairn, D. J. E. Marsh, J. Quevillon, and S. Rozier, "Structure formation and microlensing with axion miniclusters," *Phys. Rev. D* **97** (2018) no. 8, 083502, arXiv:1707.03310 [astro-ph.CO].

[208] E. W. Kolb and I. I. Tkachev, "Axion miniclusters and Bose stars," *Phys. Rev. Lett.* **71** (1993) 3051–3054, arXiv:hep-ph/9303313.

[209] E. W. Kolb and I. I. Tkachev, "Nonlinear axion dynamics and formation of cosmological pseudosolitons," *Phys. Rev. D* **49** (1994) 5040–5051, arXiv:astro-ph/9311037.

[210] E. W. Kolb and I. I. Tkachev, "Large amplitude isothermal fluctuations and high density dark matter clumps," *Phys. Rev. D* **50** (1994) 769–773, arXiv:astro-ph/9403011.

[211] E. W. Kolb and I. I. Tkachev, "Femtolensing and picolensing by axion miniclusters," *Astrophys. J. Lett.* **460** (1996) L25–L28, arXiv:astro-ph/9510043.

[212] G. Cowan, K. Cranmer, E. Gross, and O. Vitells, "Asymptotic formulae for likelihood-based tests of new physics," *Eur. Phys. J. C* **71** (2011) 1554, arXiv:1007.1727 [physics.data-an]. [Erratum: Eur.Phys.J.C 73, 2501 (2013)].

[213] S. Wilks, "The Large-Sample Distribution of the Likelihood Ratio for Testing Composite Hypotheses," *Annals Math. Statist.* **9** (1938) no. 1, 60–62.

[214] S. Chaudhuri, P. W. Graham, K. Irwin, J. Mardon, S. Rajendran, and Y. Zhao, "Radio for hidden-photon dark matter detection," *Phys. Rev.* **D92** (2015) no. 7, 075012, arXiv:1411.7382 [hep-ph].

[215] C. Abel *et al.*, "Measurement of the Permanent Electric Dipole Moment of the Neutron," *Phys. Rev. Lett.* **124** (2020) no. 8, 081803, arXiv:2001.11966 [hep-ex].

[216] G. Grilli di Cortona, E. Hardy, J. Pardo Vega, and G. Villadoro, "The QCD axion, precisely," *JHEP* **01** (2016) 034, arXiv:1511.02867 [hep-ph].

[217] M. Pospelov and A. Ritz, "Theta induced electric dipole moment of the neutron via QCD sum rules," *Phys. Rev. Lett.* **83** (1999) 2526–2529, arXiv:hep-ph/9904483.

[218] C. Abel *et al.*, "Search for Axionlike Dark Matter through Nuclear Spin Precession in Electric and Magnetic Fields," *Phys. Rev. X* **7** (2017) no. 4, 041034, arXiv:1708.06367 [hep-ph].

[219] T. S. Roussy *et al.*, "Experimental Constraint on Axionlike Particles over Seven Orders of Magnitude in Mass," *Phys. Rev. Lett.* **126** (2021) no. 17, 171301, arXiv:2006.15787 [hep-ph].

[220] I. Schulthess *et al.*, "New Limit on Axion-Dark-Matter using Cold Neutrons," arXiv:2204.01454 [hep-ex].

[221] D. Aybas *et al.*, "Search for Axionlike Dark Matter Using Solid-State Nuclear Magnetic Resonance," *Phys. Rev. Lett.* **126** (2021) no. 14, 141802, arXiv:2101.01241 [hep-ex].

[222] S. P. Chang, S. Haciomeroglu, O. Kim, S. Lee, S. Park, and Y. K. Semertzidis, "Axionlike dark matter search using the storage ring EDM method," *Phys. Rev. D* **99** (2019) no. 8, 083002, arXiv:1710.05271 [hep-ex].

[223] J. Pretz, S. Karanth, E. Stephenson, S. P. Chang, V. Hejny, S. Park, Y. Semertzidis, and H. Ströher, "Statistical sensitivity estimates for oscillating electric dipole moment measurements in storage rings," *Eur. Phys. J. C* **80** (2020) no. 2, 107, arXiv:1908.09678 [hep-ex].

[224] **JEDI** Collaboration, E. Stephenson, "A Search for Axion-like Particles with a Horizontally Polarized Beam In a Storage Ring," *PoS* **PSTP2019** (2020) 018.

[225] J. Alexander *et al.*, "The storage ring proton EDM experiment," arXiv:2205.00830 [hep-ph].

[226] S. Karanth *et al.*, "First Search for Axion-Like Particles in a Storage Ring Using a Polarized Deuteron Beam," arXiv:2208.07293 [hep-ex].

[227] P. W. Graham and S. Rajendran, "Axion Dark Matter Detection with Cold Molecules," *Phys. Rev. D* **84** (2011) 055013, arXiv:1101.2691 [hep-ph].

[228] H. Kim and G. Perez, "Oscillations of atomic energy levels induced by QCD axion dark matter," arXiv:2205.12988 [hep-ph].

[229] F. Wilczek, "Two Applications of Axion Electrodynamics," *Phys. Rev. Lett.* **58** (1987) 1799.

[230] P. Sikivie, "Invisible Axion Search Methods," *Rev. Mod. Phys.* **93** (2021) no. 1, 015004, arXiv:2003.02206 [hep-ph].

[231] Y. K. Semertzidis and S. Youn, "Axion dark matter: How to see it?," *Sci. Adv.* **8** (2022) no. 8, abm9928, arXiv:2104.14831 [hep-ph].

[232] **ADMX** Collaboration, N. Du *et al.*, "Search for Invisible Axion Dark Matter with the Axion Dark Matter Experiment," *Phys. Rev. Lett.* **120** (2018) no. 15, 151301, arXiv:1804.05750 [hep-ex].

[233] **ADMX** Collaboration, T. Braine *et al.*, "Extended Search for the Invisible Axion with the Axion Dark Matter Experiment," *Phys. Rev. Lett.* **124** (2020) no. 10, 101303, arXiv:1910.08638 [hep-ex].

[234] **ADMX** Collaboration, C. Bartram *et al.*, "Search for Invisible Axion Dark Matter in the 3.3–4.2 μeV Mass Range," *Phys. Rev. Lett.* **127** (2021) no. 26, 261803, arXiv:2110.06096 [hep-ex].

[235] **HAYSTAC** Collaboration, L. Zhong *et al.*, "Results from phase 1 of the HAYSTAC microwave cavity axion experiment," *Phys. Rev. D* **97** (2018) no. 9, 092001, arXiv:1803.03690 [hep-ex].

[236] **HAYSTAC** Collaboration, K. M. Backes *et al.*, "A quantum-enhanced search for dark matter axions," *Nature* **590** (2021) no. 7845, 238–242, arXiv:2008.01853 [quant-ph].

[237] S. Lee, S. Ahn, J. Choi, B. R. Ko, and Y. K. Semertzidis, "Axion Dark Matter Search around 6.7 μeV," *Phys. Rev. Lett.* **124** (2020) no. 10, 101802, arXiv:2001.05102 [hep-ex].

[238] J. Jeong, S. Youn, S. Bae, J. Kim, T. Seong, J. E. Kim, and Y. K. Semertzidis, "Search for Invisible Axion Dark Matter with a Multiple-Cell Haloscope," *Phys. Rev. Lett.* **125** (2020) no. 22, 221302, arXiv:2008.10141 [hep-ex].

[239] **CAPP** Collaboration, O. Kwon *et al.*, "First Results from an Axion Haloscope at CAPP around 10.7 μeV," *Phys. Rev. Lett.* **126** (2021) no. 19, 191802, arXiv:2012.10764 [hep-ex].

[240] Y. Lee, B. Yang, H. Yoon, M. Ahn, H. Park, B. Min, D. Kim, and J. Yoo, "Searching for Invisible Axion Dark Matter with an 18 T Magnet Haloscope," *Phys. Rev. Lett.* **128** (2022) no. 24, 241805, arXiv:2206.08845 [hep-ex].

[241] J. Kim *et al.*, "Near-Quantum-Noise Axion Dark Matter Search at CAPP around 9.5 μeV," arXiv:2207.13597 [hep-ex].

[242] **ADMX** Collaboration, C. Boutan *et al.*, "Piezoelectrically Tuned Multimode Cavity Search for Axion Dark Matter," *Phys. Rev. Lett.* **121** (2018) no. 26, 261302, arXiv:1901.00920 [hep-ex].

[243] T. Grenet, R. Ballou, Q. Basto, K. Martineau, P. Perrier, P. Pugnat, J. Quevillon, N. Roch, and C. Smith, "The Grenoble Axion Haloscope platform (GrAHal): development plan and first results," arXiv:2110.14406 [hep-ex].

[244] **TASEH** Collaboration, H. Chang *et al.*, "Taiwan axion search experiment with haloscope: Designs and operations," *Rev. Sci. Instrum.* **93** (2022) no. 8, 084501, arXiv:2205.01477 [physics.ins-det].

[245] **TASEH** Collaboration, H. Chang *et al.*, "First Results from the Taiwan Axion Search Experiment with a Haloscope at 19.6 μeV," *Phys. Rev. Lett.* **129** (2022) no. 11, 111802, arXiv:2205.05574 [hep-ex].

[246] **CAST** Collaboration, A. A. Melcón *et al.*, "First results of the CAST-RADES haloscope search for axions at 34.67 μeV," *JHEP* **21** (2020) 075, arXiv:2104.13798 [hep-ex].

[247] D. Alesini *et al.*, "Search for invisible axion dark matter of mass $m_a = 43$ μeV with the QUAX–$a\gamma$ experiment," *Phys. Rev. D* **103** (2021) no. 10, 102004, arXiv:2012.09498 [hep-ex].

[248] A. P. Quiskamp, B. T. McAllister, P. Altin, E. N. Ivanov, M. Goryachev, and M. E. Tobar, "Direct search for dark matter axions excluding ALP cogenesis in the 63- to 67-μeV range with the ORGAN experiment," *Sci. Adv.* **8** (2022) no. 27, abq3765, arXiv:2203.12152 [hep-ex].

[249] D. B. Kaplan, "Opening the Axion Window," *Nucl. Phys. B* **260** (1985) 215–226.

[250] S. L. Cheng, C. Q. Geng, and W. T. Ni, "Axion-photon couplings in invisible axion models," *Phys. Rev. D* **52** (1995) 3132–3135, arXiv:hep-ph/9506295.

[251] L. Di Luzio, F. Mescia, and E. Nardi, "Redefining the Axion Window," *Phys. Rev. Lett.* **118** (2017) no. 3, 031801, arXiv:1610.07593 [hep-ph].

[252] L. Di Luzio, F. Mescia, and E. Nardi, "Window for preferred axion models," *Phys. Rev. D* **96** (2017) no. 7, 075003, arXiv:1705.05370 [hep-ph].

[253] V. V. Flambaum and H. B. Tran Tan, "Oscillating nuclear electric dipole moment induced by axion dark matter produces atomic and molecular electric dipole moments and nuclear spin rotation," *Phys. Rev. D* **100** (2019) no. 11, 111301, arXiv:1904.07609 [hep-ph].

[254] J. Hong, J. E. Kim, and P. Sikivie, "Nuclear dipole radiation from $\overline{\theta}$ oscillations," *Phys. Rev. D* **42** (Sep, 1990) 1847–1850. https://link.aps.org/doi/10.1103/PhysRevD.42.1847.

[255] I. B. Khriplovich and S. K. Lamoreaux, *CP violation without strangeness: Electric dipole moments of particles, atoms, and molecules*. Springer Berlin, Heidelberg, 1997.

[256] V. V. Flambaum, I. B. Khriplovich, and O. P. Sushkov, "On the Possibility to Study P Odd and T Odd Nuclear Forces in Atomic and Molecular Experiments," *Sov. Phys. JETP* **60** (1984) 873.

[257] J. Engel, J. L. Friar, and A. C. Hayes, "Nuclear octupole correlations and the enhancement of atomic time reversal violation," *Phys. Rev. C* **61** (2000) 035502, arXiv:nucl-th/9910008.

[258] N. Auerbach, V. V. Flambaum, and V. Spevak, "Collective T- and P-odd electromagnetic moments in nuclei with octupole deformations," *Phys. Rev. Lett.* **76** (1996) 4316–4319, arXiv:nucl-th/9601046.

[259] V. Spevak, N. Auerbach, and V. V. Flambaum, "Enhanced T-odd, P-odd electromagnetic moments in reflection asymmetric nuclei," *Phys. Rev. C* **56** (1997) 1357–1369, arXiv:nucl-th/9612044.

[260] J. S. M. Ginges and V. V. Flambaum, "Violations of fundamental symmetries in atoms and tests of unification theories of elementary particles," *Phys. Rept.* **397** (2004) 63–154, arXiv:physics/0309054.

[261] L. I. Schiff, "Measurability of Nuclear Electric Dipole Moments," *Phys. Rev.* **132** (1963) 2194–2200.

[262] V. A. Dzuba, V. V. Flambaum, J. S. M. Ginges, and M. G. Kozlov, "Electric dipole moments of Hg, Xe, Rn, Ra, Pu, and TlF induced by the nuclear Schiff moment and limits on time reversal violating interactions," *Phys. Rev. A* **66** (2002) 012111, arXiv:hep-ph/0203202.

[263] V. A. Dzuba, V. V. Flambaum, and S. G. Porsev, "Calculation of (P,T)-odd electric dipole moments for the diamagnetic atoms ^{129}Xe, ^{171}Yb, ^{199}Hg, ^{211}Rn, and ^{225}Ra," *Phys. Rev. A* **80** (2009) 032120, arXiv:0906.5437 [physics.atom-ph].

[264] V. A. Dzuba, V. V. Flambaum, and J. S. M. Ginges, "Atomic electric dipole moments of He and Yb induced by nuclear Schiff moments," *Phys. Rev. A* **76** (2007) 034501, arXiv:0705.4001 [physics.atom-ph].

[265] V. V. Flambaum and H. Feldmeier, "Enhanced nuclear Schiff moment in stable and metastable nuclei," *Phys. Rev. C* **101** (2020) no. 1, 015502, arXiv:1907.07438 [nucl-th].

[266] V. F. Dmitriev, I. B. Khriplovich, and V. B. Telitsin, "Nuclear magnetic quadrupole moments in the single-particle approximation," *Phys. Rev. C* **50** (1994) 2358–2361, arXiv:nucl-th/9405016.

[267] J. de Vries, E. Epelbaum, L. Girlanda, A. Gnech, E. Mereghetti, and M. Viviani, "Parity- and Time-Reversal-Violating Nuclear Forces," *Front. in Phys.* **8** (2020) 218, arXiv:2001.09050 [nucl-th].

[268] V. V. Flambaum, D. DeMille, and M. G. Kozlov, "Time-reversal symmetry violation in molecules induced by nuclear magnetic quadrupole moments," *Phys. Rev. Lett.* **113** (2014) 103003, arXiv:1406.6479 [physics.atom-ph].

[269] W. C. Haxton and E. M. Henley, "Enhanced T-nonconserving nuclear moments," *Phys. Rev. Lett.* **51** (Nov, 1983) 1937–1940.

[270] A. Griffiths and P. Vogel, "One-body parity and time reversal violating potentials," *Phys. Rev. C* **43** (1991) 2844–2848.

[271] F. Dalton, V. V. Flambaum, and A. J. Mansour, "Enhanced Schiff and magnetic quadrupole moments in deformed nuclei and their connection to the search for axion dark matter," arXiv:2302.00214 [hep-ph].

[272] R. K. Harris, E. D. Becker, S. M. C. De Menezes, R. Goodfellow, and P. Granger, "NMR nomenclature. Nuclear spin properties and conventions for chemical shifts (IUPAC recommendations 2001)," *Pure and Applied Chemistry* **73** (2001) no. 11, 1795–1818.

[273] Institute for Rare Earths and Metals, "Rare earth prices in February 2020." https://en.institut-seltene-erden.de/rare-earth-prices-in-february-2020/. Accessed: 2022-08-10.

[274] V. V. Flambaum and V. A. Dzuba, "Electric dipole moments of atoms and molecules produced by enhanced nuclear Schiff moments," *Phys. Rev. A* **101** (2020) no. 4, 042504, arXiv:1912.03598 [physics.atom-ph].

[275] J. A. Behr, "Nuclei with enhanced Schiff moments in practical elements for atomic and molecular EDM measurements," arXiv:2203.06758 [nucl-ex].

[276] E. U. Condon, "Forced oscillations in cavity resonators," *Journal of Applied Physics* **12** (1941) no. 2, 129–132.

[277] W. B. Smythe, *Static and dynamic electricity*. New York, NY (USA); Hemisphere Publishing, 1988.

[278] R. E. Collin, *Field theory of guided waves*, vol. 5. John Wiley & Sons, 1990.

[279] J. Kim, S. Youn, J. Jeong, W. Chung, O. Kwon, and Y. K. Semertzidis, "Exploiting higher-order resonant modes for axion haloscopes," *J. Phys. G* **47** (2020) no. 3, 035203, arXiv:1910.00793 [physics.ins-det].

[280] R. A. Parker, "Static dielectric constant of rutile (TiO_2), 1.6-1060°K," *Phys. Rev.* **124** (Dec, 1961) 1719–1722.

[281] D. E. Morris, "An Electromagnetic Detector For Relic Axions,".

[282] P. Sikivie, D. B. Tanner, and Y. Wang, "Axion detection in the 10^{-4} eV mass range," *Phys. Rev. D* **50** (1994) 4744–4748, arXiv:hep-ph/9305264.

[283] G. Rybka, A. Wagner, A. Brill, K. Ramos, R. Percival, and K. Patel, "Search for dark matter axions with the Orpheus experiment," *Phys. Rev. D* **91** (2015) no. 1, 011701, arXiv:1403.3121 [physics.ins-det].

[284] B. Phillips, "The Electric Tiger experiment: a proof-of-concept for the periodic dielectric loaded resonator." Talk given at the 2nd Workshop on Microwave Cavities and Detectors for Axion Research, 2017.

[285] J. Egge, S. Knirck, B. Majorovits, C. Moore, and O. Reimann, "A first proof of principle booster setup for the MADMAX dielectric haloscope," *Eur. Phys. J. C* **80** (2020) no. 5, 392, arXiv:2001.04363 [physics.ins-det].

[286] R. Cervantes *et al.*, "Search for 70 μeV Dark Photon Dark Matter with a Dielectrically-Loaded Multi-Wavelength Microwave Cavity," arXiv:2204.03818 [hep-ex].

[287] R. Cervantes *et al.*, "ADMX-Orpheus First Search for 70 μeV Dark Photon Dark Matter: Detailed Design, Operations, and Analysis," arXiv:2204.09475 [hep-ex].

[288] C. Lee and O. Reimann, "T-RAX: Transversely Resonant Axion eXperiment," *JCAP* **09** (2022) 007, arXiv:2203.15487 [astro-ph.IM].

[289] A. P. Quiskamp, B. T. McAllister, G. Rybka, and M. E. Tobar, "Dielectric-Boosted Sensitivity to Cylindrical Azimuthally Varying Transverse-Magnetic Resonant Modes in an Axion Haloscope," *Phys. Rev. Applied* **14** (2020) no. 4, 044051, arXiv:2006.05641 [physics.ins-det].

[290] B. T. McAllister, G. Flower, L. E. Tobar, and M. E. Tobar, "Tunable Supermode Dielectric Resonators for Axion Dark-Matter Haloscopes," *Phys. Rev. Applied* **9** (2018) no. 1, 014028, arXiv:1705.06028 [physics.ins-det].

[291] **QUAX** Collaboration, D. Alesini *et al.*, "Realization of a high quality factor resonator with hollow dielectric cylinders for axion searches," *Nucl. Instrum. Meth. A* **985** (2021) 164641, arXiv:2004.02754 [physics.ins-det].

[292] R. Di Vora *et al.*, "High-Q Microwave Dielectric Resonator for Axion Dark-Matter Haloscopes," *Phys. Rev. Applied* **17** (2022) no. 5, 054013, arXiv:2201.04223 [physics.ins-det].

[293] D. Alesini *et al.*, "Search for Galactic axions with a high-Q dielectric cavity," *Phys. Rev. D* **106** (2022) no. 5, 052007, arXiv:2208.12670 [hep-ex].

[294] J. Jeong, S. Youn, S. Ahn, C. Kang, and Y. K. Semertzidis, "Phase-matching of multiple-cavity detectors for dark matter axion search," *Astropart. Phys.* **97** (2018) 33–37, arXiv:1707.05925 [astro-ph.IM].

[295] J. Yang, J. R. Gleason, S. Jois, I. Stern, P. Sikivie, N. S. Sullivan, and D. B. Tanner, "Search for 5–9 μeV Axions with ADMX Four-Cavity Array," *Springer Proc. Phys.* **245** (2020) 53–62.

[296] M. Maroudas, "Search for dark matter axions with CAST-CAPP." Talk given at the 16th Patras Workshop on Axions, WIMPs and WISPs, 2021.

[297] M. Goryachev, B. T. Mcallister, and M. E. Tobar, "Axion detection with negatively coupled cavity arrays," *Phys. Lett. A* **382** (2018) 2199–2204, arXiv:1703.07207 [physics.ins-det].

[298] A. A. Melcón *et al.*, "Axion Searches with Microwave Filters: the RADES project," *JCAP* **05** (2018) 040, arXiv:1803.01243 [hep-ex].

[299] S. Arguedas Cuendis *et al.*, "The 3 Cavity Prototypes of RADES: An Axion Detector Using Microwave Filters at CAST," *Springer Proc. Phys.* **245** (2020) 45–51, arXiv:1903.04323 [physics.ins-det].

[300] A. Álvarez Melcón *et al.*, "Scalable haloscopes for axion dark matter detection in the 30 μeV range with RADES," *JHEP* **07** (2020) 084, arXiv:2002.07639 [hep-ex].

[301] A. Díaz-Morcillo *et al.*, "Design of New Resonant Haloscopes in the Search for the Dark Matter Axion: A Review of the First Steps in the RADES Collaboration," *Universe* **8** (2021) no. 1, 5, arXiv:2111.14510 [physics.ins-det].

[302] J. Jeong, S. Youn, S. Ahn, J. E. Kim, and Y. K. Semertzidis, "Concept of multiple-cell cavity for axion dark matter search," *Phys. Lett. B* **777** (2018) 412–419, arXiv:1710.06969 [astro-ph.IM].

[303] J. Jeong, S. Youn, and J. E. Kim, "Multiple-cell cavity design for high mass axion searches," arXiv:2205.01319 [hep-ex].

[304] M. Wooten, A. Droster, A. Kenany, D. Sun, S. M. Lewis, and K. van Bibber, "Exploration of Wire Array Metamaterials for the Plasma Axion Haloscope," arXiv:2203.13945 [hep-ex].

[305] S. Bae, S. Youn, and J. Jeong, "Tunable dielectric metamaterial haloscope for high-mass axion searches," arXiv:2205.08885 [hep-ex].

[306] C.-L. Kuo, "Large-Volume Centimeter-Wave Cavities for Axion Searches," *JCAP* **06** (2020) 010, arXiv:1910.04156 [physics.ins-det].

[307] C.-L. Kuo, "Symmetrically Tuned Large-Volume Conic Shell-Cavities for Axion Searches," *JCAP* **02** (2021) 018, arXiv:2010.04337 [physics.ins-det].

[308] F. Natali, B. J. Ruck, N. O. Plank, H. J. Trodahl, S. Granville, C. Meyer, and W. R. Lambrecht, "Rare-earth mononitrides," *Progress in Materials Science* **58** (2013) no. 8, 1316–1360.

[309] A. Jain, S. P. Ong, G. Hautier, W. Chen, W. D. Richards, S. Dacek, S. Cholia, D. Gunter, D. Skinner, G. Ceder, and K. A. Persson, "Commentary: The Materials Project: A materials genome approach to accelerating materials innovation," *APL Materials* **1** (2013) no. 1, 011002.

[310] I. Petousis, D. Mrdjenovich, E. Ballouz, M. Liu, D. Winston, W. Chen, T. Graf, T. D. Schladt, K. A. Persson, and F. B. Prinz, "High-throughput screening of inorganic compounds for the discovery of novel dielectric and optical materials," *Scientific data* **4** (2017) no. 1, 1–12.

[311] D. Xue, K. Betzler, and H. Hesse, "Dielectric constants of binary rare-earth compounds," *Journal of Physics: Condensed Matter* **12** (2000) no. 13, 3113.

[312] L. V. Skripnikov and A. V. Titov, "LCAO-based theoretical study of $PbTiO_3$ crystal to search for parity and time reversal violating interaction in solids," *The Journal of Chemical Physics* **145** (2016) no. 5, 054115.

[313] J. A. Ludlow and O. P. Sushkov, "Investigating the nuclear Schiff moment of ^{207}Pb in ferroelectric $PbTiO_3$," *J. Phys. B* **46** (2013) 085001, `arXiv:1210.2117 [physics.atom-ph]`.

[314] V. Gurevich and A. Tagantsev, "Intrinsic dielectric loss in crystals," *Advances in Physics* **40** (1991) no. 6, 719–767.

[315] N. M. Alford, J. Breeze, X. Wang, S. Penn, S. Dalla, S. Webb, N. Ljepojevic, and X. Aupi, "Dielectric loss of oxide single crystals and polycrystalline analogues from 10 to 320 K," *Journal of the European Ceramic Society* **21** (2001) no. 15, 2605–2611.

[316] X. Aupi, J. Breeze, N. Ljepojevic, L. J. Dunne, N. Malde, A.-K. Axelsson, and N. M. Alford, "Microwave dielectric loss in oxides: Theory and experiment," *Journal of applied physics* **95** (2004) no. 5, 2639–2645.

[317] V. Braginsky, V. Ilchenko, and K. S. Bagdassarov, "Experimental observation of fundamental microwave absorption in high-quality dielectric crystals," *Physics Letters A* **120** (1987) no. 6, 300–305.

[318] M. E. Tobar, J. Krupka, E. N. Ivanov, and R. A. Woode, "Anisotropic complex permittivity measurements of mono-crystalline rutile between 10 and 300 K," *Journal of Applied Physics* **83** (1998) no. 3, 1604–1609.

[319] J. Krupka, K. Derzakowski, A. Abramowicz, M. E. Tobar, and R. G. Geyer, "Use of whispering-gallery modes for complex permittivity determinations of ultra-low-loss dielectric materials," *IEEE Transactions on Microwave Theory and Techniques* **47** (1999) no. 6, 752–759.

[320] J. Krupka, K. Derzakowski, M. Tobar, J. Hartnett, and R. G. Geyer, "Complex permittivity of some ultralow loss dielectric crystals at cryogenic temperatures," *Measurement Science and Technology* **10** (1999) no. 5, 387.

[321] G. Liu, S. Zhang, W. Jiang, and W. Cao, "Losses in ferroelectric materials," *Materials Science and Engineering: R: Reports* **89** (2015) 1–48.

[322] J. M. Martinis, K. B. Cooper, R. McDermott, M. Steffen, M. Ansmann, K. D. Osborn, K. Cicak, S. Oh, D. P. Pappas, R. W. Simmonds, and C. C. Yu, "Decoherence in Josephson qubits from dielectric loss," *Phys. Rev. Lett.* **95** (Nov, 2005) 210503.

[323] A. D. O'Connell, M. Ansmann, R. C. Bialczak, M. Hofheinz, N. Katz, E. Lucero, C. McKenney, M. Neeley, H. Wang, E. M. Weig, *et al.*, "Microwave dielectric loss at single photon energies and millikelvin temperatures," *Applied Physics Letters* **92** (2008) no. 11, 112903.

[324] N. Kostylev, M. Goryachev, A. D. Bulanov, V. A. Gavva, and M. E. Tobar, "Determination of low loss in isotopically pure single crystal ^{28}Si at low temperatures and single microwave photon energy," *Scientific reports* **7** (2017) no. 1, 1–8.

[325] D. S. Betts, *An Introduction to Millikelvin Technology*. Cambridge Studies in Low Temperature Physics. Cambridge University Press, 1989.

[326] H. Zu, W. Dai, and A. de Waele, "Development of dilution refrigerators—a review," *Cryogenics* **121** (2022) 103390.

[327] A. Abragam and M. Goldman, *Nuclear magnetism: order and disorder*. Clarendon Press, 1982.

[328] O. Gonen and J. Waugh, "NMR relaxation mechanisms and line widths in insulators below 1 K," *Physica A: Statistical Mechanics and its Applications* **156** (1989) no. 1, 219–226.

[329] W. de Boer and T. Niinikoski, "Dynamic proton polarization in propanediol below 0.5 K," *Nuclear Instruments and Methods* **114** (1974) no. 3, 495–498.

[330] P. Kuhns, P. Hammel, O. Gonen, and J. Waugh, "Unexpectedly rapid ^{19}F spin-lattice relaxation in CaF_2 below 1 K," *Physical Review B* **35** (1987) no. 10, 4591.

[331] J. Waugh and C. P. Slichter, "Mechanism of nuclear spin-lattice relaxation in insulators at very low temperatures," *Physical Review B* **37** (1988) no. 8, 4337.

[332] P. Phillips, D. Izzo, and K. Kundu, "Spin-lattice relaxation below 1 K: A new mechanism for unexpected nuclear spin relaxation," *Physical Review B* **37** (1988) no. 18, 10876.

[333] A. J. Vega, P. A. Beckmann, S. Bai, and C. Dybowski, "Spin-lattice relaxation of heavy spin-1/2 nuclei in diamagnetic solids: A Raman process mediated by spin-rotation interaction," *Physical Review B* **74** (2006) no. 21, 214420.

[334] A. Abragam, *The Principles of Nuclear Magnetism*. No. 32 in International series of monographs on physics. Clarendon Press, 1961.

[335] E. Krjukov, J. O'Neill, and J. Owers-Bradley, "Brute force polarization of ^{129}Xe," *Journal of low temperature physics* **140** (2005) no. 5, 397–408.

[336] J. R. Owers-Bradley, A. J. Horsewill, D. T. Peat, K. S. Goh, and D. G. Gadian, "High polarization of nuclear spins mediated by nanoparticles at millikelvin temperatures," *Physical Chemistry Chemical Physics* **15** (2013) no. 25, 10413–10417.

[337] J. H. Ardenkjær-Larsen, B. Fridlund, A. Gram, G. Hansson, L. Hansson, M. H. Lerche, R. Servin, M. Thaning, and K. Golman, "Increase in signal-to-noise ratio of >10,000 times in liquid-state NMR," *Proceedings of the National Academy of Sciences* **100** (2003) no. 18, 10158–10163.

[338] D. Lee, S. Hediger, and G. De Paëpe, "Is solid-state NMR enhanced by dynamic nuclear polarization?," *Solid State Nuclear Magnetic Resonance* **66** (2015) 6–20.

[339] J. H. Ardenkjaer-Larsen, "On the present and future of dissolution-DNP," *Journal of Magnetic Resonance* **264** (2016) 3–12.

[340] J. Eills *et al.*, "Spin hyperpolarization in modern magnetic resonance," *ChemRxiv* (2022) .

[341] D. G. Crabb and W. Meyer, "Solid polarized targets for nuclear and particle physics experiments," *Ann. Rev. Nucl. Part. Sci.* **47** (1997) 67–109.

[342] S. Goertz, W. Meyer, and G. Reicherz, "Polarized H, D and He-3 targets for particle physics experiments," *Prog. Part. Nucl. Phys.* **49** (2002) 403–489. [Erratum: Prog.Part.Nucl.Phys. 51, 309–312 (2003)].

[343] **Spin Muon** Collaboration, D. Adams *et al.*, "The polarized double cell target of the SMC," *Nucl. Instrum. Meth. A* **437** (1999) 23–67.

[344] C. Keith, "Polarized solid targets: recent progress and future prospects," *Polarized Sources, Targets And Polarimetry* (2011) 113–122.

[345] T. O. Niinikoski, *The Physics of Polarized Targets*. Cambridge University Press, 2020.

[346] G. Reicherz, "Status of Polarized Solid Targets in European High Energy Scattering Experiments." Talk given at the 24th International Spin Symposium, 2021.

[347] I. Fernando, "SpinQuest Polarized Target: An Overview." Talk given at the 24th International Spin Symposium, 2021.

[348] C. Keith, "Testing a new polarized target for CLAS12 at Jefferson Lab." Talk given at the 24th International Spin Symposium, 2021.

[349] K. Ishizaki, "La-139 polarized target study for NOPTREX." Talk given at the 2019 Workshop on Polarized Sources, Targets, and Polarimetry, 2019.

[350] C. D. Keith, J. Brock, C. Carlin, S. A. Comer, D. Kashy, J. McAndrew, D. G. Meekins, E. Pasyuk, J. J. Pierce, and M. L. Seely, "The Jefferson Lab Frozen Spin Target," *Nucl. Instrum. Meth. A* **684** (2012) 27–35, arXiv:1204.1250 [physics.ins-det].

[351] R. H. Dicke, "The measurement of thermal radiation at microwave frequencies," in *Classics in Radio Astronomy*, pp. 106–113. Springer, 1946.

[352] R. Balkin, J. Serra, K. Springmann, S. Stelzl, and A. Weiler, "White dwarfs as a probe of light QCD axions," arXiv:2211.02661 [hep-ph].

[353] **CUORE** Collaboration, C. Ligi *et al.*, "The CUORE Cryostat: A 1-Ton Scale Setup for Bolometric Detectors," *J. Low Temp. Phys.* **184** (2016) no. 3-4, 590–596, arXiv:1603.03306 [physics.ins-det].

[354] C. Alduino *et al.*, "The CUORE cryostat: An infrastructure for rare event searches at millikelvin temperatures," *Cryogenics* **102** (2019) 9–21, arXiv:1904.05745 [physics.ins-det].

[355] M. I. Hollister, R. C. Dhuley, and G. L. Tatkowski, "A large millikelvin platform at Fermilab for quantum computing applications," *IOP Conf. Ser. Mater. Sci. Eng.* **1241** (2022) 012045, arXiv:2108.10816 [physics.ins-det].

[356] P. Astone *et al.*, "First Cooling Below 0.1 K of the New Gravitational-Wave Antenna "Nautilus" of the Rome Group," *EPL* **16** (1991) 231–235.

[357] M. Cerdonio *et al.*, "The ultracryogenic gravitational-wave detector AURIGA," *Class. Quant. Grav.* **14** (1997) 1491–1494.

[358] **DEAP** Collaboration, M. G. Boulay, "DEAP-3600 Dark Matter Search at SNOLAB," *J. Phys. Conf. Ser.* **375** (2012) 012027, arXiv:1203.0604 [astro-ph.IM].

[359] **XENON** Collaboration, E. Aprile *et al.*, "Projected WIMP sensitivity of the XENONnT dark matter experiment," *JCAP* **11** (2020) 031, arXiv:2007.08796 [physics.ins-det].

[360] L. Di Luzio, B. Gavela, P. Quilez, and A. Ringwald, "An even lighter QCD axion," *JHEP* **05** (2021) 184, arXiv:2102.00012 [hep-ph].

[361] L. Di Luzio, B. Gavela, P. Quilez, and A. Ringwald, "Dark matter from an even lighter QCD axion: trapped misalignment," *JCAP* **10** (2021) 001, arXiv:2102.01082 [hep-ph].

[362] N. Crisosto, P. Sikivie, N. S. Sullivan, D. B. Tanner, J. Yang, and G. Rybka, "ADMX SLIC: Results from a Superconducting *LC* Circuit Investigating Cold Axions," *Phys. Rev. Lett.* **124** (2020) no. 24, 241101, arXiv:1911.05772 [astro-ph.CO].

[363] **DMRadio** Collaboration, L. Brouwer *et al.*, "DMRadio-m^3: A Search for the QCD Axion Below 1 μeV," arXiv:2204.13781 [hep-ex].

[364] C. Gatti and S. Tocci, "FLASH: A proposal for a 100-300 MHz haloscope." Talk given at the Workshop on Physics Opportunities at 100-500 MHz Haloscopes, 2022.

[365] A. Díaz-Morcillo, "RADES at babyIAXO in the 400 MHz frequency range." Talk given at the Workshop on Physics Opportunities at 100-500 MHz Haloscopes, 2022.

[366] M. A. Hassan, "Dielectric-loaded cavities for ADMX low-frequency searches." Talk given at the APS April Meeting, 2022.

[367] M. Cicoli, M. Goodsell, and A. Ringwald, "The type IIB string axiverse and its low-energy phenomenology," *JHEP* **10** (2012) 146, arXiv:1206.0819 [hep-th].

[368] C. B. Adams *et al.*, "Axion Dark Matter," in *2022 Snowmass Summer Study*. 3, 2022. arXiv:2203.14923 [hep-ex].

[369] J. E. Moody and F. Wilczek, "New macroscopic forces?," *Phys. Rev. D* **30** (1984) 130.

[370] B. A. Dobrescu and I. Mocioiu, "Spin-dependent macroscopic forces from new particle exchange," *JHEP* **11** (2006) 005, arXiv:hep-ph/0605342.

[371] T. M. Leslie and J. C. Long, "Prospects for electron spin-dependent short-range force experiments with rare earth iron garnet test masses," *Phys. Rev. D* **89** (2014) no. 11, 114022, arXiv:1401.6730 [hep-ph].

[372] F. Ficek, D. F. J. Kimball, M. Kozlov, N. Leefer, S. Pustelny, and D. Budker, "Constraints on exotic spin-dependent interactions between electrons from helium fine-structure spectroscopy," *Phys. Rev. A* **95** (2017) no. 3, 032505, arXiv:1608.05779 [physics.atom-ph].

[373] W. Ji, C. Fu, and H. Gao, "Searching for New Spin-Dependent Interactions with $SmCo_5$ Spin Sources and a SERF Comagnetometer," *Phys. Rev. D* **95** (2017) no. 7, 075014, arXiv:1610.09483 [physics.ins-det].

[374] Q. Wang, Z. Ouyang, Y. Lu, J. Wang, L. Zhu, and P. Luo, "Proposal for the search for exotic spin-spin interactions at the micrometer scale using functionalized cantilever force sensors," *Phys. Rev. D* **107** (2023) no. 1, 015005, arXiv:2212.11546 [hep-ex].

[375] E. G. Adelberger, B. R. Heckel, S. A. Hoedl, C. D. Hoyle, D. J. Kapner, and A. Upadhye, "Particle Physics Implications of a Recent Test of the Gravitational Inverse Sqaure Law," *Phys. Rev. Lett.* **98** (2007) 131104, arXiv:hep-ph/0611223.

[376] G. Vasilakis, J. M. Brown, T. W. Kornack, and M. V. Romalis, "Limits on new long range nuclear spin-dependent forces set with a K - He-3 co-magnetometer," *Phys. Rev. Lett.* **103** (2009) 261801, arXiv:0809.4700 [physics.atom-ph].

[377] M. P. Ledbetter, M. Romalis, and D. F. Jackson-Kimball, "Constraints on short-range spin-dependent interactions from scalar spin-spin coupling in deuterated molecular hydrogen," *Phys. Rev. Lett.* **110** (2013) no. 4, 040402, arXiv:1203.6894 [physics.atom-ph].

[378] V. M. Mostepanenko and G. L. Klimchitskaya, "The State of the Art in Constraining Axion-to-Nucleon Coupling and Non-Newtonian Gravity from Laboratory Experiments," *Universe* **6** (2020) no. 9, 147, arXiv:2009.04517 [hep-ph].

[379] A. Almasi, J. Lee, H. Winarto, M. Smiciklas, and M. V. Romalis, "New Limits on Anomalous Spin-Spin Interactions," *Phys. Rev. Lett.* **125** (2020) no. 20, 201802, arXiv:1811.03614 [physics.atom-ph].

[380] Y. Wang *et al.*, "Limits on Axions and Axionlike Particles within the Axion Window Using a Spin-Based Amplifier," *Phys. Rev. Lett.* **129** (2022) no. 5, 051801, arXiv:2201.11847 [physics.ins-det].

[381] P. W. Graham and S. Rajendran, "New Observables for Direct Detection of Axion Dark Matter," *Phys. Rev.* **D88** (2013) 035023, arXiv:1306.6088 [hep-ph].

[382] A. Garcon *et al.*, "The cosmic axion spin precession experiment (CASPEr): a dark-matter search with nuclear magnetic resonance," *Quantum Sci. Technol.* **3** (2017) no. 1, 014008, arXiv:1707.05312 [physics.ins-det].

[383] A. Garcon *et al.*, "Constraints on bosonic dark matter from ultralow-field nuclear magnetic resonance," *Sci. Adv.* **5** (2019) no. 10, eaax4539, arXiv:1902.04644 [hep-ex].

[384] T. Wu *et al.*, "Search for Axionlike Dark Matter with a Liquid-State Nuclear Spin Comagnetometer," *Phys. Rev. Lett.* **122** (2019) no. 19, 191302, arXiv:1901.10843 [hep-ex].

[385] C. Smorra *et al.*, "Direct limits on the interaction of antiprotons with axion-like dark matter," *Nature* **575** (2019) no. 7782, 310–314, arXiv:2006.00255 [physics.atom-ph].

[386] M. Jiang, H. Su, A. Garcon, X. Peng, and D. Budker, "Search for axion-like dark matter with spin-based amplifiers," *Nature Phys.* **17** (2021) no. 12, 1402–1407, arXiv:2102.01448 [hep-ph].

[387] **NASDUCK** Collaboration, I. M. Bloch, G. Ronen, R. Shaham, O. Katz, T. Volansky, and O. Katz, "New constraints on axion-like dark matter using a Floquet quantum detector," *Sci. Adv.* **8** (2022) no. 5, abl8919, arXiv:2105.04603 [hep-ph].

[388] **NASDUCK** Collaboration, I. M. Bloch, R. Shaham, Y. Hochberg, E. Kuflik, T. Volansky, and O. Katz, "Constraints on axion-like dark matter from a SERF comagnetometer," *Nature Commun.* **14** (2023) no. 1, 5784, arXiv:2209.13588 [hep-ph].

[389] J. Lee, M. Lisanti, W. A. Terrano, and M. Romalis, "Laboratory Constraints on the Neutron-Spin Coupling of feV-Scale Axions," *Phys. Rev. X* **13** (2023) no. 1, 011050, arXiv:2209.03289 [hep-ph].

[390] C. Abel *et al.*, "Search for ultralight axion dark matter in a side-band analysis of a ^{199}Hg free-spin precession signal," *SciPost Phys.* **15** (2023) no. 2, 058, arXiv:2212.02403 [nucl-ex].

[391] K. Wei *et al.*, "Dark matter search with a strongly-coupled hybrid spin system," arXiv:2306.08039 [hep-ph].

[392] Z. Xu *et al.*, "Constraining Ultralight Dark Matter through an Accelerated Resonant Search," arXiv:2309.16600 [hep-ph].

[393] Y. Rosenzweig, Y. Kats, M. Givon, Y. Japha, and R. Folman, "An atomic probe of dark matter differential interactions with elementary particles," arXiv:2312.05894 [hep-ph].

[394] X. Huang, X. Ma, W. Ji, J. Liu, and K. Wei, "Axionlike particle detection in alkali-noble-gas haloscopes," arXiv:2312.09491 [hep-ex].

[395] C. Gao, W. Halperin, Y. Kahn, M. Nguyen, J. Schütte-Engel, and J. W. Scott, "Axion Wind Detection with the Homogeneous Precession Domain of Superfluid Helium-3," *Phys. Rev. Lett.* **129** (2022) no. 21, 211801, arXiv:2208.14454 [hep-ph].

[396] S. Chigusa, D. Kondo, H. Murayama, R. Okabe, and H. Sudo, "Axion detection via superfluid ^{3}He ferromagnetic phase and quantum measurement techniques," arXiv:2309.09160 [hep-ph].

[397] J. W. Foster, C. Gao, W. Halperin, Y. Kahn, A. Mande, M. Nguyen, J. Schütte-Engel, and J. W. Scott, "The statistics and sensitivity of axion wind detection with the homogeneous precession domain of superfluid helium-3," arXiv:2310.07791 [hep-ph].

[398] P. W. Graham, S. Hacıömeroğlu, D. E. Kaplan, Z. Omarov, S. Rajendran, and Y. K. Semertzidis, "Storage ring probes of dark matter and dark energy," *Phys. Rev. D* **103** (2021) no. 5, 055010, arXiv:2005.11867 [hep-ph].

[399] R. Janish and H. Ramani, "Muon g-2 and EDM experiments as muonic dark matter detectors," *Phys. Rev. D* **102** (2020) 115018, arXiv:2006.10069 [hep-ph].

[400] N. N. Nikolaev, "Spin of protons in NICA and PTR storage rings as an axion antenna," *Pisma Zh. Eksp. Teor. Fiz.* **115** (2022) no. 11, 683–684, arXiv:2204.13448 [hep-ph].

[401] **JEDI** Collaboration, S. Karanth *et al.*, "First Search for Axionlike Particles in a Storage Ring Using a Polarized Deuteron Beam," *Phys. Rev. X* **13** (2023) no. 3, 031004, arXiv:2208.07293 [hep-ex].

[402] L. Santamaria, C. Braggio, G. Carugno, V. D. Sarno, P. Maddaloni, and G. Ruoso, "Axion dark matter detection by laser spectroscopy of ultracold molecular oxygen: a proposal," *New J. Phys.* **17** (2015) no. 11, 113025.

[403] C. Braggio *et al.*, "Axion dark matter detection by laser induced fluorescence in rare-earth doped materials," *Sci. Rep.* **7** (2017) no. 1, 15168, arXiv:1707.06103 [astro-ph.CO].

[404] J. D. Vergados, F. T. Avignone, S. Cohen, and R. J. Creswick, "Axion Detection via Atomic Excitations," arXiv:1801.02072 [hep-ph].

[405] A. Mitridate, T. Trickle, Z. Zhang, and K. M. Zurek, "Detectability of Axion Dark Matter with Phonon Polaritons and Magnons," *Phys. Rev. D* **102** (2020) no. 9, 095005, arXiv:2005.10256 [hep-ph].

[406] T. Trickle, Z. Zhang, and K. M. Zurek, "Detecting Light Dark Matter with Magnons," *Phys. Rev. Lett.* **124** (2020) no. 20, 201801, arXiv:1905.13744 [hep-ph].

[407] R. Barbieri, M. Cerdonio, G. Fiorentini, and S. Vitale, "Axion to magnon conversion: a scheme for the detection of galactic axions," *Phys. Lett. B* **226** (1989) 357–360.

[408] F. Caspers and Y. Semertzidis, "Ferrimagnetic Resonance, Magnetostatic Waves, and Open Resonators for Axion Detection," in *Workshop on the Detection of Cosmic Axions*, pp. 0173–183. 6, 1989.

[409] A. I. Kakhidze and I. V. Kolokolov, "Antiferromagnetic axions detector," *Sov. Phys. JETP* **72** (1991) 598–600.

[410] G. Ruoso, A. Lombardi, A. Ortolan, R. Pengo, C. Braggio, G. Carugno, C. S. Gallo, and C. C. Speake, "The QUAX proposal: a search of galactic axion with magnetic materials," *J. Phys. Conf. Ser.* **718** (2016) no. 4, 042051, arXiv:1511.09461 [hep-ph].

[411] R. Barbieri, C. Braggio, G. Carugno, C. S. Gallo, A. Lombardi, A. Ortolan, R. Pengo, G. Ruoso, and C. C. Speake, "Searching for galactic axions through magnetized media: the QUAX proposal," *Phys. Dark Univ.* **15** (2017) 135–141, arXiv:1606.02201 [hep-ph].

[412] S. Dimopoulos, G. D. Starkman, and B. W. Lynn, "Atomic Enhancements in the Detection of Weakly Interacting Particles," *Phys. Lett. B* **168** (1986) 145–150.

[413] M. Pospelov, A. Ritz, and M. B. Voloshin, "Bosonic super-WIMPs as keV-scale dark matter," *Phys. Rev. D* **78** (2008) 115012, arXiv:0807.3279 [hep-ph].

[414] V. A. Dzuba, V. V. Flambaum, and M. Pospelov, "Atomic Ionization by keV-scale Pseudoscalar Dark Matter Particles," *Phys. Rev. D* **81** (2010) 103520, arXiv:1002.2979 [hep-ph].

[415] A. Derevianko, V. A. Dzuba, V. V. Flambaum, and M. Pospelov, "Axio-electric effect," *Phys. Rev. D* **82** (2010) 065006, arXiv:1007.1833 [hep-ph].

[416] F. T. Avignone, III, R. L. Brodzinski, S. Dimopoulos, G. D. Starkman, A. K. Drukier, D. N. Spergel, G. Gelmini, and B. W. Lynn, "Laboratory Limits on Solar Axions From an Ultralow Background Germanium Spectrometer," *Phys. Rev. D* **35** (1987) 2752.

[417] K. Arisaka, P. Beltrame, C. Ghag, J. Kaidi, K. Lung, A. Lyashenko, R. D. Peccei, P. Smith, and K. Ye, "Expected Sensitivity to Galactic/Solar Axions and Bosonic Super-WIMPs based on the Axio-electric Effect in Liquid Xenon Dark Matter Detectors," *Astropart. Phys.* **44** (2013) 59–67, arXiv:1209.3810 [astro-ph.CO].

[418] A. H. Abdelhameed *et al.*, "New limits on the resonant absorption of solar axions obtained with a ^{169}Tm-containing cryogenic detector," *Eur. Phys. J. C* **80** (2020) no. 5, 376, arXiv:2004.08121 [hep-ex].

[419] Y. M. Gavrilyuk *et al.*, "New Constraints on the Axion–Electron Coupling Constant for Solar Axions," *JETP Lett.* **116** (2022) no. 1, 11–17.

[420] I. M. Bloch, R. Essig, K. Tobioka, T. Volansky, and T.-T. Yu, "Searching for Dark Absorption with Direct Detection Experiments," *JHEP* **06** (2017) 087, arXiv:1608.02123 [hep-ph].

[421] A. Mitridate, T. Trickle, Z. Zhang, and K. M. Zurek, "Dark matter absorption via electronic excitations," *JHEP* **09** (2021) 123, arXiv:2106.12586 [hep-ph].

[422] J. C. Slonczewski, "Effect of the axion halo on bound electrons," *Phys. Rev. D* **32** (1985) 3338–3341.

[423] P. F. Smith and J. D. Lewin, "Dark Matter Detection," *Phys. Rept.* **187** (1990) 203.

[424] H. S. Røising, B. Fraser, S. M. Griffin, S. Bandyopadhyay, A. Mahabir, S.-W. Cheong, and A. V. Balatsky, "Axion-matter coupling in multiferroics," *Phys. Rev. Res.* **3** (2021) no. 3, 033236, arXiv:2102.10171 [hep-ph].

[425] A. Balatsky and B. Fraser, "Comment on "Axion-matter coupling in multiferroics"," arXiv:2302.02174 [hep-ph].

[426] S. Alexander and R. Sims, "Detecting axions via induced electron spin precession," *Phys. Rev. D* **98** (2018) no. 1, 015011, arXiv:1702.01459 [hep-ph].

[427] Z. Wang and L. Shao, "Axion induced spin effective couplings," *Phys. Rev. D* **103** (2021) no. 11, 116021, arXiv:2102.04669 [hep-ph].

[428] C. Smith, "On the fermionic couplings of axionic dark matter," arXiv:2302.01142 [hep-ph].

[429] L. Di Luzio, H. Gisbert, and P. Sørensen, "On the oscillating electric dipole moment induced by axion-fermion couplings," arXiv:2308.16135 [hep-ph].

[430] **MADMAX Working Group** Collaboration, A. Caldwell, G. Dvali, B. Majorovits, A. Millar, G. Raffelt, J. Redondo, O. Reimann, F. Simon, and F. Steffen, "Dielectric Haloscopes: A New Way to Detect Axion Dark Matter," *Phys. Rev. Lett.* **118** (2017) no. 9, 091801, arXiv:1611.05865 [physics.ins-det].

[431] A. J. Millar, G. G. Raffelt, J. Redondo, and F. D. Steffen, "Dielectric Haloscopes to Search for Axion Dark Matter: Theoretical Foundations," *JCAP* **01** (2017) 061, arXiv:1612.07057 [hep-ph].

[432] **MADMAX** Collaboration, P. Brun *et al.*, "A new experimental approach to probe QCD axion dark matter in the mass range above 40 μeV," *Eur. Phys. J. C* **79** (2019) no. 3, 186, arXiv:1901.07401 [physics.ins-det].

[433] J. Chiles *et al.*, "New Constraints on Dark Photon Dark Matter with Superconducting Nanowire Detectors in an Optical Haloscope," *Phys. Rev. Lett.* **128** (2022) no. 23, 231802, arXiv:2110.01582 [hep-ex].

[434] L. Manenti *et al.*, "Search for dark photons using a multilayer dielectric haloscope equipped with a single-photon avalanche diode," *Phys. Rev. D* **105** (2022) no. 5, 052010, arXiv:2110.10497 [hep-ex].

[435] J. De Miguel and J. F. Hernández-Cabrera, "Discovery prospects with the Dark-photons and Axion-Like particles Interferometer-part I," arXiv:2303.03997 [hep-ph].

[436] S. Knapen, J. Kozaczuk, and T. Lin, "Dark matter-electron scattering in dielectrics," *Phys. Rev. D* **104** (2021) no. 1, 015031, arXiv:2101.08275 [hep-ph].

[437] Y. Hochberg, Y. Kahn, N. Kurinsky, B. V. Lehmann, T. C. Yu, and K. K. Berggren, "Determining Dark-Matter–Electron Scattering Rates from the Dielectric Function," *Phys. Rev. Lett.* **127** (2021) no. 15, 151802, arXiv:2101.08263 [hep-ph].

[438] S. Knapen, J. Kozaczuk, and T. Lin, "Python package for dark matter scattering in dielectric targets," *Phys. Rev. D* **105** (2022) no. 1, 015014, arXiv:2104.12786 [hep-ph].

[439] C. Boyd, Y. Hochberg, Y. Kahn, E. D. Kramer, N. Kurinsky, B. V. Lehmann, and T. C. Yu, "Directional detection of dark matter with anisotropic response functions," *Phys. Rev. D* **108** (2023) no. 1, 015015, arXiv:2212.04505 [hep-ph].

[440] A. Berlin and T. Trickle, "Absorption of Axion Dark Matter in a Magnetized Medium," arXiv:2305.05681 [hep-ph].

[441] L. L. Foldy and S. A. Wouthuysen, "On the Dirac theory of spin 1/2 particle and its nonrelativistic limit," *Phys. Rev.* **78** (1950) 29–36.

[442] P. W. Graham, D. E. Kaplan, J. Mardon, S. Rajendran, and W. A. Terrano, "Dark Matter Direct Detection with Accelerometers," *Phys. Rev. D* **93** (2016) no. 7, 075029, arXiv:1512.06165 [hep-ph].

[443] A. Pierce, K. Riles, and Y. Zhao, "Searching for Dark Photon Dark Matter with Gravitational Wave Detectors," *Phys. Rev. Lett.* **121** (2018) no. 6, 061102, arXiv:1801.10161 [hep-ph].

[444] **MAGIS-100** Collaboration, M. Abe *et al.*, "Matter-wave Atomic Gradiometer Interferometric Sensor (MAGIS-100)," *Quantum Sci. Technol.* **6** (2021) no. 4, 044003, arXiv:2104.02835 [physics.atom-ph].

[445] A. Arvanitaki, S. Dimopoulos, and K. Van Tilburg, "Sound of Dark Matter: Searching for Light Scalars with Resonant-Mass Detectors," *Phys. Rev. Lett.* **116** (2016) no. 3, 031102, arXiv:1508.01798 [hep-ph].

[446] A. Branca *et al.*, "Search for an Ultralight Scalar Dark Matter Candidate with the AURIGA Detector," *Phys. Rev. Lett.* **118** (2017) no. 2, 021302, arXiv:1607.07327 [hep-ex].

[447] J. Manley, D. Wilson, R. Stump, D. Grin, and S. Singh, "Searching for Scalar Dark Matter with Compact Mechanical Resonators," *Phys. Rev. Lett.* **124** (2020) no. 15, 151301, arXiv:1910.07574 [astro-ph.IM].

[448] D. J. E. Marsh, K.-C. Fong, E. W. Lentz, L. Smejkal, and M. N. Ali, "Proposal to Detect Dark Matter using Axionic Topological Antiferromagnets," *Phys. Rev. Lett.* **123** (2019) no. 12, 121601, arXiv:1807.08810 [hep-ph].

[449] **ALPHA** Collaboration, A. J. Millar *et al.*, "Searching for dark matter with plasma haloscopes," *Phys. Rev. D* **107** (2023) no. 5, 055013, arXiv:2210.00017 [hep-ph].

[450] R. Balafendiev, C. Simovski, A. J. Millar, and P. Belov, "Wire metamaterial filled metallic resonators," *Phys. Rev. B* **106** (2022) no. 7, 075106, arXiv:2203.10083 [hep-ph].

[451] J. Schütte-Engel, D. J. E. Marsh, A. J. Millar, A. Sekine, F. Chadha-Day, S. Hoof, M. N. Ali, K.-C. Fong, E. Hardy, and L. Smejkal, "Axion quasiparticles for axion dark matter detection," *JCAP* **08** (2021) 066, arXiv:2102.05366 [hep-ph].

[452] D. J. E. Marsh, J. I. McDonald, A. J. Millar, and J. Schütte-Engel, "Axion detection with phonon-polaritons revisited," *Phys. Rev. D* **107** (2023) no. 3, 035036, arXiv:2209.12909 [hep-ph].

[453] D. Horns, J. Jaeckel, A. Lindner, A. Lobanov, J. Redondo, and A. Ringwald, "Searching for WISPy Cold Dark Matter with a Dish Antenna," *JCAP* **04** (2013) 016, arXiv:1212.2970 [hep-ph].

[454] A. Caputo, A. J. Millar, C. A. J. O'Hare, and E. Vitagliano, "Dark photon limits: A handbook," *Phys. Rev. D* **104** (2021) no. 9, 095029, arXiv:2105.04565 [hep-ph].

[455] L. D. Landau and E. M. Lifshitz, *Electrodynamics of Continuous Media*. Pergamon, New York, 1984.

[456] S. Chikazumi, *Physics of ferromagnetism*. No. 94 in International Series of Monographs on Physics. Oxford University Press, 1997.

[457] J. M. Coey, *Magnetism and magnetic materials*. Cambridge University Press, 2010.

[458] D. M. Pozar, *Microwave engineering*. John Wiley & Sons, 2011.

[459] R. Sanders, D. Paquette, V. Jaccarino, and S. Rezende, "Radiation damping in magnetic resonance. II. Continuous-wave antiferromagnetic-resonance experiments," *Physical Review B* **10** (1974) no. 1, 132.

[460] G. Wende, "Radiation damping in FMR measurements in a nonresonant rectangular waveguide," *physica status solidi (a)* **36** (1976) no. 2, 557–567.

[461] M. A. Schoen, J. M. Shaw, H. T. Nembach, M. Weiler, and T. Silva, "Radiative damping in waveguide-based ferromagnetic resonance measured via analysis of perpendicular standing spin waves in sputtered permalloy films," *Physical Review B* **92** (2015) no. 18, 184417.

[462] L. Weymann, A. Shuvaev, A. Pimenov, A. A. Mukhin, and D. Szaller, "Magnetic equivalent of electric superradiance in yttrium-iron-garnet films," *Communications Physics* **4** (2021) no. 1, 97.

[463] J. Jaeckel and J. Redondo, "Resonant to broadband searches for cold dark matter consisting of weakly interacting slim particles," *Phys. Rev. D* **88** (2013) no. 11, 115002, arXiv:1308.1103 [hep-ph].

[464] R. Lasenby, "Parametrics of Electromagnetic Searches for Axion Dark Matter," *Phys. Rev. D* **103** (2021) no. 7, 075007, arXiv:1912.11467 [hep-ph].

[465] S. Chaudhuri, "Impedance matching to axion dark matter: considerations of the photon-electron interaction," *JCAP* **12** (2021) no. 12, 033, arXiv:2105.02005 [hep-ph].

[466] S. Emori and P. Li, "Ferrimagnetic insulators for spintronics: Beyond garnets," *Journal of Applied Physics* **129** (01, 2021) 020901.

[467] A. Stupakov, O. Perevertov, and V. Zablotskii, "Dynamical properties of magnetic barkhausen noise in a soft microalloyed steel," *IEEE Transactions on Magnetics* **51** (2015) no. 1, 1–4.

[468] D. Wolf, *Noise in Physical Systems: Proceedings of the Fifth International Conference on Noise, Bad Nauheim, Fed. Rep. of Germany, March 13–16, 1978*. Noise in physical systems : international conference : proceedings. Springer Berlin Heidelberg, 1978.

[469] O. Kypris, I. C. Nlebedim, and D. C. Jiles, "A model for the Barkhausen frequency spectrum as a function of applied stress," *Journal of Applied Physics* **115** (02, 2014) 083906. https://doi.org/10.1063/1.4866195.

[470] L. V. Meisel and P. J. Cote, "Power laws, flicker noise, and the barkhausen effect," *Phys. Rev. B* **46** (Nov, 1992) 10822–10828. https://link.aps.org/doi/10.1103/PhysRevB.46.10822.

[471] G. Manson and G. H. de Visme, "The frequency spectrum of barkhausen noise," *Journal of Physics D: Applied Physics* **5** (aug, 1972) 1389. https://dx.doi.org/10.1088/0022-3727/5/8/305.

[472] B. Cerruti, G. Durin, and S. Zapperi, "Hysteresis and noise in ferromagnetic materials with parallel domain walls," *Phys. Rev. B* **79** (Apr, 2009) 134429. https://link.aps.org/doi/10.1103/PhysRevB.79.134429.

[473] Low Noise Factory, "Cryogenic low noise amplifiers." https://lownoisefactory.com/product-category/cryogenic-amplifier/. Accessed: 2023-10-31.

[474] D. Aybas, H. Bekker, J. W. Blanchard, D. Budker, G. P. Centers, N. L. Figueroa, A. V. Gramolin, D. F. J. Kimball, A. Wickenbrock, and A. O. Sushkov, "Quantum sensitivity limits of nuclear magnetic resonance experiments searching for new fundamental physics," *Quantum Sci. Technol.* **6** (2021) no. 3, 034007, arXiv:2103.06284 [quant-ph].

[475] A. N. Ioannisian, N. Kazarian, A. J. Millar, and G. G. Raffelt, "Axion-photon conversion caused by dielectric interfaces: quantum field calculation," *JCAP* **09** (2017) 005, arXiv:1707.00701 [hep-ph].

[476] J. Egge, "Axion haloscope signal power from reciprocity," *JCAP* **04** (2023) 064, arXiv:2211.11503 [hep-ph].

[477] J. Egge *et al.*, "Experimental determination of axion signal power of dish antennas and dielectric haloscopes using the reciprocity approach," arXiv:2311.13359 [hep-ex].

[478] S. Knirck, J. Schütte-Engel, A. Millar, J. Redondo, O. Reimann, A. Ringwald, and F. Steffen, "A First Look on 3D Effects in Open Axion Haloscopes," *JCAP* **08** (2019) 026, arXiv:1906.02677 [physics.ins-det].

[479] **MADMAX** Collaboration, S. Knirck *et al.*, "Simulating MADMAX in 3D: requirements for dielectric axion haloscopes," *JCAP* **10** (2021) 034, arXiv:2104.06553 [hep-ex].

[480] T. Trickle, "Extended calculation of electronic excitations for direct detection of dark matter," *Phys. Rev. D* **107** (2023) no. 3, 035035, arXiv:2210.14917 [hep-ph].

[481] A. Esposito and S. Pavaskar, "Optimal antiferromagnets for light dark matter detection," *Phys. Rev. D* **108** (2023) no. 1, L011901, arXiv:2210.13516 [hep-ph].

[482] S. Dubovsky and G. Hernández-Chifflet, "Heating up the Galaxy with Hidden Photons," *JCAP* **12** (2015) 054, arXiv:1509.00039 [hep-ph].

[483] E. Hardy and R. Lasenby, "Stellar cooling bounds on new light particles: plasma mixing effects," *JHEP* **02** (2017) 033, arXiv:1611.05852 [hep-ph].

[484] S. Chigusa, A. Ito, K. Nakayama, and V. Takhistov, "Effects of Finite Material Size On Axion-Magnon Conversion," arXiv:2310.17704 [hep-ph].

[485] R. Essig, G. K. Giovanetti, N. Kurinsky, D. McKinsey, K. Ramanathan, K. Stifter, and T.-T. Yu, "Snowmass2021 Cosmic Frontier: The landscape of low-threshold dark matter direct detection in the next decade," in *Snowmass 2021*. 3, 2022. arXiv:2203.08297 [hep-ph].

[486] G. Krnjaic and T. Trickle, "Absorption of vector dark matter beyond kinetic mixing," *Phys. Rev. D* **108** (2023) no. 1, 015024, arXiv:2303.11344 [hep-ph].

[487] A. Caputo, A. J. Millar, and E. Vitagliano, "Revisiting longitudinal plasmon-axion conversion in external magnetic fields," *Phys. Rev. D* **101** (2020) no. 12, 123004, arXiv:2005.00078 [hep-ph].

[488] G. B. Gelmini, V. Takhistov, and E. Vitagliano, "Scalar direct detection: In-medium effects," *Phys. Lett. B* **809** (2020) 135779, arXiv:2006.13909 [hep-ph].

[489] G. B. Gelmini, A. J. Millar, V. Takhistov, and E. Vitagliano, "Probing dark photons with plasma haloscopes," *Phys. Rev. D* **102** (2020) no. 4, 043003, arXiv:2006.06836 [hep-ph].

[490] J. S. R. Chisholm, "Change of variables in quantum field theories," *Nucl. Phys.* **26** (1961) no. 3, 469–479.

[491] S. Kamefuchi, L. O'Raifeartaigh, and A. Salam, "Change of variables and equivalence theorems in quantum field theories," *Nucl. Phys.* **28** (1961) 529–549.

[492] I. B. Khriplovich and S. K. Lamoreaux, *CP violation without strangeness: electric dipole moments of particles, atoms, and molecules*. Springer Science & Business Media, 2012.

[493] Y. V. Stadnik and V. V. Flambaum, "Axion-induced effects in atoms, molecules, and nuclei: Parity nonconservation, anapole moments, electric dipole moments, and spin-gravity and spin-axion momentum couplings," *Phys. Rev. D* **89** (2014) no. 4, 043522, arXiv:1312.6667 [hep-ph].

[494] M. Kawasaki, K. Saikawa, and T. Sekiguchi, "Axion dark matter from topological defects," *Phys. Rev. D* **91** (2015) no. 6, 065014, arXiv:1412.0789 [hep-ph].

[495] A. Vaquero, J. Redondo, and J. Stadler, "Early seeds of axion miniclusters," *JCAP* **04** (2019) 012, arXiv:1809.09241 [astro-ph.CO].

[496] V. B. Klaer and G. D. Moore, "The dark-matter axion mass," *JCAP* **11** (2017) 049, arXiv:1708.07521 [hep-ph].

[497] M. Buschmann, J. W. Foster, and B. R. Safdi, "Early-Universe Simulations of the Cosmological Axion," *Phys. Rev. Lett.* **124** (2020) no. 16, 161103, arXiv:1906.00967 [astro-ph.CO].

[498] M. Gorghetto, E. Hardy, and G. Villadoro, "Axions from Strings: the Attractive Solution," *JHEP* **07** (2018) 151, arXiv:1806.04677 [hep-ph].

[499] M. Kawasaki, T. Sekiguchi, M. Yamaguchi, and J. Yokoyama, "Long-term dynamics of cosmological axion strings," *PTEP* **2018** (2018) no. 9, 091E01, arXiv:1806.05566 [hep-ph].

[500] C. A. J. O'Hare, G. Pierobon, J. Redondo, and Y. Y. Y. Wong, "Simulations of axionlike particles in the postinflationary scenario," *Phys. Rev. D* **105** (2022) no. 5, 055025, arXiv:2112.05117 [hep-ph].

[501] M. Buschmann, J. W. Foster, A. Hook, A. Peterson, D. E. Willcox, W. Zhang, and B. R. Safdi, "Dark matter from axion strings with adaptive mesh refinement," *Nature Commun.* **13** (2022) no. 1, 1049, arXiv:2108.05368 [hep-ph].

[502] A. V. Dixit, S. Chakram, K. He, A. Agrawal, R. K. Naik, D. I. Schuster, and A. Chou, "Searching for Dark Matter with a Superconducting Qubit," *Phys. Rev. Lett.* **126** (2021) no. 14, 141302, arXiv:2008.12231 [hep-ex].

[503] E. Graham *et al.*, "Rydberg-atom-based single-photon detection for haloscope axion searches," arXiv:2310.15352 [hep-ex].

[504] **BREAD** Collaboration, J. Liu *et al.*, "Broadband Solenoidal Haloscope for Terahertz Axion Detection," *Phys. Rev. Lett.* **128** (2022) no. 13, 131801, arXiv:2111.12103 [physics.ins-det].

[505] C. A. Thomson, M. Goryachev, B. T. McAllister, E. N. Ivanov, P. Altin, and M. E. Tobar, "Searching for low-mass axions using resonant upconversion," *Phys. Rev. D* **107** (2023) no. 11, 112003, arXiv:2301.06778 [hep-ex].

[506] J. D. Jackson, *Classical Electrodynamics*. Wiley, 1999.

[507] C. W. Misner, K. S. Thorne, and J. A. Wheeler, *Gravitation*. Macmillan, 1973.

[508] J. Nicolas, "Microwave ferrites," in *Handbook of Ferromagnetic Materials*, vol. 2, ch. 4, pp. 243–296. Elsevier, 1980.

[509] A. B. Fuller, *Ferrites at microwave frequencies*. No. 23 in Electromagnetic Waves Series. IET, 1987.

[510] G. F. Dionne, *Magnetic oxides*, vol. 14. Springer, 2009.

[511] Ü. Özgür, Y. Alivov, and H. Morkoç, "Microwave ferrites, part 1: fundamental properties," *Journal of materials science: Materials in electronics* **20** (2009) 789–834.

[512] H. Maier-Flaig, S. Klingler, C. Dubs, O. Surzhenko, R. Gross, M. Weiler, H. Huebl, and S. T. B. Goennenwein, "Temperature-dependent magnetic damping of yttrium iron garnet spheres," *Phys. Rev. B* **95** (Jun, 2017) 214423.

[513] S. Klingler, H. Maier-Flaig, C. Dubs, O. Surzhenko, R. Gross, H. Huebl, S. T. B. Goennenwein, and M. Weiler, "Gilbert damping of magnetostatic modes in a yttrium iron garnet sphere," *Applied Physics Letters* **110** (03, 2017) 092409.

[514] J. Krupka, P. Aleshkevych, B. Salski, and P. Kopyt, "Ferromagnetic linewidth measurements employing electrodynamic model of the magnetic plasmon resonance," *Measurement Science and Technology* **29** (jan, 2018) 025501.

[515] A. Pacewicz, J. Krupka, B. Salski, P. Aleshkevych, and P. Kopyt, "Rigorous broadband study of the intrinsic ferromagnetic linewidth of monocrystalline garnet spheres," *Scientific Reports* **9** (2019) no. 1, 9434.

[516] E. G. Spencer, R. C. LeCraw, and A. M. Clogston, "Low-temperature line-width maximum in yttrium iron garnet," *Phys. Rev. Lett.* **3** (Jul, 1959) 32–33.

[517] E. G. Spencer, R. C. LeCraw, and R. C. Linares, "Low-temperature ferromagnetic relaxation in yttrium iron garnet," *Phys. Rev.* **123** (Sep, 1961) 1937–1938.

[518] I. Boventer, M. Pfirrmann, J. Krause, Y. Schön, M. Kläui, and M. Weides, "Complex temperature dependence of coupling and dissipation of cavity magnon polaritons from millikelvin to room temperature," *Phys. Rev. B* **97** (May, 2018) 184420.

[519] M. Pfirrmann, I. Boventer, A. Schneider, T. Wolz, M. Kläui, A. V. Ustinov, and M. Weides, "Magnons at low excitations: Observation of incoherent coupling to a bath of two-level systems," *Phys. Rev. Res.* **1** (Nov, 2019) 032023.

[520] Q. H. F. Vrehen, "Absorption and Dispersion in Porous and Anisotropic Polycrystalline Ferrites at Microwave Frequencies," *Journal of Applied Physics* **40** (11, 2003) 1849–1860.

[521] C. Patton, "A review of microwave relaxation in polycrystalline ferrites," *IEEE Transactions on Magnetics* **8** (1972) no. 3, 433–439.

[522] G. White and C. Patton, "Magnetic properties of lithium ferrite microwave materials," *Journal of Magnetism and Magnetic Materials* **9** (1978) no. 4, 299–317.

[523] N. Mo, J. J. Green, P. Krivosik, and C. E. Patton, "The low field microwave effective linewidth in polycrystalline ferrites," *Journal of Applied Physics* **101** (01, 2007) 023914.

[524] P. Strange, *Relativistic Quantum Mechanics: with applications in condensed matter and atomic physics*. Cambridge University Press, 1998.

[525] V. B. Berestetskii, E. M. Lifshitz, and L. P. Pitaevskii, *Quantum Electrodynamics*, vol. 4 of *Course of Theoretical Physics*. Butterworth-Heinemann, 1982.

[526] S. Balk, J. G. Korner, and D. Pirjol, "Heavy quark effective theory at large orders in $1/m$," *Nucl. Phys. B* **428** (1994) 499–528, `arXiv:hep-ph/9307230`.

[527] A. Gardestig, K. Kubodera, and F. Myhrer, "Comparison of the heavy-fermion and Foldy-Wouthuysen formalisms at third order," *Phys. Rev. C* **76** (2007) 014005, `arXiv:0705.2885 [nucl-th]`.

[528] F. J. Dyson, "The interactions of nucleons with meson fields," *Phys. Rev.* **73** (Apr, 1948) 929–930.

[529] M. Slotnick and W. Heitler, "The charge density and magnetic moments of the nucleons," *Phys. Rev.* **75** (Jun, 1949) 1645–1663.

[530] K. M. Case, "Equivalence theorems for meson-nucleon couplings," *Phys. Rev.* **76** (Jul, 1949) 14–17.

[531] J. M. Berger, L. L. Foldy, and R. K. Osborn, "Equivalence theorems for pseudoscalar coupling," *Phys. Rev.* **87** (Sep, 1952) 1061–1065.

[532] S. D. Drell and E. M. Henley, "Pseudoscalar mesons with applications to meson-nucleon scattering and photoproduction," *Phys. Rev.* **88** (Dec, 1952) 1053–1064.

[533] G. Raffelt and D. Seckel, "Bounds on Exotic Particle Interactions from SN 1987a," *Phys. Rev. Lett.* **60** (1988) 1793.

[534] M. Carena and R. D. Peccei, "The Effective Lagrangian for Axion Emission From SN1987A," *Phys. Rev. D* **40** (1989) 652.

[535] K. Choi, K. Kang, and J. E. Kim, "Invisible Axion Emissions From SN1987A," *Phys. Rev. Lett.* **62** (1989) 849.

[536] C. Arzt, "Reduced effective Lagrangians," *Phys. Lett. B* **342** (1995) 189–195, arXiv:hep-ph/9304230.

[537] I.-T. Cheon, "Foldy Transformation in the π-Nucleus Interaction," *Progress of Theoretical Physics Supplement* **E68** (07, 1968) 146–155.

[538] M. V. Barnhill, "Ambiguity of the "Galilean-invariant" operator for pion absorption by nuclei," *Nuclear Physics A* **131** (1969) no. 1, 106–112.

[539] J. L. Friar, "Pion-nucleon absorption operator ambiguity," *Phys. Rev. C* **10** (1974) 955–957.

[540] E. De Vries, "Foldy-Wouthuysen transformations and related problems," *Fortsch. Phys.* **18** (1970) 149–182.

[541] J. P. Costella and B. H. J. McKellar, "The Foldy-Wouthuysen transformation," *Am. J. Phys.* **63** (1995) 1119, arXiv:hep-ph/9503416.

[542] J. H. Smith, E. M. Purcell, and N. F. Ramsey, "Experimental limit to the electric dipole moment of the neutron," *Phys. Rev.* **108** (1957) 120–122.

[543] R. L. Garwin and L. M. Lederman, "The electric dipole moment of elementary particles," *Il Nuovo Cimento (1955-1965)* **11** (1959) 776–780.

[544] T. Chupp, P. Fierlinger, M. Ramsey-Musolf, and J. Singh, "Electric dipole moments of atoms, molecules, nuclei, and particles," *Rev. Mod. Phys.* **91** (2019) no. 1, 015001, arXiv:1710.02504 [physics.atom-ph].

[545] R. Alarcon *et al.*, "Electric dipole moments and the search for new physics," in *Snowmass 2021*. 3, 2022. arXiv:2203.08103 [hep-ph].

[546] G. R. Burleson and H. Kendall, "An experimental search for dipole structure of the electron," *Nuclear Physics* **19** (1960) 68–78.

[547] J. Goldemberg and Y. Torizuka, "Upper limit of the electric dipole moment of the electron," *Phys. Rev.* **129** (Mar, 1963) 2580–2581.

[548] R. E. Rand, "Determination of the upper limit to the electric dipole moment of the electron at high momentum transfer," *Phys. Rev.* **140** (Dec, 1965) B1605–B1610.

[549] D. Berley, R. L. Garwin, G. Gidal, and L. M. Lederman, "Electric dipole moment of the muon," *Phys. Rev. Lett.* **1** (Oct, 1958) 263–263.

[550] D. F. Nelson, A. A. Schupp, R. W. Pidd, and H. R. Crane, "Search for an electric dipole moment of the electron," *Phys. Rev. Lett.* **2** (Jun, 1959) 492–495.

[551] D. Berley and G. Gidal, "Search for an electric dipole moment structure of the muon," *Phys. Rev.* **118** (May, 1960) 1086–1091.

[552] G. Charpak, F. Parley, R. L. Garwin, T. Muller, J. C. Sens, and A. Zichighi, "A new limit to the electric dipole moment of the muon," *Il Nuovo Cimento (1955-1965)* **22** (1961) no. 5, 1043–1050.

[553] G. Feinberg, "Effects of an electric dipole moment of the electron on the hydrogen energy levels," *Phys. Rev.* **112** (Dec, 1958) 1637–1642.

[554] E. E. Salpeter, "Some atomic effects of an electronic electric dipole moment," *Phys. Rev.* **112** (Dec, 1958) 1642–1648.

[555] P. Sandars, "The electric dipole moment of an atom," *Physics Letters* **14** (1965) no. 3, 194–196.

[556] P. G. H. Sandars, "The electric-dipole moments of an atom II. The contribution from an electric-dipole moment on the electron with particular reference to the hydrogen atom," *Journal of Physics B: Atomic and Molecular Physics* **1** (May, 1968) 511.

[557] E. D. Commins, J. D. Jackson, and D. P. DeMille, "The electric dipole moment of the electron: An intuitive explanation for the evasion of Schiff's theorem," *American Journal of Physics* **75** (06, 2007) 532–536.

[558] A. Berlin and K. Zhou, "Discovering QCD-coupled axion dark matter with polarization haloscopes," *Phys. Rev. D* **108** (2023) no. 3, 035038, `arXiv:2209.12901 [hep-ph]`.

[559] G. Bertone and M. Fairbairn, "Compact Stars as Dark Matter Probes," *Phys. Rev. D* **77** (2008) 043515, `arXiv:0709.1485 [astro-ph]`.

[560] C. Kouvaris, "WIMP Annihilation and Cooling of Neutron Stars," *Phys. Rev. D* **77** (2008) 023006, arXiv:0708.2362 [astro-ph].

[561] M. Baryakhtar, J. Bramante, S. W. Li, T. Linden, and N. Raj, "Dark Kinetic Heating of Neutron Stars and An Infrared Window On WIMPs, SIMPs, and Pure Higgsinos," *Phys. Rev. Lett.* **119** (2017) no. 13, 131801, arXiv:1704.01577 [hep-ph].

[562] R. K. Leane and J. Smirnov, "Exoplanets as Sub-GeV Dark Matter Detectors," *Phys. Rev. Lett.* **126** (2021) no. 16, 161101, arXiv:2010.00015 [hep-ph].

[563] F. Iocco, M. Taoso, F. Leclercq, and G. Meynet, "Main sequence stars with asymmetric dark matter," *Phys. Rev. Lett.* **108** (2012) 061301, arXiv:1201.5387 [astro-ph.SR].

[564] J. Casanellas and I. Lopes, "First asteroseismic limits on the nature of dark matter," *Astrophys. J. Lett.* **765** (2013) L21, arXiv:1212.2985 [astro-ph.SR].

[565] I. Goldman and S. Nussinov, "Weakly Interacting Massive Particles and Neutron Stars," *Phys. Rev. D* **40** (1989) 3221–3230.

[566] J. F. Acevedo, J. Bramante, A. Goodman, J. Kopp, and T. Opferkuch, "Dark Matter, Destroyer of Worlds: Neutrino, Thermal, and Existential Signatures from Black Holes in the Sun and Earth," arXiv:2012.09176 [hep-ph].

[567] B. Dasgupta, R. Laha, and A. Ray, "Low Mass Black Holes from Dark Core Collapse," *Phys. Rev. Lett.* **126** (2021) no. 14, 141105, arXiv:2009.01825 [astro-ph.HE].

[568] G. G. Raffelt, *Stars as laboratories for fundamental physics: The astrophysics of neutrinos, axions, and other weakly interacting particles*. University of Chicago press, 1996.

[569] D. M. Jacobs, G. D. Starkman, and B. W. Lynn, "Macro Dark Matter," *Mon. Not. Roy. Astron. Soc.* **450** (2015) no. 4, 3418–3430, arXiv:1410.2236 [astro-ph.CO].

[570] S. Burdin, M. Fairbairn, P. Mermod, D. Milstead, J. Pinfold, T. Sloan, and W. Taylor, "Non-collider searches for stable massive particles," *Phys. Rept.* **582** (2015) 1–52, arXiv:1410.1374 [hep-ph].

[571] Y. Bai, A. J. Long, and S. Lu, "Tests of Dark MACHOs: Lensing, Accretion, and Glow," *JCAP* **09** (2020) 044, arXiv:2003.13182 [astro-ph.CO].

[572] D. M. Grabowska, T. Melia, and S. Rajendran, "Detecting Dark Blobs," *Phys. Rev. D* **98** (2018) no. 11, 115020, arXiv:1807.03788 [hep-ph].

[573] D. Budker, V. V. Flambaum, X. Liang, and A. Zhitnitsky, "Axion Quark Nuggets and how a Global Network can discover them," *Phys. Rev. D* **101** (2020) no. 4, 043012, arXiv:1909.09475 [hep-ph].

[574] J. Singh Sidhu, R. M. Abraham, C. Covault, and G. Starkman, "Macro detection using fluorescence detectors," *JCAP* **02** (2019) 037, arXiv:1808.06978 [astro-ph.HE].

[575] J. S. Sidhu and G. Starkman, "Macroscopic Dark Matter Constraints from Bolide Camera Networks," *Phys. Rev. D* **100** (2019) no. 12, 123008, arXiv:1908.00557 [astro-ph.CO].

[576] L. W. Piotrowski, K. Małek, L. Mankiewicz, M. Sokołowski, G. Wrochna, A. Zadrożny, and A. F. Żarnecki, "Limits on the Flux of Nuclearites and Other Heavy Compact Objects from the Pi of the Sky Project," *Phys. Rev. Lett.* **125** (2020) no. 9, 091101, arXiv:2008.01285 [astro-ph.HE].

[577] E. T. Herrin, D. C. Rosenbaum, and V. L. Teplitz, "Seismic search for strange quark nuggets," *Phys. Rev. D* **73** (2006) 043511, arXiv:astro-ph/0505584.

[578] D. Cyncynates, J. Chiel, J. Sidhu, and G. D. Starkman, "Reconsidering seismological constraints on the available parameter space of macroscopic dark matter," *Phys. Rev. D* **95** (2017) no. 6, 063006, arXiv:1610.09680 [astro-ph.CO]. [Addendum: Phys.Rev.D 95, 129903 (2017)].

[579] S. Abbas and A. Abbas, "Volcanogenic dark matter and mass extinctions," *Astropart. Phys.* **8** (1998) 317–320, arXiv:astro-ph/9612214.

[580] J. Rafelski, L. Labun, and J. Birrell, "Compact Ultradense Matter Impactors," *Phys. Rev. Lett.* **110** (2013) no. 11, 111102, arXiv:1104.4572 [astro-ph.EP].

[581] K. M. Zurek, "Asymmetric Dark Matter: Theories, Signatures, and Constraints," *Phys. Rept.* **537** (2014) 91–121, arXiv:1308.0338 [hep-ph].

[582] E. Hardy, R. Lasenby, J. March-Russell, and S. M. West, "Big Bang Synthesis of Nuclear Dark Matter," *JHEP* **06** (2015) 011, arXiv:1411.3739 [hep-ph].

[583] M. I. Gresham, H. K. Lou, and K. M. Zurek, "Early Universe synthesis of asymmetric dark matter nuggets," *Phys. Rev. D* **97** (2018) no. 3, 036003, arXiv:1707.02316 [hep-ph].

[584] C. Kouvaris and N. G. Nielsen, "Asymmetric Dark Matter Stars," *Phys. Rev. D* **92** (2015) no. 6, 063526, arXiv:1507.00959 [hep-ph].

[585] M. I. Gresham, H. K. Lou, and K. M. Zurek, "Astrophysical Signatures of Asymmetric Dark Matter Bound States," *Phys. Rev. D* **98** (2018) no. 9, 096001, arXiv:1805.04512 [hep-ph].

[586] J. H. Chang, D. Egana-Ugrinovic, R. Essig, and C. Kouvaris, "Structure Formation and Exotic Compact Objects in a Dissipative Dark Sector," *JCAP* **03** (2019) 036, arXiv:1812.07000 [hep-ph].

[587] M. R. Buckley and A. DiFranzo, "Collapsed Dark Matter Structures," *Phys. Rev. Lett.* **120** (2018) no. 5, 051102, arXiv:1707.03829 [hep-ph].

[588] G. Krnjaic and K. Sigurdson, "Big Bang Darkleosynthesis," *Phys. Lett. B* **751** (2015) 464–468, arXiv:1406.1171 [hep-ph].

[589] W. Detmold, M. McCullough, and A. Pochinsky, "Dark Nuclei I: Cosmology and Indirect Detection," *Phys. Rev. D* **90** (2014) no. 11, 115013, arXiv:1406.2276 [hep-ph].

[590] R. Foot, "Mirror matter-type dark matter," *Int. J. Mod. Phys. D* **13** (2004) 2161–2192, arXiv:astro-ph/0407623.

[591] Z. Berezhiani, S. Cassisi, P. Ciarcelluti, and A. Pietrinferni, "Evolutionary and structural properties of mirror star MACHOs," *Astropart. Phys.* **24** (2006) 495–510, arXiv:astro-ph/0507153.

[592] G. D'Amico, P. Panci, A. Lupi, S. Bovino, and J. Silk, "Massive Black Holes from Dissipative Dark Matter," *Mon. Not. Roy. Astron. Soc.* **473** (2018) no. 1, 328–335, arXiv:1707.03419 [astro-ph.CO].

[593] D. Curtin and J. Setford, "Signatures of Mirror Stars," *JHEP* **03** (2020) 041, arXiv:1909.04072 [hep-ph].

[594] E. Witten, "Cosmic separation of phases," *Physical Review D* **30** (1984) no. 2, 272.

[595] J. A. Frieman, G. Gelmini, M. Gleiser, and E. W. Kolb, "Solitogenesis: Primordial Origin of Nontopological Solitons," *Phys. Rev. Lett.* **60** (1988) 2101.

[596] Y. Bai, A. J. Long, and S. Lu, "Dark Quark Nuggets," *Phys. Rev. D* **99** (2019) no. 5, 055047, arXiv:1810.04360 [hep-ph].

[597] C. Gross, G. Landini, A. Strumia, and D. Teresi, "Dark Matter as dark dwarfs and other macroscopic objects: multiverse relics?," arXiv:2105.02840 [hep-ph].

[598] B. Paxton, L. Bildsten, A. Dotter, F. Herwig, P. Lesaffre, and F. Timmes, "Modules for Experiments in Stellar Astrophysics (MESA)," *The Astrophysical Journal Supplement* **192** (jan, 2011) 3, arXiv:1009.1622 [astro-ph.SR].

[599] B. Paxton, M. Cantiello, P. Arras, L. Bildsten, E. F. Brown, A. Dotter, C. Mankovich, M. H. Montgomery, D. Stello, F. X. Timmes, and R. Townsend, "Modules for Experiments in Stellar Astrophysics (MESA): Planets, Oscillations, Rotation, and Massive Stars," *The Astrophysical Journal Supplement* **208** (sep, 2013) 4, arXiv:1301.0319 [astro-ph.SR].

[600] B. Paxton, P. Marchant, J. Schwab, E. B. Bauer, L. Bildsten, M. Cantiello, L. Dessart, R. Farmer, H. Hu, N. Langer, R. H. D. Townsend, D. M. Townsley, and F. X. Timmes, "Modules for Experiments in Stellar Astrophysics (MESA): Binaries, Pulsations, and Explosions," *The Astrophysical Journal Supplement* **220** (sep, 2015) 15, arXiv:1506.03146 [astro-ph.SR].

[601] B. Paxton, J. Schwab, E. B. Bauer, L. Bildsten, S. Blinnikov, P. Duffell, R. Farmer, J. A. Goldberg, P. Marchant, E. Sorokina, A. Thoul, R. H. D. Townsend, and F. X. Timmes, "Modules for Experiments in Stellar Astrophysics (MESA): Convective Boundaries, Element Diffusion, and Massive Star Explosions," *The Astrophysical Journal Supplement* **234** (feb, 2018) 34, arXiv:1710.08424 [astro-ph.SR].

[602] B. Paxton, R. Smolec, J. Schwab, A. Gautschy, L. Bildsten, M. Cantiello, A. Dotter, R. Farmer, J. A. Goldberg, A. S. Jermyn, S. M. Kanbur, P. Marchant, A. Thoul, R. H. D. Townsend, W. M. Wolf, M. Zhang, and F. X. Timmes, "Modules for Experiments in Stellar Astrophysics (MESA): Pulsating Variable Stars, Rotation, Convective Boundaries, and Energy Conservation," *The Astrophysical Journal Supplement* **243** (Jul, 2019) 10, arXiv:1903.01426 [astro-ph.SR].

[603] J. Choi, A. Dotter, C. Conroy, M. Cantiello, B. Paxton, and B. D. Johnson, "Mesa Isochrones and Stellar Tracks (MIST). I. Solar-scaled Models," *The Astrophysical Journal* **823** (June, 2016) 102, arXiv:1604.08592 [astro-ph.SR].

[604] T. O. Husser, S. Wende-von Berg, S. Dreizler, D. Homeier, A. Reiners, T. Barman, and P. H. Hauschildt, "A new extensive library of PHOENIX stellar atmospheres and synthetic spectra," *Astronomy & Astrophysics* **553** (May, 2013) A6, arXiv:1303.5632 [astro-ph.SR].

[605] A. Bailey and J. Hiatt, "Sphere drag coefficients for a broad range of mach and reynolds numbers," *AIAA Journal* **10** (1972) no. 11, 1436–1440.

[606] D. O. ReVelle, "On meteor-generated infrasound," *Journal of Geophysical Research* **81** (1976) no. 7, 1217–1230.

[607] E. A. Silber and P. G. Brown, "Optical observations of meteors generating infrasound-I: Acoustic signal identification and phenomenology," *Journal of Atmospheric and Solar-Terrestrial Physics* **119** (Nov., 2014) 116–128, arXiv:1407.6331 [physics.ao-ph].

[608] G. Whitham, "On the propagation of weak shock waves," *Journal of Fluid Mechanics* **1** (1956) no. 3, 290–318.

[609] A. D. Pierce, *Acoustics: an introduction to its physical principles and applications*. Springer, 2019.

[610] A. Sakurai, "On the problem of a shock wave arriving at the edge of a gas," *Communs. Pure and Appl. Math.* **13** (1960) .

[611] E. Quataert and J. Shiode, "Wave-driven mass loss in the last year of stellar evolution: setting the stage for the most luminous core-collapse supernovae," *MNRAS* **423** (June, 2012) L92–L96, arXiv:1202.5036 [astro-ph.SR].

[612] S. Ro and C. D. Matzner, "Shock Dynamics in Stellar Outbursts: I. Shock formation," *Astrophys. J.* **841** (2017) no. 1, 9, arXiv:1612.08997 [astro-ph.SR].

[613] J. Fuller and S. Ro, "Pre-supernova outbursts via wave heating in massive stars - II. Hydrogen-poor stars," *MNRAS* **476** (May, 2018) 1853–1868, arXiv:1710.04251 [astro-ph.SR].

[614] C. D. Matzner and S. Ro, "Wave-driven shocks in stellar outbursts: Dynamics, envelope heating, and nascent blast waves," *The Astrophysical Journal* **908** (Feb, 2021) 23. http://dx.doi.org/10.3847/1538-4357/abd03b.

[615] I. Linial, J. Fuller, and R. Sari, "Partial stellar explosions - ejected mass and minimal energy," *MNRAS* **501** (Mar., 2021) 4266–4275, arXiv:2011.12965 [astro-ph.HE].

[616] A. Gould, "Resonant enhancements in weakly interacting massive particle capture by the earth," *The Astrophysical Journal* **321** (1987) 571–585.

[617] I. Sagiv, A. Gal-Yam, E. O. Ofek, E. Waxman, O. Aharonson, S. R. Kulkarni, E. Nakar, D. Maoz, B. Trakhtenbrot, E. S. Phinney, J. Topaz, C. Beichman, J. Murthy, and S. P. Worden, "Science with a Wide-field UV Transient Explorer," *The Astronomical Journal* **147** (Apr., 2014) 79, arXiv:1303.6194 [astro-ph.CO].

[618] Ž. Ivezić, S. M. Kahn, J. A. Tyson, B. Abel, E. Acosta, R. Allsman, D. Alonso, Y. AlSayyad, S. F. Anderson, J. Andrew, J. R. P. Angel, G. Z. Angeli, R. Ansari, P. Antilogus, C. Araujo, R. Armstrong, K. T. Arndt, *et al.*, "LSST: From Science Drivers to Reference Design and Anticipated Data Products," *The Astrophysical Journal* **873** (Mar., 2019) 111, arXiv:0805.2366 [astro-ph].

[619] G. R. Ricker, J. N. Winn, R. Vanderspek, D. W. Latham, G. Á. Bakos, J. L. Bean, Z. K. Berta-Thompson, T. M. Brown, L. Buchhave, N. R. Butler, R. P. Butler, W. J. Chaplin, D. Charbonneau, J. Christensen-Dalsgaard, M. Clampin, *et al.*, "Transiting Exoplanet Survey Satellite (TESS)," in *Space Telescopes and Instrumentation 2014: Optical, Infrared, and Millimeter Wave*, J. Oschmann, Jacobus M., M. Clampin, G. G. Fazio, and H. A. MacEwen, eds., vol. 9143 of *Society of Photo-Optical Instrumentation Engineers (SPIE) Conference Series*, p. 914320. Aug., 2014. arXiv:1406.0151 [astro-ph.EP].

[620] H. Rauer *et al.*, "The plato 2.0 mission," arXiv:1310.0696 [astro-ph.EP].

[621] J. R. A. Davenport, "The kepler catalog of stellar flares," *The Astrophysical Journal* **829** (Sep, 2016) 23. http://dx.doi.org/10.3847/0004-637X/829/1/23.

[622] S. Okamoto, Y. Notsu, H. Maehara, K. Namekata, S. Honda, K. Ikuta, D. Nogami, and K. Shibata, "Statistical Properties of Superflares on Solar-type Stars: Results Using All of the Kepler Primary Mission Data," *The Astrophysical Journal* **906** (Jan., 2021) 72, arXiv:2011.02117 [astro-ph.SR].

[623] M. N. Günther, Z. Zhan, S. Seager, P. B. Rimmer, S. Ranjan, K. G. Stassun, R. J. Oelkers, T. Daylan, E. Newton, M. H. Kristiansen, K. Olah, E. Gillen, S. Rappaport, G. R. Ricker, R. K. Vanderspek, D. W. Latham, J. N. Winn, J. M. Jenkins, A. Glidden, M. Fausnaugh, A. M. Levine, J. A. Dittmann, S. N. Quinn, A. Krishnamurthy, and E. B. Ting, "Stellar Flares from the First TESS Data Release: Exploring a New Sample of M Dwarfs," *The Astronomical Journal* **159** (Feb., 2020) 60, arXiv:1901.00443 [astro-ph.EP].

[624] E. F. Schlafly and D. P. Finkbeiner, "Measuring Reddening with Sloan Digital Sky Survey Stellar Spectra and Recalibrating SFD," *The Astrophysical Journal* **737** (Aug., 2011) 103, arXiv:1012.4804 [astro-ph.GA].

[625] B. Moore, "Constraints on the global mass-to-light ratios and on the extent of dark matter halos in globular clusters and dwarf spheroidals," *The Astrophysical Journal Letters* **461** (1996) no. 1, L13.

[626] R. Ibata, C. Nipoti, A. Sollima, M. Bellazzini, S. Chapman, and E. Dalessandro, "Do globular clusters possess Dark Matter halos? A case study in NGC 2419," *Mon. Not. Roy. Astron. Soc.* **428** (2013) 3648, arXiv:1210.7787 [astro-ph.CO].

[627] P. J. E. Peebles, "Dark matter and the origin of galaxies and globular star clusters," *Astrophys. J.* **277** (1984) 470–477.

[628] P. Creasey, L. V. Sales, E. W. Peng, and O. Sameie, "Globular clusters formed within dark haloes I: present-day abundance, distribution, and kinematics," *Mon. Not. Roy. Astron. Soc.* **482** (2019) no. 1, 219–230, arXiv:1806.11118 [astro-ph.GA].

[629] B. F. Griffen, M. J. Drinkwater, P. A. Thomas, J. C. Helly, and K. A. Pimbblet, "Globular cluster formation within the Aquarius simulation," *MNRAS* **405** (June, 2010) 375–386, arXiv:0910.0310 [astro-ph.GA].

[630] T. R. Saitoh, J. Koda, T. Okamoto, K. Wada, and A. Habe, "Tidal disruption of dark matter halos around proto-globular clusters," *Astrophys. J.* **640** (2006) 22–30, arXiv:astro-ph/0511692.

[631] L. Gao, S. D. M. White, A. Jenkins, F. Stoehr, and V. Springel, "The subhalo populations of ΛCDM dark haloes," *MNRAS* **355** (Dec., 2004) 819–834, arXiv:astro-ph/0404589 [astro-ph].

[632] J. F. Navarro, C. S. Frenk, and S. D. M. White, "The Structure of cold dark matter halos," *Astrophys. J.* **462** (1996) 563–575, arXiv:astro-ph/9508025.

[633] D. Merritt, "Evolution of the dark matter distribution at the galactic center," *Phys. Rev. Lett.* **92** (2004) 201304, arXiv:astro-ph/0311594.

[634] R. K. Leane, T. Linden, P. Mukhopadhyay, and N. Toro, "Celestial-Body Focused Dark Matter Annihilation Throughout the Galaxy," arXiv:2101.12213 [astro-ph.HE].

[635] G. R. Blumenthal, S. M. Faber, R. Flores, and J. R. Primack, "Contraction of Dark Matter Galactic Halos Due to Baryonic Infall," *Astrophys. J.* **301** (1986) 27.

[636] O. Y. Gnedin and J. R. Primack, "Dark Matter Profile in the Galactic Center," *Phys. Rev. Lett.* **93** (2004) 061302, arXiv:astro-ph/0308385.

[637] A. M. Brown, T. Lacroix, S. Lloyd, C. Bœhm, and P. Chadwick, "Understanding the γ-ray emission from the globular cluster 47 Tuc: evidence for dark matter?," *Phys. Rev. D* **98** (2018) no. 4, 041301, arXiv:1806.01866 [astro-ph.HE].

[638] P. Amaro-Seoane, J. Casanellas, R. Schödel, E. Davidson, and J. Cuadra, "Probing dark matter crests with white dwarfs and IMBHs," *Mon. Not. Roy. Astron. Soc.* **459** (2016) no. 1, 695–700, arXiv:1512.00456 [astro-ph.CO].

[639] C. Knigge, D. R. Zurek, M. M. Shara, and K. S. Long, "A Far-Ultraviolet Survey of 47 Tucanae. I. Imaging," *The Astrophysical Journal* **579** (Nov., 2002) 752–759, arXiv:astro-ph/0207060 [astro-ph].

[640] R. L. Gilliland, T. M. Brown, P. Guhathakurta, A. Sarajedini, E. F. Milone, M. D. Albrow, N. R. Baliber, H. Bruntt, A. Burrows, D. Charbonneau, P. Choi, W. D. Cochran, P. D. Edmonds, S. Frandsen, J. H. Howell, D. N. C. Lin, G. W. Marcy, M. Mayor, D. Naef, S. Sigurdsson, C. R. Stagg, D. A. Vandenberg, S. S. Vogt, and M. D. Williams, "A Lack of Planets in 47 Tucanae from a Hubble Space Telescope Search," *The Astrophysical Journal Letters* **545** (Dec., 2000) L47–L51.

[641] T. Bringmann and M. Pospelov, "Novel direct detection constraints on light dark matter," *Phys. Rev. Lett.* **122** (2019) no. 17, 171801, arXiv:1810.10543 [hep-ph].

[642] **SuperCDMS** Collaboration, I. Alkhatib *et al.*, "Light Dark Matter Search with a High-Resolution Athermal Phonon Detector Operated Above Ground," arXiv:2007.14289 [hep-ex].

[643] M. A. Abramowicz, J. K. Becker, P. L. Biermann, A. Garzilli, F. Johansson, and L. Qian, "No Observational Constraints from Hypothetical Collisions of Hypothetical Dark Halo Primordial Black Holes with Galactic Objects," *The Astrophysical Journal* **705** (Nov., 2009) 659–669, arXiv:0810.3140 [astro-ph].

[644] M. Kesden and S. Hanasoge, "Transient solar oscillations driven by primordial black holes," *Phys. Rev. Lett.* **107** (2011) 111101, arXiv:1106.0011 [astro-ph.CO].

[645] P. W. Graham, R. Janish, V. Narayan, S. Rajendran, and P. Riggins, "White Dwarfs as Dark Matter Detectors," *Phys. Rev. D* **98** (2018) no. 11, 115027, arXiv:1805.07381 [hep-ph].

[646] J. Singh Sidhu and G. D. Starkman, "Reconsidering astrophysical constraints on macroscopic dark matter," *Phys. Rev. D* **101** (2020) no. 8, 083503, arXiv:1912.04053 [astro-ph.CO].

[647] G. H. Jones, M. M. Knight, K. Battams, D. C. Boice, J. Brown, S. Giordano, J. Raymond, C. Snodgrass, J. K. Steckloff, P. Weissman, *et al.*, "The science of sungrazers, sunskirters, and other near-sun comets," *Space Science Reviews* **214** (2018) no. 1, 20.

[648] P. J. Francis, "The Demographics of Long-Period Comets," *The Astrophysical Journal* **635** (Dec., 2005) 1348–1361, arXiv:astro-ph/0509074 [astro-ph].

[649] N. Brosch, V. Balabanov, and E. Behar, "Small observatories for the UV," *Astrophysics and Space Science* **354** (Nov., 2014) 205–209.

[650] J. Mathew, S. Ambily, A. Prakash, M. Sarpotdar, K. Nirmal, A. G. Sreejith, M. Safonova, J. Murthy, and N. Brosch, "Wide-field ultraviolet imager for astronomical transient studies," *Experimental Astronomy* **45** (Apr., 2018) 201–218, arXiv:1801.10405 [astro-ph.IM].

[651] S. Serjeant, M. Elvis, and G. Tinetti, "The future of astronomy with small satellites," *Nature Astronomy* **4** (Nov., 2020) 1031–1038, arXiv:2011.03478 [astro-ph.IM].

[652] M. N. Plooster, "Shock waves from line sources. numerical solutions and experimental measurements," *The physics of fluids* **13** (1970) no. 11, 2665–2675.

[653] K. Zahnle and M.-M. Mac Low, "The collision of jupiter and comet shoemaker-levy 9," *Icarus* **108** (1994) no. 1, 1–17.

[654] A. Anic, Y. Alibert, and W. Benz, "Giant collisions involving young jupiter," *Astronomy & Astrophysics* **466** (2007) no. 2, 717–728.

[655] H. Baumgardt, M. Hilker, A. Sollima, and A. Bellini, "Mean proper motions, space orbits, and velocity dispersion profiles of Galactic globular clusters derived from Gaia DR2 data," *MNRAS* **482** (Feb., 2019) 5138–5155, arXiv:1811.01507 [astro-ph.GA].

[656] I. King, "The structure of star clusters. I. an empirical density law," *The Astronomical Journal* **67** (Oct., 1962) 471.

[657] F. Campos, P. Bergeron, A. D. Romero, S. O. Kepler, G. Ourique, J. E. S. Costa, C. J. Bonatto, D. E. Winget, M. H. Montgomery, T. A. Pacheco, and L. R. Bedin, "A comparative analysis of the observed white dwarf cooling sequence from globular clusters," *MNRAS* **456** (Mar., 2016) 3729–3742, arXiv:1512.03114 [astro-ph.SR].

[658] K. Brogaard, D. A. VandenBerg, L. R. Bedin, A. P. Milone, A. Thygesen, and F. Grundahl, "The age of 47 Tuc from self-consistent isochrone fits to colour-magnitude diagrams and the eclipsing member V69," *MNRAS* **468** (June, 2017) 645–661, arXiv:1702.03421 [astro-ph.SR].

[659] N. Aghanim, Y. Akrami, M. Ashdown, J. Aumont, C. Baccigalupi, M. Ballardini, A. J. Banday, R. B. Barreiro, N. Bartolo, and et al., "Planck 2018 results," *Astronomy & Astrophysics* **641** (Sep, 2020) A6. http://dx.doi.org/10.1051/0004-6361/201833910.

[660] A. D. Ludlow, S. Bose, R. E. Angulo, L. Wang, W. A. Hellwing, J. F. Navarro, S. Cole, and C. S. Frenk, "The mass-concentration-redshift relation of cold and warm dark matter haloes," *MNRAS* **460** (Aug., 2016) 1214–1232, arXiv:1601.02624 [astro-ph.CO].

[661] B. Diemer and M. Joyce, "An Accurate Physical Model for Halo Concentrations," *The Astrophysical Journal* **871** (Feb., 2019) 168, arXiv:1809.07326 [astro-ph.CO].

[662] J. Wang, S. Bose, C. S. Frenk, L. Gao, A. Jenkins, V. Springel, and S. D. M. White, "Universal structure of dark matter haloes over a mass range of 20 orders of magnitude," *Nature* **585** (Sept., 2020) 39–42, arXiv:1911.09720 [astro-ph.CO].

[663] L. Spitzer, *Dynamical evolution of globular clusters*. 1987.

[664] E. Mamajek, "Number densities of stars of different types in the solar vicinity." http://www.pas.rochester.edu/~emamajek/memo_star_dens.html, 2021. Accessed: 2021-05-14.

[665] E. Waxman, "Ultrasat: A wide-field uv space telescope." https://www.weizmann.ac.il/ultrasat/sites/ultrasat/files/uploads/1_Eli_2020%2006%20ULTRASAT%2015%20%2B%205.pdf, 2020. Accessed: 2021-05-14.

[666] R. A. Windhorst, S. H. Cohen, N. P. Hathi, P. J. McCarthy, J. Ryan, Russell E., H. Yan, I. K. Baldry, S. P. Driver, J. A. Frogel, D. T. Hill, L. S. Kelvin, A. M. Koekemoer, M. Mechtley, R. W. O'Connell, A. S. G. Robotham, M. J. Rutkowski, M. Seibert, A. N. Straughn, R. J. Tuffs, B. Balick, H. E. Bond, H. Bushouse, D. Calzetti, M. Crockett, M. J. Disney, M. A. Dopita, D. N. B. Hall, J. A. Holtzman, S. Kaviraj, R. A. Kimble, J. W. MacKenty,

M. Mutchler, F. Paresce, A. Saha, J. I. Silk, J. T. Trauger, A. R. Walker, B. C. Whitmore, and E. T. Young, "The Hubble Space Telescope Wide Field Camera 3 Early Release Science Data: Panchromatic Faint Object Counts for 0.2-2 μm Wavelength," *The Astrophysical Journal Supplement* **193** (Apr., 2011) 27, arXiv:1005.2776 [astro-ph.CO].

[667] C. Boehm and P. Fayet, "Scalar dark matter candidates," *Nucl. Phys. B* **683** (2004) 219–263, arXiv:hep-ph/0305261.

[668] P. Fayet, "Light spin 1/2 or spin 0 dark matter particles," *Phys. Rev. D* **70** (2004) 023514, arXiv:hep-ph/0403226.

[669] J. F. Gunion, D. Hooper, and B. McElrath, "Light neutralino dark matter in the NMSSM," *Phys. Rev. D* **73** (2006) 015011, arXiv:hep-ph/0509024.

[670] H. K. Dreiner, S. Grab, D. Koschade, M. Kramer, B. O'Leary, and U. Langenfeld, "Rare meson decays into very light neutralinos," *Phys. Rev. D* **80** (2009) 035018, arXiv:0905.2051 [hep-ph].

[671] A. Badin and A. A. Petrov, "Searching for light dark matter in heavy meson decays," *Phys. Rev. D* **82** (2010) 034005, arXiv:1005.1277 [hep-ph].

[672] J. F. Kamenik and C. Smith, "FCNC portals to the dark sector," *JHEP* **03** (2012) 090, arXiv:1111.6402 [hep-ph].

[673] P. Fayet, "Constraints on light dark matter and U bosons, from ψ, Υ, K^+, π^0, η and η' decays," *Phys. Rev. D* **74** (2006) 054034, arXiv:hep-ph/0607318.

[674] B. McElrath, "Invisible quarkonium decays as a sensitive probe of dark matter," *Phys. Rev. D* **72** (2005) 103508, arXiv:hep-ph/0506151.

[675] P. Fayet, "U-boson production in e^+e^- annihilations, ψ and Υ decays, and light dark matter," *Phys. Rev. D* **75** (2007) 115017, arXiv:hep-ph/0702176.

[676] D. McKeen, "WIMPless Dark Matter and Meson Decays with Missing Energy," *Phys. Rev. D* **79** (2009) 114001, arXiv:0903.4982 [hep-ph].

[677] G. K. Yeghiyan, "Upsilon Decays into Light Scalar Dark Matter," *Phys. Rev. D* **80** (2009) 115019, arXiv:0909.4919 [hep-ph].

[678] L. Darmé, S. A. R. Ellis, and T. You, "Light Dark Sectors through the Fermion Portal," *JHEP* **07** (2020) 053, arXiv:2001.01490 [hep-ph].

[679] E. Bertuzzo and M. Taoso, "Probing light dark scalars with future experiments," *JHEP* **03** (2021) 272, arXiv:2011.04735 [hep-ph].

[680] N. Fernandez, J. Kumar, I. Seong, and P. Stengel, "Complementary Constraints on Light Dark Matter from Heavy Quarkonium Decays," *Phys. Rev. D* **90** (2014) no. 1, 015029, arXiv:1404.6599 [hep-ph].

[681] N. Fernandez, I. Seong, and P. Stengel, "Constraints on Light Dark Matter from Single-Photon Decays of Heavy Quarkonium," *Phys. Rev. D* **93** (2016) no. 5, 054023, arXiv:1511.03728 [hep-ph].

[682] D. E. Hazard and A. A. Petrov, "Lepton flavor violating quarkonium decays," *Phys. Rev. D* **94** (2016) no. 7, 074023, arXiv:1607.00815 [hep-ph].

[683] E. Bertuzzo, C. J. Caniu Barros, and G. Grilli di Cortona, "MeV Dark Matter: Model Independent Bounds," *JHEP* **09** (2017) 116, arXiv:1707.00725 [hep-ph].

[684] T. Li, X.-D. Ma, M. A. Schmidt, and R.-J. Zhang, "Implication of J/$\psi\to(\gamma+)$invisible for the effective field theories of neutrino and dark matter," *Phys. Rev. D* **104** (2021) no. 3, 035024, arXiv:2104.01780 [hep-ph].

[685] **BESIII** Collaboration, M. Ablikim *et al.*, "Search for invisible decays of ω and ϕ with J/ψ data at BESIII," *Phys. Rev. D* **98** (2018) no. 3, 032001, arXiv:1805.05613 [hep-ex].

[686] **BESIII** Collaboration, M. Ablikim *et al.*, "Search for η and η' invisible decays in J/$\psi\to\phi\eta$ and $\phi\eta$'," *Phys. Rev. D* **87** (2013) no. 1, 012009, arXiv:1209.2469 [hep-ex].

[687] **BaBar** Collaboration, J. P. Lees *et al.*, "Search for $B \to K^{(*)}\nu\overline{\nu}$ and invisible quarkonium decays," *Phys. Rev. D* **87** (2013) no. 11, 112005, arXiv:1303.7465 [hep-ex].

[688] **BaBar** Collaboration, B. Aubert *et al.*, "A Search for Invisible Decays of the Upsilon(1S)," *Phys. Rev. Lett.* **103** (2009) 251801, arXiv:0908.2840 [hep-ex].

[689] **NA62** Collaboration, E. Cortina Gil *et al.*, "Search for π^0 decays to invisible particles," *JHEP* **02** (2021) 201, arXiv:2010.07644 [hep-ex].

[690] L. N. Chang, O. Lebedev, and J. N. Ng, "On the invisible decays of the Υ and J/Ψ resonances," *Phys. Lett. B* **441** (1998) 419–424, arXiv:hep-ph/9806487.

[691] **BESIII** Collaboration, M. Ablikim *et al.*, "Search for the decay $J/\psi \to \gamma +$ invisible," *Phys. Rev. D* **101** (2020) no. 11, 112005, arXiv:2003.05594 [hep-ex].

[692] D.-N. Gao, "Analysis of $J/\psi(\eta_c) \to \gamma +$ invisible decays in the standard model," *Phys. Rev. D* **90** (2014) no. 7, 077501, arXiv:1408.4552 [hep-ph].

[693] **BaBar** Collaboration, P. del Amo Sanchez *et al.*, "Search for Production of Invisible Final States in Single-Photon Decays of $\Upsilon(1S)$," *Phys. Rev. Lett.* **107** (2011) 021804, arXiv:1007.4646 [hep-ex].

[694] L. Arnellos, W. J. Marciano, and Z. Parsa, "The Decay $\pi^0 \to \nu\bar{\nu}\gamma$," *Nucl. Phys. B* **196** (1982) 365–377.

[695] **Crystal Barrel** Collaboration, C. Amsler *et al.*, "Search for a new light gauge boson in decays of π^0 and η," *Phys. Lett. B* **333** (1994) 271–276.

[696] S. Andreas *et al.*, "Proposal for an Experiment to Search for Light Dark Matter at the SPS," arXiv:1312.3309 [hep-ex].

[697] **NA64, Physics Beyond Collider Conventional Beams working group** Collaboration, J. Bernhard, "Status and Plans for the NA64 Experiment," *J. Phys. Conf. Ser.* **1468** (2020) no. 1, 012023.

[698] **LDMX** Collaboration, T. Åkesson *et al.*, "Light Dark Matter eXperiment (LDMX)," arXiv:1808.05219 [hep-ex].

[699] **LDMX** Collaboration, T. Åkesson *et al.*, "A High Efficiency Photon Veto for the Light Dark Matter eXperiment," *JHEP* **04** (2020) 003, arXiv:1912.05535 [physics.ins-det].

[700] L. B. Okun, "Limits of electrodynamics: paraphotons?," *Sov. Phys. JETP* **56** (1982) 502.

[701] B. Holdom, "Two U(1)'s and ϵ Charge Shifts," *Phys. Lett. B* **166** (1986) 196–198.

[702] C. D. Carone and H. Murayama, "Possible light U(1) gauge boson coupled to baryon number," *Phys. Rev. Lett.* **74** (1995) 3122–3125, arXiv:hep-ph/9411256.

[703] C. D. Carone and H. Murayama, "Realistic models with a light U(1) gauge boson coupled to baryon number," *Phys. Rev. D* **52** (1995) 484–493, arXiv:hep-ph/9501220.

[704] P. Fileviez Perez and M. B. Wise, "Baryon and lepton number as local gauge symmetries," *Phys. Rev. D* **82** (2010) 011901, arXiv:1002.1754 [hep-ph]. [Erratum: Phys.Rev.D 82, 079901 (2010)].

[705] M. L. Graesser, I. M. Shoemaker, and L. Vecchi, "A Dark Force for Baryons," arXiv:1107.2666 [hep-ph].

[706] R. Essig *et al.*, "Working Group Report: New Light Weakly Coupled Particles," in *Community Summer Study 2013: Snowmass on the Mississippi*. 10, 2013. arXiv:1311.0029 [hep-ph].

[707] J. Alexander *et al.*, "Dark Sectors 2016 Workshop: Community Report," 8, 2016. arXiv:1608.08632 [hep-ph].

[708] M. Fabbrichesi, E. Gabrielli, and G. Lanfranchi, "The Dark Photon," arXiv:2005.01515 [hep-ph].

[709] A. Filippi and M. De Napoli, "Searching in the dark: the hunt for the dark photon," *Rev. Phys.* **5** (2020) 100042, arXiv:2006.04640 [hep-ph].

[710] S. N. Gninenko, "Search for invisible decays of π^0, η, η', K_S and K_L: A probe of new physics and tests using the Bell-Steinberger relation," *Phys. Rev. D* **91** (2015) no. 1, 015004, arXiv:1409.2288 [hep-ph].

[711] J. D. Bjorken, R. Essig, P. Schuster, and N. Toro, "New Fixed-Target Experiments to Search for Dark Gauge Forces," *Phys. Rev. D* **80** (2009) 075018, arXiv:0906.0580 [hep-ph].

[712] B. Batell, M. Pospelov, and A. Ritz, "Exploring Portals to a Hidden Sector Through Fixed Targets," *Phys. Rev. D* **80** (2009) 095024, arXiv:0906.5614 [hep-ph].

[713] M. Reece and L.-T. Wang, "Searching for the light dark gauge boson in GeV-scale experiments," *JHEP* **07** (2009) 051, arXiv:0904.1743 [hep-ph].

[714] S. N. Gninenko, N. V. Krasnikov, M. M. Kirsanov, and D. V. Kirpichnikov, "Missing energy signature from invisible decays of dark photons at the CERN SPS," *Phys. Rev. D* **94** (2016) no. 9, 095025, arXiv:1604.08432 [hep-ph].

[715] E. Izaguirre, G. Krnjaic, P. Schuster, and N. Toro, "Testing GeV-Scale Dark Matter with Fixed-Target Missing Momentum Experiments," *Phys. Rev. D* **91** (2015) no. 9, 094026, arXiv:1411.1404 [hep-ph].

[716] Y.-S. Tsai and V. Whitis, "Thick-Target Bremsstrahlung and Target Considerations for Secondary-Particle Production by Electrons," *Phys. Rev.* **149** (1966) 1248–1257.

[717] **MiniBooNE** Collaboration, A. A. Aguilar-Arevalo *et al.*, "The Neutrino Flux prediction at MiniBooNE," *Phys. Rev. D* **79** (2009) 072002, arXiv:0806.1449 [hep-ex].

[718] A. Berlin, S. Gori, P. Schuster, and N. Toro, "Dark Sectors at the Fermilab SeaQuest Experiment," *Phys. Rev. D* **98** (2018) no. 3, 035011, arXiv:1804.00661 [hep-ph].

[719] B. Döbrich, J. Jaeckel, and T. Spadaro, "Light in the beam dump - ALP production from decay photons in proton beam-dumps," *JHEP* **05** (2019) 213, arXiv:1904.02091 [hep-ph]. [Erratum: JHEP 10, 046 (2020)].

[720] J. Allison *et al.*, "Recent developments in Geant4," *Nucl. Instrum. Meth. A* **835** (2016) 186–225.

[721] T. Sjöstrand, S. Ask, J. R. Christiansen, R. Corke, N. Desai, P. Ilten, S. Mrenna, S. Prestel, C. O. Rasmussen, and P. Z. Skands, "An introduction to PYTHIA 8.2," *Comput. Phys. Commun.* **191** (2015) 159–177, arXiv:1410.3012 [hep-ph].

[722] D. H. Wright and M. H. Kelsey, "The Geant4 Bertini Cascade," *Nucl. Instrum. Meth. A* **804** (2015) 175–188.

[723] O. Buss, T. Gaitanos, K. Gallmeister, H. van Hees, M. Kaskulov, O. Lalakulich, A. B. Larionov, T. Leitner, J. Weil, and U. Mosel, "Transport-theoretical Description of Nuclear Reactions," *Phys. Rept.* **512** (2012) 1–124, arXiv:1106.1344 [hep-ph].

[724] **LDMX** Collaboration, "LDMX simulation and reconstruction framework." https://github.com/LDMX-Software/ldmx-sw/blob/trunk/Detectors/data/ldmx-det-v12/ecal.gdml, 2021. Accessed: 2021-10-31.

[725] J. M. Laget, "Photoproduction of vector mesons at large momentum transfer," *Phys. Lett. B* **489** (2000) 313–318, arXiv:hep-ph/0003213.

[726] **H1** Collaboration, C. Adloff *et al.*, "Elastic photoproduction of J/ψ and Υ mesons at HERA," *Phys. Lett. B* **483** (2000) 23–35, arXiv:hep-ex/0003020.

[727] V. Guzey, M. Strikman, and M. Zhalov, "Disentangling coherent and incoherent quasielastic J/ψ photoproduction on nuclei by neutron tagging in ultraperipheral ion collisions at the LHC," *Eur. Phys. J. C* **74** (2014) no. 7, 2942, arXiv:1312.6486 [hep-ph].

[728] J. Hufner and B. Z. Kopeliovich, "$J/\Psi N$ and $\Psi' N$ total cross sections from photoproduction data: failure of vector dominance," *Phys. Lett. B* **426** (1998) 154–160, arXiv:hep-ph/9712297.

[729] **BESIII** Collaboration, M. Ablikim *et al.*, "Future Physics Programme of BESIII," *Chin. Phys. C* **44** (2020) no. 4, 040001, arXiv:1912.05983 [hep-ex].

[730] A. Bharucha, D. M. Straub, and R. Zwicky, "$B \to V\ell^+\ell^-$ in the Standard Model from light-cone sum rules," *JHEP* **08** (2016) 098, arXiv:1503.05534 [hep-ph].

[731] F. Wilczek, "Decays of Heavy Vector Mesons Into Higgs Particles," *Phys. Rev. Lett.* **39** (1977) 1304.

[732] V. Mathieu, G. Fox, and A. P. Szczepaniak, "Neutral Pion Photoproduction in a Regge Model," *Phys. Rev. D* **92** (2015) no. 7, 074013, arXiv:1505.02321 [hep-ph].

[733] **JPAC** Collaboration, J. Nys, V. Mathieu, C. Fernández-Ramírez, A. N. Hiller Blin, A. Jackura, M. Mikhasenko, A. Pilloni, A. P. Szczepaniak, G. Fox, and J. Ryckebusch, "Finite-energy sum rules in eta photoproduction off a nucleon," *Phys. Rev. D* **95** (2017) no. 3, 034014, arXiv:1611.04658 [hep-ph].

[734] **CB-ELSA** Collaboration, I. Horn *et al.*, "Study of the reaction $\gamma p \to p\pi^0\eta$," *Eur. Phys. J. A* **38** (2008) 173–186, arXiv:0806.4251 [nucl-ex].

[735] **CLAS** Collaboration, M. Battaglieri *et al.*, "Measurement of Direct $f_0(980)$ Photoproduction on the Proton," *Phys. Rev. Lett.* **102** (2009) 102001, arXiv:0811.1681 [hep-ex].

[736] S.-s. Fang, A. Kupsc, and D.-h. Wei, "An overview of η and η' decays at BESIII," *Chin. Phys. C* **42** (2018) no. 4, 042002, arXiv:1710.05173 [hep-ex].

[737] **KLOE-2** Collaboration, X. Kang, "Study of η-meson Decays at KLOE/KLOE-2," *J. Phys. Conf. Ser.* **1586** (2020) no. 1, 012035, arXiv:1904.12034 [hep-ex].

[738] L. Gan, B. Kubis, E. Passemar, and S. Tulin, "Precision tests of fundamental physics with η and η' mesons," arXiv:2007.00664 [hep-ph].

[739] L. Gan *et al.*, "Eta Decays with Emphasis on Rare Neutral Modes: The JLab Eta Factory (JEF) Experiment." https://www.jlab.org/exp_prog/proposals/14/PR12-14-004.pdf, 2014.

[740] **REDTOP** Collaboration, C. Gatto, "The REDTOP experiment," arXiv:1910.08505 [physics.ins-det].

[741] G. Krnjaic, "Probing light thermal dark matter with a Higgs portal mediator," *Phys. Rev. D* **94** (2016) no. 7, 073009, arXiv:1512.04119 [hep-ph].

[742] B. Batell, A. Freitas, A. Ismail, and D. Mckeen, "Flavor-specific scalar mediators," *Phys. Rev. D* **98** (2018) no. 5, 055026, arXiv:1712.10022 [hep-ph].

[743] B. Batell, A. Freitas, A. Ismail, and D. Mckeen, "Probing light dark matter with a hadrophilic scalar mediator," *Phys. Rev. D* **100** (2019) no. 9, 095020, arXiv:1812.05103 [hep-ph].

[744] B. Batell, A. Freitas, A. Ismail, D. McKeen, and M. Rai, "Renormalizable Models of Flavor-Specific Scalars," arXiv:2107.08059 [hep-ph].

[745] Y. Kahn, G. Krnjaic, S. Mishra-Sharma, and T. M. P. Tait, "Light Weakly Coupled Axial Forces: Models, Constraints, and Projections," *JHEP* **05** (2017) 002, arXiv:1609.09072 [hep-ph].

[746] M. J. Dolan, F. Kahlhoefer, C. McCabe, and K. Schmidt-Hoberg, "A taste of dark matter: Flavour constraints on pseudoscalar mediators," *JHEP* **03** (2015) 171, arXiv:1412.5174 [hep-ph]. [Erratum: JHEP 07, 103 (2015)].

[747] S. N. Gninenko and N. V. Krasnikov, "Invisible K_L decays as a probe of new physics," *Phys. Rev. D* **92** (2015) no. 3, 034009, arXiv:1503.01595 [hep-ph].

[748] D. Barducci, M. Fabbrichesi, and E. Gabrielli, "Neutral Hadrons Disappearing into the Darkness," *Phys. Rev. D* **98** (2018) no. 3, 035049, arXiv:1806.05678 [hep-ph].

[749] A. Abada, D. Bečirević, O. Sumensari, C. Weiland, and R. Zukanovich Funchal, "Sterile neutrinos facing kaon physics experiments," *Phys. Rev. D* **95** (2017) no. 7, 075023, arXiv:1612.04737 [hep-ph].

[750] J. Heeck, "Light particles with baryon and lepton numbers," *Phys. Lett. B* **813** (2021) 136043, arXiv:2009.01256 [hep-ph].

[751] G. Alonso-Álvarez, G. Elor, M. Escudero, B. Fornal, and B. Grinstein, "The Strange Physics of Dark Baryons," arXiv:2111.12712 [hep-ph].

[752] S. Tulin, "New weakly-coupled forces hidden in low-energy QCD," *Phys. Rev. D* **89** (2014) no. 11, 114008, arXiv:1404.4370 [hep-ph].

[753] B. A. Dobrescu and C. Frugiuele, "Hidden GeV-scale interactions of quarks," *Phys. Rev. Lett.* **113** (2014) 061801, arXiv:1404.3947 [hep-ph].

[754] P. Ilten, Y. Soreq, M. Williams, and W. Xue, "Serendipity in dark photon searches," *JHEP* **06** (2018) 004, arXiv:1801.04847 [hep-ph].

[755] M. Bauer, P. Foldenauer, and J. Jaeckel, "Hunting All the Hidden Photons," *JHEP* **07** (2018) 094, arXiv:1803.05466 [hep-ph].

[756] F. Kling, "Probing light gauge bosons in tau neutrino experiments," *Phys. Rev. D* **102** (2020) no. 1, 015007, arXiv:2005.03594 [hep-ph].

[757] J. Heeck, M. Lindner, W. Rodejohann, and S. Vogl, "Non-Standard Neutrino Interactions and Neutral Gauge Bosons," *SciPost Phys.* **6** (2019) no. 3, 038, arXiv:1812.04067 [hep-ph].

[758] T. Han, J. Liao, H. Liu, and D. Marfatia, "Nonstandard neutrino interactions at COHERENT, DUNE, T2HK and LHC," *JHEP* **11** (2019) 028, arXiv:1910.03272 [hep-ph].

[759] T. Li, X.-D. Ma, and M. A. Schmidt, "General neutrino interactions with sterile neutrinos in light of coherent neutrino-nucleus scattering and meson invisible decays," *JHEP* **07** (2020) 152, arXiv:2005.01543 [hep-ph].

[760] K. Asai, S. Iwamoto, Y. Sakaki, and D. Ueda, "New physics searches at the ILC positron and electron beam dumps," arXiv:2105.13768 [hep-ph].

[761] T. H. Bauer, R. D. Spital, D. R. Yennie, and F. M. Pipkin, "The Hadronic Properties of the Photon in High-Energy Interactions," *Rev. Mod. Phys.* **50** (1978) 261. [Erratum: Rev.Mod.Phys. 51, 407 (1979)].

[762] K. S. Kolbig and B. Margolis, "Particle production in nuclei and unstable particle cross-sections," *Nucl. Phys. B* **6** (1968) 85–101.

[763] **CLAS** Collaboration, M. Battaglieri *et al.*, "Photoproduction of the ρ^0 Meson on the Proton at Large Momentum Transfer," *Phys. Rev. Lett.* **87** (2001) 172002, arXiv:hep-ex/0107028.

[764] **CLAS** Collaboration, M. Battaglieri *et al.*, "Photoproduction of the ω Meson on the Proton at Large Momentum Transfer," *Phys. Rev. Lett.* **90** (2003) 022002, arXiv:hep-ex/0210023.

[765] **CLAS** Collaboration, H. Seraydaryan *et al.*, "ϕ-meson photoproduction on hydrogen in the neutral decay mode," *Phys. Rev. C* **89** (2014) no. 5, 055206, arXiv:1308.1363 [hep-ex].

[766] **CLAS** Collaboration, B. Dey, C. A. Meyer, M. Bellis, and M. Williams, "Data analysis techniques, differential cross sections, and spin density matrix elements for the reaction $\gamma p \to \phi p$," *Phys. Rev. C* **89** (2014) no. 5, 055208, arXiv:1403.2110 [nucl-ex]. [Addendum: Phys.Rev.C 90, 019901 (2014)].

[767] E. Chudakov, S. Gevorkyan, and A. Somov, "Photoproduction of ω mesons off nuclei and impact of polarization on the meson-nucleon interaction," *Phys. Rev. C* **93** (2016) no. 1, 015203, arXiv:1508.00422 [hep-ph].

[768] T. Ishikawa *et al.*, "ϕ photo-production from Li, C, Al, and Cu nuclei at $E_\gamma = 1.5$–2.4 GeV," *Phys. Lett. B* **608** (2005) 215–222, arXiv:nucl-ex/0411016.

[769] **CLAS** Collaboration, M. H. Wood *et al.*, "Absorption of the ω and ϕ Mesons in Nuclei," *Phys. Rev. Lett.* **105** (2010) 112301, arXiv:1006.3361 [nucl-ex].

[770] A. Sibirtsev, H.-W. Hammer, U.-G. Meissner, and A. W. Thomas, "ϕ-meson photoproduction from nuclei," *Eur. Phys. J. A* **29** (2006) 209–220, arXiv:nucl-th/0606044.

[771] E. P. Wigner, "On Unitary Representations of the Inhomogeneous Lorentz Group," *Annals of Mathematics* **40** (1939) 149–204.

[772] S. Weinberg, "Feynman Rules for Any Spin. II. Massless Particles," *Phys. Rev.* **134** (1964) B882–B896.

[773] S. Weinberg, "Photons and Gravitons in S-Matrix Theory: Derivation of Charge Conservation and Equality of Gravitational and Inertial Mass," *Phys. Rev.* **135** (1964) B1049–B1056.

[774] S. Weinberg, "Photons and Gravitons in Perturbation Theory: Derivation of Maxwell's and Einstein's Equations," *Phys. Rev.* **138** (1965) B988–B1002.

[775] S. Weinberg and E. Witten, "Limits on massless particles," *Phys. Lett. B* **96** (1980) 59–62.

[776] F. A. Berends, G. J. H. Burgers, and H. van Dam, "On the theoretical problems in constructing interactions involving higher-spin massless particles," *Nucl. Phys. B* **260** (1985) 295–322.

[777] F. A. Berends, G. J. H. Burgers, and H. Van Dam, "On spin three self interactions," *Z. Phys. C* **24** (1984) 247–254.

[778] X. Bekaert, N. Boulanger, and S. Leclercq, "Strong obstruction of the Berends–Burgers–van Dam spin-3 vertex," *J. Phys. A* **43** (2010) 185401, arXiv:1002.0289 [hep-th].

[779] P. Schuster and N. Toro, "On the theory of continuous-spin particles: wavefunctions and soft-factor scattering amplitudes," *JHEP* **09** (2013) 104, arXiv:1302.1198 [hep-th].

[780] P. Schuster and N. Toro, "On the theory of continuous-spin particles: helicity correspondence in radiation and forces," *JHEP* **09** (2013) 105, arXiv:1302.1577 [hep-th].

[781] P. Schuster and N. Toro, "Continuous-spin particle field theory with helicity correspondence," *Phys. Rev. D* **91** (2015) 025023, arXiv:1404.0675 [hep-th].

[782] V. O. Rivelles, "Gauge theory formulations for continuous and higher spin fields," *Phys. Rev. D* **91** (2015) no. 12, 125035, arXiv:1408.3576 [hep-th].

[783] V. O. Rivelles, "Remarks on a gauge theory for continuous spin particles," *Eur. Phys. J. C* **77** (2017) no. 7, 433, arXiv:1607.01316 [hep-th].

[784] X. Bekaert and E. D. Skvortsov, "Elementary particles with continuous spin," *Int. J. Mod. Phys. A* **32** (2017) no. 23n24, 1730019, arXiv:1708.01030 [hep-th].

[785] M. Najafizadeh, "Modified Wigner equations and continuous spin gauge field," *Phys. Rev. D* **97** (2018) no. 6, 065009, arXiv:1708.00827 [hep-th].

[786] P. Schuster and N. Toro, "A new class of particle in 2 + 1 dimensions," *Phys. Lett. B* **743** (2015) 224–227, arXiv:1404.1076 [hep-th].

[787] X. Bekaert, M. Najafizadeh, and M. R. Setare, "A gauge field theory of fermionic continuous-spin particles," *Phys. Lett. B* **760** (2016) 320–323, arXiv:1506.00973 [hep-th].

[788] M. Najafizadeh, "Supersymmetric continuous spin gauge theory," *JHEP* **03** (2020) 027, arXiv:1912.12310 [hep-th].

[789] M. Najafizadeh, "Off-shell supersymmetric continuous spin gauge theory," *JHEP* **02** (2022) 038, arXiv:2112.10178 [hep-th].

[790] R. R. Metsaev, "BRST-BV approach to continuous-spin field," *Phys. Lett. B* **781** (2018) 568–573, arXiv:1803.08421 [hep-th].

[791] I. L. Buchbinder, V. A. Krykhtin, and H. Takata, "BRST approach to Lagrangian construction for bosonic continuous spin field," *Phys. Lett. B* **785** (2018) 315–319, arXiv:1806.01640 [hep-th].

[792] K. Alkalaev, A. Chekmenev, and M. Grigoriev, "Unified formulation for helicity and continuous spin fermionic fields," *JHEP* **11** (2018) 050, arXiv:1808.09385 [hep-th].

[793] I. L. Buchbinder, S. Fedoruk, A. P. Isaev, and V. A. Krykhtin, "Towards Lagrangian construction for infinite half-integer spin field," *Nucl. Phys. B* **958** (2020) 115114, arXiv:2005.07085 [hep-th].

[794] I. L. Buchbinder, S. J. Gates, and K. Koutrolikos, "Superfield continuous spin equations of motion," *Phys. Lett. B* **793** (2019) 445–450, arXiv:1903.08631 [hep-th].

[795] I. L. Buchbinder, M. V. Khabarov, T. V. Snegirev, and Y. M. Zinoviev, "Lagrangian formulation for the infinite spin N=1 supermultiplets in d=4," *Nucl. Phys. B* **946** (2019) 114717, arXiv:1904.05580 [hep-th].

[796] I. L. Buchbinder, S. Fedoruk, and A. P. Isaev, "Massless infinite spin (super)particles and fields," *Proc. Steklov Inst. Math.* **309** (2020) 46–56, arXiv:1911.00362 [hep-th].

[797] I. L. Buchbinder, S. A. Fedoruk, A. P. Isaev, and V. A. Krykhtin, "On the off-shell superfield Lagrangian formulation of $4D$, N=1 supersymmetric infinite spin theory," *Phys. Lett. B* **829** (2022) 137139, arXiv:2203.12904 [hep-th].

[798] Y. M. Zinoviev, "Infinite spin fields in $d = 3$ and beyond," *Universe* **3** (2017) no. 3, 63, arXiv:1707.08832 [hep-th].

[799] K. B. Alkalaev and M. A. Grigoriev, "Continuous spin fields of mixed-symmetry type," *JHEP* **03** (2018) 030, arXiv:1712.02317 [hep-th].

[800] C. Burdík, V. K. Pandey, and A. Reshetnyak, "BRST–BFV and BRST–BV descriptions for bosonic fields with continuous spin on $R^{1,d-1}$," *Int. J. Mod. Phys. A* **35** (2020) no. 26, 2050154, arXiv:1906.02585 [hep-th].

[801] R. R. Metsaev, "Continuous spin gauge field in (A)dS space," *Phys. Lett. B* **767** (2017) 458–464, arXiv:1610.00657 [hep-th].

[802] R. R. Metsaev, "Fermionic continuous spin gauge field in (A)dS space," *Phys. Lett. B* **773** (2017) 135–141, arXiv:1703.05780 [hep-th].

[803] R. R. Metsaev, "Continuous-spin mixed-symmetry fields in AdS(5)," *J. Phys. A* **51** (2018) no. 21, 215401, arXiv:1711.11007 [hep-th].

[804] M. V. Khabarov and Y. M. Zinoviev, "Infinite (continuous) spin fields in the frame-like formalism," *Nucl. Phys. B* **928** (2018) 182–216, arXiv:1711.08223 [hep-th].

[805] R. R. Metsaev, "Light-cone continuous-spin field in AdS space," *Phys. Lett. B* **793** (2019) 134–140, arXiv:1903.10495 [hep-th].

[806] R. R. Metsaev, "Mixed-symmetry continuous-spin fields in flat and AdS spaces," *Phys. Lett. B* **820** (2021) 136497, arXiv:2105.11281 [hep-th].

[807] R. R. Metsaev, "Cubic interaction vertices for continuous-spin fields and arbitrary spin massive fields," *JHEP* **11** (2017) 197, arXiv:1709.08596 [hep-th].

[808] X. Bekaert, J. Mourad, and M. Najafizadeh, "Continuous-spin field propagator and interaction with matter," *JHEP* **11** (2017) 113, arXiv:1710.05788 [hep-th].

[809] R. R. Metsaev, "Cubic interaction vertices for massive/massless continuous-spin fields and arbitrary spin fields," *JHEP* **12** (2018) 055, arXiv:1809.09075 [hep-th].

[810] V. O. Rivelles, "A gauge field theory for continuous spin tachyons." 7, 2018.

[811] F. A. Berends, G. J. H. Burgers, and H. van Dam, "Explicit construction of conserved currents for massless fields of arbitrary spin," *Nucl. Phys. B* **271** (1986) 429–441.

[812] G. J. Iverson and G. Mack, "Theory of weak interactions with "continuous-spin" neutrinos," *Phys. Rev. D* **2** (Nov, 1970) 2326–2333. https://link.aps.org/doi/10.1103/PhysRevD.2.2326.

[813] J. Yngvason, "Zero-mass infinite spin representations of the Poincare group and quantum field theory," *Commun. Math. Phys.* **18** (1970) 195–203.

[814] G. Iverson and G. Mack, "Quantum fields and interactions of massless particles: the continuous spin case," *Annals of Physics* **64** (1971) 211–253.

[815] A. Chakrabarti, "Remarks on lightlike continuous spin and spacelike representations of the Poincare group," *J. Math. Phys.* **12** (1971) 1813–1822.

[816] L. F. Abbott, "Massless particles with continuous spin indices," *Phys. Rev. D* **13** (Apr, 1976) 2291–2294. https://link.aps.org/doi/10.1103/PhysRevD.13.2291.

[817] K. Hirata, "Quantization of Massless Fields with Continuous Spin," *Prog. Theor. Phys.* **58** (1977) 652–666.

[818] X. Bekaert, N. Boulanger, and P. Sundell, "How higher-spin gravity surpasses the spin two barrier: no-go theorems versus yes-go examples," *Rev. Mod. Phys.* **84** (2012) 987–1009, arXiv:1007.0435 [hep-th].

[819] A. M. Khan and P. Ramond, "Continuous spin representations from group contraction," *J. Math. Phys.* **46** (2005) 053515, arXiv:hep-th/0410107 [hep-th].

[820] L. P. S. Singh and C. R. Hagen, "Lagrangian formulation for arbitrary spin. I. The boson case," *Phys. Rev. D* **9** (1974) 898–909.

[821] L. P. S. Singh and C. R. Hagen, "Lagrangian formulation for arbitrary spin. II. The fermion case," *Phys. Rev. D* **9** (1974) 910–920.

[822] C. Fronsdal, "Massless fields with integer spin," *Phys. Rev. D* **18** (1978) 3624.

[823] J. Fang and C. Fronsdal, "Massless fields with half-integral spin," *Phys. Rev. D* **18** (1978) 3630.

[824] X. Bekaert and J. Mourad, "The continuous spin limit of higher spin field equations," *JHEP* **0601** (2006) 115, arXiv:hep-th/0509092 [hep-th].

[825] P. Schuster and N. Toro, "A gauge field theory of continuous-spin particles," *JHEP* **10** (2013) 061, arXiv:1302.3225 [hep-th].

[826] A. Nicolis, R. Rattazzi, and E. Trincherini, "Galileon as a local modification of gravity," *Phys. Rev. D* **79** (2009) 064036, arXiv:0811.2197 [hep-th].

[827] T. Ortín, *Gravity and Strings*. Cambridge University Press, 2004.

[828] M. Maggiore, *Gravitational waves: Volume 1: Theory and experiments*. OUP Oxford, 2007.

[829] B. de Wit and D. Z. Freedman, "Systematics of higher-spin gauge fields," *Phys. Rev. D* **21** (1980) 358.

[830] A. Y. Segal, "Point particle in general background fields and generalized equivalence principle," in *International Conference on Quantization, Gauge Theory, and Strings: Conference Dedicated to the Memory of Professor Efim Fradkin*, pp. 443–451. 8, 2000. arXiv:hep-th/0008105.

[831] A. Y. Segal, "Point particle in general background fields and free gauge theories of traceless symmetric tensors," *Int. J. Mod. Phys. A* **18** (2003) 4999–5021, arXiv:hep-th/0110056.

[832] M. J. Strassler, "Field theory without Feynman diagrams: One loop effective actions," *Nucl. Phys. B* **385** (1992) 145–184, arXiv:hep-ph/9205205.

[833] C. Schubert, "Perturbative quantum field theory in the string-inspired formalism," *Phys. Rept.* **355** (2001) 73–234, arXiv:hep-th/0101036.

[834] J. P. Edwards and C. Schubert, "Quantum mechanical path integrals in the first quantised approach to quantum field theory," 12, 2019. arXiv:1912.10004 [hep-th].

[835] R. P. Feynman, "Mathematical formulation of the quantum theory of electromagnetic interaction," *Phys. Rev.* **80** (Nov, 1950) 440–457. https://link.aps.org/doi/10.1103/PhysRev.80.440.

[836] A. Font, F. Quevedo, and S. Theisen, "A comment on continuous spin representations of the Poincare group and perturbative string theory," *Fortsch. Phys.* **62** (2014) 975–980, arXiv:1302.4771 [hep-th].

[837] E. Titchmarsh, *The Theory of Functions*. Oxford University Press, 1939.